

A Thesis Submitted for the Degree of PhD at the University of Warwick

Permanent WRAP URL:

<http://wrap.warwick.ac.uk/163388>

Copyright and reuse:

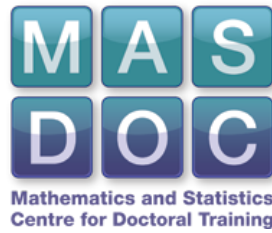
This thesis is made available online and is protected by original copyright.

Please scroll down to view the document itself.

Please refer to the repository record for this item for information to help you to cite it.

Our policy information is available from the repository home page.

For more information, please contact the WRAP Team at: wrap@warwick.ac.uk



Liquid Marble Formation: Development
of a Computational Model from
Experiments

by

Jesse Pritchard

Thesis

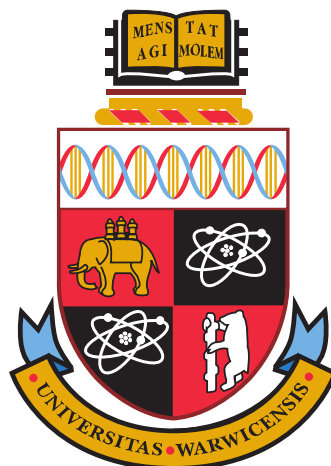
Submitted for the degree of

Doctor of Philosophy

Mathematics Institute

The University of Warwick

January 2021



Contents

List of Figures	xxxiv
List of Tables	xxxv
Acknowledgments	xxxvi
Declarations	xxxvii
List of Abbreviations	xxxviii
Abstract	xxxix
Chapter 1 Introduction	1
1.1 Liquid Marbles	2
1.1.1 Formation	3
1.1.2 Structure of the Shell	6
1.1.3 Properties	8
1.1.4 Applications	11
1.1.5 Deformed Liquid Marbles	17
1.1.6 Project Motivation	23
1.2 Drop Dynamics with a Particle-Laden Interface and Impacts onto Powder Beds	24
1.3 Surface Rheology and its Application to Dynamics of Particle-Laden Interfaces	26
1.4 Drop Impact onto Superhydrophobic Impermeable Rigid Substrates .	28
1.5 Organisation	29
Chapter 2 Experiments	33
2.1 Materials	34
2.2 Methods	35
2.2.1 Image Analysis	39

2.3	Results	42
2.3.1	Characteristic Impacts on Rigid Impermeable Superhydrophobic Substrates	43
2.3.2	Characteristic Impacts on Superhydrophobic Powder Beds	55
2.3.3	Comparison between Impacts on Rigid Impermeable Superhydrophobic Substrates and Superhydrophobic Powder Beds	65
2.3.4	Marble Formation as a Function of Maximum Spread	71
Chapter 3 Mathematical Models		80
3.1	Problem Formulation	81
3.1.1	Co-ordinate System	82
3.1.2	Qualitative Descriptions of the Dynamics	84
3.2	Development of a Mathematical Model for Liquid Marble Formation via Drop Impact	87
3.2.1	Liquid-Gas Surface Equations	88
3.2.2	Boundary Conditions at the Liquid-Solid Interface	91
3.2.3	Boundary Conditions for the Surface Equations	92
3.2.4	Inviscid Bulk Equations	93
3.2.5	Viscous Bulk Equations	106
3.3	Suspended Inviscid Drop Oscillations with Dilatational Surface Viscosity	109
3.3.1	Derivation of the Damped Nonlinear Oscillator	110
3.3.2	Critical Amplitude	115
3.3.3	Analytic Solution in the Overdamped Limit	116
Chapter 4 Boundary Integral Method and Boundary Element Method		117
4.1	Irrotational Bulk Drop Flow within the Inviscid Model	118
4.2	Formulation of the Boundary Integral Equation in Three Dimensions	119
4.2.1	Boundary Conditions	122
4.3	Application of the Boundary Integral Equation	122
4.3.1	Identifying the Boundary	123
4.3.2	Applied Boundary Conditions	123
4.3.3	Axisymmetry of the Boundary Integral Equation	123

4.4	Bernoulli Equation at the Drop Boundary	124
4.5	Numerical Method	125
4.5.1	Interpolation of Variables between Nodes	126
4.5.2	Discretising the Boundary Integral Equation	132
4.5.3	Discrete Time Evolution using a Runge-Kutta Scheme	134
4.5.4	Nodes Moving to and from the Solid Substrate	137
4.5.5	Adaptive Time Stepping	139
4.5.6	Mesh Redistribution	141
4.6	Numerical Validation	143
4.6.1	Free Surface Oscillations	144
4.6.2	Drop Impact	164
4.7	Shortcomings of using the Boundary Element Method and Inviscid Model for Drop Impact	170
4.7.1	Physically-Motivated Topological Changes	170
4.7.2	Unphysical Splashing due to the Inviscid Bulk Flow Assumption	179
4.8	Numerical Investigation of the Damped Nonlinear Oscillator Model .	182
4.8.1	Validation for Small Amplitude Oscillations	183
4.8.2	Large Amplitude Oscillations	193
Chapter 5 Volume-of-Fluid Method		204
5.1	The ‘One-Fluid’ Approach to the Modelling of a Multi-Phase System	204
5.1.1	Application to the Viscous Model	207
5.2	Numerical Implementation using a Volume-of-Fluid Method in Basilisk	210
5.2.1	Volume-of-Fluid Methods	211
5.2.2	Basilisk Implementation	214
5.3	Added Functionality: Implicit Scheme to Solve for the Effective Sur- face Tension	218
5.3.1	Finding an Implicit Solution Iteratively	218
5.3.2	Validation of Dilatational Surface Viscosity Implementation .	222
5.3.3	Curvature Limitation	231
Chapter 6 Drop Impact		233
6.1	Spread Dynamics and Timescales for Interaction with the Substrate .	234

6.1.1	Slip Length: Numerical Justification	234
6.1.2	Pinning Radius	236
6.1.3	Validation against Experiments	237
6.2	Retraction and Rebound Dynamics	243
6.2.1	Rigid Substrate Impacts	243
6.2.2	Powder Bed Impacts	247
Chapter 7 Liquid Marble Formation		256
7.1	Encapsulation of Simulated Drops	257
7.2	Choice of β	260
7.2.1	Forming a Spherical Liquid Marble	261
7.3	Simulation Results	265
7.3.1	Overview of Liquid Marble Formation	265
7.3.2	No Liquid Marble Formation	271
7.3.3	Spherical Liquid Marble Formation	273
7.3.4	Deformed Liquid Marble Formation	276
7.3.5	Effect of large β	291
Chapter 8 Summary and Future Work		292
Bibliography		315
Appendix A Derivation of the Surface Divergence Operator in Axisymmetric Coordinates		316
Appendix B Proof of Surface Area Conservation from Zero Surface Divergence of Surface Velocity		318
Appendix C Axisymmetric Kernels for the Boundary Integral Equation		320
Appendix D Computation of Spline Coefficients		323
D.1	Cubic Splines	324
D.1.1	Continuity at Interior Nodes	324
D.1.2	Generating the Matrix Equation	325
D.1.3	End Conditions	325
D.2	Quintic Splines	326
D.2.1	Continuity at Interior Nodes	327

D.2.2	Generating the Matrix Equations	327
D.2.3	End Conditions	329
Appendix E Populating the Matrices for the Discretised Boundary		
Integral Equation		332

List of Figures

Chapter 1 Introduction	1
1.1 Liquid marble composed of a water drop (radius 1mm) and a shell formed of hydrophobic lycopodium grains (typical size $20\mu\text{m}$), at rest on a glass plate.	3
1.2 Schematic for the formation of a liquid marble from a drop rolling on a hydrophobic powder bed.	4
1.3 Schematic of liquid marble formation via drop impact: a liquid drop (a) released from rest above a powder bed, (b) reaching a maximum spreading diameter, and (c) forming a liquid marble following retraction.	5
1.4 Schematic showing the effect of substrate hydrophobicity on liquid condensation when the substrate is coated with superhydrophobic nanoparticles. Liquid marbles can form when the underlying substrate is superhydrophobic.	5
1.5 Schematic showing a formed oil liquid marble immersed in water due to the destabilisation of a granular raft lying at an oil-water interface.	6
1.6 Schematic representation of adhered (left) hydrophobic, and (right) hydrophilic particles at a liquid-gas interface, with the liquid-solid interface between the liquid and solid substrate replaced by multiple solid-solid contacts and pockets of gas separating the liquid-gas interface from the solid substrate.	7
1.7 Close-up images taken of the surface of water liquid marbles, coated in (left) $20\mu\text{m}$ lycopodium grains, and (right) 130nm PVDF nanobeads.	7
1.8 Close-up images taken of the surface of water liquid marbles coated in a mono-layer of mono-dispersed polystyrene particles of sizes $15\mu\text{m}$, $30\mu\text{m}$, $50\mu\text{m}$, $75\mu\text{m}$, $100\mu\text{m}$	8

1.9	Schematic of a proposed liquid marble formation process; with (a) a liquid drop lying atop the pillars of a structured superhydrophobic solid surface, and (b) the pillars detaching from the substrate due to surface tension forces from the drop and assembling a conformal surface texture that becomes the liquid marble shell.	8
1.10	(Left) Diagram showing a liquid marble lying atop a liquid surface, with pockets of air between adhered particles separating the interior of the liquid marble from the supporting liquid. (Right) Experimental image of a distilled water liquid marble (volume $120\mu\text{L}$) coated in PVDF particles (size 130nm) floating on a distilled water surface. . .	11
1.11	Experimental images showing the evaporation process of a water liquid marble (volume $5\text{-}10\mu\text{L}$) coated in graphite powder (size $2\text{-}30\mu\text{m}$), with buckling of the encapsulating shell following sufficient evaporation of the interior liquid.	11
1.12	Opening of the magnetic shell of a liquid marble to expose the liquid interior, shown in (a) an experiment, and (b) a diagram. A magnet is placed beneath the underlying substrate, pulling the magnetic particles in the shell of the liquid marble towards the magnet, tangentially along the liquid-gas interface.	14
1.13	Revealing the contamination of a water surface with a water liquid marble coated in PVDF powder particles. (Left) Liquid marble at rest on an uncontaminated water surface. (Right) PVDF particles lying upon a water surface coated in silicone oil following the destruction of a floating liquid marble.	15
1.14	(Left) A macroscopic oil liquid marble with an encapsulating shell of transparent microscopic oil liquid marbles, each with a hydrophobic silica nanoparticle shell. (Right) A macroscopic oil liquid marble re-configured into a hemisphere following forced wetting on a patch of liquid, exhibiting properties of the macroscopic marble which are similar to a compound lens.	16

1.15	(d) Optical microscope images demonstrating the control of the shape of a deposited macroscopic oil liquid marble. Cross-sectional diagrams and images from experiments of compound lens (macroscopic oil liquid marble) deposition on a wettable patch on a (e) hydrophobic and (f) hydrophilic substrate, and (g) the introduction of an immiscible third fluid phase within the deposited compound lens.	17
1.16	Profiles of liquid marbles obtained from water drop impact experiments onto a superhydrophobic powder bed, for a drop with initial diameter $D_0 = 2.1\text{mm}$, and for impact speeds of (a) $U_0 = 1.14\text{ m/s}$, (b) $U_0 = 1.56\text{ m/s}$, (c) $U_0 = 1.66\text{ m/s}$, (d) $U_0 = 1.84\text{ m/s}$. Red lines and markers added by the original author.	18
1.17	Deformed liquid marbles formed in drop impact experiments. The liquid drop is water with an initial spherical diameter of 2mm , and the hydrophobic particles are of average size $25\mu\text{m}$	21
1.18	Change in arrested shape for pseudo-spherical deformed liquid marbles (initial drop diameter $D_0 = 3\text{mm}$, mean particle size $\bar{d}_p = 25\mu\text{m}$) following impact with a solid substrate. Impact speeds of (a) $U_0 = 0.96\text{m/s}$, and (b) $U_0 = 1.39\text{m/s}$. Scale bars are 2mm long.	22
Chapter 2 Experiments		33
2.1	Histogram showing the distribution of geometric diameters of solid particles used in experiments, as calculated using an API Aerosizer [®] particle size analyzer. The y-axis shows the (normalised) number of particles within a particular size range.	34
2.2	Photographs and diagrams of the experimental setup for drop impacts onto treated superhydrophobic glass surfaces and superhydrophobic powder beds.	36
2.3	Photographs showing (top) a superhydrophobic powder bed post-impact, including (top-right) a close-up of liquid marbles at rest on the powder surface, and (bottom) a treated superhydrophobic glass slide.	37

2.4	Comparison between drop impact experiments on treated superhydrophobic glass from (top) set A; providing a well-resolved view of spreading dynamics but a limited view of post-rebound dynamics, and (bottom) set B; providing a less-resolved view of drop spread but fully capturing post-rebound dynamics. Scale bar has a width of 2mm. . . .	39
2.5	Liquid marbles with overlaid smooth boundaries and centroids. The impact Weber number for each experiment is: (a) $We = 49$, (b) $We = 59$, (c) $We = 69$, (d) $We = 79$	40
2.6	Example of the process of approximating the surface area of a liquid marble: (a) Identify the boundary (red) of the two dimensional image of the drop and calculate the centroid of the filled shape, (b) Draw a line (blue) through the centroid that can reasonably act as an axis of symmetry for the drop shape - this splits the boundary into a left and right component (green and pink), (c-d) Construct a surface-of-revolution using the left and right components of the drop boundary. The ‘true’ surface area is approximated as the average of the approximations in (c) and (d).	42
2.7	Spreading factor versus impact Weber number for drop impact on a rigid impermeable superhydrophobic substrate with experiments from (top) set A, and (bottom) set B. Power law approximations are provided for both sets of experiments for $We > 20$. The R-squared value and mean squared error are (top) $R^2 = 0.9815$ and $MSE = 2.6 \times 10^{-3}$, (bottom) $R^2 = 0.9965$ and $MSE = 8.3 \times 10^{-4}$	45
2.8	Drop impact experiment (from set B, $We = 9$) on a rigid impermeable superhydrophobic substrate, showing no satellite droplet ejection. Scale bar has a width of 2mm.	47
2.9	Drop impact experiment (from set B, $We = 51$) on a rigid impermeable superhydrophobic substrate, showing the ejection of satellite droplets. Scale bar has a width of 2mm.	48
2.10	Drop impact experiment (from set B, $We = 98$) on a rigid impermeable superhydrophobic substrate, showing the ejection of satellite droplets. Scale bar has a width of 2mm.	49

2.11	Drop impact experiment (from set B, $We = 150$) on a rigid impermeable superhydrophobic substrate, showing the onset of the fingering instability. At 2.00ms the receding rim of the drop is experiencing a slight perturbation which continues through 3.50ms, and ultimately causes the drop to lose axisymmetry as is evident in the irregular drop shape at 16.00ms. Scale bar has a width of 2mm.	50
2.12	Drop impact experiment (from set B, $We = 223$) on a rigid impermeable superhydrophobic substrate. The fingering instability appears at the end of the drop spreading regime (at 2.50ms), which breaks axisymmetry and causes the drop to jet at an angle off the vertical, with irregular surface waves propagating along the drop interface. Scale bar has a width of 2mm.	51
2.13	Drop impact experiment (from set B, $We = 244$) on a rigid impermeable superhydrophobic substrate. Splashing occurs soon after contact is made with the substrate. Scale bar has a width of 2mm.	52
2.14	Drop impact on a rigid impermeable superhydrophobic substrate, with $We = 3.5$ and $\gamma = 1.35$. Limits on the value of the contact angle for (top) spreading, and (bottom) retraction, are given by straight lines drawn at the contact line. These images show (left) the drops as recorded, (middle-left) the drops with a greater contrast and imposed contact angle lines, and (middle-right)-(right) close-ups at the contact line.	54
2.15	Drop impact on a rigid impermeable superhydrophobic substrate, with $We = 49$. Limits on the value of the contact angle for (top) part-way through retraction, and (bottom) just prior to rebound, are given by straight lines drawn at the contact line. These images show (left) the drops as recorded, (middle-left) the drops with a greater contrast and imposed contact angle lines, and (middle-right)-(right) close-ups at the contact line.	55

2.16	Spreading factor versus impact Weber number for drop impact onto a superhydrophobic powder bed with experiments from (top) set A, and (bottom) set B. Power law approximations are provided for both sets of experiments for $We > 20$. The R-squared value and mean squared error are (top) $R^2 = 0.9486$ and $MSE = 5.2 \times 10^{-3}$, (bottom) $R^2 = 0.9363$ and $MSE = 6.7 \times 10^{-3}$	58
2.17	Drop impact experiment (from set B, $We = 15$) on a superhydrophobic powder bed, with partial coating of the drop interface and no satellite droplet ejection. Scale bar has a width of 2mm.	59
2.18	Drop impact experiment (from set B, $We = 25$) on a superhydrophobic powder bed, with partial coating of the drop interface and satellite droplet ejection. Scale bar has a width of 2mm.	60
2.19	Drop impact experiment (from set B, $We = 36$) on a superhydrophobic powder bed, with drop encapsulation occurring at 13.00ms due to ejection of a large satellite droplet. Afterwards, the drop is still able to oscillate in the air until returning to the powder bed. Scale bar has a width of 2mm.	61
2.20	Drop impact experiment (from set B, $We = 52$) on a superhydrophobic powder bed, showing the formation of a spherical liquid marble. Encapsulation of the drop occurs due to a satellite drop ejection soon after 7.50ms, after which the drop pulls itself together, the proceeding oscillations are then quickly damped and a spherical liquid marble is formed at 25.00ms. The drop continues its flight through the air; all the while maintaining its spherical shape. Scale bar has a width of 2mm.	62
2.21	Drop impact experiment (from set B, $We = 68$) on a superhydrophobic powder bed, showing the formation of a deformed liquid marble. Encapsulation of the drop occurs due to a satellite drop ejection at 9.50ms just as the drop has lifted off from the powder bed. The drop attempts to minimise its surface area until the interface becomes jammed at 17.50ms. This shape is maintained for the remainder of the experiment until coming back into contact with the powder bed. Scale bar has a width of 2mm.	63

2.22	Drop impact experiment (from set B, $We = 78$) on a superhydrophobic powder bed, showing the formation of a deformed liquid marble. The desire for drops in experiments prior to this has been to form back into a sphere (the drop's minimum surface area state), so the creation of such an elongated liquid marble is testament to the effects of very tight powder packing on the drop interface. Given the marble shape remains almost unchanged from when the drop was encapsulated (at 8.25ms), it seems the powder packing was already close to the critical value for liquid marble formation at encapsulation. Scale bar has a width of 2mm.	64
2.23	Drop impact experiment (from set A, $We = 156$) showing splashing soon after contact is made with the superhydrophobic powder bed. Scale bar has a width of 2mm.	65
2.24	Spreading factor versus impact Weber number for all sets of experiments. Also included are data points calculated using a theoretical model which incorporates the effects of crater formation. Experimental parameters from the set B powder bed experiments are used to obtain the model results.	66
2.25	Comparison of drop impacts on (a) a rigid impermeable superhydrophobic substrate, and (b) a superhydrophobic powder bed. (a) $D_0 = 1.94\text{mm}$ and $We = 3.5$, with spreading factor $\gamma = 1.35$, (b) $D_0 = 1.99\text{mm}$ and $We = 3.5$, with spreading factor $\gamma = 1.33$. Scale bar has a width of 2mm.	67
2.26	Comparison of drop impacts on (a) a rigid impermeable superhydrophobic substrate, and (b) a superhydrophobic powder bed. (a) $D_0 = 1.94\text{mm}$ and $We = 9$, with spreading factor $\gamma = 1.52$, (b) $D_0 = 1.99\text{mm}$ and $We = 9$, with spreading factor $\gamma = 1.52$. Scale bar has a width of 2mm.	68
2.27	Comparison of drop impacts on (a) a rigid impermeable superhydrophobic substrate, and (b) a superhydrophobic powder bed. (a) $D_0 = 1.94\text{mm}$ and $We = 14$, with spreading factor $\gamma = 1.62$, (b) $D_0 = 1.99\text{mm}$ and $We = 15$, with spreading factor $\gamma = 1.67$. Scale bar has a width of 2mm.	68

2.28	Comparison of drop impacts on (a) a rigid impermeable superhydrophobic substrate, and (b) a superhydrophobic powder bed. (a) $D_0 = 1.94\text{mm}$ and $We = 24$, with spreading factor $\gamma = 1.87$, (b) $D_0 = 1.99\text{mm}$ and $We = 25$, with spreading factor $\gamma = 1.87$. Scale bar has a width of 2mm.	69
2.29	Comparison of drop impacts on (a-b) a rigid impermeable superhydrophobic substrate, and (c-d) a superhydrophobic powder bed. (a-b) $D_0 = 1.94\text{mm}$ and $We = 35$, with spreading factor $\gamma = 2.06$, (c) $D_0 = 1.99\text{mm}$ and $We = 36$, with spreading factor $\gamma = 2.07$, (d) $D_0 = 1.99\text{mm}$ and $We = 36$, with spreading factor $\gamma = 2.14$. Scale bar has a width of 2mm.	70
2.30	Diagram showing the difference between the spreading diameter \hat{D}_{max} , and the contact line diameter \hat{D}_{CL} , for a drop in contact with a solid substrate.	72
2.31	Drop impact experiment on a superhydrophobic powder bed (from set B) showing the ejection of a satellite drop that takes no adsorbed powder along with it; reducing the surface area and mass of the primary drop but <i>not</i> reducing the mass of adsorbed powder.	73
2.32	Drop impact experiment on a superhydrophobic powder bed (from set B) showing the ejection of a satellite drop that causes the encapsulation of the primary drop. Before pinch-off, the drop maintains a small region of clean interface at the drop apex. The top of the drop is then ejected, taking some adsorbed powder along with it, thus also reducing the total mass of adsorbed powder on the primary drop interface. . .	74
2.33	Drop impact experiment on a superhydrophobic powder bed (from set B) showing the ejection of a satellite drop while encapsulated. . . .	76
2.34	Values of $\alpha_{encap}^{(spr)}$, $\alpha_{freeze}^{(spr)}$, and $\alpha_{final}^{(spr)}$ for set B powder bed experiments that exhibit encapsulation and (possibly) liquid marble formation. . .	78

Chapter 3 Mathematical Models

3.1	Diagram showing an axisymmetric drop domain Ω in the (r, z) -plane with a one dimensional boundary curve representation for the interface \mathcal{S}_{LG} , with arclength s , normal vector \mathbf{n} , tangent vector \mathbf{t} , and line element ds	83
3.2	Stages preceding (potential) liquid marble formation. (a) Spherical drop with radius \hat{R}_0 with clean liquid-gas interface \mathcal{S}_{LG} impacts the substrate with speed \hat{U}_0 . (b) The drop spreads along the substrate while adsorbing powder to the liquid-solid interface \mathcal{S}_{LS} . (c) Following maximum spread, the drop retracts, and a vertical jet forms along the z -axis. Some adsorbed powder moves onto \mathcal{S}_{LG} from \mathcal{S}_{LS} . (d) The drop rebounds from the substrate and oscillates within the gas. . . .	85
3.3	Diagram showing the drop flow profile within a boundary layer beside the liquid-solid interface. Very close to the substrate, the flow profile is radial and linear in z . The slip length in this case is the same as the diameter of an individual powder particle, \bar{d}_p , and this determines the value of the slip velocity at the liquid-solid interface.	92
3.4	Diagram showing (a) the drop at maximum spread, with maximum contact line radius \bar{r}_{CL} and a uniform coating of powder on its liquid-solid interface \mathcal{S}_{LS} , followed by retraction of the drop with the contact line reducing to $r_{CL}(t) < \bar{r}_{CL}$ for some time t . We have (b) $\alpha_{encap} < 1$, whereby the powder more densely packs onto the liquid-gas interface \mathcal{S}_{LG} , (c) $\alpha_{encap} = 1$, whereby the powder maintains the same packing on \mathcal{S}_{LG} , or (d) $\alpha_{encap} > 1$, whereby the powder is more sparsely packed on \mathcal{S}_{LG}	100
3.5	Example plots for the constitutive equation for λ^s (blue curve) provided by (3.2.37) and a constitutive equation that has $\lambda^s \rightarrow 0$ as $A \rightarrow \infty$ (red curve). Both curves diverge to infinity when the free surface area A converges to the freezing area A_{freeze} , but the blue curve is zero at the encapsulation area $A = A_{encap}$, while the red curve that takes a small positive value $\epsilon > 0$	104

Chapter 4 Boundary Integral Method and Boundary Element Method 117

4.1	Diagram showing a three dimensional domain Ω bounded by a smooth surface \mathcal{S} and containing an interior ball of radius ε , centred at the point $\underline{\mathbf{x}} \in \Omega$. Ω_ε is the reduced domain $\Omega - B_\varepsilon(\underline{\mathbf{x}})$ with unit normal $\underline{\mathbf{n}}$ to the boundary $\partial\Omega_\varepsilon \equiv \mathcal{S} \cup \mathcal{S}_\varepsilon$	120
4.2	Diagram showing the decomposition of an axisymmetric drop boundary in the (r, z) -plane when the drop is (left) <i>away from</i> , and (right) <i>in contact with</i> , the solid substrate. The boundary curve Γ is divided into N subintervals denoted $\Gamma_1, \dots, \Gamma_N$ where each subinterval is bounded by two nodes (shown as white and green circles). Counting of nodes and subintervals begins at the top intersection with the z -axis (axis of symmetry) and continues clockwise (s -increasing) until the second intersection with the z -axis. A white (green) node corresponds to the imposing of a Dirichlet (Neumann) boundary condition, that is, imposing a value of ϕ ($\partial\phi/\partial n$).	126
4.3	Height of drop apex with respect to the drop centre of mass (for increasing N) for a suspended drop released from rest with initial shape given by (4.6.6) with $\varepsilon = 0.05$. Black dotted vertical lines indicate the (dimensionless) theoretical oscillation period for a second axisymmetric spherical mode ($2\pi/\sqrt{8}$).	148
4.4	Errors in the conservation of drop (top) volume, and (bottom) total energy, as calculated using the l_2 - and l_∞ -norms (4.6.5), for a suspended drop released from rest with initial shape given by (4.6.6) with $\varepsilon = 0.05$, for varied $h = 1/N$. Power laws are fitted with: (top) Error $\sim h^{2.04}$, with an R-squared value and mean square error of: $R^2 = 1.00$ and $\text{MSE} = 2.13 \times 10^{-2}$ for the l_2 -norm and $R^2 = 1.00$ and $\text{MSE} = 9.30 \times 10^{-6}$ for the l_∞ -norm, and (bottom) Error $\sim h^{2.15}$ and $\sim h^{2.24}$ for the l_2 - and l_∞ -norms, respectively, with an R-squared value and mean square error of: $R^2 = 1.00$ and $\text{MSE} = 1.50 \times 10^{-2}$ for the l_2 -norm, and $R^2 = 0.99$ and $\text{MSE} = 5.63 \times 10^{-5}$ for the l_∞ -norm.	149
4.5	Profiles of oscillations in the (r, z) -plane for a suspended drop released from rest with initial shape given by (4.6.6) with $\varepsilon = 0.5$. Snapshots taken at times (left-to-right): $t = 0.0, 0.8, 1.6, 2.0, 3.2$	150

4.6	Errors in the conservation of drop (top) volume, and (bottom) total energy, as calculated using the l_2 - and l_∞ -norms (4.6.5), for a suspended drop released from rest with initial shape given by (4.6.6) with $\epsilon = 0.5$, for varied $h = 1/N$. Power laws are fitted with: (top) Error $\sim h^{2.26}$ and $\sim h^{2.27}$ for the l_2 - and l_∞ -norms respectively, with an R-squared value and mean square error of: $R^2 = 1.00$ and $MSE = 1.39 \times 10^{-2}$ for the l_2 -norm and $R^2 = 1.00$ and $MSE = 1.10 \times 10^{-5}$ for the l_∞ -norm, and (bottom) Error $\sim h^{2.46}$ and $\sim h^{2.32}$ for the l_2 - and l_∞ -norms respectively, with an R-squared value and mean square error of: $R^2 = 1.00$ and $MSE = 7.17 \times 10^{-2}$ for the l_2 -norm and $R^2 = 1.00$ and $MSE = 1.50 \times 10^{-5}$ for the l_∞ -norm.	151
4.7	Height of drop apex with respect to the drop centre of mass (for increasing N) for a suspended drop released from rest with initial shape given by (4.6.6) with $\epsilon = 0.5$. The drop is experiencing (dilatational) surface viscous effects corresponding to (constant) $\lambda^s = 1$	154
4.8	(Top) Effective surface tension, and (b) total energy (for increasing N) for a suspended drop released from rest with initial shape given by (4.6.6) with $\epsilon = 0.5$. The drop is experiencing (dilatational) surface viscous effects corresponding to (constant) $\lambda^s = 1$. The pink dotted line in the bottom plot indicates the total energy corresponding to the drop being at rest with spherical shape (the minimum surface energy state).	155
4.9	(Top) Comparison of the observed (from simulations) and theoretical energy decay rate (4.6.7, calculated using the $N = 170$ simulation), and (b) energy decay rate error (for increasing N) for a suspended drop released from rest with initial shape given by (4.6.6) with $\epsilon = 0.5$. The drop is experiencing (dilatational) surface viscous effects corresponding to (constant) $\lambda^s = 1$. The energy decay rate error is defined as the normed-difference of the observed and theoretical decay rates. Fitted power laws for the errors are $\sim h^{1.80}$ with $R^2 = 1.00$ and $MSE = 4.25 \times 10^{-1}$ for the l_2 -norm, and $\sim h^{1.71}$ with $R^2 = 0.99$ and $MSE = 3.70 \times 10^{-3}$ for the l_∞ -norm.	156

4.10	Height of drop apex with respect to the drop centre of mass (for increasing N) for a suspended drop released from rest with initial shape given by (4.6.6) with $\epsilon = 0.5$. The drop is experiencing (dilatational) surface viscous effects corresponding to (constant) $\lambda^s = 10$	157
4.11	(Top) Effective surface tension, and (b) total energy (for increasing N) for a suspended drop released from rest with initial shape given by (4.6.6) with $\epsilon = 0.5$. The drop is experiencing (dilatational) surface viscous effects corresponding to (constant) $\lambda^s = 10$. The pink dotted line in the bottom plot indicates the total energy corresponding to the drop being at rest with spherical shape (the minimum surface energy state).	158
4.12	(Top) Comparison of the observed (from simulations) and theoretical energy decay rate (4.6.7, calculated using the $N = 170$ simulation), and (b) energy decay rate error (for increasing N) for a suspended drop released from rest with initial shape given by (4.6.6) with $\epsilon = 0.5$. The drop is experiencing (dilatational) surface viscous effects corresponding to (constant) $\lambda^s = 10$. The energy decay rate error is defined as the normed-difference of the observed and theoretical decay rates. Fitted power laws for the errors are $\sim h^{2.03}$ with $R^2 = 1.00$ and $MSE = 3.45 \times 10^{-1}$ for the l_2 -norm, and $\sim h^{2.12}$ with $R^2 = 0.99$ and $MSE = 1.00 \times 10^{-3}$ for the l_∞ -norm.	159
4.13	Height of drop apex with respect to the drop centre of mass (for increasing N) for a suspended drop released from rest with initial shape given by (4.6.6) with $\epsilon = 0.5$. The drop is experiencing (dilatational) surface viscous effects corresponding to (constant) $\lambda^s = 100$	160
4.14	Effective surface tension (for increasing N) for a suspended drop released from rest with initial shape given by (4.6.6) with $\epsilon = 0.5$. Plots show (top) linear-scale, and (bottom) semilog-scale. The drop is experiencing (dilatational) surface viscous effects corresponding to (constant) $\lambda^s = 100$	161

4.15	Total energy (for increasing N) for a suspended drop released from rest with initial shape given by (4.6.6) with $\epsilon = 0.5$. The drop is experiencing (dilatational) surface viscous effects corresponding to (constant) $\lambda^s = 100$. The pink dotted line in the bottom plot indicates the total energy corresponding to the drop being at rest with spherical shape (the minimum surface energy state). Plots show (top) from time $t = 0$ to $t = 10$, and (bottom) a close-up view of fluctuations from time $t = 8$ to $t = 10$	162
4.16	(Top) Comparison of the observed (from simulations) and theoretical energy decay rate (4.6.7, calculated using the $N = 170$ simulation), and (b) energy decay rate error (for increasing N) for a suspended drop released from rest with initial shape given by (4.6.6) with $\epsilon = 0.5$. The drop is experiencing (dilatational) surface viscous effects corresponding to (constant) $\lambda^s = 100$. The energy decay rate error is defined as the normed-difference of the observed and theoretical decay rates. Fitted power laws for the errors are $\sim h^{2.21}$ with $R^2 = 0.99$ and $MSE = 1.99 \times 10^{-1}$ for the l_2 -norm, and $\sim h^{1.94}$ with $R^2 = 0.99$ and $MSE = 8.40 \times 10^{-5}$ for the l_∞ -norm.	163
4.17	Comparison between a drop impact experiment on a rigid impermeable superhydrophobic substrate (contact angle 180°), and a simulation using our boundary element model, with conditions: $\hat{R}_0 = 1.14\text{mm}$, $\hat{U}_0 = 0.35\text{m/s}$ ($We = 3.5$). Top to bottom, comparisons are made at 0ms, 0.925ms, 2.05ms from the moment of contact between the drop and the solid substrate. The simulation uses $N = 102$ elements, a maximum time step of $\tau = 5 \times 10^{-4}$, with nodes redistributed every 50 time steps, and quintic splines used to approximate the boundary. Figure continues on next page.	165
4.17	(cont) Top to bottom, comparisons are made at 3.55ms, 4.675ms. . .	166

4.18	Comparison between a drop impact experiment on a rigid impermeable superhydrophobic substrate, and a simulation using our boundary element model, with conditions: $\hat{R}_0 = 1.75\text{mm}$, $\hat{U}_0 = 0.41\text{m/s}$ ($\text{We} = 8.1$). Top to bottom, comparisons are made at 0.0ms, 2.7ms, 4.5ms, 4.9ms. Simulation used $N = 202$ elements, maximum time step $\tau = 4 \times 10^{-4}$, nodes redistributed every 50 time steps, quintic splines used.	168
4.18 (cont)	Top to bottom, comparisons are made at 5.9ms, 6.1ms, 6.3ms, 6.7ms. Figure continues on next page.	169
4.18 (cont)	Top to bottom, comparisons are made at 7.1ms, 8.0ms.	170
4.19	Photographs taken of a (water) drop impact experiment onto a rigid impermeable superhydrophobic substrate, exhibiting drying-out of the drop centre. Top photo shows the earliest time. Initial spherical drop diameter $\hat{D}_0 = 4\text{mm}$, with vertical impact speed $\hat{U}_0 = 0.14\text{m/s}$, and associated impact Weber number $\text{We} = 1.1$	174
4.20	BEM simulation exhibiting drying-out of the drop centre, with impact Weber number $\text{We} = 6.9$. The simulation uses $N = 302$ elements, a maximum time step of $\tau = 6.25 \times 10^{-5}$, with nodes redistributed every 400 time steps, and cubic splines used to approximate the drop boundary. Drop impacts with a spherical shape (top left), followed by snapshots (middle left) - (bottom left) - (top right) - (middle right), ending with a snapshot moments prior to the centre drying-out (bottom right).	175

- 4.21 BEM simulation with the same initial drop shape and velocity profile as Figure 4.20, with $N = 152$ elements, a maximum time step of $\tau = 5 \times 10^{-4}$, with redistribution every 50 time steps, and quintic splines used to approximate the boundary. An additional term for the surface pressure to stop drying-out of the centre is applied (4.7.1) on the top part of the drop boundary near the axis of symmetry, with $\epsilon = 0.02$ and $m = 4$. The snapshots show (top left) moments prior to drying-out, leading into (bottom left) where the top boundary is prevented from drying-out by the additional force-field term. Then, (top right) the snapshot shows the drop continuing to retract inwards until (bottom right) where the snapshot is taken moments prior to the drop touching the axis of symmetry and trapping an interior gas bubble. 178
- 4.22 Photographs of a (water) drop impact experiment onto a rigid superhydrophobic substrate (contact angle of 161°), exhibiting the trapping of an interior bubble after potential drying-out of the drop centre. Initial spherical drop diameter $\hat{D}_0 = 2\text{mm}$, with vertical impact speed $\hat{U}_0 = 0.58\text{m/s}$, and associated impact Weber number $We = 9.2$. White scale bar on the left-most drop image has length 1mm. Additional markers added by original author. 178
- 4.23 BEM simulation exhibiting drop splashing, with impact Weber number $We = 28$. The simulation uses $N = 152$ elements, a maximum time step of $\tau = 5 \times 10^{-4}$, with nodes redistributed every 50 time steps, and quintic splines used to approximate the drop boundary. Order of snapshots is (top left) - (middle left) - (bottom left) - (top right) - (middle right) - (bottom right). The final snapshot is taken moments before the drop splashes with pinch-off highlighted with red circles. . 180
- 4.24 BEM simulation exhibiting drop splashing, with impact Weber number $We = 43$. The simulation uses $N = 182$ elements, a maximum time step of $\tau = 1 \times 10^{-4}$, with nodes redistributed every 100 time steps, and quintic splines used to approximate the drop boundary. Order of snapshots is (top left) - (middle left) - (bottom left) - (top right) - (middle right) - (bottom right). The final snapshot is taken moments before the drop splashes with pinch-off highlighted with red circles. . 181

4.25	<i>Small amplitude suspended inviscid drop oscillations with small $\lambda^s > 0$ against a damped nonlinear oscillator:</i> Plots showing, for $\lambda^s = 0$ to $\lambda^s = 2 \times 10^2$ (top) BEM simulations showing the evolution of the height of the drop apex starting from rest with initial shape (4.6.6) with $\epsilon = 0.05$, and (bottom) the solution to the ordinary differential equation (3.3.17) describing a damped nonlinear oscillator, for the amplitude $a(t)$. BEM simulations use $N = 240$ elements, a constant time step of $\tau = 1 \times 10^{-4}$, no redistribution of nodes, and cubic splines approximating the drop boundary.	184
4.26	<i>Small amplitude suspended inviscid drop oscillations with large $\lambda^s > 0$ against a damped nonlinear oscillator:</i> Plots showing, for $\lambda^s = 2 \times 10^2$ to $\lambda^s = 1 \times 10^4$ (top) BEM simulations showing the evolution of the height of the drop apex starting from rest with initial shape (4.6.6) with $\epsilon = 0.05$, and (bottom) the solution to the ordinary differential equation (3.3.17) describing a damped nonlinear oscillator, for the amplitude $a(t)$. Simulation parameters given in the caption of Figure 4.25.	185
4.27	<i>Transition from overdamped to underdamped motion for large $\lambda^s > 0$:</i> Plots showing the height of drop apex in BEM simulations, overlaid with the solution of the damped nonlinear oscillator (3.3.17), and the analytic solution in the overdamped limit (3.3.21), with pink dotted lines indicating the critical band $[1 - a_c, 1 + a_c]$ inside of which drop oscillations are underdamped, and outside of which drop oscillations are overdamped. Critical amplitude a_c given by (3.3.19). Simulation parameters given in the caption of Figure 4.25. Cases shown are for (a) $\lambda^s = 2 \times 10^2$, (b) $\lambda^s = 4 \times 10^2$, (c) $\lambda^s = 1 \times 10^3$, (d) $\lambda^s = 2 \times 10^3$, (e) $\lambda^s = 4 \times 10^3$, (f) $\lambda^s = 1 \times 10^4$	186

4.28	<i>Small amplitude suspended inviscid drop oscillations with small $\lambda^s > 0$ against a damped nonlinear oscillator:</i> Plots showing, for $\lambda^s = 1 \times 10^{-1}$ to $\lambda^s = 2 \times 10^2$ (top) BEM simulations showing the evolution of the effective surface tension starting from rest with initial shape (4.6.6) with $\epsilon = 0.05$, and (bottom) the effective spring constant (3.3.16) from the damped nonlinear oscillator model. Simulation parameters given in the caption of Figure 4.25.	188
4.29	<i>Small amplitude suspended inviscid drop oscillations with large $\lambda^s > 0$ against a damped nonlinear oscillator:</i> Plots showing, for $\lambda^s = 2 \times 10^2$ to $\lambda^s = 1 \times 10^4$ (top) BEM simulations showing the evolution of the effective surface tension starting from rest with initial shape (4.6.6) with $\epsilon = 0.05$, and (bottom) the effective spring constant (3.3.16) from the damped nonlinear oscillator model. Simulation parameters given in the caption of Figure 4.25.	189
4.30	<i>Small amplitude suspended inviscid drop oscillations with large $\lambda^s > 0$ against a damped nonlinear oscillator:</i> Plot showing, for $\lambda^s = 1 \times 10^3$ to $\lambda^s = 1 \times 10^4$ the effective spring constant (3.3.16) from the damped nonlinear oscillator model overlaid with the analytic solution to the effective surface tension in the overdamped limit (3.3.23), given by dotted lines of similar colour.	190
4.31	<i>Drift in effective surface tension for small amplitude suspended inviscid drop oscillations with large $\lambda^s > 0$:</i> Plots showing, (top) for $\lambda^s = 1 \times 10^3, 2 \times 10^3, 4 \times 10^3$, the surface viscous term $W(t) = \sigma_{\text{eff}} - 1$ with data taken from Figure 4.29 with imposed dotted lines indicating $\bar{W}(t)$ (4.8.3), and (bottom) spatial convergence of the effective surface tension to the damped nonlinear oscillator solution with $N = 120, 170, 240$, and $\lambda^s = 2 \times 10^3$. BEM simulation the same as described in the caption of Figure 4.25, with differing N	192

4.32	<i>Large amplitude suspended inviscid drop oscillations with small $\lambda^s > 0$ against a toy damped nonlinear oscillator:</i> Plots showing, for $\lambda^s = 0$ to $\lambda^s = 1 \times 10^1$ (top) BEM simulations showing the evolution of the height of the drop apex starting from rest with initial shape (4.6.6) with $\epsilon = 0.5$, and (bottom) the solution to the toy damped nonlinear oscillator model (4.8.4), for the amplitude $a(t)$, with γ chosen to maximise resemblance to the BEM simulations. BEM simulations use $N = 240$ elements, a constant time step of $\tau = 1 \times 10^{-4}$, no redistribution of nodes, and cubic splines approximating the drop boundary.	195
4.33	<i>Large amplitude suspended inviscid drop oscillations with small $\lambda^s > 0$ against a toy damped nonlinear oscillator:</i> Plots showing, for $\lambda^s = 1 \times 10^{-2}$ to $\lambda^s = 1 \times 10^1$ (top) BEM simulations showing the evolution of the effective surface tension starting from rest with initial shape (4.6.6) with $\epsilon = 0.5$, and (bottom) the effective spring constant (3.3.16) from the damped nonlinear oscillator model. Simulation parameters given in the caption of Figure 4.32.	196
4.34	Plots showing, for BEM simulations with parameters given in the caption of Figure 4.32: (top) for $\lambda^s = 0$ to $\lambda^s = 1 \times 10^1$, total drop energy, in which the pink dotted line corresponding to zero kinetic energy and the surface energy attained at a sphere (the minimum surface energy state) and (bottom) for $\lambda^s = 1 \times 10^0, 1 \times 10^1$ the theoretical energy decay rate as calculated with (4.6.7).	197
4.35	<i>Small amplitude suspended inviscid drop oscillations with small $\lambda^s > 0$ against a damped nonlinear oscillator:</i> Plots showing, for $\lambda^s = 1 \times 10^1$ to $\lambda^s = 1 \times 10^3$ (top) BEM simulations showing the evolution of the height of the drop apex starting from rest with initial shape (4.6.6) with $\epsilon = 0.5$, and (bottom) the solution to the toy damped nonlinear oscillator model (4.8.4), for the amplitude $a(t)$, with γ chosen to maximise resemblance to the BEM simulations. Simulation parameters given in the caption of Figure 4.32	199

4.36	<i>Large amplitude suspended inviscid drop oscillations with large $\lambda^s > 0$ against a toy damped nonlinear oscillator:</i> Plots showing, for $\lambda^s = 1 \times 10^1$ to $\lambda^s = 1 \times 10^3$ (top) BEM simulations showing the evolution of the effective surface tension starting from rest with initial shape (4.6.6) with $\epsilon = 0.5$, and (bottom) the effective spring constant (3.3.16) from the damped nonlinear oscillator model. Simulation parameters given in the caption of Figure 4.32.	200
4.37	<i>Large amplitude suspended inviscid drop oscillations with large $\lambda^s > 0$ against a toy damped nonlinear oscillator:</i> Plots showing in semi-log scale, for $\lambda^s = 1 \times 10^1$ to $\lambda^s = 1 \times 10^3$ (top) BEM simulations showing the evolution of the effective surface tension starting from rest with initial shape (4.6.6) with $\epsilon = 0.5$, and (bottom) the effective spring constant (3.3.16) from the damped nonlinear oscillator model. Simulation parameters given in the caption of Figure 4.32.	201
4.38	Plot showing, for BEM simulations with parameters given in the caption of Figure 4.32: for $\lambda^s = 1 \times 10^1$ to $\lambda^s = 1 \times 10^3$, total drop energy, in which the pink dotted line corresponding to zero kinetic energy and the surface energy attained at a sphere (the minimum surface energy state).	202
4.39	Plots showing, for BEM simulations with parameters given in the caption of Figure 4.32, the theoretical energy decay rate as calculated with (4.6.7) for (top) $\lambda^s = 1 \times 10^1$ to $\lambda^s = 1 \times 10^3$, and (bottom) a close-up view of cases with $\lambda^s = 2 \times 10^2, 4 \times 10^2, 1 \times 10^3$	203

Chapter 5 Volume-of-Fluid Method **204**

5.1	Two dimensional diagrammatic example of a two-phase fluid domain, with immiscible fluid subdomains Ω_1 and Ω_2 . The interfaces between the two fluids are denoted collectively by \mathcal{S}	205
5.2	Two dimensional example of a two-phase fluid domain from Figure 5.1 partitioned into grid cells. The grey cells on the outer perimeter of the domain are ‘ghost’ cells; extra grid cells outside the fluid domain that make it easier to numerically implement boundary conditions for the flow.	212

5.3	Two dimensional example of grid cells containing segments of the fluid-fluid boundary with (left) the fluid-fluid interface, and (right) the corresponding values of the volume fraction (5.2.1) within each cell. . . .	213
5.4	Diagram illustrating the search for the implicit value of the effective surface tension, beginning with an initial guess $\sigma_{\text{eff}}^{(0)}$ and ending with σ_{eff}^* .	222
5.5	Comparison for the height of the drop apex (from the centre of mass of the drop) for suspended drops released from rest with initial shape (4.6.6) with $\epsilon = 0.5$, and small λ^s , from simulations using (top) a VoF implementation using Basilisk, and (bottom) a BEM implementation using purpose-built code described in §4.5. The details of the BEM simulations can be found in the caption of Figure 4.32. The VoF simulations are run in a 6×6 domain with adaptive mesh refinement and a smallest grid cell diameter of $6/2^9 \approx 0.01$	225
5.6	Comparison for the effective surface tension for suspended drops released from rest with initial shape (4.6.6) with $\epsilon = 0.5$, and small λ^s , from simulations using (top) a VoF implementation using Basilisk, and (bottom) a BEM implementation using purpose-built code described in §4.5. The details of the BEM simulations can be found in the caption of Figure 4.32, and for the VoF simulations in the caption of Figure 5.5.	226
5.7	Comparison for the total energy for suspended drops released from rest with initial shape (4.6.6) with $\epsilon = 0.5$, and small λ^s , from simulations using (top) a VoF implementation using Basilisk, and (bottom) a BEM implementation using purpose-built code described in §4.5. The details of the BEM simulations can be found in the caption of Figure 4.32, and for the VoF simulations in the caption of Figure 5.5.	227
5.8	Comparison for the height of the drop apex (from the centre of mass of the drop) for suspended drops released from rest with initial shape (4.6.6) with $\epsilon = 0.5$, and large λ^s , from simulations using (top) a VoF implementation using Basilisk, and (bottom) a BEM implementation using purpose-built code described in §4.5. The details of the BEM simulations can be found in the caption of Figure 4.32, and for the VoF simulations in the caption of Figure 5.5.	228

5.9	Comparison for the effective surface tension for suspended drops released from rest with initial shape (4.6.6) with $\epsilon = 0.5$, and large λ^s , from simulations using (top) a VoF implementation using Basilisk, and (bottom) a BEM implementation using purpose-built code described in §4.5. The details of the BEM simulations can be found in the caption of Figure 4.32, and for the VoF simulations in the caption of Figure 5.5.	229
5.10	Comparison for the total energy for suspended drops released from rest with initial shape (4.6.6) with $\epsilon = 0.5$, and large λ^s , from simulations using (top) a VoF implementation using Basilisk, and (bottom) a BEM implementation using purpose-built code described in §4.5. The details of the BEM simulations can be found in the caption of Figure 4.32, and for the VoF simulations in the caption of Figure 5.5.	230

Chapter 6 Drop Impact

233

6.1	Spreading factor as a function of imposed slip length for multiple impact Weber number drop impact simulations. The minimum cell size in all simulations is approximately $5.86\mu\text{m}$. For reference, note that the mean powder particle diameter is $23.72\mu\text{m}$, and the initial drop diameter is 2mm. Data points on the <i>left</i> of the minimum cell size correspond to a ‘numerical’ slip length on the order of the minimum cell size, and simulations for the data points on the <i>right</i> are assumed to be well-resolved at their imposed slip lengths.	236
6.2	Spreading time (from the moment of contact with the substrate to the moment maximum spread is reached) and contact time (total time on the substrate, so spreading time plus retraction time) for drop impact experiments and simulations. Experimental data is gathered from rigid impermeable superhydrophobic substrate experiments and superhydrophobic powder bed experiments discussed in Chapter 2. The simulations are run in Basilisk using our VoF implementation, with contact times given with and without the inclusion of a pinning radius (see §6.1.2), and with the spreading time shared by both types of simulation.	239

6.3	Spreading factor plotted against the impact Weber number for our VoF drop impact simulations using Basilisk, along with data from (top) our drop impact experiments on rigid impermeable superhydrophobic substrates and superhydrophobic powder beds, and from (bottom) drop impact experiments on micro-textured rigid superhydrophobic substrates (un-filled markers), and surfaces exhibiting the Leidenfrost effect (filled markers).	240
6.4	Outlines of drops from drop impact simulations with VoF using Basilisk, overlaid onto drop impact experiments on rigid impermeable superhydrophobic substrates (as shown in Chapter 2). The dimensionless time of $t = 0.00$ indicates the moment of contact between the drop and substrate in both the simulations and experiments. The images on the right with $t = 0.56$ are at the approximate time when the drops reach their maximum spread (recall that this is We -independent). The experiments shown are representative of other experiments with their impact Weber numbers.	241
6.5	Outlines of drops from drop impact simulations with VoF using Basilisk, overlaid onto drop impact experiments on superhydrophobic powder beds (as shown in Chapter 2). The dimensionless time of $t = 0.00$ indicates the moment of contact between the drop and substrate in both the simulations and experiments. The images on the right with $t = 0.56$ are at the approximate time when the drops reach their maximum spread (recall that this is We -independent). The experiments shown are representative of other experiments with their impact Weber number.	242
6.6	Drop shape from a $We = 45$ ($\gamma = 2.31$) simulation overlaid onto a $We = 45$ ($\gamma = 2.27$) rigid substrate experiment. The moment of contact (at dimensionless time $t = 0.00$) is synchronised between the simulation and experiment. The top row of images is overlaid with a simulation <i>without</i> a pinning radius. The bottom row of images is overlaid with a simulation <i>with</i> a pinning radius of $r_{pin} = 0.5$ reducing the dynamic contact angle from 160° to 120° when reached by the receding contact line.	245

6.7	Drop shape from a $We = 61$ ($\gamma = 2.53$) simulation overlaid onto a $We = 61$ ($\gamma = 2.49$) rigid substrate experiment. The moment of contact (at dimensionless time $t = 0.00$) is synchronised between the simulation and experiment. The top row of images is overlaid with a simulation <i>without</i> a pinning radius. The bottom row of images is overlaid with a simulation <i>with</i> a pinning radius of $r_{pin} = 0.5$ reducing the dynamic contact angle from 160° to 120° when reached by the receding contact line.	246
6.8	Drop shape from a $We = 66$ ($\gamma = 2.59$) simulation overlaid onto a $We = 68$ ($\gamma = 2.53$) rigid substrate experiment. The moment of contact (at dimensionless time $t = 0.00$) is synchronised between the simulation and experiment. The top row of images is overlaid with a simulation <i>without</i> a pinning radius. The bottom row of images is overlaid with a simulation <i>with</i> a pinning radius of $r_{pin} = 0.5$ reducing the dynamic contact angle from 160° to 120° when reached by the receding contact line.	247
6.9	Drop shapes from $We = 45$ ($\gamma = 2.31$) simulations overlaid onto a $We = 46$ ($\gamma = 2.23$) powder bed experiment. The moment of contact (at dimensionless time $t = 0.00$) is synchronised between the simulation and experiment. The top (bottom) row is overlaid with a simulation <i>without</i> (<i>with</i>) a pinning radius of r_{pin} which reduces the otherwise constant contact angle when passed over by the receding contact line. Images span from part way through retraction along the powder bed to the moment of encapsulation for the primary drop in the non-pinning simulation.	250

6.10	Drop shapes from $We = 61$ ($\gamma = 2.53$) simulations overlaid onto a $We = 62$ ($\gamma = 2.53$) powder bed experiment. The moment of contact (at dimensionless time $t = 0.00$) is synchronised between the simulation and experiment. The top (bottom) row is overlaid with a simulation <i>without</i> (<i>with</i>) a pinning radius of r_{pin} which reduces the otherwise constant contact angle when passed over by the receding contact line. Images span from part way through retraction along the powder bed to the moment of encapsulation for the primary drop in the non-pinning simulation.	251
6.11	Drop shapes from $We = 66$ ($\gamma = 2.59$) simulations overlaid onto a $We = 68$ ($\gamma = 2.61$) powder bed experiment. The moment of contact (at dimensionless time $t = 0.00$) is synchronised between the simulation and experiment. The top (bottom) row is overlaid with a simulation <i>without</i> (<i>with</i>) a pinning radius of r_{pin} which reduces the otherwise constant contact angle when passed over by the receding contact line. Images span from part way through retraction along the powder bed to the moment of encapsulation for the primary drop in the non-pinning simulation.	252
6.12	Coefficient of restitution as calculated for drop impact experiments onto rigid impermeable superhydrophobic substrates and superhydrophobic powder beds, for a wide range of impact Weber numbers. Also shown are data points from drop impact simulations <i>without</i> a pinning radius, for $35 \leq We \leq 87$. Coefficient of restitution is calculated as $\epsilon = \sqrt{h_R/h_0}$ for greatest rebound height, h_R , of the primary drop, and initial drop height h_0 (released from rest to obtain the associated impact Weber number).	254
6.13	Drop shapes from $We = 45$ ($\gamma = 2.31$) simulations (without a pinning radius) overlaid onto a $We = 52$ ($\gamma = 2.35$) powder bed experiment. The moment of contact (at dimensionless time $t = 0.00$) is synchronised between the simulation and experiment. Images span from part way through retraction along the powder bed to the moment of encapsulation for the primary drop in the non-pinning simulation.	255

7.1 Amended plot from Figure 2.34, with the original data points $\alpha_{encap}^{(spr)}$, $\alpha_{freeze}^{(spr)}$, and $\alpha_{final}^{(spr)}$ scaled to relate to the maximum contact area with the substrate, rather than the spreading area. The scaled parameters α_{encap} , α_{freeze} , and α_{final} are shown as functions of the spreading factor γ , calculated for powder bed experiments from Chapter 2, supplemented with data points from drop impact simulations (purple stars) conducted in Chapter 6. These stars indicate the value of α_{encap} for each simulation according to the line-of-best-fit for the existing experimental data points. For the $We = 87$ data point, the corresponding value of α_{encap} sits on the horizontal α_{freeze} line, indicating simultaneous encapsulation and deformed liquid marble formation. 259

7.2 Maximum visible drop radius and maximum contact line radius, both taken at the moment of maximum spread for clean drop impact simulations as a function of the impact Weber number. See Figure 2.30 for a representation of the drop spread diameter compared to the contact line diameter. 260

7.3 Plots from encapsulation to when the drop reaches the apex of its rebound from the substrate for simulations with $We = 40$ ($\gamma = 2.19$), with (top) a surface area plot showing the clean case, along with surface viscous simulations with $\beta = 0.05, 0.5, 5$, and also showing the spherical surface area. Also shown is (bottom) the ratio of the drop's primary and secondary axes for $\beta = 0.5$, overlaid with the same data taken from powder bed experiments with $We = 41$ ($\gamma = 2.16, 2.17$) representing the extreme cases for this We . Encapsulation in experiments is matched to occur at the start of the plot. 263

7.4	Plots from encapsulation to when the drop reaches the apex of its rebound from the substrate for simulations with $We = 45$ ($\gamma = 2.31$), with (top) a surface area plot showing the clean case, along with surface viscous simulations with $\beta = 0.05, 0.5, 5$, and also showing the spherical surface area. Also shown is (bottom) the ratio of the drop's primary and secondary axes for $\beta = 0.5$, overlaid with the same data taken from powder bed experiments with $We = 46$ ($\gamma = 2.23, 2.25$) representing the extreme cases for this We . Encapsulation in experiments is matched to occur at the start of the plot.	264
7.5	Drop profiles at encapsulation for $35 \leq We \leq 57$. The red outlines indicate the primary drop at the moment of encapsulation - any other drops in the simulation are ignored in the subsequent dynamics. The impact Weber number for each simulation or experiment is provided above each drop profile, with the spreading factor provided below. . .	268
7.6	Drop profiles at encapsulation for $61 \leq We \leq 87$. The red outlines indicate the primary drop at the moment of encapsulation - any other drops in the simulation are ignored in the subsequent dynamics. The impact Weber number for each simulation or experiment is provided above each drop profile, with the spreading factor provided below. . .	269
7.7	Drop profiles for deformed liquid marbles obtained for $51 \leq We \leq 78$. The impact Weber number for each simulation or experiment is provided above each drop profile, with the spreading factor provided below.	270
7.8	Plots for the liquid marble simulation arising from a $We = 40$ impact. (Top) The surface areas of both liquid-solid and liquid-gas interfaces, along with the encapsulation and freezing areas up to the point of encapsulation. Once encapsulated, the liquid-gas surface area for the surface viscous simulation is overlaid, and the (time dependent) encapsulation and freezing areas are continued accordingly. (Bottom) The dilatational surface viscous coefficient λ^s and effective surface tension σ_{eff} over the course of the simulation.	272

7.9	Plots for the liquid marble simulation arising from a $We = 45$ impact. (Top) The surface areas of both liquid-solid and liquid-gas interfaces, along with the encapsulation and freezing areas up to the point of encapsulation. Once encapsulated, the liquid-gas surface area for the surface viscous simulation is overlaid, and the (time dependent) encapsulation and freezing areas are continued accordingly. (Bottom) The dilatational surface viscous coefficient λ^s (log-scale) and effective surface tension σ_{eff} over the course of the simulation.	274
7.10	Drop profile comparisons from the moment of encapsulation between the simulation with $We = 45$ and $\gamma = 2.31$, and a powder bed experiment with $We = 57$ and $\gamma = 2.45$. The dimensionless time taken between images in the experiment is the same as that in the simulation, and $t = 3.38$ is the time of encapsulation for the primary drop in the simulation. The first six pairs of images show where the simulation and experiment match best (just post-encapsulation), and end with images showing that they eventually move out of phase with one another.	275
7.11	Surface area plot for the clean $We = 51$ simulation and overlaid surface viscous simulation post-encapsulation. (Top) Includes pre-encapsulation behaviour. (Bottom) Focus on the surface viscous case from encapsulation to liquid marble formation (both marked with stars). The lines for the liquid-gas surface area, encapsulation area and freezing area terminate at freezing; where the simulation ends.	277
7.12	Post-encapsulation plot of the dilatational surface viscous coefficient λ^s (log-scale) and effective surface tension σ_{eff} over the course of the $We = 51$ liquid marble simulation.	278
7.13	Drop profile comparison from the moment of encapsulation to the moment of deformed liquid marble formation between the simulation with $We = 51$ and $\gamma = 2.40$, and a powder bed experiment with $We = 52$ and $\gamma = 2.60$. The dimensionless time $t = 0.00$ corresponds to the moment the drop first comes into contact with the substrate.	279

7.14	Surface area plot for the clean $We = 61$ simulation and overlaid surface viscous simulation post-encapsulation. The encapsulation and freezing areas change according to the surface viscous simulation. (Top) Includes pre-encapsulation behaviour. (Bottom) Focus on the surface viscous case from encapsulation to liquid marble formation.	282
7.15	Post-encapsulation plot of the dilatational surface viscous coefficient λ^s (log-scale) and effective surface tension σ_{eff} over the course of the $We = 61$ liquid marble simulation.	283
7.16	Comparisons of interesting observed phenomena in the $We = 61$ ($\gamma = 2.53$) simulation, with examples of the same phenomena occurring in our drop impact experiments: (a) $We = 62$ ($\gamma = 2.53$) experiment showing ejection of a clean satellite followed by a continuous reduction in surface area to encapsulation in the right-most image. (b) $We = 62$ ($\gamma = 2.53$) experiment showing ejection of a satellite post-encapsulation. (c) $We = 68$ ($\gamma = 2.56$) experiment showing the ‘squashing’ of the drop surface leading to deformed liquid marble formation in the right-most image.	284
7.17	Surface area plot for the clean $We = 71$ simulation and overlaid surface viscous simulation post-encapsulation. The encapsulation and freezing areas change according to the surface viscous simulation. (Top) Includes pre-encapsulation behaviour. (Bottom) Focus on the surface viscous case from encapsulation to liquid marble formation.	286
7.18	Plot of the dilatational surface viscous coefficient λ^s (log-scale) and effective surface tension σ_{eff} over the course of the $We = 71$ liquid marble simulation.	287
7.19	Drop profile comparison from the moment of encapsulation to the moment of deformed liquid marble formation between the simulation with $We = 71$ and $\gamma = 2.66$, and a powder bed experiment with $We = 78$ and $\gamma = 2.69$. Encapsulation is on the far left, with the deformed liquid marble on the far right, and intermediary images between them. In both cases there is little variation between the shape at encapsulation and of the deformed liquid marble; a slight retraction of the drop neck into the bulk of the drop is sufficient to cause interfacial freezing. . .	288

7.20	Examples of deformed liquid marbles created at the moment of encapsulation in powder bed impact experiments, and the $We = 87$ ($\gamma = 2.83$) simulation. The deformed liquid marble in the simulation (outlined in red) forms as an immediate result of a satellite drop ejection.	289
7.21	Drop profiles showing (left) the drop at encapsulation for $We = 71$ ($\gamma = 2.66$) and the remaining images show the liquid marble created using $\beta = 0.5$, $\beta = 5$, and $\beta = 10$	291

List of Tables

Chapter 2 Experiments	33
2.1 Properties of de-ionised water (at 20°C) used in drop impact experiments.	35
2.2 Details for each experimental run.	38
Chapter 3 Mathematical Models	80
3.1 Dimensional scales for mathematical models.	88
Chapter 4 Boundary Integral Method and Boundary Element Method	117
4.1 Each row indicates the distribution of ϕ_j , r_j , and z_j at the start of the i -th local time step of the RK4 numerical scheme, for $j = 1, \dots, N + 1$, at time T	137

Acknowledgements

First and foremost, I would like to thank Dr. James Sprittles and Dr. Mykyta Chubynsky for their tireless support during the course of my PhD, and without whose continuing efforts this work would not have been possible. I also thank Dr. Jeremy Marston for his guidance during my research visit to Texas Tech University in Lubbock, Texas.

I owe many thanks to those involved in the MASDOC doctoral training centre, supported by EPSRC grant EP/HO23364/1, for their PhD course. I would also like to thank those involved in the Micro and Nano Flows Research Group, particularly those based at the University of Warwick, with whom I enjoyed an excellent collaborative environment in which to share ideas and discuss ongoing research in a variety of interesting fields relating to multiscale fluid dynamics.

I would like to thank those closest to me for their continued support throughout the course of my time at the University of Warwick. I thank Tommy-Joe and Sue for their unlimited patience and generous hospitality during my long period of study - you are both like family to me. I also thank Evonne, Howard, and Sophie, some of the most thoughtful and compassionate people I have ever had the privilege to meet, for the years of support, encouragement, and unbounded generosity.

Finally, I thank Frankie for being my inspiration for the last eight years, and to whom I dedicate this work. Without your love and unwavering support I would not be the man I am today, and without you continuing to act as a steady, guiding light that has led me through difficult periods of self-doubt, nothing accomplished here would have been possible. I look forward to our future adventures together once the world settles back down.

Declarations

I declare that, to the best of my knowledge, the content in this thesis is original and is formed by my own work, conducted under the supervision of Dr. James Sprittles.

This thesis is submitted to the University of Warwick in support of my application for the degree of Doctor of Philosophy. It has been composed by myself and has not been submitted in any previous application for any degree, and has not been submitted to any other higher education institution.

List of Abbreviations

BEM boundary element method

BIM boundary integral method

PVDF polyvinylidene flouride

VoF volume-of-fluid

Abstract

This thesis presents novel experimental and computational modelling investigations of liquid marble formation via drop impact onto a superhydrophobic powder bed. A mathematical model is formulated for this process, and following numerical implementation, the first reporting of simulations for liquid marble formation via drop impact is made, for a wide range of impact Weber numbers. These simulations are validated by comparison to drop impact experiments.

The adhered particle coating on the surface of the impacted drop creates energy dissipating effects, which are captured by a model based on incorporating a surface viscosity with a dominant dilatational component. Following physically-motivated simplifying assumptions, surface viscous effects appear via a spatially independent effective surface tension, which differs from the usual value only after the drop is completely encapsulated in particles. Following analysis of the experimental data, a novel relationship is identified between the maximum spreading diameter of the drop with the powder bed, and the surface area of the drop when it becomes encapsulated, and when (and if) it becomes a deformed liquid marble due to particle jamming at its interface. This relationship is used in the model to provide a constitutive equation for the surface viscous effects, and to identify encapsulation and deformed liquid marble formation in simulations.

Additionally, a novel third-order damped oscillator model is derived for a suspended inviscid oscillating drop experiencing the effects of a dilatational component of surface viscosity. This model predicts that with a sufficiently large dilatational surface viscous coefficient, a transition from overdamped to underdamped motion occurs over the course of a drop's oscillations, which is not predicted in existing (linear) approximations, and is validated following numerical simulations. For small amplitude oscillations, an analytic solution for the motion in the overdamped limit is derived, and an analogue of the effective surface tension is presented.

Chapter 1

Introduction

The primary focus of this thesis is the development of a novel mathematical model that describes the formation of ‘liquid marbles’ via liquid drop impact onto beds of solid superhydrophobic powder particles. The models presented in this thesis are justified empirically from experiments conducted for this body of work, along with observations made in existing research. This thesis provides, to our knowledge, the first report of numerical simulations for liquid marble formation via drop impact. In addition, a novel third-order damped nonlinear oscillator model is developed and presented, which describes (approximately) the dynamics of suspended inviscid drop oscillations with effects of dilatational surface viscosity.

We begin this chapter by introducing liquid marbles; describing their structural and dynamic properties, their applications to solving real-world issues, and open problems that remain unexplored. The motivations for the research undertaken in this thesis are then outlined, followed by a discussion of topics related to important aspects of liquid marble formation via drop impact. These topics cover the effect of a particle-laden interface on drop dynamics, and the interactions between a liquid drop and deformable powder bed following a high speed impact. Also included are justifications for rheological assumptions and simplifications that are made during the development of a mathematical model, and the implementation of a numerical simulation. This chapter concludes with an outline of the organisation of the remainder of the thesis.

Oral presentations on the research presented in this thesis were given at workshops organised by the ‘Micro & Nano Flows’ research group on the 13th of December 2016 at the University of Warwick, the 23rd of May 2017 at The University of Edinburgh, and the 19th of December 2018 at the University of Glasgow. Additionally,

an oral presentation was given at the ‘UK Fluids Network Special Interest Group on Drop Dynamics’ workshop on the 19th of September 2018 at the University of Oxford.

1.1 Liquid Marbles

The term ‘liquid marble’ describes the object formed when a liquid drop is completely encapsulated by a shell-like structure, typically consisting of solid particles, that prevents the interior liquid from interacting with nearby solid surfaces and other liquids [1]. In general, the shell of a liquid marble prevents the adhesion of the interior drop’s molecules to those of a solid substrate (that is, it prevents ‘wetting’), instead providing the liquid marble with an effective contact angle of 180° with that substrate, meaning it can be made to move freely without small volumes of the interior liquid breaking off and remaining on the substrate [1, 2].

In most cases, the solid particles adhered to the surface of a liquid drop, which constitute the shell of a liquid marble, are hydrophobic (‘water-repelling’), and are much smaller than the drop itself. The first liquid marbles manufactured consisted of small amounts of liquid (with volumes of $1\text{-}10\text{mm}^3$ of either water, glycerol, or a water-glycerol mixture) coated with lycopodium grains (chemically treated in order to increase their hydrophobicity) of typical size $20\mu\text{m}$ [1]. The experiments from [1] showed that forming a liquid marble allowed liquids of varying viscosities to be transported along an otherwise wettable solid substrate at high speeds, with little imposed force. A liquid marble from [1] is shown in Figure 1.1 at rest on a glass plate, which the interior liquid would wet in the absence of the surrounding shell.



Figure 1.1: Liquid marble composed of a water drop (radius 1mm) and a shell formed of hydrophobic lycopodium grains (typical size $20\mu\text{m}$), at rest on a glass plate. Obtained from [1].

We will now discuss existing research on the processes behind the formation of liquid marbles (including how they are created in experiments), the structure of the encapsulating shell, their properties, and their varied applications. Existing research focuses primarily on liquid marbles that retain a spherical shape in the absence of external forcing, with less attention paid to the formation and properties of ‘deformed’ liquid marbles, that is, those that attain an arrested non-spherical shape after surface oscillations have decayed. Examining the process of liquid marble formation via drop impact is the focus of this thesis, with particular attention paid to the formation of deformed liquid marbles. This section concludes with a description of existing research involving deformed liquid marbles and the motivations for this particular project. An interested reader is directed to prominent review articles [3–10] for further information on liquid marbles.

1.1.1 Formation

When a sufficiently small¹ solid particle comes into contact with a fluid-fluid interface (at equilibrium) from the bulk of either fluid, the adsorption of that particle to the interface is preferable (in terms of reducing the total surface free energy of the system) as long as the contact angle between the particle and either fluid is not 180° [3, 11]. In the context of liquid marble formation, for liquid drops (with sizes on the order of

¹Small enough such that the fluid-fluid interface with which it interacts appears flat at the length-scale of the particle diameter.

1mm) lying in an immiscible fluid, contact with small solid particles (with sizes on the order of 1nm-10 μ m) that are neither completely wetting nor completely nonwetting (that is, with contact angles of neither 0° nor 180° with the liquid, respectively) will cause the particles to adhere to the drop’s fluid-fluid interface. Although the particles adhering to the surface of a liquid drop do not strictly require a contact angle of greater than 90° to form an encapsulating shell, this is preferred as it increases the distance between the interior liquid and anything outside the liquid marble (see Figure 1.6).

The easiest method of forming liquid marbles is therefore one in which the number of particle-liquid contacts is maximised in the easiest way; typically achieved by depositing a liquid drop onto a bed of hydrophobic particles and rolling it around until a full coating has been attained [3] (see Figure 1.2). Liquid marbles have also been formed by drop impacts onto hydrophobic powder beds [12–17] (see Figure 1.3), high-speed mixing of liquids and hydrophobic particles [18], applying a magnetic field to direct a magnetic hydrophobic powder to ‘collect’ a drop that has wetted a hydrophilic substrate [19], inducing condensation on rigid superhydrophobic substrates that have been coated in hydrophobic particles [20] (see Figure 1.4), and destabilisation of granular rafts formed at oil-water interfaces [21] (see Figure 1.5). Liquid marbles have also been observed in nature; with the hydrophobic wax-like secretions of gall aphids coming into contact with and encapsulating its liquid excrement (honeydew) upon exiting their bodies [22, 23].

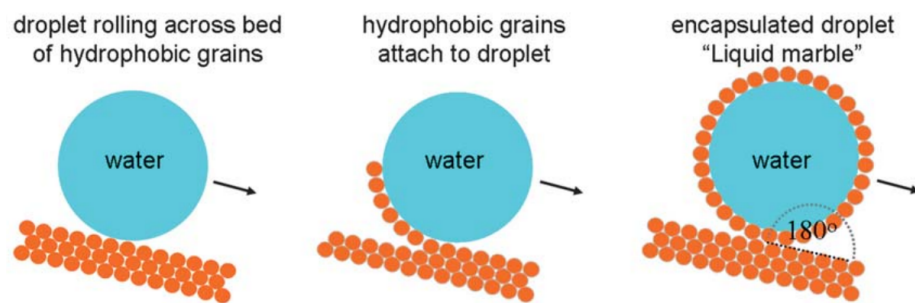


Figure 1.2: Schematic for the formation of a liquid marble from a drop rolling on a hydrophobic powder bed. Obtained from [3].

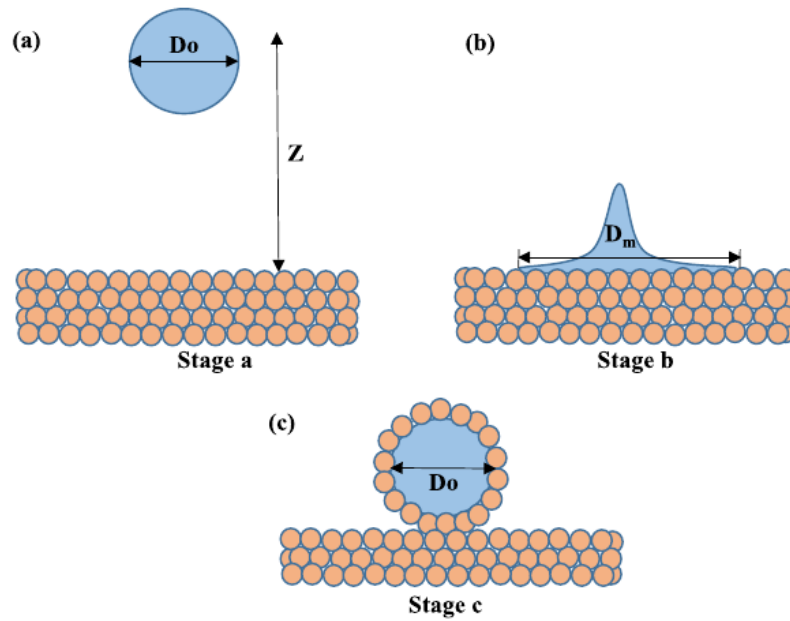


Figure 1.3: Schematic of liquid marble formation via drop impact: a liquid drop (a) released from rest above a powder bed, (b) reaching a maximum spreading diameter, and (c) forming a liquid marble following retraction. Obtained from [16].

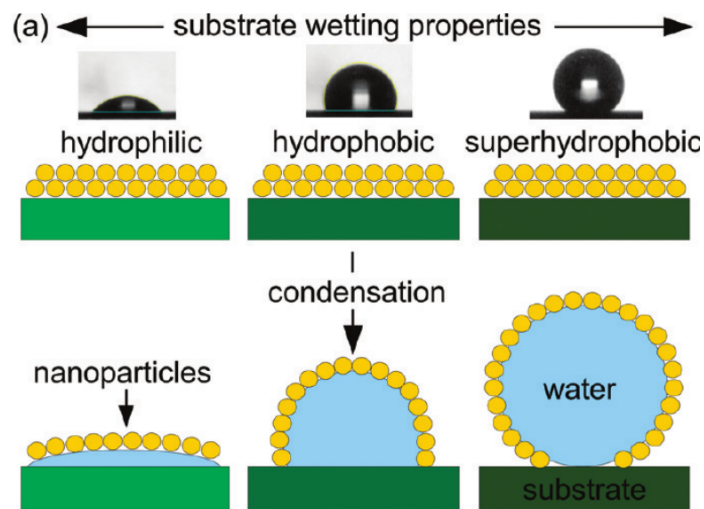


Figure 1.4: Schematic showing the effect of substrate hydrophobicity on liquid condensation when the substrate is coated with superhydrophobic nanoparticles. Liquid marbles can form when the underlying substrate is superhydrophobic. Obtained from [20].

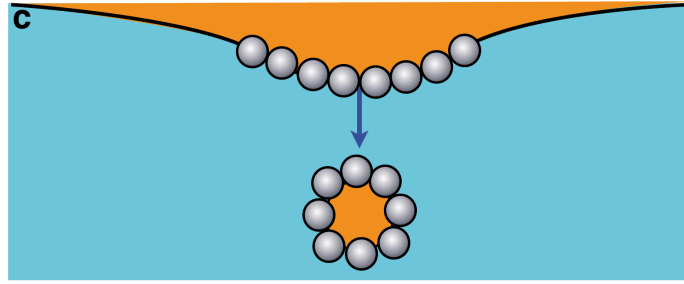


Figure 1.5: Schematic showing a formed oil liquid marble immersed in water due to the destabilisation of a granular raft lying at an oil-water interface. Obtained from [21].

1.1.2 Structure of the Shell

As previously mentioned, the defining property of a liquid marble is that the exterior shell prevents interactions of the interior liquid with other liquids and solid surfaces [1, 11]. For a liquid marble at rest on a solid substrate, what would have been the liquid-solid interface with the drop wetting the substrate is replaced by a collection of solid-solid contacts (particles touching the substrate) with pockets of gas between them that separate liquid-gas interfaces from the solid substrate [11, 24] (see Figure 1.6).

For many liquid marbles, their surfaces appear similar to the examples in Figure 1.7, where the surface of a liquid marble coated with $30\mu\text{m}$ lycopodium grains exhibits vast gaps of free liquid-gas interface [11] between particle clusters, and similarly, where the surface of a liquid marble coated with 130nm polyvinylidene fluoride (PVDF) nanobeads shows tall aggregates of the coating separated by wide clearings of the liquid-gas interface [24]. In cases where the particles used to form the shell are mono-dispersed (that is, with a single consistent size and shape) and form a close-packed monolayer on the drop interface, the surface structure can be reminiscent of a hexagonal lattice [25], in which there still remain small pockets of liquid-gas interface visible between the particles (see Figure 1.8).

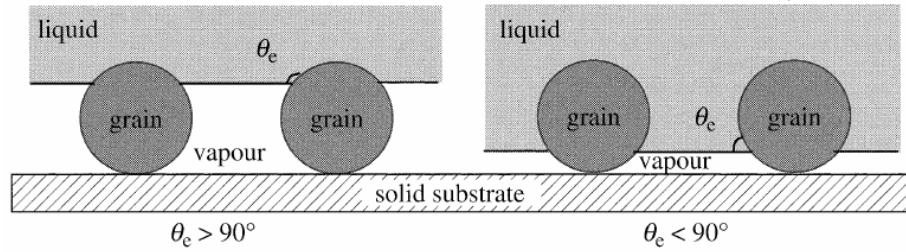


Figure 1.6: Schematic representation of adhered (left) hydrophobic, and (right) hydrophilic particles at a liquid-gas interface, with the liquid-solid interface between the liquid and solid substrate replaced by multiple solid-solid contacts and pockets of gas separating the liquid-gas interface from the solid substrate. Obtained from [11].

The structure of a liquid marble shell is therefore similar to that of a superhydrophobic surface; where air pockets are trapped between small solid pillars, which reduces the liquid-solid contact area (and increases the apparent contact angle) of the liquid lying atop the substrate. Unlike drops on a superhydrophobic surface, where nonwetting is caused by the surface texture of the solid substrate (inducing a so-called ‘Cassie-Baxter’ state between a drop and the substrate [26]), for liquid marbles, this texture conforms to the shape of the drop. This conceptual similarity is discussed in [6], with a novel suggestion that superhydrophobic surfaces may be constructed using sufficiently weak links between the pillars and the substrate such that surface tension forces would detach the pillars to form an encapsulating shell (hence forming a liquid marble, see Figure 1.9).

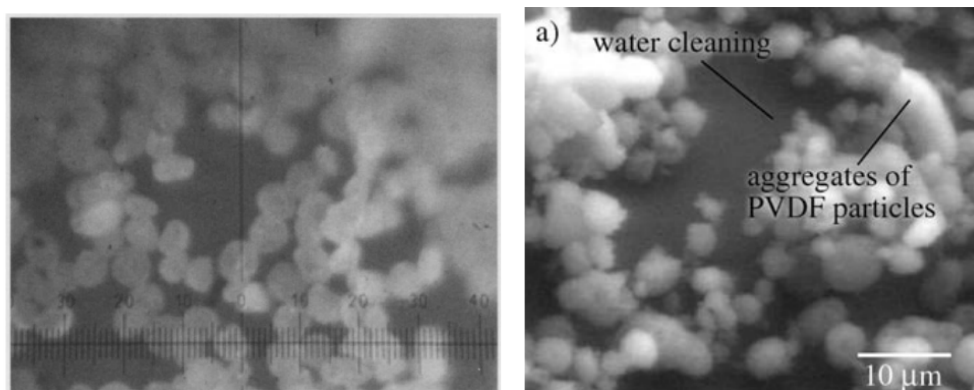


Figure 1.7: Close-up images taken of the surface of water liquid marbles, coated in (left) 20 μ m lycopodium grains: obtained from [11], and (right) 130nm PVDF nanobeads: obtained from [24].

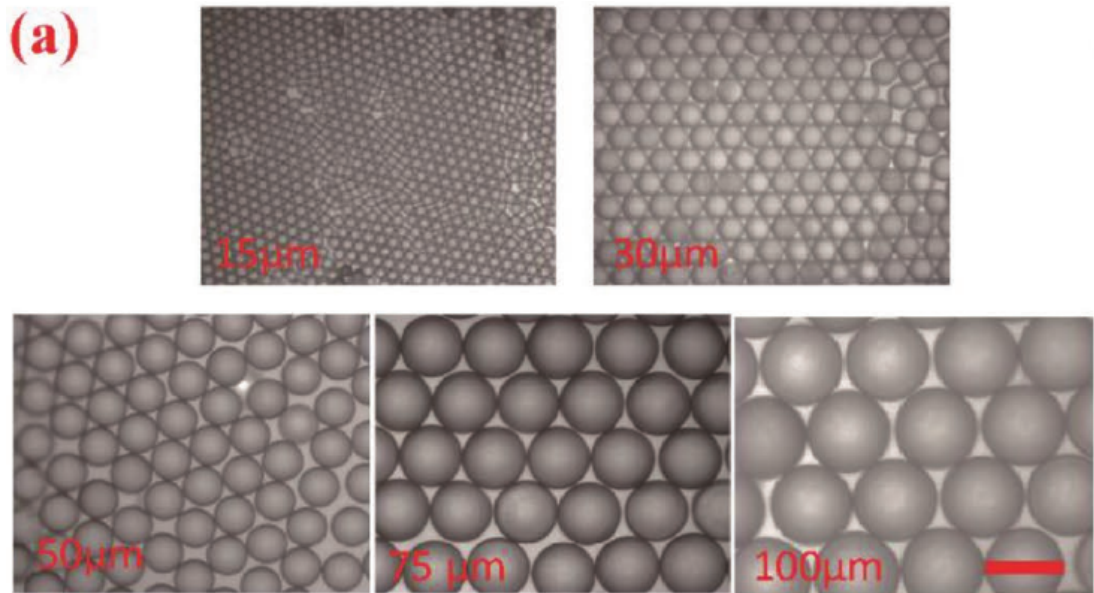


Figure 1.8: Close-up images taken of the surface of water liquid marbles coated in a mono-layer of mono-dispersed polystyrene particles of sizes $15\mu\text{m}$, $30\mu\text{m}$, $50\mu\text{m}$, $75\mu\text{m}$, $100\mu\text{m}$. Obtained from [25].

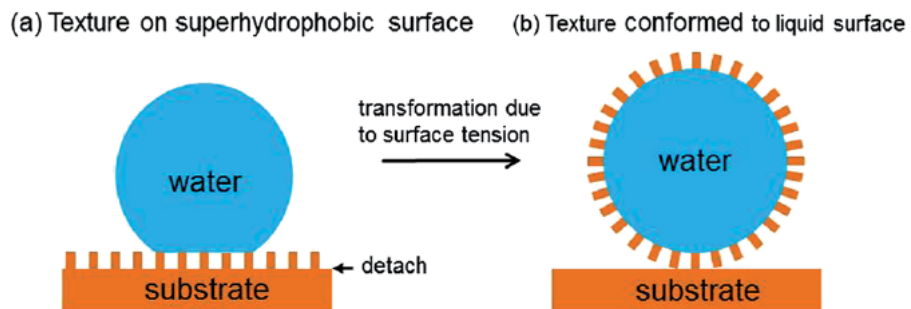


Figure 1.9: Schematic of a proposed liquid marble formation process; with (a) a liquid drop lying atop the pillars of a structured superhydrophobic solid surface, and (b) the pillars detaching from the substrate due to surface tension forces from the drop and assembling a conformal surface texture that becomes the liquid marble shell. Obtained from [6].

1.1.3 Properties

Liquid marbles exhibit numerous properties that make them useful in a wide range of emerging applications (see §1.1.4). Provided here is an overview of some of these properties.

- *Ability to float on liquid surfaces:* The structure of the encapsulating shell prevents liquids as well as solids from interacting with the interior of a liquid marble, meaning they can float atop liquid surfaces [11, 24] (see Figure 1.10). The difference in surface tension between the liquid marble interior and that of the supporting liquid surface is important in determining the lifetime of a floating liquid marble; a lower surface tension of the supporting liquid can make it energetically favourable for particles to detach from the surface of the liquid marble and adhere to the surface of the supporting liquid [27].
- *Reduced or enhanced evaporation rates:* The gaps between adhered particles in the encapsulating shell permit the exchange of gas between the interior and exterior of a liquid marble. The evaporation rate for a liquid marble depends on the size and hydrophobic properties of the particles constituting the shell, as well as the choice of liquid interior [28, 29]. Water liquid marbles (radius 1mm) with a shell consisting of polytetrafluoroethylene (PTFE) powder (of size 5-6 μ m) have been shown to reduce the evaporation rate by 25-40% compared to liquid drops of the same volume [30], and a graphite shell has been shown to produce marbles that exhibit double the lifetime of liquid drops of the same volume [31] by reducing the evaporation rate. Liquid marbles can also exhibit a *shorter* lifetime than liquid drops [32], whereby a higher evaporation rate emerges due to an increased liquid-gas surface area following ‘buckling’ of the powder shell (see example of buckling in Figure 1.11).
- *Elastic properties:* Liquid marbles can be modelled as volumes of liquid encapsulated by a membrane which provides elastic properties [33]. The robustness and elastic properties of liquid marbles under compression between parallel plates, impact with a solid substrate, and impact with other liquid marbles have been the subject of much research [11, 19, 25, 33–38].
- *Effective surface tension:* Liquid marbles have been modelled as having an ‘effective surface tension’; a modification of the existing surface tension of the interior liquid, that incorporates the solid particle-particle interactions in the encapsulating shell (be they capillary, hydrostatic, or electrostatic in nature, among other possibilities) [12, 27, 34, 38–46]. The effective surface tension has been shown to be predictive of the lifetime [29] and robustness of a liquid mar-

ble [47]. Multiple methods have been developed for calculating the effective surface tension for liquid marbles, and particle-laden interfaces in general, in both static and dynamic settings (see a recent review article [10]). The effective surface tension for water liquid marbles (volumes 10-1000 μL) coated in a powdered polymerised perfluoroethyl alkyl acrylate monomer mixture (P-Zonyl-TAN) (sizes 8 μm , 20 μm , and 60 μm) has been shown to decrease as adhered particle size is increased [29]. This reduction in effective surface tension was reported to describe an increase in repulsive solid particle-particle forces, which correlated to an observed decrease in the lifetime for a liquid marble resting upon liquid surfaces, due to the widened gaps between adhered particles allowing earlier coalescence of the liquid phases. An effective surface tension appears in the models for liquid marble formation given in Chapter 3, but arises as a consequence of modelling assumptions and is independent of the existing notions described here.

- *Amenability to manipulation:* Liquid marbles play an important role as transportable liquid micro-reservoirs [1], and can be easily moved (without leakage of the liquid interior) along inclined solid substrates through the work of gravity alone, even when the liquid interior has a viscosity much greater than water [1, 11]. There are many examples of magnetic materials being used to construct the liquid marble shell, so that an applied magnetic field actuates motion of the liquid marble along solid substrates or liquid surfaces [19, 41, 48–51], or lifts the liquid marble into the air without any guiding surface [43]. Actuation of liquid marbles via magnetic fields has also been conducted in cases where the liquid, rather than the shell, is magnetic; examples include the use of ferrofluid [52] and liquid metal [45, 53] for the interior drops. Liquid marbles have also been controlled using electric fields [11, 39, 54, 55], and with acoustic waves [56]. An interested reader is directed to a review in [7] on the manipulation of liquid marbles, for further information.

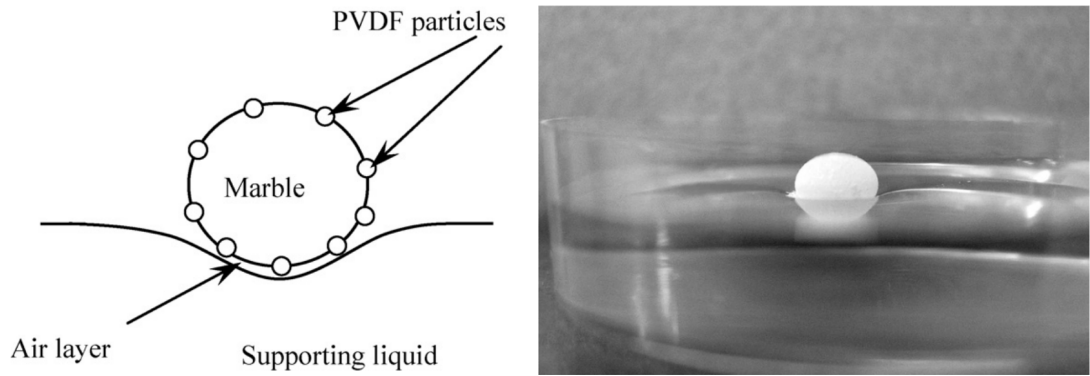


Figure 1.10: (Left) Diagram showing a liquid marble lying atop a liquid surface, with pockets of air between adhered particles separating the interior of the liquid marble from the supporting liquid, obtained from [27]. (Right) Experimental image of a distilled water liquid marble (volume $120\mu\text{L}$) coated in PVDF particles (size 130nm) floating on a distilled water surface, obtained from [57].

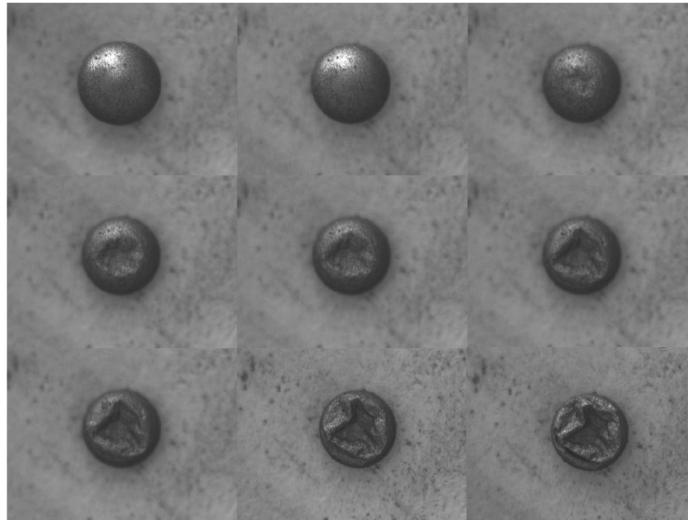


Figure 1.11: Experimental images showing the evaporation process of a water liquid marble (volume $5\text{-}10\mu\text{L}$) coated in graphite powder (size $2\text{-}30\mu\text{m}$), with buckling of the encapsulating shell following sufficient evaporation of the interior liquid. Obtained from [31].

1.1.4 Applications

Liquid marbles have undergone significant study, and many viable applications to real-world problems have been proposed. Discussed here are some examples highlighting their versatility. An interested reader is directed to review articles describing

applications of liquid marbles [3, 6, 9, 58, 59] for further information.

Micro-Reactors

Liquid marbles can be used as micro-scale reactors for purposes involving instigating chemical reactions and enabling biological processes within the marble interior. Described here are the liquid marble properties that promote their suitability as micro-reactors, techniques that have been developed to aid in conducting micro-reactor experiments, and examples of application within existing research.

As discussed in §1.1.3, the interior of a liquid marble can be prevented from interacting with liquids and solid surfaces on the other side of the encapsulating shell, depending on the characteristics of the particles that constitute the shell; meaning an interior aqueous solution can be kept safe from contamination, including the prevention of biohazard exposure [59]. The chemical characteristics of the marble shell play an important role in micro-reactor applications; either by remaining chemically inert [31] to allow chemical reactions to occur within the interior unimpeded, having bio-compatible properties [50] that aid the growth of biological cultures, or by themselves acting as a catalyst that instigates chemical reactions within the interior liquid [60–62]. The ability to create bespoke encapsulating shells that extend the lifetime of the liquid marble or increase the robustness due to external forcing allow a wide range of micro-reactor experiments to be conducted. Further, the three dimensional medium of the marble interior represents a realistic environment for biological processes, and the wide range of volumes for liquid marbles (typically 10-1000 μ L) also permits a plethora of micro-scale phenomena that can be observed [59].

Regarding the mechanics of micro-reactors experiments, liquid marbles with magnetic particles forming the encapsulating shells have been made to open and close reversibly upon application of a magnetic field [19, 43]. Placing a magnet *beneath* a liquid marble with a magnetic shell (and solid substrate onto which it is resting) can cause the adhered particles within the shell to be pulled downwards towards the magnet, moving tangentially along the liquid surface, opening a clean liquid-gas interfacial region (see Figure 1.12). This provides a mechanism for observation of processes occurring within the interior drop, which has also been achieved with transparent liquid marbles created with fumed silica nanoparticles [32], but with the additional ability to add or remove biological and chemical agents during

experiments without having to ‘break through’ the shell. The controlled opening and closing of the encapsulating shell has also been conducted for silicone oil liquid marbles coated in a multitude of spherical non-magnetic nanoparticles (including for silica, dyed polyethylene, and clay) using applied electric fields [63]. Alternatively, two liquid marbles with magnetically opened shells can be moved into contact with one another and merged into a larger liquid marble; providing a convenient method of combining two aqueous solutions [19]. Controlled rotation of liquid marbles with a magnetic shell [64] has also been achieved experimentally, and can aid in the mixing of chemical and biological components within the marble interior.

Examples of applications for liquid marbles as micro-scale bio-reactors include, but are not limited to: human blood typing [65], investigating the growth of lung cancer stem cells [66], engineering three dimensional toroidal biological tissues [67], and cultivation of micro-organism cultures [68]. As micro-scale chemical reactors, applications include the synthesis of: graphene nanocomposites [69], Janus particles (that is, particles with regions of differing hydrophobicities) [70, 71], and colour pigment [72], and also the instigation of chemical reactions brought on by the particle coating, such as reduction of methylene blue from the interior aqueous solution [61, 62], and the hydrogenation of maleic acid in dry water [60].

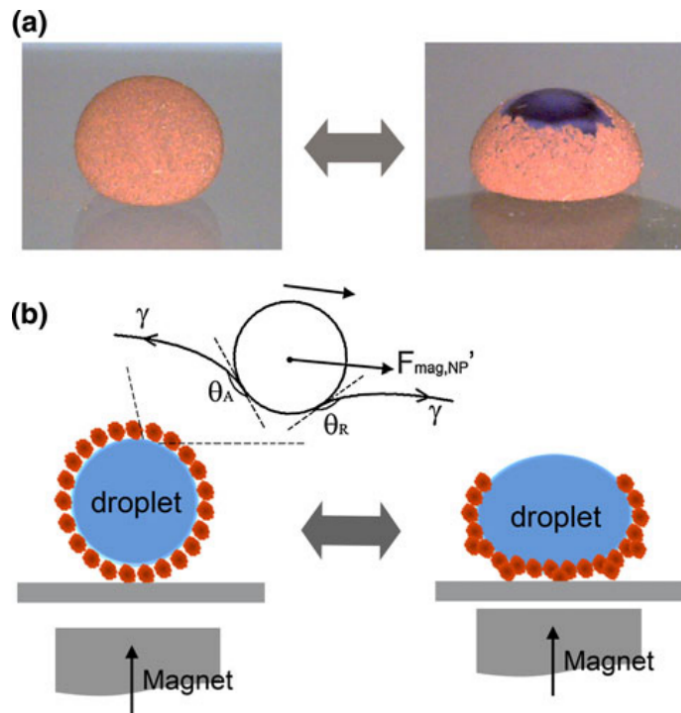


Figure 1.12: Opening of the magnetic shell of a liquid marble to expose the liquid interior, shown in (a) an experiment, and (b) a diagram. A magnet is placed beneath the underlying substrate, pulling the magnetic particles in the shell of the liquid marble towards the magnet, tangentially along the liquid-gas interface. Obtained from [43].

Detecting Contamination

Liquid marbles can be used to detect contamination of a liquid surface, or within a surrounding gas, without taking samples of these phases. Contamination detection typically relies on the exploitation of certain properties of the particles forming a liquid marble's encapsulating shell, and with specific particle coatings chosen to best detect specific contaminants. The free exchange of gases through the encapsulating shell of a liquid marble has led to the development of 'gas-sensing' liquid marbles; purposefully chosen combinations of a liquid interior and adhered particles that cause chemical reactions which act as visual indicators of exposure to different chemicals, such as ammonia and hydrochloric gases [73].

Water liquid marbles (volume $10\mu\text{L}$) with a PVDF (size 130nm) coating have been used to detect contamination of a water surface [27]. Figure 1.13 shows a liquid marble at rest upon an uncontaminated water surface, and also the remains of a

liquid marble that has burst upon contact with a thin silicone oil film. The oil film sufficiently reduces the surface tension of the supporting water surface such that it is energetically favourable for the particles adhered to a liquid marble to instead detach from the drop and adhere to that surface. Liquid marbles have also been used to detect the pH of supporting liquid surfaces, making use of manufactured particles that change from hydrophobic to hydrophilic when put into contact with a low pH (acidic) material [74]. Such liquid marbles were shown to lie at rest upon liquid surfaces with neutral to high pH (alkaline), and collapse upon the introduction of low pH substances.

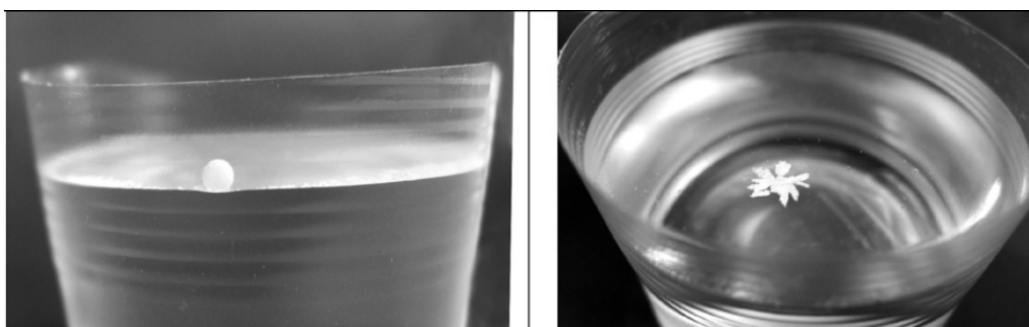


Figure 1.13: Revealing the contamination of a water surface with a water liquid marble coated in PVDF powder particles. (Left) Liquid marble at rest on an uncontaminated water surface. (Right) PVDF particles lying upon a water surface coated in silicone oil following the destruction of a floating liquid marble. Obtained from [27].

Additional Applications

Novel and interesting uses for liquid marbles continue to be devised. A recent article [75] describes the production of multi-scale liquid marbles that mimic the structure of a mosquito eye (see Figures 1.14-1.15). The liquid marble consists of an oil drop (size 0.5-5mm), coated with a close-packed hexagonal lattice monolayer of ‘microlenses’, which are smaller transparent oil liquid marbles (size 25-250 μ m) each with a non-close-packed hexagonal monolayer of silica nanoparticles (size 120-600nm). The resulting macro liquid marble is referred to as a ‘compound lens’ and contains a hierarchy of characteristic length-scales that closely resemble the eyes of mosquitoes and similar insects, as well as matching optical and anti-fogging properties. Given each compound lens is a liquid marble (with a coating of smaller liquid marbles),

they are easily transportable and can be made to form stationary arrays, with each macro liquid marble led to pre-placed patches of liquid with which the liquid marble coalesces, while retaining a monolayer coating of micro-lenses at its interface. Patch shapes and wetting properties of the underlying substrate can be varied, and an additional immiscible liquid phase can be added, leading to a variety of compound lens configurations that can differ in optical properties (see Figure 1.15). This study presents a development of liquid marbles for use within vision system applications, including medical imaging, reconnaissance, and robotics.

Other applications of liquid marbles include but are not limited to: foam stabilisation [76], ‘dry water’ storage [18], production of ‘designer particles’ from hollow encapsulating shells following evaporation of the interior liquid [40], oil and water separation [21, 49], reduction of plastic waste in DNA processing [77], and collision-based computing [51].

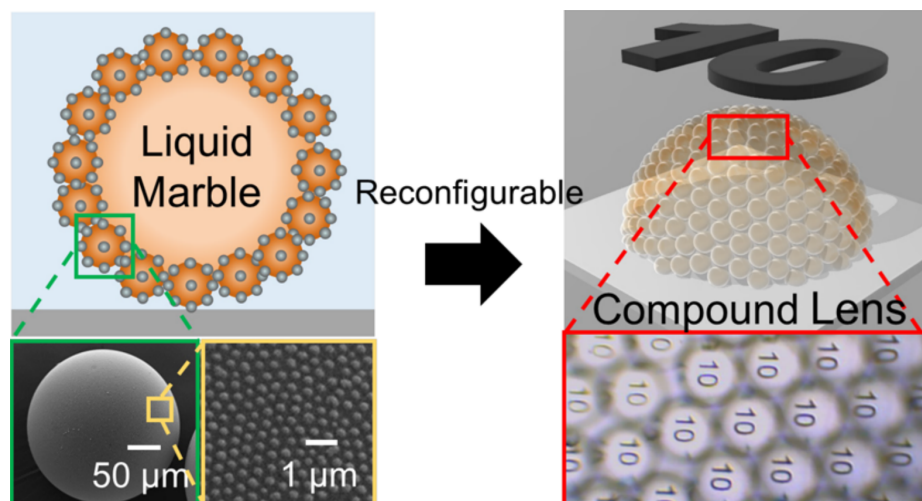


Figure 1.14: (Left) A macroscopic oil liquid marble with an encapsulating shell of transparent microscopic oil liquid marbles, each with a hydrophobic silica nanoparticle shell. (Right) A macroscopic oil liquid marble reconfigured into a hemisphere following forced wetting on a patch of liquid, exhibiting properties of the macroscopic marble which are similar to a compound lens. Obtained from [75].

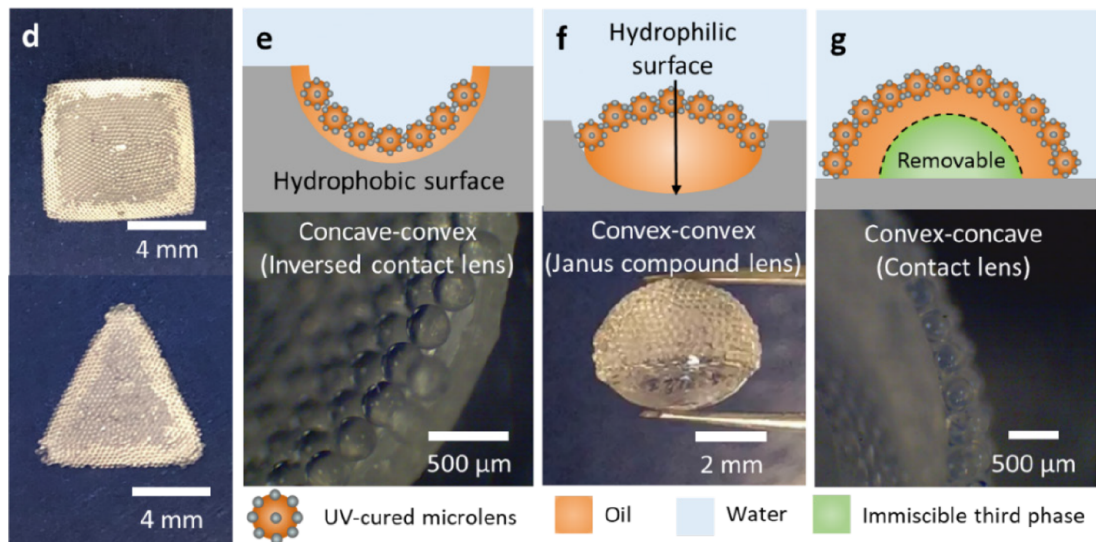


Figure 1.15: (d) Optical microscope images demonstrating the control of the shape of a deposited macroscopic oil liquid marble. Cross-sectional diagrams and images from experiments of compound lens (macroscopic oil liquid marble) deposition on a wettable patch on a (e) hydrophobic and (f) hydrophilic substrate, and (g) the introduction of an immiscible third fluid phase within the deposited compound lens. Obtained from [75].

1.1.5 Deformed Liquid Marbles

We now focus attention on ‘deformed liquid marbles’, which are liquid marbles that maintain arrested non-spherical shapes once external forcing is removed and surface oscillations have decayed. They form as a result of adhered particles on the surface of the liquid marble approaching close-packing, which ‘jams’ the interface and prevents any further reduction in drop surface area [13–15]. This is in contrast to liquid marbles with sufficiently sparse particle coatings (which have primarily been discussed up to now), where the adhered particles can freely rearrange during drop oscillations and (importantly) as the surface area reduces to that of a sphere (the minimal surface energy state). The formation and properties of deformed liquid marbles have gained considerably less attention than their un-deformed counterparts. Provided here is an overview of the extent of current research on deformed liquid marbles (given primarily by [13–15]), and the open questions that provide avenues for future research.

Deformed liquid marbles can be created by impacting a liquid drop onto a hydrophobic powder bed at sufficiently high speeds, the first examples of which were

documented and described in [13, 14]. For experiments with an impact speed above a critical threshold, it was found that during post-rebound oscillations, the particles adhered to the surface of the drop during contact with the powder bed were able to reach a jammed state, whereby further change in drop shape was prevented, and the drop surface was immobilised (described as ‘freezing drop oscillations’). The liquid marbles maintained whatever shape they were in at the moment of jamming for the remainder of their time in the air, until they fell back to the powder bed. Past this threshold, the shapes of deformed liquid marbles tend to become more elongated and cylindrical [13, 15]; moving further away from a spherical shape until a high enough impact speed is reached for prompt splashing to occur upon contact with the powder bed, after which point the arrested shapes are irregular due to an unstable radial ejection of satellite droplets on the substrate.

In Figure 1.16, we see the profiles of deformed liquid marbles as compared to a spherical liquid marble, all of which were obtained through the same set of drop impact experiments onto superhydrophobic powder beds, with different impact speeds [13]. These experiments were conducted using pure water drops with equilibrium diameters of $D_0 = 2.1\text{mm}$, and hydrophobised glass beads with mean diameter $\bar{d}_p = 31\mu\text{m}$ and apparent contact angles of $160\text{-}170^\circ$ with water. A critical impact speed of $U_0^* = 1.56\text{m/s}$ was identified as the point of transition from spherical to deformed liquid marbles being created upon rebound.

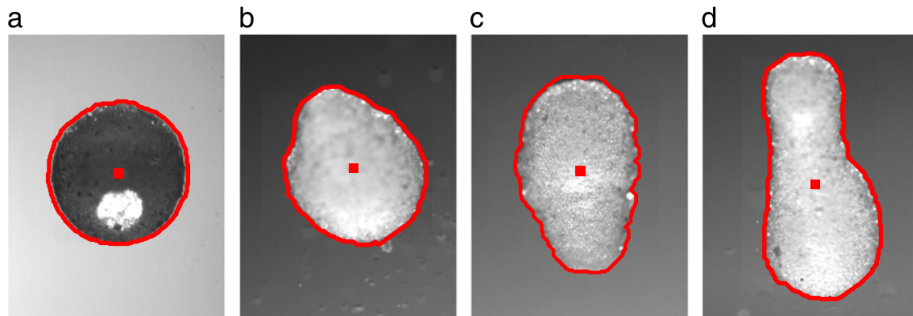


Figure 1.16: Profiles of liquid marbles obtained from water drop impact experiments onto a superhydrophobic powder bed, for a drop with initial diameter $D_0 = 2.1\text{mm}$, and for impact speeds of (a) $U_0 = 1.14\text{ m/s}$, (b) $U_0 = 1.56\text{ m/s}$, (c) $U_0 = 1.66\text{ m/s}$, (d) $U_0 = 1.84\text{ m/s}$. Red lines and markers added by the original author. Obtained from [13].

Further experiments [15] found that critical impact speeds for deformed liquid

marble formation (when using water drops) depend primarily on the diameter of the impacting drops, with no quantifiable dependence on particle size; the critical impact speeds were found to be $U_0^* = 2.1\text{m/s}$, $U_0^* = 1.5\text{m/s}$, and $U_0^* = 1.3\text{m/s}$ for initial drop diameters of $D_0 = 1\text{mm}$, $D_0 = 2\text{mm}$, and $D_0 = 3\text{mm}$, respectively. The particles used in these experiments were hydrophobised glass beads, with a variety of sizes ranging from $\bar{d}_p = 25\text{-}500\mu\text{m}$. By considering the Weber number [78] (a dimensionless parameter that provides a measure of the relative importance of fluid inertia and surface tension) at the moment of impact, given by

$$\text{We} = \frac{\rho U_0^2 D_0}{\sigma}, \quad (1.1.1)$$

for liquid density ρ , and surface tension of the liquid-gas interface σ , the critical impact speeds given above collapse into a critical impact Weber number range of $\text{We}^* = 60\text{-}70$. Deformed liquid marbles have also been created with higher viscosity liquids [14], though less research has been conducted on their formation, and a similar critical threshold has not been reported. Note that while the length-scale given in the definition of the Weber number (1.1.1) is the diameter of the drop, the characteristic length-scale for the mathematical models presented in Chapter 3 is the drop radius; the diameter is presented here for consistency with existing research on this topic.

Scaling laws have been developed that describe a monotonic increase in maximum spreading diameter of a drop impacting a hydrophobic powder bed, with an increase in the impact Weber number, based upon experimental data and energy-based arguments [13, 15, 16]. Therefore, an increased We means an increased maximum spreading diameter, which corresponds to a greater maximum contact area between the drop and substrate, and so a larger number of particles that come into contact with, and adhere to, the drop surface. Reaching a critical We threshold for deformed liquid marble formation can therefore be re-imagined as adhering a critical mass of particles on the free surface that will approach sufficiently close-packing, so as to jam the interface upon rebound from the powder bed, before the minimum surface area shape can be attained. However, how much powder is required to encapsulate a drop, and to create a deformed liquid marble remains an open question [15, 16]. Although spreading diameters can be determined visually in experiments, it is difficult to gauge how much powder has actually been adsorbed to the drop interface, and this is complicated further by the ejection of satellite droplets during rebound from the powder bed (as well as splashing while on the powder bed) which remove volumes of liquid

and masses of adsorbed powder particles from the primary drop.

Estimates have been made regarding a necessary condition for drop encapsulation, namely a *minimum* value of the maximum contact area between the drop and powder bed, after which encapsulation *can* occur. A condition on the maximum contact area D_{\max} deemed necessary for encapsulation in [15] postulates that

$$D_{\max} > 1.67D_0. \quad (1.1.2)$$

This is based on a calculation of the minimum (spherical) surface area of liquid drops that have been encapsulated in powder bed impact experiments, taking into account volume lost due to the ejection of un-coated satellite drops. A similar condition in [16] is postulated *a priori*, and compares directly the surface area of a sphere with the initial volume of the impacting drop, with the maximum contact area (idealised as an axisymmetric circular disc) to find a necessary condition of

$$D_{\max} \geq 2D_0, \quad (1.1.3)$$

for encapsulation. To our knowledge, further study demonstrating a relationship between the maximum contact area and the surface area of the drop *at the moment* of encapsulation remains unreported. There has not been a similar condition reported for a spreading diameter that, once exceeded, yields deformed liquid marbles, though it is asserted in [15] that a jammed interface requires “that the liquid free surface vanish entirely”, that is, encapsulation is necessary for the creation of deformed liquid marbles.

It is postulated in [15] that the rate of change of surface coverage in adhered particles may influence the formation of deformed liquid marbles and the shapes that are exhibited. This is asserted following observations made for the highest We experiments that yield deformed liquid marbles prior to prompt splashing; where high horizontal retraction and vertical rebound speeds were reported, which led to complicated arrested shapes that were far from spherical (see Figure 1.17). To our knowledge, the effect of the rate of change of surface coverage relating to the formation of liquid marbles has not been investigated to date.

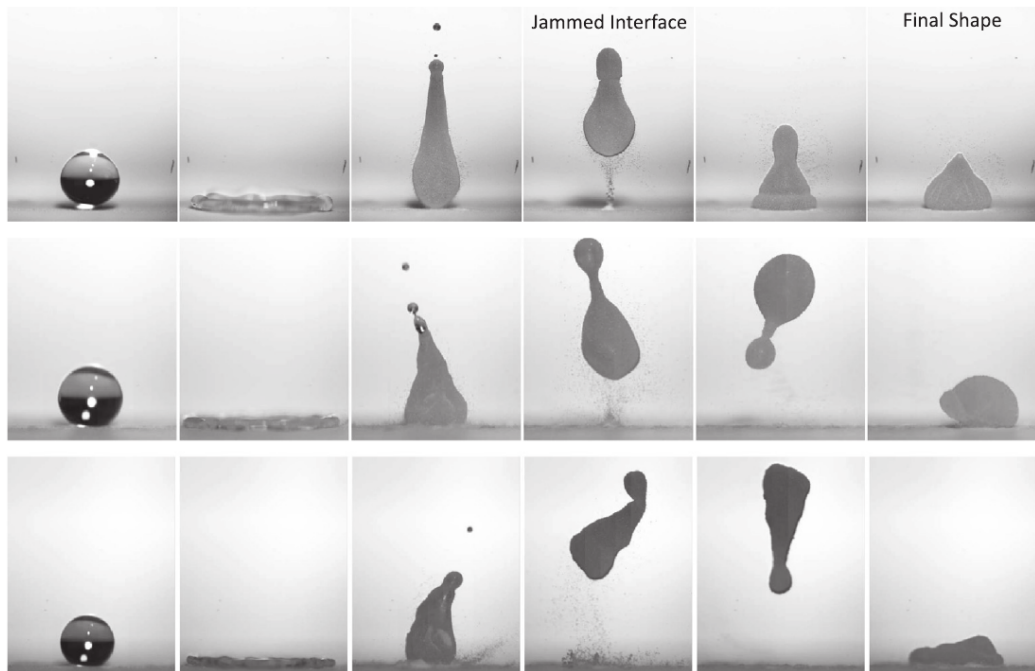
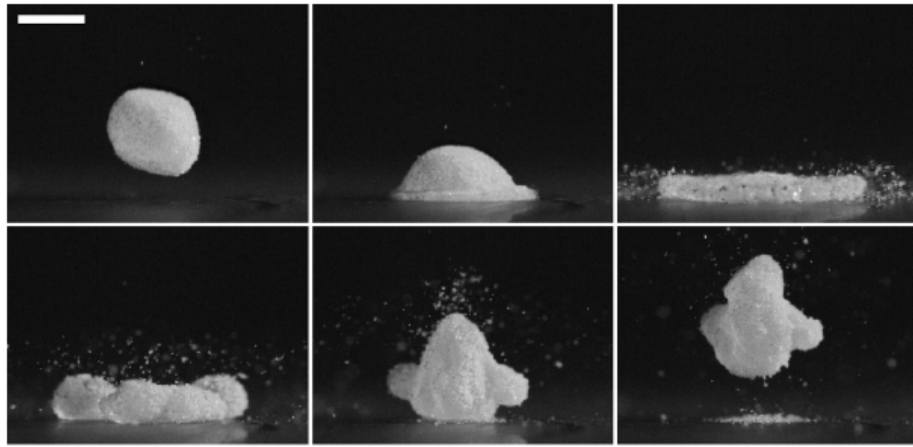
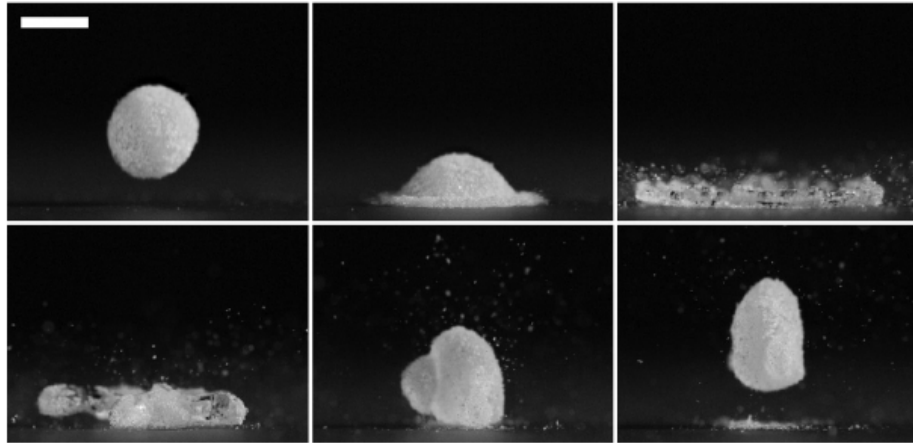


Figure 1.17: Deformed liquid marbles formed in drop impact experiments. The liquid drop is water with an initial spherical diameter of 2mm, and the hydrophobic particles are of average size $25\mu\text{m}$. Obtained from [15].

Impact dynamics of liquid marbles (including deformed liquid marbles) were investigated experimentally in [79]. When impacting a rigid impermeable substrate, the particular shape of a deformed liquid marble was found to have no substantial effect on the maximum spreading diameter. This is intuitive given that the ‘effective surface tension’ (described in §1.1.3) quickly returns to the value of the underlying liquid surface tension as the adhered particles move apart from one another during the drop spreading regime. It was also shown that pseudo-spherical deformed liquid marbles can significantly change their shape, yet maintain a non-spherical arrested shape upon impact and rebound from a rigid impermeable substrate (see Figure 1.18). The process of particle rearrangement on the surface of an impacting deformed liquid marble as a result of the impact remains unexplored.



(a)



(b)

Figure 1.18: Change in arrested shape for pseudo-spherical deformed liquid marbles (initial drop diameter $D_0 = 3\text{mm}$, mean particle size $\bar{d}_p = 25\mu\text{m}$) following impact with a solid substrate. Impact speeds of (a) $U_0 = 0.96\text{m/s}$, and (b) $U_0 = 1.39\text{m/s}$. Scale bars are 2mm long. Obtained from [79].

Particle-laden interfaces, particularly those with a high concentration of adhered particles, have been reported to exhibit surface viscoelastic effects [80–91]. These effects may play a significant role in drop dynamics during the period in drop impact experiments between the complete encapsulation of the drop, and the jamming of the interface that signifies deformed liquid marble formation. A study on the dissipative effects of the adhered particle coating on drop dynamics following impact with a hydrophobic powder bed but prior to liquid marble formation has not been conducted.

Recently, drops of an aqueous solution containing polyethylene oxide impacting a thin superhydrophobic sol-gel film consisting of SiO_2 nanoparticles (size 20nm) were shown to produce ‘local’ jamming of adhered particles upon rebound from the

substrate, with only a partial surface coverage [92]. Unlike previous cases where deformed liquid marbles are formed when the entire drop surface is immobilised simultaneously, these drops consist of coated regions that exhibit ‘sharp’ curvatures and appear partially immobilised, while the clean regions move freely. The local jamming effect was reportedly “not easy to achieve” with low viscosity liquids, with greater success reported for high viscosity aqueous solutions. Given that local jamming is ‘easier’ with higher viscosity liquids, processes behind deformed liquid marble formation, and liquid marble formation process via drop impact in general, may be governed by parameters that differ significantly with fluid viscosity.

1.1.6 Project Motivation

The objective of this body of research is to develop an experimentally-motivated mathematical model to describe the formation of liquid marbles via liquid drop impact onto a superhydrophobic powder bed, and to produce the first numerical simulations of this process. Ultimately, we look to make *a priori* predictions of the outcomes from these impacts, for example, whether a spherical or deformed liquid marble is created (if either), and the time it takes for ‘final’ shapes to be attained. To this end, we work on some of the open questions presented in §1.1.5; in particular, we aim to study the dissipative effects of the particle-laden interface on drop dynamics, particularly during the intermediary period between encapsulation and jamming, and to determine the relationship between the maximum contact area (between the drop and powder bed) and the surface area of the drop at encapsulation and at the moment of particle-jamming at its interface.

The research undertaken here may prove useful in emerging applications for liquid marbles, as well as being of fundamental interest. For example, examining the dissipative effects on post-rebound drop dynamics due to adhered particles may help in the determination of a relationship between the oscillation damping time (that is, the time for drop oscillations to completely decay between encapsulation and forming a sphere) for un-deformed liquid marbles created by drop impacts, and physical parameters. This could then help in improving the efficiency of automated liquid marble generation, by choosing experimental parameters so that, for example, impacting drops reach a spherical shape prior to landing back on the powder bed.

Accomplishing the stated objective requires a combination of numerically sim-

ulating (i) drop impacts onto superhydrophobic powder beds, and (ii) the surface rheological effects brought on by a densely-packed particle-laden fluid-fluid interface. What follows are sections motivating the methods taken in this body of work to achieve these goals.

1.2 Drop Dynamics with a Particle-Laden Interface and Impacts onto Powder Beds

Within the existing research literature there are many examples of numerical simulations conducted for particle-laden interfaces separating immiscible fluids. Particle-based methods (that is, where individual solid particles are considered explicitly) have been used to simulate a variety of phenomena in this field, including the effect of a colloidal particle coating on a suspended drop in shear flow [93, 94], the production of bijels and Pickering emulsions [94–98], the dynamics of magnetic Janus particles on a fluid-fluid interface under an imposed magnetic field [99–101], and interfacial jamming of adhered particles [102–104]. However, although particle-based approaches have been used to successfully model phenomena we are interested in (jamming effects in particular), we instead opt for a continuum representation of the particle coating; a justification of which is given below. A discussion of how particle-based methods could be used to advance the research presented in this thesis is given in Chapter 8.

While simulations in which the solid particles are fully realised² can accurately reproduce a range of phenomena observed in experiments [93, 94, 98, 105], using these methods in our case would require computational resources in excess of what we have available, to reproduce dynamics that we believe may adequately (though less accurately) be resolved using computationally cheaper methods which follow from certain simplifying assumptions. A fully realised particle-based simulation is, for example, necessarily three dimensional (compared to two dimensional in continuum approaches where an axisymmetry assumption can be made), and capturing the energy dissipative effects of the particle dynamics would require an accurate resolution of the flow between adhered particles, which would be challenging to implement, especially as

²Whereby the sizes and shapes of particles, as well as their ‘hard-core’ interactions (that is, where particles are prevented from intersecting each other) are captured.

the inter-particle distance becomes small when close to jamming. A particle-based approach is feasible in principle, and larger systems than ours have been considered, for example, in a numerical study on the formation of bijels and Pickering emulsions [98], on the order of 10^5 - 10^6 solid particles are considered (compared to $\sim 10^3$ particles that adhere to the drop surface in our motivating experiments), but these simulations are computationally very expensive; running in parallel using up to 262,144 cores, compared to our simulations which run on a single core.

Additional approximations in particle-based approaches can be made to make simulations computationally cheaper, but this comes at the expense of accuracy. For example, the research in [104, 106] represents adhered particles as points on the fluid-fluid interface, and represents their interactions with one another through a repulsive force that increases sharply from zero as neighbouring particles ‘intersect’ (that is, they come within a distance of one another that represents two particle radii). These ‘soft-core’ interactions can produce meaningful jamming effects at a fluid-fluid interface [104] and permit (computationally) cheap simulations to be run, but modelling the particles this way may not necessarily correctly reproduce the flow field between them, especially for a densely packed interface, hence energy dissipation due to this inter-particle flow may not be reproduced accurately.

To our knowledge, there are no particle-based methods that have been shown to both adequately reproduce the energy dissipating effects that we desire, and are sufficiently (computationally) cheap to run, given our available computational resources. A continuum approximation of the particle coating, whereby individual particles are no longer resolved and instead are characterised collectively using continuous variables, by contrast, can produce energy dissipating effects (with an easily-adjustable ‘strength’), and also provides additional benefits over particle-based approaches. Firstly, the continuous variables characterising the particle coating can be easily incorporated into flow equations that govern the system, and in particular can be described by a well-established continuum model for surface viscosity (which provides desired energy dissipation, to be discussed in §1.3). As previously mentioned, computational and modelling complexity can also be reduced by moving from three to two dimensions under an assumption of axisymmetry. Further, calibration is easy under a continuum assumption; for example, as shown in §7.2, the ‘strength’ of surface viscous effects in our model is calibrated to match the decay in drop oscillations

in simulations with those observed in experiments, by changing the value of a single parameter. By contrast, in a particle-based simulation, it is not clear how this could be so easily achieved. For these reasons, we adopt the continuum approach for modelling the particle coating in this thesis.

Few numerical simulations have been reported for liquid drop impacts onto powder beds. The most promising example is from a recent article [107], which boasts the “first numerical study on droplet impact on particles placed above a substrate”, in which the adhesion of multiple hydrophobic particles to the surface of the impacting drop is resolved, and a power law relating the impact Weber number to the maximum spreading diameter is attained, which is similar to that which is observed in experiments. However, it is notable that this is achieved only with a small number of solid particles, each of which is much larger than in our motivating experiments ($\bar{d}_p/D_0 = 0.14$ in [107] versus $\bar{d}_p/D_0 \approx 0.01$ in experiments), and with low impact Weber numbers ($We \leq 14$ in [107] versus $We = 60-70$ for deformed liquid marble formation in experiments). As will be discussed in §1.4 and in Chapter 2, treating the deformable powder bed as rigid and impermeable is a reasonable (as well as being the simplest) approximation to make, and by assuming this in our model, we benefit from the extensive research devoted to drop impacts onto such substrates.

1.3 Surface Rheology and its Application to Dynamics of Particle-Laden Interfaces

Particle-laden interfaces have been reported to exhibit surface viscoelastic properties, which become more prevalent as the concentration of solid particles at the interface is increased [80–91]. As mentioned in §1.1.3, there is existing research on the elastic properties of liquid marbles, brought on by the adhered particles at the drop interface, however, these cases consider mostly small deformations, whereby the adhered particles return to their initial positions upon relaxation of an applied external force. In contrast, drops in powder bed impact experiments exhibit significant deformations, far in excess of the elastic limit, which suggests that surface elastic effects are likely negligible for these cases. Given this, we henceforth neglect the effects of surface elasticity, and focus instead on the effects of surface viscosity alone.

Surface viscosity is a two dimensional analogue of bulk viscosity³, whereby energy dissipating effects follow as a consequence of contamination at a fluid-fluid interface, commonly by surfactants or proteins [108], or, as in this work, by small solid particles. In our case, surface viscosity is brought on by hydrodynamic interactions within a thin layer at the fluid-fluid interface, which is modelled as a surface phase; a continuum that describes a combination of the fluid-fluid interface and the solid particles adsorbed to it. The model used in this thesis for incorporating surface viscous effects is the ‘Boussinesq-Scriven constitutive law’ [109], and expresses the surface stress tensor, denoted by $\underline{\underline{\mathbf{\Pi}}}^s$, as

$$\underline{\underline{\mathbf{\Pi}}}^s = (\sigma + [\lambda^s - \mu^s] \nabla_s \cdot \mathbf{v}^s) \underline{\underline{\mathbf{P}}}^s + \mu^s \underline{\underline{\mathbf{P}}}^s \cdot \left(\nabla_s \mathbf{v}^s + (\nabla_s \mathbf{v}^s)^T \right) \cdot \underline{\underline{\mathbf{P}}}^s, \quad (1.3.1)$$

for surface tension σ , velocity of the interface \mathbf{v}^s , surface divergence operator ∇_s , surface projection tensor $\underline{\underline{\mathbf{P}}}^s$, and shear and dilatational surface viscous coefficients μ^s and λ^s , respectively. A description of the surface operators in (1.3.1) is given in Chapter 3 on mathematical modelling.

Equation (1.3.1) represents the surface stress tensor similarly to the (Newtonian) stress tensors within bulk fluids, with separate shear and dilatational components for viscous stress. The size of the surface shear viscosity coefficient μ^s describes the resistance to shearing motion at the interface, whereas the surface dilatational viscosity coefficient λ^s describes the resistance to change in surface area. The Boussinesq-Scriven constitutive law is well-established and has been utilised in a wide range of analytical and computational studies, including multiple parameter studies for drops under different flow conditions in which the effect of variation in both viscosity coefficients is identified [110–115].

In our models (presented in Chapter 3), the surface stress tensor appears alongside the bulk stress tensors from both bulk fluids in the force balance equation at the liquid-gas interface of the drop. As will be discussed (see Chapter 3), the dominant motion preceding liquid marble formation in our experiments appears to be dilatational (that is, surface area change) rather than shearing at the interface. Then, given that using the dilatational component of surface viscosity alone simplifies the model significantly, and doing so still provides energy dissipation at the drop interface, we neglect the shear component in our model by setting $\mu^s = 0$ in equation (1.3.1). For small oscillations, it is known that the dissipative effect of the dilatational compo-

³Similar to surface tension being a two dimensional (surface) analogue of bulk pressure.

ment (when assuming a zero shear component) vanishes in the linear approximation [116, 117], however this is not an area of concern for our research, as we are focused mostly in large drop deformations.

To the best of our knowledge, only linear-order approximations have been studied for a suspended oscillating inviscid drop [116–119], so the effects of the dilatational component vanish when the shear component is set to zero in these studies. Therefore, in addition to modelling and simulating liquid marble formation, we present a derivation and numerical validation of a novel third-order model for a suspended oscillating inviscid drop, under the effect of a dilatational surface viscosity. As will be shown, our novel damped *nonlinear* oscillator model reveals a transition between overdamped and underdamped motion when crossing a critical oscillation amplitude that is observed in simulations but is not predicted in the linear approximation.

1.4 Drop Impact onto Superhydrophobic Impermeable Rigid Substrates

Given the aforementioned decision to treat the solid particles as a continuum once they have adhered to the surface of the drop rather than resolving them individually, we also do not resolve the particles that constitute the powder bed, and instead treat the bed as an impermeable solid substrate. Recall, our objectives are to study the dissipative effects of the particle coating (primarily) during the period between encapsulation and liquid marble formation, and to relate the maximum contact area with the surface area of the drop at these critical post-rebound events (again, encapsulation and deformed liquid marble formation). We are therefore satisfied with the impact phase as long as we attain good agreement between our simulations and powder bed experiments in terms of the maximum spreading diameter, and achieve reasonable agreement in terms of drop shapes exhibited when lifting-off from the substrate. We will now briefly discuss our justification for the additional assumption of neglecting the deformability of the powder bed, and refer the reader to latter parts of the thesis where necessary.

Accurately reproducing the maximum spreading diameter is an important aspect of our simulations, as it correlates to the outcome of drop impact experiments on a powder bed (see §1.1.5). Within existing research, scaling laws for the maxi-

imum spreading diameter in terms of the impact Weber number have been developed (theoretically and empirically) for drop impacts onto hydrophobic powder beds and hydrophobic solid substrates, and are presented in Chapter 2 alongside our own experimental results. Ultimately, we find that the values of the maximum spreading diameter from our experiments match well between both types of substrate, albeit with larger variation between individual powder bed impact experiments at any particular We , and in particular, the scaling laws we observe in our experiments on both types of substrate agree with each other (and with existing results). We are therefore satisfied that modelling the substrate as rigid permits a good approximation of the maximum spreading diameter on a deformable powder bed.

Regarding drop shapes exhibited when lifting-off from the substrate, we conclude in Chapter 2 that for low We , there is good agreement between experiments onto both substrates, and for moderate-to-high We impacts the agreement is still reasonable. However, the low reproducibility of drop shapes in powder bed experiments (likely caused by heterogeneity of the powder bed) means that any deterministic approach would likely fail in matching all cases that may appear. Ultimately, given our research priorities, we are satisfied in using the simplifying assumption of a rigid substrate, and resolving substrate deformation is an avenue for future work (see Chapter 8).

Finally, by using the rigid approximation, we benefit from the extensive experimental, modelling, and simulation studies that have been conducted on drop impacts onto solid surfaces, including for superhydrophobic surfaces (see prominent review articles [120, 121]).

1.5 Organisation

This thesis is organised into eight chapters; a brief description of the content within each future chapter is given here.

In Chapter 2, data from experiments of liquid drops impacting rigid impermeable superhydrophobic substrates and superhydrophobic powder beds is presented and discussed. Attention is paid to the change in maximum spreading diameter along the substrate as the impact speed is increased (characterised by the impact Weber number, We) and the resultant change in drop shapes exhibited. Comparisons are made between drop impacts onto the two kinds of substrate, highlighting similarities

and points of divergence. For powder bed impacts, the transition from drops partially coated in powder post-rebound, to fully coated drops, to spherical liquid marbles, to the formation of deformed liquid marbles, and finally splashing, is presented as We is increased between experiments. Using data extracted from experiments, a novel relationship is presented between the maximum spreading diameter of the drop on the superhydrophobic powder bed, and the surface area of the drop at the moments of: complete encapsulation in solid particles, and spherical/deformed liquid marble formation (if it occurs).

In Chapter 3, novel mathematical models for liquid marble formation via drop impact are derived, under the separate assumptions of inviscid and viscous bulk flows within the liquid drop and exterior gas. Assumptions made here arise from empirical observations following the experiments in Chapter 2, and from existing research into liquid marble formation, drop impacts, and the surface rheological properties of particle-laden interfaces. The adhered particles on the drop surface are modelled as a continuum, affecting drop dynamics through a dilatational surface viscosity, which is implemented with the Boussinesq-Scriven constitutive law (1.3.1). An assumption of inviscid bulk flows, negligible particle inertia at the drop surface, and negligible surface shear viscosity leads to (dilatational) surface viscosity being incorporated via an effective surface tension. The deformable superhydrophobic powder bed is modelled as a superhydrophobic rigid impermeable substrate. A viscous-bulk model is developed owing to cumbersome numerical and technical challenges related to simulating the drop impact with an inviscid bulk flow assumption and chosen numerical implementation. A novel third-order damped nonlinear oscillator model is also derived for suspended inviscid drop oscillations with surface viscous effects stemming from a nonzero dilatational surface viscous coefficient. This contrasts with existing linear approximations, whereby the dilatational viscosity effect vanishes when zero surface shear viscosity is considered.

Chapter 4 describes the development of a boundary integral method to be applied to the inviscid bulk model presented in Chapter 3. A corresponding numerical boundary element method is derived, and a detailed description of its computational implementation (created specifically for this body of research) is given. The implementation of the boundary element method is validated for suspended drop oscillations against known theoretical results, and against expected orders of convergence

under mesh refinement. Implementation of surface viscosity is validated with respect to known energy decay rates, and the novel damped nonlinear oscillator model for suspended inviscid drop oscillations is validated against numerical simulations for small amplitude oscillations. An investigation is conducted showing the qualitative similarities between a ‘toy’ nonlinear oscillator based upon our damped nonlinear oscillator, and *large* amplitude drop oscillations. Numerical challenges when simulating a high-speed drop impact with an inviscid-bulk assumption, and with a boundary element method are discussed.

Chapter 5 introduces the volume-of-fluid method; a numerical method capable of handling viscous bulk flows and changes in drop topology, both of which caused difficulty with the use of the inviscid model and a boundary element method in Chapter 4. A discussion is given on how the viscous model from Chapter 3 was implemented using a well-documented and commonly used software program that is capable of running volume-of-fluid simulations. Functionality added to this software for this research, such as the use of an effective surface tension and the application of a curvature-limiting condition, are discussed. The implementation of a nonzero dilatational surface viscosity is validated by comparing the results of volume-of-fluid and boundary element method (from Chapter 4) simulations of suspended inviscid drop oscillations.

The results of our drop impact simulations are provided in Chapter 6 using the viscous-bulk model from Chapter 3 implemented with the volume-of-fluid method discussed in Chapter 5. The maximum spreading diameters of drops within simulations are validated against those in drop impact experiments onto both kinds of substrate from Chapter 2. The use of an empirically-motivated pinning radius is used to better match drop impact simulations to rigid substrate impacts, but does not improve agreement with powder bed experiments, for reasons later discussed.

Chapter 7 presents the first reporting of simulations for liquid marble formation via drop impact, for a wide range of We . The model from Chapter 2 for the relationship between the maximum spreading diameter, and drop surface area at encapsulation and liquid marble formation, is adjusted to account for the difference observed in simulations between the largest diameter of the drop at maximum spread and the contact line diameter, which is not visible in experiments. The surface area corresponding to encapsulation and liquid marble formation for use in simulations

is then calculated using the maximum spreading diameters from drop impact simulations presented in Chapter 6. The strength of dilatational surface viscous effects in simulations is calibrated with reference to drop impact experiments. Results are presented for simulations running from the moment of encapsulation, until liquid marble formation (if it occurs), using drop impact simulations from Chapter 6 as initial conditions, with dilatational surface viscosity providing dissipative effects on drop dynamics. The process of liquid marble formation in simulations is compared to drop impact experiments onto superhydrophobic powder beds from Chapter 2.

Finally, the research conducted in this thesis is summarised and avenues for future work are discussed in Chapter 8.

Chapter 2

Experiments

This chapter presents novel experiments that were conducted to aid in the development of a mathematical model to describe liquid marble formation (including for deformed liquid marbles) via drop impact onto superhydrophobic powder beds (existing research discussed in §1.1.5), and for our subsequent numerical simulations to be compared against. Two types of experiment were conducted, namely, (i) drop impacts onto superhydrophobic powder beds, and (ii) drop impacts onto flat rigid impermeable superhydrophobic substrates. These latter (simpler) experiments were performed to investigate how well superhydrophobic powder bed impacts can be approximated by impacts onto a rigid impermeable superhydrophobic substrate. One may expect, *a priori*, for the two to be similar for low impact Weber numbers, where only a small amount of powder is adsorbed to the drop interface. Similar experiments for both kinds of impacting surfaces appear in literature, but do not present sufficient qualitative and quantitative data that we require to develop our model, or to compare simulations against.

All experiments presented in this chapter were conducted while on a research visit to the Chemical Engineering department at Texas Tech University in Lubbock, Texas, under the guidance of Dr. Jeremy Marston, who has pioneered research into liquid marble formation via drop impact with superhydrophobic powders, as well as ultra-high-speed imaging of fluid dynamics phenomena.

2.1 Materials

The particles used to form the powder beds in experiments are soda lime solid glass microspheres (Cospheric, USA) that arrive pre-treated with a hydrophobic nano-coating. The stated particle density from the supplier is 2.45g/cc, and after conducting a time-of-flight measurement using an API Aerosizer[®] particle size analyzer, the geometric mean particle diameter is found to be approximately 23.72 μm . The distribution of particle diameters from this measurement is shown in Figure 2.1.

For the powder beds, a square bowl is filled with the hydrophobised solid glass microspheres and packed tightly (a description of this process is given in §2.2). For the rigid impermeable superhydrophobic substrates, glass microscope slides are used; first washed with acetone and de-ionised water and then immersed for a few seconds in a liquid suspension (Glaco Mirror Coat) containing silica nanoparticles, before being left to air dry for five minutes. The slides are then heat cured on a hot plate at 120°C for a further five minutes, after which the slides exhibit superhydrophobic properties due to the aggregation of nanoparticles across their surfaces. The liquid used in all experiments is de-ionised water, the properties of which (at 20°C) are provided in Table 2.1.

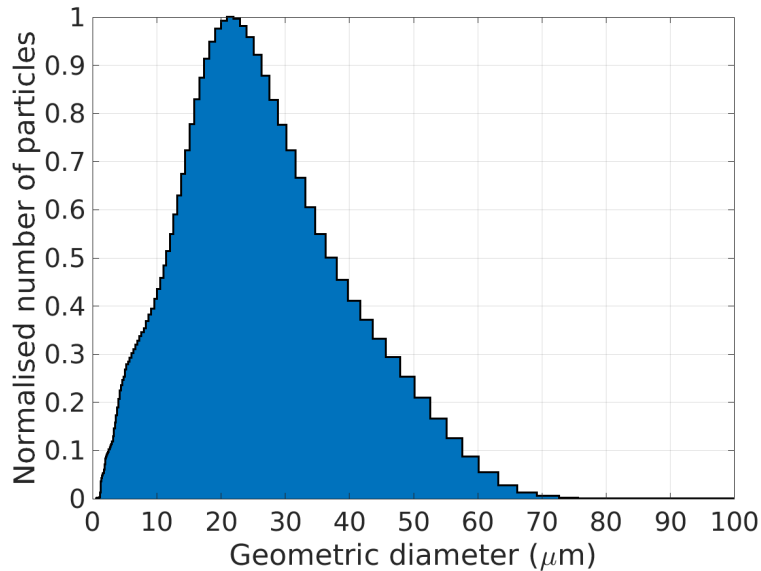


Figure 2.1: Histogram showing the distribution of geometric diameters of solid particles used in experiments, as calculated using an API Aerosizer[®] particle size analyzer. The y-axis shows the (normalised) number of particles within a particular size range.

Table 2.1: Properties of de-ionised water (at 20°C) used in drop impact experiments.

Density	Dynamic Viscosity	Surface Tension
998 kg/m ³	10 ⁻³ N·s/m ²	72.75 × 10 ⁻³ N/m

2.2 Methods

To prepare the powder beds, the solid particles are first poured into the cavity of the square bowl until it is overfilled, after which a flat solid surface is pressed down firmly on top of the powder to maximise the particle packing fraction. This solid surface is then pulled horizontally along the top of the bowl to prevent powder particles from being lifted from the bed as it is removed, which can occur when pulling the solid surface away vertically, as particles may stick to it. A straight edge is then placed across the width of the cavity opening and pulled across it (with the straight edge maintaining contact with the bowl rim) to scrape away excess powder and to ensure a flat impacting powder surface. The bowl is then brushed with lint-free cloth to remove any remaining powder particles not part of the powder bed. Finally, the filled bowl is weighed to allow a calculation of the powder packing fraction. The packing fraction, φ_{avg} , is taken as an average for the whole powder bed and calculated as

$$\varphi_{avg} = \frac{\text{Filled bowl mass} - \text{Empty bowl mass}}{\text{Powder density} \times \text{Cavity volume}}. \quad (2.2.1)$$

A packing fraction of $0.60 \leq \varphi_{avg} \leq 0.64$ is achieved for all powder bed experiments, with any beds falling outside this range being emptied and remade. The theoretical maximum packing fraction for a collection of uniform spheres is approximately 0.74 [122] assuming a perfect lattice formation, whereas a non-perfect random arrangement can reach a maximum packing fraction of approximately 0.64 [123], which is close to the value we achieve; therefore demonstrating the robust method of powder packing used for the experiments.

The experimental setups for impacts onto treated glass and powder beds are shown in Figure 2.2, and close-ups of both types of substrate are shown in Figure 2.3. Water drops are made by feeding de-ionised water through a rubber tube connecting a 30ml syringe to a glass capillary that is clamped into position at a given height and with a vertical orientation (perpendicular to the impacting surface). The thin end of the capillary (where the drops emerge) is hydrophobised using the same method described earlier for the hydrophobisation of the glass slides; this is to ensure that

drops do not wet the outside of the capillary when forced out, meaning that drop size is determined by the size of the capillary opening (along with the value of liquid surface tension).

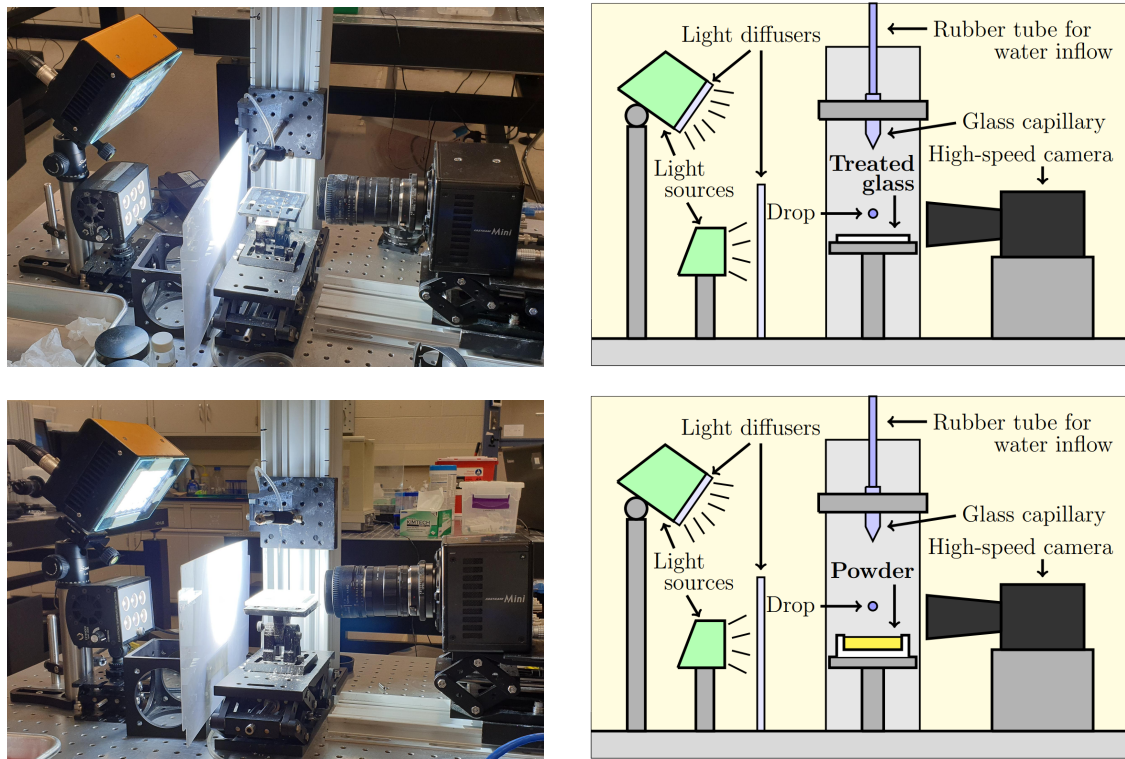


Figure 2.2: Photographs and diagrams of the experimental setup for drop impacts onto treated superhydrophobic glass surfaces and superhydrophobic powder beds.

By gently pressing on the syringe pump, water forms into a drop at the opening of the glass capillary, and pinches off after reaching a certain size. It is important that this is done slowly in order to ensure zero kinetic energy within the drop when it starts to fall (so that an accurate approximation of the impact speed can be made), and that no extra liquid is added to the drop prior to pinch-off (ensuring a repeatable drop size). Once pinched off from the capillary, drops fall and impact the substrate, spread along it until reaching a maximum extension, subsequently retract and rebound from the substrate, and then oscillate in the air before eventually falling back to it. In the powder bed case, powder particles adhere to the surface of the drop during the spreading and retraction phases, and craters may form upon impact. With sufficient powder coverage, the rebounded drops may take an arrested non-spherical shape (that is, they may form a deformed liquid marble) as the powder on the drop interface prevents it from forming back into its minimal surface area shape - a sphere (as

discussed in §1.1.5). The impact speed, \hat{U}_0 , is varied by changing the height of the capillary opening with respect to the substrate. We estimate the drop impact speed, \hat{U}_0 , using the relation $\hat{U}_0 = \sqrt{2\hat{g}\hat{H}}$, where $\hat{g} \approx 9.81 \text{ m/s}^2$ denotes acceleration due to gravity, and \hat{H} denotes the height of the bottom of the drop with respect to the surface of the substrate. The range of drop heights and impact speeds for our experiments are $4.6 \leq \hat{H} \leq 466.7 \text{ mm}$ and $0.30 \leq \hat{U}_0 \leq 3.02 \text{ m/s}$, respectively.

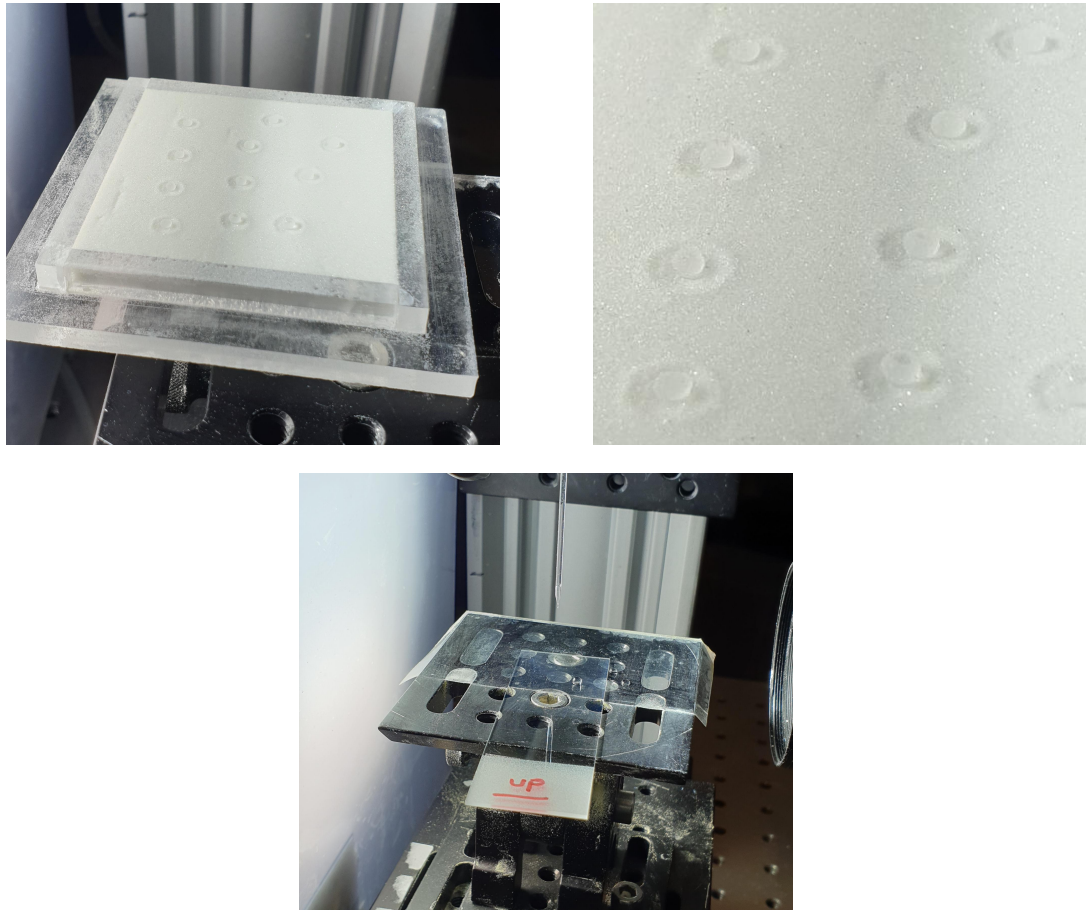


Figure 2.3: Photographs showing (top) a superhydrophobic powder bed post-impact, including (top-right) a close-up of liquid marbles at rest on the powder surface, and (bottom) a treated superhydrophobic glass slide.

The experiments are illuminated using two light sources, each placed behind light diffusers to maximise contrast of the impacting drops with the background for the sake of visual analysis. Experiments are recorded at 4000 frames per second using a monochrome FASTCAM Mini UX100 high-speed camera, and Photron FASTCAM Viewer software is used to play back recorded videos and to extract still images.

Four sets of experiments are conducted in total; two sets of experiments for impacts onto rigid impermeable superhydrophobic substrates (that is, on the treated glass slides), and two sets of experiments for impacts onto superhydrophobic powder beds. The difference between these two sets for a particular substrate is the camera position; experiments from set A provide a close-up view of spreading and retraction dynamics, whereas experiments from set B have the camera positioned further away so as to fully capture the drop oscillations post-rebound that occur out of frame in set A experiments. An example of the difference between set A and set B experiments is shown in Figure 2.4. For each set of experiments, the drop diameter, visible height above the substrate captured by the camera, and the width (and length) that each (square) pixel represents, is given in Table 2.2. The error in measurements of visual data is expected to be on the order of 1 pixel.

Given the focus of this body of research is primarily on dynamics that occur post-rebound, the majority of references made later in this thesis to data and images from the experiments presented in this chapter are with respect to those from set B. As such, the name of the set is often not mentioned unless the corresponding data or images are from set A experiments.

Table 2.2: Details for each experimental run.

Set	Substrate	Drop diameter (mm)	Visible height above substrate (mm)	Pixel width (μm)
A	Glass slide	1.90	7.68	8.62
A	Powder bed	1.90	8.01	8.62
B	Glass slide	1.94	21.72	23.54
B	Powder bed	1.99	21.16	22.82

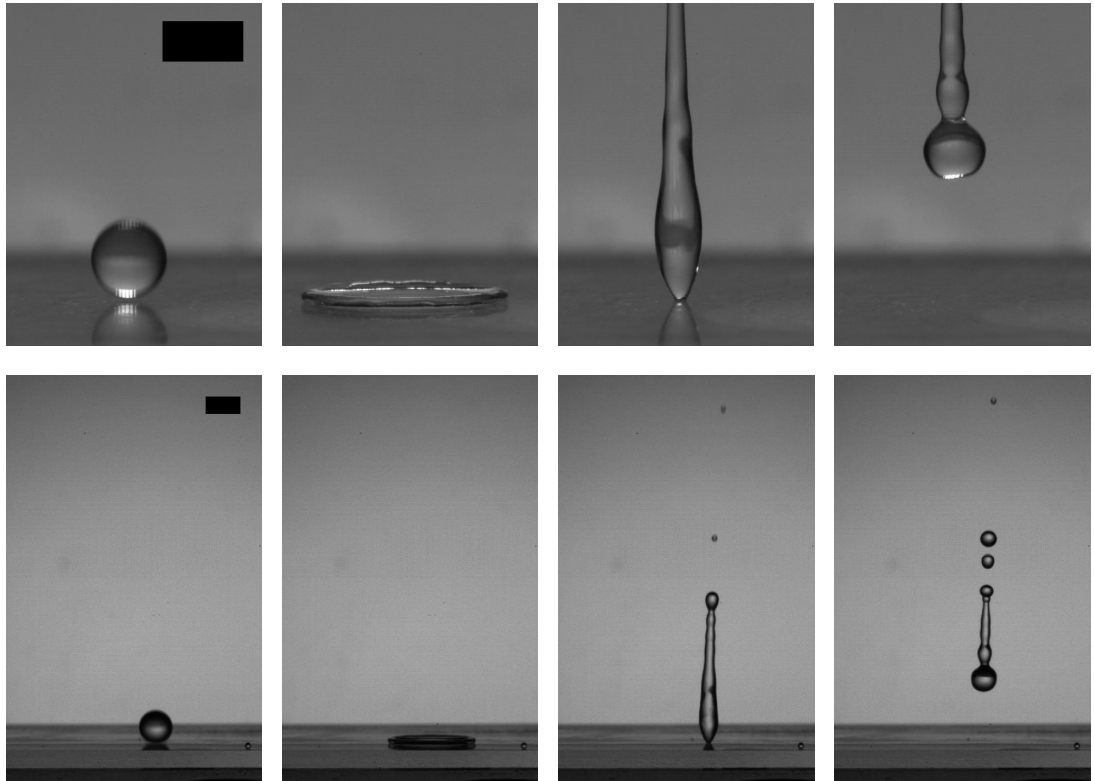


Figure 2.4: Comparison between drop impact experiments on treated superhydrophobic glass from (top) set A; providing a well-resolved view of spreading dynamics but a limited view of post-rebound dynamics, and (bottom) set B; providing a less-resolved view of drop spread but fully capturing post-rebound dynamics. Scale bar has a width of 2mm.

After conducting a drop impact experiment on treated glass, the substrate is tilted so that any drops lying near the impact zone roll off the glass slide. If water is left behind after rebound, meaning there has been partial penetration of the substrate micro-structure, the glass slide is horizontally shifted so that a non-wetted region becomes the new impact zone. If there is insufficient non-wetted space, the slide is replaced. Similarly, after each impact on a powder bed, the bowl is shifted so that the impact zone moves to a region of undisturbed powder, and if no such region exists, the bowl is emptied and the powder bed is remade.

2.2.1 Image Analysis

Following completion of experiments, image analysis is conducted to provide a variety of measurements; most importantly for the maximum spreading diameter and an

approximation of drop surface area. The maximum spreading diameter is easy to measure as it only requires pin-pointing the extreme left- and right-most pixels of the drop at maximum extension, whereas other quantities rely on data that is harder to obtain, such as the shape of the drop boundary.

To obtain an outline of the shape for a coated drop, a frame is taken from experiments and the contrast is altered so that the drop profile appears as a black mass of pixels on a white background. The pixels at the boundary of the drop are then taken and ordered sequentially. As this ordered boundary data is taken directly from pixels, the boundary is not smooth; which can introduce spurious results when calculating quantities such as surface area (in fact this gets worse as multiple layers of powder adhere to the drop interface). We therefore smooth the boundary data, and do so by using Savitzky-Golay filtering [124]. Figure 2.5 shows images of liquid marbles overlaid with smoothed boundaries, constructed using the above process, along with identification of their centroids (that is, the two dimensional centre of mass).

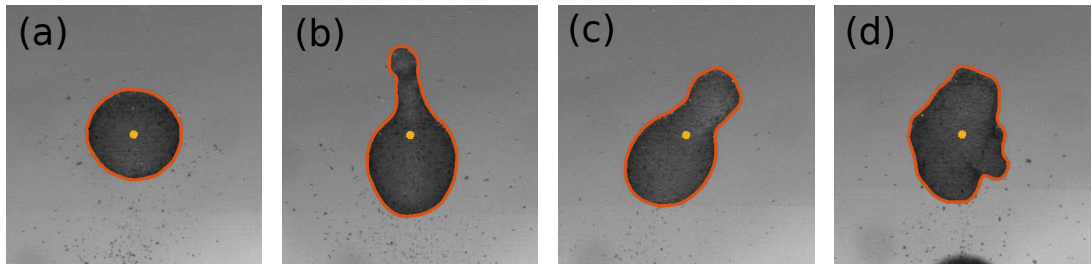


Figure 2.5: Liquid marbles with overlaid smooth boundaries and centroids. The impact Weber number for each experiment is: (a) $We = 49$, (b) $We = 59$, (c) $We = 69$, (d) $We = 79$.

Approximating Surface Area from Images

Recall that relating the surface area of a drop at the moment of encapsulation and at liquid marble formation, to the maximum contact area, is one of the goals of this body of research (see §1.1.6). It is therefore important to obtain an accurate approximation of the drop surface area, and described here is our method for achieving this.

To obtain an approximation of drop surface area with just one camera view, we have to assume that the images we see from experiments are representative of an

axisymmetric shape, which appears to be the case (in varying degrees) for all but the highest impact Weber numbers, where the drop experiences splashing or the fingering instability (where the rim of the spreading drop splits into liquid ‘fingers’). Approximating the surface area under an axisymmetry assumption requires the choosing of an appropriate axis of symmetry. Prior to impact, the axis of symmetry is the vertical line that traces the drop’s descent onto the substrate, so assuming axisymmetry is maintained during the impact and after rebound, this axis will be unchanged throughout the experiment. We do observe however that liquid marbles will often rotate in the air after forming, likely caused by heterogeneity of the powder bed, but fortunately the drops still appear to maintain reasonable axisymmetry about a now-rotated axis.

For our approximation, we choose an axis of symmetry by drawing a straight line connecting two points of the drop boundary such that this line passes through the drop centroid, and that the orientation of this line matches closely to the visual evolution of the axis in an experiment (see example in Figure 2.6). This axis splits the drop shape into two components, referred to as left and right components. Two approximations are then made for the drop surface area by assuming each component, when made into a surface-of-revolution, is representative of the three dimensional drop shape. The surface area for the liquid marble, A_{LM} , is then taken as the average of these two approximations, that is,

$$A_{LM} = \frac{1}{2} \left(2\pi \int_{\text{left}} r \, ds + 2\pi \int_{\text{right}} r \, ds \right), \quad (2.2.2)$$

where ds denotes the line element along the drop boundary in the left or right component. Ultimately, we find that after applying this averaging, surface area calculations are not particularly sensitive to the precise placement of the axis of symmetry, as long as a ‘sensible’ choice is made.

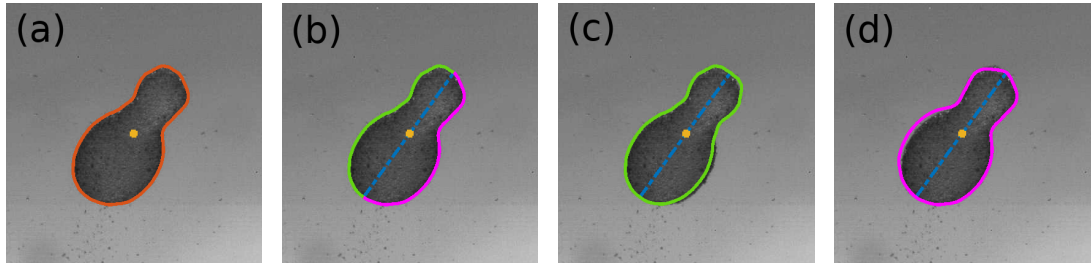


Figure 2.6: Example of the process of approximating the surface area of a liquid marble: (a) Identify the boundary (red) of the two dimensional image of the drop and calculate the centroid of the filled shape, (b) Draw a line (blue) through the centroid that can reasonably act as an axis of symmetry for the drop shape - this splits the boundary into a left and right component (green and pink), (c-d) Construct a surface-of-revolution using the left and right components of the drop boundary. The ‘true’ surface area is approximated as the average of the approximations in (c) and (d).

2.3 Results

In this section we discuss results of the experiments outlined earlier in this chapter. We begin by describing characteristic impacts on rigid impermeable superhydrophobic substrates and superhydrophobic powder beds, showing a range of possible dynamics as the impact Weber number is increased. We then compare drop dynamics for impacts on both types of substrate to determine at what impact Weber numbers they are similar and when they diverge. Finally, we investigate the relationship between the maximum spreading diameter and the surface area of the drop when it becomes encapsulated (that is, fully coated in powder), and either when it becomes a deformed liquid marble, or after it *quickly* returns to a spherical shape.

We denote the initial (dimensional) diameter of the spherical drop prior to impact by \hat{D}_0 , and the (dimensional) maximum spreading diameter by \hat{D}_{\max} . Then, we define the (dimensionless) ‘spreading factor’ as

$$\gamma := \frac{\hat{D}_{\max}}{\hat{D}_0}, \quad (2.3.1)$$

which we consider in place of the maximum spreading diameter for the remainder of this thesis.

We are unable to identify the position of the contact line in our experiments until the drop is at least part-way through the retraction process and only then for impacts onto rigid substrates (see discussion on the dynamic contact angle in §2.3.1). Hence, references to the maximum spreading diameter and spreading factor as in (2.3.1) always refer to the maximum visible diameter of the drop, rather than the position of the contact line. References later in the thesis to the location of the contact line are made explicitly clear.

2.3.1 Characteristic Impacts on Rigid Impermeable Superhydrophobic Substrates

We consider here the simpler experiments of drop impact onto a rigid impermeable superhydrophobic substrate. The more complex case of drop impact onto a superhydrophobic powder bed is considered in §2.3.2.

Maximum Spread

The experiments from both sets A and B are conducted under the same conditions, and the slight deviation between their results is a possible indication of dynamics at higher impact Weber numbers being sensitive to preparation techniques for the substrate.

Provided in Figure 2.7 are plots for the spreading factor γ against the impact Weber number for both sets of experiments. We separate experiments into four regimes that provide an overview of the outcomes that are observed. The first regime is for impacts that exhibit no satellite droplet ejection (see example in Figure 2.8), which is seen for the lowest impact Weber numbers. The majority of experiments *do* eject satellite droplets without any signs of axisymmetry-breaking instabilities (see Figures 2.9 and 2.10); these appear at slightly higher impact Weber numbers than experiments with no satellite ejection and persist for a wide range of We . Increasing the impact Weber number within this regime forces the drop to spread further out on the substrate, which results in a stronger vertical jet forming during retraction, that in turn causes the drop to become more elongated prior to rebound. For large enough impact Weber numbers, we see the onset of the fingering instability; whereby small perturbations appear on the rim of the drop as it retracts, which can cause a

minor break in axisymmetry visible in post-rebound dynamics (see Figure 2.11). For even larger impact Weber numbers, we see that the fingering instability takes hold during drop spreading (see Figure 2.12), which irrevocably destroys any notion of axisymmetry as surface waves are irregularly propagated along the drop boundary as the fingers retract back into the primary drop. The distinction made between the two fingering instability regimes has to do with the timing of a break in axisymmetry; if a noticeable break occurs during spreading, this is classed as showing the fingering instability, whereas if surface perturbations only appear during retraction, then this is classed as the ‘onset of fingering’. The two scenarios, whilst very similar, are separated to highlight the gradual shift from stable impacts to splashing. Eventually the impact Weber number is so large that splashing occurs soon after contact is made with the substrate (see Figure 2.13); such experiments are not on the plots in Figure 2.7 as it does not make sense to characterise such drop spreads with a single number, and this is not the focus of our study.

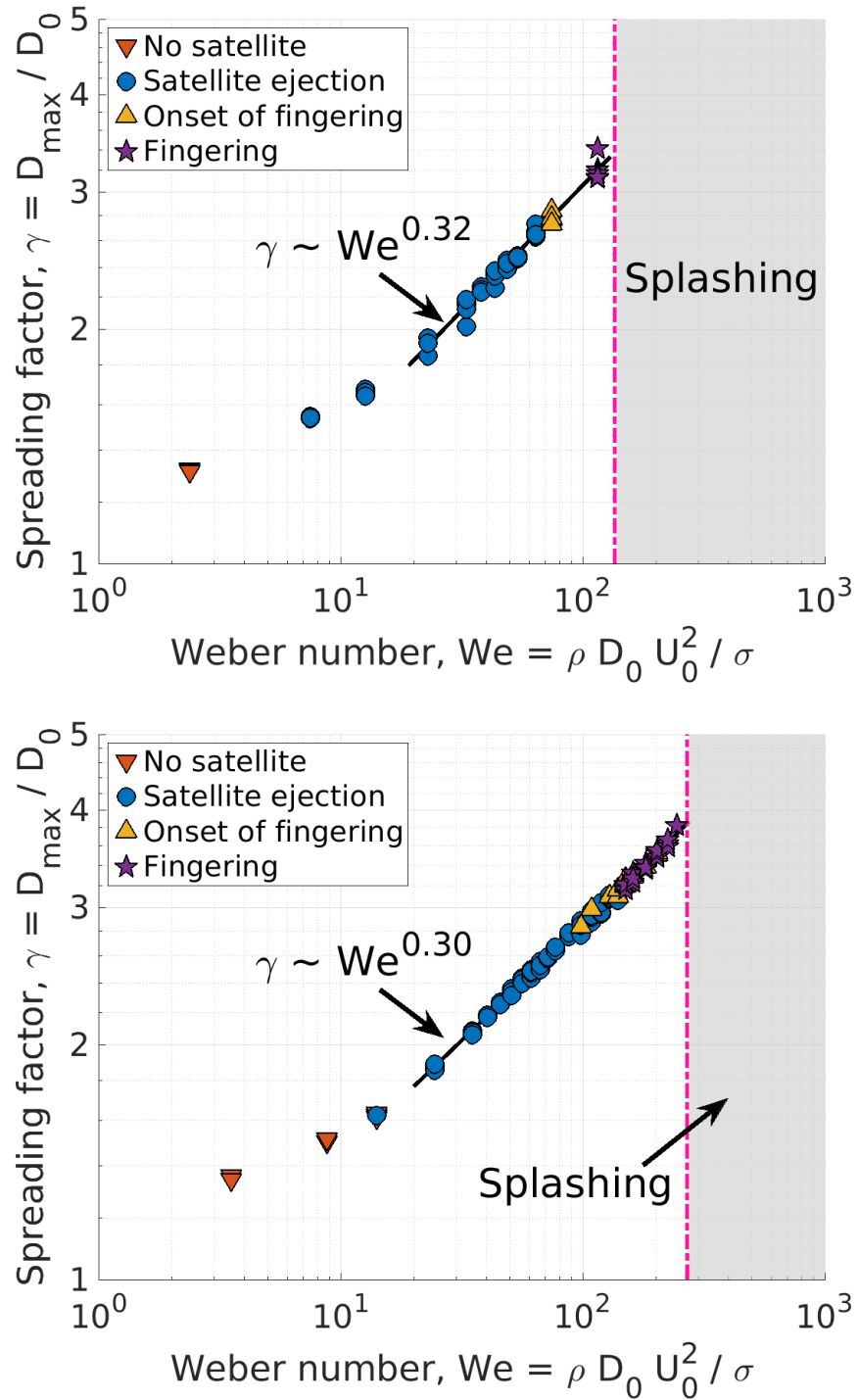


Figure 2.7: Spreading factor versus impact Weber number for drop impact on a rigid impermeable superhydrophobic substrate with experiments from (top) set A, and (bottom) set B. Power law approximations are provided for both sets of experiments for $We > 20$. The R-squared value and mean squared error are (top) $R^2 = 0.9815$ and $MSE = 2.6 \times 10^{-3}$, (bottom) $R^2 = 0.9965$ and $MSE = 8.3 \times 10^{-4}$.

For both sets A and B, experiments with $We > 20$ appear to behave differently to those with $We < 20$; this is similarly observed in the literature [125, 126] for impacts

onto superhydrophobic surfaces, though both here and in previous publications the evidence for a true regime change is weak. Logarithmic plots are used to provide an approximate scaling of the spreading factor γ with the impact Weber number; in set A we see a scaling of $We^{0.32}$ and in set B we see a scaling of $We^{0.3}$. In the literature, similar scaling laws for the spreading factor in terms of the impact Weber number have been observed between $\gamma \sim We^{0.25}$ and $\gamma \sim We^{0.5}$ [121, 127]. However, these values as well as ours may not reflect the true scaling behaviour that one may find for $We \rightarrow \infty$, because of the narrow range of We accessible and small values of γ . For low impact Weber number ($We < 20$), it is even less clear that a scaling law is appropriate; as the impact Weber number approaches zero, one would expect the spreading factor to reach unity, and regardless, the focus of this thesis is with phenomena that occur outside of this range. Nevertheless these scalings provide confidence that our results are not in contradiction with the published experimental literature on this topic.

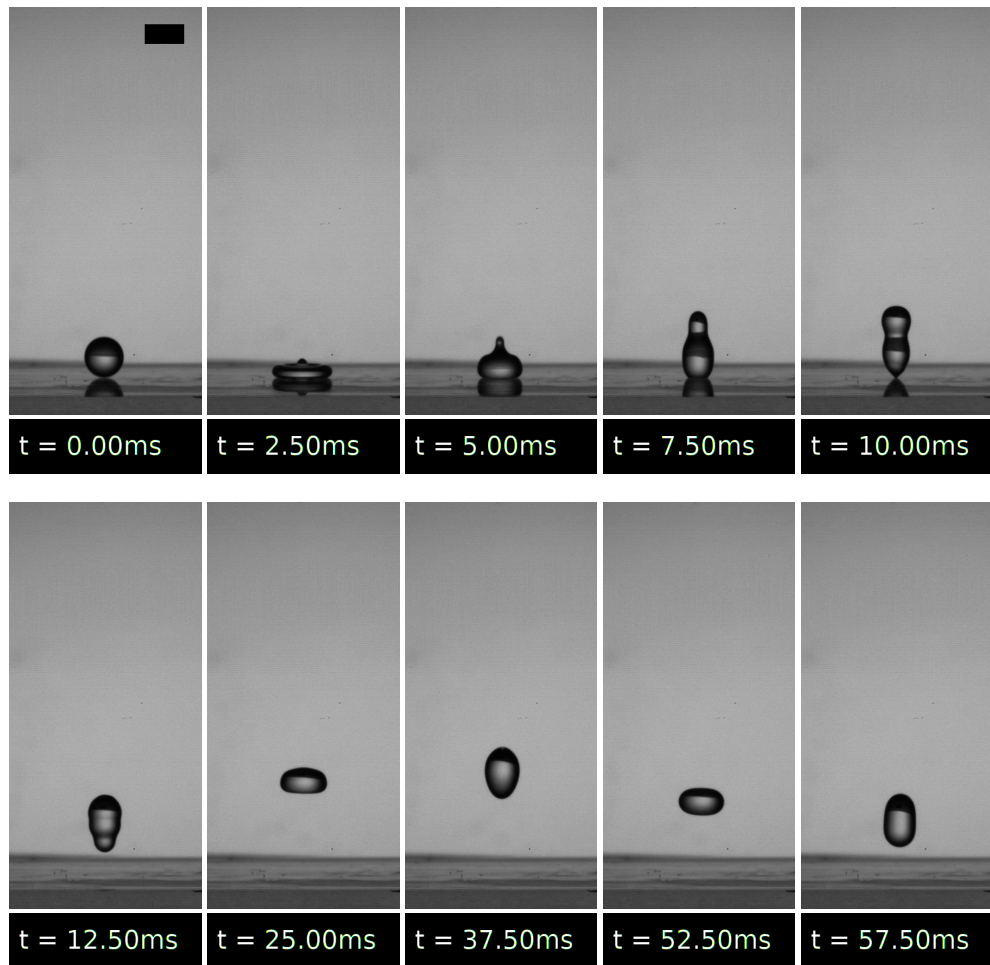


Figure 2.8: Drop impact experiment (from set B, $We = 9$) on a rigid impermeable superhydrophobic substrate, showing no satellite droplet ejection. Scale bar has a width of 2mm.

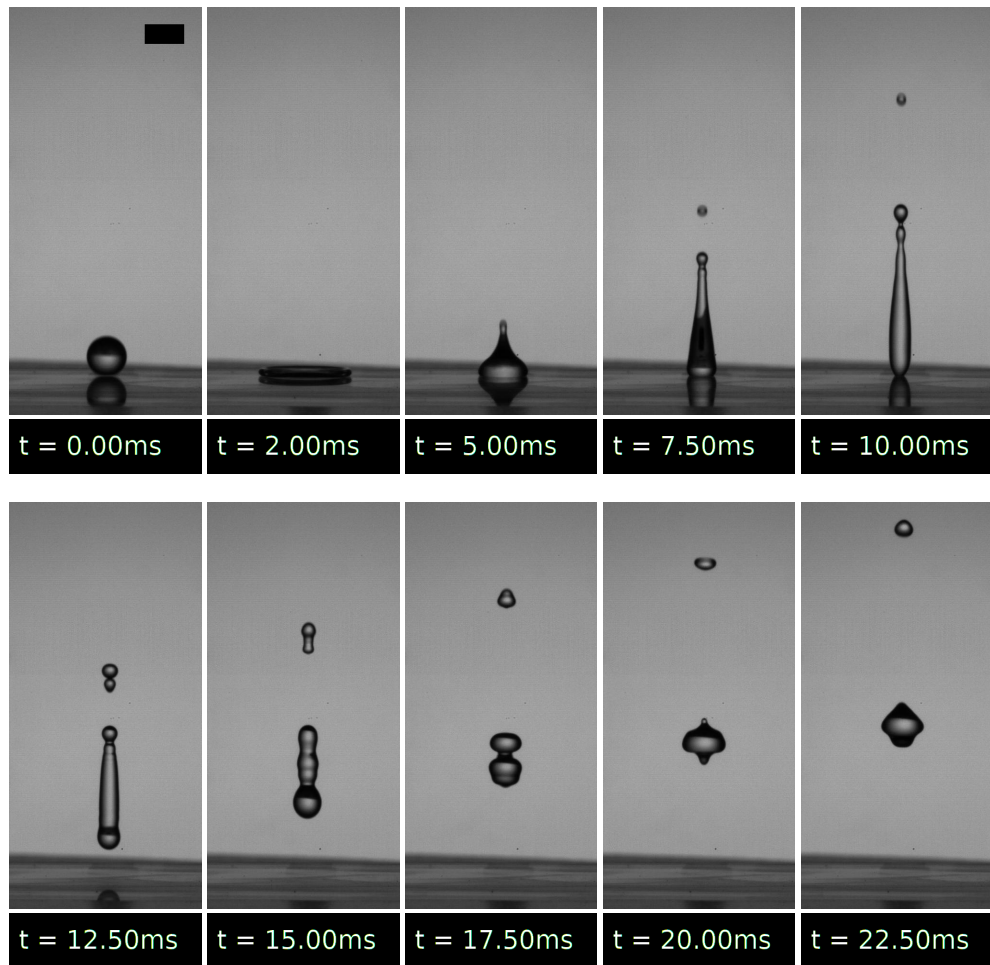


Figure 2.9: Drop impact experiment (from set B, $We = 51$) on a rigid impermeable superhydrophobic substrate, showing the ejection of satellite droplets. Scale bar has a width of 2mm.

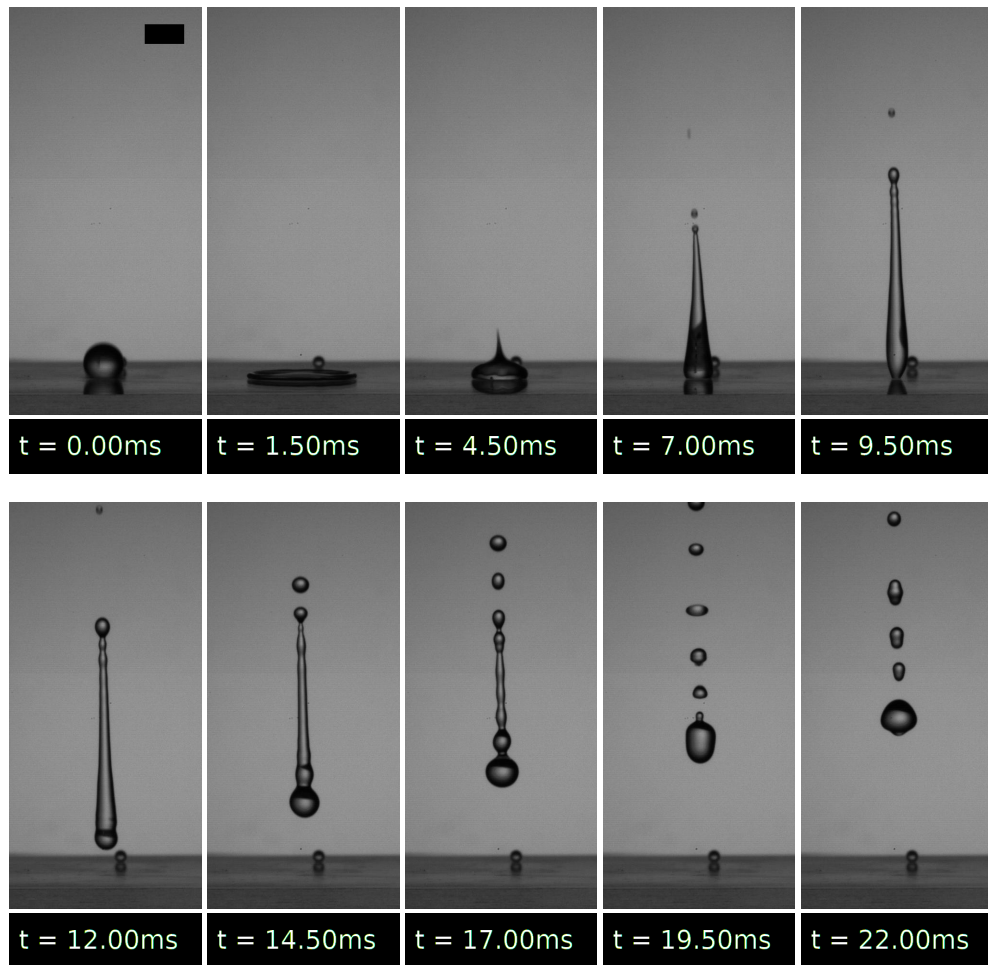


Figure 2.10: Drop impact experiment (from set B, $We = 98$) on a rigid impermeable superhydrophobic substrate, showing the ejection of satellite droplets. Scale bar has a width of 2mm.

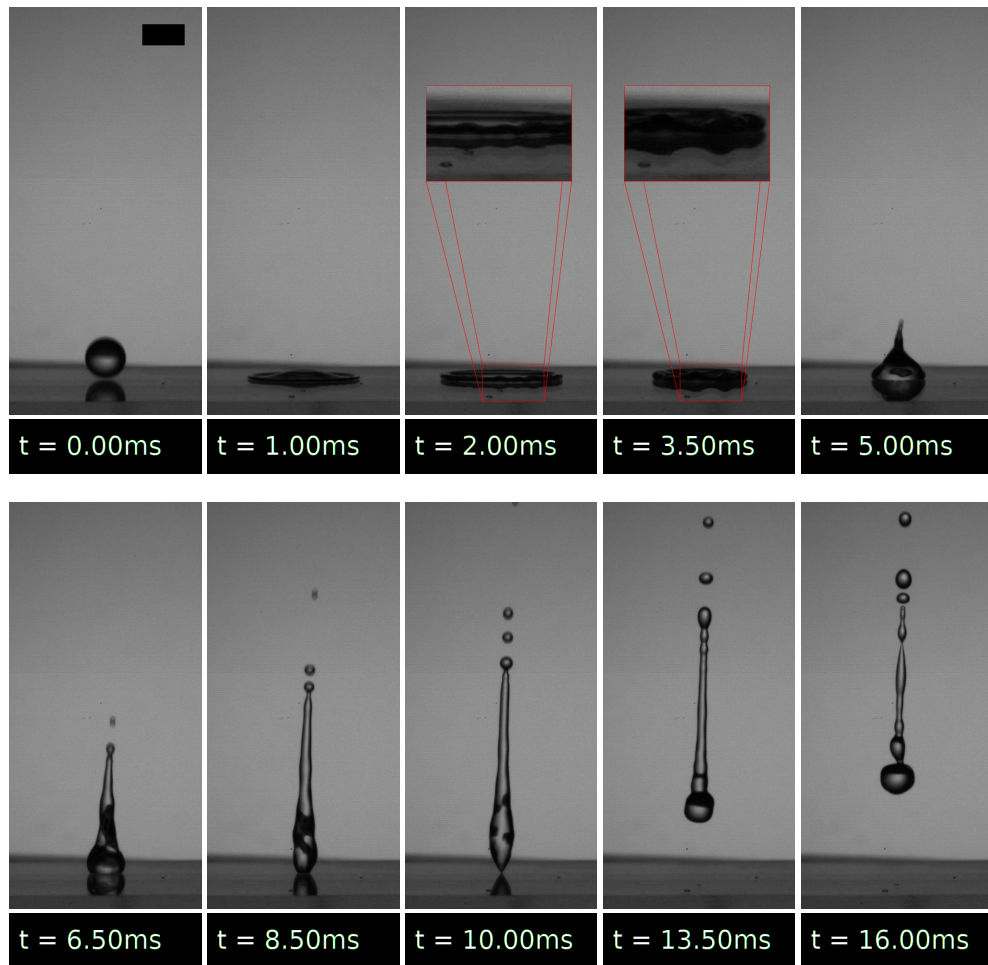


Figure 2.11: Drop impact experiment (from set B, $We = 150$) on a rigid impermeable superhydrophobic substrate, showing the onset of the fingering instability. At 2.00ms the receding rim of the drop is experiencing a slight perturbation which continues through 3.50ms, and ultimately causes the drop to lose axisymmetry as is evident in the irregular drop shape at 16.00ms. Scale bar has a width of 2mm.

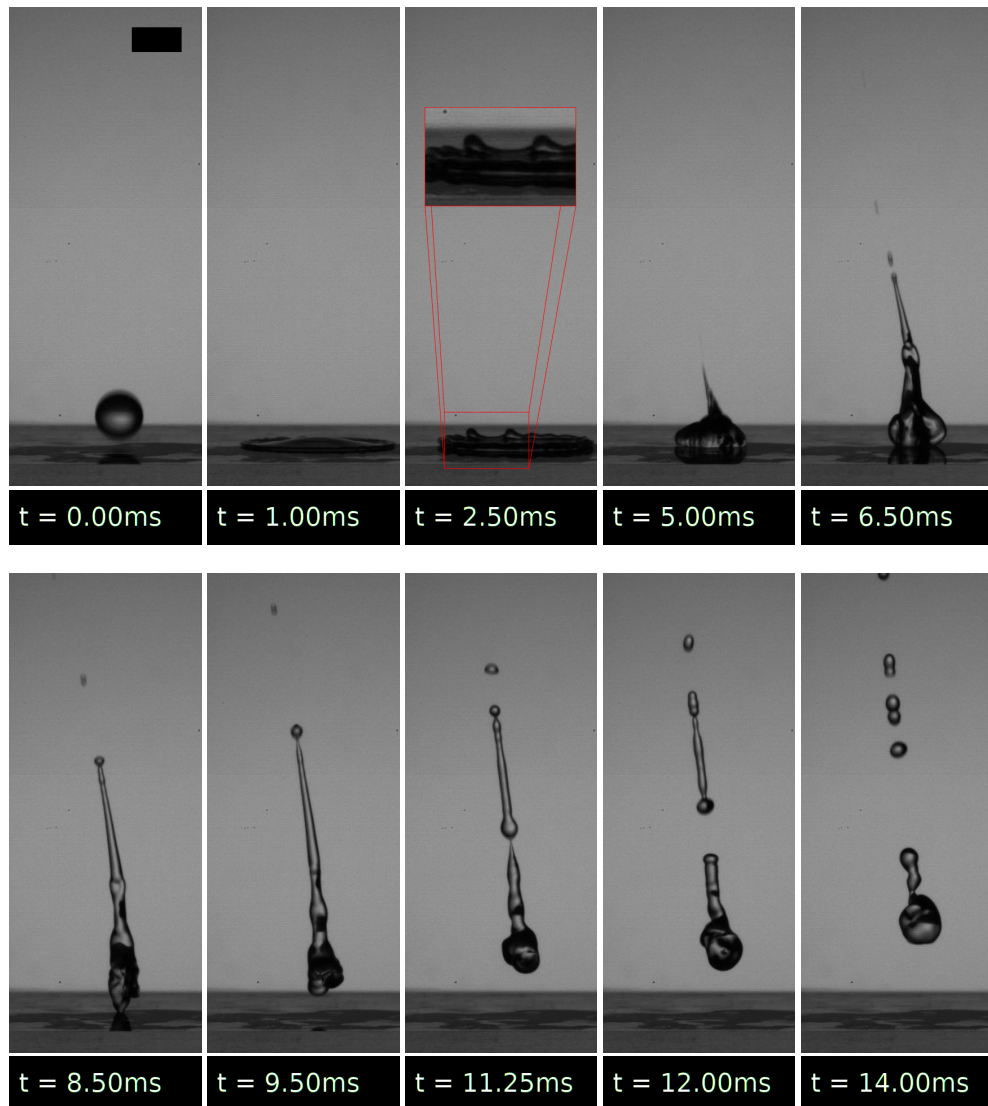


Figure 2.12: Drop impact experiment (from set B, $We = 223$) on a rigid impermeable superhydrophobic substrate. The fingering instability appears at the end of the drop spreading regime (at 2.50ms), which breaks axisymmetry and causes the drop to jet at an angle off the vertical, with irregular surface waves propagating along the drop interface. Scale bar has a width of 2mm.

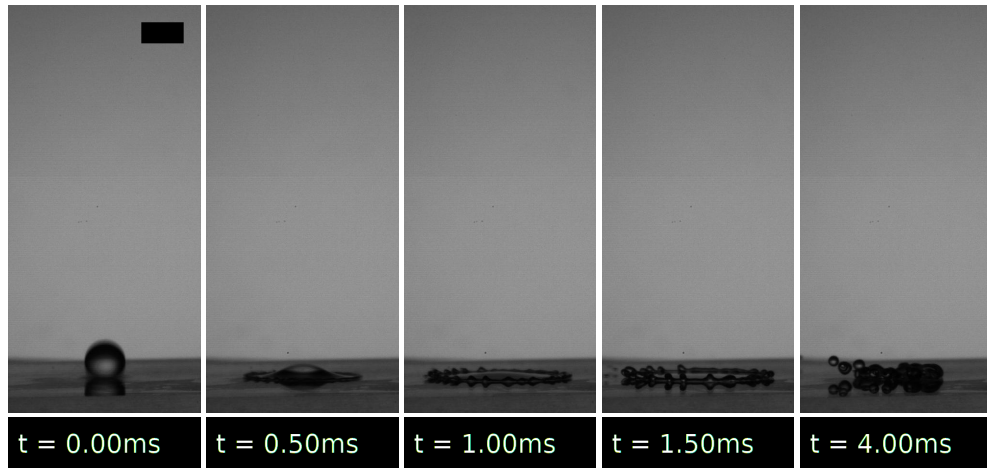


Figure 2.13: Drop impact experiment (from set B, $We = 244$) on a rigid impermeable superhydrophobic substrate. Splashing occurs soon after contact is made with the substrate. Scale bar has a width of 2mm.

Dynamic Contact Angle

We discuss here the change in contact angle between the drop and rigid substrate observed in our drop impact experiments. While it is not the focus of the research presented in this thesis considering we do not observe a change in contact angle in our powder bed impact experiments, we show in Chapter 6 that by incorporating these effects using a simple dynamic contact angle model, our simulations of drop impact can be made to better match rigid substrate impact experiments. In particular, we note a steady reduction in the dynamic contact angle as the contact line recedes, with the largest reduction coinciding with contact line pinning on the substrate at some horizontal radius from the drop centre.

When referring to contact angles in this thesis, it is always assumed these are ‘apparent’ angles [128] (limited in our case by the visible length-scale provided by the camera); the ‘true’ angle at a microscopic level could be acting differently, but considerations of its value falls outside the scope of this thesis.

Liquid drops are known to exhibit dynamic contact angles on many types of substrate (including superhydrophobic substrates [129]), with significant variation often observed depending on whether there is advancing or receding motion at the contact line. Accurate measurements of dynamic contact angles are notoriously difficult, particularly on hydrophobic substrates where measuring the angle within a cusp-like

geometry becomes even more complex. We therefore show that the contact angle between the drop and substrate is dynamic in our experiments by using a simple approach of approximating intervals inside which the contact angle lies by constructing tangent lines to the free surface drawn at the contact line.

Approximations for the contact angle are not possible while the drop is spreading for anything but the lowest impact Weber numbers; this is because the time between the moment of impact to maximum spread is at most 3ms whereas frames are captured every 0.25ms (as our focus is on liquid marble formation, which occurs on a longer time scale), so motion blur, as well as the view of the contact line being obscured by the rim of the spreading drop, prevents any approximation. Given that retraction is a slower process than spreading (taking approximately 7ms compared to 2-3ms for spreading), it is possible to provide approximations for the contact angle during retraction for a much wider range of impact Weber numbers. Figure 2.14 shows images from an experiment (from set A) with $We = 3.5$ and $\gamma = 1.35$, so the deformation of the drop during the impact is small. In these images, we see snapshots from the (albeit short) spreading and retraction phases of the impact; overlaid on both are reasonable choices (as made by eye) for upper and lower bounds for the contact angle θ_c , in this case, estimating that $150^\circ \leq \theta_c \leq 170^\circ$, which incidentally confirms that the substrate is superhydrophobic. At this low impact Weber however, it is not possible to discern whether there is a change in the contact angle, but this measurement will motivate the value of θ_c eventually chosen in our computational model.

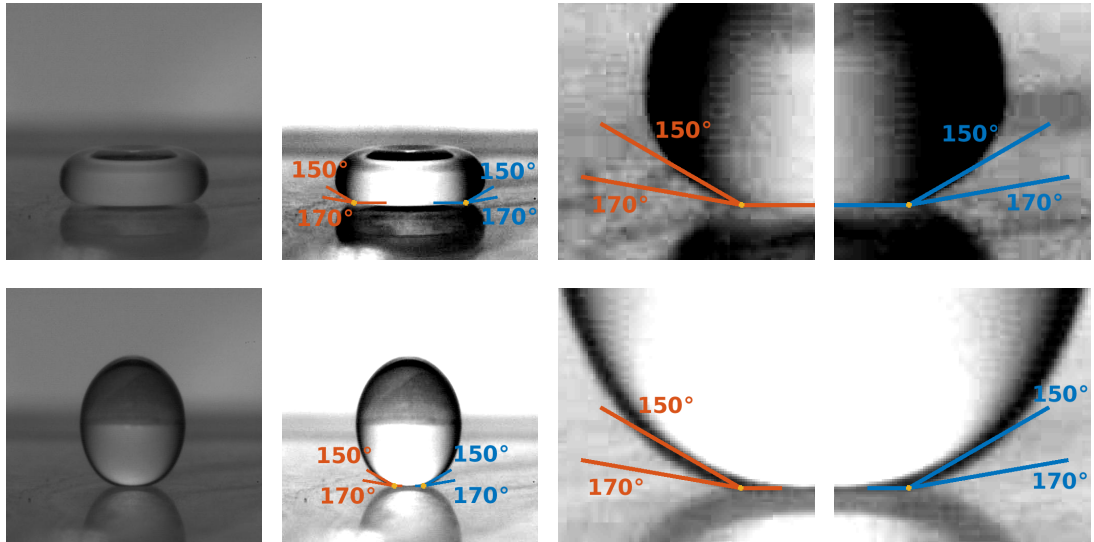


Figure 2.14: Drop impact on a rigid impermeable superhydrophobic substrate, with $We = 3.5$ and $\gamma = 1.35$. Limits on the value of the contact angle for (top) spreading, and (bottom) retraction, are given by straight lines drawn at the contact line. These images show (left) the drops as recorded, (middle-left) the drops with a greater contrast and imposed contact angle lines, and (middle-right)-(right) close-ups at the contact line.

Figure 2.15 shows images from an experiment (from set A) with $We = 49$, in which we see two snapshots at different moments of retraction. The contact angle now appears to lie between 130° and 155° part-way through retraction, and between 115° and 140° just prior to rebound, which confirms that the contact angle is dynamic. In most cases where a change in contact angle is observable in our experiments (which is always during retraction), the most significant change in the dynamic contact angle takes place when contact line appears to be pinned on the substrate. We approximate that pinning occurs at a roughly constant horizontal radius from the drop centre (the ‘pinning radius’), which is between 0.25-0.5 times the initial drop radius. When a dynamic contact angle is incorporated into our computational model to better match rigid substrate impacts (see §6.1.2), we adopt the simplest approximation, namely that the dynamic contact angle is constant (independent of the contact line speed and equal to 160° , in agreement with Figure 2.14) during the spreading phase and part-way through retraction *until* the contact line recedes to an appropriately chosen pinning radius, at which point the dynamic contact angle smoothly transitions to a lower value which is then maintained until rebound. The ultimate test for our

measurements is our ability to describe these experiments with our computational model with the extracted angles (see §6.2.1 for comparisons with our simulations).

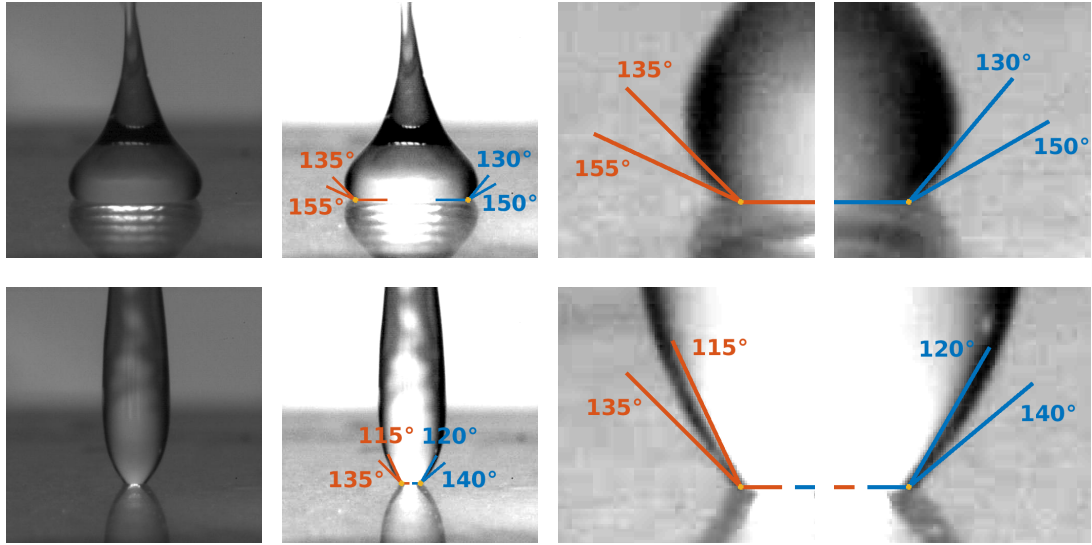


Figure 2.15: Drop impact on a rigid impermeable superhydrophobic substrate, with $We = 49$. Limits on the value of the contact angle for (top) part-way through retraction, and (bottom) just prior to rebound, are given by straight lines drawn at the contact line. These images show (left) the drops as recorded, (middle-left) the drops with a greater contrast and imposed contact angle lines, and (middle-right)-(right) close-ups at the contact line.

2.3.2 Characteristic Impacts on Superhydrophobic Powder Beds

Here we look at how the dynamics of drop impacts onto superhydrophobic powder beds change as the impact Weber number is increased in experiments, and distinguish between several regimes of phenomena that are observed.

Maximum Spread

As with the rigid substrate impacts, both sets of experiments here are conducted under the same conditions, so deviation between results are likely to be the result of slight variations in setup, particularly the packing of the powder bed.

Plots of the spreading factor γ against the impact Weber number for impacts on superhydrophobic powder beds are provided in Figure 2.16 for both sets A and B. Sev-

eral distinct phenomena are highlighted, which are similar to those given in existing research [13, 15], except that we distinguish between drops becoming encapsulated and being ‘liquid marbles’. In the context of discussions in §1.1, all encapsulated drops exhibited in our experiments are liquid marbles, but for this body of research, we reserve the term ‘liquid marble’ for encapsulated drops that either quickly return to and maintain a spherical shape after encapsulation but prior to returning to the powder bed (‘spherical liquid marbles’), or become deformed liquid marbles following particle jamming at the drop interface (as described in §1.1.5).

The first two regimes, which are observed for lower impact Weber numbers, are of drops that attain only a partial coating of powder on their interfaces, with distinctions made between cases that do *not* eject satellite droplets (see Figure 2.17) and those that do (see Figure 2.18). Following this, there is a narrow range of impact Weber numbers where the drop can become encapsulated, but no liquid marble (neither spherical nor deformed) is created, and so the drop interface is fully coated in powder but stops oscillating only when the drop returns to the powder bed (see Figure 2.19). Interestingly, encapsulation of impacted drops is only observed in these experiments post-rebound; an important detail that is incorporated into the mathematical models formulated in Chapter 3.

Spherical liquid marbles are seen to form for $We > 40$; in this case drop oscillations quickly decay, and the drop attains a spherical shape (often) before reaching the apex of its rebound flight (see Figure 2.20). Deformed liquid marbles start to appear from $We > 52$; recall that these are encapsulated drops that maintain an arrested non-spherical shape due to a tight packing of powder on their interfaces (see §1.1.5). In Figure 2.21 we see the creation of a deformed liquid marble shortly after encapsulation as a result of its elongated neck being pulled into the rest of the drop. Another example in Figure 2.22 shows an experiment where encapsulation and deformed liquid marble formation occur almost simultaneously; clearly the powder packing on the interface at the moment of encapsulation is sufficiently tight as to prevent any reduction in surface area, as was possible in the previous example. At very high impact Weber numbers ($We > 115$), splashing occurs soon after the moment of impact on the powder bed; deformed liquid marbles are still produced (see Figure 2.23), but these cases are beyond the scope of this thesis and so are neglected. A more detailed discussion of the evolution in observed phenomena (as We is increased)

in experiments that exhibit liquid marble formation is postponed to Chapter 7, where our numerical simulations are compared to our experiments.

Similar to our experiments on rigid impermeable superhydrophobic substrates in §2.3.1, we fit a scaling law to the spreading factor for $We > 20$. In this case, set A provides a scaling of $We^{0.32}$ and set B provides a scaling of $We^{0.33}$. Similar experiments of drop impacts onto hydrophobic powder beds found that the spreading factor scaled as $We^{0.4}$ [13], and $We^{0.32}$ [15, 16]. Additionally, an energy-based argument given in [15] provides a theoretical scaling of $We^{1/3}$ for the maximum spreading diameter for small $We \leq 10$, and a scaling of $We^{1/2}$ for large $We \geq 100$. These results confirm that our findings are consistent with existing research. However, it is unclear whether there is any deep physical significance to the scaling we observe; the limited data points for $We < 20$ obscures what could be a continuous change in slope. As such, we claim no great importance to this fitted law other than by a crude comparison to the similar scaling law fit on rigid substrate impacts for similar We in §2.3.1.

We find a critical impact Weber number threshold for the creation of deformed liquid marbles to be $We^* \approx 50$, which is close to existing results of $We^* = 60-70$ [13, 15]. The small difference is most likely due to different definitions of what a deformed liquid marble is. Within existing research, deformed liquid marbles are characterised as having sufficiently non-spherical arrested shapes. This is subtly different to our definition, where a deformed liquid marble is classed as an encapsulated drop that exhibits a seemingly-instantaneous transition to an arrested shape, which means that some of our ‘deformed liquid marbles’ are *quasi*-spherical and so would not be classed as being deformed in past research. Classifying deformed liquid marbles this way, particularly by distinguishing them from the creation of spherical liquid marbles (whereby an encapsulated drop exhibits a fast but *continuous* decay in drop oscillations to a spherical shape) is better suited to our research on modelling liquid marble formation, as will become apparent in Chapter 3, where energy dissipating effects (leading to oscillatory decay) and jamming of the interface (creation of a deformed liquid marble) are distinct, but connected, processes.

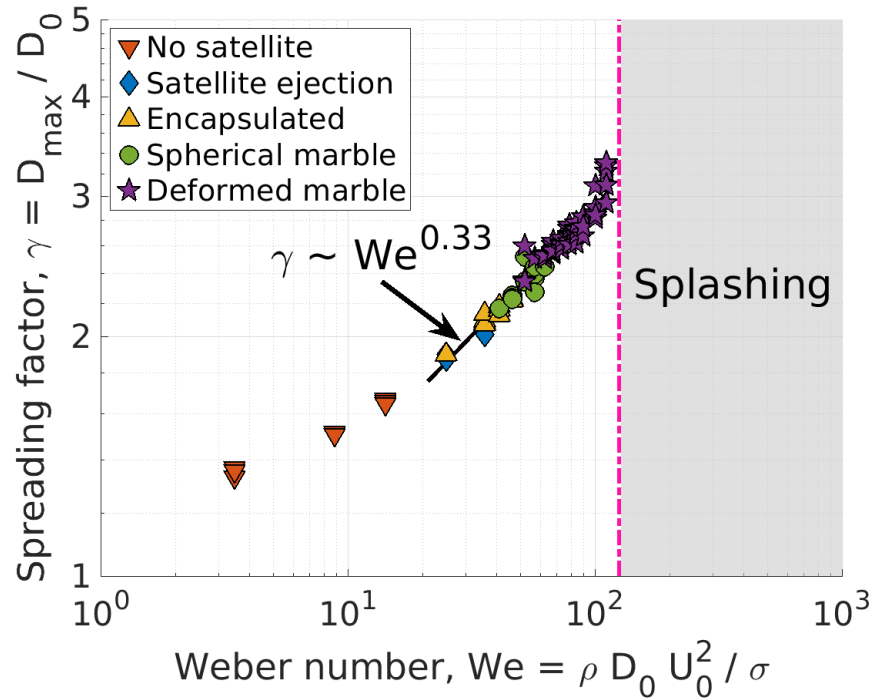
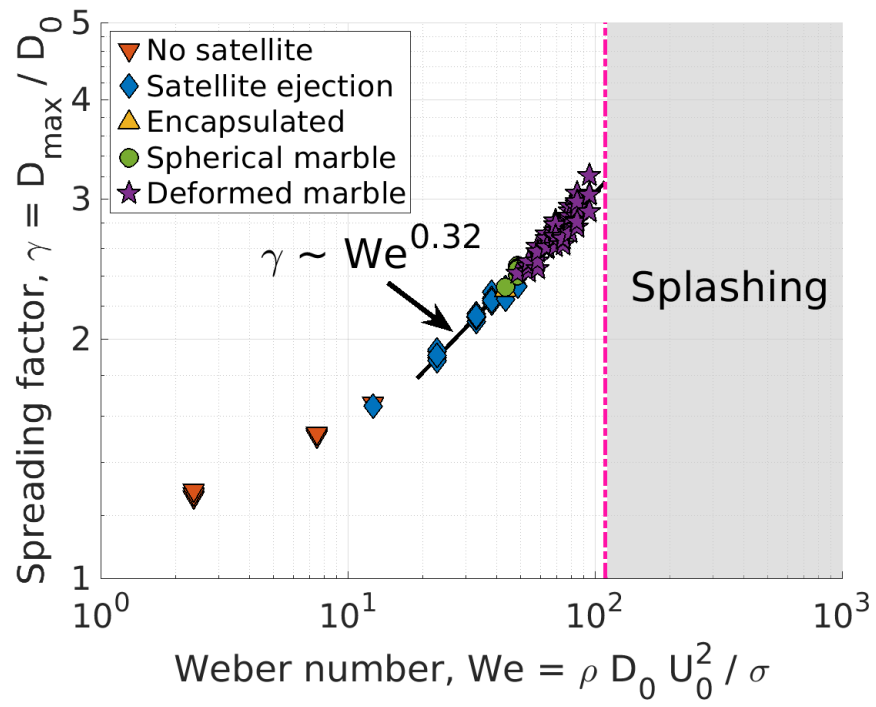


Figure 2.16: Spreading factor versus impact Weber number for drop impact onto a superhydrophobic powder bed with experiments from (top) set A, and (bottom) set B. Power law approximations are provided for both sets of experiments for $We > 20$. The R-squared value and mean squared error are (top) $R^2 = 0.9486$ and $MSE = 5.2 \times 10^{-3}$, (bottom) $R^2 = 0.9363$ and $MSE = 6.7 \times 10^{-3}$.

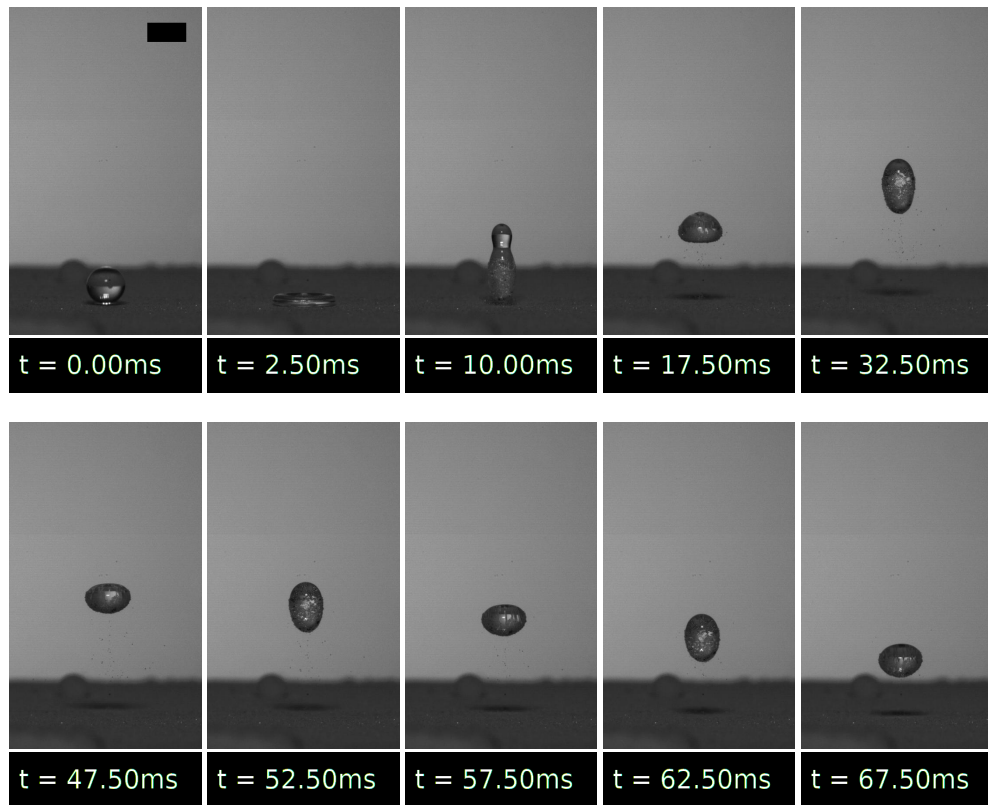


Figure 2.17: Drop impact experiment (from set B, $We = 15$) on a superhydrophobic powder bed, with partial coating of the drop interface and no satellite droplet ejection. Scale bar has a width of 2mm.

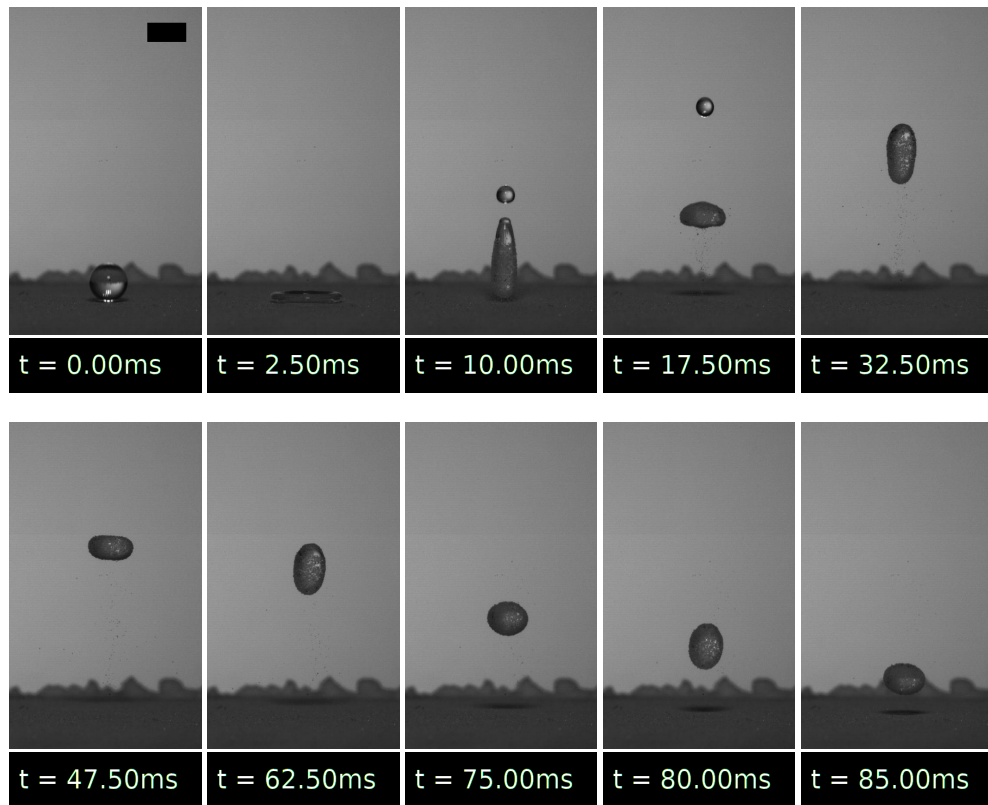


Figure 2.18: Drop impact experiment (from set B, $We = 25$) on a superhydrophobic powder bed, with partial coating of the drop interface and satellite droplet ejection. Scale bar has a width of 2mm.

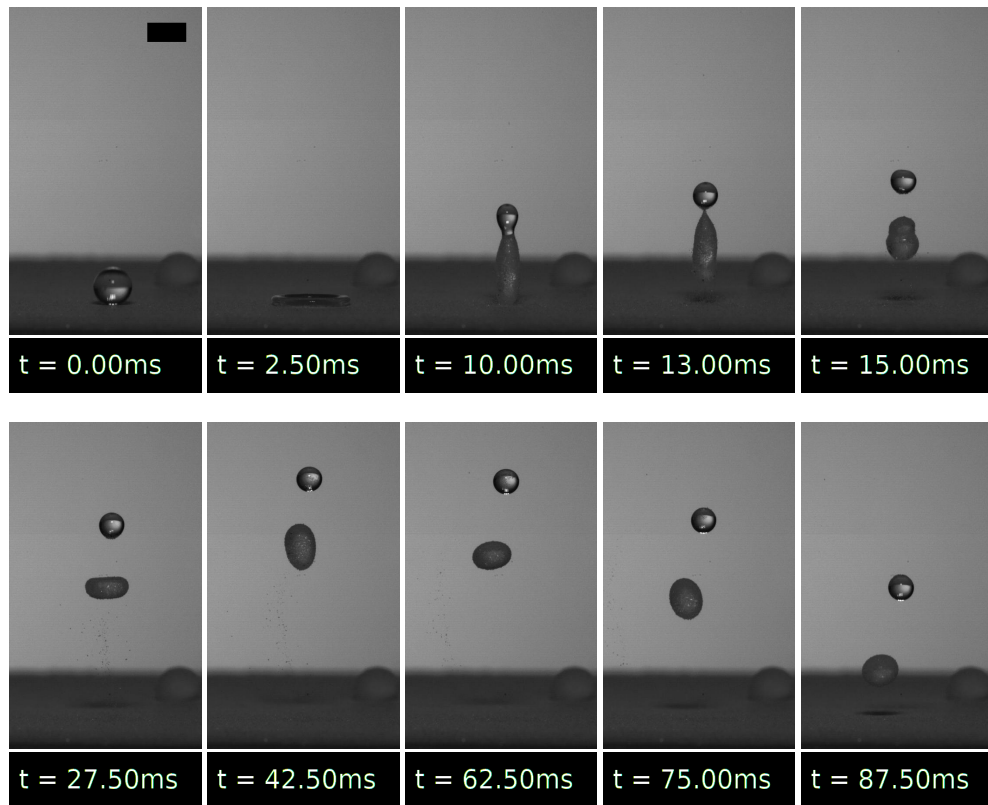


Figure 2.19: Drop impact experiment (from set B, $We = 36$) on a superhydrophobic powder bed, with drop encapsulation occurring at 13.00ms due to ejection of a large satellite droplet. Afterwards, the drop is still able to oscillate in the air until returning to the powder bed. Scale bar has a width of 2mm.

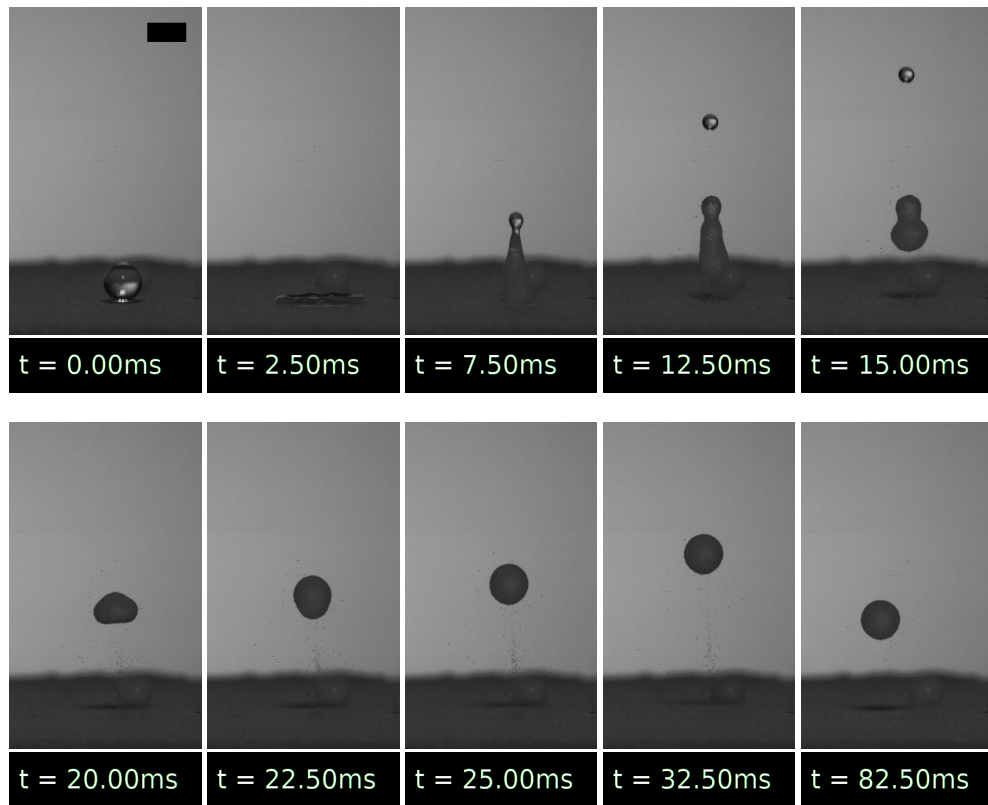


Figure 2.20: Drop impact experiment (from set B, $We = 52$) on a superhydrophobic powder bed, showing the formation of a spherical liquid marble. Encapsulation of the drop occurs due to a satellite drop ejection soon after 7.50ms, after which the drop pulls itself together, the proceeding oscillations are then quickly damped and a spherical liquid marble is formed at 25.00ms. The drop continues its flight through the air; all the while maintaining its spherical shape. Scale bar has a width of 2mm.

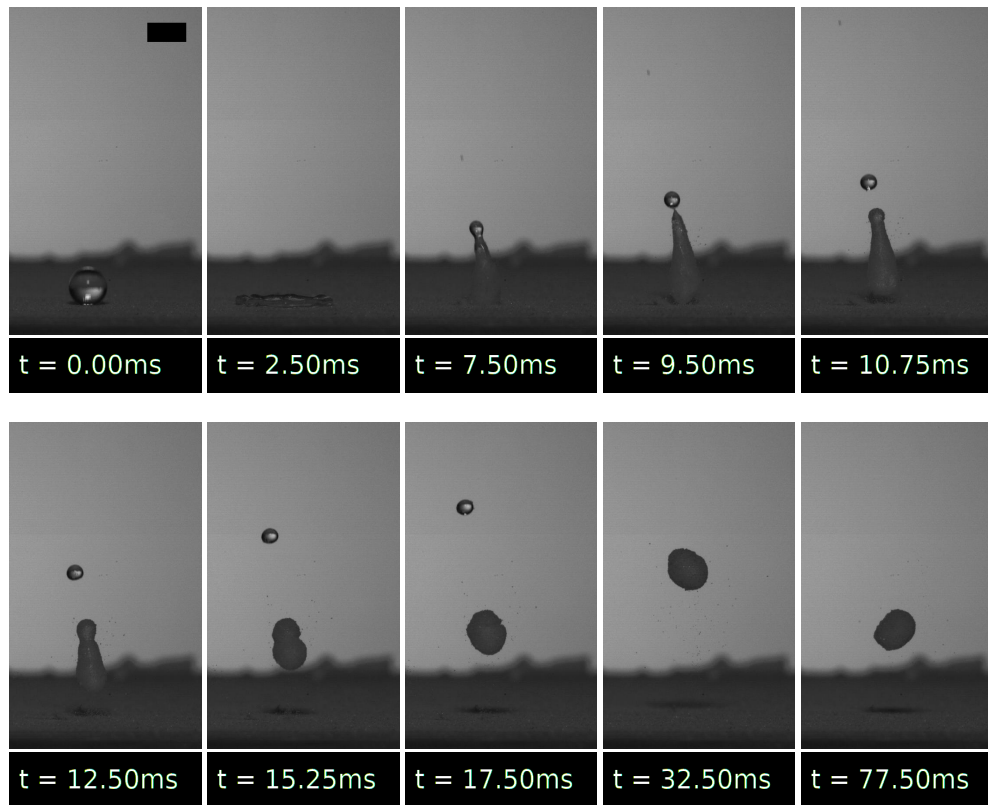


Figure 2.21: Drop impact experiment (from set B, $We = 68$) on a superhydrophobic powder bed, showing the formation of a deformed liquid marble. Encapsulation of the drop occurs due to a satellite drop ejection at 9.50ms just as the drop has lifted off from the powder bed. The drop attempts to minimise its surface area until the interface becomes jammed at 17.50ms. This shape is maintained for the remainder of the experiment until coming back into contact with the powder bed. Scale bar has a width of 2mm.

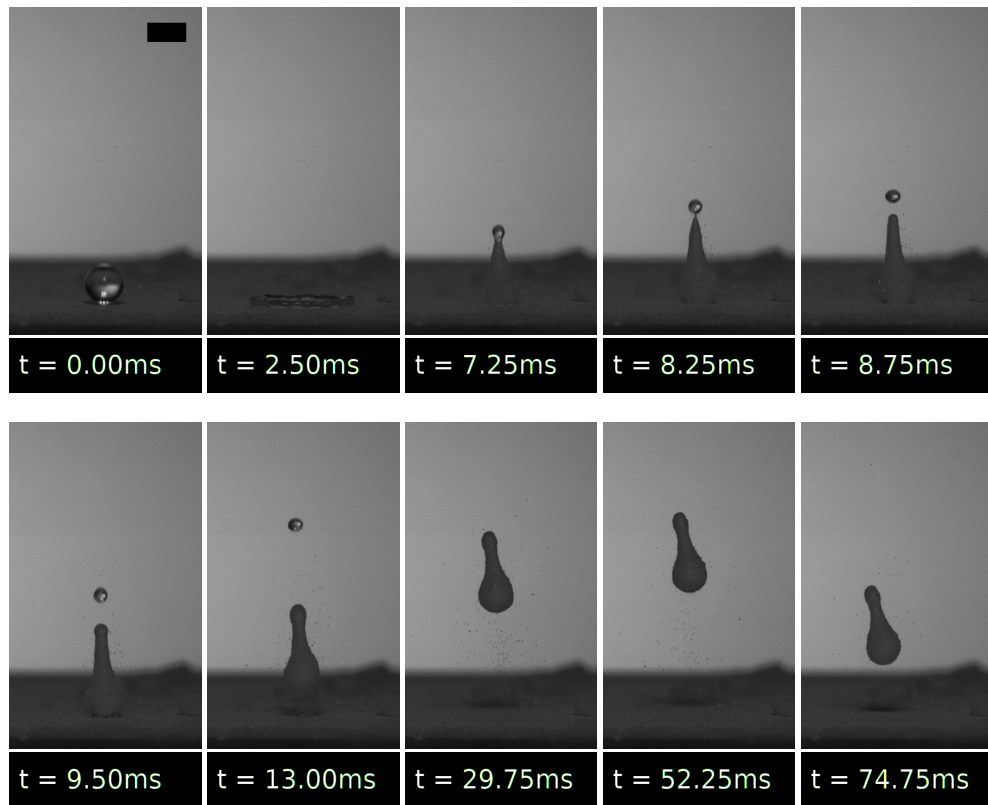


Figure 2.22: Drop impact experiment (from set B, $We = 78$) on a superhydrophobic powder bed, showing the formation of a deformed liquid marble. The desire for drops in experiments prior to this has been to form back into a sphere (the drop's minimum surface area state), so the creation of such an elongated liquid marble is testament to the effects of very tight powder packing on the drop interface. Given the marble shape remains almost unchanged from when the drop was encapsulated (at 8.25ms), it seems the powder packing was already close to the critical value for liquid marble formation at encapsulation. Scale bar has a width of 2mm.

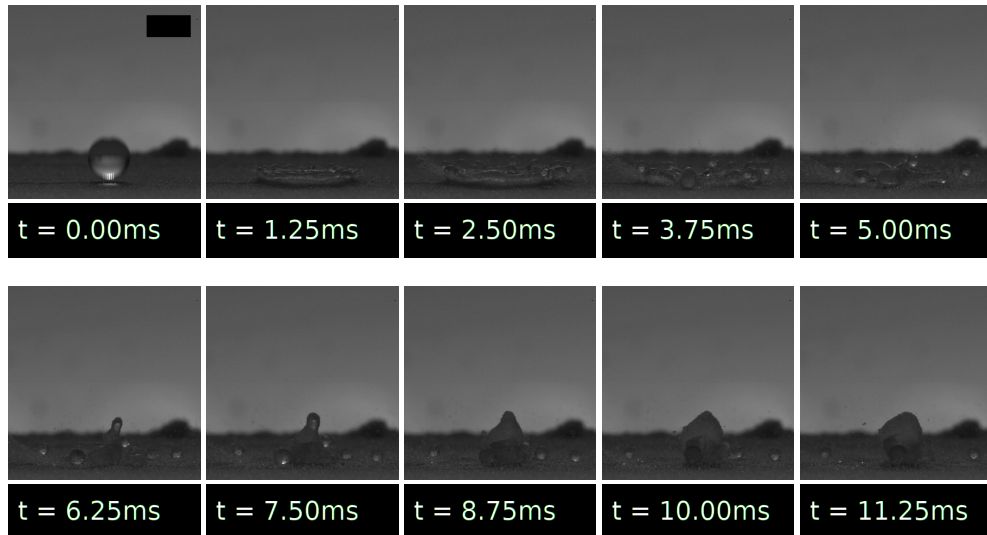


Figure 2.23: Drop impact experiment (from set A, $We = 156$) showing splashing soon after contact is made with the superhydrophobic powder bed. Scale bar has a width of 2mm.

2.3.3 Comparison between Impacts on Rigid Impermeable Superhydrophobic Substrates and Superhydrophobic Powder Beds

In the previous two subsections, we have seen that drop impacts onto both types of substrate produce similar scaling laws for the spreading factor when $We > 20$. Provided in Figure 2.24 is a combined plot of the spreading factor against impact Weber numbers for all four sets of experiments; we see that as well as having similar scaling behaviour, there is good agreement on the actual value of the spreading factor across a wide range of We (albeit with a wider variance for the powder bed impacts). Note that there is a slight vertical shift in the spreading factor for set A experiments as compared to those from set B, which may be due to a more robust setup for the latter due to greater experience in experimentation when they were conducted. Ultimately this slight variation is reasonable as the set B experiments are almost exclusively used for motivating the forthcoming computational model on liquid marble formation and for comparisons against simulations, with set A experiments largely neglected following this chapter. Also included in this plot are predictions of the spreading factor from a recently derived theoretical model for liquid drop impacts onto hydrophobic

powder beds [16], which incorporates an empirical estimate for the effect of crater formation. Equations from this model are not included here (an interested reader is directed to the cited article), but take into account the properties of the flow at impact, and the packing fraction of the powder bed. The data points presented for this model use the experimental parameters for the set B powder bed experiments. Interestingly, the model matches well with experiments on both substrates, providing additional indications that substrate deformation is likely not important, at least for reproducing the spreading factor.

The similarity between the experiments on different substrates prompts further investigation. Although a particular value for the spreading factor is not entirely indicative of rebound dynamics, the data presented in Figure 2.24 suggest that for a range of impact Weber numbers, impacts on superhydrophobic powder beds may be reasonably approximated by impacts on rigid impermeable superhydrophobic substrates.

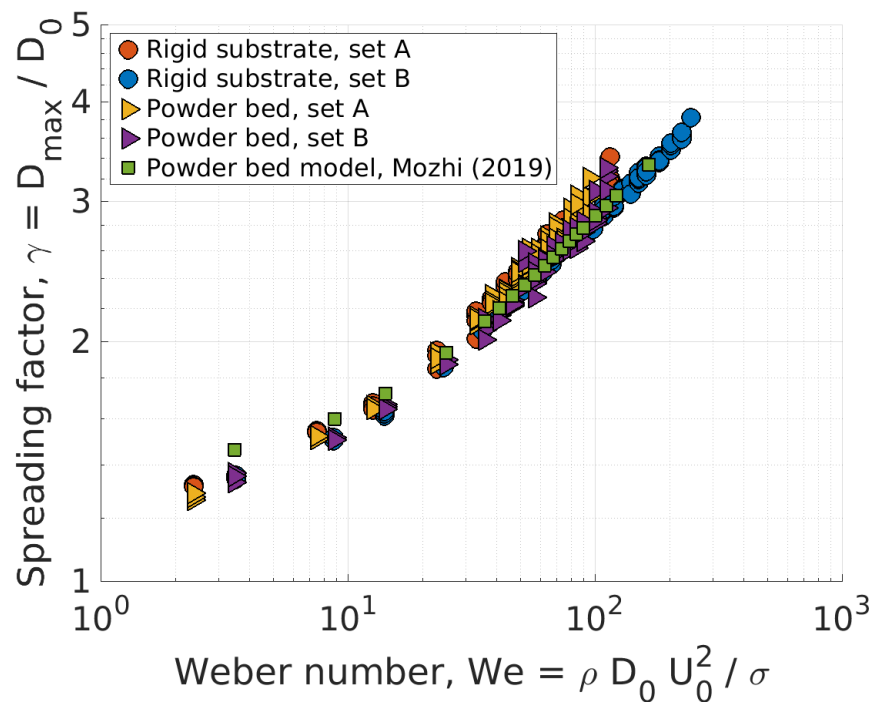


Figure 2.24: Spreading factor versus impact Weber number for all sets of experiments. Also included are data points calculated using the theoretical model in [16] which incorporates the effects of crater formation. Experimental parameters from the set B powder bed experiments are used to obtain the model results.

Provided in Figures 2.25-2.28 are visual comparisons between impacts on rigid

impermeable superhydrophobic substrates and superhydrophobic powder beds for similar impact Weber numbers ranging from $3.5 \leq We \leq 25$. The drop dynamics in each of these presented experiments is characteristic of those observed in all experiments for the stated impact Weber number. Through spreading, retraction, and for some time after rebound, the drop shapes exhibit striking similarities, for example the intricate ‘spinning-tops’ at $t = 15.00\text{ms}$ in Figures 2.27-2.28 appears for both types of substrate. The similarities in drop shape, while holding for a significant length of time, eventually break down in these experiments due to an accumulation of small differences over a long period of time.

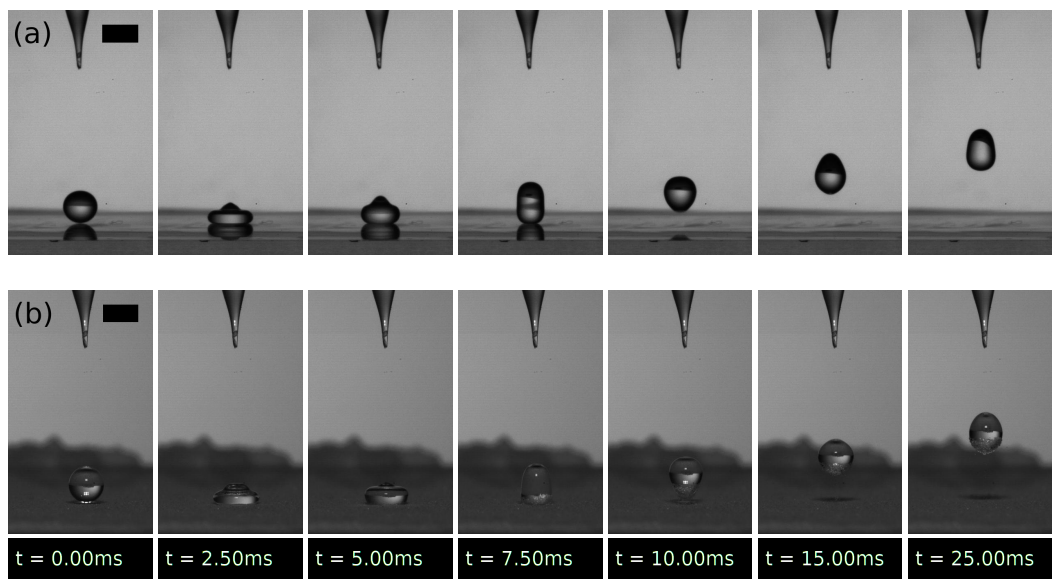


Figure 2.25: Comparison of drop impacts on (a) a rigid impermeable superhydrophobic substrate, and (b) a superhydrophobic powder bed. (a) $D_0 = 1.94\text{mm}$ and $We = 3.5$, with spreading factor $\gamma = 1.35$, (b) $D_0 = 1.99\text{mm}$ and $We = 3.5$, with spreading factor $\gamma = 1.33$. Scale bar has a width of 2mm .

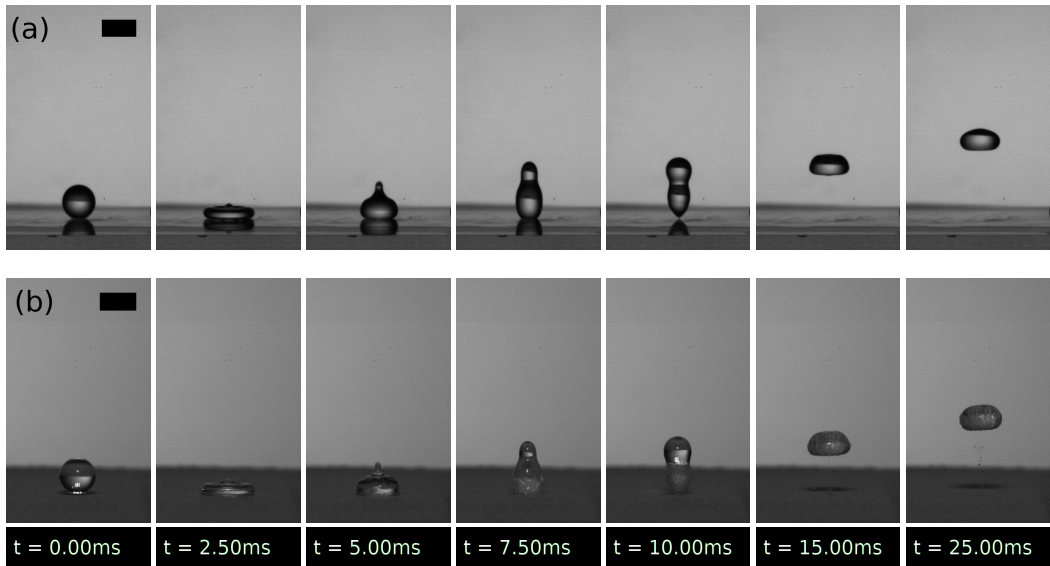


Figure 2.26: Comparison of drop impacts on (a) a rigid impermeable superhydrophobic substrate, and (b) a superhydrophobic powder bed. (a) $D_0 = 1.94\text{mm}$ and $We = 9$, with spreading factor $\gamma = 1.52$, (b) $D_0 = 1.99\text{mm}$ and $We = 9$, with spreading factor $\gamma = 1.52$. Scale bar has a width of 2mm.

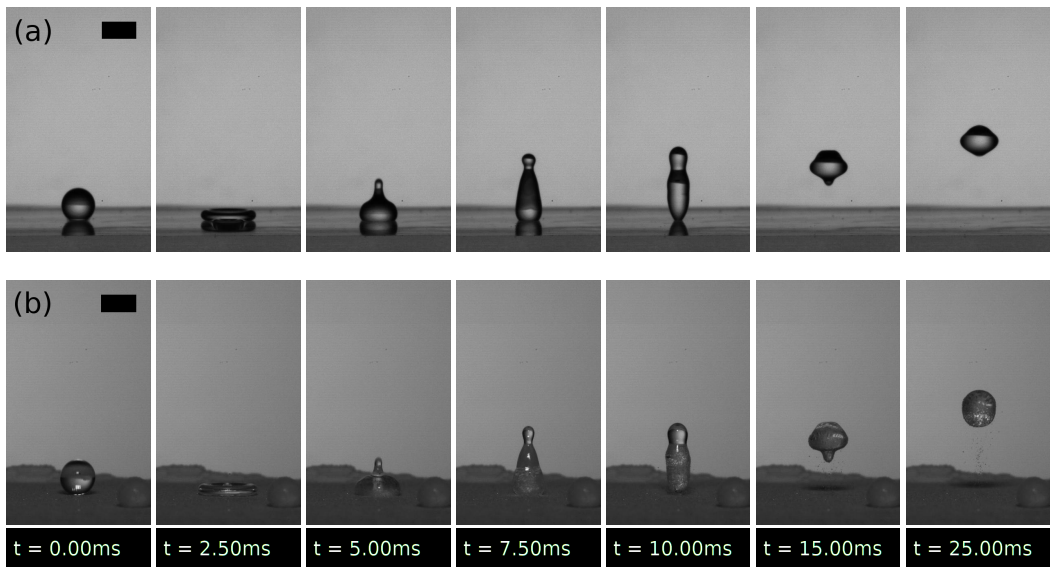


Figure 2.27: Comparison of drop impacts on (a) a rigid impermeable superhydrophobic substrate, and (b) a superhydrophobic powder bed. (a) $D_0 = 1.94\text{mm}$ and $We = 14$, with spreading factor $\gamma = 1.62$, (b) $D_0 = 1.99\text{mm}$ and $We = 15$, with spreading factor $\gamma = 1.67$. Scale bar has a width of 2mm.

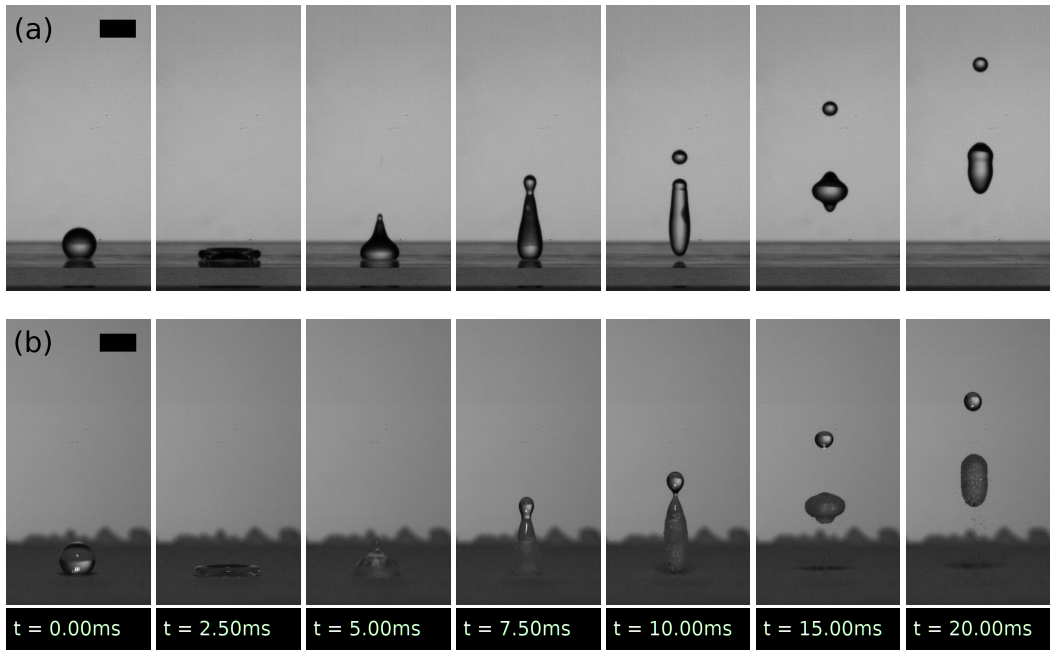


Figure 2.28: Comparison of drop impacts on (a) a rigid impermeable superhydrophobic substrate, and (b) a superhydrophobic powder bed. (a) $D_0 = 1.94\text{mm}$ and $We = 24$, with spreading factor $\gamma = 1.87$, (b) $D_0 = 1.99\text{mm}$ and $We = 25$, with spreading factor $\gamma = 1.87$. Scale bar has a width of 2mm.

For higher impact Weber numbers ($We \geq 36$), the similarity between the two types of experiments breaks down as portrayed in Figure 2.29; in fact drop shapes between individual powder bed experiments also differ. Before this, impacts onto superhydrophobic powder beds were reproducible, however we see here that this is not the case; at time $t = 7.50\text{ms}$ the difference in powder coverage between the (c) and (d) is quite considerable, indicating that interactions between the drop and the powder bed have started to become very important. By contrast, impacts on rigid impermeable superhydrophobic substrates continue to be reproducible, as seen in (a) and (b).

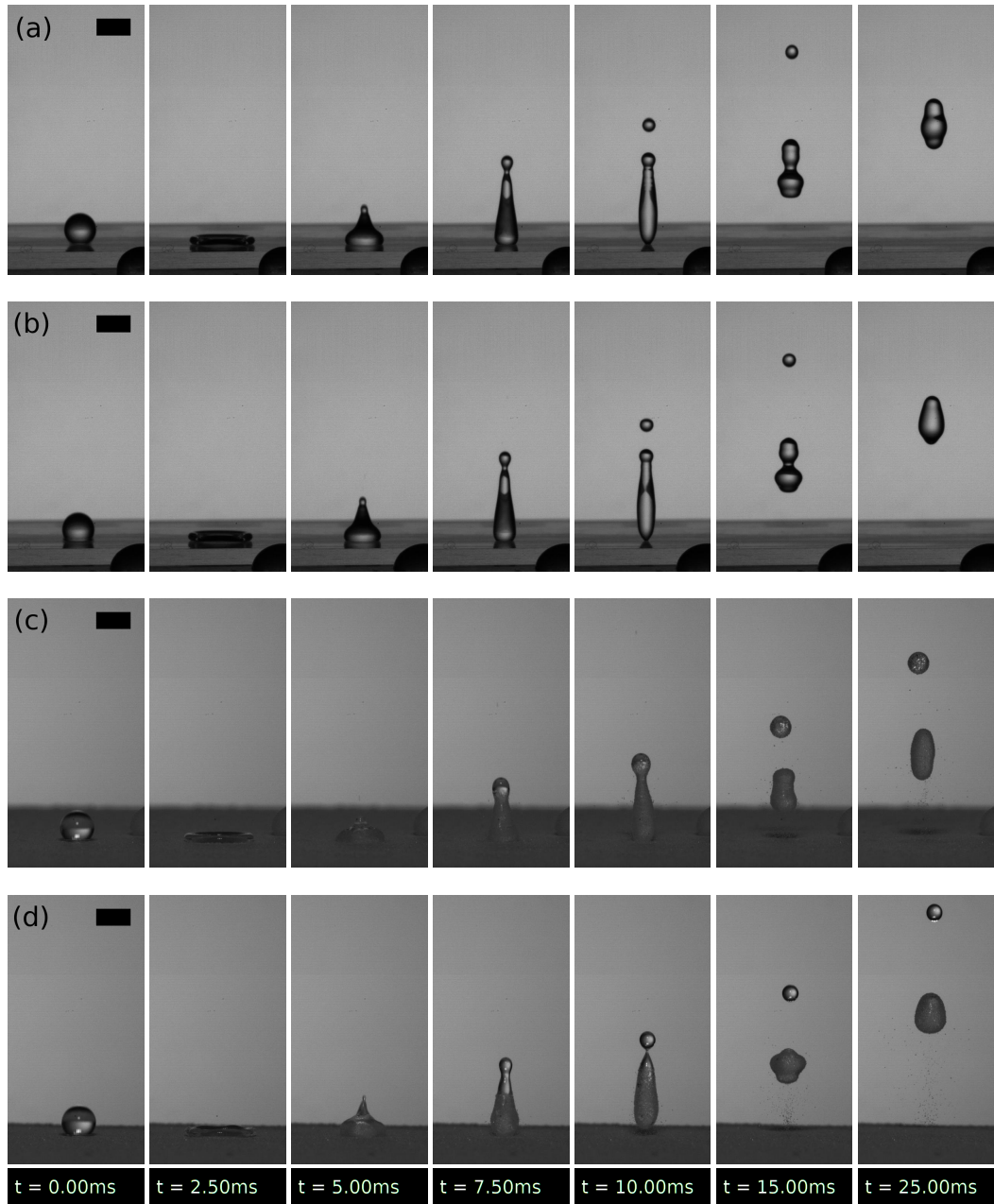


Figure 2.29: Comparison of drop impacts on (a-b) a rigid impermeable superhydrophobic substrate, and (c-d) a superhydrophobic powder bed. (a-b) $D_0 = 1.94\text{mm}$ and $We = 35$, with spreading factor $\gamma = 2.06$, (c) $D_0 = 1.99\text{mm}$ and $We = 36$, with spreading factor $\gamma = 2.07$, (d) $D_0 = 1.99\text{mm}$ and $We = 36$, with spreading factor $\gamma = 2.14$. Scale bar has a width of 2mm.

We have seen here that for a range of low impact Weber numbers, drop shapes exhibited in experiments for impacts onto superhydrophobic powder beds are largely similar to those seen after impacts on rigid impermeable superhydrophobic substrates. This has important modelling consequences as for a first approximation, it allows the powder bed to be considered rigid and impermeable; this avoids the complexity of having to capture bed deformation via some complex solid mechanics model, but its inclusion poses an interesting avenue for future research (see Chapter 8).

2.3.4 Marble Formation as a Function of Maximum Spread

For superhydrophobic powder beds, as the impact Weber number increases, so does the propensity for the drop to form (increasingly non-spherical) liquid marbles. One would expect that this trend is due to an increased mass of powder adsorbing to the drop interface for higher impact Weber numbers, and this powder reaching some critical packing threshold at earlier times in the impact process. Two obvious explanations for the adsorption of more powder particles are (i) the greater momentum at the moment of impact allowing for deeper penetration of the powder bed, and (ii) because of the enlarged maximum contact area between the drop and powder bed (due to greater spreading). Penetration of the powder bed is not a quantity that is measurable in these experiments, whereas the maximum contact area is indirectly measured via the maximum spreading diameter \hat{D}_{\max} (the contact area is defined as the disc with the perimeter of the contact line, rather than the *full* drop spread, see Figure 2.30); hence this latter factor is what we focus on.

We investigate, in turn, how the change in the maximum spreading diameter affects the two critical moments in liquid marble formation; namely drop encapsulation (full coverage of the drop interface in adhered particles) and the jamming of the drop interface (formation of a deformed liquid marble). In the remainder of this thesis, we refer to the jamming of particles at the interface as ‘interfacial freezing’ or ‘drop freezing’, following the initial description of deformed liquid marble formation as “freezing drop oscillations” [13].

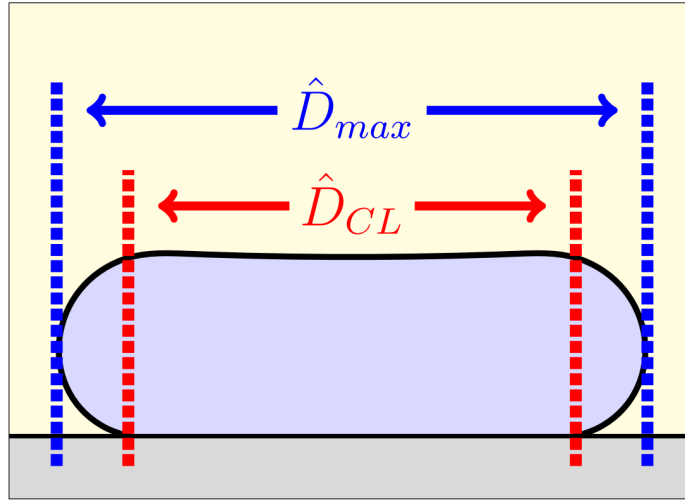


Figure 2.30: Diagram showing the difference between the spreading diameter \hat{D}_{max} , and the contact line diameter \hat{D}_{CL} , for a drop in contact with a solid substrate.

Encapsulation

Before encapsulation, the drop interface is split into a clean region and a powder coated region, with encapsulation occurring when the surface area of the clean region goes to zero and the powder coats the entire interface. At maximum spread, the powder coated region of the drop interface is exactly the part of the drop in contact with the powder bed, and it is after the drop starts to retract that we see the powder spread along the rest of the interface. We wish to know what relationship (if any) exists between the surface area of all powder coated regions (this includes partially coated satellite drops) at the moment of encapsulation, and the maximum contact area between the drop and the powder bed. We make an assumption from the outset that all powder particles that adhere to the surface of the drop have done so by the time maximum spread is reached, that is, no extra particles are adhered during retraction.

Recall that we are not able to make a direct measurement of the contact area, and instead rely on comparisons to the ‘spreading area’, which we define as the area of a disc with diameter \hat{D}_{max} , that is,

$$\hat{A}_{spread} = \frac{\pi \hat{D}_{max}^2}{4}. \quad (2.3.2)$$

Importantly, we cannot make a direct comparison between the surface area of the primary drop at encapsulation and the spreading area because of satellite drop

ejection. Before encapsulation, ejections of satellite drops are not of particular interest in almost all cases, because while they do reduce the surface area of the primary drop, they do *not* reduce the mass of powder adhered to its interface (see Figure 2.31). Satellite drop ejections can become important if they lead to the primary drop becoming encapsulated, however in many cases, encapsulation occurs via a continuous reduction of the surface area of the clean region of the interface to zero, rather than because of a satellite drop ejection (although satellite drops may have been ejected earlier on). In those cases, the mass of powder on the drop interface at encapsulation is the same as it was at maximum spread. However, there are also cases (as in Figure 2.32) where the ejection of a satellite drop is the *direct cause* of encapsulation for the primary drop. For these cases, the satellite drop takes with it some (though often small) mass of powder and (importantly) the remaining clean region of the interface, so that when it detaches, powder now coats the entirety of the primary drop interface. Unlike the previous scenario, the mass of powder on the primary drop interface is no longer equal to what it was at maximum spread.

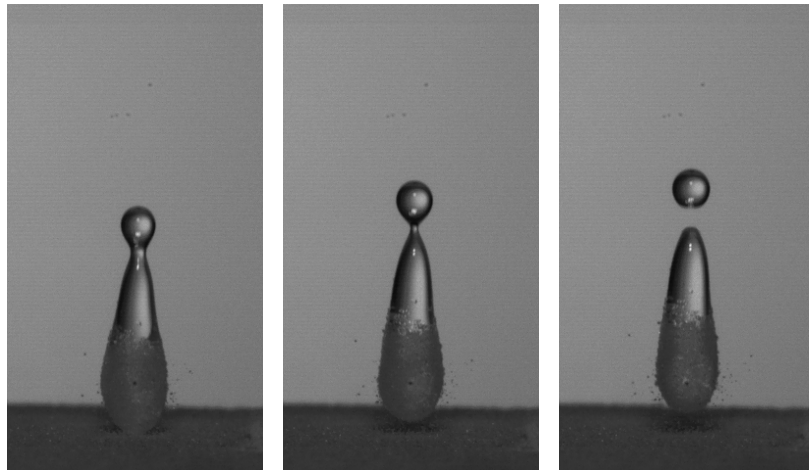


Figure 2.31: Drop impact experiment on a superhydrophobic powder bed (from set B) showing the ejection of a satellite drop that takes no adsorbed powder along with it; reducing the surface area and mass of the primary drop but *not* reducing the mass of adsorbed powder.

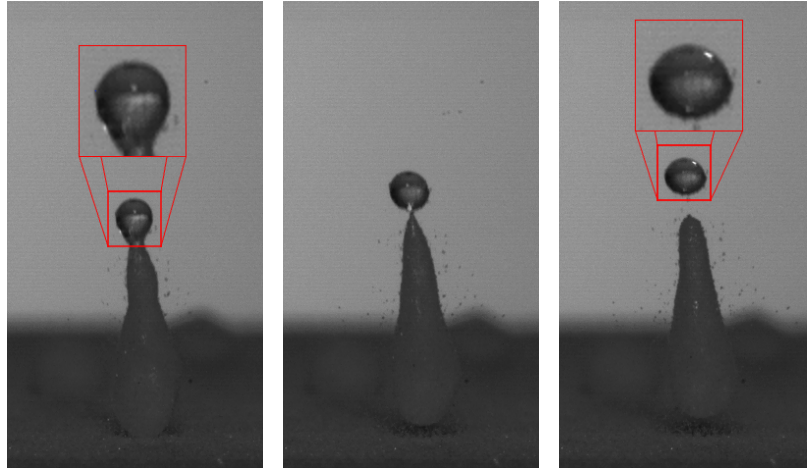


Figure 2.32: Drop impact experiment on a superhydrophobic powder bed (from set B) showing the ejection of a satellite drop that causes the encapsulation of the primary drop. Before pinch-off, the drop maintains a small region of clean interface at the drop apex. The top of the drop is then ejected, taking some adsorbed powder along with it, thus also reducing the total mass of adsorbed powder on the primary drop interface.

To capture the properties of both these scenarios, we recognise that what we are truly interested in is the total surface area the powder covers just as the drop became encapsulated, which we denote by $\hat{A}_{encap}^{(0)}$ and call the (dimensional) ‘initial encapsulation area’; which is the sum of the surface area of the primary drop plus the powder coated surface area of any partially coated satellite. Considering this quantity in particular, as opposed to the surface area of the primary drop alone, is an important modelling aspect in §3.2.4.

By defining the number

$$\alpha_{encap}^{(spr)} = \frac{\hat{A}_{encap}^{(0)}}{\hat{A}_{spread}}, \quad (2.3.3)$$

where (recall) \hat{A}_{spread} is given in equation (2.3.2), we then have a quantity that describes the extent of the powder coverage across all powder coated regions at encapsulation as a proportion of the spreading area. Naively, we may expect that $\alpha_{encap}^{(spr)}$ takes a constant value, meaning that the drop surface area covered by powder at the moment of encapsulation is some fixed proportion of the spreading area, and we may further expect that this constant would be such that the aforementioned surface area is equal to the maximum contact area. However, as will be shown later in this section,

$\alpha_{encap}^{(spr)}$ is *not* constant.

Interfacial Freezing

As discussed previously (see §1.1.5 and §2.3.2), the freezing of a drop interface is the result of a tight packing of adsorbed powder preventing further surface area reduction. As such, the freezing (interfacial jamming) process is best described in terms of powder ‘concentration’, that is, the mass of powder present per unit area of the drop interface. However, as mentioned earlier in this section, the only relevant quantity we are able to measure/approximate directly is drop surface area. We therefore make the simplest assumption that powder concentration is spatially constant within connected powder coated regions, but that it can vary in time. Under this assumption, powder concentration is inversely proportional to the surface area of the powder coated region in question, hence powder concentration rising to a critical packing threshold is equivalent to the powder coated surface area reducing to a critical area threshold.

Our aim here is to construct a similar expression to (2.3.3) but regarding freezing instead of encapsulation. This requires us to define the notion of a (dimensional) ‘initial freezing area’, $\hat{A}_{freeze}^{(0)}$, which acts as the critical area threshold just described. Given that it is because of an explicit assumption on powder concentration that we are able to solely deal with surface areas, we must take special care with satellite drop ejections that reduce the total mass of adsorbed powder on the primary drop interface. With this in mind let \hat{M} , \hat{c} , and \hat{A} denote the total mass of adsorbed powder, powder concentration (spatially constant by assumption), and surface area of the powder coated region, respectively. These are related in the following way,

$$\hat{c} = \frac{\hat{M}}{\hat{A}} \quad \text{or equivalently} \quad \hat{A} = \frac{\hat{M}}{\hat{c}} \quad \text{or equivalently} \quad \hat{M} = \hat{c}\hat{A}. \quad (2.3.4)$$

If we consider a scenario whereby there is no reduction in mass of adsorbed powder for the primary drop, then the drop interface should freeze once the surface area of the drop falls to $\hat{A}_{freeze}^{(0)}$. We therefore define this quantity as

$$\hat{A}_{freeze}^{(0)} = \frac{\hat{M}_{spread}}{\hat{c}_{freeze}}, \quad (2.3.5)$$

where \hat{M}_{spread} is the total powder mass adsorbed to the drop interface through interaction with the powder bed (which we assume is adhered once the drop has reached

maximum spread), and \hat{c}_{freeze} represents the critical packing threshold necessary for interfacial freezing (particle jamming). We would like to compare this initial freezing area in (2.3.5) across different drop impact experiments, but given that many experiments *do* exhibit pinch-off events that reduce the adsorbed powder mass (either as a catalyst for encapsulation as in Figure 2.32, or while the drop is already encapsulated as in Figure 2.33), this requires some careful attention.

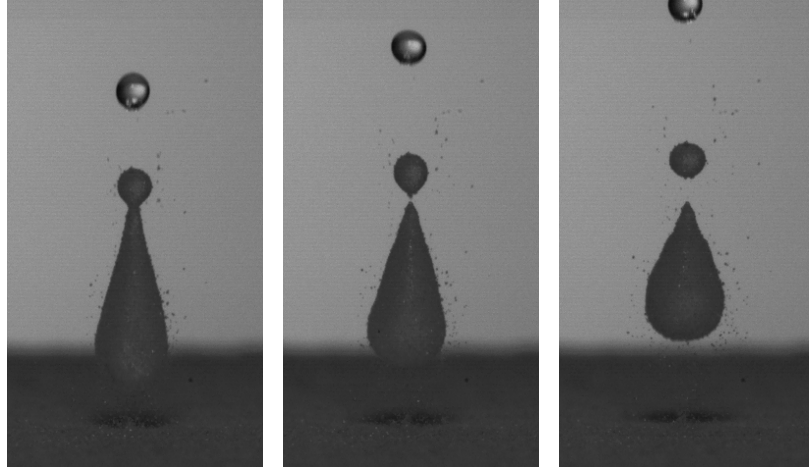


Figure 2.33: Drop impact experiment on a superhydrophobic powder bed (from set B) showing the ejection of a satellite drop while encapsulated.

The total surface area of the primary drop is clearly not continuous through a pinch-off event, nor is the total mass of adsorbed powder on the primary drop *if* the satellite drop has some powder coating on its interface. On the other hand, powder concentration on coated regions *is* continuous through all pinch-off events because the powder mass lost to a satellite drop is proportional to the powder coated surface area lost (by assumption of a spatially constant powder concentration).

Suppose that a drop experiences $n \in \mathbb{N}$ satellite drop ejections that remove powder from the primary drop before eventually the drop freezes due to the powder concentration reaching the freezing threshold \hat{c}_{freeze} . Let $\hat{M}_i^{(-)}$ and $\hat{M}_i^{(+)}$ denote the mass of adsorbed powder on the primary drop interface immediately before and after the i -th pinch-off event respectively, for $i = 1, \dots, n$. Let $\hat{A}_i^{(-)}$ and $\hat{A}_i^{(+)}$ denote the powder coated surface area of the primary drop for these same events, respectively. Finally, let \hat{M}_{n+1} and \hat{A}_{n+1} denote the adsorbed powder mass, and surface area of the primary drop at the moment of freezing some time after all of these satellite drop ejections, respectively.

As powder mass is only lost at discrete pinch-off events, we can write the powder mass at the moment of eventual freezing as the original mass multiplied by the proportion of mass still remaining after each ejection, that is,

$$\hat{M}_{n+1} = \hat{M}_{spread} \cdot \frac{\hat{M}_1^{(+)}}{\hat{M}_1^{(-)}} \cdot \frac{\hat{M}_2^{(+)}}{\hat{M}_2^{(-)}} \cdot \dots \cdot \frac{\hat{M}_n^{(+)}}{\hat{M}_n^{(-)}}. \quad (2.3.6)$$

Using the relation in (2.3.4) for powder mass, we can rewrite this equation as

$$\hat{c}_{freeze} \hat{A}_{n+1} = \hat{M}_{spread} \cdot \frac{\hat{A}_1^{(+)}}{\hat{A}_1^{(-)}} \cdot \frac{\hat{A}_2^{(+)}}{\hat{A}_2^{(-)}} \cdot \dots \cdot \frac{\hat{A}_n^{(+)}}{\hat{A}_n^{(-)}}, \quad (2.3.7)$$

where we have used the fact that powder concentration is continuous through ejection events. Dividing both sides through by \hat{c}_{freeze} and using (2.3.5) then gives us

$$\hat{A}_{n+1} = \hat{A}_{freeze}^{(0)} \cdot \frac{\hat{A}_1^{(+)}}{\hat{A}_1^{(-)}} \cdot \frac{\hat{A}_2^{(+)}}{\hat{A}_2^{(-)}} \cdot \dots \cdot \frac{\hat{A}_n^{(+)}}{\hat{A}_n^{(-)}},$$

or equivalently,

$$\hat{A}_{freeze}^{(0)} = \hat{A}_{n+1} \cdot \frac{\hat{A}_1^{(-)}}{\hat{A}_1^{(+)}} \cdot \frac{\hat{A}_2^{(-)}}{\hat{A}_2^{(+)}} \cdot \dots \cdot \frac{\hat{A}_n^{(-)}}{\hat{A}_n^{(+)}}. \quad (2.3.8)$$

where the right hand side of (2.3.8) is made up exclusively of terms that are directly measurable from experiments. Importantly, the surface area immediately following a pinch-off event is *not* the same as the surface area before the next pinch-off event (for example, $\hat{A}_1^{(+)} \neq \hat{A}_2^{(-)}$) because of dynamics causing surface area change between these events. Therefore (2.3.8) allows us to calculate, for any experiment that produces a liquid marble, a value of the initial freezing area $\hat{A}_{freeze}^{(0)}$, that is, the critical area threshold for interfacial freezing.

We can now define the number

$$\alpha_{freeze}^{(spr)} = \frac{\hat{A}_{freeze}^{(0)}}{\hat{A}_{spread}}, \quad (2.3.9)$$

which describes the critical area threshold for freezing as a proportion of the spreading area, similar to the condition for encapsulation in equation (2.3.3).

Comparison of Initial Encapsulation Areas and Initial Freezing Areas

A plot for $\alpha_{encap}^{(spr)}$ and $\alpha_{freeze}^{(spr)}$ against the spreading diameter γ is provided in Figure 2.34 using data gathered from the set B powder bed experiments. The vertical axis is denoted by $\alpha^{(spr)}$ that represents the surface area of a drop at the given critical event, divided by the spreading area. Data is provided for almost all experiments that

exhibit drop encapsulation, with exceptions for cases of an obscured view or a drop rotating toward/away from the camera meaning we cannot obtain a reliable surface area measurement. Though not part of the motivation for $\alpha_{freeze}^{(spr)}$, this parameter has been extended to include data points for experiments in which spherical liquid marbles are created, which are referred to as $\alpha_{final}^{(spr)}$ as they pertain to a liquid marble with particle concentration less than the value at critical freezing. A distinction is also made in this plot for deformed liquid marbles that are created instantaneously following encapsulation.

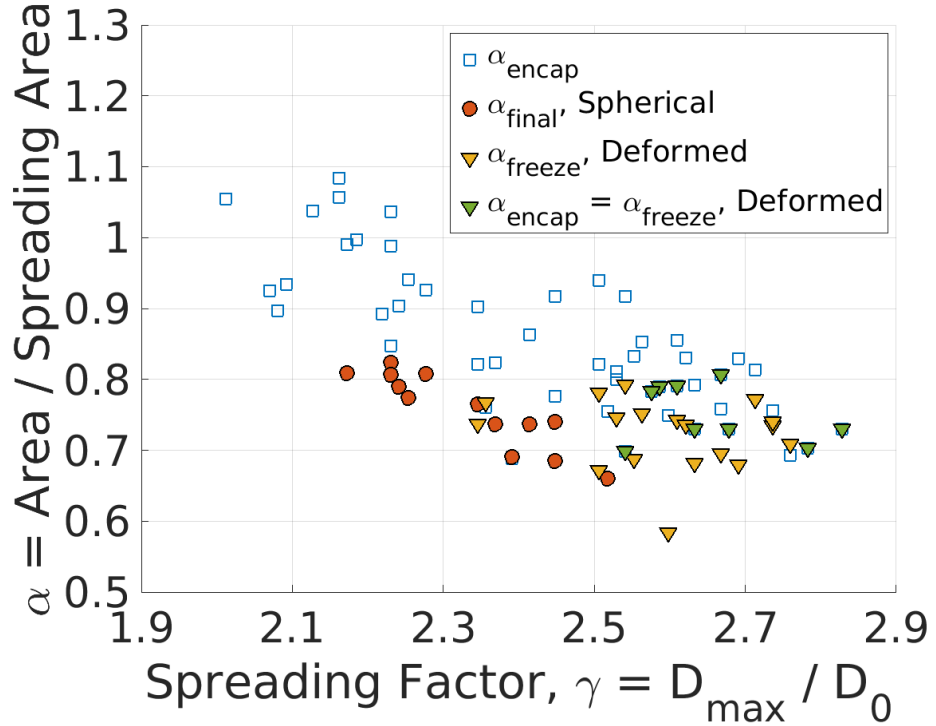


Figure 2.34: Values of $\alpha_{\text{encap}}^{(spr)}$, $\alpha_{\text{freeze}}^{(spr)}$, and $\alpha_{\text{final}}^{(spr)}$ for set B powder bed experiments that exhibit encapsulation and (possibly) liquid marble formation.

Interestingly, $\alpha_{\text{encap}}^{(spr)}$ decreases (on average) as the spreading factor increases, in other words, the surface area of the drop at encapsulation decreases as a proportion of the spreading area, as the spreading factor increases. Also, for some low spreading factor experiments, we see that $\alpha_{\text{encap}}^{(spr)} > 1$, meaning that the surface area at encapsulation is *larger* than the spreading area, which itself is larger than the maximum contact area, which suggests that the powder particles are spreading out further along the portion of the drop interface not in contact with the bed, than they were when first adhered on the underside of the drop. There is a similar decreasing trend for data points corresponding to spherical liquid marbles, however, the inclusion of these

data points primarily works to show the minimum surface area (as a proportion of the spreading area) for experiments that do not exhibit deformed liquid marbles. By contrast, there is no clear monotonic trend in data points for deformed liquid marbles, with corresponding data clustered around an average value of $\alpha^{(spr)} = 0.75$. In combination with the spherical liquid marble data points, this plot indicates that if a drop can reduce to a surface area that is 0.75 times its spreading area, then it is likely to become a deformed liquid marble, and this is almost guaranteed for $\gamma \geq 2.5$. Finally, the downward trend of $\alpha_{encap}^{(spr)}$ leads to a decreasing interval of surface areas between encapsulation and interfacial freezing, culminating in several points where $\alpha_{encap}^{(spr)} = \alpha_{freeze}^{(spr)}$, that is, where the two events occur simultaneously.

The concepts within this subsection on initial encapsulation and initial freezing areas represent novel results from an investigation into the relationship between the surface area of a drop at encapsulation and liquid marble formation, and the maximum spreading diameter (used in lieu of the maximum contact area, which is not possible to directly obtain from our experiments). The novel parameters presented here are important in our mathematical model for liquid marble formation via drop impact, and are discussed again in §3.2.4 with regards to model development. In §7.1, an amended version of Figure 2.34 is presented which bridges the connection to the maximum contact area by way of comparisons to numerical simulation of drop spreading conducted in Chapter 6, and from that amended data, a linear model for α_{encap} (the equivalent of $\alpha_{encap}^{(spr)}$ but corresponding to the maximum contact area) in terms of γ is given and then utilised in our simulations of liquid marble formation.

The next chapter focuses on the development of a mathematical model for liquid marble formation via drop impact, that is motivated by the experiments in this chapter, exploiting similarities between impacts onto powder beds and rigid impermeable superhydrophobic substrates from §2.3.3, and utilising the concepts introduced in this section.

Chapter 3

Mathematical Models

In this chapter we formulate two (novel) mathematical models which describe the formation of liquid marbles via drop impact onto a superhydrophobic powder bed, which differ only in their distinct assumptions of the importance of viscosity in the bulk flows of the liquid drop and exterior gas. These models describe the spreading, retraction, and rebound dynamics of the impacting drop, coupled with the effects of the powder particles adsorbed to its interface - focusing on their dissipative effects on drop energy, and the interfacial freezing phenomenon (corresponding to deformed liquid marble formation) that is observed at higher impact Weber numbers (as discussed in Chapter 2 and §1.1.5). We first consider the model in which bulk flows in the liquid drop and exterior gas are inviscid and discuss the interesting (and unexpected) consequences this has on the coupled surface equations. Owing to shortcomings of the inviscid model in simulating the drop spread dynamics (discussed in §4.7), we then introduce a model with viscous bulk flows whilst retaining the interesting surface equations that arise as a consequence of the inviscid model, an approach whose validity we will analyse and discuss. Many of the assumptions made during the development of these mathematical models are motivated by observations of liquid marble formation in the experiments presented in Chapter 2, and from existing research.

As discussed in §1.3, the effects of the adsorbed powder particles on the drop interface are modelled in this thesis via surface viscous forces. Surface viscosity is implemented using the Boussinesq-Scriven constitutive law (1.3.1), which is simplified in this chapter following observations from experiments.

In addition to the models for liquid marble formation, this chapter concludes with the development of a novel third-order damped oscillator model for a suspended

inviscid oscillating drop experiencing (dilatational) surface viscous effects. This model contrasts with existing (linear) approximations, in which dilatational surface viscosity effects vanish when considering zero shear surface viscosity.

For the remainder of this thesis, variables containing the ‘hat’ notation, for example $\hat{\mathbf{x}}$, denote dimensional variables, and variables without this notation denote their dimensionless counterparts. The dimensional scales relating the two are provided in Table 3.1.

3.1 Problem Formulation

Consider a drop of initially spherical shape with radius \hat{R}_0 and diameter $\hat{D}_0 = 2\hat{R}_0$, of an incompressible Newtonian fluid with (constant) density $\hat{\rho}_0$, and bulk dynamic viscosity $\hat{\mu}$. Denote the domain contained within the drop by Ω , and the bulk velocity by $\hat{\mathbf{u}}$. The smooth interface \mathcal{S}_{LG} , separating the bulk liquid drop phase from an exterior gas phase, is characterised by the (constant) surface tension $\hat{\sigma}_0$, along with surface shear and surface dilatational viscosity coefficients $\hat{\mu}^s$ and $\hat{\lambda}^s$, respectively (see equation 1.3.1), both of which may vary due to the presence of adsorbed particles on the drop interface. We denote the velocity of the liquid-gas interface \mathcal{S}_{LG} (also known as the surface velocity) by $\hat{\mathbf{v}}^s$. Initially, the liquid-gas interface \mathcal{S}_{LG} is ‘clean’, that is, without any particle coating, which we suppose gives (dimensionless) $\lambda^s = \mu^s = 0$ in line with conventional models. For a clean interface, the surface velocity $\hat{\mathbf{v}}^s$ is equal to the velocity of the bulk fluid at the interface, that is, $\hat{\mathbf{u}} = \hat{\mathbf{v}}^s$. In powder coated regions of the interface however, $\hat{\mathbf{v}}^s$ denotes the velocity of the continuum of particles adsorbed to the drop surface, which may differ from $\hat{\mathbf{u}}$ due to, for example, slip at the interface between the bulk liquid and solid particles. As will be shown, these two quantities are related within the model presented in this thesis, but a more general model that lifts some of our simplifying assumptions may prescribe completely different dynamics to $\hat{\mathbf{u}}$ and $\hat{\mathbf{v}}^s$.

Beneath the drop there exists an isotropic superhydrophobic powder bed, modelled in our case as a flat rigid impermeable superhydrophobic substrate. The justification for neglecting the effect of crater formation, and deformation of the substrate more generally, is provided in §1.4 and §2.3.3. Future research that could extend the models presented here may include the effects of substrate deformation, as is

discussed in Chapter 8.

We denote by \mathcal{S}_{LS} (when it exists) the interface between the drop and the solid substrate. Whilst some boundary conditions to the bulk flow are applied on \mathcal{S}_{LS} , it is not a free surface and there are no surface equations that hold on it, hence \mathcal{S}_{LS} will be treated differently from \mathcal{S}_{LG} . The drop boundary, denoted by $\partial\Omega$, therefore consists of the union of the liquid-gas and liquid-solid interfaces when the drop is in contact with the substrate ($\partial\Omega \equiv \mathcal{S}_{LG} \cup \mathcal{S}_{LS}$), and just the liquid-gas interface otherwise ($\partial\Omega \equiv \mathcal{S}_{LG}$).

3.1.1 Co-ordinate System

We adopt a cylindrical co-ordinate system (r, θ, z) , where r and z denote the radial and axial coordinates, respectively, and θ denotes the azimuthal angle about the z -axis. The z -axis (where $r = 0$) is chosen to coincide with the vertical axis (perpendicular to the substrate) that passes through the centre of mass of the (spherical) drop prior to impact, and the r -axis (where $z = 0$) is chosen to coincide with the surface of the flat solid substrate. In line with observations made in Chapter 2, the problem is assumed (as a first approximation) to be axisymmetric with respect to this co-ordinate system (that is, with no variation in dynamics with respect to the azimuthal angle θ), and as such, the complexity of this problem reduces from three to two spatial dimensions. Whilst the axis of symmetry for some drops is seen to rotate in our experiments some time after rebound, drop dynamics appear symmetric about the rotated axis. Instabilities that cause an irrevocable loss of axisymmetry only occur in our experiments for very high impact Weber numbers (see §2.3.2), and reproducing these effects are outside the scope of the models presented here.

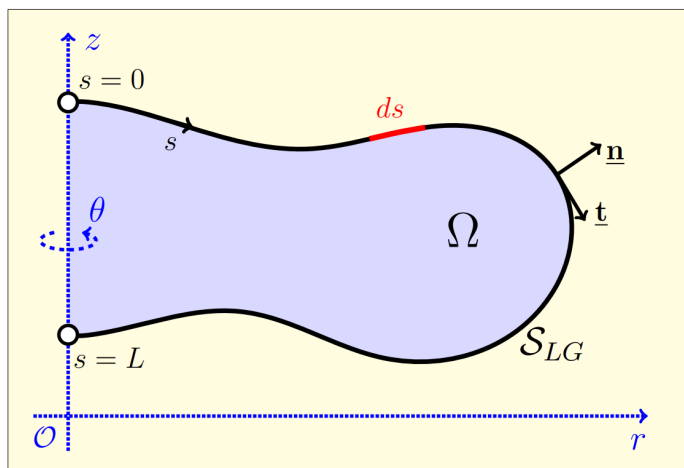


Figure 3.1: Diagram showing an axisymmetric drop domain Ω in the (r, z) -plane with a one dimensional boundary curve representation for the interface \mathcal{S}_{LG} , with arclength s , normal vector $\underline{\mathbf{n}}$, tangent vector $\underline{\mathbf{t}}$, and line element ds .

The reduction via axisymmetry means that the drop's liquid-gas interface \mathcal{S}_{LG} can be considered, in the (r, z) -plane, as a one dimensional boundary curve with a single parameter that spans the interface (see Figure 3.1). This parameter is chosen to be the arclength, s , and ranges from $s = 0$ where the curve 'first' intersects the axis of symmetry (without loss of generality choose the intersection with greatest z coordinate), to $s = L > 0$ at the second intersection, or at the contact line where it meets the liquid-solid interface \mathcal{S}_{LS} , if the latter interface exists.

We denote the unit tangent vector at the liquid-gas interface \mathcal{S}_{LG} in the (r, z) -plane pointing in the direction of s -increasing by $\underline{\mathbf{t}}$, and the associated unit normal vector by $\underline{\mathbf{n}}$. We note that

$$\underline{\mathbf{t}} \cdot \underline{\mathbf{e}}_\theta = \underline{\mathbf{t}} \cdot \underline{\mathbf{n}} = 0,$$

and

$$\underline{\mathbf{t}} = \frac{\partial r}{\partial s} \underline{\mathbf{e}}_r + \frac{\partial z}{\partial s} \underline{\mathbf{e}}_z \quad \text{and} \quad \underline{\mathbf{n}} = -\frac{\partial z}{\partial s} \underline{\mathbf{e}}_r + \frac{\partial r}{\partial s} \underline{\mathbf{e}}_z,$$

where $\underline{\mathbf{e}}_r$, $\underline{\mathbf{e}}_\theta$, and $\underline{\mathbf{e}}_z$ denote the unit vectors along the r -, θ -, and z -axes respectively. There is a second tangent vector at the interface, pointing in the direction of θ -increasing, but we need not consider this because of axisymmetry.

The surface divergence operator is defined on the interface \mathcal{S}_{LG} as [130]

$$\nabla_s := \underline{\underline{\mathbf{P}}}^s \cdot \nabla, \tag{3.1.1}$$

where $\underline{\underline{\mathbf{P}}}^s \equiv \underline{\underline{\mathbf{I}}} - \underline{\mathbf{n}}\underline{\mathbf{n}}$ is the surface projection operator, and $\underline{\underline{\mathbf{I}}}$ is the identity matrix,

so that ∇_s is the projection of the classical divergence operator onto the interfacial tangent space. In an axisymmetric formulation this is given by (see Appendix A for derivation), for $r \neq 0$:

$$\begin{aligned}\nabla_s \cdot \underline{\mathbf{a}}^s &= \frac{\partial a_t^s}{\partial s} + \frac{a_t^s}{r} (\underline{\mathbf{t}} \cdot \underline{\mathbf{e}}_r) + a_n^s (\nabla_s \cdot \underline{\mathbf{n}}), \\ &= \frac{\partial a_t^s}{\partial s} + \frac{a_t^s}{r} \frac{\partial r}{\partial s} + a_n^s (\nabla_s \cdot \underline{\mathbf{n}}),\end{aligned}\tag{3.1.2}$$

for a vector $\underline{\mathbf{a}}^s = a_t^s \underline{\mathbf{t}} + a_n^s \underline{\mathbf{n}}$ defined on the boundary curve. The surface divergence of the unit normal (equal to twice the mean curvature κ), is given by [131]

$$\nabla_s \cdot \underline{\mathbf{n}} = 2\kappa = \begin{cases} \frac{\partial z}{\partial s} \frac{\partial^2 r}{\partial s^2} - \frac{\partial r}{\partial s} \frac{\partial^2 z}{\partial s^2} - \frac{1}{r} \frac{\partial z}{\partial s}, & r > 0 \\ -2 \frac{\partial^2 z}{\partial s^2}, & r = 0. \end{cases}\tag{3.1.3}$$

Throughout this thesis, the term $(\nabla_s \cdot \underline{\mathbf{n}})$ will commonly be referred to as the curvature.

3.1.2 Qualitative Descriptions of the Dynamics

The stages (potentially) leading to liquid marble formation are illustrated in Figure 3.2 and described here. Moving with (constant) downward vertical velocity $\hat{U}_0 \underline{\mathbf{e}}_z$, the (spherical) drop of radius \hat{R}_0 impacts the substrate and spreads along it until reaching a maximum extension, then retracts, with a vertical jet forming along the z -axis culminating in the drop rebounding from the substrate and oscillating in the surrounding gas. In the midst of these stages, solid powder particles have adsorbed to the liquid-solid interface \mathcal{S}_{LS} through contact with the substrate, which move, during retraction, to the liquid-gas interface \mathcal{S}_{LG} . The adsorbed particles affect flow dynamics, particularly after rebound while the surface area of the liquid-gas interface attempts to decrease towards its minimum value (at a sphere). With sufficient particle coverage, the drop may become encapsulated, leading (potentially) to spherical/deformed liquid marble formation.

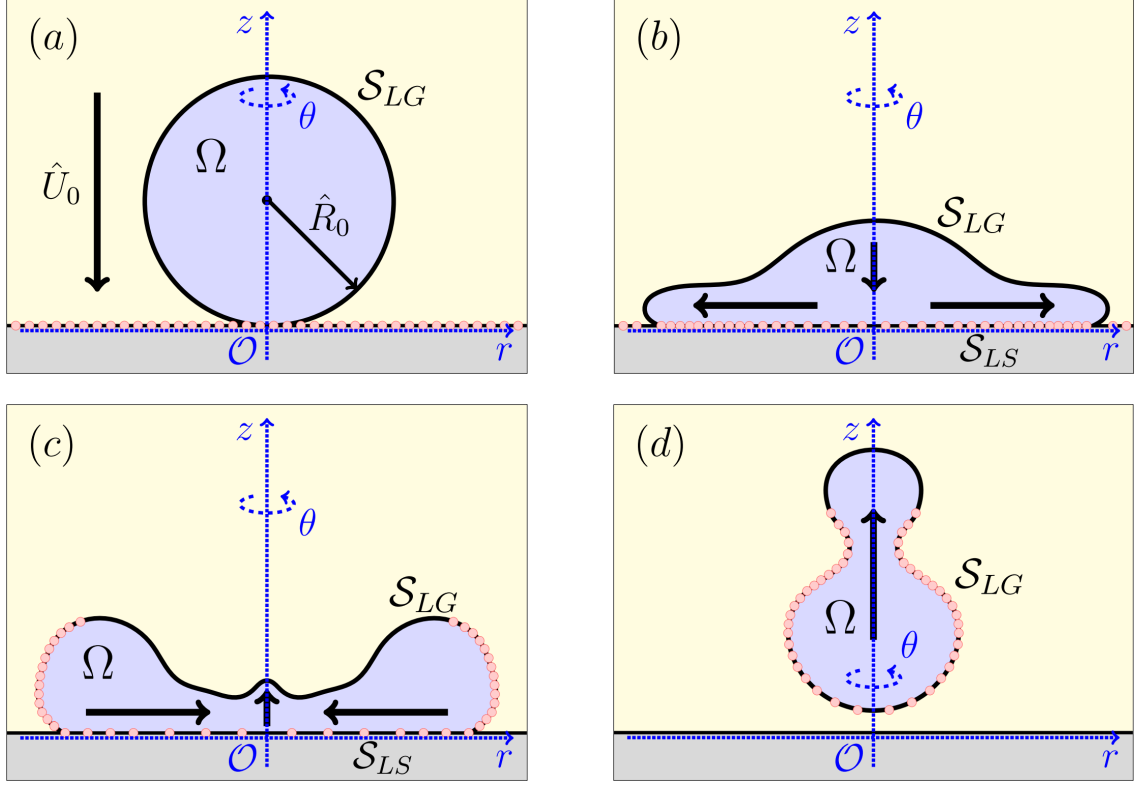


Figure 3.2: Stages preceding (potential) liquid marble formation. (a) Spherical drop with radius \hat{R}_0 with clean liquid-gas interface \mathcal{S}_{LG} impacts the substrate with speed \hat{U}_0 . (b) The drop spreads along the substrate while adsorbing powder to the liquid-solid interface \mathcal{S}_{LS} . (c) Following maximum spread, the drop retracts, and a vertical jet forms along the z -axis. Some adsorbed powder moves onto \mathcal{S}_{LG} from \mathcal{S}_{LS} . (d) The drop rebounds from the substrate and oscillates within the gas.

As per the discussion in §1.2, we treat the adhered particle coating on the drop surface as a continuum. Also recall that per the discussion in §1.3, we model the effects of the (continuum) particle coating using surface viscosity, which is incorporated using the Boussinesq-Scriven constitutive law (1.3.1). This constitutive law contains surface shear and surface dilatational viscous coefficients $\hat{\mu}^s$ and $\hat{\lambda}^s$, respectively, which we consider to be negligible for a clean interface, and otherwise depend on the concentration of adhered particles within the region under consideration. Given this, let \hat{c} (units kg/m^2) denote the (dimensional) concentration of adhered particles on the drop surface. Once the drop and substrate have come into contact, the entire liquid-solid interface \mathcal{S}_{LS} is assumed to instantaneously attain a nonzero concentration of adhered powder particles, so (dimensionless) $c > 0$ everywhere on \mathcal{S}_{LS} , while $c = 0$

everywhere on \mathcal{S}_{LG} . During retraction, the particles make their way from the liquid-solid interface \mathcal{S}_{LS} to the liquid-gas interface \mathcal{S}_{LG} , meaning we then have $c > 0$ in some regions of \mathcal{S}_{LG} , which (importantly) means that μ^s and λ^s are no longer negligible. As previously highlighted, the liquid-solid interface \mathcal{S}_{LS} is not a free surface, and is instead considered an extension of the bulk domain on the surface of the solid substrate where boundary conditions are applied. As such, the adhered particle coating on \mathcal{S}_{LS} does not affect flow dynamics.

For our models, we consider the simplest case, whereby we set (dimensionless) $\mu^s = 0$ in the forthcoming model equations and so only the surface dilatational component of surface viscosity can affect flow dynamics. The motion on the drop surface as observed in our experiments (see Chapter 2) is not *purely* dilatational, as it would be only in the case of uniform expansion/contraction of the drop surface area. However, it appears justified to claim that surface dilatation must be *at least* about as important as shearing motion in our experiments, given that for post-rebound drop dynamics, there is clearly surface dilatation, particularly for higher impact Weber number cases where surface area change acts as a catalyst for interfacial freezing, while there is no *clear* surface shearing. To achieve the correct dissipative effects, we can increase the dilatational surface viscous coefficient as appropriate (and is done in §7.2 to match oscillatory decay observed in experiments). Although (as discussed in §3.3) dilatational surface viscous effects vanish in the limit of small deformations, we are focused primarily on cases with large drop deformations. We postpone an explanation of how incorporating $\mu^s > 0$ in the forthcoming surface equations would impact the mathematical model to Chapter 8, where it is discussed as a possible extension of the research presented in this thesis.

We incorporate the effects relating the drop spreading over discrete particles in the powder bed into our model via a slip length that affects the bulk drop flow in a small boundary layer within the drop, close to the substrate. Incorporating small-scale asperities on a substrate into a slip length on an effective smooth surface (in our case the surface of the rigid impermeable substrate) is a standard way of modelling drop spreading on (macroscopically) flat superhydrophobic surfaces [132]. The modelling for the slip length is found in §3.2.2, and only applies to the model which approximates both bulk flows as viscous.

3.2 Development of a Mathematical Model for Liquid Marble Formation via Drop Impact

We will now derive a set of equations that, for the problem formulation in §3.1, will describe the liquid marble formation process following drop impact onto a superhydrophobic powder bed. We begin with development of the surface equations followed by their boundary conditions at an intersection with the axis of symmetry, or where the liquid-gas and liquid-solid interfaces meet (at the contact line), and conclude with development of the bulk equations. The choice of whether or not to consider the bulk flows as inviscid turns out to be very consequential; an inviscid assumption considerably simplifies the surface equations. Given the problem contains complex surface phenomena, it is important to distinguish between what equations hold on the interface because of assumptions relating directly to interfacial quantities, and what holds because of choices made regarding bulk flows. Hence, the model is constructed in this somewhat unorthodox way of developing surface equations first, followed by bulk equations.

Given that we present two (very similar) models that differ only on their modelling of the importance of viscosity in the bulk flows, we introduce the Reynolds number [133], given by

$$\text{Re} = \frac{\hat{\rho}_0 \hat{U} \hat{D}_0}{\hat{\mu}}, \quad (3.2.1)$$

which is a dimensionless number that relates the relative importance of bulk inertial and bulk viscous forces for (in our case) the liquid drop. Recall that drop impact experiments presented in Chapter 2 were characterised by their impact Weber number. If we calculate the impact Reynolds number (so with $\hat{U} = \hat{U}_0$ in equation 3.2.1) for those experiments, we see that encapsulation is observed for experiments with $\text{Re}_{\text{impact}} > 1600$, and deformed liquid marbles are created for $\text{Re}_{\text{impact}} > 2600$. So in all cases that we are interested in, the Reynolds number, at least at the moment of impact, is high. Note that the length scale used in (3.2.1) is the initial drop diameter rather than the initial drop radius (as in the forthcoming dimensional scales), which is chosen to ensure consistency with the Weber number as introduced in (1.1.1).

All variables that are given in their dimensionless form in this thesis use the scales provided in Table 3.1. These scales are based on the balance of inertial and capillary forces; which is the most appropriate for our high Reynolds number problem.

Table 3.1: Dimensional scales for mathematical models.

Length	Bulk Density	Surface Tension
\hat{R}_0	$\hat{\rho}_0$	$\hat{\sigma}_0$
Time	Velocity	Powder Concentration
$\sqrt{\hat{\rho}_0 \hat{R}_0^3 / \hat{\sigma}_0}$	$\sqrt{\hat{\sigma}_0 / \hat{\rho}_0 \hat{R}_0}$	$\hat{\rho}_0 \hat{R}_0$
Bulk Pressure	Bulk Viscosity	Dilatational Surface Viscosity Coefficient
$\hat{\sigma}_0 / \hat{R}_0$	$\sqrt{\hat{\sigma}_0 \hat{\rho}_0 \hat{R}_0}$	$\sqrt{\hat{\sigma}_0 \hat{\rho}_0 \hat{R}_0^3}$

3.2.1 Liquid-Gas Surface Equations

We begin with a derivation of the kinematic condition for the drop's liquid-gas interface \mathcal{S}_{LG} , which describes the interface's evolution in time, followed by a corresponding momentum equation for this interface.

Let Ω_G denote the exterior gas domain and recall that Ω denotes the interior liquid drop domain. Let $f(\mathbf{x}, t) = 0$ be the implicit equation of the liquid-gas interface \mathcal{S}_{LG} such that $f < 0$ for $\mathbf{x} \in \Omega$ and $f > 0$ for $\mathbf{x} \in \Omega_G$, where \mathbf{x} and t denote space and time, respectively. Consider the unit normal $\mathbf{n} = \nabla f / |\nabla f|$ pointing from the liquid phase (where $f < 0$) into the gas phase (where $f > 0$). By continuity of the function f , the following (dimensionless) condition can be retrieved,

$$\frac{\partial f}{\partial t} + \underline{\mathbf{v}}^s \cdot \nabla f = \frac{\partial f}{\partial t} + (\underline{\mathbf{v}}^s \cdot \mathbf{n}) |\nabla f| = 0 \quad \text{on } \mathcal{S}_{LG}, \quad (3.2.2)$$

where (recall) $\underline{\mathbf{v}}^s$ is the (dimensionless) surface velocity at \mathcal{S}_{LG} . The kinematic condition (3.2.2) specifies the shape of the interface over time in terms of the normal projection of $\underline{\mathbf{v}}^s$ and holds for any smooth fluid-fluid interface moving in space [134]. Note that equation (3.2.2) implicitly defines the normal component of $\underline{\mathbf{v}}^s$ but does not define its component tangential to the liquid-gas interface. Although a future equation (c.f. equation 3.2.23) does provide a condition on the derivative of $\underline{\mathbf{v}}^s$ (and so on $\underline{\mathbf{v}}^s \cdot \underline{\mathbf{t}}$), there still remain degrees of freedom for its tangential component that are left undefined, however, as will be shown, an evaluation of $\underline{\mathbf{v}}^s \cdot \underline{\mathbf{t}}$ is never required, and the use of equation (3.2.23) and knowledge of $\underline{\mathbf{v}}^s \cdot \mathbf{n}$ are sufficient for our model.

Suppose that there is zero mass flux to the interface from either bulk fluid, that is,

$$(\underline{\mathbf{u}} - \underline{\mathbf{v}}^s) \cdot \mathbf{n} = (\underline{\mathbf{u}}_G - \underline{\mathbf{v}}^s) \cdot \mathbf{n} = 0 \quad \text{on } \mathcal{S}_{LG}, \quad (3.2.3)$$

where $\underline{\mathbf{u}}$ and $\underline{\mathbf{u}}_G$ denote the bulk velocity in the liquid and gas phases, respectively.

Using equation (3.2.3), we can then re-frame the kinematic condition (3.2.2) in terms of the bulk liquid drop velocity (instead of the surface velocity), so that we have:

$$\frac{\partial f}{\partial t} + (\mathbf{u} \cdot \mathbf{n}) |\nabla f| = 0 \quad \text{on } \mathcal{S}_{LG}. \quad (3.2.4)$$

The general formulation for the (dimensional) conservation of momentum equation at the liquid-gas interface \mathcal{S}_{LG} is the following [135]:

$$\begin{aligned} \hat{\rho}^s \frac{\hat{D}_s \hat{\mathbf{v}}^s}{D\hat{t}} - \hat{\rho} (\hat{\mathbf{u}} - \hat{\mathbf{v}}^s) (\hat{\mathbf{u}} - \hat{\mathbf{v}}^s) \cdot \mathbf{n} + \hat{\rho}_G (\hat{\mathbf{u}}_G - \hat{\mathbf{v}}^s) (\hat{\mathbf{u}}_G - \hat{\mathbf{v}}^s) \cdot \mathbf{n} \\ = \mathbf{n} \cdot \left(\hat{\underline{\underline{\mathbf{P}}}}_G - \hat{\underline{\underline{\mathbf{P}}}} \right) + \hat{\nabla}_s \cdot \hat{\underline{\underline{\mathbf{P}}}}^s + \hat{\rho}^s \hat{\mathbf{F}}^s \quad \text{on } \mathcal{S}_{LG}, \end{aligned} \quad (3.2.5)$$

where $\hat{\underline{\underline{\mathbf{P}}}}$ and $\hat{\underline{\underline{\mathbf{P}}}}_G$, and $\hat{\rho}$ and $\hat{\rho}_G$, are the bulk stress tensors and bulk densities of the liquid and gas phases, respectively. Also, $\hat{\rho}^s$ (units kg/m²) is the surface density, $\hat{\rho}^s \hat{\mathbf{F}}^s$ (units kg/m.s²) is a surface body force, $\hat{D}_s/D\hat{t} \equiv \partial/\partial\hat{t} + \hat{\mathbf{v}}^s \cdot \hat{\nabla}_s$ is the surface advective operator, and $\hat{\underline{\underline{\mathbf{P}}}}^s$ is the surface stress tensor. Recall the definition of the surface divergence operator $\hat{\nabla}_s$ (in dimensionless form) in (3.1.1).

For our case, we immediately disregard the second and third terms on the left hand side of equation (3.2.5) because of the zero mass flux condition (3.2.3). We suppose that there are no surface body forces acting on the liquid-gas interface (so $\hat{\mathbf{F}}^s = \hat{\mathbf{0}}$), and following discussions in §1.3 and §3.1.2, the surface stress tensor is given by the Boussinesq-Scriven constitutive law (1.3.1) with (dimensionless) $\mu^s = 0$, that is,

$$\hat{\underline{\underline{\mathbf{P}}}}^s = \left(\hat{\sigma}_0 + \lambda^s \hat{\nabla}_s \cdot \hat{\mathbf{v}}^s \right) \hat{\underline{\underline{\mathbf{P}}}}^s, \quad (3.2.6)$$

where recall (see §3.1.2), the surface tension of the clean liquid-gas interface is assumed constant, in line with conventional models.

We are left with (i) a term consisting of stress tensors from the bulk liquid and gas phases, which will be considered later when discussing the bulk equations, (ii) a surface viscous term by way of the surface stress tensor with constitutive equation (3.2.6), and (iii) a surface inertial term given by the surface advective operator applied to the surface velocity. As a further simplification of equation (3.2.5), we choose to neglect the effects of surface inertia (as has been done in existing research on particle-laden interfaces [104, 136, 137]). We will now briefly discuss why this is justified by way of a crude model for calculating the Reynolds number at the liquid-gas interface.

Consider the following dimensionless parameter which describes the relationship between surface inertial and surface viscous forces within the liquid-gas interface \mathcal{S}_{LG} ,

which we call the ‘surface Reynolds number’:

$$\text{Re}_s := \frac{\hat{\rho}^s \hat{U}^s \hat{R}_0}{\hat{\lambda}^s}, \quad (3.2.7)$$

where \hat{U}^s is the characteristic flow speed within the liquid-gas interface. Similar to the classical Reynolds number (3.2.1), if we find that $\text{Re}_s \ll 1$, we conclude that surface inertial terms are negligible and so neglect their contributions to equation (3.2.5). We will now consider the ‘pessimistic’ scenario with regards to neglecting surface inertia, in which we maximise the values of the surface density, $\hat{\rho}^s$, and the characteristic flow speed within the liquid-gas interface, \hat{U}^s , within the limits of our motivating experiments.

The surface density $\hat{\rho}^s$ represents, per unit area, the mass of a small layer at the liquid-gas interface. Given that the density of the solid particles is greater than the density of the liquid drop (see §2.1), the largest value of $\hat{\rho}^s$ corresponds to the scenario in which the density of the small layer is *equal*¹ to the density of the solid particles. Supposing this is the case, then by multiplying the particle density by the thickness of the interfacial layer, which is on the scale of the particle diameter ($\bar{d}_p = 23.72\mu\text{m}$), we obtain a maximal estimate for the surface density of:

$$\begin{aligned} \hat{\rho}^s &= \left(2.45 \times 10^3 \frac{\text{kg}}{\text{m}^3} \right) \cdot (2.372 \times 10^{-5} \text{m}) \\ &\approx 5.8 \times 10^{-2} \frac{\text{kg}}{\text{m}^2}. \end{aligned}$$

Given that kinetic energy is maximised at the moment of impact, with energy lost during the impact phase, the maximum value that the characteristic flow speed \hat{U}^s within the liquid-gas interface can attain is the impact speed \hat{U}_0 . The impact speeds we ultimately consider in our simulations of liquid marble formation lie within the range of 1-2m/s, so for sake of argument suppose that $\hat{U}^s = 2\text{m/s}$. We consider water drops which have an initial spherical radius of $\hat{R}_0 = 10^{-3}\text{m}$, so using the dimensional scales provided in Table 3.1 and properties of water in Table 2.1, we have that the surface dilatational viscosity coefficient satisfies

$$\begin{aligned} \hat{\lambda}^s &\approx \lambda^s \cdot \sqrt{72.75 \times 10^3} \frac{\text{kg}}{\text{s}} \\ &\approx \lambda^s \cdot (2.7 \times 10^2) \frac{\text{kg}}{\text{s}}. \end{aligned}$$

¹This would require there to be *no* gaps between solid particles at the interface, which is not possible with spherical particles, but we consider this as the absolute limit of possible values.

Combining all terms together, our maximal surface Reynolds number is

$$\begin{aligned} \text{Re}_s^{(\max)} &\approx \frac{(5.8 \times 10^{-2} \frac{\text{kg}}{\text{m}^2}) (2 \frac{\text{m}}{\text{s}}) (10^{-3} \text{m})}{\lambda^s \cdot (2.7 \times 10^2) \frac{\text{kg}}{\text{s}}} \\ &\approx \frac{4 \times 10^{-7}}{\lambda^s}. \end{aligned}$$

As will be shown in Chapter 7, λ^s is *significantly* larger than 4×10^{-7} through the course of our simulations; typically taking values of order 1-100 prior to liquid marble formation. Given then that even in the case of a maximised surface Reynolds number, we still have $\text{Re}_s \ll 1$, we are satisfied that (for our problem) surface viscous forces dominate surface inertial forces at the liquid-gas interface. We therefore neglect the first term in (3.2.5), and so our conservation of momentum equation at the liquid-gas interface \mathcal{S}_{LG} is given by:

$$\underline{\mathbf{n}} \cdot (\underline{\hat{\boldsymbol{\Pi}}} - \underline{\hat{\boldsymbol{\Pi}}}_G) = \hat{\nabla}_s \cdot \underline{\hat{\boldsymbol{\Pi}}}^s \quad \text{on } \mathcal{S}_{LG}. \quad (3.2.8)$$

In summary, the (dimensional) surface equations at the liquid-gas interface \mathcal{S}_{LG} are the kinematic condition (3.2.4), and the conservation of momentum equation (3.2.8), where the surface stress tensor is given by (3.2.6).

3.2.2 Boundary Conditions at the Liquid-Solid Interface

We incorporate the effects of substrate permeability for the powder bed, modelled in our case as rigid and *impermeable*, via a (dimensionless) Beavers-Joseph boundary condition [138] at an effective flat liquid-solid interface:

$$u_r = \frac{K^{1/2}}{\alpha_{BJ}} \frac{\partial u_r}{\partial z} \quad \text{at } z = 0, \quad (3.2.9)$$

where K is the permeability of the substrate, α_{BJ} is the Beavers-Joseph coefficient, and $u_r \equiv \underline{\mathbf{u}} \cdot \underline{\mathbf{e}}_r$ is the bulk radial velocity. Given that (dimensional) permeability \hat{K} scales with area, specifically the area of pores on a surface, and that the ‘pores’ of a powder bed are on the order of particle size, we suppose that $K = \bar{d}_p^2$, where \bar{d}_p is the (dimensionless) mean particle diameter. If we assume that the Beavers-Joseph coefficient α_{BJ} is unity, for sake of argument, then equation (3.2.9) reduces to

$$u_r = \bar{d}_p \frac{\partial u_r}{\partial z} \quad \text{at } z = 0. \quad (3.2.10)$$

This boundary condition then allows us to calculate the radial velocity at the liquid-solid interface \mathcal{S}_{LS} , where \bar{d}_p acts as a slip length (see Figure 3.3).

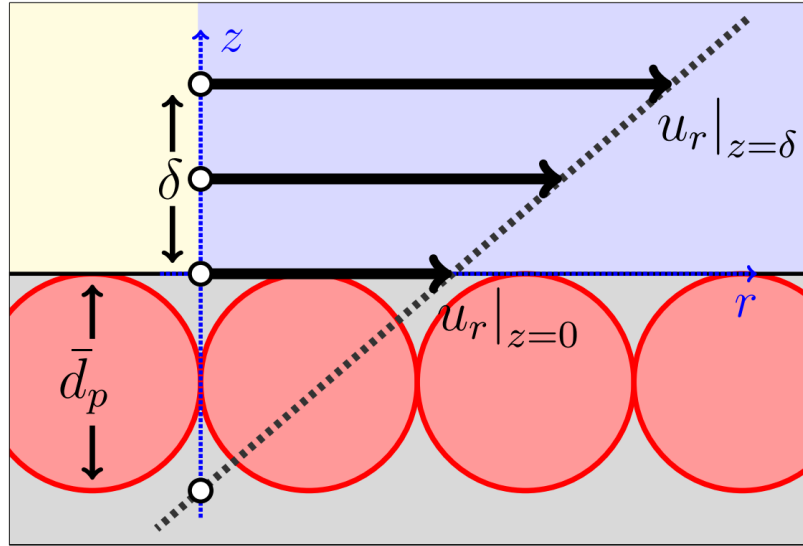


Figure 3.3: Diagram showing the drop flow profile within a boundary layer beside the liquid-solid interface. Very close to the substrate, the flow profile is radial and linear in z . The slip length in this case is the same as the diameter of an individual powder particle, \bar{d}_p , and this determines the value of the slip velocity at the liquid-solid interface.

By impermeability, the axial velocity $u_z \equiv \mathbf{u} \cdot \mathbf{e}_z$ at the liquid-solid interface \mathcal{S}_{LS} is given by

$$u_z = 0 \quad \text{at } z = 0. \quad (3.2.11)$$

3.2.3 Boundary Conditions for the Surface Equations

We apply boundary conditions where the liquid-gas interface \mathcal{S}_{LG} touches the axis of symmetry, and, if the liquid-solid interface \mathcal{S}_{LS} exists, at the contact line. As a result of the forthcoming formulation of the bulk equations (see §3.2.4), we find that surface viscous effects are only triggered upon encapsulation of the drop (which occurs after the drop has rebounded, in accordance with experimental observations), and when they *are* triggered, they take the form of an effective surface tension. Ultimately, this means that we do not require boundary conditions on the surface velocity \mathbf{v}^s at the axis (or at the contact line) at any point in the model, and so the boundary conditions on the surface equations are purely geometric.

At the axis of symmetry, we require on \mathcal{S}_{LG} :

$$\mathbf{n} \cdot \mathbf{e}_r = 0 \quad \text{at } r = 0, \quad (3.2.12)$$

which ensures the liquid-gas interface \mathcal{S}_{LG} remains smooth across the axis. When the liquid-solid interface \mathcal{S}_{LS} does *not* exist, (3.2.12) applies at the apex and bottom of the drop. When the drop is in contact with the solid substrate (so \mathcal{S}_{LS} *does* exist), (3.2.12) continues to apply at the drop apex, but at the other end of the liquid-gas interface (now at the contact line), we prescribe a contact angle θ_c . Given we have not observed a dynamic contact angle in our powder bed impact experiments, we consider the simplest case, that the contact angle θ_c is constant.

In §6.1.2, we will show that by incorporating a ‘pinning radius’, as observed experimentally in §2.3.1, for drop impacts onto rigid substrates) into our numerical simulations for the retraction phase, post-rebound drop dynamics can be made to better match those particular experiments. For that case, we provide the following simple empirical dynamic contact angle model:

$$\begin{aligned}
u_r^{(CL)} > 0 &\implies \theta_c = \theta_1, \\
r^{(CL)} > r_{pin} \quad \text{and} \quad u_r^{(CL)} < 0 &\implies \theta_c = \theta_1, \\
r^{(CL)} < r_{pin} \quad \text{and} \quad u_r^{(CL)} < 0 &\implies \theta_c = \theta_0 < \theta_1, \\
r^{(CL)} = r_{pin} \quad \text{and} \quad u_r^{(CL)} < 0 &\implies \text{set } u_r^{(CL)} = 0 \quad \text{while } \theta_c \rightarrow \theta_0,
\end{aligned} \tag{3.2.13}$$

where $u_r^{(CL)}$ is the contact line speed, $r^{(CL)}$ is the position of the contact line, and θ_1 and θ_0 are contact angles with the substrate. During drop spreading and part-way through retraction, the contact angle is kept constant (equal to θ_1), and when the contact line recedes back to the pinning radius $r_{pin} > 0$, it remains stationary while the contact angle smoothly transitions from θ_1 to θ_0 . The receding motion then continues with the smaller contact angle θ_0 until the drop rebounds from the substrate.

3.2.4 Inviscid Bulk Equations

The first model for the bulk equations is for inviscid liquid and gas flows. We first assume that both flows are incompressible, so we have

$$\nabla \cdot \mathbf{u} = 0 \quad \text{in } \Omega, \tag{3.2.14}$$

and

$$\nabla \cdot \mathbf{u}_G = 0 \quad \text{in } \Omega_G. \tag{3.2.15}$$

For the phenomena we are interested in modelling and simulating (see §1.1.6), the impact Reynolds number, as discussed earlier in this section, exceeds $\text{Re} = 1600$

(where encapsulation is seen to occur). Such large impact Reynolds numbers indicate that the contribution from bulk inertial forces greatly outweigh those from bulk viscous forces at the start of the dynamics, and hence it is a reasonable first approximation to consider an inviscid bulk flow within the drop through all subsequent dynamics. The (dimensional) constitutive equation for the bulk stress tensor in the drop is then given by

$$\underline{\hat{\boldsymbol{\Pi}}} = -\hat{p}\underline{\mathbf{I}}. \quad (3.2.16)$$

Therefore the conservation of momentum equation in the drop takes the form of the (dimensionless) Euler equations [133],

$$\frac{\partial \underline{\mathbf{u}}}{\partial t} + (\underline{\mathbf{u}} \cdot \nabla) \underline{\mathbf{u}} = -\nabla p + \underline{\mathbf{g}} \quad \text{in } \Omega, \quad (3.2.17)$$

where (dimensionless) $\underline{\mathbf{g}} = \hat{\underline{\mathbf{g}}} / (\hat{\sigma}_0 / \hat{\rho}_0 \hat{R}_0^2)$ denotes acceleration due to gravity.

We will consider the gas to be inviscid and dynamically passive so that without loss of generality we take the pressure in the gas, p_G , equal to zero. This eliminates any contributions from the bulk stress tensor in the gas domain to flow dynamics in the gas bulk and on the drop interface.

Combining the (dimensional) constitutive equations for the bulk and surface stress tensors, (3.2.16) and (3.2.6) respectively, with the conservation of momentum equation for the liquid-gas interface (3.2.8), and then expanding out gives

$$\hat{\nabla}_s \left(\hat{\sigma}_0 + \hat{\lambda}^s \hat{\nabla}_s \cdot \hat{\underline{\mathbf{v}}}^s \right) - \left(\hat{\sigma}_0 + \hat{\lambda}^s \hat{\nabla}_s \cdot \hat{\underline{\mathbf{v}}}^s \right) \left(\hat{\nabla}_s \cdot \underline{\mathbf{n}} \right) \underline{\mathbf{n}} = -\hat{p} \underline{\mathbf{n}} \quad \text{on } \mathcal{S}_{LG}. \quad (3.2.18)$$

Recall here that by axisymmetry, the model is two dimensional and therefore vector variables taking values on the drop interface can be split into a component normal to the interface (parallel to the normal vector $\underline{\mathbf{n}}$), and a component tangent to the interface in the (r, z) -plane (parallel to the tangent vector $\underline{\mathbf{t}}$). Also recall that there exists a second tangent vector that is parallel to the θ -axis, but this is unimportant because of axisymmetry. As such, we split equation (3.2.18) into normal and tangential components, respectively,

$$- \left(\hat{\sigma}_0 + \hat{\lambda}^s \hat{\nabla}_s \cdot \hat{\underline{\mathbf{v}}}^s \right) \left(\hat{\nabla}_s \cdot \underline{\mathbf{n}} \right) \underline{\mathbf{n}} = -\hat{p} \underline{\mathbf{n}} \quad \text{on } \mathcal{S}_{LG}, \quad (3.2.19)$$

and

$$\hat{\nabla}_s \left(\hat{\sigma}_0 + \hat{\lambda}^s \hat{\nabla}_s \cdot \hat{\underline{\mathbf{v}}}^s \right) = \hat{\underline{\mathbf{0}}} \quad \text{on } \mathcal{S}_{LG}. \quad (3.2.20)$$

We now simplify these equations. For the tangential projection, recall that $\hat{\sigma}_0$ is constant (so $\hat{\nabla}_s \hat{\sigma}_0 = \hat{0}$ on \mathcal{S}_{LG}), and integrate equation (3.2.20) over the entire liquid-gas interface to obtain

$$\hat{\lambda}^s \hat{\nabla}_s \cdot \hat{\underline{\mathbf{v}}}^s = \hat{W}(\hat{t}) \quad \text{on } \mathcal{S}_{LG}, \quad (3.2.21)$$

where $\hat{W}(\hat{t})$ is constant along \mathcal{S}_{LG} , but we are careful to note that there is still a time dependency. The normal projection (3.2.19), has the surface viscous term $\hat{\lambda}^s \hat{\nabla}_s \cdot \hat{\underline{\mathbf{v}}}^s$ lying within parentheses with the liquid surface tension, and so will affect the flow in the same manner; hence we can think of this combined term as an *effective surface tension*;

$$\hat{\sigma}_{\text{eff}}(\hat{t}) \equiv \hat{\sigma}_0 + \hat{\lambda}^s \hat{\nabla}_s \cdot \hat{\underline{\mathbf{v}}}^s = \hat{\sigma}_0 + \hat{W}(\hat{t}), \quad (3.2.22)$$

where we have used equation (3.2.21) to show that similarly, this effective surface tension is also spatially independent. It was important here to present equation (3.2.22) in its dimensional form to make it clear that the surface viscous term is additive to the surface tension of the underlying liquid. Now we use the dimensional scales in Table 3.1 and rewrite equation (3.2.22) in its dimensionless form:

$$\sigma_{\text{eff}}(t) \equiv 1 + \lambda^s \nabla_s \cdot \underline{\mathbf{v}}^s = 1 + W(t), \quad (3.2.23)$$

and then incorporate this into the normal stress condition (3.2.19), likewise in dimensionless form, to obtain:

$$p = \sigma_{\text{eff}}(t) (\nabla_s \cdot \underline{\mathbf{n}}) \quad \text{on } \mathcal{S}_{LG}, \quad (3.2.24)$$

where the dot product with $\underline{\mathbf{n}}$ has been applied to both sides.

The important unexpected consequence of this is that when considering an inviscid bulk flow, the (dilatational) surface viscous effects manifest themselves everywhere on the interface simultaneously via an effective surface tension, independent of how large the powder concentration (and so λ^s) is in any particular region. The consequences of this model for an effective surface tension are considered below for different scenarios.

Partially Coated Liquid-Gas Interface

If we consider a drop that has a partial but not full coating of powder on its liquid-gas interface \mathcal{S}_{LG} (so the drop is not yet encapsulated), then as stated in §3.1 we must

have $\lambda^s = 0$ in the regions *without* a powder coating. Therefore $W(t) = \lambda^s \nabla_s \cdot \underline{\mathbf{v}}^s = 0$ in these regions also, and as $W(t)$ is spatially independent, we must have that $W(t) = 0$ along the *entire* liquid-gas interface. The consequence of this is that if there is only a *partial* coating of powder on \mathcal{S}_{LG} , then there are *no* surface viscous effects felt anywhere, and so drop dynamics continue as if there is a completely clean interface. Given that, as stated in §2.3.2, encapsulation is always observed *after* the drop has rebounded from the powder bed in our experiments, we likewise suppose that encapsulation can only occur post-rebound in our model. Therefore, as long as the liquid-solid interface \mathcal{S}_{LS} exists, there are no surface viscous effects whatsoever and while equation (3.2.23) still holds (with $W(t) = 0$), it is not used in the model.

Now consider the case of a partially coated *rebounded* drop. Given that $W(t) = 0$ everywhere on \mathcal{S}_{LG} , it must be that within powder coated regions (where $\lambda^s \neq 0$), we have $\nabla_s \cdot \underline{\mathbf{v}}^s = 0$, in other words, the surface area of the powder coated region *cannot* change and so must stay constant (see Appendix B for proof of this result). An important consequence of this is that knowing the surface area of the entire liquid-gas interface and knowing the (fixed) surface area of the powder region is sufficient for tracking the point on the interface separating the clean and powder regions, without the need for an advection equation. In terms of motivating this, the constant-area condition on the powder region follows from the inviscid assumption in both bulk flows and the surface-inviscid assumption in the clean regions of the interface; namely that there can be no force acting on the powder region from these locations to compress it - so the powder is unrestrained in its movements.

Fully Coated Liquid-Gas Interface

For the case of a fully coated (encapsulated) drop, $\lambda^s \neq 0$ everywhere and consequently $W(t)$ is no longer identically zero and is therefore an unknown. Recall that for encapsulation to occur in our model, the drop has rebounded from the substrate and so there is no liquid-solid interface. We will now derive an additional expression for $W(t)$, showing that it is determined by the distribution of the normal component of $\underline{\mathbf{v}}^s$ on the liquid-gas interface \mathcal{S}_{LG} , and is independent of the tangential component of $\underline{\mathbf{v}}^s$.

Since λ^s is now nowhere zero, we can divide both sides of (the dimensionless form of) equation (3.2.21) by λ^s and then integrate over the liquid-gas interface \mathcal{S}_{LG}

to obtain:

$$W(t) \int_{\mathcal{S}_{LG}} \frac{1}{\lambda^s} dS = \int_{\mathcal{S}_{LG}} \frac{W(t)}{\lambda^s} dS = \int_{\mathcal{S}_{LG}} \nabla_s \cdot \underline{\mathbf{v}}^s dS, \quad (3.2.25)$$

which yields

$$W(t) = \frac{\int_{\mathcal{S}_{LG}} \nabla_s \cdot \underline{\mathbf{v}}^s dS}{\int_{\mathcal{S}_{LG}} 1/\lambda^s dS}, \quad (3.2.26)$$

where dS denotes an area element of the interface \mathcal{S}_{LG} . Recall the axisymmetric form of the surface divergence term $\nabla_s \cdot (\cdot)$ provided by equation (3.1.2) and apply it to the surface velocity:

$$\nabla_s \cdot \underline{\mathbf{v}}^s = \frac{1}{r} \frac{\partial}{\partial s} (r \underline{\mathbf{v}}^s \cdot \underline{\mathbf{t}}) + (\nabla_s \cdot \underline{\mathbf{n}})(\underline{\mathbf{u}} \cdot \underline{\mathbf{n}}), \quad (3.2.27)$$

where we have also used the zero mass flux condition (3.2.3) to replace $(\underline{\mathbf{v}}^s \cdot \underline{\mathbf{n}})$ with $(\underline{\mathbf{u}} \cdot \underline{\mathbf{n}})$.

Transforming the surface integrals in (3.2.26) into line integrals via axisymmetry, using equation (3.2.27), and through recognition that $r = 0$ and $\underline{\mathbf{v}}^s \cdot \underline{\mathbf{t}}$ is bounded when $s = 0$ and $s = L$ (both at the axis of symmetry), we obtain the following expression for $W(t)$:

$$\begin{aligned} W(t) &= \frac{1}{\int_{\mathcal{S}_{LG}(t)} 1/\lambda^s dS(t)} 2\pi \int_0^{L(t)} \left(\frac{1}{r} \frac{\partial}{\partial s} (r \underline{\mathbf{v}}^s \cdot \underline{\mathbf{t}}) + (\nabla_s \cdot \underline{\mathbf{n}})(\underline{\mathbf{u}} \cdot \underline{\mathbf{n}}) \right) r ds(t) \\ &= \frac{1}{\int_{\mathcal{S}_{LG}(t)} 1/\lambda^s dS(t)} 2\pi \int_0^{L(t)} \left(\frac{\partial}{\partial s} (r \underline{\mathbf{v}}^s \cdot \underline{\mathbf{t}}) + (\nabla_s \cdot \underline{\mathbf{n}})(\underline{\mathbf{u}} \cdot \underline{\mathbf{n}}) r \right) ds(t) \\ &= \frac{1}{\int_{\mathcal{S}_{LG}(t)} 1/\lambda^s dS(t)} 2\pi \int_0^{L(t)} (\nabla_s \cdot \underline{\mathbf{n}})(\underline{\mathbf{u}} \cdot \underline{\mathbf{n}}) r ds(t) \\ &\equiv \frac{1}{\int_{\mathcal{S}_{LG}(t)} 1/\lambda^s dS(t)} \int_{\mathcal{S}_{LG}(t)} (\nabla_s \cdot \underline{\mathbf{n}})(\underline{\mathbf{u}} \cdot \underline{\mathbf{n}}) dS(t), \end{aligned} \quad (3.2.28)$$

where ds denotes a line element on the one dimensional boundary curve representation of \mathcal{S}_{LG} . As well as highlighting the independence of calculating $W(t)$ from the tangential velocity at the interface, this formulation is useful numerically as it expresses $W(t)$ in terms of variables that are used often (for other purposes) during our numerical simulations. Additionally, an expression for the tangential component of the surface velocity can be derived, but it does not appear in any of the flow equations within this model, and so is not included here.

We will now move on to discuss the two critical events that can occur following drop impact onto a superhydrophobic powder bed; the moments of encapsulation and liquid marble formation (specifically deformed liquid marble formation, in which

interfacial freezing occurs). In terms of the dynamics, once encapsulated, a drop immediately enters the surface viscous regime whereby the presence of powder on the drop interface affects flow dynamics, and at some point the drop interface may freeze (that is, the adhered particles jam on the interface). Instead of discussing these processes in the order they occur, we will deal with the concepts of encapsulation and freezing first, and end with the intermediary surface viscous regime. This is because the discussion of the surface viscous regime introduces a constitutive equation for the surface viscous coefficient λ^s that relies on parameters directly related to the moments of encapsulation and interfacial freezing, which need to have already been introduced.

Encapsulation

Discussed here are the same concepts presented in §2.3.4, which originally described the relationship (as observed in our experiments) between the surface area of the liquid drop at the moments of encapsulation and (deformed) liquid marble formation, and the spreading area. The difference being that here we formulate these concepts with respect to the maximum contact area rather than the spreading area, and justify their inclusion in our model through the context of differing powder concentrations on the liquid-gas and liquid-solid interfaces of the drop. We first discuss the concepts related to encapsulation, and then those on interfacial freezing.

Denote the maximum contact area between the liquid drop and solid substrate by

$$A_{contact} = \pi \bar{r}_{CL}^2, \quad (3.2.29)$$

where \bar{r}_{CL} denotes the maximum radial coordinate attained by the contact line (which is achieved at maximum spread). We suppose, as a first approximation, that all solid particles that will adsorb to \mathcal{S}_{LS} through contact with the substrate have done so by the time the drop has reached maximum spread, and further that the concentration of this particle coating on \mathcal{S}_{LS} , denoted by c_{LS} , is constant in both time and space. Then, the total mass of adsorbed particles on \mathcal{S}_{LS} , which is also the *maximum* mass of adsorbed particles on the drop surface at any time post-maximum spread, is given by

$$M_{spread} = c_{LS} \cdot A_{contact}. \quad (3.2.30)$$

Let c_{LG} denote the concentration of powder particles in the (non-empty) powder

coated region of \mathcal{S}_{LG} for a partially coated drop (so prior to encapsulation), and assume that c_{LG} is also constant in time and space, but not necessarily equal to c_{LS} . Note that with a constant c_{LG} , the surface area of the powder coated region must be constant, which agrees with what we found to be the case for our model earlier in this section (recall that $\nabla_s \cdot \underline{\mathbf{v}}^s = 0$ wherever $\lambda^s \neq 0$, as long as $\lambda^s = 0$ somewhere), so this assumption of a uniform concentration within the powder region is reasonable as a first approximation. Given that c_{LS} is (assumed) constant and that powder mass is conserved on the drop surface, then as the contact line recedes (so the contact area between the drop and substrate reduces), some powder *must* move to the liquid-gas interface \mathcal{S}_{LG} and by doing so transitions from a concentration of c_{LS} to c_{LG} . This transition between concentrations would take place across some finite time and region, but given that encapsulation does not occur in our model until after rebound (and encapsulation is required for surface viscous effects to trigger), we do not expect there to be any situation in which drop dynamics are altered while there is a transition of concentrations underway, so we assume for simplicity that it is instantaneous. This process of transitioning between constant concentrations, and that such a transition occurs over a small finite time, are choices made to simplify the model and this is only one of the possible scenarios; further experimental and theoretical evidence (for example, involving particle dynamics) backing this assumption is outside the scope of this thesis and is an avenue for future research, as discussed in Chapter 8.

If we define the following ratio

$$\alpha_{encap} \equiv \frac{c_{LS}}{c_{LG}}, \quad (3.2.31)$$

then as shown in Figure 3.4, there are three scenarios that can occur with regards to the powder coating as the contact line recedes from maximum spread: if $\alpha_{encap} < 1$ (> 1) then the powder concentration increases (decreases) for powder that moves to the liquid-gas interface, thus decreasing (increasing) the surface area that this powder covers, whereas if $\alpha_{encap} = 1$ means that concentration is maintained as powder moves between interfaces, and so the surface area of the entire powder region across both interfaces stays equal to the maximum contact area with the substrate, $A_{contact}$.

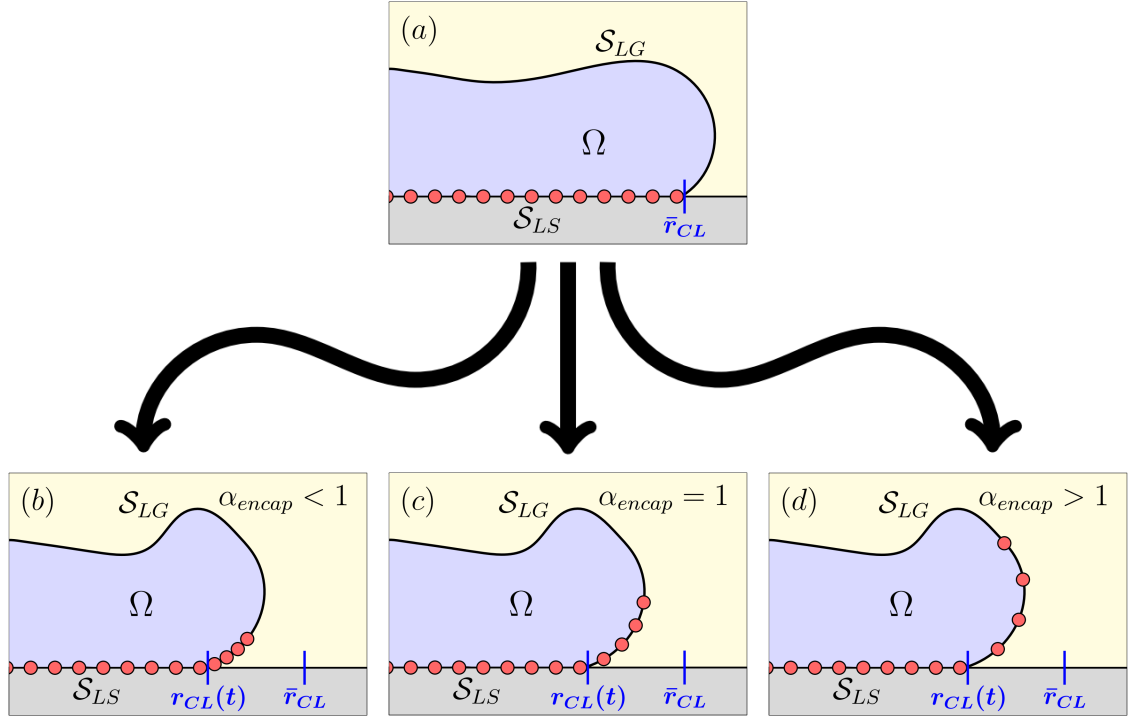


Figure 3.4: Diagram showing (a) the drop at maximum spread, with maximum contact line radius \bar{r}_{CL} and a uniform coating of powder on its liquid-solid interface \mathcal{S}_{LS} , followed by retraction of the drop with the contact line reducing to $r_{CL}(t) < \bar{r}_{CL}$ for some time t . We have (b) $\alpha_{encap} < 1$, whereby the powder more densely packs onto the liquid-gas interface \mathcal{S}_{LG} , (c) $\alpha_{encap} = 1$, whereby the powder maintains the same packing on \mathcal{S}_{LG} , or (d) $\alpha_{encap} > 1$, whereby the powder is more sparsely packed on \mathcal{S}_{LG} .

When fully rebounded from the substrate, the surface area of the powder coated region remains constant and with a uniform concentration c_{LG} , and so encapsulation of the drop is equivalent to the total surface area of the liquid-gas interface reducing to the powder coated surface area. This is the same quantity described in §2.3.4 as the ‘initial encapsulation area’, and is given here by

$$A_{encap}^{(0)} = \alpha_{encap} \cdot A_{contact}. \quad (3.2.32)$$

Importantly, once the initial encapsulation area has been reached, the surface area of the drop is still able to change, meaning that the powder concentration on the drop surface (while still assumed uniform) can now vary from c_{LG} . When providing a constitutive equation for λ^s later in this subsection, we would like to know the surface area of the drop, for all time, that corresponds to the powder concentration being *equal* to c_{LG} . If the powder mass on the drop surface stays constant from

maximum spread to encapsulation, then this is equal to the initial encapsulation area (3.2.32), but because of satellite drop ejections that remove powder mass from the primary drop, this may change. Given that (by assumption) powder concentration is always uniform in the powder coated region of the liquid-gas interface, it is therefore continuous through pinch-off events. Consequently, the surface area corresponding to a concentration of c_{LG} after the pinch-off event is given by the ratio of the surface area of the primary drop immediately after pinch-off, over the powder coated surface area immediately prior to pinch-off (see initial discussion in §2.3.4). Hence the (time dependent) ‘encapsulation area’, denoted by $A_{encap}(t)$, evaluated after the j -th pinch-off event ($j \in \mathbb{N}$), is calculated as

$$A_{encap}(t_j^+) = A_{encap}(t_j^-) \cdot \frac{A_p(t_j^+)}{A_p(t_j^-)}, \quad (3.2.33)$$

where t_j^- and t_j^+ denote the times immediately before and after the j -th pinch-off event, and $A_p(t)$ denotes the surface area of the powder coated region of the primary drop at time t . The encapsulation area $A_{encap}(t)$ is therefore piecewise constant in time, reducing only at discrete pinch-off events where powder mass is lost from the primary drop surface. Up to the first pinch-off event which reduces powder mass on the primary drop surface, we have $A_{encap}(t) = A_{encap}^{(0)}$.

Once encapsulated, the drop enters the surface viscous regime where $W(t) \neq 0$, and surface area conservation for the powder region of \mathcal{S}_{LG} no longer holds. An important consideration is that after a drop has been encapsulated, it is considered encapsulated for all future time; it may be the case that, after encapsulation, surface viscous effects are weak enough to allow the drop surface area to increase above $A_{encap}(t)$, as the process is highly nonlinear and involves large deformations of the liquid-gas interface. If this is the case, then the drop is assumed to remain in the surface viscous regime but with a powder concentration on \mathcal{S}_{LG} *less* than c_{LG} (so for example, we assume that ‘holes’ within the powder coating cannot re-open). The dynamics of being within the surface viscous regime, and the effects from the surface area of the liquid-gas interface increasing past $A_{encap}(t)$ are discussed shortly.

Interfacial Freezing

As has been discussed previously, the interfacial freezing phenomenon is caused by the jamming of particles at the drop interface preventing further surface area change. For

this to occur, the concentration of the adhered powder particles must reach a critical threshold, which we denote by c_{freeze} . Given that we have assumed the concentration of the particle coating is spatially constant post-encapsulation, particle concentration scales as the reciprocal of drop surface area, so the concentration reaching c_{freeze} corresponds to the surface area reaching the ‘initial freezing area’ $A_{freeze}^{(0)}$ (as in §2.3.4). If we assume that no satellite drop ejection has taken place that has removed powder mass from the primary drop surface, then the powder mass at maximum spread is the same as at interfacial freezing, so we have:

$$c_{LS} \cdot A_{contact} = M_{spread} = c_{freeze} \cdot A_{freeze}^{(0)},$$

where we have used equation (3.2.30). Dividing the left and right sides of this equation through by c_{freeze} , we obtain:

$$A_{freeze}^{(0)} = \alpha_{freeze} \cdot A_{contact}, \quad (3.2.34)$$

where

$$\alpha_{freeze} \equiv \frac{c_{LS}}{c_{freeze}}. \quad (3.2.35)$$

As with the previous discussion on encapsulation, we seek the surface area of the primary drop, over time, corresponding to the freezing threshold for powder concentration, c_{freeze} . Hence, as with equation (3.2.33), the (time dependent) ‘freezing area’, denoted by $A_{freeze}(t)$ is evaluated immediately after the j -th pinch-off event ($j \in \mathbb{N}$) as

$$A_{freeze}(t_j^+) = A_{freeze}(t_j^-) \cdot \frac{A_p(t_j^+)}{A_p(t_j^-)}, \quad (3.2.36)$$

where t_j^- and t_j^+ denote the times immediately before and after the j -th pinch-off event, and $A_p(t)$ denotes the surface area of the powder coated region of the primary drop at time t . Similarly, up to the first pinch-off event which reduces powder mass on the primary drop, we have $A_{freeze}(t) = A_{freeze}^{(0)}$ as given in (3.2.34).

Surface Viscous Regime

Now that we have introduced variables associated with encapsulation and interfacial freezing, here follows a discussion on the modelling of the intermediary surface viscous regime.

Recall that the surface viscous regime is initiated after the drop is encapsulated, because the liquid-gas surface area A has reduced to (or below) the initial encapsulation area $A_{encap}^{(0)}$. Once encapsulated, drop dynamics are affected by surface viscosity

via the effective surface tension (3.2.23 and 3.2.28). What remains is to provide the *simplest* constitutive equation for the dilatational surface viscous coefficient λ^s that satisfies the assumptions we have made in the construction of this model thus far. As such, we suppose λ^s takes the following form:

$$\lambda^s(A, t) = \beta \cdot \frac{(A_{encap}(t) - A)}{(A - A_{freeze}(t))}, \quad (3.2.37)$$

where $\beta > 0$ is a dimensionless parameter. This is the constitutive equation used for the simulations of liquid marble formation presented in Chapter 7, and holds for $A_{freeze}(t) < A \leq A_{encap}(t)$.

According to equation (3.2.37), as A approaches the freezing area $A_{freeze}(t)$, the surface viscous coefficient λ^s (and hence surface viscous stress) diverges to infinity, which can have strong effects on drop dynamics, and drives energy dissipation at the drop interface. As will be seen in our simulations for liquid marble formation in Chapter 7, the surface viscous stresses provided by equation (3.2.37) can delay the drop surface area from reaching $A_{freeze}(t)$ (as compared to a clean simulation) but does not prevent it from occurring indefinitely, and so when $A = A_{freeze}(t)$ (equivalently, the powder concentration has reached c_{freeze}) we claim that interfacial freezing has occurred, and the drop is now a deformed liquid marble.

As A approaches the encapsulation area $A_{encap}(t)$ from below, λ^s in (3.2.37) converges to zero and so the differences between the dynamics of the encapsulated drop and a clean drop vanish. Importantly, if A *does* leave the interval between encapsulation and freezing areas (by increasing above $A_{encap}(t)$), we set $\lambda^s(A, t) = 0$ until $A \leq A_{encap}(t)$. While keeping track of the surface area of the primary drop corresponding to the critical freezing threshold (that is, $A_{freeze}(t)$) is a clear requirement for determining when interfacial freezing occurs, there is no fundamental significance in the value of the powder concentration at encapsulation, c_{LG} . However, considering that the surface viscous dynamics are most interesting and prominent when A is close to the freezing area, for simplicity we use the concentration c_{LG} (and so a surface area of $A_{encap}(t)$) to signify negligible surface viscous effects.

An important assumption at the beginning of this chapter is that $\lambda^s \neq 0$ for a coated region of the liquid-gas interface, and the condition on equation (3.2.37) that $\lambda^s = 0$ for $A > A_{encap}(t)$ appears to not satisfy this. Alternatively, a constitutive equations for λ^s that *certainly* satisfies this, is one that decays to zero as the surface area $A \rightarrow \infty$ (example presented in Figure 3.5 compared to equation 3.2.37), but as

just explained, the physics is most rich near interfacial freezing, so one may expect (3.2.37) to provide reasonable results.

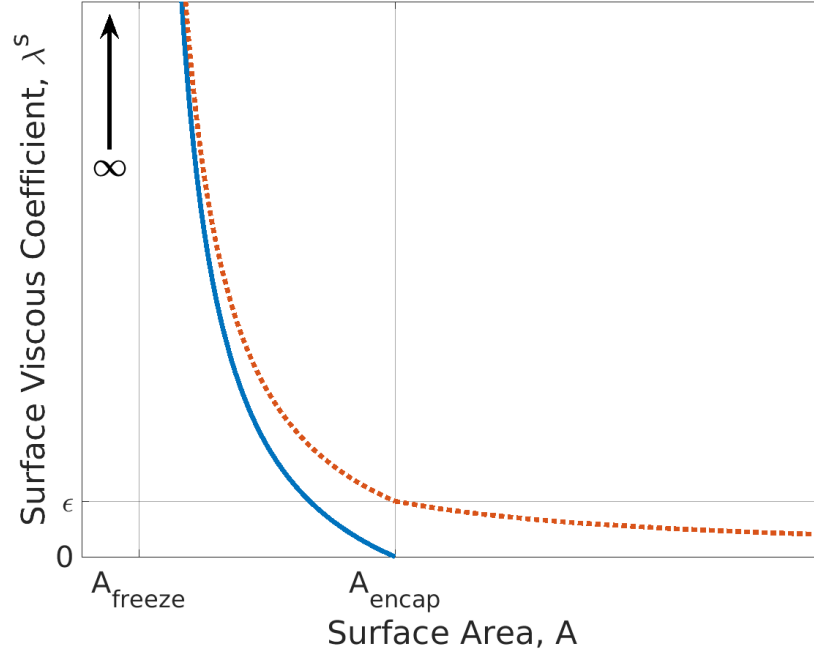


Figure 3.5: Example plots for the constitutive equation for λ^s (blue curve) provided by (3.2.37) and a constitutive equation that has $\lambda^s \rightarrow 0$ as $A \rightarrow \infty$ (red curve). Both curves diverge to infinity when the free surface area A converges to the freezing area A_{freeze} , but the blue curve is zero at the encapsulation area $A = A_{encap}$, while the red curve that takes a small positive value $\epsilon > 0$.

Limits on the Effective Surface Tension

Recall that the (dimensional) effective surface tension, $\hat{\sigma}_{\text{eff}}(\hat{t})$, is the sum of the reference surface tension of the liquid, $\hat{\sigma}_0$, and surface viscous contributions from the powder, $\hat{\lambda}^s \hat{\nabla}_s \cdot \hat{\mathbf{v}}^s$. Using the definition of the time dependent function $W(t)$ (equation 3.2.21) and its representation given by (3.2.28), we have (in dimensionless form)

$$\sigma_{\text{eff}}(A, t) = 1 + \lambda^s(A, t) \left(\frac{\int_{\mathcal{S}_{LG}(t)} (\nabla_s \cdot \mathbf{n})(\mathbf{u} \cdot \mathbf{n}) \, dS(t)}{\int_{\mathcal{S}_{LG}(t)} 1 \, dS(t)} \right). \quad (3.2.38)$$

We have given a constitutive equation for λ^s (3.2.37) such that it can only take non-negative values, but no such condition exists on the curvature $(\nabla_s \cdot \mathbf{n})$ or normal velocity $(\mathbf{u} \cdot \mathbf{n})$ at the interface \mathcal{S}_{LG} , hence the integral on the right hand side of (3.2.38) is able to take any real value. When this integral is positive, we have $\sigma_{\text{eff}}(A, t) \geq 1$ meaning that the effective surface tension is stronger than the reference value of the

underlying liquid and so the liquid-gas interface more aggressively tries to reduce its surface area. On the other hand, if this integral is negative, then there are two possibilities that we consider separately. If $-1 \leq \lambda^s \nabla_s \cdot \underline{\mathbf{v}}^s < 0$, then $0 \leq \sigma_{\text{eff}}(A, t) < 1$ and so the liquid-gas interface will still try to reduce its surface area but the effective surface tension is weaker than the reference value of the underlying liquid, which allows regions of high curvature to persist for longer than they would in the case of a clean drop, therefore increasing the time it takes to smooth the interface and reduce back to a sphere. If $\lambda^s \nabla_s \cdot \underline{\mathbf{v}}^s < -1$, then $\sigma_{\text{eff}}(A, t) < 0$ and it is then beneficial (energetically speaking) for the surface area of the liquid-gas interface to *increase*.

The effective surface tension is time dependent so throughout the course of the dynamics, each one of these situations may occur at some point, particularly if the drop-shape at encapsulation is very deformed, with a complex distribution of curvatures and normal velocities at its interface. However, allowing the effective surface tension to become negative is problematic; small perturbations at the interface will grow very fast even over short intervals of time and allowing this as a possibility is not feasible as spurious surface waves (brought on by numerical errors) that are normally damped out of existence are instead exacerbated and forced to grow. Therefore we do not allow the surface tension to become negative and instead suppose that the minimum value for $\sigma_{\text{eff}}(A, t)$ is a small constant (taken to be equal to 10^{-5} in simulations presented later in this thesis). Ultimately, for our liquid marble simulations in Chapter 7, this limitation is rarely triggered, and even then only near the end of a simulation just before the creation of a deformed liquid marble; where the surface area of the drop approaches the freezing area.

Boundary Condition at the Axis of Symmetry

Finally, we impose the following symmetry boundary condition on the bulk flow within the liquid drop at the axis of symmetry:

$$u_r = 0 \quad \text{at } r = 0. \quad (3.2.39)$$

Summary of the Inviscid Model

In summary, the flow in the bulk liquid drop satisfies the incompressible Euler equations (3.2.17) and (3.2.14). The exterior gas is treated as dynamically passive and

its sole contribution is via a constant atmospheric pressure. At the liquid-gas interface \mathcal{S}_{LG} , the kinematic condition (3.2.4) holds, as does equation (3.2.24), where the effective surface tension is given by (3.2.38), and the dilatational surface viscous coefficient is given by (3.2.37). At the axis of symmetry, the boundary condition (3.2.39) holds in the bulk liquid drop, as does the boundary condition (3.2.12) at any intersection of the liquid-gas interface \mathcal{S}_{LG} with the axis of symmetry. At the liquid-solid interface \mathcal{S}_{LS} (if it exists), impermeability is applied as a boundary condition for the bulk drop flow (3.2.11), and at the contact line (where \mathcal{S}_{LG} and \mathcal{S}_{LS} meet), a *constant* contact angle is imposed. The initial encapsulation and initial freezing areas (3.2.32) and (3.2.34), respectively, are determined by the values of α_{encap} (3.2.31) and α_{freeze} (3.2.35), respectively, as well as the maximum contact area of the impacting drop with the substrate. Upon encapsulation, which occurs post-rebound and is when the drop surface area is below the initial encapsulation area, surface viscous effects are triggered, and a deformed liquid marble is created when (and if) the surface area of the encapsulated drop reaches the (time dependent) freezing area.

3.2.5 Viscous Bulk Equations

After constructing the inviscid bulk equations and presenting the new and interesting consequences that follow from their coupling to the surface equations, the next step was to implement the model numerically and to simulate drop impacts (which is discussed in Chapter 4 using a boundary integral method and corresponding boundary element method). After some time, it became clear that the simulations for the impact itself did not accurately capture dynamics observed in experiments which are associated with a drop spreading over a superhydrophobic substrate (see §4.7 for details). Experimental phenomena corresponding to low impact Weber numbers can be reproduced effectively, but this is for drops that barely deform from a sphere when in contact with the substrate and are of no interest for our objective of studying liquid marble formation. At higher impact Weber numbers, problems arise when considering thin films of liquid; particularly those that follow the thick liquid rim that forms behind the advancing contact line during spreading (see Figures 4.23-4.24). In our simulations of the inviscid model, these thin films break as the liquid-gas interface behind the advancing rim moves closer and closer to the substrate until the two meet, which results in drops splashing *much* earlier than has been observed in experiments

with similar parameters.

While a high impact Reynolds number may allow dynamics on the length-scale of the radius of the drop to be considered inviscid, within the thin films of the spreading (and later, retracting) drop, the local length-scale is *much* smaller and on par with the size of the viscous boundary layer at the substrate. Hence bulk viscosity is very important in these areas, and is the mechanism one would expect to prevent breaking of the thin films observed in simulations of the inviscid model. Therefore for the second model, we suppose that both liquid and gas flows are viscous; this will mean incorporating an additional boundary condition, which is the condition for slip length (3.2.10) at the liquid-solid interface \mathcal{S}_{LS} .

We only expect viscosity to be important during the impact itself (when these thin films exist), and once the drop has rebounded (or retracted significantly so that there are no thin films) we claim that it is moving with sufficient speed that the effects of bulk viscosity are not that important and that post-rebound, both models would likely produce similar dynamics because the motion has returned to being on par with the length-scale of the drop. For this reason, we suppose that the effective surface tension (developed in §3.2.4) carries over to this model. What this means is that we take the conventional boundary condition for the normal stress at the interface between two viscous flows, and replace the surface tension with our *effective* surface tension, that is, we have

$$\underline{\mathbf{n}} \cdot \left(\underline{\underline{\mathbf{\Pi}}}_G - \underline{\underline{\mathbf{\Pi}}} \right) \cdot \underline{\mathbf{n}} = \sigma_{\text{eff}}(A, t) (\nabla_s \cdot \underline{\mathbf{n}}) \quad \text{on } \mathcal{S}_{LG}. \quad (3.2.40)$$

The effective surface tension $\sigma_{\text{eff}}(A, t)$ is given by equation (3.2.38) which is repeated here for convenience,

$$\sigma_{\text{eff}}(A, t) = 1 + \lambda^s(A, t) \left(\frac{\int_{\mathcal{S}_{LG}(t)} (\nabla_s \cdot \underline{\mathbf{n}}) (\underline{\mathbf{u}} \cdot \underline{\mathbf{n}}) \, dS(t)}{\int_{\mathcal{S}_{LG}(t)} 1 \, dS(t)} \right),$$

with the constitutive equation (3.2.37) for $\lambda^s(A, t)$, likewise repeated for convenience:

$$\lambda^s(A, t) = \beta \cdot \frac{(A_{\text{encap}}(t) - A)}{(A - A_{\text{freeze}}(t))}.$$

For the tangential stress balance equation, we continue with the conventional boundary condition for free surface flows, namely:

$$\underline{\mathbf{n}} \cdot \left(\underline{\underline{\mathbf{\Pi}}}_G - \underline{\underline{\mathbf{\Pi}}} \right) \cdot \underline{\mathbf{t}} = 0. \quad (3.2.41)$$

The constitutive equations for the liquid and gas bulk stress tensors in this viscous formulation are given by, respectively,

$$\underline{\underline{\mathbf{\Pi}}} = -p\underline{\underline{\mathbf{I}}} + \text{Oh} \left(\nabla \underline{\mathbf{u}} + (\nabla \underline{\mathbf{u}})^T \right), \quad (3.2.42)$$

and

$$\underline{\underline{\mathbf{\Pi}}}_G = -p_G \underline{\underline{\mathbf{I}}} + \mu_G \text{Oh} \left(\nabla \underline{\mathbf{u}}_G + (\nabla \underline{\mathbf{u}}_G)^T \right), \quad (3.2.43)$$

where $\text{Oh} \equiv \hat{\mu} / \sqrt{\hat{\rho}_0 \hat{\sigma}_0 \hat{R}_0}$ is the Ohnesorge number (a dimensionless parameter relating bulk viscous forces to bulk inertial and surface tension forces) [78] as calculated for the liquid bulk, and where $\hat{\mu}$ and μ_G are the dimensional bulk viscosity and dimensionless gas viscosity respectively. The gas dynamics in principle could be neglected, but it is convenient to include them because the numerical method used for the viscous case models both domains with a single set of governing equations (see Chapter 5 on the volume-of-fluid method). The conservation of momentum equations within the liquid and gas then take the form of the (dimensionless) Navier-Stokes equations [133], that is,

$$\frac{\partial \underline{\mathbf{u}}}{\partial t} + (\underline{\mathbf{u}} \cdot \nabla) \underline{\mathbf{u}} = -\nabla p + \underline{\mathbf{g}} + \text{Oh} \nabla^2 \underline{\mathbf{u}} \quad \text{in } \Omega, \quad (3.2.44)$$

in the liquid drop, and

$$\rho_G \left[\frac{\partial \underline{\mathbf{u}}_G}{\partial t} + (\underline{\mathbf{u}}_G \cdot \nabla) \underline{\mathbf{u}}_G \right] = -\nabla p_G + \rho_G \underline{\mathbf{g}} + \mu_G \text{Oh} \nabla^2 \underline{\mathbf{u}}_G \quad \text{in } \Omega_G, \quad (3.2.45)$$

in the exterior gas. As with the inviscid model we assume both flows are incompressible, so equations (3.2.14) and (3.2.15) hold in the liquid and gas, repeated for convenience:

$$\nabla \cdot \underline{\mathbf{u}} = 0 \quad \text{in } \Omega, \quad \text{and} \quad \nabla \cdot \underline{\mathbf{u}}_G = 0 \quad \text{in } \Omega_G.$$

Finally, we impose the following symmetry boundary condition on the bulk flows within the liquid drop and exterior gas at the axis of symmetry, in addition to the condition (3.2.39) from the inviscid model (which is also applied to the gas bulk):

$$\frac{\partial}{\partial r} (\underline{\mathbf{u}} \cdot \underline{\mathbf{e}}_z) = 0 \quad \text{and} \quad \frac{\partial}{\partial r} (\underline{\mathbf{u}}_G \cdot \underline{\mathbf{e}}_z) = 0 \quad \text{at } r = 0. \quad (3.2.46)$$

Summary of the Viscous Model

In summary, the flow in the bulk liquid drop and exterior gas satisfy the incompressible Navier-Stokes equations (3.2.44) and (3.2.14), and (3.2.45) and (3.2.15), respectively. At the liquid-gas interface \mathcal{S}_{LG} , the kinematic condition (3.2.4) holds,

as do the normal and tangential stress balance equations (3.2.40) and (3.2.41), respectively, where the effective surface tension is given by (3.2.38), and the dilatational surface viscous coefficient is given by (3.2.37). At the axis of symmetry, boundary conditions (3.2.39) and (3.2.46) hold in the liquid and gas bulk flows, as does the boundary condition (3.2.12) at any intersection of the liquid-gas interface \mathcal{S}_{LG} with the axis of symmetry. At the liquid-solid interface \mathcal{S}_{LS} (if it exists), impermeability is applied as a boundary condition for the bulk drop flow (3.2.11), as is a slip length condition (3.2.10), and at the contact line (where \mathcal{S}_{LG} and \mathcal{S}_{LS} meet), a *constant* contact angle is imposed, except in §6.2.1 where the dynamic contact angle model (3.2.13) is used. The roles and definitions of the encapsulation and freezing areas are the same as in the summary of the inviscid model in §3.2.4.

3.3 Suspended Inviscid Drop Oscillations with Dilatational Surface Viscosity

We will now derive an ordinary differential equation (with a form similar to a damped harmonic oscillator, but nonlinear) that approximates the motion of a point on the surface of an incompressible suspended oscillating inviscid drop, experiencing the effects of a nonzero dilatational component of surface viscosity. Similar ordinary differential equations have been derived [116–119] to describe the amplitudes of waves experiencing surface viscous effects but they only approximate these effects up to linear order, and these linear effects vanish in the case of zero shear surface viscosity and zero bulk viscosity that we consider here. In contrast, our novel *third-order* approximation predicts complicated drop behaviour that matches simulation results (see §4.8) for oscillations of an inviscid drop with a *possibly large* (constant) dilatational surface viscous coefficient λ^s and zero shear surface viscous coefficient and is the lowest-order approximation that provides damping. In particular, it predicts for large λ^s that a drop experiences overdamped motion when the amplitude is relatively large², and transitions to underdamped motion once the amplitude falls below some critical threshold.

²The relative size of the amplitude in this context depends on the chosen value of λ^s .

3.3.1 Derivation of the Damped Nonlinear Oscillator

Consider a drop oscillation that is dominated by a single axisymmetric harmonic mode, with *small* amplitude. Let x denote the displacement of a point on the drop boundary (denoted by \mathcal{S}) from the drop centre (drop bulk denoted by Ω), then, in dimensionless form, x is given by³

$$x(t, \psi) = 1 + a(t)P_n(\cos \psi) + \sum_{\substack{m=0 \\ m \neq n}}^{\infty} b_m(t)P_m(\cos \psi), \quad (3.3.1)$$

where $\psi \in [0, \pi]$ is the polar angle in spherical coordinates (with the centre of this coordinate system coinciding with the drop centre), and where P_n denotes the Legendre polynomial of order n , corresponding to the axisymmetric mode that dominates the drop oscillation. The term with factor $a(t)$ corresponds to the excitation of the dominant n -th mode, and without loss of generality, the corrections to the deformation are expanded over all spherical harmonics, with amplitudes given by $b_m(t)$, where *at least at early times*, $b_m(t)$ is small compared to $a(t)$ ⁴, and we *assume* that they remain small compared to $a(t)$ at all times of interest, as discussed in more detail at the end of this section.

Consider first the case of a clean interface (so with *no* surface viscous effects), then supposing that the bulk drop flow is inviscid, there is no mechanism for damping of drop oscillations. Hence, every point on the drop boundary follows (in the linear approximation) a simple harmonic oscillation that satisfies the following ordinary differential equation, which is the linear approximation of the *exact* nonlinear equation for $a(t)$:

$$\frac{d^2 a}{dt^2} = -\omega_{0,n}^2 a, \quad (3.3.2)$$

where $\omega_{0,n}$ is the undamped angular frequency of the n -th axisymmetric spherical harmonic mode, given by [139]

$$\omega_{0,n}^2 = n(n-1)(n+2). \quad (3.3.3)$$

Looking at (3.3.3) in its dimensional form, we have

$$\hat{\omega}_{0,n}^2 = n(n-1)(n+2) \frac{\hat{\sigma}_0}{\hat{\rho}_0 \hat{R}_0^3}, \quad (3.3.4)$$

³Neglecting the possibility of x becoming multi-valued due to, for example, ‘folding’ of the drop surface.

⁴That is, the characteristic sizes of $b_m(t)$ are much smaller than that of $a(t)$.

highlighting in particular the (constant) surface tension $\hat{\sigma}_0$ that was otherwise hidden through non-dimensionalisation. By imposing an everywhere nonzero dilatational surface viscous coefficient $\hat{\lambda}^s$, recall from §3.2.4 that in the case of an inviscid bulk flow (and zero shear surface viscosity), dilatational surface viscous effects are manifested in an *effective* surface tension $\hat{\sigma}_{\text{eff}}$ (3.2.22) that replaces the *base* surface tension of the clean interface. By replacing the constant surface tension with our effective surface tension in (3.3.4), we can therefore incorporate surface viscous effects into this harmonic oscillator model and investigate the implications of doing so. Including $\hat{\sigma}_{\text{eff}}$ and then making the equation dimensionless (recall dimensional scales in Table 3.1), we obtain a new quantity $\omega_{\text{eff},n}^2$, given by

$$\begin{aligned}\omega_{\text{eff},n}^2 &= n(n-1)(n+2)\sigma_{\text{eff}} \\ &= \omega_{0,n}^2 [1 + W(t)] \\ &= \omega_{0,n}^2 \left[1 + \lambda^s \frac{\int_{\mathcal{S}} (\nabla_s \cdot \underline{\mathbf{n}}) (\underline{\mathbf{u}} \cdot \underline{\mathbf{n}}) \, dS}{\int_{\mathcal{S}} 1 \, dS} \right].\end{aligned}\tag{3.3.5}$$

Using (3.3.5) in place of $\omega_{0,n}^2$ in (3.3.2), we obtain an altered version of this oscillator, given by

$$\frac{d^2 a}{dt^2} = -\omega_{\text{eff},n}^2 a,\tag{3.3.6}$$

which describes the oscillation of an inviscid drop with surface viscous effects (arising from a constant $\lambda^s > 0$ and $\mu^s = 0$). We now seek to obtain the lowest order approximation of the integrals in (3.3.5) that, as we will see, provides damping. As will be shown, the lowest-order nonzero terms that make up the expansion of the numerator integral in (3.3.5) are *second*-order in a , which results in an additional term in (3.3.6) that is then *third*-order in a .

To evaluate (3.3.5), we consider in turn, the three constituent factors within the integrand of the numerator integral, using the representation of the deformation in (3.3.1). The normal velocity, which is the time derivative of the displacement of the interface, is therefore given by

$$\underline{\mathbf{u}} \cdot \underline{\mathbf{n}} = \frac{da}{dt} P_n(\cos \psi) + \sum_{\substack{m=0 \\ m \neq n}}^{\infty} \frac{db_m}{dt} P_m(\cos \psi),\tag{3.3.7}$$

the curvature $\nabla_s \cdot \underline{\mathbf{n}}$ is given by

$$\nabla_s \cdot \underline{\mathbf{n}} = 2 + (n-1)(n+2)a(t)P_n(\cos \psi) + \mathcal{O}(a^2) + \mathcal{O}(b_m),\tag{3.3.8}$$

where 2 is the dimensionless curvature of the sphere, and $(n-1)(n+2)$ is the pre-factor for the linear term in $a(t)$ as calculated in [140] for the n -th axisymmetric spherical harmonic mode, and the area element dS is given by

$$dS = [1 + 2a(t)P_n(\cos \psi) + \mathcal{O}(a^2) + \mathcal{O}(b_m)] \sin \psi \, d\psi \, d\theta, \quad (3.3.9)$$

where θ is the azimuthal angle. Note that unlike the expansion for $\underline{\mathbf{u}} \cdot \underline{\mathbf{n}}$ (3.3.7) which is given explicitly, the expansions of $\nabla_s \cdot \underline{\mathbf{n}}$ (3.3.8) and dS (3.3.9) group together all second- and higher-order terms in a that emerge, and also terms multiplied by b_m (including cross-terms also multiplied by powers of a). It is not clear *a priori* which of b_m and a^2 is larger (in order), hence for now, we keep track of both. Ultimately, all grouped terms contribute to higher order within the numerator integral of (3.3.5) following multiplication, than the terms given explicitly.

We now use (3.3.7), (3.3.8), and (3.3.9) to express the numerator integral of (3.3.5), and will now consider explicitly all terms up to *and including* $\mathcal{O}(a^2)$ and $\mathcal{O}(b_m)$. Note that as we assume $b_m \ll a$ for all $m \geq 0$, we then have $a \cdot b_m \ll a^2$, and so terms of order $a \cdot b_m$ are grouped with other small terms and are not given explicitly. With this in mind, we have

$$\begin{aligned} \int_S (\nabla_s \cdot \underline{\mathbf{n}}) (\underline{\mathbf{u}} \cdot \underline{\mathbf{n}}) \, dS &= \int_{\theta=0}^{\theta=2\pi} \int_{\psi=0}^{\psi=\pi} \left[2 \frac{da}{dt} P_n(\cos \psi) + 4a \frac{da}{dt} P_n^2(\cos \psi) \right. \\ &\quad \left. + (n-1)(n+2)a \frac{da}{dt} P_n^2(\cos \psi) \right. \\ &\quad \left. + 2 \sum_{\substack{m=0 \\ m \neq n}}^{\infty} \frac{db_m}{dt} P_m(\cos \psi) + \text{smaller terms} \right] \sin \psi \, d\psi \, d\theta \\ &= 2\pi \int_{\xi=-1}^{\xi=1} \left[2 \frac{da}{dt} P_n(\xi) + \{4 + (n-1)(n+2)\} a \frac{da}{dt} P_n^2(\xi) \right. \\ &\quad \left. + 2 \sum_{\substack{m=0 \\ m \neq n}}^{\infty} \frac{db_m}{dt} P_m(\xi) + \text{smaller terms} \right] d\xi \\ &= 2\pi \left[0 + \{4 + (n-1)(n+2)\} a \frac{da}{dt} \frac{2}{2n+1} \right. \\ &\quad \left. + 4 \frac{db_0}{dt} \right] + \text{smaller terms} \\ &= 4\pi \left[\frac{4 + (n-1)(n+2)}{2n+1} a \frac{da}{dt} + 2 \frac{db_0}{dt} \right] + \text{smaller terms}, \end{aligned} \quad (3.3.10)$$

where we have used the variable substitution $\xi = \cos \psi$, and the properties of Legendre polynomials under integration [141], in particular that

$$\int_{\xi=-1}^{\xi=1} P_m(\xi) d\xi = 0,$$

for $m \geq 1$,

$$\int_{\xi=-1}^{\xi=1} P_m(\xi)P_n(\xi) d\xi = \frac{2}{2n+1}\delta_{mn},$$

for $n, m \geq 0$, and *importantly* that $P_0(\xi) = 1$; from which emerged the b_0 term. This term provides a contribution to *roughly* the same order as the $a(t)$ term from the expansion of the deformation (3.3.1) *even if* $b_0 = \mathcal{O}(a^2)$ (which it indeed is, as we will see shortly), and it is the *only* b_m term that can contribute to the lowest order. It may seem that to evaluate b_0 , we will need to go beyond the linear approximation given by (3.3.2), but in reality, we can obtain it from incompressibility.

To obtain an expression for $b_0(t)$ in terms of $a(t)$, we expand the surface integral of the normal velocity $\mathbf{u} \cdot \mathbf{n}$ (equivalent to the bulk integral of $\nabla \cdot \mathbf{u}$) into a sum over all spherical harmonics, as done previously for (3.3.10). Doing so by only explicitly considering terms up to and including $\mathcal{O}(a^2)$ and $\mathcal{O}(b_m)$, we have

$$\begin{aligned} 0 &= \int_{\Omega} \nabla \cdot \mathbf{u} dV = \int_S \mathbf{u} \cdot \mathbf{n} dS \\ &= 2\pi \int_{\xi=-1}^{\xi=1} \left[\frac{da}{dt} P_n(\xi) + 2a \frac{da}{dt} P_n^2(\xi) \right. \\ &\quad \left. + \sum_{\substack{m=0 \\ m \neq n}}^{\infty} \frac{db_m}{dt} P_m(\xi) + \text{smaller terms} \right] d\xi \\ &= 2\pi \left[0 + 2a \frac{da}{dt} \frac{2}{2n+1} + 2 \frac{db_0}{dt} \right] + \text{smaller terms} \\ &= 4\pi \left[\frac{d}{dt} \left(\frac{a^2}{2n+1} \right) + \frac{db_0}{dt} \right] + \text{smaller terms}, \end{aligned} \tag{3.3.11}$$

where the first equality holds by incompressibility. Hence for incompressibility to hold up to order a^2 , we must have

$$\frac{db_0}{dt} = -\frac{d}{dt} \left(\frac{a^2}{2n+1} \right), \quad \text{or equivalently,} \quad b_0(t) = -\frac{a^2}{2n+1} + \mathcal{C}, \tag{3.3.12}$$

where \mathcal{C} is a constant and equal to zero, because for a sphere (where $a(t) = 0$) we must have $b_0(t) = 0$. So in fact, $b_0 = \mathcal{O}(a^2)$.

Using (3.3.12) in (3.3.10), we then find the following representation of the numerator integral in (3.3.5):

$$\int_S (\nabla_s \cdot \mathbf{n}) (\mathbf{u} \cdot \mathbf{n}) \, dS = \frac{4\pi(n-1)(n+2)}{2n+1} a \frac{da}{dt} + \text{smaller terms.} \quad (3.3.13)$$

In the lowest order, the surface area of the drop is given by

$$\int_S 1 \, dS \approx 4\pi, \quad (3.3.14)$$

meaning we can finally get the lowest-order approximation of $W(t)$ from (3.3.5). Combining (3.3.13), (3.3.14), and (3.3.5), we then have the second-order approximation (so up to a^2)

$$\omega_{\text{eff},n}^2 \approx \omega_{0,n}^2 k_{\text{eff},n}, \quad (3.3.15)$$

where

$$k_{\text{eff},n} = 1 + \lambda^s a \frac{da}{dt} \frac{(n-1)(n+2)}{2n+1} \quad (3.3.16)$$

is the second-order approximation of the effective surface tension, which we call the ‘effective spring constant’ for the n -th axisymmetric harmonic mode. This leads to the *damped nonlinear* oscillator given by the following ordinary differential equation:

$$\begin{aligned} \frac{d^2 a}{dt^2} &= -\omega_{0,n}^2 k_{\text{eff},n} a \\ &= -\omega_{0,n}^2 a - \frac{\omega_{0,n}^2 \lambda^s (n-1)(n+2)}{2n+1} a^2 \frac{da}{dt} \\ &= -\omega_{0,n}^2 a - 2\zeta_n \omega_{0,n} \frac{da}{dt}, \end{aligned} \quad (3.3.17)$$

where

$$\zeta_n = \frac{\omega_{0,n} \lambda^s a^2 (n-1)(n+2)}{2(2n+1)}. \quad (3.3.18)$$

Note that (3.3.17)-(3.3.18) represents a third-order approximation of (3.3.6) given that it contains a term proportional to $a^2 da/dt$, which is missing from approximations in [116–119].

The form of (3.3.17) with ζ_n is the standard representation for a damped harmonic oscillator, and is co-opted for this damped nonlinear oscillator. For a harmonic oscillator with $\zeta_n > 1$, the dynamical system is *overdamped*, so it decays towards a steady state exponentially without oscillation, and does so slower for larger ζ_n . For $\zeta_n < 1$, the system is *underdamped*, so it gradually decays to a steady state while still oscillating at a different frequency from the undamped oscillator [142].

Our derivation started with the linear equation (3.3.2), which neglects all nonlinear terms that are independent of λ^s . A single nonlinear, third-order term multiplied

by λ^s via (3.3.5) by contrast *is* considered, and is the lowest order term to provide damping in the case of $\lambda^s > 0$ and $\mu^s = 0$. For sufficiently large λ^s , when the included third-order term is much larger than the neglected terms that do not contain λ^s , dominance of the included term is expected. For λ^s not so large (when it is less obvious that these terms can be neglected), it is useful to consider possible effects of the neglected terms. First, these second- and third-order terms can modify the frequency of oscillation slightly or introduce small ‘distortions’ to drop motion, but both of these effects are not of interest to us here. More interestingly, in the case of resonant coupling between the modes, whereby the natural frequency of oscillation for the initially-dominant mode can be written as a sum (with integer coefficients) of the natural frequencies of other modes [143], the amount of energy transferred between them can become large over time. This transfer of energy in the case of resonant coupling can significantly decrease the amplitude of oscillation for the primary mode, invalidate our assumption that the displacement at the drop surface is proportional to the amplitude of the primary mode, and modify our result for $W(t)$ significantly. Our considerations remain valid as long as this energy transfer associated with resonant coupling is small compared to the total energy of the initially-dominant mode during the time interval of interest. In practice, there are relatively few second-order resonances (the lowest being between the 5th and 8th modes [144]), with effects of third-order resonances being much weaker and taking place on a longer timescale. For example, as will be shown for subsequent numerical simulations for the 2nd mode in §4.8, effects from the third-order resonant coupling between the 2nd and 4th mode [145] are not apparent.

3.3.2 Critical Amplitude

Turning our attention now to where the transition between overdamped and underdamped motion occurs, we rearrange equation (3.3.18) to find the critical amplitude a_c at which $\zeta_n = 1$, which is given as

$$a_c = \sqrt{\frac{2(2n+1)}{\omega_{0,n}\lambda^s(n-1)(n+2)}}. \quad (3.3.19)$$

So for sufficiently small λ^s , the critical amplitude a_c is *larger* than the initial amplitude, so only underdamped motion is experienced. As λ^s is increased, there comes a point at which this critical amplitude is *less* than the initial amplitude; at which

point the drop experiences both damping regimes during its dynamics.

3.3.3 Analytic Solution in the Overdamped Limit

In the overdamped limit, we have $\zeta_n \gg 1$, and so the term containing the first derivative of the amplitude $a(t)$ in (3.3.17) dominates the term containing its second derivative. In the lowest approximation, we neglect the effects of the second derivative entirely by setting the left hand side of the un-approximated oscillator (3.3.6) equal to zero, which is equivalent to setting $\sigma_{\text{eff}} = 0$. This is then (approximately) equivalent to setting the effective spring constant $k_{\text{eff},n}$ in equations (3.3.15) and (3.3.16) equal to zero, which leads to the first-order equation in $a(t)$ given by:

$$1 + \frac{\lambda^s(n-1)(n+2)}{2n+1} a \frac{da}{dt} = 0. \quad (3.3.20)$$

Solving (3.3.20) for $a(t)$ then provides an analytic solution to the *nonlinear* damped oscillator (3.3.17) in the overdamped limit. Recognising that $d(a^2)/dt = 2a da/dt$, we solve (3.3.20) and find

$$a(t) = \sqrt{a_0^2 - 2Bt}, \quad (3.3.21)$$

where a_0 is the amplitude of the perturbation at time $t = 0$, and

$$B = \frac{(2n+1)}{\lambda^s(n-1)(n+2)}. \quad (3.3.22)$$

Using this approximation (3.3.21) for the amplitude in the overdamped limit, we can directly calculate d^2a/dt^2 and with it, a higher-order approximation of σ_{eff} in the overdamped limit using (3.3.6), given by:

$$\sigma_{\text{eff}}(t) = \left(\frac{B}{\omega_{0,n}(a_0^2 - 2Bt)} \right)^2. \quad (3.3.23)$$

The damped nonlinear oscillator (3.3.17) presented in this section is validated numerically in §4.8 by comparing the predicted behaviour of the amplitude $a(t)$ and effective spring constant $k_{\text{eff},n}$ against boundary element method simulations for small amplitude suspended inviscid drop oscillations, with (constant) values of λ^s spanning multiple orders of magnitude. Large amplitude oscillations are also investigated, and although they lie outside the range of validity for this model given their nonlinear drop deformations, they are shown to exhibit a similar transition between overdamped and underdamped motion that can be described well qualitatively with a ‘toy’ version of our model (that is, with parameters chosen to best match exhibited behaviour).

Chapter 4

Boundary Integral Method and Boundary Element Method

In this chapter we formulate a boundary integral method (BIM) for the inviscid model from §3.2.4 and discuss the associated computational boundary element method (BEM) that is implemented and solved numerically using code created for this body of research. The implementation of the BEM is validated by presenting our simulations with comparisons to experimental images and theoretical results, where applicable, for suspended drop oscillations (separately with a clean interface and with dilatational surface viscosity) and for drop impacts with low impact Weber numbers. We then discuss the shortcomings of the BIM and BEM in resolving the impact phase of the problem, and justify why focus was moved onto the viscous model (see §3.2.5) and solving it with a volume-of-fluid method, which is discussed in Chapter 5. We conclude with a numerical validation of the novel damped nonlinear oscillator model presented in §3.3 for a suspended oscillating inviscid drop experiencing the effects of a dilatational surface viscosity, with respect to small amplitude drop oscillations, and also discuss how this model can qualitatively describe large amplitude drop oscillations.

BIMs involve constructing a boundary integral equation that allows flow variables to be calculated at a fluid boundary, using *only* knowledge of the boundary geometry, and of other flow variables evaluated *at* this boundary. Once all values of these variables have been solved for, a second boundary integral equation allows us to then evaluate flow variables *inside* the bulk (if we so wish). Given that the focus of the research presented here (see §1.1.6 and the mathematical problem formulation in §3.1)

is on liquid marble formation, which is governed by processes associated to particles adhered to the drop interface, we are only interested in the evolution of the boundary itself; so we do not need to solve for the flow inside the drop.

4.1 Irrotational Bulk Drop Flow within the Inviscid Model

We will assume that the flow within the liquid drop in the inviscid model (see §3.2.4) is irrotational (that is, $\nabla \times \underline{\mathbf{u}} = \underline{\mathbf{0}}$), so then the bulk drop velocity can be expressed as

$$\underline{\mathbf{u}} = \nabla\phi, \quad (4.1.1)$$

within the drop domain Ω , where ϕ is known as the ‘velocity potential’. We will now show how this expression affects the flow equations in the bulk liquid drop.

Applying (4.1.1) to the (dimensionless form of the) Euler equations (3.2.17) and then integrating in space provides us with the (dimensionless) unsteady Bernoulli equations [133], given by

$$\frac{\partial\phi}{\partial t} + \frac{1}{2}|\nabla\phi|^2 + p + gz = C(t), \quad (4.1.2)$$

which holds everywhere within the drop domain Ω and on the drop liquid-gas interface \mathcal{S}_{LG} , and where gz is the potential of the gravitational acceleration term $\underline{\mathbf{g}}$, and $C(t)$ is a time dependent function. Without loss of generality, $C(t)$ can be absorbed into the potential ϕ (because ϕ only needs to be known up to an additive constant), so the right hand side of (4.1.2) is set equal to zero for sake of simplicity.

Applying (4.1.1) to the incompressibility condition (3.2.14) shows that the velocity potential solves Laplace’s equation in the drop domain, that is,

$$\nabla^2\phi = 0 \quad \text{in } \Omega. \quad (4.1.3)$$

This equation is crucial to the development of a BIM as we will see in the following section, in which we present a formulation of the boundary integral equation in three dimensions for a general case. In §4.3.3, we apply this formulation to our model and discuss the role axisymmetry plays in simplifying the method.

4.2 Formulation of the Boundary Integral Equation in Three Dimensions

The boundary integral equation utilised in this body of research is similar to those used in existing research [131, 146–149], with formulations like the one presented here being well-documented. Given the code used to implement the BEM corresponding to the forthcoming boundary integral equation was built specifically for this body of research, we present this formulation to provide the reader with an understanding of how the boundary integral equation is derived, and how it is applied to the inviscid model given in §3.2.4.

Consider a three dimensional volume, Ω , with smooth boundary $\partial\Omega \equiv \mathcal{S}$. For any pair of twice-continuously-differentiable functions, ϕ and ψ , defined on the closed set $\Omega \cup \mathcal{S} \subset \mathbb{R}^3$, Green’s second identity dictates [150] that

$$\int_{\Omega} (\phi \nabla^2 \psi - \psi \nabla^2 \phi) \, d\Omega = \int_{\mathcal{S}} \left(\phi \frac{\partial \psi}{\partial n} - \psi \frac{\partial \phi}{\partial n} \right) \, dS, \quad (4.2.1)$$

where $\partial/\partial n \equiv \mathbf{n} \cdot \nabla$ denotes the directional derivative in the direction of \mathbf{n} , the outward-pointing unit normal at the interface \mathcal{S} , and dS denotes an area element on \mathcal{S} .

Fix a point $\mathbf{x} \in \Omega$ (known as the ‘singularity point’), let $\underline{\boldsymbol{\xi}} \in \Omega \cup \mathcal{S}$ (known as the ‘field variable’) and define the following function

$$G(\mathbf{x}, \underline{\boldsymbol{\xi}}) := \frac{1}{4\pi |\mathbf{x} - \underline{\boldsymbol{\xi}}|}, \quad (4.2.2)$$

which is known as the ‘free-space Green’s function for Laplace’s equation in three dimensions’ [150]. Our aim is to replace the function ψ in Green’s second identity (4.2.1) with G . However, G exhibits a singularity at the point $\underline{\boldsymbol{\xi}} = \mathbf{x}$, so this point will have to be treated carefully when the function is integrated. To this end, let $\varepsilon > 0$ be a small constant and define the reduced domain $\Omega_{\varepsilon} := \Omega - B_{\varepsilon}(\mathbf{x})$, where $B_{\varepsilon}(\mathbf{x})$ (with boundary $\mathcal{S}_{\varepsilon}$) is the ball of radius ε , with centre \mathbf{x} (see Figure 4.1). The boundary to this reduced domain now consists of two distinct (smooth) surfaces, given by $\partial\Omega_{\varepsilon} \equiv \mathcal{S} \cup \mathcal{S}_{\varepsilon}$. Notice that G is both twice-continuously-differentiable and a solution to Laplace’s equation in the reduced domain Ω_{ε} , that is,

$$\nabla^2 G = 0 \quad \text{in } \Omega_{\varepsilon}, \quad (4.2.3)$$

where ∇ represents differentiation with respect to the field variable $\underline{\boldsymbol{\xi}}$. Hence G satisfies the conditions of ψ in Ω_{ε} .

Suppose that ϕ solves Laplace's equation over the *entire* domain Ω , that is, $\nabla^2\phi = 0$ in Ω . Then, applying Green's second identity (4.2.1) to Ω_ε with $\psi = G$ yields

$$\begin{aligned} 0 &= \int_{\Omega_\varepsilon} (\phi \nabla^2 G - G \nabla^2 \phi) \, d\Omega_\varepsilon \\ &= \int_{\partial\Omega_\varepsilon} \left(\phi \frac{\partial G}{\partial n} - G \frac{\partial \phi}{\partial n} \right) \, d\Omega_\varepsilon \\ &\equiv \int_{\mathcal{S}} \left(\phi \frac{\partial G}{\partial n} - G \frac{\partial \phi}{\partial n} \right) \, dS + \int_{\mathcal{S}_\varepsilon} \left(\phi \frac{\partial G}{\partial n} - G \frac{\partial \phi}{\partial n} \right) \, dS_\varepsilon, \end{aligned} \quad (4.2.4)$$

where dS_ε is a surface element on \mathcal{S}_ε .

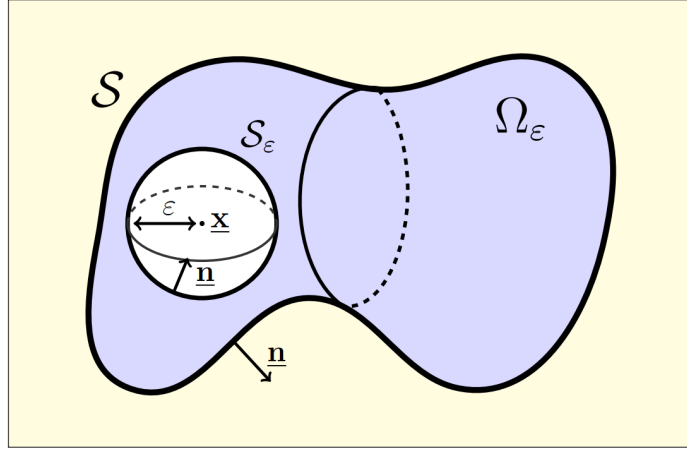


Figure 4.1: Diagram showing a three dimensional domain Ω bounded by a smooth surface \mathcal{S} and containing an interior ball of radius ε , centred at the point $\underline{x} \in \Omega$. Ω_ε is the reduced domain $\Omega - B_\varepsilon(\underline{x})$ with unit normal \underline{n} to the boundary $\partial\Omega_\varepsilon \equiv \mathcal{S} \cup \mathcal{S}_\varepsilon$.

The aim now is to frame the integral over \mathcal{S}_ε in equation (4.2.4) in such a way that taking the limit $\varepsilon \rightarrow 0$ produces a term that makes sense analytically. As such, consider a spherical coordinate system with origin point \underline{x} (the centre of the epsilon-ball) and write the function G as

$$G(\underline{x}, \underline{\xi}) = \frac{1}{4\pi R}, \quad (4.2.5)$$

with $R = |\underline{x} - \underline{\xi}|$. When restricted to the surface of the epsilon-ball, with $\underline{\xi} \in \mathcal{S}_\varepsilon$, the normal derivative of G is then given by

$$\left. \frac{\partial G}{\partial n} \right|_{\mathcal{S}_\varepsilon} = \left. \frac{\partial}{\partial R} \left(\frac{1}{4\pi R} \right) \right|_{R=\varepsilon} = - \left. \frac{1}{4\pi R^2} \right|_{R=\varepsilon} = - \frac{1}{4\pi \varepsilon^2}. \quad (4.2.6)$$

Applying (4.2.5) and (4.2.6) to the integral over \mathcal{S}_ε in equation (4.2.4) then yields

$$\int_{\mathcal{S}_\varepsilon} \left(\phi \frac{\partial G}{\partial n} - G \frac{\partial \phi}{\partial n} \right) \, dS_\varepsilon = - \frac{1}{4\pi \varepsilon^2} \int_{\mathcal{S}_\varepsilon} \phi \, dS_\varepsilon - \frac{1}{4\pi \varepsilon} \int_{\mathcal{S}_\varepsilon} \frac{\partial \phi}{\partial n} \, dS_\varepsilon. \quad (4.2.7)$$

Let $\langle \cdot \rangle$ denote the map that returns the (arithmetic) mean of a function over a particular domain, that is,

$$\langle a \rangle := \frac{\int_X a \, dX}{\text{Vol}(X)}, \quad (4.2.8)$$

for some function a on a domain X , and where dX and $\text{Vol}(X)$ denote an *element*, and the *volume* of the domain X , respectively. For functions ϕ and $\partial\phi/\partial n$ over the domain \mathcal{S}_ε , this map returns

$$\langle \phi \rangle = \frac{1}{4\pi\varepsilon^2} \int_{\mathcal{S}_\varepsilon} \phi \, dS_\varepsilon \quad \text{and} \quad \left\langle \frac{\partial\phi}{\partial n} \right\rangle = \frac{1}{4\pi\varepsilon^2} \int_{\mathcal{S}_\varepsilon} \frac{\partial\phi}{\partial n} \, dS_\varepsilon, \quad (4.2.9)$$

hence equation (4.2.7) can be written as

$$\int_{\mathcal{S}_\varepsilon} \left(\phi \frac{\partial G}{\partial n} - G \frac{\partial\phi}{\partial n} \right) dS_\varepsilon = -\langle \phi \rangle - \varepsilon \left\langle \frac{\partial\phi}{\partial n} \right\rangle. \quad (4.2.10)$$

By reducing the size of the interior ball ($\varepsilon \rightarrow 0$), the second term on the right hand side in (4.2.10) tends to zero because $\partial\phi/\partial n$ is bounded on \mathcal{S}_ε , and the first term converges to the value of ϕ at the centre of the ball (by continuity of ϕ [151]). That is, as $\varepsilon \rightarrow 0$,

$$\int_{\mathcal{S}_\varepsilon} \left(\phi \frac{\partial G}{\partial n} - G \frac{\partial\phi}{\partial n} \right) dS_\varepsilon \rightarrow -\phi(\underline{\mathbf{x}}). \quad (4.2.11)$$

Finally, we substitute (4.2.11) into (4.2.4) to obtain

$$\phi(\underline{\mathbf{x}}) + \int_{\mathcal{S}} \phi(\underline{\boldsymbol{\xi}}) \frac{\partial G}{\partial n}(\underline{\mathbf{x}}, \underline{\boldsymbol{\xi}}) \, dS = \int_{\mathcal{S}} G(\underline{\mathbf{x}}, \underline{\boldsymbol{\xi}}) \frac{\partial\phi}{\partial n}(\underline{\boldsymbol{\xi}}) \, dS. \quad (4.2.12)$$

This equation allows ϕ to be evaluated within the interior of the domain by calculating surface integrals at its boundary, however, an applied boundary condition (see §4.2.1) does not supply sufficient information to immediately calculate these integrals. Hence, we first need to solve for ϕ and $\partial\phi/\partial n$ on the boundary \mathcal{S} itself (note that G and $\partial G/\partial n$ are known explicitly), so we must construct a similar equation to (4.2.12) with the singularity point $\underline{\mathbf{x}}$ on the boundary.

Up to now, $\underline{\mathbf{x}}$ has existed within the open domain Ω , but if we take $\underline{\mathbf{x}}$ to a limiting value $\underline{\mathbf{x}}_0$ on the boundary \mathcal{S} (see [146], details are not provided here) then the difference this makes to equation (4.2.12) is the inclusion of a pre-factor of one-half to the function ϕ at the singularity point $\underline{\mathbf{x}}_0$, that is,

$$\frac{1}{2}\phi(\underline{\mathbf{x}}_0) + \int_{\mathcal{S}} \phi(\underline{\boldsymbol{\xi}}) \frac{\partial G}{\partial n}(\underline{\mathbf{x}}_0, \underline{\boldsymbol{\xi}}) \, dS = \int_{\mathcal{S}} G(\underline{\mathbf{x}}_0, \underline{\boldsymbol{\xi}}) \frac{\partial\phi}{\partial n}(\underline{\boldsymbol{\xi}}) \, dS. \quad (4.2.13)$$

Equation (4.2.13) is known as the ‘boundary integral equation in three dimensions’ and all of its terms take their values at the interface \mathcal{S} . With an appropriately applied

boundary condition on \mathcal{S} , the boundary integral equation can be used to solve for ϕ and $\partial\phi/\partial n$ everywhere on the boundary \mathcal{S} (see §4.2.1), and then if desired, equation (4.2.12) can be used to solve for ϕ anywhere in the domain Ω .

4.2.1 Boundary Conditions

To solve the boundary integral equation (4.2.13), it is necessary to impose a boundary condition at \mathcal{S} regarding the function ϕ . If a Dirichlet condition is imposed (that is, ϕ takes pre-determined values on the boundary), then the boundary integral equation can be solved everywhere for the normal derivative, $\partial\phi/\partial n$. If a Neumann condition is imposed, then $\partial\phi/\partial n$ takes pre-determined values and ϕ is solved for, up to an additive constant (because we are imposing a derivative). Alternatively, if there are mixed boundary conditions, that is, Dirichlet in some regions of the interface and Neumann in others, then the boundary integral is solved for all unknowns simultaneously.

4.3 Application of the Boundary Integral Equation

We now relate the boundary integral equation formulation from the previous section to the inviscid model in §3.2.4. Due to incompressibility, the velocity potential ϕ as defined in (4.1.1) solves Laplace's equation within the bulk drop domain Ω , so clearly satisfies the conditions of ϕ as defined in §4.2. We will use the velocity potential ϕ along with the free-space Green's function G , as defined in (4.2.2), to construct the boundary integral equation (4.2.13) over the boundary of the drop. We will now discuss what we mean by the 'boundary', that is, under which conditions we mean the liquid-gas interface \mathcal{S}_{LG} , and when we mean the liquid-gas *and* liquid-solid interfaces $\mathcal{S}_{LG} \cup \mathcal{S}_{LS}$. This is followed by a description of the boundary conditions applied at each interface, and concludes with a simplification of the boundary integral equation (4.2.13) due to axisymmetry of our domain.

4.3.1 Identifying the Boundary

When the drop is *away* from the solid substrate (that is, when the liquid-solid interface \mathcal{S}_{LS} does *not* exist), the drop interface is *just* the liquid-gas interface \mathcal{S}_{LG} , which is sufficiently smooth to satisfy the conditions for the boundary \mathcal{S} in §4.2, and so we can construct the boundary integral equation (4.2.13) for $\mathcal{S} = \mathcal{S}_{LG}$. When the liquid-solid interface \mathcal{S}_{LS} *does* exist, a contact angle is imposed at the contact line which, in general, produces a corner where the interfaces \mathcal{S}_{LG} and \mathcal{S}_{LS} meet (meaning the two interfaces when combined together are *not* smooth). In our BEM, the contact angle is imposed when constructing the computational mesh (rather than via a flow equation) so we can choose to keep it at an *exact* value throughout a simulation. We take advantage of this and impose a contact angle of $\theta_c = 180^\circ$, which simultaneously mimics a completely non-wetting substrate, and is the *only* contact angle that ensures a smooth geometric transition between the liquid-gas and liquid-solid interfaces (that is, it avoids corners on the boundary \mathcal{S}). Therefore when in contact with the solid substrate, for the purposes of constructing the boundary integral equation (4.2.13), we treat the entire drop boundary as a free surface (so $\mathcal{S} = \mathcal{S}_{LG} \cup \mathcal{S}_{LS}$), but with distinct boundary conditions for \mathcal{S}_{LG} and \mathcal{S}_{LS} (discussed below).

4.3.2 Applied Boundary Conditions

On the liquid-gas interface \mathcal{S}_{LG} we impose a Dirichlet boundary condition on ϕ and solve for the normal velocity $\partial\phi/\partial n$. On the liquid-solid interface \mathcal{S}_{LS} (when it exists) we must impose impermeability of the substrate (3.2.11), given here as:

$$\mathbf{e}_z \cdot \nabla\phi = \frac{\partial\phi}{\partial z} = 0 \quad \text{at } z = 0.$$

Given that the liquid-solid interface \mathcal{S}_{LS} is flat (the same shape as the substrate), the unit normal defined at this interface is parallel to the z -axis, hence the above condition is equivalent to imposing a Neumann boundary condition:

$$\frac{\partial\phi}{\partial n} = 0 \quad \text{at } z = 0. \tag{4.3.1}$$

4.3.3 Axisymmetry of the Boundary Integral Equation

Given our model is axisymmetric, the boundary integral equation (4.2.13) can be simplified by integrating through the azimuthal angle θ to retrieve an integral over

a one dimensional boundary curve (denoted in this chapter by Γ). To this end, we identify (r_0, z_0) and (R, Z) as the radial and axial component pair for the singularity point $\underline{\mathbf{x}}_0$ and field variable $\underline{\boldsymbol{\xi}}$, respectively, and denote the components of $\underline{\mathbf{n}}$ with (n_r, n_z) . The axisymmetric form of the boundary integral equation (4.2.13) is then given by [131]

$$\frac{1}{2}\phi(\underline{\mathbf{x}}_0) + \int_{\Gamma} h(\underline{\mathbf{x}}_0, \underline{\boldsymbol{\xi}})\phi(\underline{\boldsymbol{\xi}}) ds = \int_{\Gamma} k(\underline{\mathbf{x}}_0, \underline{\boldsymbol{\xi}})\frac{\partial\phi}{\partial n}(\underline{\boldsymbol{\xi}}) ds, \quad (4.3.2)$$

for integration kernels h and k with

$$h(\underline{\mathbf{x}}_0, \underline{\boldsymbol{\xi}}) = R \int_0^{2\pi} \frac{\partial G}{\partial n}(\underline{\mathbf{x}}_0, \underline{\boldsymbol{\xi}}) d\theta \quad \text{and} \quad k(\underline{\mathbf{x}}_0, \underline{\boldsymbol{\xi}}) = R \int_0^{2\pi} G(\underline{\mathbf{x}}_0, \underline{\boldsymbol{\xi}}) d\theta. \quad (4.3.3)$$

These integration kernels can be expanded out analytically, yielding expressions in terms of complete elliptic integrals (see derivation in Appendix C). These kernels are then given by

$$k = \frac{R}{\pi A^{1/2}} K(m), \quad (4.3.4)$$

and

$$h = \frac{R}{\pi A^{1/2}} E(m) \left[\frac{n_r}{2R} - \frac{(z_0 - Z)n_z + (r_0 - R)n_r}{B} \right] - \frac{n_r}{2\pi A^{1/2}} K(m), \quad (4.3.5)$$

where $K(m) = \int_0^{\pi/2} (1 - m \sin^2 \zeta)^{-1/2} d\zeta$ and $E(m) = \int_0^{\pi/2} (1 - m \sin^2 \zeta)^{1/2} d\zeta$ are complete elliptic integrals of the first and second kind respectively, and where we define the following terms:

$$A = (r_0 + R)^2 + (z_0 - Z)^2, \quad B = (r_0 - R)^2 + (z_0 - Z)^2, \quad m = \frac{4Rr_0}{A}. \quad (4.3.6)$$

Now that we have a simplified axisymmetric boundary integral equation (4.3.2) that can be solved for the distribution of ϕ and $\partial\phi/\partial n$, what remains is to evolve the problem in time. Hence, we move on to solving the Bernoulli equation (4.1.2) at the liquid-gas portion of the boundary Γ .

4.4 Bernoulli Equation at the Drop Boundary

Interfacial quantities on the boundary curve Γ can be decomposed into components normal and tangential to the interface in the (r, z) -plane. Hence on Γ , the bulk drop velocity can be decomposed as

$$\begin{aligned} \underline{\mathbf{u}} &= \nabla\phi = (\underline{\mathbf{n}} \cdot \nabla\phi) \underline{\mathbf{n}} + (\underline{\mathbf{t}} \cdot \nabla\phi) \underline{\mathbf{t}} \\ &= \frac{\partial\phi}{\partial n} \underline{\mathbf{n}} + \frac{\partial\phi}{\partial s} \underline{\mathbf{t}}, \end{aligned} \quad (4.4.1)$$

for outward-pointing normal $\underline{\mathbf{n}}$ and tangent vector $\underline{\mathbf{t}}$, where the arclength s spans the *entire* curve Γ (both the liquid-gas and liquid-solid interfaces).

The Bernoulli equation (4.1.2) describes the evolution of the velocity potential ϕ throughout the drop domain. Given that the problem of simulating drop dynamics has reduced to solving for ϕ and $\partial\phi/\partial n$ exclusively on the drop boundary, we are only interested in how ϕ evolves *at* the boundary. For the liquid-gas portion of the boundary curve Γ , we apply (4.4.1) and the (normal component of the) conservation of momentum equation (3.2.24) to (4.1.2) to obtain the Bernoulli equation at the liquid-gas interface:

$$\frac{\partial\phi}{\partial t} = -\frac{1}{2} \left[\left(\frac{\partial\phi}{\partial n} \right)^2 + \left(\frac{\partial\phi}{\partial s} \right)^2 \right] - \sigma_{\text{eff}} (\nabla_s \cdot \underline{\mathbf{n}}) - gz. \quad (4.4.2)$$

Recall (see equation 3.2.23) that without surface viscosity, the (dimensionless) effective surface tension σ_{eff} takes a value of unity.

4.5 Numerical Method

We will now discuss how the inviscid model is solved numerically using a BEM with a coupled time-advancement scheme. We begin with a discretisation of the drop boundary, and follow with subsections focused on the discretisation of the boundary integral equation (4.3.2), a description of the scheme used for time-advancement, and a discussion of the techniques used for adaptive time stepping and mesh refinement.

To numerically solve the boundary integral equation (4.3.2), we use the ‘collocation method’ [146], whereby we select a discrete collection of distinct points (nodes) on the boundary curve Γ and solve the boundary integral equation at each of these points, in turn (that is, with $\underline{\mathbf{x}}_0$ located at each node). To this end, we begin by selecting $N + 1$ nodes on the (one dimensional) boundary curve Γ , with a node placed at each of the (two) intersections of Γ with the axis of symmetry, and the remaining $N - 1$ nodes placed elsewhere in the curve ‘interior’. At every node, either the velocity potential ϕ or normal velocity $\partial\phi/\partial n$ is imposed (see §4.3.2 on applied boundary conditions), with the other variable to be solved for with the boundary integral equation. Between each pair of adjacent nodes is a connected subinterval of the boundary curve Γ , with a total of N such subintervals. Starting from the apex of the drop (at the node placed at the higher intersection with the axis of symmetry), we sequentially

number the nodes (and subintervals) in the order that they appear as Γ is traversed for (arclength) s -increasing until the final node is reached at the lower intersection with the axis of symmetry (see Figure 4.2). Nodes are therefore numbered 1 to $N + 1$, and the subintervals are denoted Γ_1 to Γ_N .

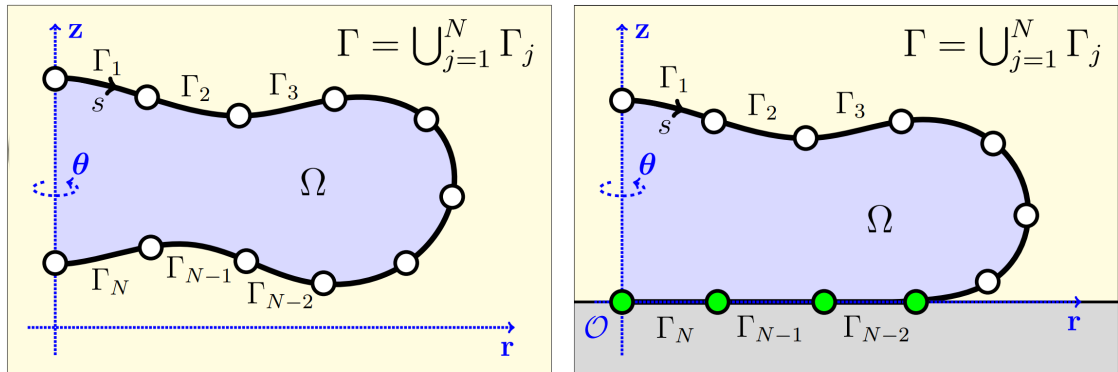


Figure 4.2: Diagram showing the decomposition of an axisymmetric drop boundary in the (r, z) -plane when the drop is (left) *away from*, and (right) *in contact with*, the solid substrate. The boundary curve Γ is divided into N subintervals denoted $\Gamma_1, \dots, \Gamma_N$ where each subinterval is bounded by two nodes (shown as white and green circles). Counting of nodes and subintervals begins at the top intersection with the z -axis (axis of symmetry) and continues clockwise (s -increasing) until the second intersection with the z -axis. A white (green) node corresponds to the imposing of a Dirichlet (Neumann) boundary condition, that is, imposing a value of ϕ ($\partial\phi/\partial n$).

Using this subdivision, we can express the boundary integral equation (4.3.2) as sums of integrals over the subintervals of Γ :

$$\frac{1}{2}\phi(\underline{\mathbf{x}}_0) + \sum_{j=1}^N \int_{\Gamma_j} h(\underline{\mathbf{x}}_0, \underline{\boldsymbol{\xi}})\phi(\underline{\boldsymbol{\xi}}) ds = \sum_{j=1}^N \int_{\Gamma_j} k(\underline{\mathbf{x}}_0, \underline{\boldsymbol{\xi}}) \frac{\partial\phi}{\partial n}(\underline{\boldsymbol{\xi}}) ds. \quad (4.5.1)$$

What follows is a discussion on the interpolation of variables between nodes.

4.5.1 Interpolation of Variables between Nodes

Given that variables (in our case, the boundary coordinates, velocity potential, and normal velocity) are only given *at* the nodes, to accurately solve the boundary integral equation (4.5.1), it is necessary to approximate how these quantities vary on the subintervals *between* the nodes. We will now discuss the chosen form of interpolation for each of these variables, as well as how the complete elliptic integrals $K(m)$ and

$E(m)$ that partly constitute the axisymmetric integration kernels k (4.3.4) and h (4.3.5) are approximated.

Boundary Coordinates

We denote our approximation of the ‘true’ boundary curve $\Gamma = \cup_{j=1}^N \Gamma_j$ by $\bar{\Gamma} = \cup_{j=1}^N \bar{\Gamma}_j$, with each subinterval approximation $\bar{\Gamma}_j \approx \Gamma_j$ referred to as a ‘boundary element’ (or simply ‘element’). As is standard practice for BEMs [146], our approximation for the boundary takes the form of a system of splines, that is, for each element $\bar{\Gamma}_j$, we associate two unique polynomials that each describe the variation of one of the boundary coordinates within that element. These splines are constructed to be continuous through nodes, with additional conditions on continuous-differentiability depending on the order of the approximating polynomials used.

Define $l_1 = 0$, and for $j = 2, \dots, N + 1$, define l_j as the sum of linear distances between consecutive nodes leading up to the j -th node, that is,

$$l_j = l_{j-1} + \sqrt{(r_j - r_{j-1})^2 + (z_j - z_{j-1})^2}, \quad (4.5.2)$$

where (r_k, z_k) denotes the radial and axial coordinate pair for the k -th node, for $k \in \{j, j - 1\}$. Let $l \in [0, l_{N+1}]$ denote the ‘spline parameter’; this will act as the variable used to traverse the approximating splines that constitute the boundary elements. A value of $l \in (l_j, l_{j+1})$ corresponds to a position within the interior of the j -th boundary element $\bar{\Gamma}_j$, with $l = l_k$ corresponding to the position of the k -th node, for $j = 1, \dots, N$ and $k = 1, \dots, N + 1$.

For $l \in [l_j, l_{j+1}]$ (where $j = 1, \dots, N + 1$), the splines that describe the geometry of the element $\bar{\Gamma}_j$ are given by

$$S_r^{(j)}(l) := r_j + \sum_{m=1}^M a_{m,r}^{(j)} (l - l_j)^m, \quad (4.5.3)$$

and

$$S_z^{(j)}(l) := z_j + \sum_{m=1}^M a_{m,z}^{(j)} (l - l_j)^m, \quad (4.5.4)$$

where M is the order of the approximating polynomial, and $a_{m,r}^{(j)}$ and $a_{m,z}^{(j)}$ denote polynomial coefficients for the approximations of the radial and axial boundary coordinates, respectively. The radial and axial boundary coordinates associated with a realisation of the spline parameter l are then given by, respectively, $R(l) = S_r^{(j)}(l)$ and $Z(l) = S_z^{(j)}(l)$, where j is the largest of $\{1, \dots, N + 1\}$ such that $l \geq l_j$.

All BEM simulations conducted for this research use $M = 3$ ('cubic splines', examples in [116, 152–154]) or $M = 5$ ('quintic splines', examples in [131, 149]) for the boundary elements on the liquid-gas portion of the boundary $\bar{\Gamma}$. The choice of which order splines to use is made before the start of a simulation. Cubic splines are the lowest-order splines that ensure continuity of curvature for interior nodes, whereas quintic splines provide additional continuity constraints between nodes and allow for superior approximations of a complex interface, but are more computationally expensive to use as more polynomial coefficients must be solved for when building the system of splines. On the (flat) liquid-solid portion of the boundary $\bar{\Gamma}$, we use $M = 1$ ('linear splines', example in [155]).

We now discuss the conditions that are applied to the system of splines to uniquely determine the polynomial coefficients; starting with the drop being *away* from the solid substrate, where M stays constant, and then when *in contact with* the solid substrate, where M reduces to 1 on the liquid-solid interface. Throughout numerical simulations, M stays constant along the liquid-gas interface, that is, we never change between $M = 3$ and $M = 5$. The process of calculating the polynomial coefficients using the imposed conditions discussed below is provided in Appendix D.

Determination of Spline Coefficients: Away from the Solid Substrate

Suppose the drop is *away* from the solid substrate, so there is no liquid-solid interface, and we have a constant $M = 3$ or $M = 5$. To uniquely determine the spline coefficients from (4.5.3) and (4.5.4), we impose continuity conditions between elements at the interior $N - 1$ nodes, and symmetry conditions at the (two) nodes lying on the axis of symmetry at either end of the free surface.

For each coordinate (axial and radial), there are a total of N splines, each with M unknown coefficients, hence a total of MN unknowns. In other words we must impose MN conditions (for each coordinate) on this system of splines for it to be uniquely determined. We start by imposing continuity of position between adjacent splines at all interior nodes, that is,

$$S_r^{(j)}(l_{j+1}) = S_r^{(j+1)}(l_{j+1}) \quad \text{and} \quad S_z^{(j)}(l_{j+1}) = S_z^{(j+1)}(l_{j+1}), \quad (4.5.5)$$

for $j = 1, \dots, N - 1$. Further, we impose that the first $M - 1$ derivatives of the splines (with respect to the spline parameter l) are also continuous through the interior

nodes, that is,

$$\frac{d^p S_r^{(j)}}{dl^p}(l_{j+1}) = \frac{d^p S_r^{(j+1)}}{dl^p}(l_{j+1}) \quad \text{and} \quad \frac{d^p S_z^{(j)}}{dl^p}(l_{j+1}) = \frac{d^p S_z^{(j+1)}}{dl^p}(l_{j+1}), \quad (4.5.6)$$

for $p = 1, \dots, M - 1$ and $j = 1, \dots, N - 1$.

Notice that by definition (see equations 4.5.3-4.5.4), $S_r^{(1)}(l_1) = r_1 \equiv 0$ and $S_z^{(1)}(l_1) = z_1$, that is, the splines approximating the first element touch the first node (which lies on the axis of symmetry). This is not automatically true for the final element and final node, to force this we impose

$$S_r^{(N)}(l_{N+1}) = r_{N+1} \equiv 0 \quad \text{and} \quad S_z^{(N)}(l_{N+1}) = z_{N+1}. \quad (4.5.7)$$

We have thus far imposed a total of $M(N - 1) + 1$ conditions on the system of splines. The final $M - 1$ equations take the form of symmetry conditions at the axis of symmetry, namely,

$$\frac{d^2 S_r^{(1)}}{dl^2}(l_1) = 0 \quad \text{and} \quad \frac{dS_z^{(1)}}{dl}(l_1) = 0, \quad (4.5.8)$$

and

$$\frac{d^2 S_r^{(N)}}{dl^2}(l_{N+1}) = 0 \quad \text{and} \quad \frac{dS_z^{(N)}}{dl}(l_{N+1}) = 0, \quad (4.5.9)$$

for $M = 3$, and

$$\frac{d^2 S_r^{(1)}}{dl^2}(l_1) = \frac{d^4 S_r^{(1)}}{dl^4}(l_1) = 0 \quad \text{and} \quad \frac{dS_z^{(1)}}{dl}(l_1) = \frac{d^3 S_z^{(1)}}{dl^3}(l_1) = 0 \quad (4.5.10)$$

and

$$\frac{d^2 S_r^{(N)}}{dl^2}(l_{N+1}) = \frac{d^4 S_r^{(N)}}{dl^4}(l_{N+1}) = 0 \quad \text{and} \quad \frac{dS_z^{(N)}}{dl}(l_{N+1}) = \frac{d^3 S_z^{(N)}}{dl^3}(l_{N+1}) = 0. \quad (4.5.11)$$

for $M = 5$.

Determination of Spline Coefficients: In Contact with the Solid Substrate

Suppose the drop is in contact with the solid substrate, so the liquid-solid interface exists. Let N_{LG} and N_{LS} denote the number of elements on the liquid-gas and liquid-solid portions of the drop surface, respectively, with $N = N_{LG} + N_{LS}$. Then there are $N_{LS} + 1$ nodes lying *on* the solid substrate and N_{LG} nodes *away* from it. There are therefore a total of MN_{LG} unknown coefficients for the liquid-gas portion of the boundary $\bar{\Gamma}$ and N_{LS} unknown coefficients on the liquid-solid portion (recall we use linear splines at the liquid-solid interface), with $M = 3$ or $M = 5$.

Recall that the j -th spline touches the j -th node by definition; this holds for *all* splines regardless of polynomial order, for $j = 1, \dots, N$. By enforcing that all (linear) splines on the liquid-solid interface also touch the $(j + 1)$ -th node, that is, with (4.5.5) holding for $j = N_{LG} + 1, \dots, N - 1$ and (4.5.7) holding for the final spline, we ensure continuity of position between adjacent splines lying on the liquid-solid interface. Through the interior nodes of the liquid-gas interface, we impose continuity of position and of the first $M - 1$ derivatives (with respect to l), that is, (4.5.5) and (4.5.6) hold for $p = 1, \dots, M - 1$ and $j = 1, \dots, N_{LG} - 1$. We have now imposed $M(N_{LG} - 1) + N_{LS}$ conditions, leaving M conditions still remaining.

At the first node (where the liquid-gas interface meets the axis of symmetry), we impose symmetry boundary conditions, so (4.5.8) holds for $M = 3$ and (4.5.10) for $M = 5$. The remaining conditions enforce the highest degree of smoothness at the contact line, where the approximating splines reduce to linear order. We therefore impose continuity through the contact line node, that is, (4.5.5) for $j = N_{LG}$, as well as the following conditions on the derivatives:

$$\frac{d^p S_r^{(N_{LG})}}{dl^p}(l_{N_{LG}+1}) = \frac{d^p S_r^{(N_{LG}+1)}}{dl^p}(l_{N_{LG}+1}), \quad (4.5.12)$$

and

$$\frac{d^p S_z^{(N_{LG})}}{dl^p}(l_{N_{LG}+1}) = \frac{d^p S_z^{(N_{LG}+1)}}{dl^p}(l_{N_{LG}+1}), \quad (4.5.13)$$

for $p = 1$ when $M = 3$ and $p = 1, 2$ when $M = 5$.

After constructing the approximated boundary $\bar{\Gamma}$ in either of the scenarios outlined above, we are able to approximate the arclength of the entire drop boundary, which we use to interpolate the velocity potential ϕ and normal velocity $\partial\phi/\partial n$.

Arclength as a Function of the Spline Parameter

Let $s(l)$ denote the arclength of the approximated boundary curve $\bar{\Gamma}$, that is, the distance along the approximating system of splines from node 1 (at the highest intersection with the axis of symmetry) to the point on the boundary with associated spline parameter $l \in [0, l_{N+1}]$. For $j = 1, \dots, N + 1$, define $s_j \equiv s(l_j)$ and let $s_1 \equiv s(l_1) = 0$; these values then correspond to the arclength at each node. Consider a point within the j -th element $\bar{\Gamma}_j$ (for $j = 1, \dots, N$) with associated spline parameter $\tilde{l} \in [l_j, l_{j+1}]$. The arclength at this point is then given by

$$s(\tilde{l}) = s_j + \int_{l_j}^{\tilde{l}} \sqrt{\left(\frac{dR}{dl}\right)^2 + \left(\frac{dZ}{dl}\right)^2} dl, \quad (4.5.14)$$

that is, the arclength up to the j -th node plus the remaining distance along the boundary element $\bar{\Gamma}_j$, where the derivatives of R and Z are calculated using (4.5.3) and (4.5.4), respectively. The integral in (4.5.14) is approximated using Gauss-Legendre quadrature with $M + 1$ integration points, so we have

$$s(\bar{l}) \approx s_j + \sum_{\chi=1}^{M+1} w_\chi \sqrt{\left(\left.\frac{dR}{dl}\right|_{l=\xi_\chi}\right)^2 + \left(\left.\frac{dZ}{dl}\right|_{l=\xi_\chi}\right)^2} \quad (4.5.15)$$

where w_χ and ξ_χ represent the standard Gaussian weights and abscissae [156], respectively, along the j -th element up to the point $l = \bar{l}$.

Velocity Potential and Normal Velocity

The velocity potential ϕ and normal velocity $\partial\phi/\partial n$ are interpolated linearly along boundary elements, which is a standard choice for boundary element implementations [131, 146–148, 157]. Over the j -th element (so $s \in [s_j, s_{j+1}]$), the interpolated quantities are therefore given by

$$\begin{aligned} \phi(s) &= \phi_j \left(\frac{s_{j+1} - s}{s_{j+1} - s_j}\right) + \phi_{j+1} \left(\frac{s - s_j}{s_{j+1} - s_j}\right), \\ \text{and} \quad \frac{\partial\phi}{\partial n}(s) &= \left(\frac{\partial\phi}{\partial n}\right)_j \left(\frac{s_{j+1} - s}{s_{j+1} - s_j}\right) + \left(\frac{\partial\phi}{\partial n}\right)_{j+1} \left(\frac{s - s_j}{s_{j+1} - s_j}\right), \end{aligned} \quad (4.5.16)$$

for $j = 1, \dots, N$, where ϕ_k and $(\partial\phi/\partial n)_k$ denote the values of ϕ and $\partial\phi/\partial n$ at node k , for $k \in \{j, j + 1\}$.

Axisymmetric Integration Kernels

The remaining terms in the boundary integral equation (4.5.1) are the kernels k and h , which are given in terms of the elliptic integrals $K(m)$ and $E(m)$. These are both geometric quantities and as such, we do not have to choose a method of interpolation, instead, once the boundary elements have been constructed, approximations for these integrals (found in [156] with errors of $\mathcal{O}(10^{-8})$) can be found anywhere on the boundary, with

$$\begin{aligned} K(m) &\approx A_c(1 - m) + B_c(1 - m) \ln(1 - m), \\ \text{and} \quad E(m) &\approx \tilde{A}_c(1 - m) + \tilde{B}_c \ln(1 - m), \end{aligned} \quad (4.5.17)$$

for known quartic polynomials A_c , B_c , \tilde{A}_c and \tilde{B}_c , and with

$$1 - m = \frac{B}{A}, \quad (4.5.18)$$

where m , A and B are given in §4.3.3.

Now that we can approximate each term in the boundary integral equation (4.5.1) along the *entire* drop boundary, we move onto a discussion of how this equation is solved at the nodes.

4.5.2 Discretising the Boundary Integral Equation

We will now consider the approximate form of the boundary integral equation (4.5.1), that is, with integrals over the boundary elements $\bar{\Gamma}_j$ rather than the ‘true’ subintervals Γ_j . This approximate form is given by:

$$\frac{1}{2}\phi(\underline{\mathbf{x}}_0) + \sum_{j=1}^N \int_{\bar{\Gamma}_j} h(\underline{\mathbf{x}}_0, \underline{\boldsymbol{\xi}}) \phi(\underline{\boldsymbol{\xi}}) \, ds = \sum_{j=1}^N \int_{\bar{\Gamma}_j} k(\underline{\mathbf{x}}_0, \underline{\boldsymbol{\xi}}) \frac{\partial \phi}{\partial n}(\underline{\boldsymbol{\xi}}) \, ds. \quad (4.5.19)$$

Given the chosen form of interpolation for the velocity potential ϕ and normal velocity $\partial\phi/\partial n$ along boundary elements is linear (see equation 4.5.16), we can rewrite (4.5.19) as

$$\begin{aligned} \frac{1}{2}\phi(\underline{\mathbf{x}}_0) + \sum_{j=1}^N & \left(\phi_j \int_{l_j}^{l_{j+1}} \left(\frac{s_{j+1} - s(l)}{s_{j+1} - s_j} \right) h(\underline{\mathbf{x}}_0, \underline{\boldsymbol{\xi}}(l)) J(l) \, dl \right. \\ & \left. + \phi_{j+1} \int_{l_j}^{l_{j+1}} \left(\frac{s(l) - s_j}{s_{j+1} - s_j} \right) h(\underline{\mathbf{x}}_0, \underline{\boldsymbol{\xi}}(l)) J(l) \, dl \right) \\ & = \sum_{j=1}^N \left(\left(\frac{\partial \phi}{\partial n} \right)_j \int_{l_j}^{l_{j+1}} \left(\frac{s_{j+1} - s(l)}{s_{j+1} - s_j} \right) k(\underline{\mathbf{x}}_0, \underline{\boldsymbol{\xi}}(l)) J(l) \, dl \right. \\ & \left. + \left(\frac{\partial \phi}{\partial n} \right)_{j+1} \int_{l_j}^{l_{j+1}} \left(\frac{s(l) - s_j}{s_{j+1} - s_j} \right) k(\underline{\mathbf{x}}_0, \underline{\boldsymbol{\xi}}(l)) J(l) \, dl \right). \end{aligned} \quad (4.5.20)$$

with the Jacobian

$$J(l) = \sqrt{\left(\frac{dR}{dl} \right)^2 + \left(\frac{dZ}{dl} \right)^2}, \quad (4.5.21)$$

expressing a change of integration variable from the arclength s to the spline parameter l . Notice that equation (4.5.20) contains the value of ϕ and $\partial\phi/\partial n$ at every node, what remains is to consider the singularity point $\underline{\mathbf{x}}_0$ at each of these nodes, in turn.

Let $\underline{\mathbf{x}}_i = (r_i, z_i)$ for $i = 1, \dots, N + 1$, denote the position of the nodes on the boundary $\bar{\Gamma}$, and consider the boundary integral equation (4.5.20) with the singularity point $\underline{\mathbf{x}}_0$ at each of these positions, separately. The resulting collection of $N + 1$ simultaneous boundary integral equations can be formulated into a discrete $(N + 1) \times (N + 1)$ matrix equation, given by

$$\underline{\underline{\mathbf{H}}} \cdot \underline{\underline{\boldsymbol{\Phi}}} = \underline{\underline{\mathbf{K}}} \cdot \underline{\underline{\mathbf{V}}}, \quad (4.5.22)$$

with vectors

$$(\underline{\Phi})_j = \phi_j \quad \text{and} \quad (\underline{\mathbf{V}})_j = \left(\frac{\partial \phi}{\partial n} \right)_j \quad (4.5.23)$$

and matrices

$$\begin{aligned} (\underline{\mathbf{H}})_{i,j} = & \frac{1}{2} \delta_{ij} + \int_{l_{j-1}}^{l_j} \left(\frac{s(l) - s_{j-1}}{s_j - s_{j-1}} \right) h(\underline{\mathbf{x}}_i, \underline{\boldsymbol{\xi}}(l)) J(l) dl \\ & + \int_{l_j}^{l_{j+1}} \left(\frac{s_{j+1} - s(l)}{s_{j+1} - s_j} \right) h(\underline{\mathbf{x}}_i, \underline{\boldsymbol{\xi}}(l)) J(l) dl, \end{aligned} \quad (4.5.24)$$

and

$$\begin{aligned} (\underline{\mathbf{K}})_{i,j} = & \int_{l_{j-1}}^{l_j} \left(\frac{s(l) - s_{j-1}}{s_j - s_{j-1}} \right) k(\underline{\mathbf{x}}_i, \underline{\boldsymbol{\xi}}(l)) J(l) dl \\ & + \int_{l_j}^{l_{j+1}} \left(\frac{s_{j+1} - s(l)}{s_{j+1} - s_j} \right) k(\underline{\mathbf{x}}_i, \underline{\boldsymbol{\xi}}(l)) J(l) dl, \end{aligned} \quad (4.5.25)$$

for $i, j = 1, \dots, N + 1$. The ‘Kronecker delta’ δ_{ij} is given by

$$\delta_{ij} = \begin{cases} 1, & i = j \\ 0, & i \neq j. \end{cases} \quad (4.5.26)$$

For $j = 1$, the first integrals in (4.5.24)-(4.5.25) are not evaluated (as there is no l_0), and similarly for $j = N + 1$ the second integrals are ignored (as there is no l_{N+2}).

Equation (4.5.22) constitutes the fully-discretised form of the boundary integral equation (4.5.1). The elements of the matrices $\underline{\mathbf{H}}$ and $\underline{\mathbf{K}}$ are entirely geometric and can be calculated once the boundary has been approximated by splines. Populating these matrices (which are dense) constitutes the majority of computation time spent in our BEM simulations. Once the matrices have been populated, then at each node, a boundary condition is imposed that *either* defines ϕ_j or $(\partial \phi / \partial n)_j$ (see §4.3.2), and then the boundary integral (matrix) equation (4.5.22) is solved for all unknowns simultaneously.

A detailed description on how the matrices $\underline{\mathbf{H}}$ and $\underline{\mathbf{K}}$ in equation (4.5.22) are populated, including the approximation of each constituent boundary integral, is provided in [131]. A description of this process is also given in Appendix E for the convenience of an interested reader. We move on to discussing the numerical scheme used to evolve the system in time.

4.5.3 Discrete Time Evolution using a Runge-Kutta Scheme

After the discretised boundary integral equation (4.5.20) has been solved, so that we know the values of ϕ and $\partial\phi/\partial n$ at every node at time T , say, we then numerically advance the system to time $T+\tau$ for time step $\tau > 0$. We have to advance (in time) the boundary itself, as well as the velocity potential ϕ ; for this we use discrete analogues of the kinematic equation (3.2.4) and Bernoulli equation (4.4.2), respectively. We first present these discretised evolution equations and then discuss the Runge-Kutta scheme used to advance the corresponding variables.

Discretised Kinematic Boundary Equation

We choose to advance the liquid-gas portion of the approximated boundary curve $\bar{\Gamma}$ in the direction normal to the boundary itself. So for some smooth function $F(\underline{\mathbf{x}}, t)$ defined throughout three dimensional space, we have that the full time-derivative of F at $\underline{\mathbf{x}} \in \bar{\Gamma}$ on the liquid-gas interface is given by

$$\begin{aligned}\frac{dF}{dt} &= \frac{\partial F}{\partial t} + \frac{\partial \phi}{\partial n} \underline{\mathbf{n}} \cdot \nabla F \\ &= \frac{\partial F}{\partial t} + \frac{\partial \phi}{\partial n} \frac{\partial F}{\partial n}.\end{aligned}\tag{4.5.27}$$

On the liquid-solid interface (including at the contact line), impermeability of the substrate is imposed, so $\partial\phi/\partial n = 0$ and hence using equation (4.5.27) to advance nodes on the liquid-solid interface would result in *stationary* nodes. For this reason, we instead evolve this part of the boundary in the tangential direction; so for $F(\underline{\mathbf{x}}, t)$ for $\underline{\mathbf{x}} \in \bar{\Gamma}$ on the liquid-solid interface, we have

$$\begin{aligned}\frac{dF}{dt} &= \frac{\partial F}{\partial t} + \frac{\partial \phi}{\partial s} \underline{\mathbf{t}} \cdot \nabla F \\ &= \frac{\partial F}{\partial t} + \frac{\partial \phi}{\partial s} \frac{\partial F}{\partial s}.\end{aligned}\tag{4.5.28}$$

We can now apply equations (4.5.27) and (4.5.28) to the boundary coordinates of all nodes, resulting in a vector equation for the *entire* computational domain $\bar{\Gamma}$ that describes its evolution in time. In (scalar) component form, this vector equation is given by (for $j = 1, \dots, N$):

$$\frac{dr_j}{dt} = \left(\frac{\partial \phi}{\partial n} \right)_j (\underline{\mathbf{n}}_j \cdot \underline{\mathbf{e}}_r) \quad \text{and} \quad \frac{dz_j}{dt} = \left(\frac{\partial \phi}{\partial n} \right)_j (\underline{\mathbf{n}}_j \cdot \underline{\mathbf{e}}_z),\tag{4.5.29}$$

for $z_j > 0$ (on the liquid-gas interface), where $\underline{\mathbf{n}}_j$ denotes the normal at node j , and

$$\frac{dr_j}{dt} = \frac{\partial \phi_j}{\partial s} \quad \text{and} \quad \frac{dz_j}{dt} = \left(\frac{\partial \phi}{\partial n} \right)_j \equiv 0,\tag{4.5.30}$$

for $z_j = 0$ (on the liquid-solid interface). Note that components (4.5.29) represent a discretisation of the kinematic boundary condition (3.2.4) for the liquid-gas interface.

Discretised Bernoulli Equation

Equation (4.4.2) provides the partial time-derivative of the velocity potential ϕ at the liquid-gas interface. We must evaluate this equation at each of the nodes on this interface, and advance them in time consistent with the advancement of the boundary coordinates in (4.5.29), namely that they evolve in the direction normal to the interface. We first apply (4.5.27) to ϕ_j for all nodes j on the liquid-gas interface, that is,

$$\frac{d\phi_j}{dt} = \frac{\partial\phi_j}{\partial t} + \left(\frac{\partial\phi}{\partial n}\right)_j^2, \quad (4.5.31)$$

for $z_j > 0$. Combining this with (4.4.2) then gives us the discretised Bernoulli equation at the liquid-gas interface:

$$\frac{d\phi_j}{dt} = \frac{1}{2} \left[\left(\frac{\partial\phi}{\partial n}\right)_j^2 - \left(\frac{\partial\phi_j}{\partial s}\right)^2 \right] - \sigma_{\text{eff}} (\nabla_s \cdot \mathbf{n}) - gz, \quad (4.5.32)$$

for $z_j > 0$.

Runge-Kutta Scheme

To evolve in time, we couple the discretised equations (4.5.29), (4.5.30), and (4.5.32) together and use an explicit fourth-order Runge-Kutta scheme (RK4) [158] to simultaneously advance them forward in discrete time steps. This is a standard choice for evolving a system of equations at an interface in time within a BEM simulation (examples include [131, 147, 159–162]).

As an explicit scheme, only information within the simulation at the start of the current time is required to progress to the next time; this limits the number of variables stored and also allows for easy resumption of simulations, as the conditions at the end of any particular run can be used as initial conditions for another. As a fourth-order scheme, advancing the system forward a single ‘global’ time step involves computing four smaller ‘local’ time steps, each evolving the system forward in time a fraction of the way. Each set of four ‘local’ evolutions are then combined in such a way as to provide the new starting configuration at the next global time. The primary benefit of such a high-order scheme is the stability provided at relatively large time

steps, and for simulations that run for extended periods of time. What follows is a description of how the Runge-Kutta scheme is enacted.

Suppose that at time T , we have solved the boundary integral equation (4.5.20) for a boundary that (for sake of argument) is *away* from the substrate. Then, let $\{\phi_j^{(T)}\}$, $\{r_j^{(T)}\}$, and $\{z_j^{(T)}\}$ denote the sets containing the velocity potential, radial coordinate, and axial coordinate at every node at time T , respectively, for $j = 1, \dots, N + 1$. We want to advance these sets to $\{\phi_j^{(T+\tau)}\}$, $\{r_j^{(T+\tau)}\}$, and $\{z_j^{(T+\tau)}\}$, that is, their respective values at time $T + \tau$ for a global time step $\tau > 0$. To this end, for $j = 1, \dots, N + 1$ define

$$\zeta_{i,j}^{\phi} = \frac{d\phi_j^i}{dt} \quad \text{and} \quad \zeta_{i,j}^r = \frac{dr_j^i}{dt} \quad \text{and} \quad \zeta_{i,j}^z = \frac{dz_j^i}{dt}, \quad (4.5.33)$$

where ϕ_j^i , r_j^i , and z_j^i denote the values of the velocity potential, radial coordinate and axial coordinate of the nodes j , where $i \in \{1, 2, 3, 4\}$ notes that the value of this variable corresponds to the state of the computational domain at the start of each *local* time step when using RK4. The value each variable takes at the start of each local time step (so for each i) is given in Table 4.1.

Once all local time steps have been evaluated, the value of each variable at the next ‘global’ time $T + \tau$ is given by:

$$\begin{aligned} \phi_j^{(T+\tau)} &= \phi_j^{(T)} + \frac{\tau}{6} \left(\zeta_{0,j}^{\phi} + 2\zeta_{1,j}^{\phi} + 2\zeta_{2,j}^{\phi} + \zeta_{3,j}^{\phi} \right) \\ r_j^{(T+\tau)} &= r_j^{(T)} + \frac{\tau}{6} \left(\zeta_{0,j}^r + 2\zeta_{1,j}^r + 2\zeta_{2,j}^r + \zeta_{3,j}^r \right) \\ z_j^{(T+\tau)} &= z_j^{(T)} + \frac{\tau}{6} \left(\zeta_{0,j}^z + 2\zeta_{1,j}^z + 2\zeta_{2,j}^z + \zeta_{3,j}^z \right), \end{aligned} \quad (4.5.34)$$

for $j = 1, \dots, N + 1$.

When there *is* contact with the solid substrate, we continue to evolve the velocity potential for nodes that are *away* from the substrate (that is, on the liquid-gas interface), and continue imposing $\partial\phi/\partial n = 0$ for all nodes *on* the substrate. If during a local time step, a node that began on the liquid-gas interface moves below $z = 0$ (the substrate), the process of evaluating local time steps continues, and a judgement is made after evolution to the next global time using (4.5.34) on whether a node is moved from the liquid-gas to liquid-solid interface. Treatment of nodes that move from the liquid-gas to liquid-solid interface is discussed in §4.5.4.

Table 4.1: Each row indicates the distribution of ϕ_j , r_j , and z_j at the start of the i -th local time step of the RK4 numerical scheme, for $j = 1, \dots, N + 1$, at time T .

i	Initial ϕ_j	Initial r_j	Initial z_j
1	$\phi_j^{(T)}$	$r_j^{(T)}$	$z_j^{(T)}$
2	$\phi_j^{(T)} + \frac{1}{2}\zeta_{0,j}^\phi$	$r_j^{(T)} + \frac{1}{2}\zeta_{0,j}^r$	$z_j^{(T)} + \frac{1}{2}\zeta_{0,j}^z$
3	$\phi_j^{(T)} + \frac{1}{2}\zeta_{1,j}^\phi$	$r_j^{(T)} + \frac{1}{2}\zeta_{1,j}^r$	$z_j^{(T)} + \frac{1}{2}\zeta_{1,j}^z$
4	$\phi_j^{(T)} + \zeta_{2,j}^\phi$	$r_j^{(T)} + \zeta_{2,j}^r$	$z_j^{(T)} + \zeta_{2,j}^z$

The basic¹ numerical procedure therefore, once given a distribution of boundary coordinates (r_j, z_j) and imposed boundary conditions for ϕ_j or $(\partial\phi/\partial n)_j$ at nodes $j = 1, \dots, N + 1$ is:

1. Construct an approximate boundary $\bar{\Gamma}$ using a system of splines with appropriate continuity conditions at (r_j, z_j) (see §4.5.1),
2. Populate the matrices for the discretised boundary integral equation and solve it for the unknown values of ϕ_j and $(\partial\phi/\partial n)_j$ (see Appendix E),
3. Advance the coordinates of the nodes (r_j, z_j) , and value of the velocity potential ϕ_j on the liquid-gas interface in time, in accordance with equations (4.5.29)-(4.5.30) and (4.5.32) respectively, using the RK4 scheme described above.

To advance forward a simple global time step, the above procedure is repeated four times. This process continues until the simulation ends.

4.5.4 Nodes Moving to and from the Solid Substrate

Nodes lying on the solid substrate, including the node at the contact line, are all evolved in the radial direction as per (4.5.30). In this subsection, we describe our numerical implementation of how drops spread on a completely non-wetting (180° contact angle) solid impermeable substrate; in particular how they appear to ‘roll’ along it, which is achieved by moving nodes from the liquid-gas to the liquid-solid interface of the drop (rather than solely via a continuously moving contact line). We end with a brief overview on the progress made regarding node *detachment* from the

¹That is, without adaptive refinement of the mesh and time step; both to be discussed.

solid substrate (that is, with nodes moving from the liquid-solid to liquid-gas interface) before the shortcomings of the BEM became apparent and focus was moved to the volume-of-fluid method and viscous model (see a discussion on these shortcomings in §4.7). Given the lack of published literature regarding numerical techniques used to implement drop spreading on a completely non-wetting solid substrate, the techniques presented here are novel, and have been validated for low Weber number drop impact simulations using the BEM described in this chapter (see §4.6).

Drop impact simulations begin with the drop in contact with the solid substrate, with the $(N+1)$ -th node, located at the bottom of the drop, being the sole node at $z = 0$ (on the substrate). At this node we apply impermeability (that is, $(\partial\phi/\partial n)_{N+1} = 0$), but as it is the *only* node on the substrate, the element connecting it to its nearest neighbour is *not* given as a linear spline. As the drop descends and (in particular) the N -th node moves closer to $z = 0$, the spline that connects it to the $(N+1)$ -th node almost always moves below the surface of the substrate (there are no conditions that impose the spline must lie above $z = 0$). Many techniques has been trialled in this work to avoid the splines falling below $z = 0$; including complex schemes that redistribute nodes in a way such that the contact line ‘slides’ radially-outward (this looks like the extension and contraction of a linear spline on the substrate) whenever the approximating spline ‘touches down’. However, this issue was ultimately found to have negligible effects on spreading dynamics and the techniques developed to avoid it were computationally cumbersome. The spline going below $z = 0$ is un-physical but ultimately has little affect on the drop dynamics, which is influenced most strongly by the nodal positions.

When the N -th node is sufficiently close to the solid substrate, the kinematic equation (given discretely in 4.5.29) will naturally force this node onto or below the substrate. When the latter happens (given the former happens with probability zero), the simulation reverts to the previous global time and the global time step is reduced to a value that would have the node lie exactly *on* the substrate. This reduced global time step is calculated assuming that time-evolution is linear (recall RK4 is *not* linear) so we actually expect the node to be evolved to a position *closer* to the substrate. If the new node location has vertical coordinate less than 10^{-5} , it is shifted vertically to lie *on* the substrate and the node is from now on, considered part of the liquid-solid interface (and the new position of the contact line unless multiple nodes

descended simultaneously). If the new node location has vertical coordinate *greater* than 10^{-5} , then we continue the simulation, with the most likely outcome being that the node joins the liquid-solid interface after the *next* global time step, using the above process.

Occasionally, when a collection of nodes on the liquid-gas interface near the contact line node are all close to the solid substrate, the node that is *not* adjacent to the contact line node touches down first (that is, it penetrates the substrate as described above). In such cases, all nodes between the newly-formed contact line node and the *old* contact line node are forced down vertically to $z = 0$, and join the liquid-solid interface.

Nodes can also be relocated between the liquid-gas and liquid-solid interfaces through mesh redistribution (see §4.5.6), but other than through that mechanism, there is no way for nodes to move *off* the substrate because the normal velocity on the liquid-solid interface is taken to be zero. So in particular, during retraction on the solid, the receding motion is given solely by the radial evolution of the contact line node (4.5.30), rather than also allowing the drop to ‘roll’ back into itself (as is implemented for spreading motion). This method is still qualitatively correct as the contact line moves with the speed of the fluid at the solid substrate, however, for the drop to rebound, there has to be a mechanism in place for the final nodes on the liquid-solid interface to lift off from the substrate. In the final stages of retraction, when the contact line radius is sufficiently small as to allow the liquid-solid interface to be represented by a single element (subtended between a node at the axis and a node at the contact line, see §4.5.6), multiple implementations of node ‘lift-off’ were trialled. However, the shortcomings of using a BEM (see §4.7) became apparent before implementation of such a technique was completed.

4.5.5 Adaptive Time Stepping

Given the large deformations that occur during drop impact experiments, and the various time-scales with which motion occurs, it is sensible to allow for adaptive time stepping. The jetting behaviour seen in drop impact experiments onto rigid impermeable superhydrophobic substrates in §2.3.1, for example, is clearly much faster than any visible motion at the start of the retraction process (where the drop is almost stationary at maximum spread), and as our model treats the powder bed

as a rigid impermeable superhydrophobic substrate, we may expect to see a similar disparity in time-scales in our simulations. It would be inefficient to have a single (small) time step to cover both of these cases, so we employ the use of bounds on the time step so that it only reduces when necessary, and is able to increase where appropriate.

The first bound is a one dimensional Courant-Friedrichs-Lewy *like* condition [163],

$$\tau \leq 0.2 \min_{j=1,\dots,N+1} \left(\frac{\Delta_j s}{(\partial\phi/\partial n)_j} \right) \quad (4.5.35)$$

where $\Delta_j s$ denotes the distance between node j and either of its immediate neighbours. This condition states that the time step cannot exceed a pre-determined multiple, 0.2, of the minimum of the ratio of element length adjacent to a node, to that node's normal velocity. Its purpose is for the simulation to avoid under-resolving waves propagated along the boundary elements, and the value of 0.2 was chosen in our case through trial-and-error. This bound is used in [148] with a small constant in place of $\Delta_j s$, however, the dependence on size of the elements surrounding each node as in (4.5.35) allows for a time-bound better suited across multiple simulations. The second bound (taken from [159] where it is used in a study of surface tension driven pinch-off for deforming inviscid drops) is given by

$$\tau \leq 0.4 \min_{j=1,\dots,N+1} (\Delta_j s)^{3/2}, \quad (4.5.36)$$

and like the previous bound, aims to allow for greater resolution for capillary waves at the smallest-element scale.

A mechanism is also implemented for the time step to *increase*, as long as this increase does not then force either of the above bounds (4.5.35)-(4.5.36) to be violated. Every 25 global time steps, the initial distribution of coordinates and imposed boundary conditions is stored for all nodes. The system is then evolved for two consecutive global time steps (with the second global time step set equal to the first) and the new node locations are noted. The system is reverted to the stored state and a single large global time step (equal to the sum of the previous two) is used; if the greatest distance in position between any node and its counterpart (in the alternate evolution) is less than 1% the length of the smallest element across both evolutions, then the time step is doubled. There is a maximum time step, τ_{max} , that is defined at the start of a simulation, and any time step doubling as described here which exceeds

this is ignored and τ_{max} is used instead.

4.5.6 Mesh Redistribution

The BEM numerically implemented in this work maintains a constant number of elements N throughout individual simulations, so mesh *refinement* takes the form of mesh *redistribution*, that is, the re-positioning of nodes along the boundary $\bar{\Gamma}$. Redistribution of nodes is conducted using the chosen forms of interpolation in §4.5.1; calculating the new position of a node using the constructed splines and the new value of the velocity potential using linear interpolation. When it occurs, redistribution is *always* administered just after the system of splines has been constructed and *before* the matrices of the discretised boundary integral equation (see Appendix E) have been populated. Once the nodes have been redistributed, a new system of splines is created and the numerical procedure continues as before. We discuss here why mesh redistribution is often necessary, and describe the method of implementation, with references to how this is achieved in similar works.

Without redistribution, the positions of nodes are evolved throughout the course of a simulation, with the individual elements increasing and decreasing in size dynamically. In certain scenarios, such as for flows exhibiting an oscillatory behaviour, individual elements can similarly oscillate between small and large sizes frequently, and redistribution is *not* necessary, as there are no *permanently* under-resolved regions of the interface. Redistribution *can* be employed in a case like this, and is done so primarily to avoid smaller element sizes triggering a reduction in the time step (by bounds given in §4.5.5), and therefore increasing the computational run-time past acceptable limits.

However, there are many scenarios whereby, without redistribution, nodes have a tendency to cluster over the course of a simulation, leaving regions of the interface chronically under-resolved. An example of this is that for a kinematic equation that evolves the computational mesh in the normal direction to the interface, like our own (4.5.29), application to a sphere moving with a constant downward-vertical velocity results in nodes on the lower hemisphere clustering at the drop side (where the unit normal has no vertical component), and nodes on the upper hemisphere clustering towards the axis of symmetry. Clustering is by no means exclusive to this particular choice of how the mesh is evolved, and this can occur for a variety of kinematic equa-

tions and complex drop boundaries. It does however highlight a particular scenario in which redistribution is *necessary* to accurately resolve the drop interface, rather than employing it to avoid a (computationally intensive) small time step.

Furthermore, when a BEM is coupled with a free surface tracking scheme, unphysical instabilities are known to occur after long periods of simulation [162] whereby spurious oscillatory patterns emerge with adjacent nodes moving in opposite directions to one another (described as a ‘zig-zag’ instability). It has been theorised [162] that this instability could be caused by a clustering of nodes over time that skews the distribution of element sizes. This instability has been observed during simulations of the BEM developed in this chapter, and we find that it can be delayed significantly (ideally past the run-time of the simulation) through the regular redistribution of nodes. It should be noted here that every instance of node redistribution introduces numerical errors into the simulation due to variables taking on approximated values using the chosen forms of interpolation, which in particular, can significantly reduce bulk kinetic energy if utilised too often. Hence, redistribution often only occurs in our BEM simulations after a large number of time steps have elapsed.

The simplest choice for node redistribution, which is employed here (as well as in [148, 160, 162, 164], among others), is to update the mesh after a fixed number of time steps (or after a set time has elapsed, which is set prior to simulation) so that *all* elements are of equal length. This is simple to implement, staves off the zig-zag instability, and avoids particularly small element sizes unnecessarily reducing the time step. A variation of this technique is used in [165], whereby a constant element length Δs is enforced for all elements, apart from the first and final elements having a set length $\Delta s/2$. After a single global time step, this mesh is altered so that all elements are the same length, before reverting (at the next global time step) to lengths Δs for the interior elements and $\Delta s/2$ at the first and final elements. This ‘staggered grid’ approach is reported to work well, and was trialled with our own simulations, with ‘staggering’ occurring after a set number of time steps (rather than at every step), but it was ultimately not used as it is almost indistinguishable from enforcing constant element lengths.

Specialist node redistribution schemes have been developed, for example, in [159] (which describes surface tension driven pinch-off dynamics in inviscid flow), when close to pinch-off, the mesh is dynamically altered so that the distance between

adjacent nodes is proportional to their distance to the location of the minimum ‘neck’ radius. Additional nodes are then added where necessary so that the distance between adjacent nodes does not exceed a pre-determined multiple of the minimum neck radius. This technique allows for high-resolution of the region surrounding the pinch-off location. Preliminary work was made to implement this scheme into simulations (including the ability to add and remove nodes), foreseeing that we would have to resolve pinch-off events (as is seen in experiments in Chapter 2). However, the BEM was abandoned before this was put into effect (see §4.7).

When the drop is in contact with the solid substrate, many nodes may attach themselves to the liquid-solid interface (see §4.5.4 for a description of this mechanism). Given that the number of nodes is fixed at the start of a simulation, this can mean that (even after redistribution to equal sized elements) a large proportion of the nodes are lying on the flat substrate and *not* on the mobile liquid-gas interface, the latter consisting of regions of high curvature and interesting surface waves. Given the desire to accurately resolve the free surface dynamics, we limit the number of nodes that lie on the solid substrate to a maximum of 10% of all nodes. Let L_{LG} and L_{LS} denote the total arclength of the liquid-gas and liquid-solid portions of the approximated boundary $\bar{\Gamma}$ before redistribution (also define $L = L_{LG} + L_{LS}$), and fix the nodes on the axis of symmetry and at the contact line in their relative positions. We then provide each interface with a proportionate share of the remaining $N - 2$ nodes (with the cap of 10% of the total nodes on the liquid-solid substrate), that is, we allocate

$$\min \left(\left\lfloor \frac{L_{LS}}{L} (N - 2) \right\rfloor, \left\lfloor \frac{N + 1}{10} - 2 \right\rfloor \right),$$

nodes to the interior of the liquid-solid interface, and the remaining nodes to the interior of the liquid-gas interface.

4.6 Numerical Validation

In this section, we discuss how the implementation of the BEM (described in §4.5) is numerically validated against theoretical and experimental results (where applicable) for drop oscillations with clean and surface viscous interfaces, and for low Weber number impacts onto a rigid impermeable solid substrate. In turn, we discuss matters relating to free surface oscillations, that is, oscillating drops without consideration of solid substrates or gravity, followed by drop impacts.

Typical computational times for numerical simulations using the BEM described in this chapter are on the order of days; for cubic splines this means one-to-two days for simulations of suspended free surface oscillations without surface viscous effects, two-to-three days for suspended oscillations *with* surface viscous effects, and three-to-four days for simulations of drop impact. For quintic splines, these times are extended; with two-to-four days for suspended free surface oscillations without surface viscous effects, three-to-five days for suspended oscillations *with* surface viscous effects, and four-to-six days for drop impact. Owing to shortcomings related to simulations of drop impact (see §4.7), only low impact Weber number cases of drop impact are able to be simulated, with no simulation resolved up to the point of rebound, hence the drop impact computational times stated above are much lower than they would be for a fully-realised drop impact simulation.

For the validation study on free surface oscillations presented in §4.6.1, cubic splines are used to approximate the drop boundary, whereas when validating the success of drop impact simulations in §4.6.2, quintic splines are used. For sake of space, a validation study on free surface oscillations when using quintic splines is not presented. For drop impacts, interactions with the solid substrate can lead to complicated drop profiles appearing even for low impact Weber numbers, and so while the (higher order) quintic splines are computationally expensive, their ability to provide a higher accuracy solution for the drop shape and velocity distribution for a given number of nodes, as compared to cubic splines, is a worthwhile investment. Additionally, the use of quintic splines provides further assurance that the eventual shortcomings of the BEM presented in this chapter are not simply due to the order of the boundary approximation used.

4.6.1 Free Surface Oscillations

Within this subsection, we focus on suspended oscillating drops, whereby there are no gravitational effects, and *no* solid substrate. We begin with convergence results for small and large amplitude oscillations for drops with a clean interface, before moving onto results for oscillating drops experiencing effects corresponding to a (constant) dilatational surface viscous coefficient $\lambda^s > 0$.

Validation: Convergence without Surface Viscosity

The spatial-convergence rate for BEMs that employ the collocation method (as is done so here) depends on the chosen order of approximation for the velocity potential ϕ and normal velocity $\partial\phi/\partial n$ along boundary elements. If we let h denote the typical element length, and let W denote the order of approximation for ϕ (and $\partial\phi/\partial n$), then the error is expected to reduce as h^{W+1} , as $h \rightarrow 0$ [166]. We approximate both of these variables linearly (4.5.16), so we therefore expect to find approximately second-order convergence in numerical error as the mesh is refined.

The flows inside and outside of the drop are assumed incompressible and inviscid (see §3.2.4), hence the model (in the absence of surface viscosity) perfectly conserves drop volume and total drop energy. In the absence of gravitational forces, total drop energy, E , is the sum of bulk kinetic energy, E_K , and surface energy, E_S . Drop volume (denoted by Vol), bulk kinetic, and surface energy are given (in dimensionless form) by

$$Vol(\Omega) = \int_{\Omega} 1 \, dV \quad \text{and} \quad E_K(\Omega) = \int_{\Omega} \frac{1}{2} |\nabla\phi|^2 \, dV \quad \text{and} \quad E_S(\mathcal{S}) = \int_{\mathcal{S}} 1 \, dS, \quad (4.6.1)$$

for a volume element dV and surface element dS in the domain Ω and on the drop boundary \mathcal{S} , respectively. We measure the convergence of the numerical solution as calculated by the BEM by comparing volume and (total) energy conservation as the typical element length h is decreased between simulations.

Each integral in (4.6.1) can be written as an integral over the (one dimensional) boundary curve Γ (equivalently $\bar{\Gamma}$ for the boundary approximation), which will allow these quantities to be calculated during simulations. By noting the following:

$$\frac{1}{2} \nabla \cdot (r \mathbf{e}_r) = \frac{1}{2r} \frac{\partial}{\partial r} (r^2) = \frac{2r}{2r} = 1,$$

we can replace the 1 in the integrand for $Vol(\Omega)$ in (4.6.1) by $\frac{1}{2} \nabla \cdot (r \mathbf{e}_r)$, and then use the divergence theorem to consider integration over the boundary \mathcal{S} , and finally

reduce this to an integral over Γ by axisymmetry. Consequently, we have:

$$\begin{aligned}
Vol(\Omega) &= \int_{\Omega} \frac{1}{2} \nabla \cdot (r \underline{\mathbf{e}}_r) \, dV \\
&= \frac{1}{2} \int_{\mathcal{S}} \underline{\mathbf{n}} \cdot (r \underline{\mathbf{e}}_r) \, dS \\
&= \frac{1}{2} \int_{\mathcal{S}} r n_r \, dS \\
&= \pi \int_{\Gamma} R^2 n_r \, ds \\
&= -\pi \int_{\Gamma} R^2 \frac{\partial Z}{\partial s} \, ds,
\end{aligned} \tag{4.6.2}$$

where ds denotes a line element on Γ . Note that we refer to the radial and axial coordinates of the curve Γ by (R, Z) , consistent with §4.5.1. For the bulk kinetic energy $E_K(\Omega)$, we use the divergence theorem and incompressibility (that is, $\nabla^2 \phi = 0$) to obtain,

$$\begin{aligned}
E_K(\Omega) &= \frac{1}{2} \int_{\Omega} \nabla \phi \cdot \nabla \phi \, dV \\
&= \frac{1}{2} \int_{\Omega} [\nabla \cdot (\phi \nabla \phi) - \phi \nabla^2 \phi] \, dV \\
&= \frac{1}{2} \int_{\mathcal{S}} \underline{\mathbf{n}} \cdot (\phi \nabla \phi) \, dS \\
&= \frac{1}{2} \int_{\mathcal{S}} \phi \frac{\partial \phi}{\partial n} \, dS \\
&= \pi \int_{\Gamma} \phi \frac{\partial \phi}{\partial n} R \, ds.
\end{aligned} \tag{4.6.3}$$

Finally, for surface energy $E_S(\mathcal{S})$, we have

$$E_S(\mathcal{S}) = \int_{\mathcal{S}} 1 \, dS = 2\pi \int_{\Gamma} R \, ds. \tag{4.6.4}$$

Let $\bar{\mathcal{S}}$ denote the surface-of-revolution formed by rotating the approximated boundary curve $\bar{\Gamma}$ about the z -axis, and let $\bar{\Omega}$ denote the volume enclosed by $\bar{\mathcal{S}}$. Terms $\bar{\mathcal{S}}$ and $\bar{\Omega}$ therefore denote the approximations for the *full* drop boundary \mathcal{S} and drop domain Ω , respectively, following construction of the boundary splines (see §4.5.1). The integrals for drop volume $Vol(\bar{\Omega})$, kinetic energy $E_K(\bar{\Omega})$, and surface energy $E_S(\bar{\mathcal{S}})$ (4.6.2)-(4.6.4) are evaluated after every (global) time step during simulations, and standard Gauss-Legendre quadrature is used on each approximating spline, with $M + 1$ quadrature points (for spline-order M , consistent with §4.5).

Consider the l_2 - and l_∞ -norms, given by [167]

$$\|\underline{\mathbf{y}}\|_2 = \sqrt{y_1^2 + y_2^2 + \dots + y_Y^2} \quad \text{and} \quad \|\underline{\mathbf{y}}\|_\infty = \max(|y_1|, |y_2|, \dots, |y_Y|), \tag{4.6.5}$$

respectively, for vector $\underline{\mathbf{y}} = y_i, i = 1, \dots, Y$ and $1 \leq Y \in \mathbb{N}$. Both of the above norms are used to evaluate errors within simulations, with each y_i in (4.6.5) corresponding to the (absolute) difference between the calculated volume (or total energy) at the i -th time step and its initial value, with Y equal to the running total number of (global) time steps that have elapsed.

Small Amplitude Oscillations

We consider a suspended drop released from rest, with initial shape given by

$$(R(\psi), Z(\psi)) = [1 + \epsilon P_2(\cos \psi)] (\sin \psi, \cos \psi), \quad (4.6.6)$$

for polar angle $\psi \in [0, \pi]$, where P_2 is the Legendre polynomial of order 2, and with $\epsilon = 0.05$. This particular drop shape (4.6.6), induces an axisymmetric spherical (second) harmonic with a 5%-amplitude; which is small enough for us to compare the resulting dynamics to linear theory [140].

Six separate simulations are considered, with the number of elements in successive simulations increasing by a factor of approximately $\sqrt{2}$. In all simulations, a constant (dimensionless) time step of $\tau = 1 \times 10^{-3}$ is enforced, and nodes are redistributed every 100 time steps to ensure every boundary element has the same length. The total run-time is $t = 15$, and cubic splines are used to approximate the geometry of the drop boundary.

Shown in Figure 4.3 is the height of the drop apex (that is, the distance between the drop centre of mass and the drop apex) over the course of these simulations. Overlaid is the theoretical oscillation frequency for a drop experiencing a small amplitude (second) axisymmetric harmonic oscillation of the form given by (4.6.6) [139]. This plot shows that the oscillation frequency observed within the simulations maintains good agreement with the theoretical result for longer stretches of time as the number of elements increases (equivalently, as h decreases).

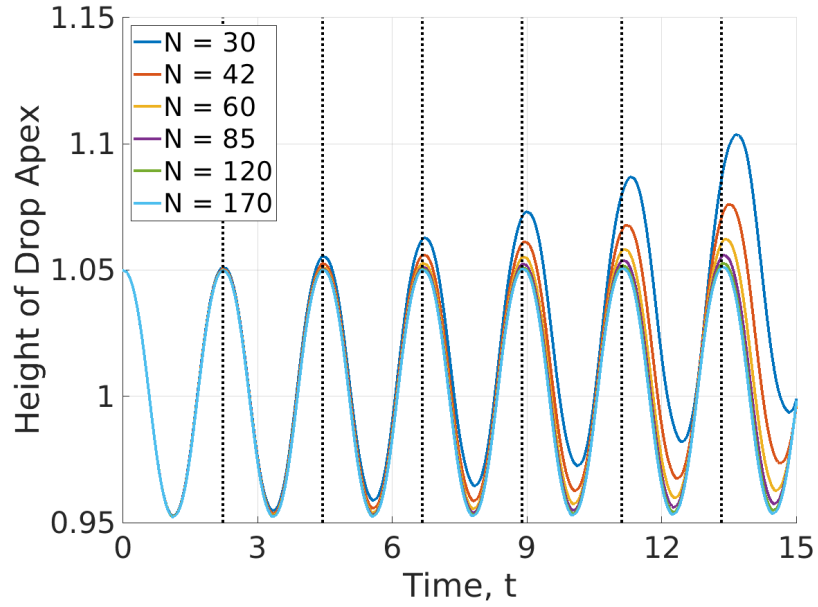


Figure 4.3: Height of drop apex with respect to the drop centre of mass (for increasing N) for a suspended drop released from rest with initial shape given by (4.6.6) with $\epsilon = 0.05$. Black dotted vertical lines indicate the (dimensionless) theoretical oscillation period for a second axisymmetric spherical mode ($2\pi/\sqrt{8}$).

Given the surface area of the drop varies during a simulation while the number of nodes stays constant, we consider spatial convergence with respect to the number of nodes used as opposed to element lengths (which are necessarily changing size on average). See Figure 4.4, where power laws for $h = 1/N$ have been constructed for errors calculated with the l_2 - and l_∞ -norms (4.6.5), for volume and (total) energy. For volume, the errors as calculated using both the l_2 - and l_∞ -norms appear to decay as approximately $h^{2.04}$. For (total) energy, the l_2 - and l_∞ -norms suggest errors decay as approximately $h^{2.15}$ and $h^{2.24}$, respectively. These obtained power-laws are sufficiently close to the theoretical result of h^2 for the decay of numerical errors to provide confidence that the numerical implementation of the BEM works well for small amplitude oscillations. We now turn our attention to large amplitude oscillations.

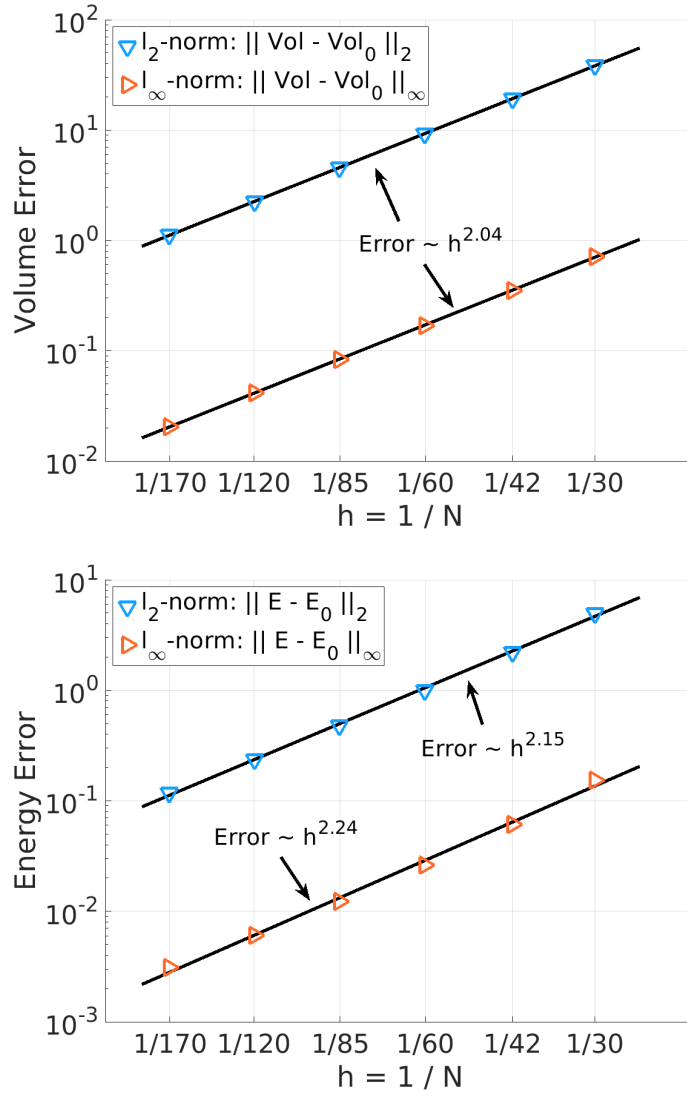


Figure 4.4: Errors in the conservation of drop (top) volume, and (bottom) total energy, as calculated using the l_2 - and l_∞ -norms (4.6.5), for a suspended drop released from rest with initial shape given by (4.6.6) with $\epsilon = 0.05$, for varied $h = 1/N$. Power laws are fitted with: (top) $\text{Error} \sim h^{2.04}$, with an R-squared value and mean square error of: $R^2 = 1.00$ and $\text{MSE} = 2.13 \times 10^{-2}$ for the l_2 -norm and $R^2 = 1.00$ and $\text{MSE} = 9.30 \times 10^{-6}$ for the l_∞ -norm, and (bottom) $\text{Error} \sim h^{2.15}$ and $\sim h^{2.24}$ for the l_2 - and l_∞ -norms, respectively, with an R-squared value and mean square error of: $R^2 = 1.00$ and $\text{MSE} = 1.50 \times 10^{-2}$ for the l_2 -norm, and $R^2 = 0.99$ and $\text{MSE} = 5.63 \times 10^{-5}$ for the l_∞ -norm.

Large Amplitude Oscillations

As before, we consider a suspended drop released from rest with initial shape given by (4.6.6), but now with $\epsilon = 0.5$. Note that this starting shape has the same form as the small amplitude case but with a *much* larger amplitude of 50%, and as such the resulting oscillations are not well-approximated with the previous theoretical results (which assume linearity of drop motion). Hence we focus just on the convergence of volume and (total) energy errors. Across five simulations, a constant time step of $\tau = 5 \times 10^{-4}$ is enforced, with node redistribution taking place every 200 time steps to ensure uniform sizes of boundary elements. The total run-time is $t = 15$, and cubic splines are used in all simulations to approximate the geometry of the drop boundary. Provided in Figure 4.5 are snapshots of the drop shape evolution during the first period of oscillation.

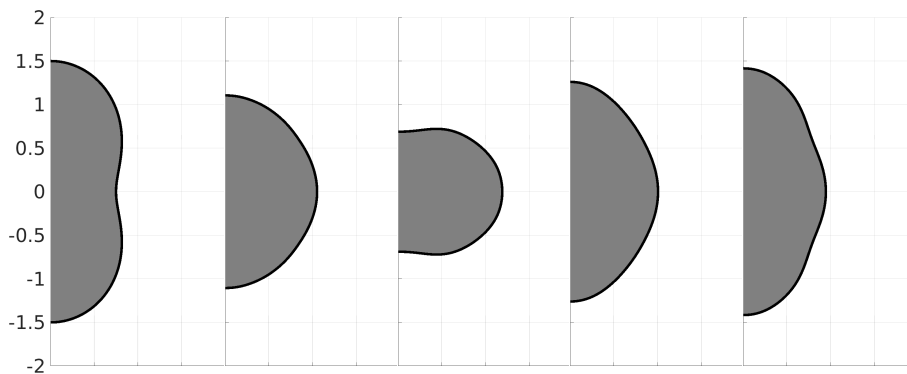


Figure 4.5: Profiles of oscillations in the (r, z) -plane for a suspended drop released from rest with initial shape given by (4.6.6) with $\epsilon = 0.5$. Snapshots taken at times (left-to-right): $t = 0.0, 0.8, 1.6, 2.0, 3.2$.

As with the small amplitude oscillations, power laws for $h = 1/N$ are constructed for errors calculated with the l_2 - and l_∞ -norms, for volume and (total) energy. For volume, the l_2 - and l_∞ -norms appear to suggest errors decay as approximately $h^{2.26}$ and $h^{2.27}$, respectively. On the other hand, for (total) energy, the l_2 - and l_∞ -norms appear to suggest errors decay as approximately $h^{2.32}$ and $h^{2.46}$, respectively. Again, these fitted power-laws are sufficiently close to the theoretical result of h^2 to provide confidence in the numerical implementation for clean drop oscillations.

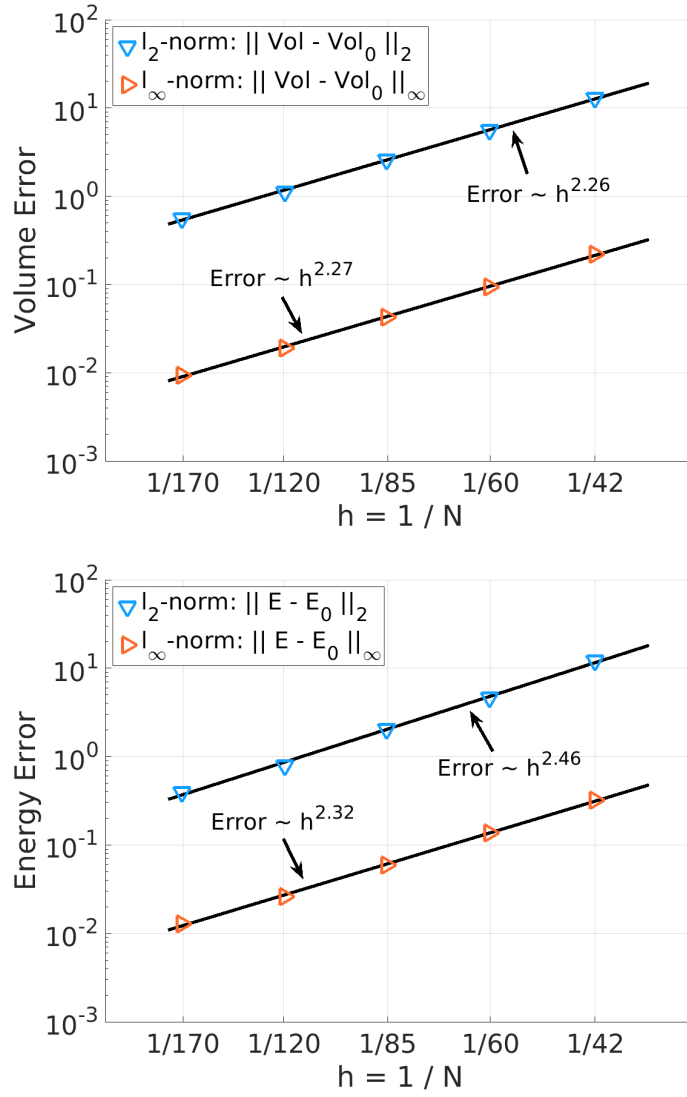


Figure 4.6: Errors in the conservation of drop (top) volume, and (bottom) total energy, as calculated using the l_2 - and l_∞ -norms (4.6.5), for a suspended drop released from rest with initial shape given by (4.6.6) with $\epsilon = 0.5$, for varied $h = 1/N$. Power laws are fitted with: (top) $\text{Error} \sim h^{2.26}$ and $\sim h^{2.27}$ for the l_2 - and l_∞ -norms respectively, with an R-squared value and mean square error of: $R^2 = 1.00$ and $\text{MSE} = 1.39 \times 10^{-2}$ for the l_2 -norm and $R^2 = 1.00$ and $\text{MSE} = 1.10 \times 10^{-5}$ for the l_∞ -norm, and (bottom) $\text{Error} \sim h^{2.46}$ and $\sim h^{2.32}$ for the l_2 - and l_∞ -norms respectively, with an R-squared value and mean square error of: $R^2 = 1.00$ and $\text{MSE} = 7.17 \times 10^{-2}$ for the l_2 -norm and $R^2 = 1.00$ and $\text{MSE} = 1.50 \times 10^{-5}$ for the l_∞ -norm.

Now that the numerical implementation of the BEM has been validated for suspended drop oscillations with clean interfaces, we move on to discuss the implementation of surface viscosity.

Validation: Energy Decay Rate due to Dilatational Surface Viscosity

An equation for the energy decay rate for an inviscid drop experiencing surface viscous (and also surface elastic) effects is provided in [116]. For our case, where we neglect surface elastic effects and consider only the dilatational component of surface viscosity, this energy decay rate is given by (assuming λ^s is nowhere zero):

$$\frac{dE(\Omega)}{dt} = -\frac{1}{\int_S 1/\lambda^s dS} \left(\int_S (\nabla_s \cdot \underline{\mathbf{n}})(\underline{\mathbf{u}} \cdot \underline{\mathbf{n}}) dS \right)^2. \quad (4.6.7)$$

We will now show that the implementation of dilatational surface viscosity in our BEM is valid by comparing the *observed* energy decay rate in our simulations for a variety of N , against the theoretical energy decay rate (4.6.7) as calculated for a large- N simulation (given it should be *close* to the ‘true’ solution). Note that equation (4.6.7) is not *truly* theoretical as it must be evaluated using approximate values of its constituent terms during a simulation, but showing that our observed decay rates converge to the value as calculated per (4.6.7) during a simulation, is sufficient for validating the surface viscous implementation.

A comparison is made between the observed energy decay rate and (4.6.7) in three separate cases, with (constant) $\lambda^s = 1, 10, 100$. In all cases, we consider a suspended drop being released from rest with initial shape given by (4.6.6) with $\epsilon = 0.5$ (the same as for the large amplitude oscillation for the clean interface). For convenience, the initial shape is repeated here:

$$(R(\psi), Z(\psi)) = [1 + \epsilon P_2(\cos \psi)] (\sin \psi, \cos \psi),$$

for polar angle $\psi \in [0, \pi]$, and where P_2 is the Legendre polynomial of order 2. To separate energy decay due to dilatational surface viscosity from decay due to redistribution of nodes (which occurs even on a clean interface due to numerical errors), we forego redistribution entirely and allow elements to change in size through the course of a simulation without interference. Additionally, the time step is kept constant at $\tau = 1 \times 10^{-4}$, and cubic splines are used to approximate the drop boundary.

In each case (so for $\lambda^s = 1, 10, 100$), the height of the drop apex shows *little*

variation between simulations for differing N , but shows clear convergence to a solution as N is increased (see Figures 4.7, 4.10, and 4.13). Similarly, we observe the effective surface tensions $\sigma_{\text{eff}}(t)$ clearly converge to a solution as the mesh is refined, and little variation is shown between the coarsest and finest meshes for $\lambda^s = 1$ and $\lambda^s = 10$, with a more pronounced difference (albeit still slight) in the latter stages of the simulations for $\lambda^s = 100$ (see Figures 4.8, 4.11, and 4.14). In contrast, the increase in N has a clear effect on the (total) energy, where we observe noticeable fluctuations for the coarsest mesh as compared to the finest mesh (see Figures 4.8, 4.11, and 4.15).

With these fluctuations in (total) energy in mind, in Figures 4.9, 4.12, and 4.16 are plots comparing how well the observed energy decay rates within simulations match the theoretical decay rate provided by (4.6.7) as calculated from the finest mesh simulation. This is a more sensitive quantity than those previously discussed as it is the rate of change in time of the energy. We see that the observed energy decay rate converges to the theoretical decay rate as measured by the l_2 - and l_∞ -norms, as $h = 1/N$ decreases. Fitting a power-law through the results, we observe that the ‘energy decay rate error’, that is, the normed-difference between the observed and theoretical energy decay rates, appears to reduce as *around* h^2 as $h \rightarrow 0$, and this holds across the three values of λ^s (in line with theoretical BEM convergence rates, see discussion earlier in this section). Note that as λ^s is increased, the time-window in which *all* meshes ‘hug’ the theoretical solution increases, after which the observed decay rates appear to drift apart. This may correlate with the findings of the damped nonlinear oscillator in §3.3, whereby an increase in λ^s corresponds to a decreased critical wave amplitude corresponding to the transition between overdamped and underdamped motion. In this context, there is better agreement between the observed and theoretical energy decay rates when the motion is overdamped, with a divergence corresponding to a transition to underdamped motion, which occurs later for cases with larger λ^s . If this is the case, then after this transition has occurred, the motion is underdamped so the drop starts oscillating. At this point, numerical instabilities begin to grow and are magnified in the plots for the energy decay rate due to them showing a time derivative of a fluctuating quantity (the total energy), and so are sensitive to fluctuations. However, given there is convergence to the theoretical result in line with the convergence for the volume and total energy (see ‘energy decay rate

error' plots in Figures 4.9, 4.12, and 4.16), this does not negate the validity of the implementation.

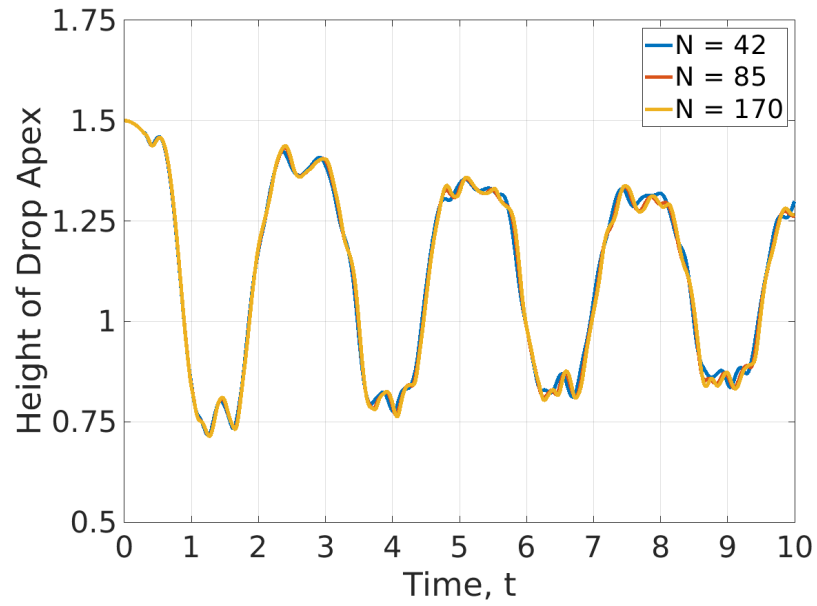


Figure 4.7: Height of drop apex with respect to the drop centre of mass (for increasing N) for a suspended drop released from rest with initial shape given by (4.6.6) with $\epsilon = 0.5$. The drop is experiencing (dilatational) surface viscous effects corresponding to (constant) $\lambda^s = 1$.

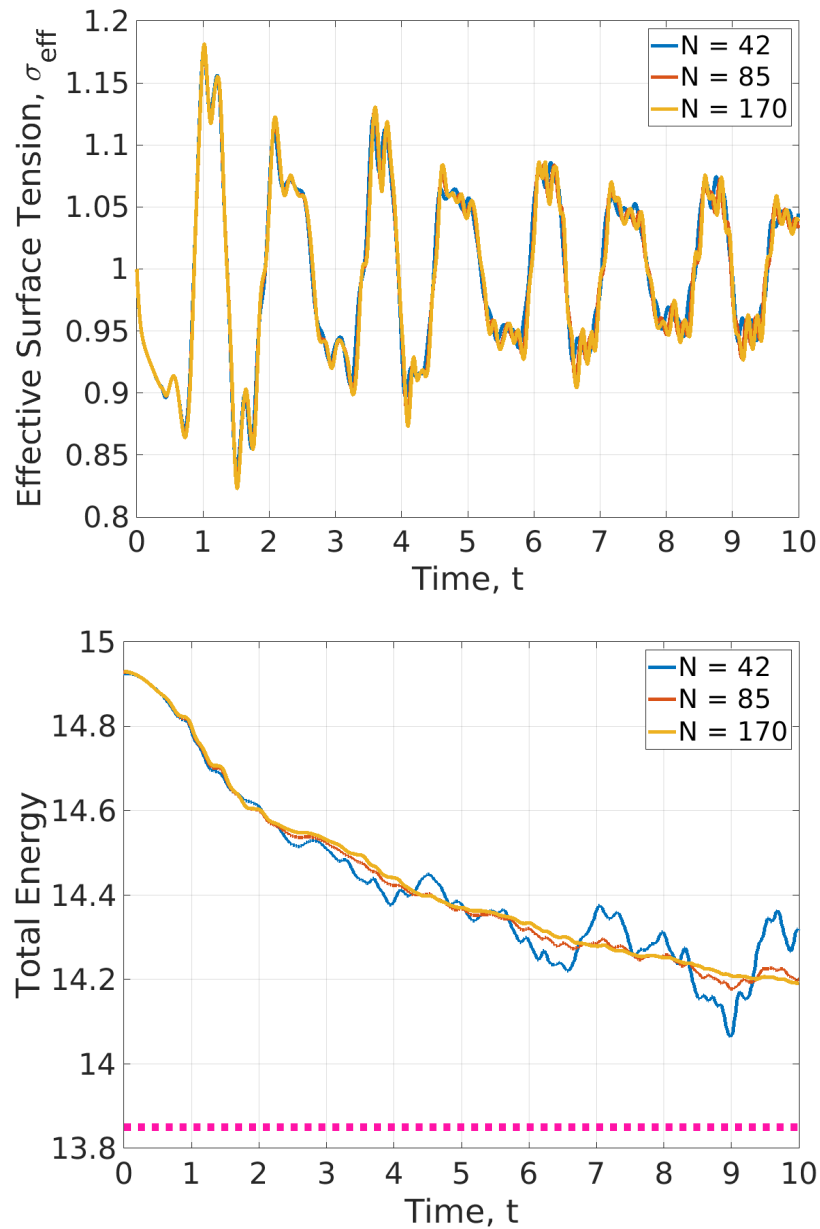


Figure 4.8: (Top) Effective surface tension, and (b) total energy (for increasing N) for a suspended drop released from rest with initial shape given by (4.6.6) with $\epsilon = 0.5$. The drop is experiencing (dilatational) surface viscous effects corresponding to (constant) $\lambda^s = 1$. The pink dotted line in the bottom plot indicates the total energy corresponding to the drop being at rest with spherical shape (the minimum surface energy state).

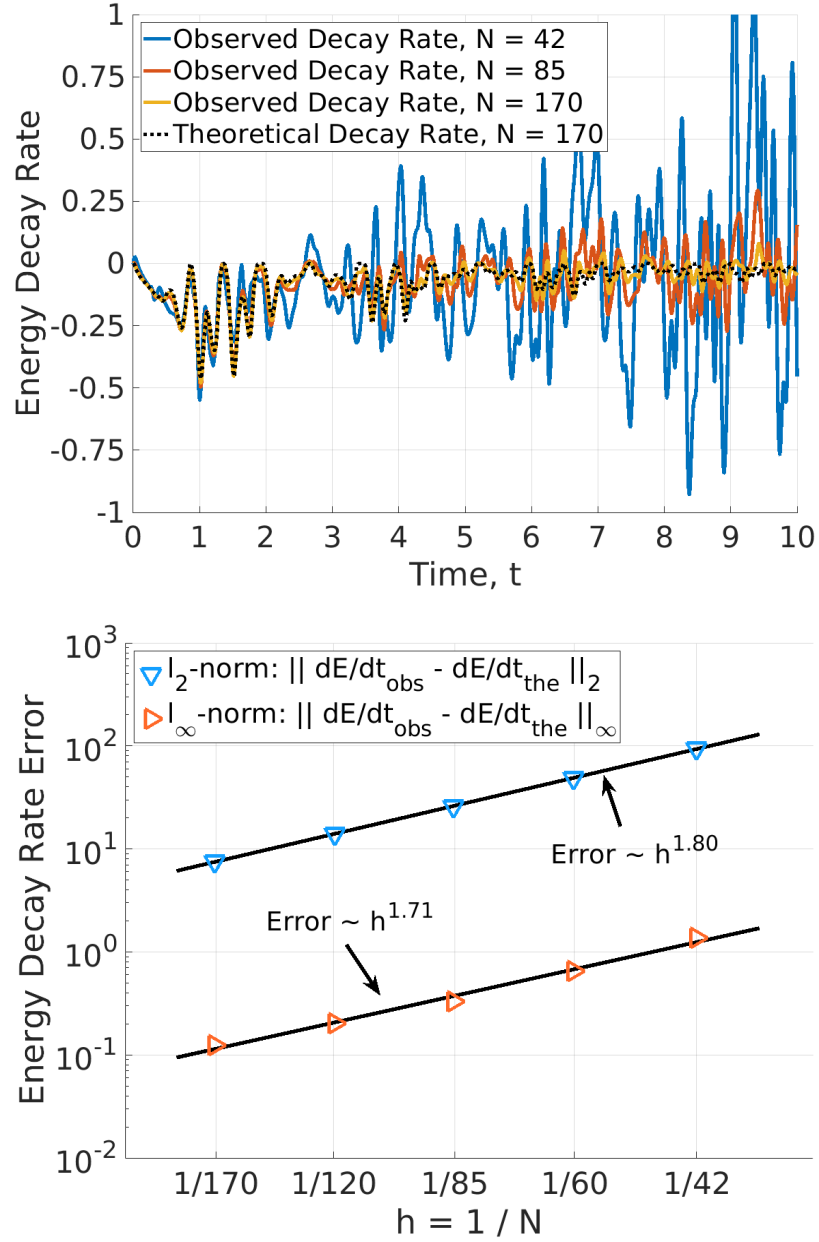


Figure 4.9: (Top) Comparison of the observed (from simulations) and theoretical energy decay rate (4.6.7, calculated using the $N = 170$ simulation), and (b) energy decay rate error (for increasing N) for a suspended drop released from rest with initial shape given by (4.6.6) with $\epsilon = 0.5$. The drop is experiencing (dilatational) surface viscous effects corresponding to (constant) $\lambda^s = 1$. The energy decay rate error is defined as the normed-difference of the observed and theoretical decay rates. Fitted power laws for the errors are $\sim h^{1.80}$ with $R^2 = 1.00$ and $\text{MSE} = 4.25 \times 10^{-1}$ for the l_2 -norm, and $\sim h^{1.71}$ with $R^2 = 0.99$ and $\text{MSE} = 3.70 \times 10^{-3}$ for the l_∞ -norm.

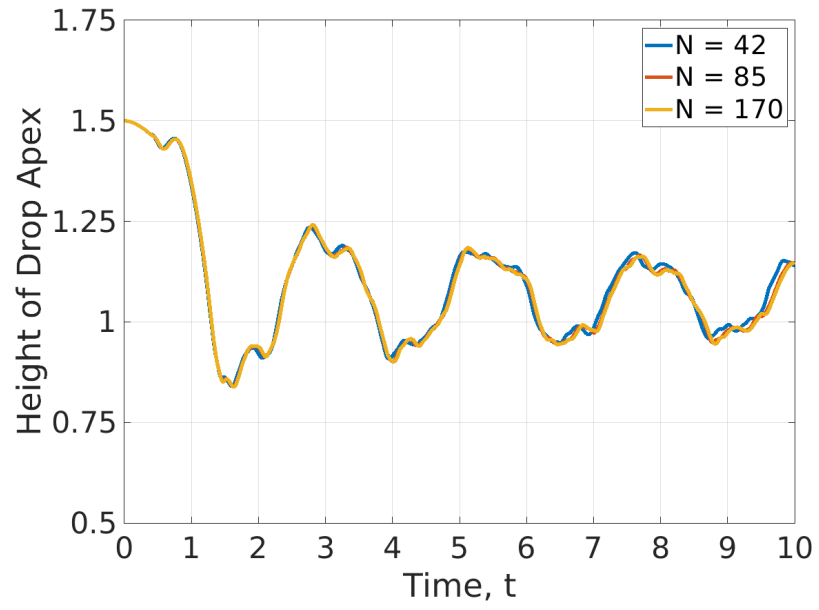


Figure 4.10: Height of drop apex with respect to the drop centre of mass (for increasing N) for a suspended drop released from rest with initial shape given by (4.6.6) with $\epsilon = 0.5$. The drop is experiencing (dilatational) surface viscous effects corresponding to (constant) $\lambda^s = 10$.

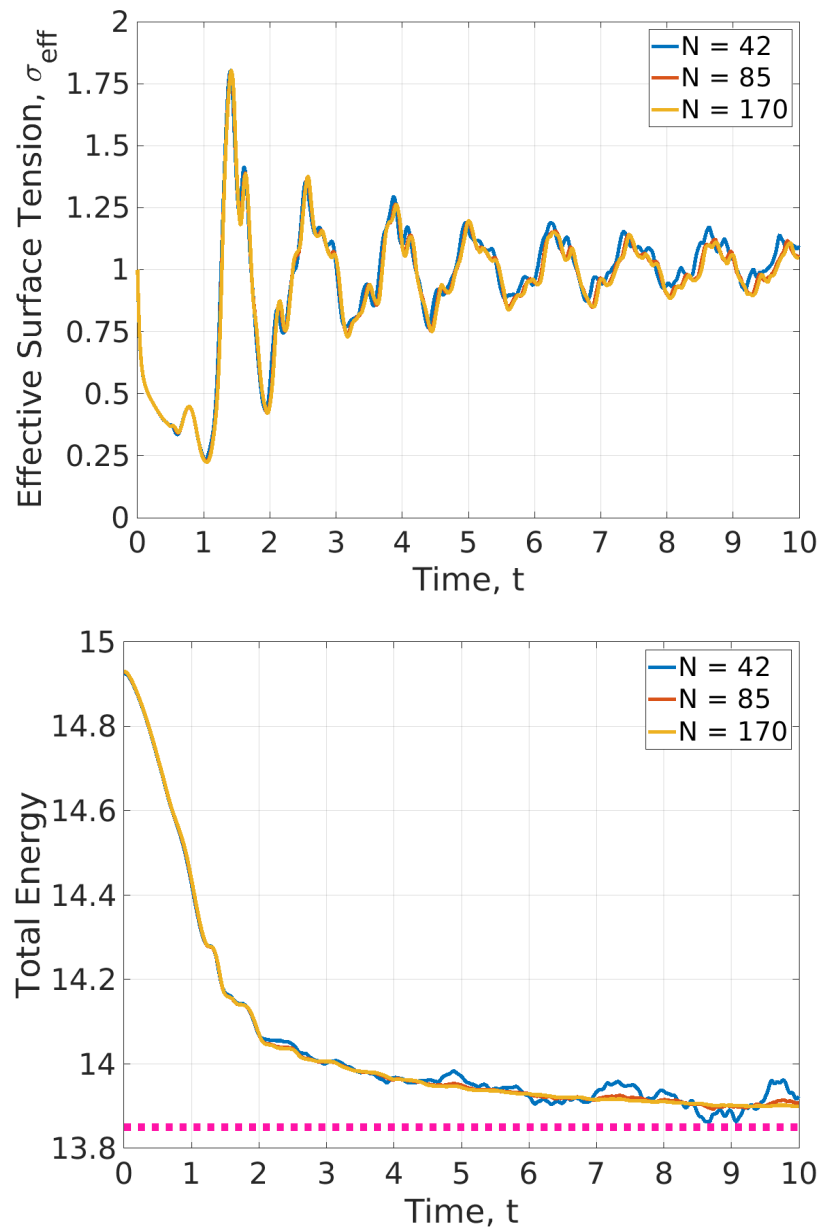


Figure 4.11: (Top) Effective surface tension, and (b) total energy (for increasing N) for a suspended drop released from rest with initial shape given by (4.6.6) with $\epsilon = 0.5$. The drop is experiencing (dilatational) surface viscous effects corresponding to (constant) $\lambda^s = 10$. The pink dotted line in the bottom plot indicates the total energy corresponding to the drop being at rest with spherical shape (the minimum surface energy state).

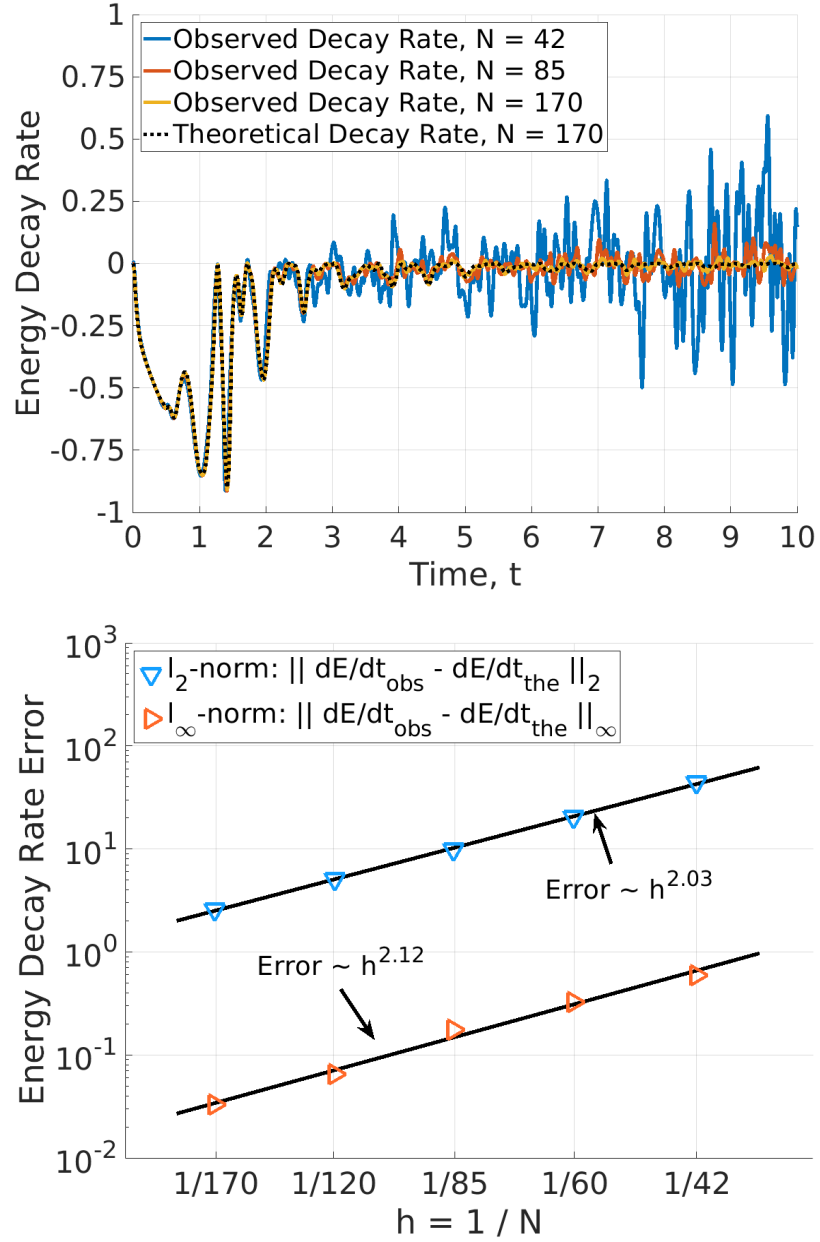


Figure 4.12: (Top) Comparison of the observed (from simulations) and theoretical energy decay rate (4.6.7, calculated using the $N = 170$ simulation), and (b) energy decay rate error (for increasing N) for a suspended drop released from rest with initial shape given by (4.6.6) with $\epsilon = 0.5$. The drop is experiencing (dilatational) surface viscous effects corresponding to (constant) $\lambda^s = 10$. The energy decay rate error is defined as the normed-difference of the observed and theoretical decay rates. Fitted power laws for the errors are $\sim h^{2.03}$ with $R^2 = 1.00$ and $\text{MSE} = 3.45 \times 10^{-1}$ for the l_2 -norm, and $\sim h^{2.12}$ with $R^2 = 0.99$ and $\text{MSE} = 1.00 \times 10^{-3}$ for the l_∞ -norm.

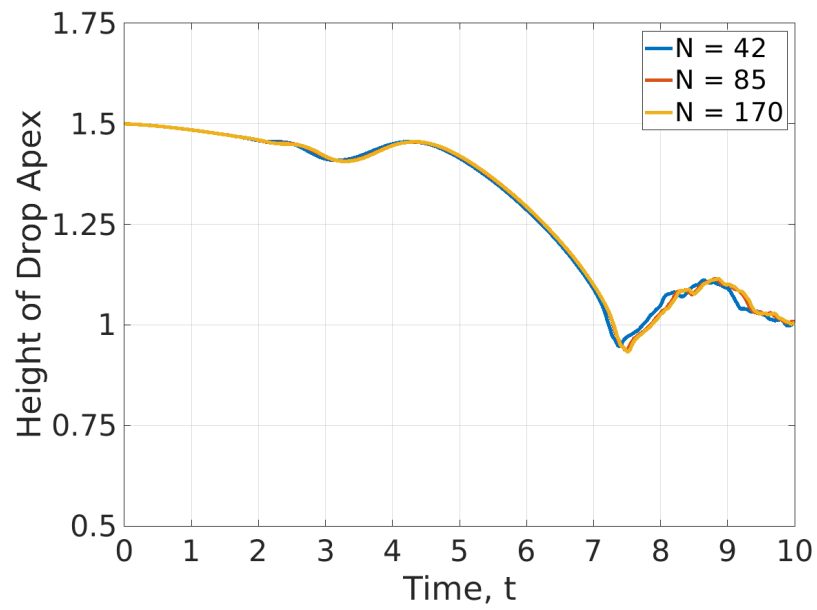


Figure 4.13: Height of drop apex with respect to the drop centre of mass (for increasing N) for a suspended drop released from rest with initial shape given by (4.6.6) with $\epsilon = 0.5$. The drop is experiencing (dilatational) surface viscous effects corresponding to (constant) $\lambda^s = 100$.

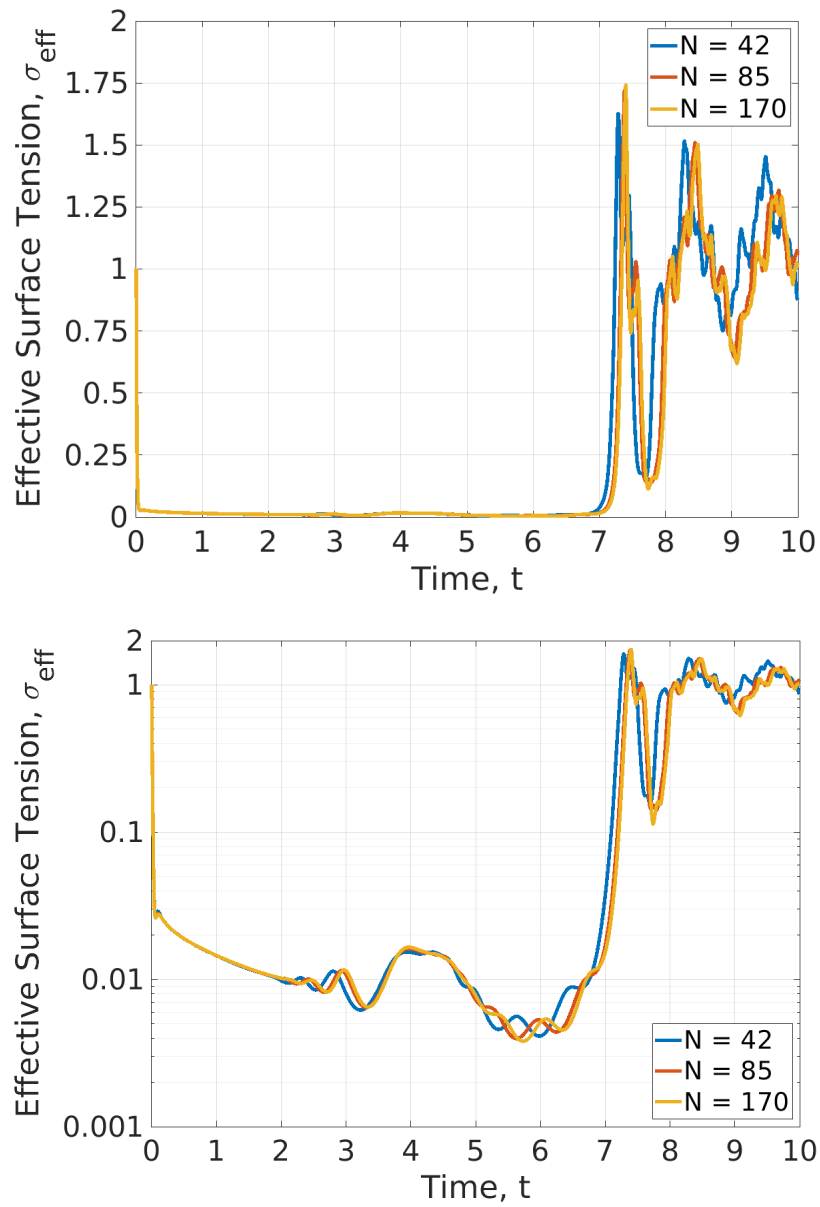


Figure 4.14: Effective surface tension (for increasing N) for a suspended drop released from rest with initial shape given by (4.6.6) with $\epsilon = 0.5$. Plots show (top) linear-scale, and (bottom) semilog-scale. The drop is experiencing (dilatational) surface viscous effects corresponding to (constant) $\lambda^s = 100$.

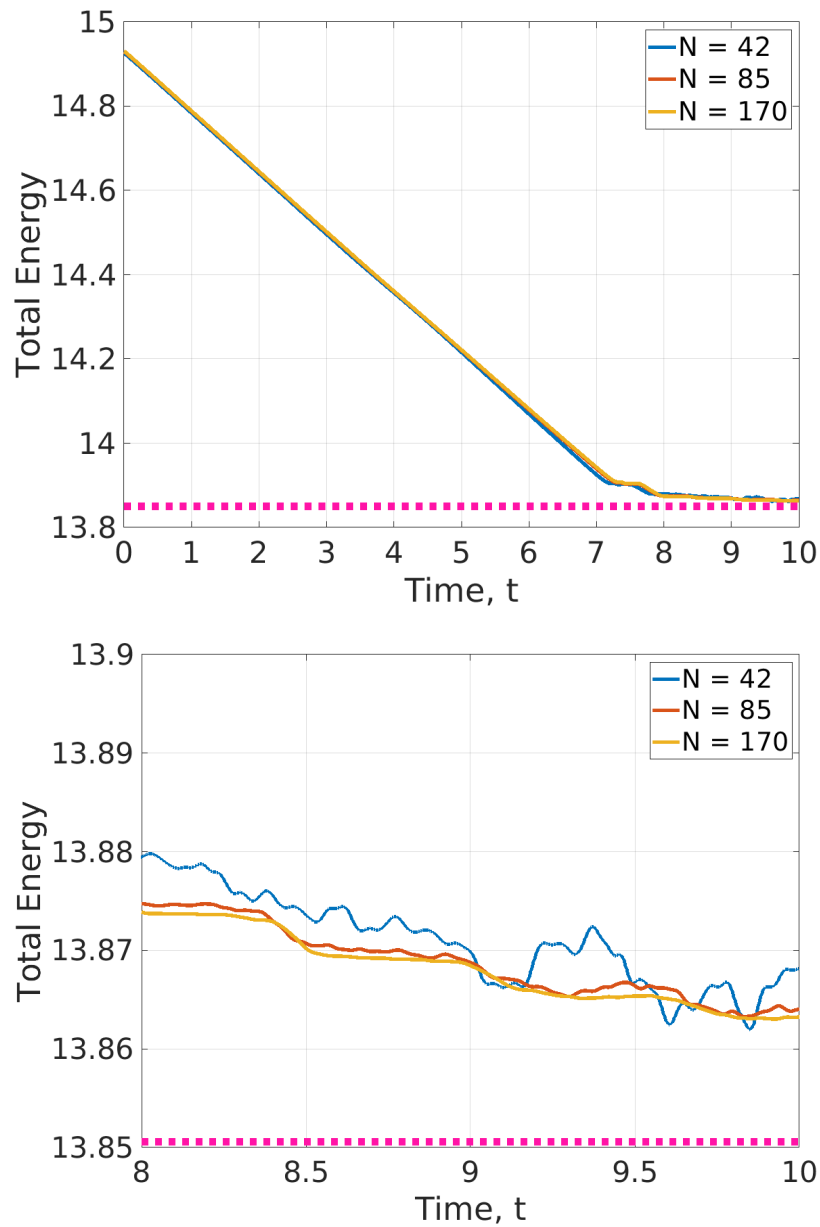


Figure 4.15: Total energy (for increasing N) for a suspended drop released from rest with initial shape given by (4.6.6) with $\epsilon = 0.5$. The drop is experiencing (dilatational) surface viscous effects corresponding to (constant) $\lambda^s = 100$. The pink dotted line in the bottom plot indicates the total energy corresponding to the drop being at rest with spherical shape (the minimum surface energy state). Plots show (top) from time $t = 0$ to $t = 10$, and (bottom) a close-up view of fluctuations from time $t = 8$ to $t = 10$.

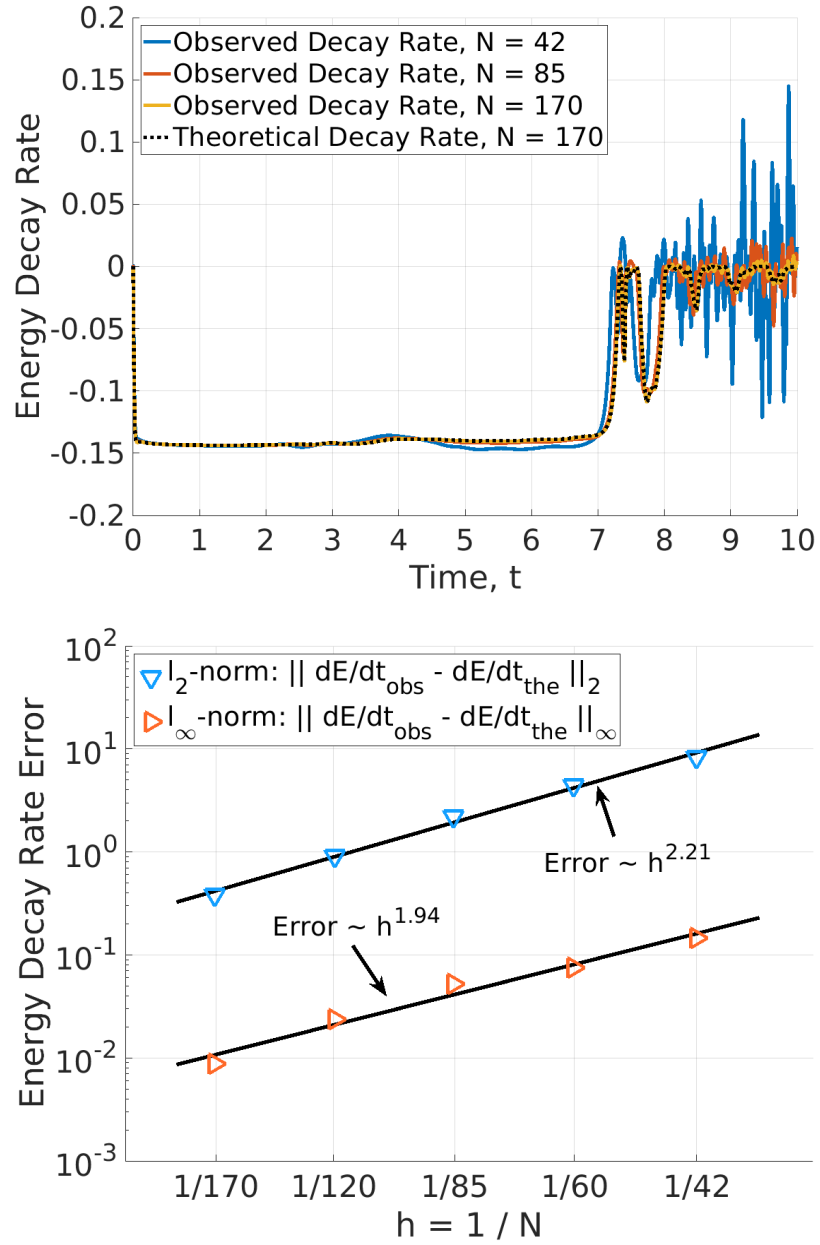


Figure 4.16: (Top) Comparison of the observed (from simulations) and theoretical energy decay rate (4.6.7, calculated using the $N = 170$ simulation), and (b) energy decay rate error (for increasing N) for a suspended drop released from rest with initial shape given by (4.6.6) with $\epsilon = 0.5$. The drop is experiencing (dilatational) surface viscous effects corresponding to (constant) $\lambda^s = 100$. The energy decay rate error is defined as the normed-difference of the observed and theoretical decay rates. Fitted power laws for the errors are $\sim h^{2.21}$ with $R^2 = 0.99$ and $\text{MSE} = 1.99 \times 10^{-1}$ for the l_2 -norm, and $\sim h^{1.94}$ with $R^2 = 0.99$ and $\text{MSE} = 8.40 \times 10^{-5}$ for the l_∞ -norm.

4.6.2 Drop Impact

This subsection is dedicated to validating the numerical implementation of drop impact onto a rigid impermeable superhydrophobic substrate using the methods described in this chapter. Owing to unforeseen fundamental issues with employing a BEM for the drop impact problem, along with using the inviscid model (see §3.2.4), validation is limited to low impact Weber number cases, and a discussion of these fundamental issues is found in §4.7.

In Figure 4.17 we see comparisons between a drop impact experiment conducted in [168], and a BEM simulation conducted with the numerical implementation described in this chapter. The experiment is of a water drop impacting onto a hydrophobically-treated glass surface with an equilibrium contact angle of 180° . The water drop has initial radius $\hat{R}_0 = 1.14\text{mm}$, and impacts the substrate vertically with speed $\hat{U}_0 = 0.35\text{m/s}$, which corresponds to impact Weber number of $We \approx 3.5$. The BEM simulation uses $N = 102$ elements, with a maximum time step of $\tau = 5 \times 10^{-4}$, with nodes redistributed every 50 time steps, and quintic splines employed to approximate the drop boundary. All outputted images from the BEM simulation are for the same time as their experimental counterpart, with $\hat{t} = 0\text{ms}$ corresponding to the moment of contact between drop and substrate.

Across all pairs of images, we see good agreement, with similar drop shapes forming in the BEM simulation as in the experiment. The drop shapes from the experiment are slightly ‘taller’, but this is likely due to the impact in the experiment taking place while the drop is slightly non-spherical, as opposed to a perfect sphere in the simulation.

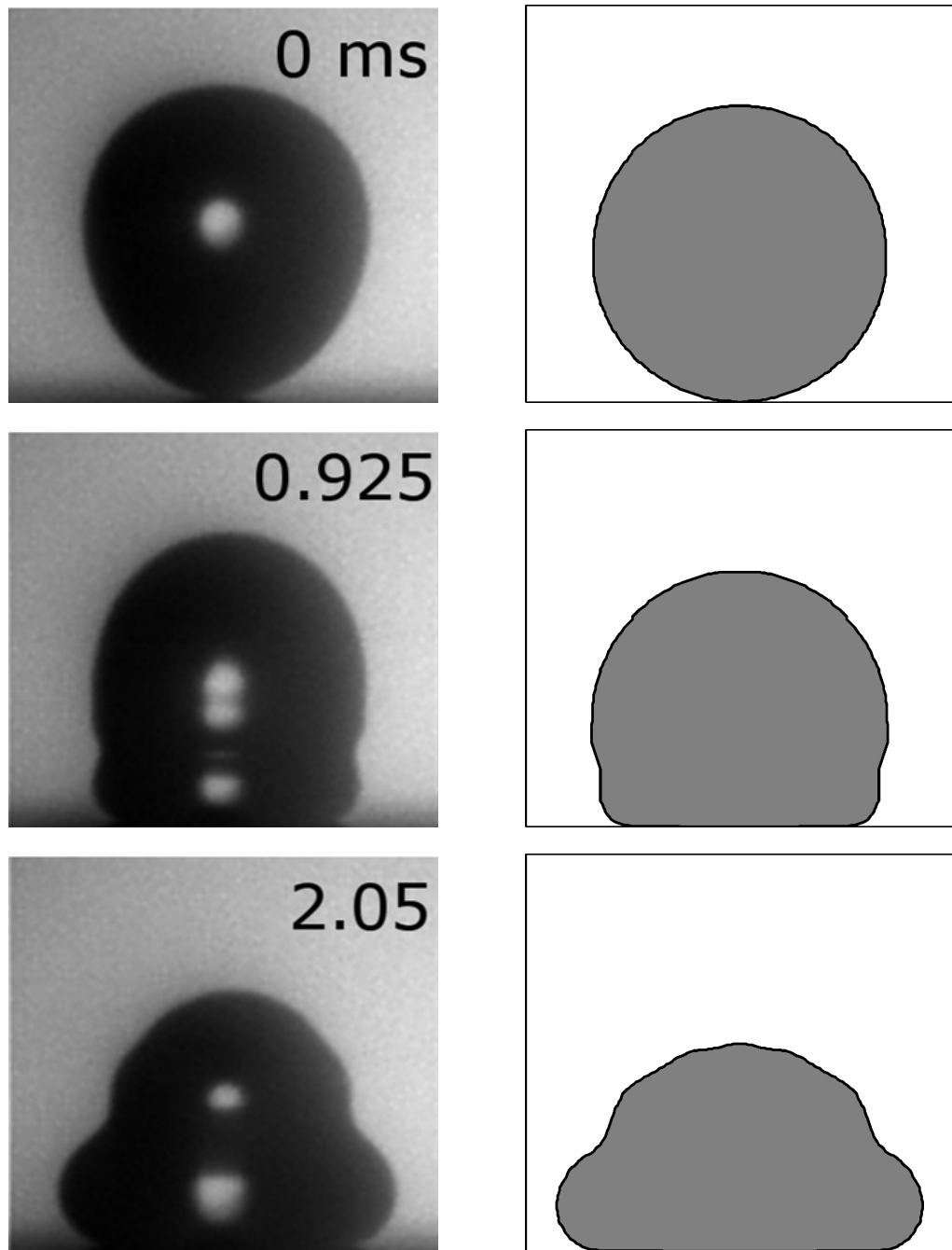


Figure 4.17: Comparison between a drop impact experiment from [168] on a rigid impermeable superhydrophobic substrate (contact angle 180°), and a simulation using our boundary element model, with conditions: $\hat{R}_0 = 1.14\text{mm}$, $\hat{U}_0 = 0.35\text{m/s}$ ($We = 3.5$). Top to bottom, comparisons are made at 0ms, 0.925ms, 2.05ms from the moment of contact between the drop and the solid substrate. The simulation uses $N = 102$ elements, a maximum time step of $\tau = 5 \times 10^{-4}$, with nodes redistributed every 50 time steps, and quintic splines used to approximate the boundary. Figure continues on next page.

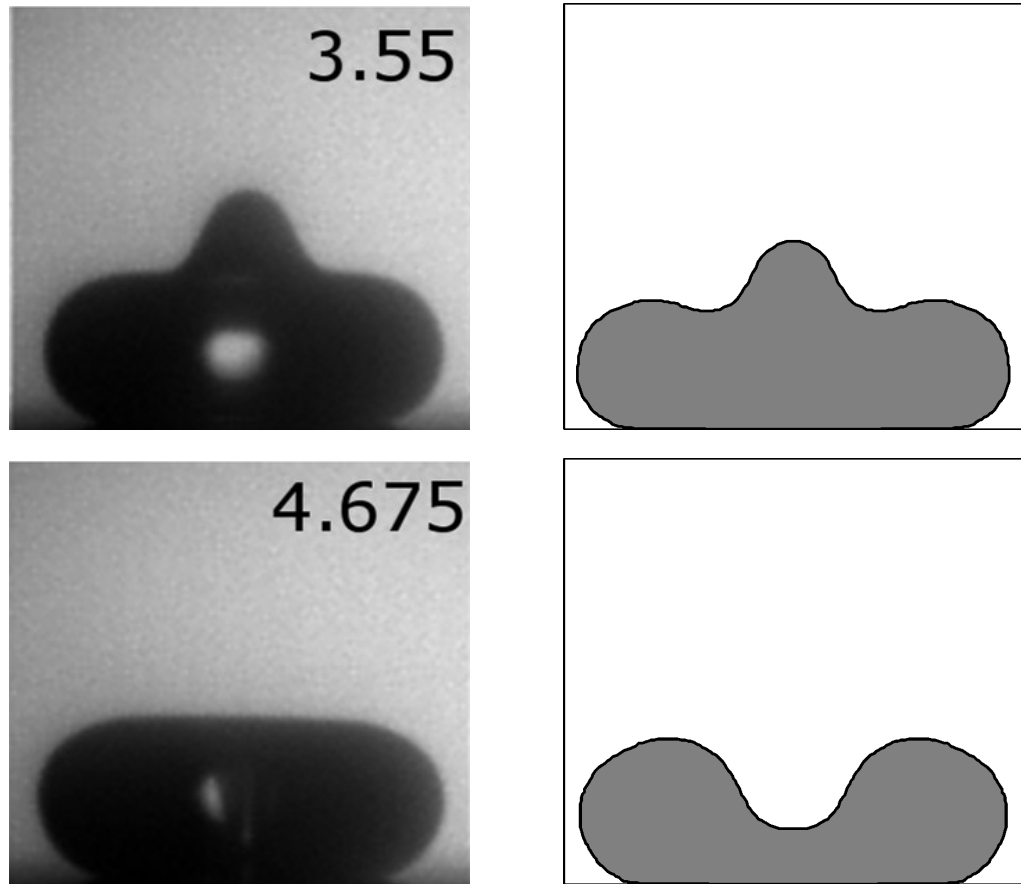


Figure 4.17: (cont) Top to bottom, comparisons are made at 3.55ms, 4.675ms.

Validation: Recreation of the Pyramidal Structure

We provide additional validation of the numerical implementation by comparing to an experiment [127] that exhibits a detailed ‘pyramidal structure’ as surface waves are propagated towards the axis of symmetry during the initial stages of drop impact. The experiment of interest has a water drop with spherical equilibrium radius of $\hat{R}_0 = 1.75\text{mm}$ impacting a superhydrophobic solid surface (contact angle not given) with impact speed $\hat{U}_0 = 0.41\text{m/s}$ which corresponds to impact Weber number of $We = 8$. The drop in the experiment has experienced significant free surface oscillations during free fall, and impacts the substrate with a pronounced non-spherical shape. This shape is approximated within [127] and we use their approximation, which is to suppose an initial shape given by (4.6.6) with $\epsilon = 0.29$. The BEM simulation uses $N = 202$ elements, with a maximum time step of $\tau = 4 \times 10^{-4}$, with nodes distributed every 50 time steps, and quintic splines employed to approximate the drop boundary. All outputted images from the BEM simulation are for the same

time as their experimental counterpart, with $\hat{t} = 0\text{ms}$ corresponding to the moment of contact between drop and substrate.

As shown in Figures 4.18, there is good agreement between the BEM simulation and experiment; in particular the pyramidal ‘steps’ are reproduced with good resemblance to the experiment. The ratio of drop height to drop diameter is also matched well, and the drop shape comparisons when the micro-jet is formed in the experiments at the axis of symmetry is also good; although there is no predicted pinch-off in our simulation, likely due to a lack of resolution in the neck region where extremely large curvatures are generated.

With these two examples, it is clear the numerical implementation of the BEM is capable of accurately reproducing drop impacts at low impact Weber numbers. The next step was to validate the implementation against experiments for higher impact Weber numbers, however in the process of doing this, it became clear that there are fundamental issues with using a BEM and the inviscid model (see §3.2.4) for these cases. The next section discusses what these issues are and how they led to the use of the viscous model (see §3.2.5) with a volume-of-fluid method (see Chapter 5).

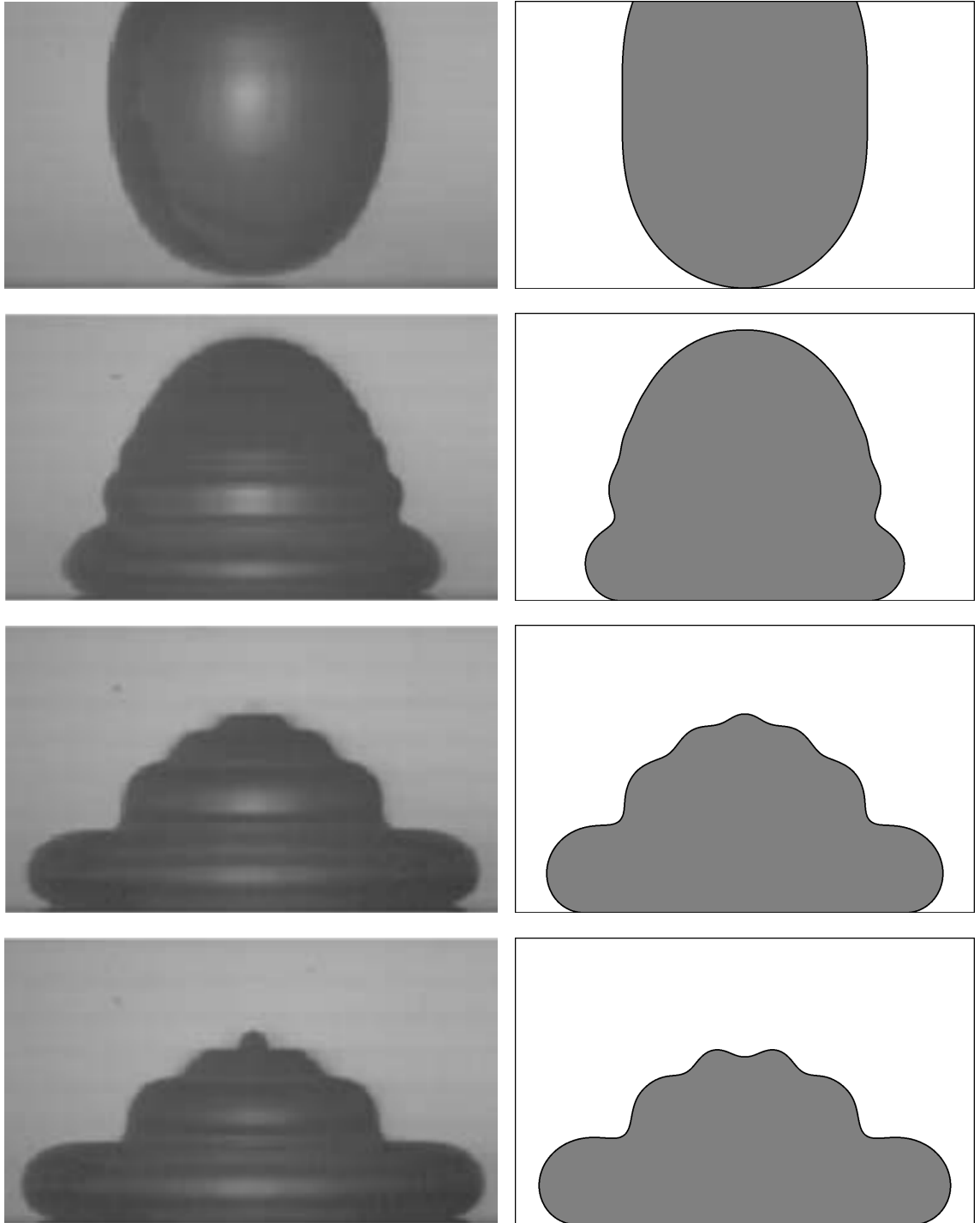


Figure 4.18: Comparison between a drop impact experiment from [127] on a rigid impermeable superhydrophobic substrate, and a simulation using our boundary element model, with parameters: $\hat{R}_0 = 1.75\text{mm}$, $\hat{U}_0 = 0.41\text{m/s}$ ($We = 8.1$). Top to bottom, comparisons are made at 0.0ms, 2.7ms, 4.5ms, 4.9ms. The simulation uses $N = 202$ elements, a maximum time step of $\tau = 4 \times 10^{-4}$, with nodes redistributed every 50 time steps, and uses quintic splines.

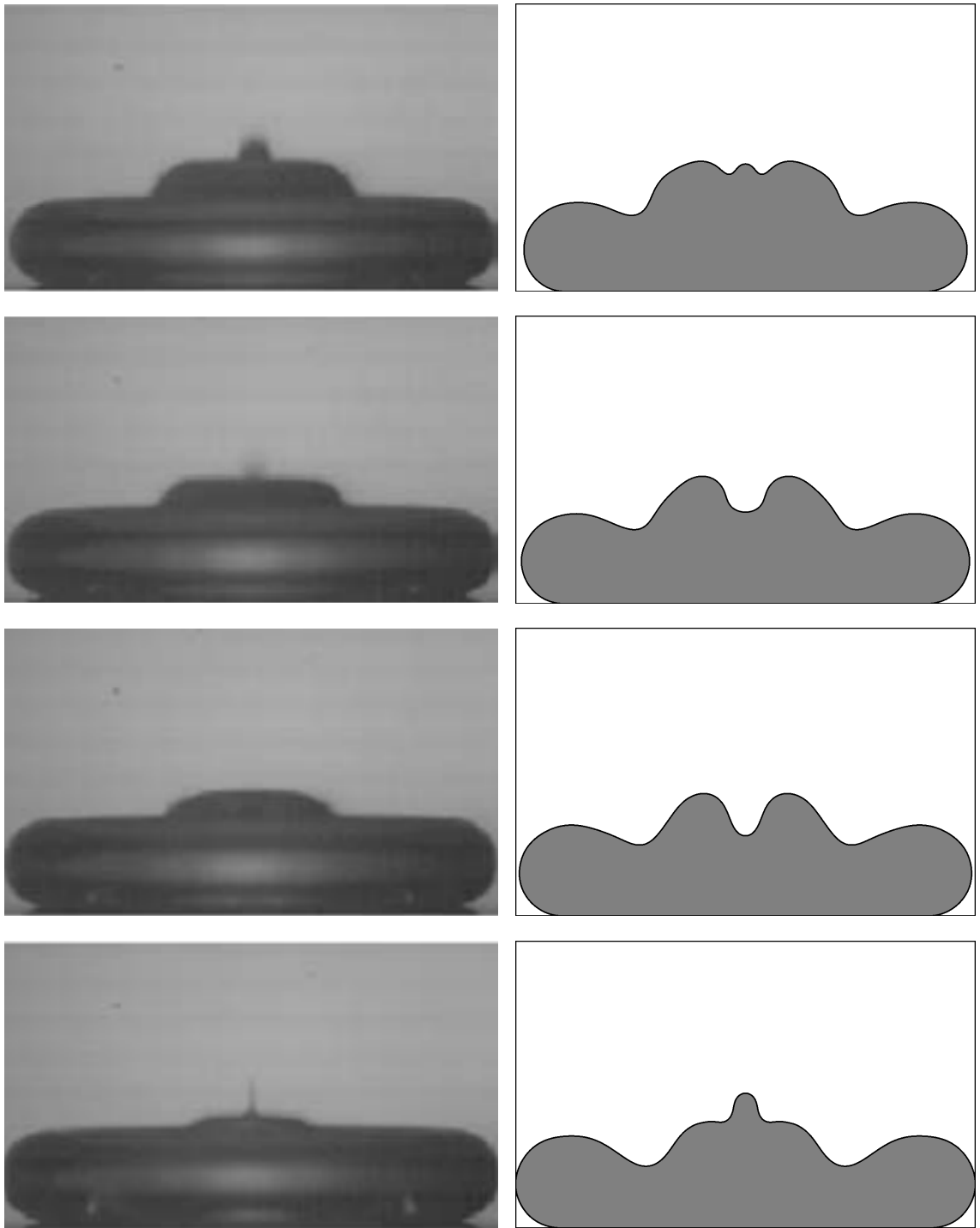


Figure 4.18: (cont) Top to bottom, comparisons are made at 5.9ms, 6.1ms, 6.3ms, 6.7ms. Figure continues on next page.

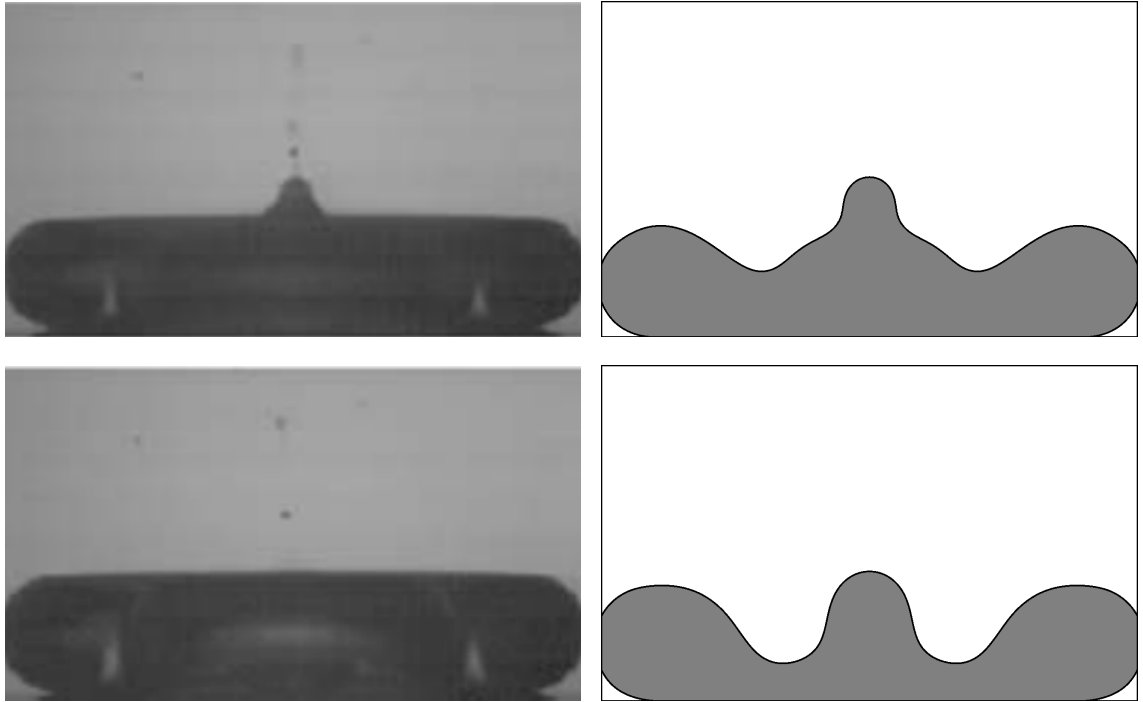


Figure 4.18: (cont) Top to bottom, comparisons are made at 7.1ms, 8.0ms.

4.7 Shortcomings of using the Boundary Element Method and Inviscid Model for Drop Impact

This section is focused on the shortcomings that were discovered when using a BEM to model drop impacts using the inviscid model (see §3.2.4), and how these insurmountable issues led to the development of the viscous model (see §3.2.5), which is implemented numerically using a volume-of-fluid method (see Chapter 5). The discussion of these shortcomings is split into two parts: beginning with topological changes, which pose a problem for BEM simulations as there is no *natural* mechanism to incorporate this phenomenon within a BIM/BEM framework, and then how the assumption of inviscid flow *throughout* the drop leads to unphysical splashing in our simulations.

4.7.1 Physically-Motivated Topological Changes

BEMs do not naturally resolve topological changes; while there may be multiple *distinct* boundaries for a single fluid domain, the merging of multiple boundaries

or division of a single boundary typically cannot occur without intervention. While there are examples of specialist forms of intervention employed to allow simulations to traverse *through* pinch-off events (to be discussed), there is insufficient reporting for all types of topological change we observe in experiments and in our simulations. What follows are three examples of physically-motivated topological changes that have occurred during drop impact simulations using the BEM formulated in this chapter.

Pinch-off of Satellite Droplets

Recall (see §1.1.6 and §3.1) that the focus for this numerical implementation is to simulate liquid marble formation, which occurs as a result of drop impact onto a superhydrophobic powder bed. In our case, we model the powder bed as a rigid impermeable superhydrophobic substrate, and as we have seen from experiments (see Chapter 2), that drop impacts onto both kinds of substrate often result in pinch-off events due to satellite droplet ejection. Provided our simulations did *not* experience the issues yet to be described, it was therefore imperative that a numerical scheme was to be coupled to our BEM implementation to allow simulation *through* pinch-off events.

Fortunately, work has been done on simulating these events in BEM simulations; one example in [169] gives that when the ‘neck’ of a drop reaches a small radius (fixed prior to simulation), the node at this point on the boundary is immediately shifted to the axis of symmetry and the value of the velocity potential at this node is then extrapolated from its value at the neighbouring nodes. The nodes lying on the now-removed portion of the drop boundary are then either placed onto the primary drop or removed entirely from the simulation, with the now-ejected satellite droplet no longer considered computationally. Other examples of BEM simulations evolving *through* pinch-off events include [152, 170–172]. The kind of implementation just described would likely work well as it ultimately involves shifting one of the connections to the axis of symmetry to a new location, with the focus being on how best to estimate the new value of the velocity potential. Clearly then, although incorporating the ejection of satellite drops into our computational model would increase complexity, there are methods known to account for such events.

We will now discuss different forms of topological change that further increase

the complexity of any necessary intervention; the ‘drying-out’ of the drop at the axis of symmetry, and interior bubble formation within the drop, neither of which are well-documented as being modelled with a BEM.

Drying-out at the Axis of Symmetry

As illustrated in Figure 4.19 and discussed in [127], there exist scenarios (typically for low impact Weber numbers) in which water drop impacts onto rigid impermeable superhydrophobic substrates lead to the apparent ‘drying-out’ of the drop at the axis of symmetry. That is, surface waves propagated from the impact with the substrate causing the drop apex to oscillate so strongly that the apex appears to briefly touch the substrate and dry-out completely. Whether or not there still exists a thin film of liquid lying atop the substrate at this point, this is at least an ‘apparent’ topological change (from a sphere to a toroid) that can affect our ability to simulate drop impact, and it must be handled carefully.

Shown in Figure 4.20 is a BEM simulation showcasing this phenomenon, in which the propagation of surface waves from the contact line region causes the drop apex to oscillate and approach the substrate until the node at the drop apex finally touches down (which causes the simulation to crash due to both nodes on the axis of symmetry occupying the same location). For a viscous model, this topological change could be avoided due to what is likely a low effective Reynolds number (and hence non-negligible influence of bulk viscosity) within the thin film region at the axis of symmetry moments prior to dry-out, due to the small local length-scale (much smaller than the drop radius). However, for the inviscid model, viscosity is assumed negligible everywhere and so the dry-out seems unavoidable.

Implementing the dry-out itself is a difficult task; unlike satellite drop ejection which essentially involves moving one of the (two) nodes on the axis of symmetry to a new location, dry-out would require merging both nodes together and simultaneously detaching them from the axis of symmetry. We would also need to create a new spline construction method (now that the boundary is a closed loop away from the axis of symmetry), and populating the matrices in the discretised boundary integral equation (4.5.22) would need extra consideration due to there now being singular integrals at every node (nodes on the axis of symmetry currently experience no singular integrals, see Appendix E). Additional difficulties emerge after such a transition

scheme is implemented, including how re-connection with the axis of symmetry is handled; for example, we would need exactly two nodes to be placed back onto the axis simultaneously and it is unclear what the conditions for such a trigger would be.

So although dry-out is a realistic phenomenon that may occur during drop impact simulations, it would require special care to treat a topological change such as this. We will now discuss a different method of dealing with the dry-out that was attempted, and how this led us to even further numerical complications relating to the formation of an interior bubble.

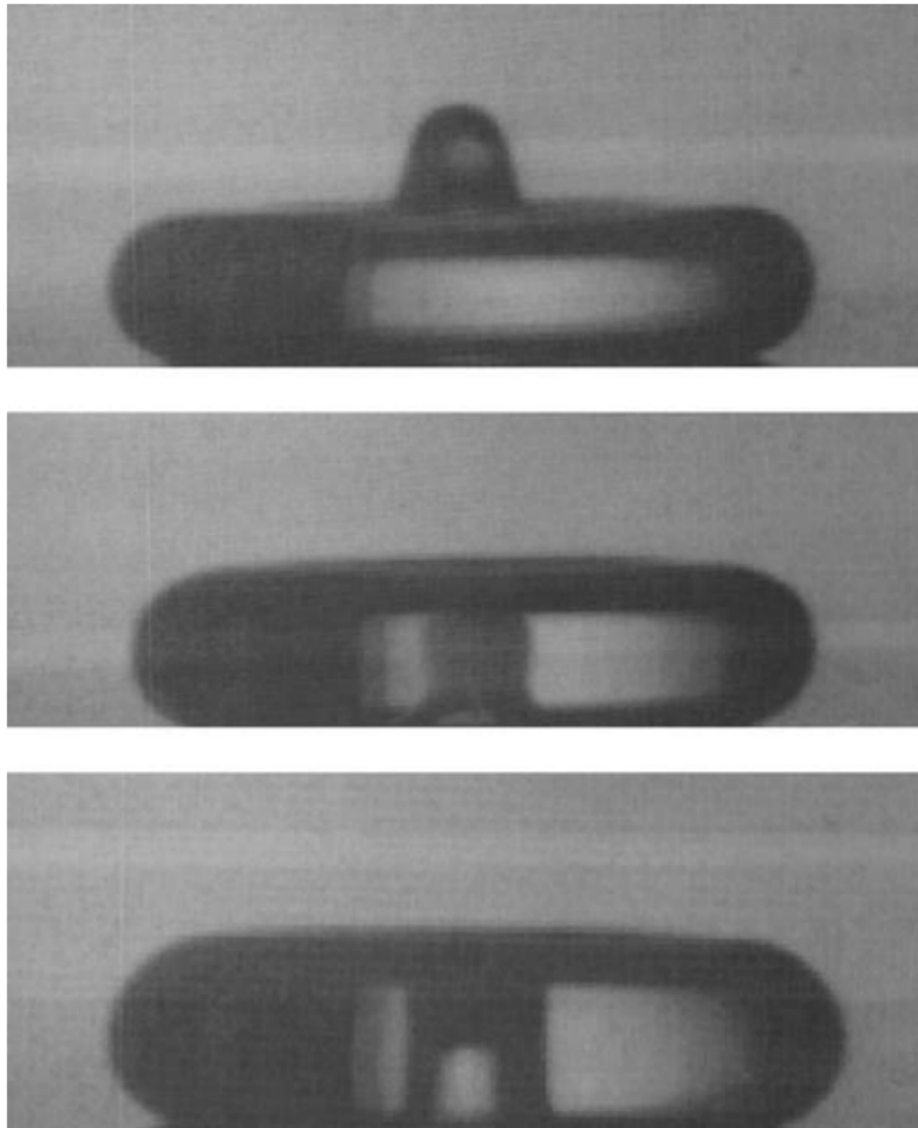


Figure 4.19: Photographs taken from [127] of a (water) drop impact experiment onto a rigid impermeable superhydrophobic substrate, exhibiting drying-out of the drop centre. Top photo shows the earliest time. Initial spherical drop diameter $\hat{D}_0 = 4\text{mm}$, with vertical impact speed $\hat{U}_0 = 0.14\text{m/s}$, and associated impact Weber number $We = 1.1$.

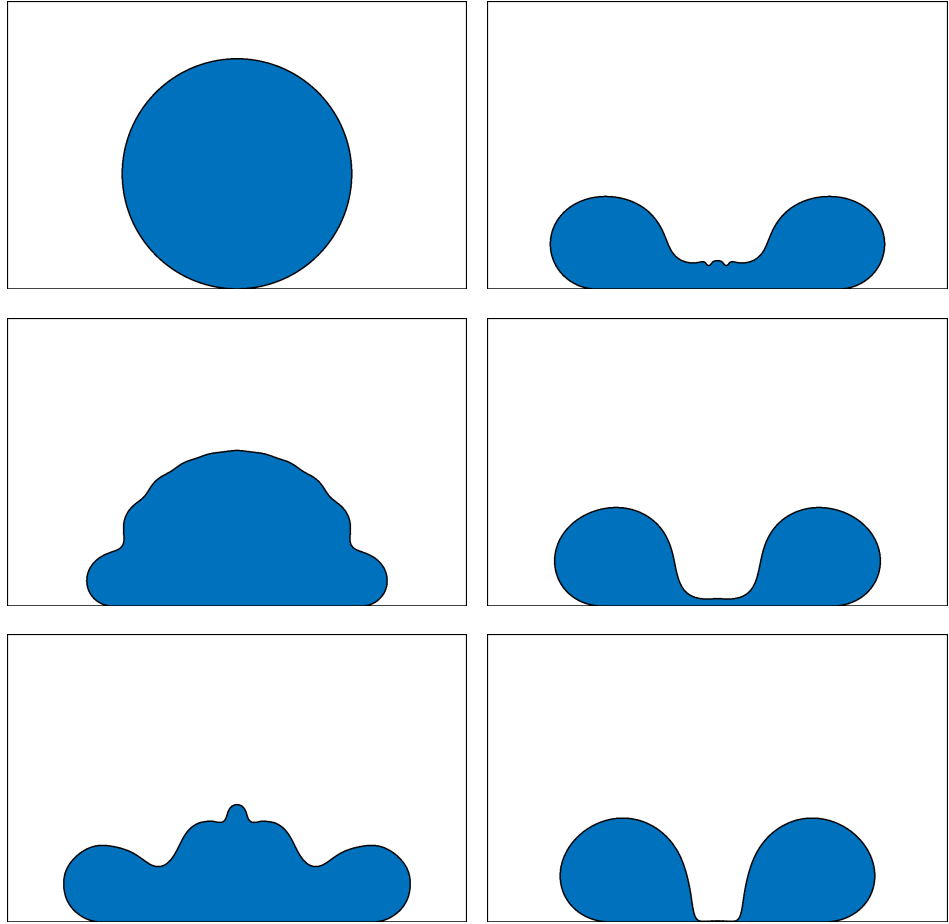


Figure 4.20: BEM simulation exhibiting drying-out of the drop centre, with impact Weber number $We = 6.9$. The simulation uses $N = 302$ elements, a maximum time step of $\tau = 6.25 \times 10^{-5}$, with nodes redistributed every 400 time steps, and cubic splines used to approximate the drop boundary. Drop impacts with a spherical shape (top left), followed by snapshots (middle left) - (bottom left) - (top right) - (middle right), ending with a snapshot moments prior to the centre drying-out (bottom right).

Entrapped Bubble Formation

Given that allowing dry-out to occur is a computational and theoretical difficulty in terms of a BEM implementation, we decided to *stop* it occurring and instead mimic its effects. Recall from equation (3.2.24) that at the drop interface, pressure is given as the effective surface tension σ_{eff} multiplied by the curvature ($\nabla_s \cdot \mathbf{n}$). If we instead consider the following equation for pressure at the interface,

$$p = \sigma_{\text{eff}}(\nabla_s \cdot \mathbf{n}) + \left(\frac{\varepsilon}{Z}\right)^m \quad (4.7.1)$$

where $\epsilon > 0$ is a small constant and with $m \in \mathbb{N}$, then the (new) second term on the right hand side represents a repulsive force that diverges as the axial coordinate Z of the drop's liquid-gas interface goes to zero. Applying this new pressure equation on the drop boundary near its apex should then prevent the drop apex from reaching the substrate. Equation (4.7.1) is then incorporated into the drop dynamics via a modified Bernoulli equation that only holds on the boundary *nearby* the drop apex; this equation is given by

$$\frac{d\phi}{dt} = \frac{1}{2} \left[\left(\frac{\partial\phi}{\partial n} \right)^2 - \left(\frac{\partial\phi}{\partial s} \right)^2 \right] - \sigma_{\text{eff}}(\nabla_s \cdot \mathbf{n}) - gz - \left(\frac{\epsilon}{z} \right)^m. \quad (4.7.2)$$

We hoped that this departure from the pressure equation provided by the inviscid model (3.2.24) would provide minimal deviation from the ‘true’ drop dynamics and resemble experiments where drying-out is believed to occur.

Provided in Figure 4.21 is a BEM simulation incorporating the new Bernoulli equation (4.7.2) in a small region around the apex to avoid dry-out. The initial shape and velocity profile are the same as for the simulation in Figure 4.20 that exhibited dry-out at the axis of symmetry, with details on the mesh size and time stepping given in the caption. As expected, the inclusion of the repulsive term prevents the nodes near the drop apex from reaching the substrate. However as the drop retracts, the drop apex remains *near* the substrate while the ‘rim’ of the drop moves towards the axis of symmetry, with the simulation suggesting the formation of an interior bubble. Although unexpected, this does appear to be realistic as demonstrated in Figure 4.22 where under similar conditions, an interior bubble is formed during a drop impact onto a rigid impermeable superhydrophobic substrate, *after* apparent dry-out of the drop centre [173].

This interior bubble phenomenon poses a challenge of increased difficulty from the drying-out of the drop centre. Given this appears to be a realistic phenomenon, it is unfeasible to try and avoid this formation in a similar manner to the dry-out, and even if this was attempted (also with a repulsive force field, say), it would result in a case-by-case application of a vertical repulsive field to only specific regions of the boundary which would vary across different impact speeds. If somehow a mechanism was introduced to capture the bubble formation by creating a new distinct boundary (the boundary of the bubble) to the bulk drop domain, then this would require *substantial* effort to reformulate the current numerical implementation which *explicitly* relies on there being a single continuous boundary. Furthermore, this ‘boundary-

dividing' process would have to be adaptive and run without intervention, given the possibility of bubble break-up and formation of multiple bubbles.

Fortunately, the apparent drying-out of the drop centre for impacts onto superhydrophobic rigid substrates has only been observed for low speed impacts, with an associated impact Weber number of $We < 15$ [127, 173], so this particular phenomenon is likely avoidable at higher impact Weber numbers. Although the interior bubble was formed *after* the drop centre had dried-out in our simulation, it is not clear whether similar bubbles are formed where dry-out does *not* occur, particularly for high impact Weber number cases. Unfortunately, we were not able to determine whether interior bubbles form during retraction for higher impact Weber number cases, as additional issues arose when considering the spreading phase of the impact for higher impact Weber numbers. These issues are directly related to the bulk drop domain being inviscid and will now be discussed.

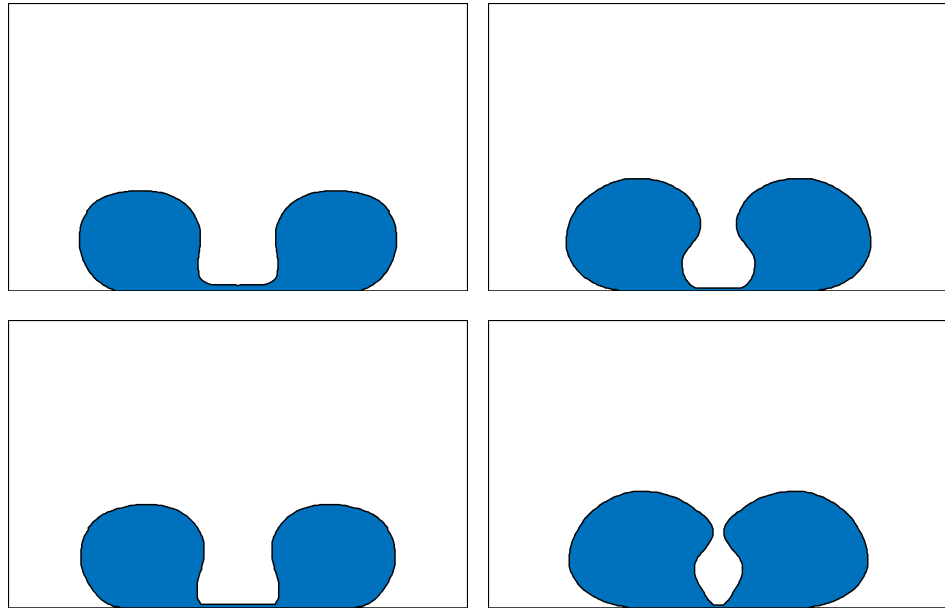


Figure 4.21: BEM simulation with the same initial drop shape and velocity profile as Figure 4.20, with $N = 152$ elements, a maximum time step of $\tau = 5 \times 10^{-4}$, with redistribution every 50 time steps, and quintic splines used to approximate the boundary. An additional term for the surface pressure to stop drying-out of the centre is applied (4.7.1) on the top part of the drop boundary near the axis of symmetry, with $\epsilon = 0.02$ and $m = 4$. The snapshots show (top left) moments prior to drying-out, leading into (bottom left) where the top boundary is prevented from drying-out by the additional force-field term. Then, (top right) the snapshot shows the drop continuing to retract inwards until (bottom right) where the snapshot is taken moments prior to the drop touching the axis of symmetry and trapping an interior gas bubble.

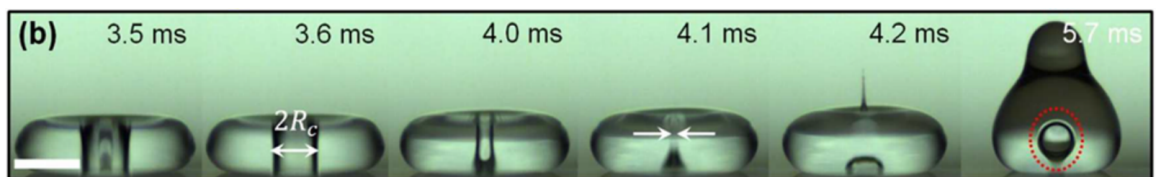


Figure 4.22: Photographs taken from [173] of a (water) drop impact experiment onto a rigid superhydrophobic substrate (contact angle of 161°), exhibiting the trapping of an interior bubble after potential drying-out of the drop centre. Initial spherical drop diameter $\hat{D}_0 = 2\text{mm}$, with vertical impact speed $\hat{U}_0 = 0.58\text{m/s}$, and associated impact Weber number $We = 9.2$. White scale bar on the left-most drop image has length 1mm. Additional markers added by original author.

4.7.2 Unphysical Splashing due to the Inviscid Bulk Flow Assumption

In addition to multiple issues with topological change at low impact Weber numbers due to dry-out and interior bubble formation (which are both physically realistic phenomena), we also observe topological changes for higher impact Weber numbers in the form of splashing. However, splashing in our simulations is observed for *much* lower impact Weber numbers than is seen experimentally in Chapter 2 for impacts onto rigid impermeable superhydrophobic substrates, and in similar experiments in literature.

Shown in Figures 4.23 - 4.24 are two examples of simulations that lead to unphysical splashing; the first with an impact Weber number of $We = 28$ and the second with $We = 43$. By comparison, splashing is not observed in our experiments for impacts onto a rigid impermeable superhydrophobic substrate until $We > 150$ for set A, and for $We > 240$ for set B. Similar works in literature have observed critical impact Weber numbers for splashing following drop impact onto rigid superhydrophobic substrates, each depending on the particular structure of the substrate, but in each case, splashing is seen to occur for $We = \mathcal{O}(100)$. For example, splashing occurs for water drops of millimetre size for $We > 130$ in [174], $We > 180$ in [175], and $We > 320$ in [176]. These results (as well as our own) indicate that we are therefore observing truly unphysical splashing in our BEM simulations.

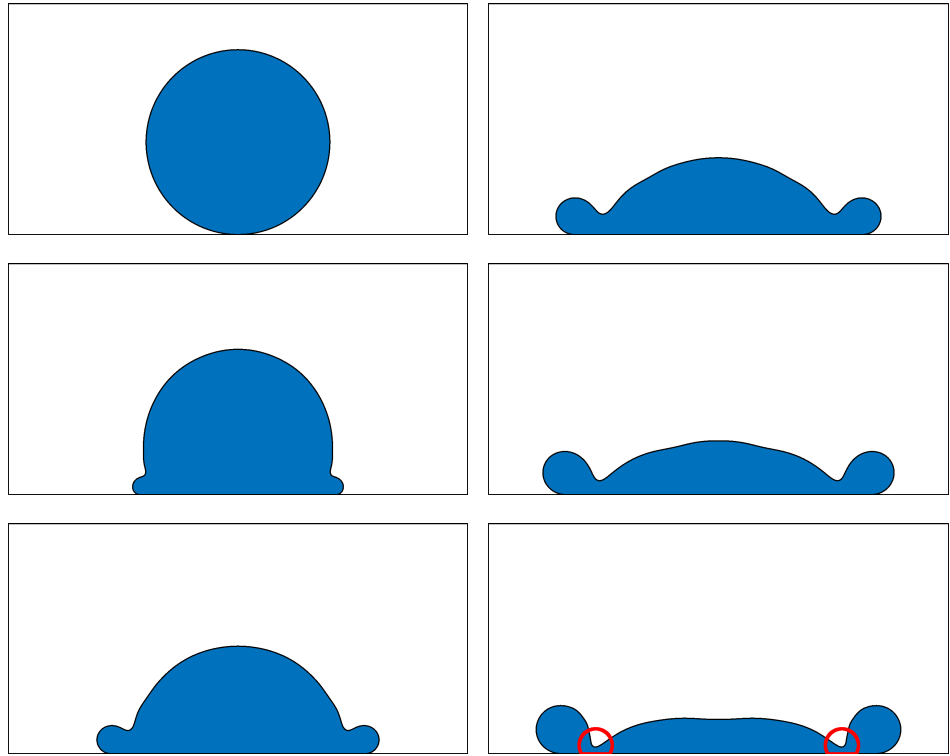


Figure 4.23: BEM simulation exhibiting drop splashing, with impact Weber number $We = 28$. The simulation uses $N = 152$ elements, a maximum time step of $\tau = 5 \times 10^{-4}$, with nodes redistributed every 50 time steps, and quintic splines used to approximate the drop boundary. Order of snapshots is (top left) - (middle left) - (bottom left) - (top right) - (middle right) - (bottom right). The final snapshot is taken moments before the drop splashes with pinch-off highlighted with red circles.

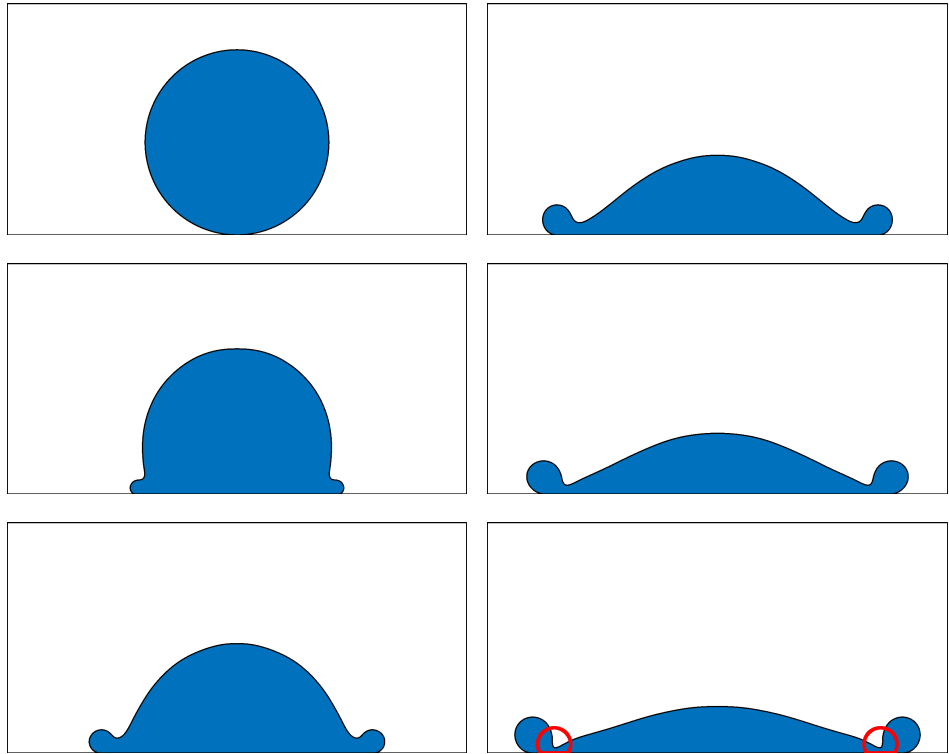


Figure 4.24: BEM simulation exhibiting drop splashing, with impact Weber number $We = 43$. The simulation uses $N = 182$ elements, a maximum time step of $\tau = 1 \times 10^{-4}$, with nodes redistributed every 100 time steps, and quintic splines used to approximate the drop boundary. Order of snapshots is (top left) - (middle left) - (bottom left) - (top right) - (middle right) - (bottom right). The final snapshot is taken moments before the drop splashes with pinch-off highlighted with red circles.

The cause of this appears to be due to bulk drop flow being assumed inviscid *everywhere*. While this inviscid assumption appears to be a valid approximation when considering flow at the length-scale of the initial drop radius \hat{R}_0 (given the impact Reynolds number is typically at least of order $\mathcal{O}(100)$), the films of bulk drop liquid that spread along the solid substrate have their own length-scales (namely their thickness, \hat{h}_{film} say) that are much *much* smaller than the initial drop radius (that is, $\hat{h}_{film} \ll \hat{R}_0$). Part way through the spreading phase, the film thickness approaches the length-scale of the viscous boundary layer in the immediate vicinity of the substrate. When considering a viscous flow, shear stresses in this boundary layer are significant and so are the effects of viscosity, which given the thickness of the film, correspond to an ‘effective’ Reynolds number *much* smaller than at the moment of impact. This increased shear stress then prevents the top interface from

touching the substrate, unless the impact speed is *very* large. By contrast, our model is both inviscid (*and* irrotational, which is necessary for use of the boundary integral method), so any viscous contributions are ignored, and so are any shear stresses; hence there is no mechanism to stop the top interface from further thinning and coming into contact with the substrate (which causes splashing).

At this point the usage of the BEM and inviscid model becomes untenable. The BEM is not naturally suited to topological changes, but owing to techniques developed in literature, pinch-off due to satellite droplet ejection is possible to simulate. However, both the potential for the drop to dry-out and form interior bubbles pose much greater challenges to incorporate into the method. Even if those topological issues were dealt with, the greater challenge comes from the use of the inviscid model itself; the thin liquid films that form as a drop spreads along the solid substrate *cannot* be well-resolved because bulk viscosity is an important parameter within those films and is neglected in the inviscid model. While it may have been possible to re-construct the numerical method to incorporate multiple distinct drop boundaries merging and dividing adaptively, the fundamental assumption of a *global* inviscid bulk drop flow renders us unable to simulate the dynamics within the spreading drop films.

For this reason, the BEM and inviscid model were dropped from consideration and the focus was moved onto the viscous model (see §3.2.5). Whereas the BEM used here was almost-entirely developed for this thesis, subsequent work used a well-documented open-source code that implements a volume-of-fluid method, which is fully capable of running viscous drop impacts and is discussed in Chapter 5. The final section of this chapter is on the numerical validation of the damped nonlinear oscillator model formulated in §3.3 for small amplitude drop oscillations, with subsequent investigations presented related to large amplitude drop oscillations.

4.8 Numerical Investigation of the Damped Non-linear Oscillator Model

We now present a validation of the (novel) damped nonlinear oscillator model formulated in §3.3, by comparing to numerical simulations conducted using the BEM described earlier in this chapter for a suspended inviscid oscillating drop. Addition-

ally, we show that for large amplitude oscillations, which exhibit nonlinear deformations of the interface (and so are outside the scope of the oscillator model), there are qualitative similarities between the behaviour of the drop surface and the effective surface tension as calculated in BEM simulations, and their evaluations in the nonlinear oscillator model for ‘toy’ values of the key parameters.

4.8.1 Validation for Small Amplitude Oscillations

We first compare the evolution of the amplitude $a(t)$ as calculated from equation (3.3.17) against the height of the drop apex for a BEM simulation whereby a suspended inviscid drop is released from rest with initial shape given by (4.6.6) with (small) $\epsilon = 0.05$, for varying λ^s . Figure 4.25 shows a comparison between the damped nonlinear oscillator model and the BEM simulations for values of λ^s small enough that motion is entirely underdamped, and we see that there is good agreement between the two. In Figure 4.26 we show cases for larger λ^s , that exhibit both overdamped and underdamped motion as predicted in the nonlinear oscillator model; as λ^s is increased, we see a slower descent to the radius of the sphere (zero amplitude), with all cases ending up in the underdamped regime with decaying small amplitude oscillations.

In Figure 4.27 we impose (on top of BEM simulations, and solutions to the ordinary differential equation) separately for different values of λ^s , the critical amplitude ‘band’ $[1 - a_c, 1 + a_c]$ (see §3.3 and equation 3.3.19), inside of which the drop is predicted to experience *underdamped* motion, and outside of which the drop is predicted to experience *overdamped* motion. We see the bands accurately bound the size of decaying oscillations that occur during the underdamped motion and effectively ‘trap’ the height of the drop apex once entered. Note that the analytic solution in the overdamped limit (3.3.21) is also overlaid onto the amplitude results in Figure 4.27.

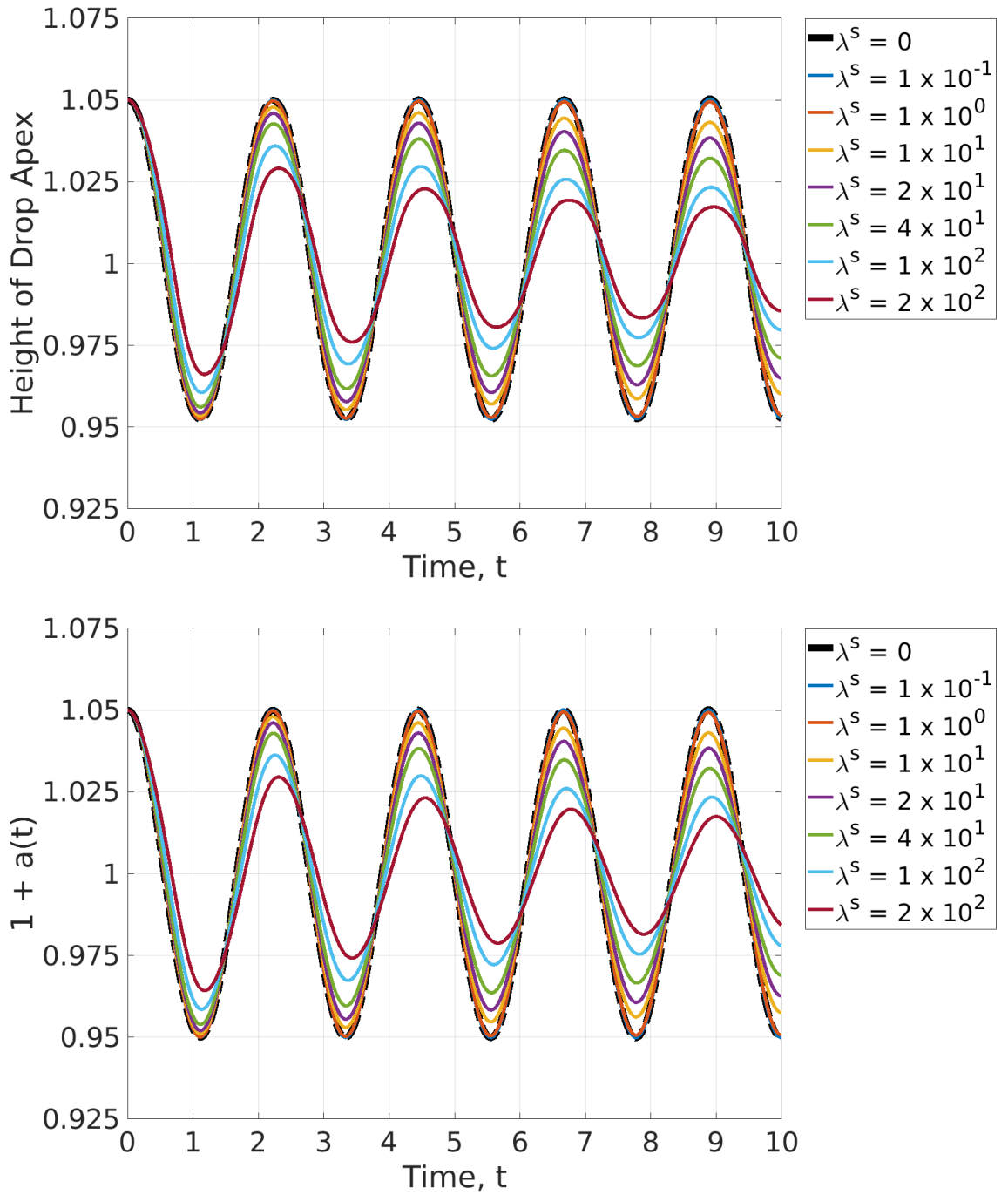


Figure 4.25: *Small amplitude suspended inviscid drop oscillations with small $\lambda^s > 0$ against a damped nonlinear oscillator*: Plots showing, for $\lambda^s = 0$ to $\lambda^s = 2 \times 10^2$ (top) BEM simulations showing the evolution of the height of the drop apex starting from rest with initial shape (4.6.6) with $\epsilon = 0.05$, and (bottom) the solution to the ordinary differential equation (3.3.17) describing a damped nonlinear oscillator, for the amplitude $a(t)$. BEM simulations use $N = 240$ elements, a constant time step of $\tau = 1 \times 10^{-4}$, no redistribution of nodes, and cubic splines approximating the drop boundary.

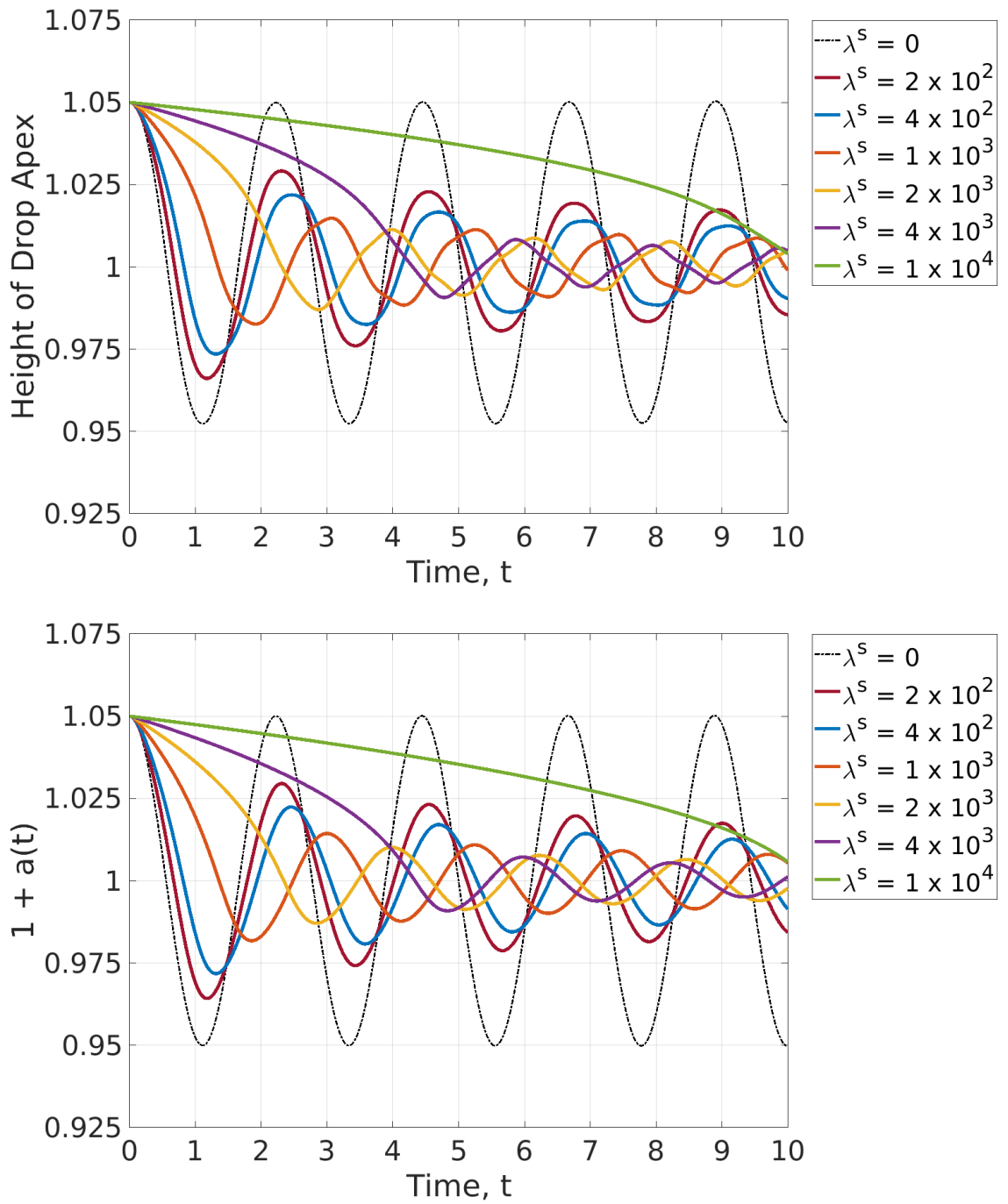


Figure 4.26: *Small amplitude suspended inviscid drop oscillations with large $\lambda^s > 0$ against a damped nonlinear oscillator*: Plots showing, for $\lambda^s = 2 \times 10^2$ to $\lambda^s = 1 \times 10^4$ (top) BEM simulations showing the evolution of the height of the drop apex starting from rest with initial shape (4.6.6) with $\epsilon = 0.05$, and (bottom) the solution to the ordinary differential equation (3.3.17) describing a damped nonlinear oscillator, for the amplitude $a(t)$. Simulation parameters given in the caption of Figure 4.25.

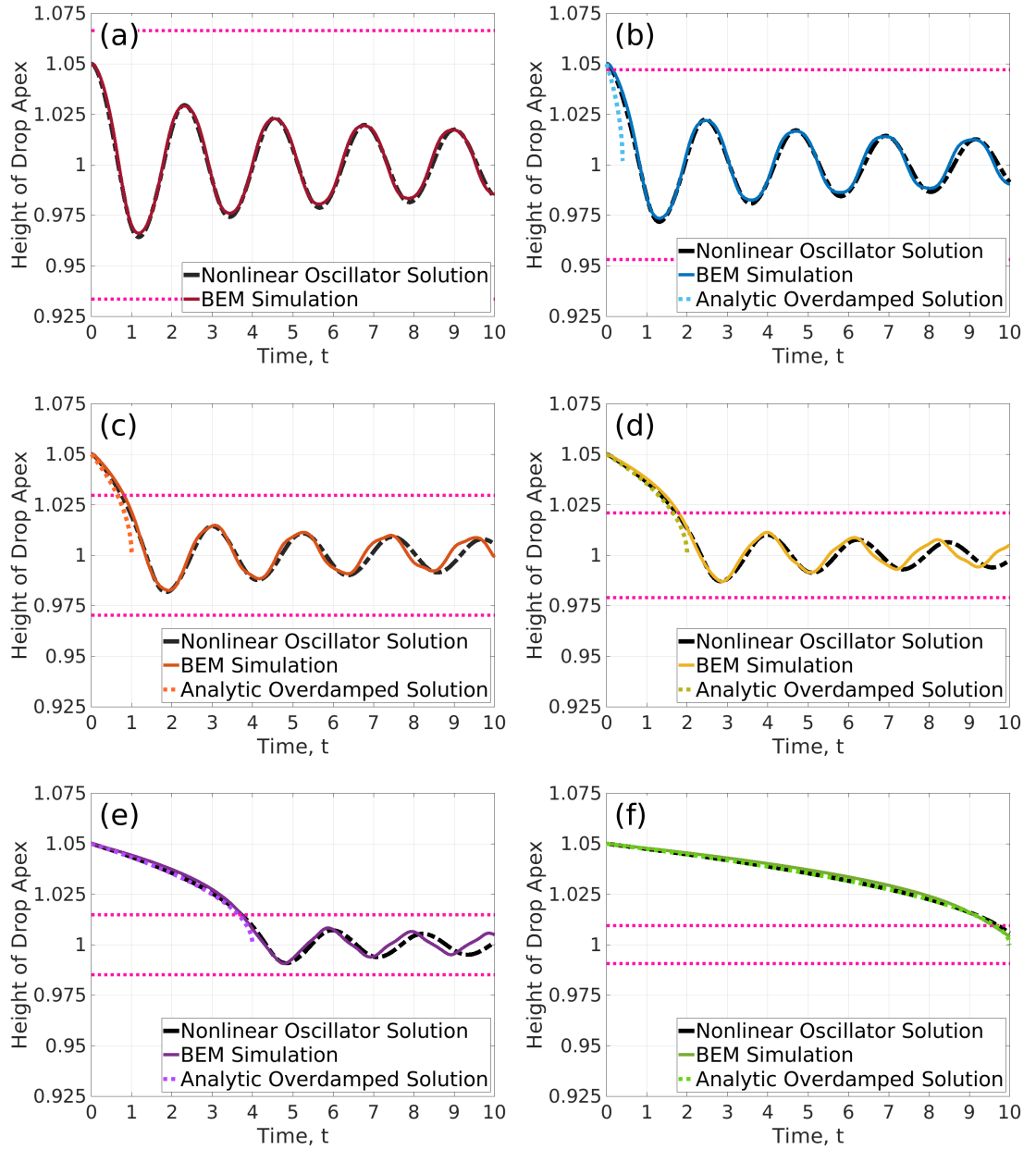


Figure 4.27: *Transition from overdamped to underdamped motion for large $\lambda^s > 0$* : Plots showing the height of drop apex in BEM simulations, overlaid with the solution of the damped nonlinear oscillator (3.3.17), and the analytic solution in the overdamped limit (3.3.21), with pink dotted lines indicating the critical band $[1 - a_c, 1 + a_c]$ inside of which drop oscillations are underdamped, and outside of which drop oscillations are overdamped. Critical amplitude a_c given by (3.3.19). Simulation parameters given in the caption of Figure 4.25. Cases shown are for (a) $\lambda^s = 2 \times 10^2$, (b) $\lambda^s = 4 \times 10^2$, (c) $\lambda^s = 1 \times 10^3$, (d) $\lambda^s = 2 \times 10^3$, (e) $\lambda^s = 4 \times 10^3$, (f) $\lambda^s = 1 \times 10^4$.

Shown in Figures 4.28-4.29 are comparisons between the effective surface tension

and the effective spring constant (recall equation 3.3.16) for the same simulations as just discussed, similarly split into small and large λ^s cases. We see good agreement between the effective spring constant and effective surface tension, particularly for small λ^s , and good results for large λ^s other than the vertical drift that emerges as the simulation progresses. Disregarding the vertical drift for now (discussed shortly), qualitatively the results match well, indicating that once λ^s increases sufficiently as to where a_c is *less* than the initial amplitude a_0 , that further increase of λ^s appears to preserve effective surface tension oscillations, but translates them along the x-axis so that they occur later in time. Shown in Figure 4.30 is the effective surface tension for the damped nonlinear oscillator for the cases with the largest λ^s , with overlaid analytic solutions in the overdamped limit as given by (3.3.23).

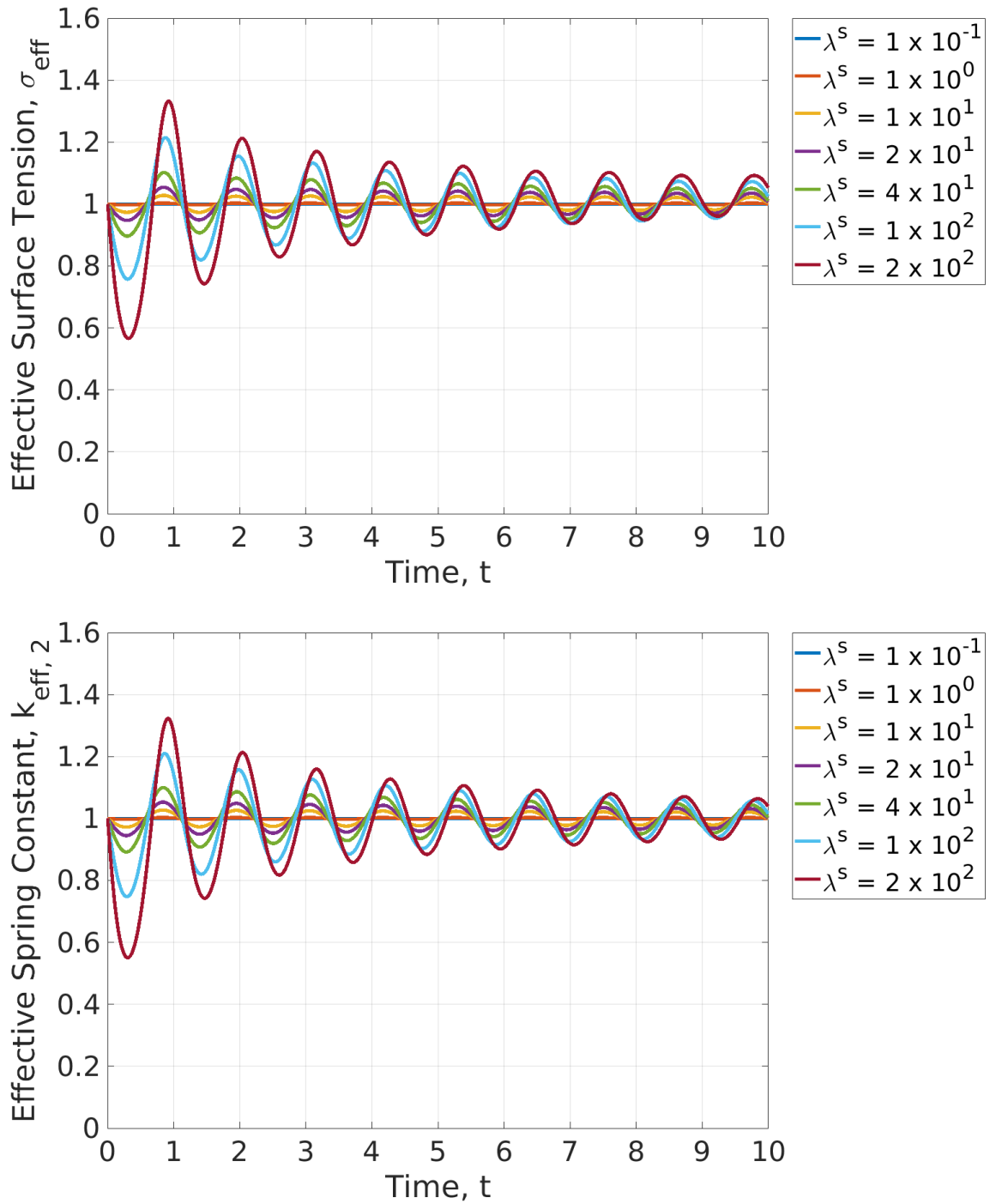


Figure 4.28: *Small amplitude suspended inviscid drop oscillations with small $\lambda^s > 0$ against a damped nonlinear oscillator*: Plots showing, for $\lambda^s = 1 \times 10^{-1}$ to $\lambda^s = 2 \times 10^2$ (top) BEM simulations showing the evolution of the effective surface tension starting from rest with initial shape (4.6.6) with $\epsilon = 0.05$, and (bottom) the effective spring constant (3.3.16) from the damped nonlinear oscillator model. Simulation parameters given in the caption of Figure 4.25.

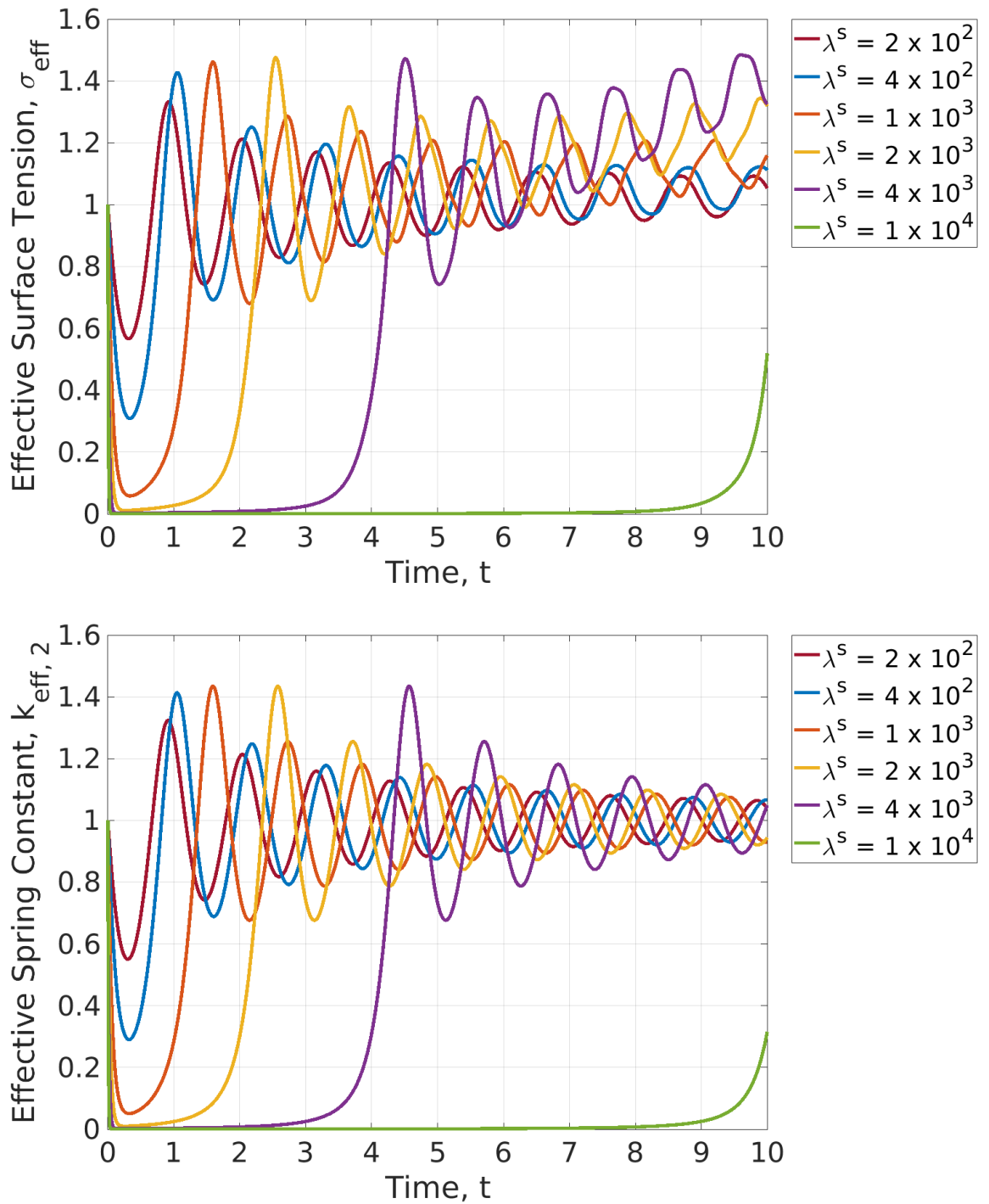


Figure 4.29: *Small amplitude suspended inviscid drop oscillations with large $\lambda^s > 0$ against a damped nonlinear oscillator*: Plots showing, for $\lambda^s = 2 \times 10^2$ to $\lambda^s = 1 \times 10^4$ (top) BEM simulations showing the evolution of the effective surface tension starting from rest with initial shape (4.6.6) with $\epsilon = 0.05$, and (bottom) the effective spring constant (3.3.16) from the damped nonlinear oscillator model. Simulation parameters given in the caption of Figure 4.25.

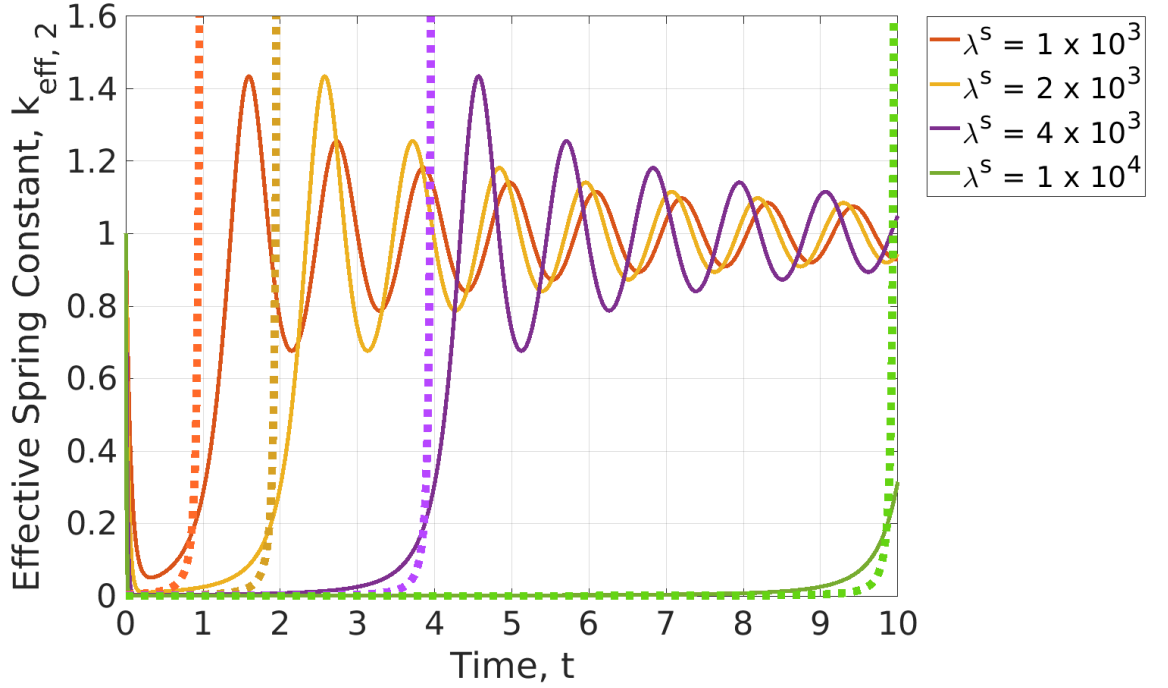


Figure 4.30: *Small amplitude suspended inviscid drop oscillations with large $\lambda^s > 0$ against a damped nonlinear oscillator*: Plot showing, for $\lambda^s = 1 \times 10^3$ to $\lambda^s = 1 \times 10^4$ the effective spring constant (3.3.16) from the damped nonlinear oscillator model overlaid with the analytic solution to the effective surface tension in the overdamped limit (3.3.23), given by dotted lines of similar colour.

We will now discuss why the vertical drift occurs in the BEM simulations in Figure 4.29, and how it can be diminished with mesh refinement, as to then validate the oscillator model. Recall that the effective surface tension is given as $\sigma_{\text{eff}} = 1 + W(t)$ (3.2.23) and also recall the integral representation of $W(t)$ (3.2.28), repeated here for the case of a constant λ^s :

$$W(t) = \lambda^s \frac{\int_{\mathcal{S}} (\nabla_s \cdot \underline{\mathbf{n}}) (\underline{\mathbf{u}} \cdot \underline{\mathbf{n}}) \, dS}{\int_{\mathcal{S}} 1 \, dS}.$$

This ratio of integrals constitute the mean (recall 4.2.8) of the integrand in the numerator integral. Therefore, the vertical drift in the effective surface tension as seen in Figure 4.29 is likely due to a similar drift in the mean of the integrand. This can either be due to spurious waves forming at the interface (affecting both curvature $\nabla_s \cdot \underline{\mathbf{n}}$ and normal velocity $\underline{\mathbf{u}} \cdot \underline{\mathbf{n}}$), or due to numerical errors in solving the boundary integral equation (affecting just the normal velocity $\underline{\mathbf{u}} \cdot \underline{\mathbf{n}}$), a mix of the two, or something else entirely.

We hypothesise that this is due to numerical errors in calculating $\underline{\mathbf{u}} \cdot \underline{\mathbf{n}}$ that result

in a *mean* normal velocity of the interface that is nonzero, and will show why this is believed to be the case. Note that if the mean normal velocity *is* drifting from zero (in either direction), we must have

$$\langle \underline{\mathbf{u}} \cdot \underline{\mathbf{n}} \rangle = \frac{\int_S \underline{\mathbf{u}} \cdot \underline{\mathbf{n}} \, dS}{\int_S 1 \, dS} \neq 0, \quad (4.8.1)$$

where $\langle \cdot \rangle$ denotes the arithmetic mean (recall 4.2.8). Given that the oscillation amplitudes currently under consideration are small, we approximate the curvature as being the curvature of a sphere with (dimensionless) radius R_{sph} , namely as $2/R_{\text{sph}}$. Note however that while $R_{\text{sph}} = 1$ initially, if the mean normal velocity at the interface is *not* zero, then the drop volume must also be changing because of the following relationship with bulk compressibility

$$\int_{\Omega} \nabla \cdot \underline{\mathbf{u}} \, dV = \int_S \underline{\mathbf{n}} \cdot \underline{\mathbf{u}} \, dS,$$

which holds by the divergence theorem. Given this, we calculate R_{sph} as a function of (the evolving) volume of the spherical drop, that is with

$$R_{\text{sph}} = \left(\text{Volume} \cdot \frac{3}{4\pi} \right)^{1/3}. \quad (4.8.2)$$

Therefore, we approximate $W(t)$ (denote the approximation by $\bar{W}(t)$) as the following

$$W(t) \approx \bar{W}(t) = \frac{2\lambda^s}{R_{\text{sph}}} \langle \underline{\mathbf{u}} \cdot \underline{\mathbf{n}} \rangle. \quad (4.8.3)$$

To clarify, (4.8.3) is an approximation for the *drift* in $W(t)$ and omits the oscillations.

In Figure 4.31, we see $W(t)$ plotted for three large values of λ^s , with overlaid lines showing the value of $\bar{W}(t)$ as calculated by (4.8.3). The drift seen in $W(t)$ is likewise observed for $\bar{W}(t)$, indicating that this was a reasonable approximation to make and importantly that errors in calculating $\underline{\mathbf{u}} \cdot \underline{\mathbf{n}}$ do *seem* to be causing this drift to occur. Fortunately, also shown in Figure 4.31 is signs of convergence towards oscillation around $\sigma_{\text{eff}} = 1$ as the mesh is refined (with increased number of nodes N).

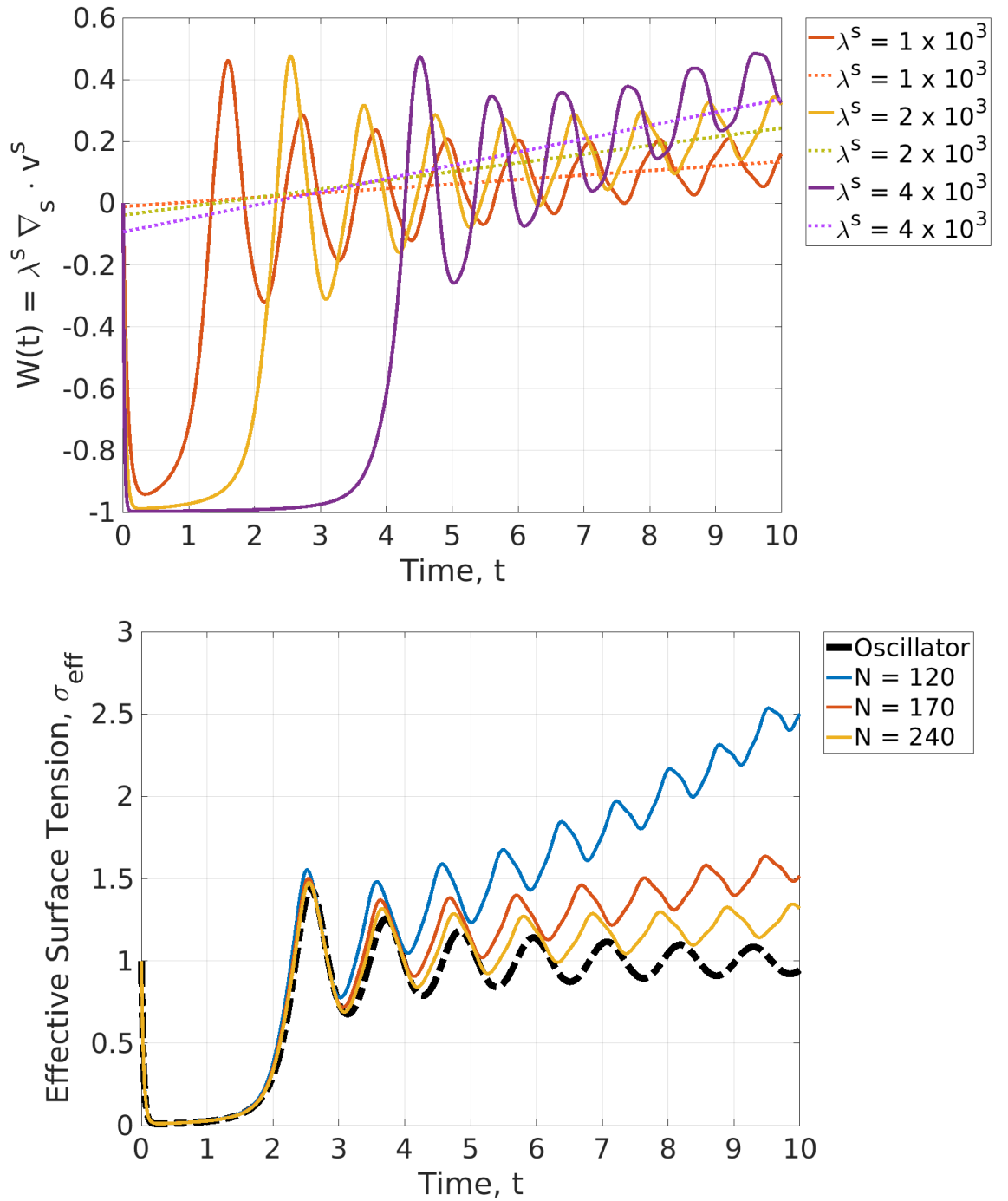


Figure 4.31: *Drift in effective surface tension for small amplitude suspended inviscid drop oscillations with large $\lambda^s > 0$* : Plots showing, (top) for $\lambda^s = 1 \times 10^3, 2 \times 10^3, 4 \times 10^3$, the surface viscous term $W(t) = \sigma_{\text{eff}} - 1$ with data taken from Figure 4.29 with imposed dotted lines indicating $\bar{W}(t)$ (4.8.3), and (bottom) spatial convergence of the effective surface tension to the damped nonlinear oscillator solution with $N = 120, 170, 240$, and $\lambda^s = 2 \times 10^3$. BEM simulation the same as described in the caption of Figure 4.25, with differing N .

4.8.2 Large Amplitude Oscillations

Given our model accurately predicts the damping behaviour of small amplitude dilatational surface viscous oscillations, we now turn to simulating large amplitude oscillations and similarly varying λ^s and noting its effects. Given the ordinary differential equation for the damped nonlinear oscillator (3.3.17) was derived for small amplitude (linear) oscillations, it will not apply to the following case, as the dynamics are nonlinear and excite multiple modes of oscillation. However, the case we consider exhibits a particular dominant harmonic mode, so we provide evaluations of the damped nonlinear oscillator (3.3.17) that are chosen to best match the visual evolution of the height of the drop apex in order to provide qualitative insight into the dynamics. We then compare the transitions from overdamped to underdamped motion, and how the effective surface tension compares to the effective spring constant.

We consider drops starting from rest with initial shape given by (4.6.6) with $\epsilon = 0.5$. It is important to note that this initial shape does *not* have the same volume as the unit sphere, and so therefore does *not* have an equilibrium radius of unity. Ultimately this is not important to the dynamics shown here as this study is qualitative in focus; but this is why oscillations of the drop height are not centred at unity. As for the small amplitude cases, the dilatational surface viscous coefficient λ^s is taken to be a nonzero constant *everywhere* on the drop interface \mathcal{S} with $\lambda^s = 1 \times 10^{-2}$ to $\lambda^s = 1 \times 10^3$. For all simulations, there is *no* redistribution of nodes (so energy decay is primarily due to surface viscous effects), a maximum time step of $\tau_{max} = 1 \times 10^{-4}$ is used at the beginning of all simulations, with enforced time-bounds (4.5.35) and (4.5.36) reducing the time step where appropriate (see §4.5.5). Simulations are run up to $t = 10$, and cubic splines are used to approximate the drop shape.

To make comparisons of the large amplitude oscillations to a damped nonlinear oscillator, we utilise our model (3.3.17) to motivate a ‘toy’ ordinary differential equation for the amplitude $a(t)$:

$$\frac{d^2a}{dt^2} = -2\gamma\omega_0a\frac{da}{dt} - \omega_0^2a, \quad (4.8.4)$$

where ω_0 is chosen to match the oscillation frequency of the clean drop, and γ is chosen so that the time and amplitude of the first local minimum in the height of the

drop apex matches (as best we can) those same quantities for a particular λ^s . This is used to match the large amplitude dynamics *qualitatively* and the values chosen for ω_0 and γ have no analytical relation to quantities from the BEM simulations.

As with the small amplitude oscillations, we separate simulations that exhibit a transition between overdamped and underdamped motion (large λ^s) from purely underdamped oscillations (small λ^s). In Figure 4.32, we show a plot for the height of the drop apex for BEM simulations that appear to exhibit solely *underdamped* motion, and a plot for the amplitude $a(t)$ using the toy model (4.8.4) with parameters chosen to best match the dynamics of the former. In this, we see that the clean BEM simulation ($\lambda^s = 0$) exhibits a fairly stable oscillation, albeit with nonlinearities causing small-scale fluctuations. As λ^s increases to 1, we see drop oscillations decay and the lower amplitude oscillations exhibit a different angular frequency from the clean case (as is expected for underdamped motion). For $\lambda^s = 10$, there is a short delay before the drop oscillations quickly decay to much lower amplitudes, which is *not* exhibited by the ‘equivalent’ case in the damped nonlinear oscillator, and is an early suggestion of the disparity between (initially) large and small amplitude oscillations. Generally, the damped nonlinear oscillator (with appropriately chosen parameters) provides a good qualitative description of large amplitude oscillations.

We now turn our attention to the effective surface tension and effective spring constant (see Figure 4.33). As λ^s is increased, we see larger amplitude oscillations in the effective surface tension as was observed in the small amplitude case, except with pronounced differences with the damped oscillator due to coupling between modes. There is some agreement between the two however as the oscillation frequency is similar between the $\lambda^s = 1 \times 10^1$ and $\gamma = 1 \times 10^0$ cases.

Of greater note is the behaviour of the total energy (kinetic energy plus surface energy) as λ^s is increased. Figure 4.34 shows the total energy and also the (theoretical) energy decay rate (as calculated with equation 4.6.7). For $\lambda^s = 1 \times 10^{-2}, 1 \times 10^{-1}$, the total energy stays roughly constant, as one may expect given almost no change in drop height amplitude over the course of the simulation. For $\lambda^s = 1 \times 10^0, 1 \times 10^1$, we see large energy decays, with the rate of energy decay increasing as λ^s is increased. This behaviour for the total energy is consistent with the critical amplitude (given for small amplitude oscillations by equation 3.3.19) approaching the initial amplitude of the drop height as it correlates to critical damping of drop oscillations. As an ad-

ditional confirmation for the faster loss of drop energy, we see the theoretical energy decay rate increase between $\lambda^s = 1 \times 10^0$ and $\lambda^s = 1 \times 10^1$ in the initial stages of the dynamics.

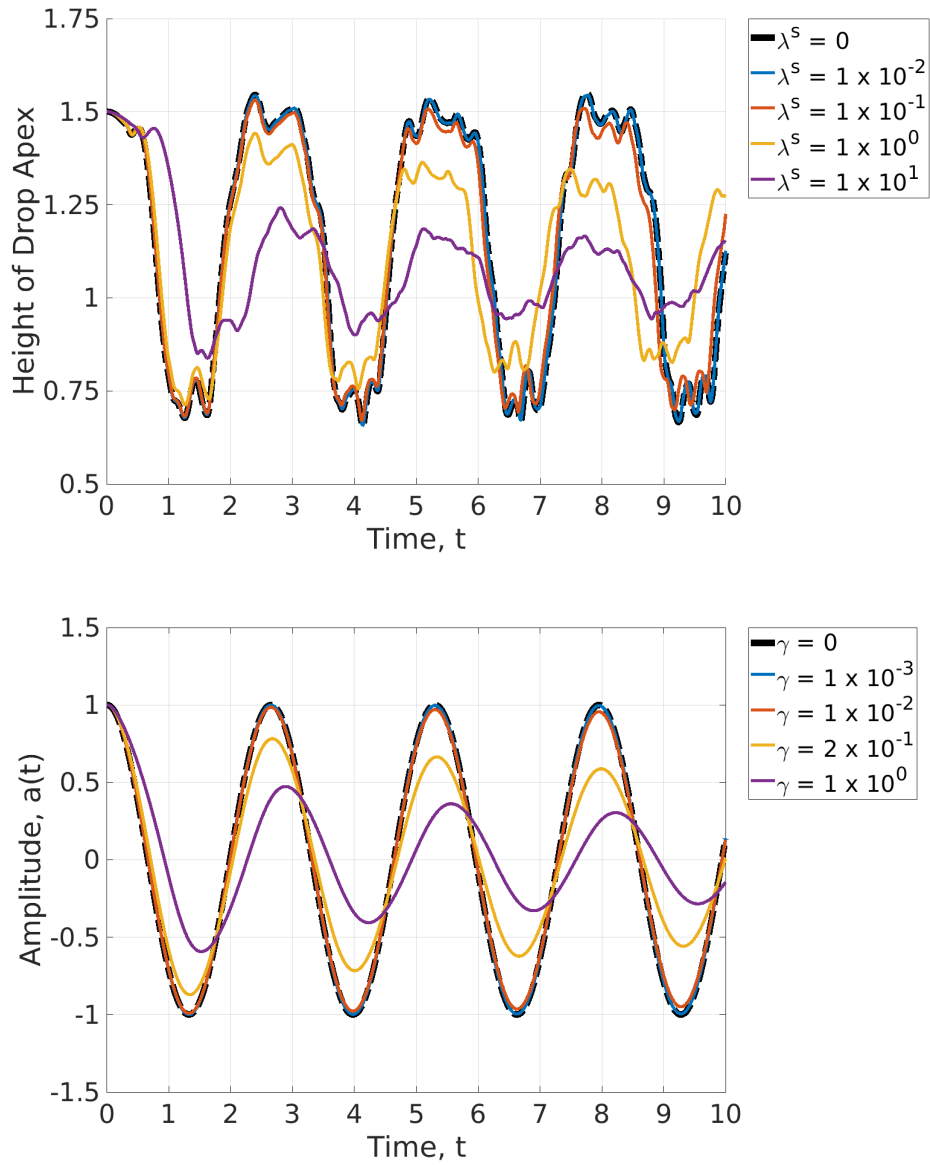


Figure 4.32: *Large amplitude suspended inviscid drop oscillations with small $\lambda^s > 0$ against a toy damped nonlinear oscillator*: Plots showing, for $\lambda^s = 0$ to $\lambda^s = 1 \times 10^1$ (top) BEM simulations showing the evolution of the height of the drop apex starting from rest with initial shape (4.6.6) with $\epsilon = 0.5$, and (bottom) the solution to the toy damped nonlinear oscillator model (4.8.4), for the amplitude $a(t)$, with γ chosen to maximise resemblance to the BEM simulations. BEM simulations use $N = 240$ elements, a constant time step of $\tau = 1 \times 10^{-4}$, no redistribution of nodes, and cubic splines approximating the drop boundary.

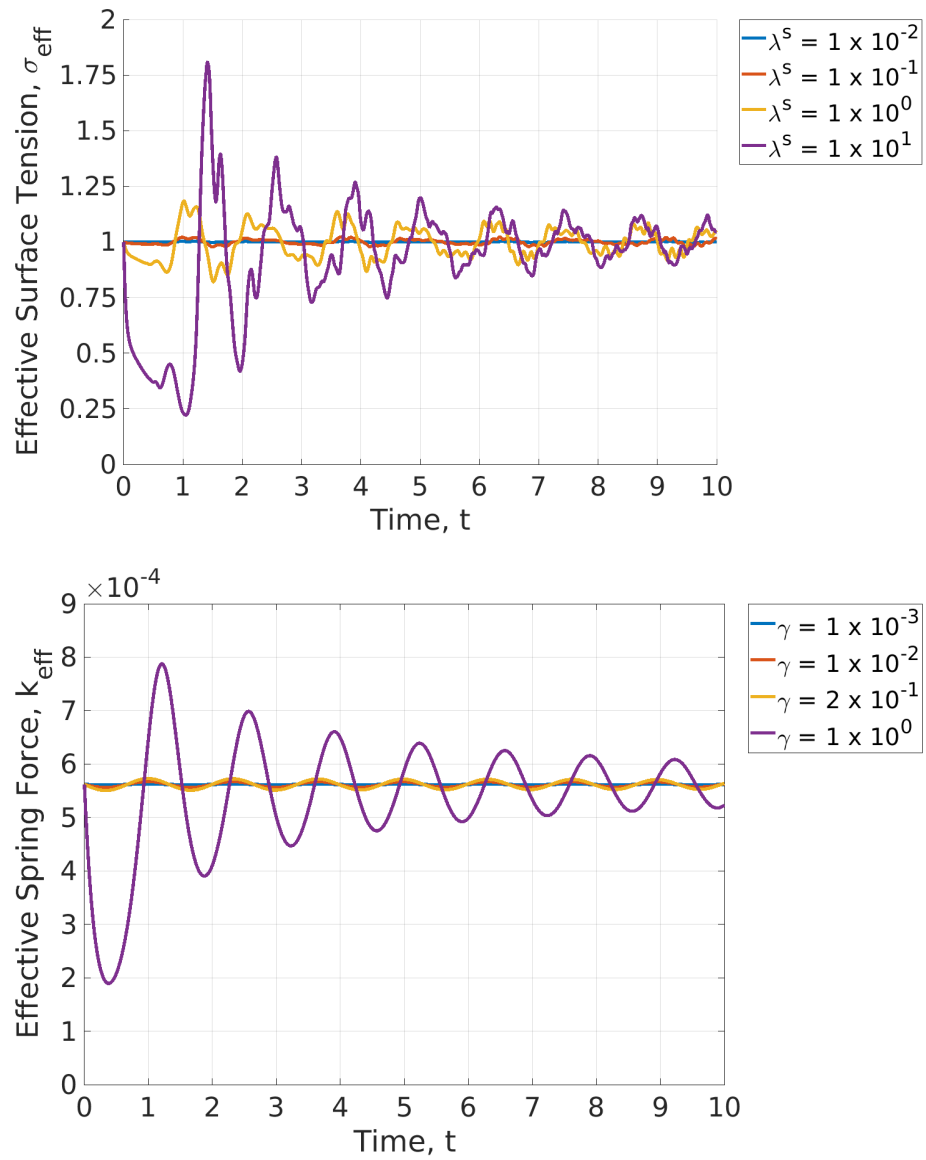


Figure 4.33: *Large amplitude suspended inviscid drop oscillations with small $\lambda^s > 0$ against a toy damped nonlinear oscillator:* Plots showing, for $\lambda^s = 1 \times 10^{-2}$ to $\lambda^s = 1 \times 10^1$ (top) BEM simulations showing the evolution of the effective surface tension starting from rest with initial shape (4.6.6) with $\epsilon = 0.5$, and (bottom) the effective spring constant (3.3.16) from the damped nonlinear oscillator model. Simulation parameters given in the caption of Figure 4.32.

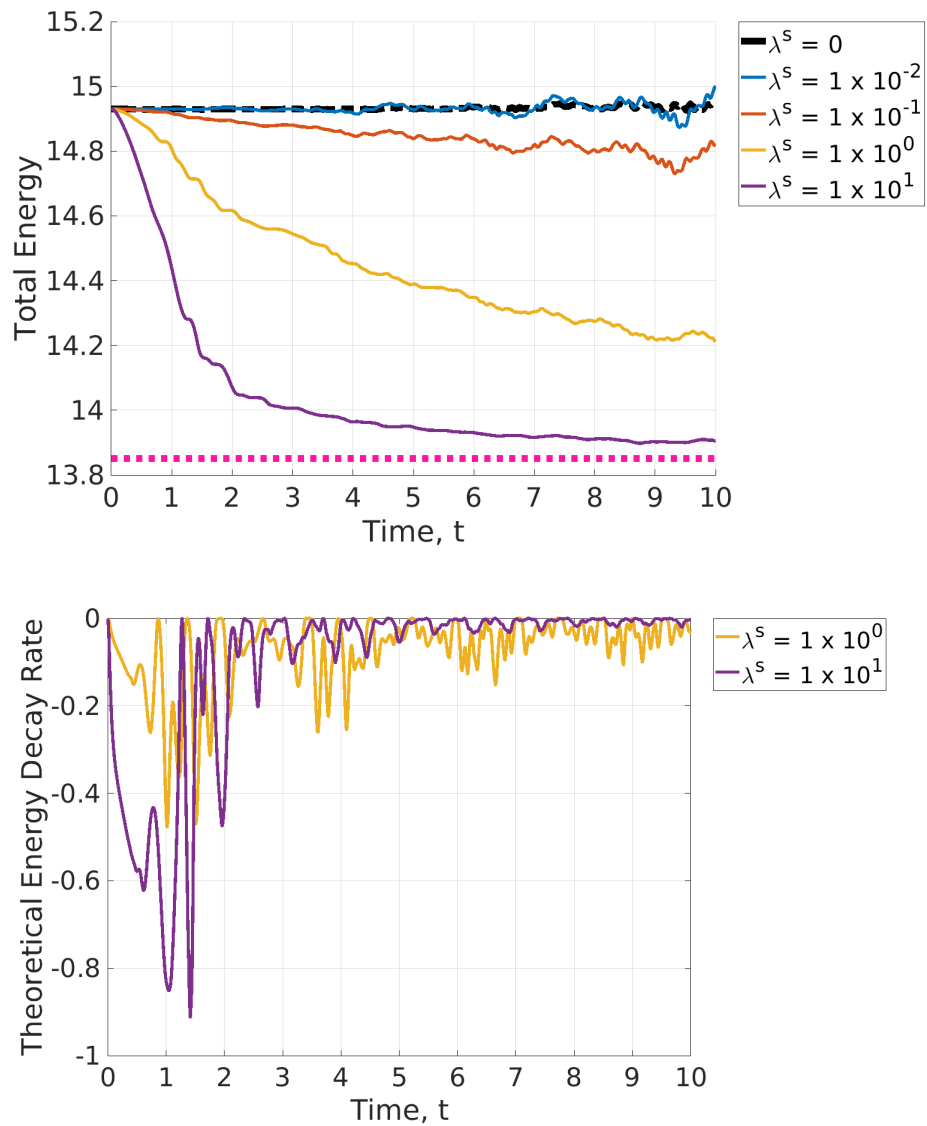


Figure 4.34: Plots showing, for BEM simulations with parameters given in the caption of Figure 4.32: (top) for $\lambda^s = 0$ to $\lambda^s = 1 \times 10^1$, total drop energy, in which the pink dotted line corresponding to zero kinetic energy and the surface energy attained at a sphere (the minimum surface energy state) and (bottom) for $\lambda^s = 1 \times 10^0, 1 \times 10^1$ the theoretical energy decay rate as calculated with (4.6.7).

For the larger λ^s cases, that exhibit *both* underdamping and overdamping, the transition to lower amplitude oscillations is more abrupt than for the small amplitude case (see Figure 4.35), with the initial trajectory of the height of the drop apex being almost linear until dramatically falling to the lower amplitude. This is in contrast to the toy damped nonlinear oscillator (4.8.4) which exhibits a smoother descent to smaller amplitude oscillations.

For the effective surface tension (see Figure 4.36), we see qualitatively similar behaviour again in the large amplitude case as seen with the small amplitude case, whereby an increase in λ^s (or γ for the nonlinear toy oscillator) shifts the oscillations to a later point in time. Similar to the evolution of the drop height (and unlike the effective spring constant), the increase of the effective surface tension from its lowest point up to unity (or nearby) is *not* sinusoidal, likely due to nonlinear effects in the form of the simultaneous excitation of multiple harmonic modes.

With regards to the total energy (see Figure 4.38), we see that the energy experiences a slower decay as λ^s is increased past a critical threshold, as one should expect for an overdamped system. The total energy decay appears to be linear in time, until the total energy approaches the surface energy of the sphere (the lowest surface energy state). This is confirmed in the theoretical energy decay rate plot (see Figure 4.39) whereby large values of λ^s correspond to an apparent convergence to a linear energy decay rate for the course of the simulation.

The next chapter returns to the primary focus of this thesis, which is liquid marble formation via drop impact onto a superhydrophobic powder bed. It introduces the volume-of-fluid method, which is the numerical scheme used to solve the viscous model for liquid marble formation presented in §3.2.5. The simulations presented in this section on large amplitude drop oscillations experiencing (dilatational) surface viscous effects are used in Chapter 5 to validate the implementation of surface viscosity, given that our BEM is highly accurate when solving complex interfacial phenomena. The damped nonlinear oscillator model presented in §3.3 and validated in this section is briefly discussed again in Chapter 7 regarding the predicted transition between overdamped and underdamped motion, and how it relates the formation of spherical liquid marbles in our simulations.

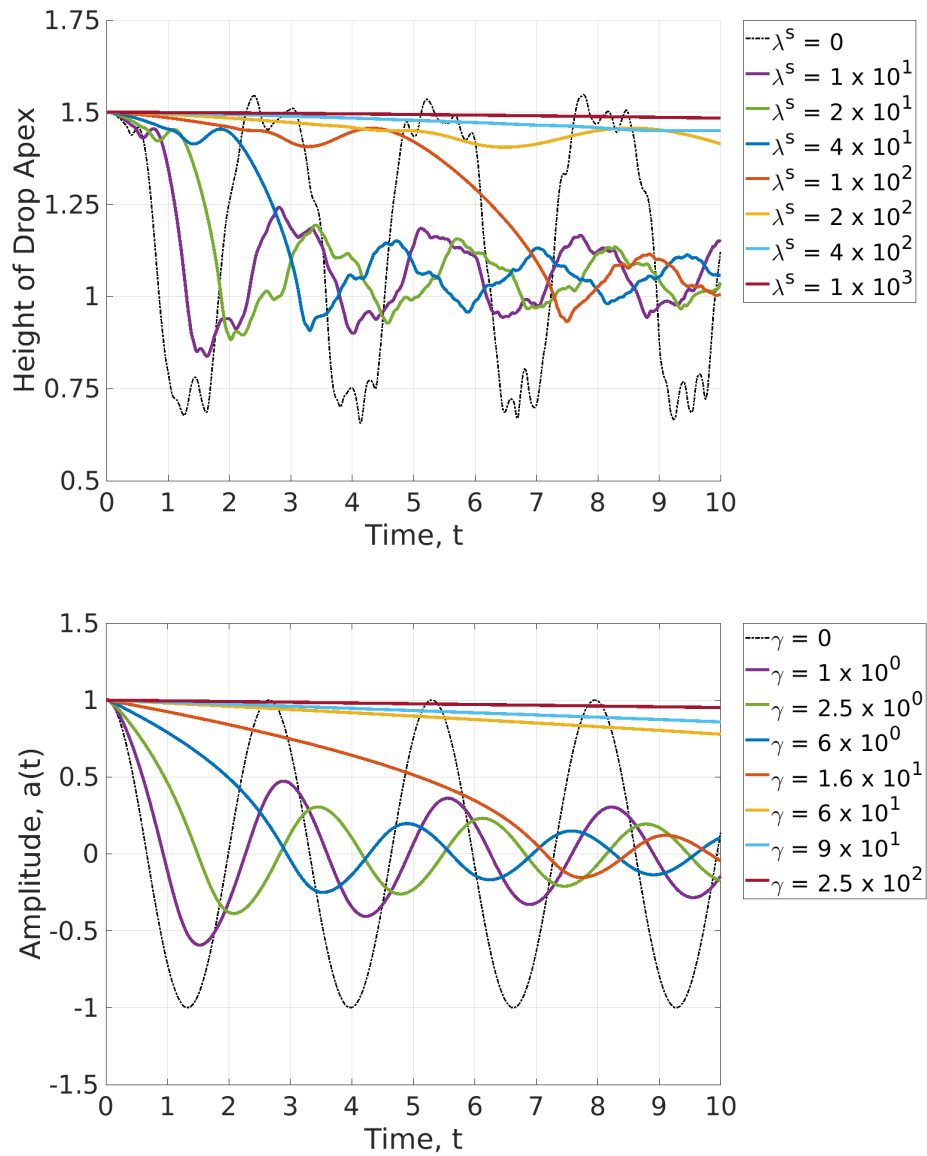


Figure 4.35: *Small amplitude suspended inviscid drop oscillations with small $\lambda^s > 0$ against a damped nonlinear oscillator*: Plots showing, for $\lambda^s = 1 \times 10^1$ to $\lambda^s = 1 \times 10^3$ (top) BEM simulations showing the evolution of the height of the drop apex starting from rest with initial shape (4.6.6) with $\epsilon = 0.5$, and (bottom) the solution to the toy damped nonlinear oscillator model (4.8.4), for the amplitude $a(t)$, with γ chosen to maximise resemblance to the BEM simulations. Simulation parameters given in the caption of Figure 4.32

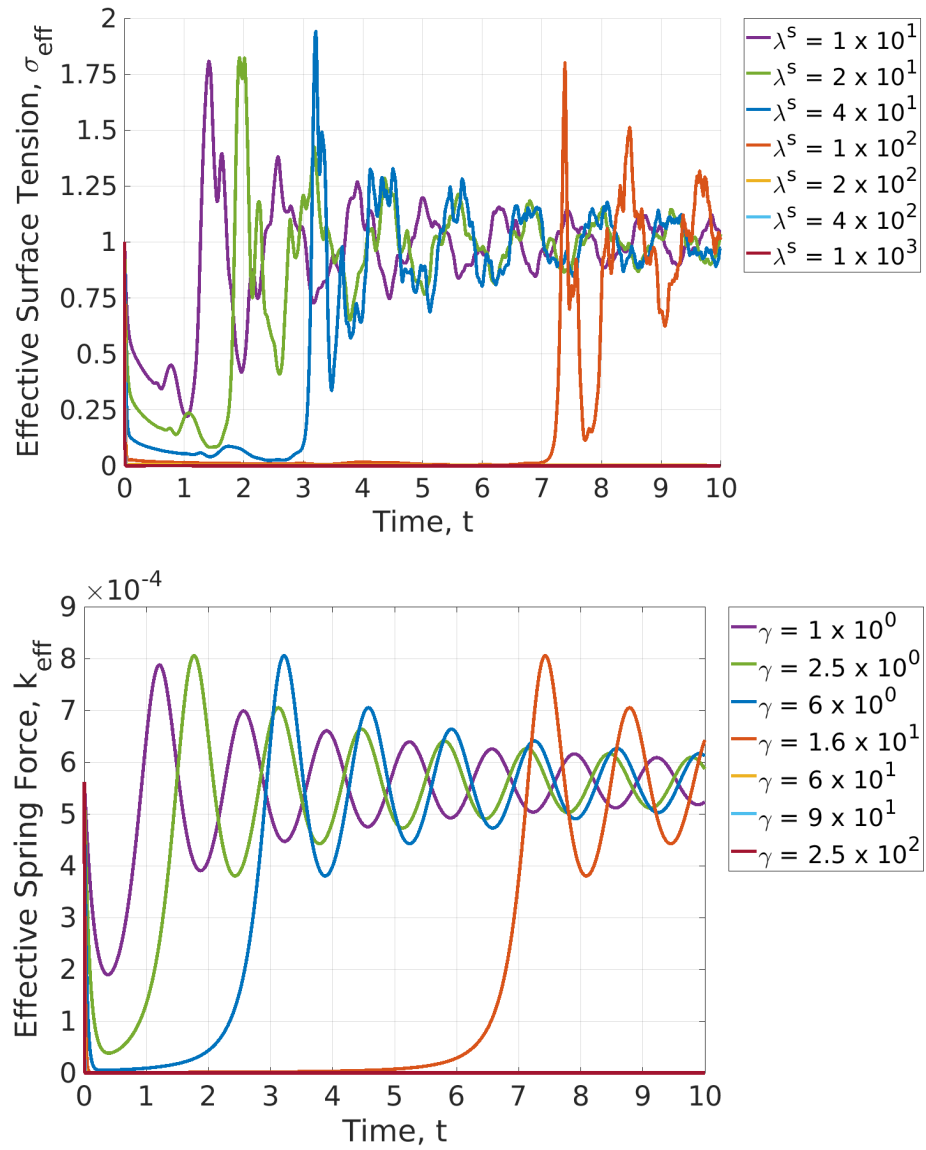


Figure 4.36: *Large amplitude suspended inviscid drop oscillations with large $\lambda^s > 0$ against a toy damped nonlinear oscillator:* Plots showing, for $\lambda^s = 1 \times 10^1$ to $\lambda^s = 1 \times 10^3$ (top) BEM simulations showing the evolution of the effective surface tension starting from rest with initial shape (4.6.6) with $\epsilon = 0.5$, and (bottom) the effective spring constant (3.3.16) from the damped nonlinear oscillator model. Simulation parameters given in the caption of Figure 4.32.

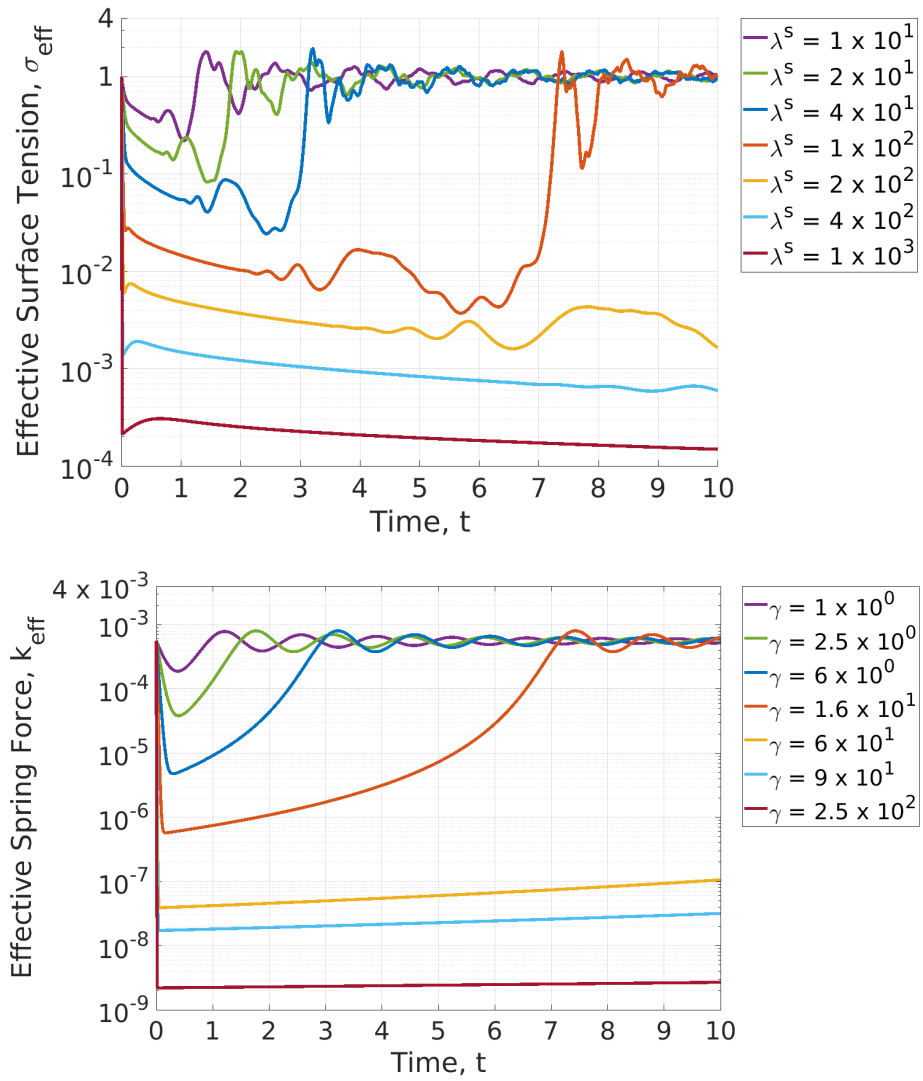


Figure 4.37: *Large amplitude suspended inviscid drop oscillations with large $\lambda^s > 0$ against a toy damped nonlinear oscillator*: Plots showing in semi-log scale, for $\lambda^s = 1 \times 10^1$ to $\lambda^s = 1 \times 10^3$ (top) BEM simulations showing the evolution of the effective surface tension starting from rest with initial shape (4.6.6) with $\epsilon = 0.5$, and (bottom) the effective spring constant (3.3.16) from the damped nonlinear oscillator model. Simulation parameters given in the caption of Figure 4.32.

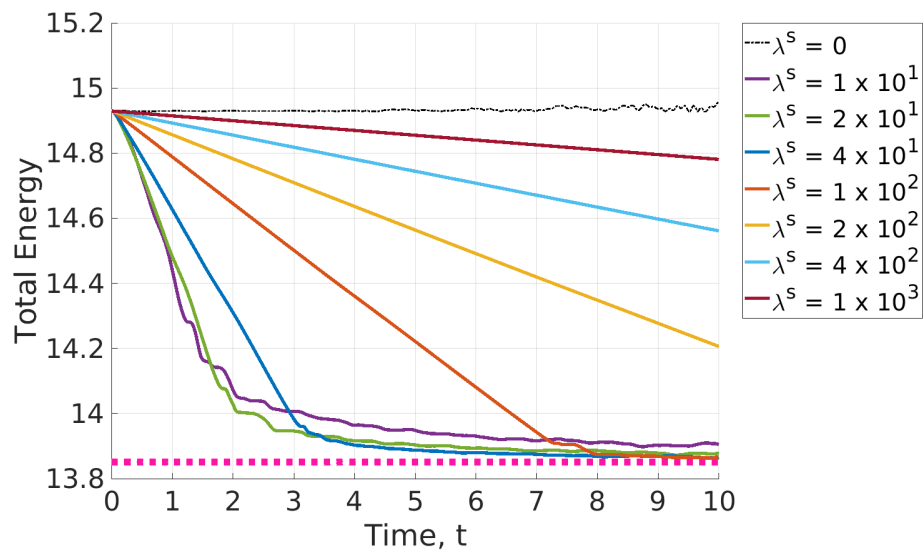


Figure 4.38: Plot showing, for BEM simulations with parameters given in the caption of Figure 4.32: for $\lambda^s = 1 \times 10^1$ to $\lambda^s = 1 \times 10^3$, total drop energy, in which the pink dotted line corresponding to zero kinetic energy and the surface energy attained at a sphere (the minimum surface energy state).

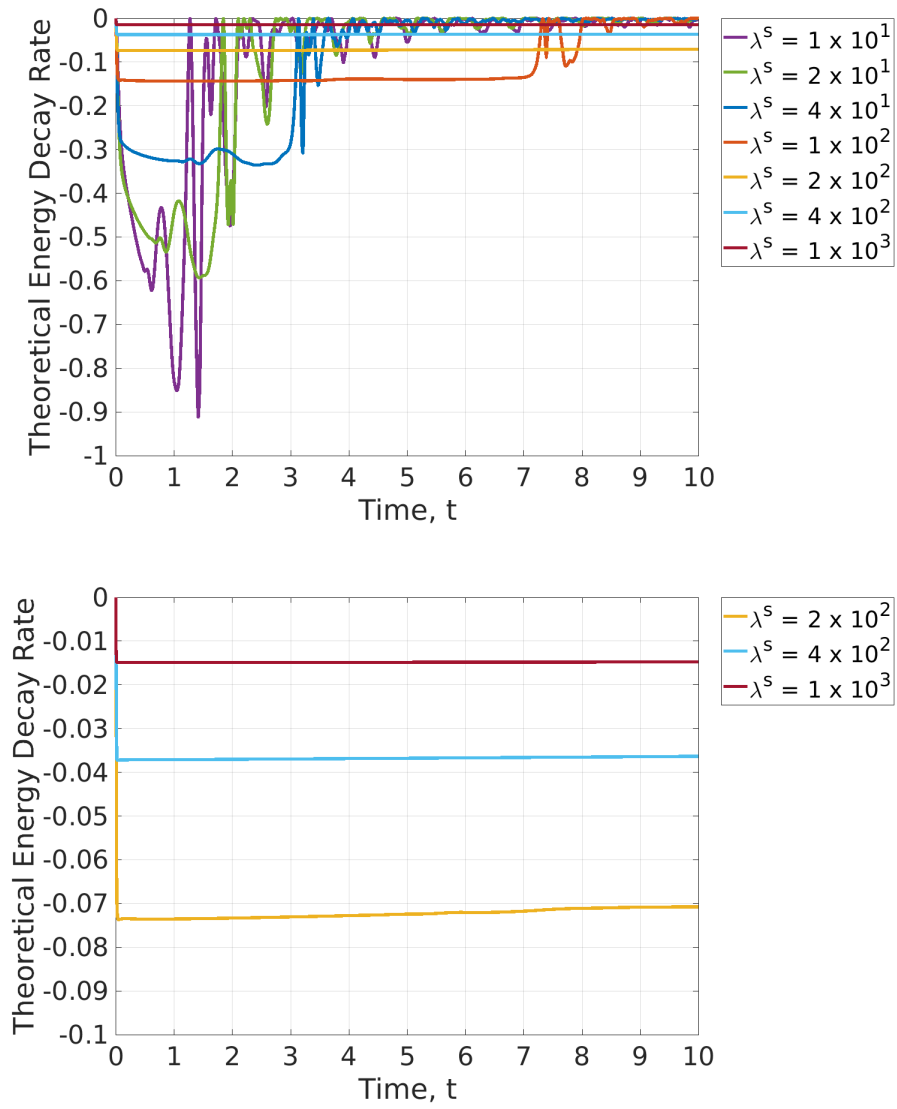


Figure 4.39: Plots showing, for BEM simulations with parameters given in the caption of Figure 4.32, the theoretical energy decay rate as calculated with (4.6.7) for (top) $\lambda^s = 1 \times 10^1$ to $\lambda^s = 1 \times 10^3$, and (bottom) a close-up view of cases with $\lambda^s = 2 \times 10^2, 4 \times 10^2, 1 \times 10^3$.

Chapter 5

Volume-of-Fluid Method

In this chapter, we provide an overview of the ‘one-fluid’ formulation applied to the viscous model (see §3.2.5) for liquid marble formation, followed by a description of the numerical implementation (with the open-source software, Basilisk [177]) using a volume-of-fluid (VoF) method. Given that the VoF method is implemented using pre-existing software (unlike the BEM code with formulation described in Chapter 4), the description of the method itself and its numerical implementation will be brief, with references given to prominent review articles for further information. This chapter ends with a discussion of additional functionality specifically developed in Basilisk for this body of research, in particular the inclusion of dilatational surface viscosity as per our model (see Chapter 3) via an effective surface tension.

The primary benefits of using a VoF method in contrast to a BEM are the ease at which topological changes can be accounted for, and that the viscous Navier-Stokes equations can be solved. We begin with a discussion of the analytical ‘one-fluid’ framework that the numerical VoF method is built upon; modelling a multi-phase fluid domain with a single set of governing equations.

5.1 The ‘One-Fluid’ Approach to the Modelling of a Multi-Phase System

The ‘one-fluid’ formulation is well established and documented, and an interested reader is advised to consult [178, 179] for details. Presented here is an explanation and high-level overview of this formulation.

Consider a domain occupied by only two immiscible bulk fluids referred to as fluids 1 and 2, with bulk subdomains Ω_1 and Ω_2 , respectively, separated by a fluid-fluid interface \mathcal{S} . Importantly, the fluid domains Ω_1 and Ω_2 are not necessarily connected, and so multiple interfaces may exist, but we assume their properties are fundamentally the same. We suppose that fluid 1 is immersed within fluid 2 (although some Ω_2 ‘bubbles’ may be immersed within Ω_1), see Figure 5.1 for an example in two dimensions.

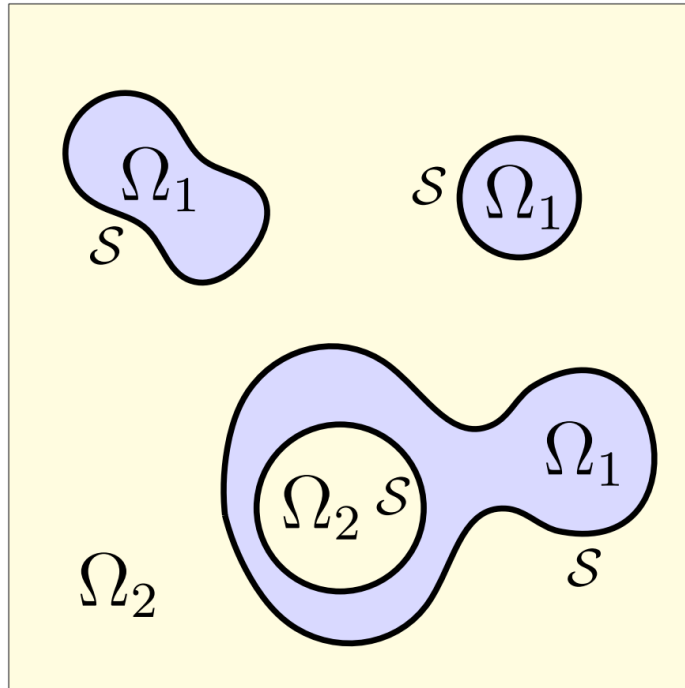


Figure 5.1: Two dimensional diagrammatic example of a two-phase fluid domain, with immiscible fluid subdomains Ω_1 and Ω_2 . The interfaces between the two fluids are denoted collectively by \mathcal{S} .

Given that we seek to use a single set of governing equations to model the *entire* fluid domain, we must be able to distinguish between the different fluids to know when to use their distinct material properties (for example, bulk density and bulk viscosity). To do this, we introduce the characteristic function χ , defined as

$$\chi(\underline{\mathbf{x}}) = \begin{cases} 1, & \underline{\mathbf{x}} \in \Omega_1 \\ 0, & \underline{\mathbf{x}} \in \Omega_2, \end{cases} \quad (5.1.1)$$

for $\underline{\mathbf{x}} = (x, y, z) \in \Omega_1 \cup \Omega_2$. Global parameters that appear within the (global) governing equations are then constructed using this characteristic function in combination with the associated parameters for the distinct fluids. For example, if the bulk den-

sities of fluids 1 and 2 are constant, namely, ρ_1 and ρ_2 , respectively, then the *global* bulk density ρ is given as

$$\rho(\underline{\mathbf{x}}) = \rho_1\chi(\underline{\mathbf{x}}) + \rho_2[1 - \chi(\underline{\mathbf{x}})]. \quad (5.1.2)$$

Similarly, constant bulk viscosities μ_1 and μ_2 in fluids 1 and 2, respectively, give rise to the (global) bulk viscous parameter μ with

$$\mu(\underline{\mathbf{x}}) = \mu_1\chi(\underline{\mathbf{x}}) + \mu_2[1 - \chi(\underline{\mathbf{x}})]. \quad (5.1.3)$$

Within the interior of either fluid subdomain, the gradient of χ is equal to zero, whereas the gradient across the sharp interface \mathcal{S} is necessarily nonzero. To evaluate this gradient, it is convenient to express χ as the following integral:

$$\chi(\underline{\mathbf{x}}) = \int_{\Omega_1} \delta(x - \bar{x})\delta(y - \bar{y})\delta(z - \bar{z}) \, d\bar{x} \, d\bar{y} \, d\bar{z}, \quad (5.1.4)$$

where δ is the Dirac delta function. Note that $\chi(\underline{\mathbf{x}}) = 1$ if $\underline{\mathbf{x}} \in \Omega_1$, and $\chi(\underline{\mathbf{x}}) = 0$ otherwise, as expected.

By taking the gradient of (5.1.4) and applying some manipulation (see Chapter 3 in [180] for details), we eventually obtain

$$\nabla\chi(\underline{\mathbf{x}}) = -\delta(n)\underline{\mathbf{n}}, \quad (5.1.5)$$

where $\underline{\mathbf{n}}$ is the unit normal on the interface \mathcal{S} pointing *into* Ω_2 , and where the parameter n is the local coordinate normal to the interface, so that $n = 0$ when $\underline{\mathbf{x}} \in \mathcal{S}$ (that is, $n = 0$ at any point on a fluid-fluid interface and nonzero otherwise) and, in particular, the normal derivative of n at the interface is 1. Using (5.1.5), the gradients of material properties can then be calculated, and so for the case of constant bulk densities in both fluids (so 5.1.2 holds), the gradient of the global density is given by

$$\nabla\rho = (\rho_2 - \rho_1)\delta(n)\underline{\mathbf{n}}. \quad (5.1.6)$$

A similar expression holds for the global viscosity coefficient μ using (5.1.5) and (5.1.3).

Some variables are only defined on the fluid interface \mathcal{S} itself (for example, surface tension σ) and are incorporated into the governing bulk flow equations using delta functions. For viscous bulk fluids with a shared interface that exhibits *no* surface viscous effects, the (global) Navier-Stokes equations then take the form

$$\rho \left[\frac{\partial \underline{\mathbf{u}}}{\partial t} + (\underline{\mathbf{u}} \cdot \nabla) \underline{\mathbf{u}} \right] = -\nabla p + \rho \underline{\mathbf{f}} + \nabla \cdot (2\mu \underline{\mathbf{D}}) - \delta(n)\sigma(\nabla_s \cdot \underline{\mathbf{n}})\underline{\mathbf{n}}, \quad (5.1.7)$$

for a force per unit mass $\underline{\mathbf{f}}$, curvature $\nabla_s \cdot \underline{\mathbf{n}}$, and rate-of-strain tensor $\underline{\underline{\mathbf{D}}}$ given by

$$\underline{\underline{\mathbf{D}}} = \frac{1}{2} \left[\nabla \underline{\mathbf{u}} + (\nabla \underline{\mathbf{u}})^T \right], \quad (5.1.8)$$

where the superscript T denotes matrix transposition. It is emphasised that equation (5.1.7) holds even when ρ and μ are discontinuous across the sharp interface \mathcal{S} . For an explanation on including surface forces in this manner, and the validity of this approach in general, the reader is directed to [178].

As the interface \mathcal{S} evolves in time, its shape and that of the regions occupied by the subdomains Ω_1 and Ω_2 may change, but the identity of each fluid particle (that is, the identity of which immiscible fluid they belong to) is retained, thus the material derivative of the characteristic function χ must be zero, that is:

$$\frac{\partial \chi}{\partial t} + \nabla \cdot (\chi \underline{\mathbf{u}}) = 0. \quad (5.1.9)$$

Equation (5.1.9) then describes the evolution of the interface \mathcal{S} , which is the only region within the global fluid domain where the spatial gradient of χ is nonzero.

So for two distinct immiscible fluids, occupying subdomains Ω_1 and Ω_2 , and sharing a common (possibly disconnected) interface \mathcal{S} , their bulk momentum equations can be combined with a conservation of momentum equation at the interface to form a *single* momentum equation in the form of (5.1.7). The kinematic equation describing the motion of the fluid interface \mathcal{S} takes the form of (5.1.9), which now describes advection of the characteristic function.

5.1.1 Application to the Viscous Model

We now apply the ‘one-fluid’ formulation to the viscous model; the full details for the bulk and surface equations from this model and applied boundary conditions are found in §3.2.5. Repeated here for the convenience of the reader is an overview of the model and the aspects that are ‘non-standard’, that is, the boundary conditions on the liquid-gas interface directly relating to surface viscosity (via an effective surface tension), and a slip condition applied at the solid substrate.

Reminder of the Viscous Model

In the viscous model, the flow within the liquid and gas domains satisfies the incompressible Navier-Stokes equations (3.2.44)-(3.2.45) with (3.2.14)-(3.2.15), and the

conventional tangential stress boundary condition holds at any liquid-gas interface (3.2.41). The (unconventional) normal stress boundary condition (3.2.40) is given by

$$(p - p_G) - \underline{\mathbf{n}} \cdot \left(\underline{\underline{\mathbf{D}}} - \underline{\underline{\mathbf{D}}}_G \right) \cdot \underline{\mathbf{n}} = \sigma_{\text{eff}}(A, t) (\nabla_s \cdot \underline{\mathbf{n}}),$$

with rate-of-strain tensors $\underline{\underline{\mathbf{D}}}$ and $\underline{\underline{\mathbf{D}}}_G$ defined as in (5.1.8) for the liquid and gas domains, respectively. The *effective* surface tension σ_{eff} (3.2.38) is how surface viscosity enters the system, with

$$\sigma_{\text{eff}}(A, t) = 1 + \lambda^s(A, t) \left(\frac{\int_{S_{LG}(t)} (\nabla_s \cdot \underline{\mathbf{n}}) (\underline{\mathbf{u}} \cdot \underline{\mathbf{n}}) \, dS(t)}{\int_{S_{LG}(t)} 1 \, dS(t)} \right),$$

where the dilatational surface viscous coefficient $\lambda^s(A, t)$ (3.2.37) is a function of the liquid-gas surface area A , and the time-dependent encapsulation and freezing areas $A_{\text{encap}}(t)$ and $A_{\text{freeze}}(t)$, respectively:

$$\lambda^s(A, t) = \beta \cdot \frac{(A_{\text{encap}}(t) - A)}{(A - A_{\text{freeze}}(t))},$$

for constant $\beta > 0$.

The kinematic condition (3.2.4) describing the motion of the fluid interface in time (defined by $f(\underline{\mathbf{x}}, t) = 0$) is given by

$$\frac{\partial f}{\partial t} + (\underline{\mathbf{u}} \cdot \underline{\mathbf{n}}) |\nabla f| = 0,$$

and the Navier-slip (3.2.10) and impermeability (3.2.11) boundary conditions are applied at the liquid-solid interface (defined as the plane at $z = 0$), respectively given by

$$\underline{\mathbf{u}} \cdot \underline{\mathbf{e}}_r = \bar{d}_p \frac{\partial}{\partial z} (\underline{\mathbf{u}} \cdot \underline{\mathbf{e}}_r) \quad \text{at } z = 0,$$

and

$$\underline{\mathbf{u}} \cdot \underline{\mathbf{e}}_z = 0 \quad \text{at } z = 0.$$

A condition is also applied at the contact line defining the contact angle between the liquid drop and solid substrate.

At the axis of symmetry, conditions (3.2.39) and (3.2.46) hold within the liquid and gas bulk flows, given by:

$$\underline{\mathbf{u}} \cdot \underline{\mathbf{e}}_r = \frac{\partial}{\partial r} (\underline{\mathbf{u}} \cdot \underline{\mathbf{e}}_z) = 0 \quad \text{and} \quad \underline{\mathbf{u}}_G \cdot \underline{\mathbf{e}}_r = \frac{\partial}{\partial r} (\underline{\mathbf{u}}_G \cdot \underline{\mathbf{e}}_z) = 0 \quad \text{at } r = 0,$$

and at an intersection of the liquid-gas interface with the axis of symmetry, the geometric boundary condition (3.2.12) is applied:

$$\underline{\mathbf{n}} \cdot \underline{\mathbf{e}}_r = 0 \quad \text{at } r = 0.$$

For the remaining fluid boundary that exists ‘at infinity’, we suppose there is zero velocity and zero pressure, that is,

$$|\underline{\mathbf{u}}_G| \rightarrow 0 \quad \text{and} \quad p_G \rightarrow 0 \quad \text{as} \quad |\underline{\mathbf{x}}| \rightarrow \infty. \quad (5.1.10)$$

Application of the One-Fluid Approach

With the introduction of the characteristic function χ , as mentioned in the previous subsection, the kinematic equation (3.2.4) describing the evolution of the drop interface is replaced by the advection equation for the characteristic function itself, given by

$$\frac{\partial \chi}{\partial t} + \nabla \cdot (\chi \tilde{\underline{\mathbf{u}}}) = 0, \quad (5.1.11)$$

where the variable $\tilde{\underline{\mathbf{u}}}$ represents the (dimensionless) velocity field across the *entire* multi-phase domain (in contrast to variables without a tilde which have throughout this thesis typically denoted bulk liquid drop properties alone). Similarly \tilde{p} will denote the (dimensionless) pressure field across the entire multi-phase domain, and $\tilde{\underline{\underline{\mathbf{D}}}}$ the (dimensionless) rate-of-strain tensor.

For the bulk fluids, the (dimensionless) conservation of momentum equations for the liquid drop (3.2.44) and exterior gas (3.2.45) are combined with the normal stress boundary condition at the fluid interface (3.2.40) to form the *global* momentum conservation equation given by

$$\tilde{\rho} \left[\frac{\partial \tilde{\underline{\mathbf{u}}}}{\partial t} + (\tilde{\underline{\mathbf{u}}} \cdot \nabla) \tilde{\underline{\mathbf{u}}} \right] = -\nabla \tilde{p} + \tilde{\rho} \underline{\mathbf{g}} + \text{Oh} \nabla \cdot \left(2\tilde{\mu} \tilde{\underline{\underline{\mathbf{D}}}} \right) - \delta(n) \sigma_{\text{eff}} (\nabla_s \cdot \underline{\mathbf{n}}) \underline{\mathbf{n}}. \quad (5.1.12)$$

The coefficients $\tilde{\rho}$ and $\tilde{\mu}$ represent the global (dimensionless) bulk density and bulk viscosity coefficients, respectively, and are given by

$$\tilde{\rho} = \chi + \rho_G (1 - \chi) \quad (5.1.13)$$

and

$$\tilde{\mu} = \chi + \mu_G (1 - \chi). \quad (5.1.14)$$

Recall here that $\rho_G = \hat{\rho}_G / \hat{\rho}$ and $\mu_G = \hat{\mu}_G / \hat{\mu}$ are the ratios of the dimensional gas and liquid density, and viscosity, respectively.

Additionally, incompressibility for both liquid and gas bulk flows (3.2.14) - (3.2.15) leads to incompressibility of the entire flow field, that is,

$$\nabla \cdot \tilde{\underline{\mathbf{u}}} = 0. \quad (5.1.15)$$

To see why (5.1.15) holds, consider the following representation of the (global) velocity field $\tilde{\mathbf{u}}$ in terms of the velocities of the liquid and gas phases, \mathbf{u} and \mathbf{u}_G , respectively:

$$\tilde{\mathbf{u}} = \mathbf{u}\chi + \mathbf{u}_G(1 - \chi). \quad (5.1.16)$$

Taking the divergence of (5.1.16), we have

$$\begin{aligned} \nabla \cdot \tilde{\mathbf{u}} &= (\mathbf{u} - \mathbf{u}_G) \cdot \nabla \chi + (\nabla \cdot \mathbf{u})\chi + (\nabla \cdot \mathbf{u}_G)(1 - \chi) \\ &= -\delta(n)(\mathbf{u} - \mathbf{u}_G) \cdot \mathbf{n} + \begin{cases} \nabla \cdot \mathbf{u}, & \mathbf{x} \in \Omega \\ \nabla \cdot \mathbf{u}_G, & \mathbf{x} \in \Omega_G \end{cases} \\ &= 0, \end{aligned} \quad (5.1.17)$$

using equations (5.1.1) and (5.1.5) in addition to the incompressibility conditions in the liquid and gas bulk flows, and the continuity of normal velocity to the interface \mathcal{S} .

The boundary conditions are incorporated numerically at the boundaries of the computational domain. The Navier-slip (3.2.10) and impermeability (3.2.11) conditions are imposed at the liquid-solid interface (where $z = 0$) with the contact angle imposed at the contact line. The symmetry conditions (3.2.39), (3.2.46), and (3.2.12) are imposed at the axis of symmetry (where $r = 0$), and are given by the following in the one-fluid formulation:

$$\tilde{\mathbf{u}} \cdot \mathbf{e}_r = 0 \quad \frac{\partial}{\partial r}(\tilde{\mathbf{u}} \cdot \mathbf{e}_z) = 0 \quad \frac{\partial \chi}{\partial r} = 0 \quad \text{at } r = 0. \quad (5.1.18)$$

Finally, the conditions in (5.1.10) are imposed ‘at infinity’.

5.2 Numerical Implementation using a Volume-of-Fluid Method in Basilisk

This section will provide a brief overview of the VoF method and its implementation using Basilisk. Basilisk is an open-source software package that is popular in the field of computational fluid mechanics that allows users to solve fluid flow problems, including the use of VoF methods to solve multi-phase flows. Basilisk is the successor to the open-source software package Gerris [181]; with Basilisk improving upon the numerical solvers used by Gerris, whilst also providing additional functionality. Using its own programming language, ‘Basilisk C’ (an extension of the C programming

language), users are able to, among other things, easily define flow fields, apply boundary conditions at the edge of the domain, and control the dynamic refinement of the computational mesh, all using a set of in-built functions and solvers. All of this, and more, can be done in Basilisk in both two and three dimensions, and made parallelisable to efficiently run large programs on multiple cores simultaneously. Basilisk is also well-tested and -documented, so this quality assurance as well as the features outlined above have made it popular in the computational fluid mechanics community and a good choice for implementing our model. An interested reader is directed to [178, 179] for additional details on the VoF method and to [177, 182] for further information on Basilisk.

Typical computational times in Basilisk when using the VoF method described in this chapter are on the order of days; taking two-to-three days to simulate the drop’s interaction with the solid substrate and subsequent rebound oscillations up to the point of encapsulation, followed by an additional one-to-four days simulating drop oscillations under the effects of surface viscosity. The relatively wide estimate in computational time for simulating the surface viscous regime following rebound from the substrate is due to the decreasing window of modelling time in which the moments of encapsulation and interfacial freezing occur, as the impact Weber number is increased (noted in experiments in §2.3.4, and discussed later with respect to numerical simulations in §7.1).

5.2.1 Volume-of-Fluid Methods

VoF methods are numerical implementations of fluid flow models that are formulated using a single set of governing equations (that is, with a one-fluid approach as discussed in §5.1), and are solved on Eulerian grids where the fluid domain is partitioned into a finite number of distinct ‘cells’. An example of such a partition of a fluid domain is shown in Figure 5.2, where for simplicity all cells are the same size. The computational domain is typically *larger* than the underlying fluid domain because additional ‘ghost’ cells are added *outside* the fluid domain for the implementation of boundary conditions.

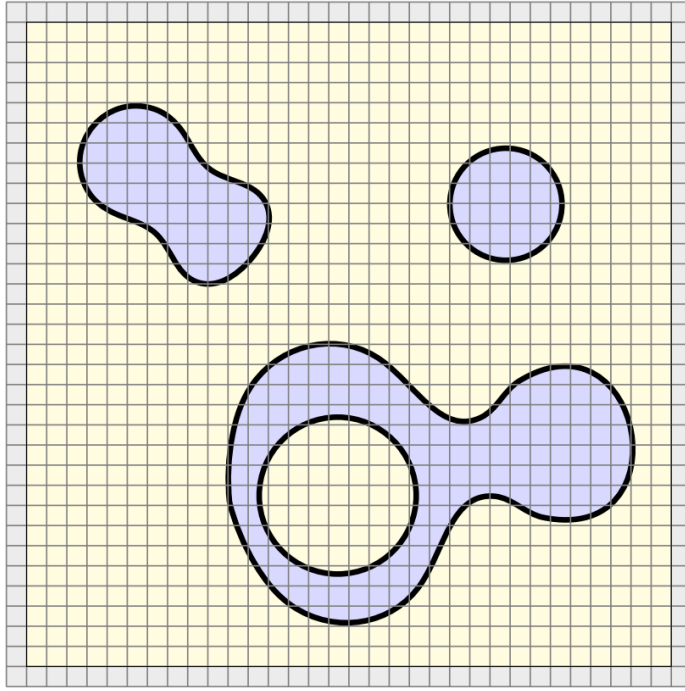


Figure 5.2: Two dimensional example of a two-phase fluid domain from Figure 5.1 partitioned into grid cells. The grey cells on the outer perimeter of the domain are ‘ghost’ cells; extra grid cells outside the fluid domain that make it easier to numerically implement boundary conditions for the flow.

In each grid cell, flow variables (for example, velocity and pressure) are ‘volume-averaged’, that is, integrals are taken of these variables over the volume (in three dimensions) or area (in two dimensions) of the cell. Volume-averaging thus *discretises* the flow; providing a single evaluation of each flow variable in every one of the grid cells that partition the fluid domain. The momentum equation is solved (along with applied boundary conditions) using these discretised variables, the details of this process are outside the scope of this thesis and can be found in [177].

We will focus briefly on a particular flow variable and its discretised form because it is at the core of representing free surface flows in VoF methods; that of the characteristic function χ . Suppose the grid cells are ordered so that (i, j) denotes the cell on the i -th row and j -th column of the mesh with $1 \leq i, j \leq N$ for some integer N (for simplicity this assumes all cells within the mesh are the same size and that the domain is square), then the volume fraction for this cell, denoted by C_{ij} , is given by

$$C_{ij} = \frac{1}{\Delta x \Delta y} \int \int_{(i,j)} \chi(x, y) \, dx \, dy, \quad (5.2.1)$$

where Δx and Δy denote the width of the cell in each coordinate direction. The volume fraction C_{ij} then represents the proportion of the cell in question that contains liquid, so a cell entirely inside (or outside) a drop will have $C_{ij} = 1$ (or $C_{ij} = 0$), and a cell containing part of the fluid interface will have $0 < C_{ij} < 1$. Therefore with this spatial discretisation, fluid interfaces are represented by cells that have volume fractions strictly between 0 and 1. An example of a fluid interface and the surrounding region being converted into values of the volume fraction is shown in Figure 5.3.

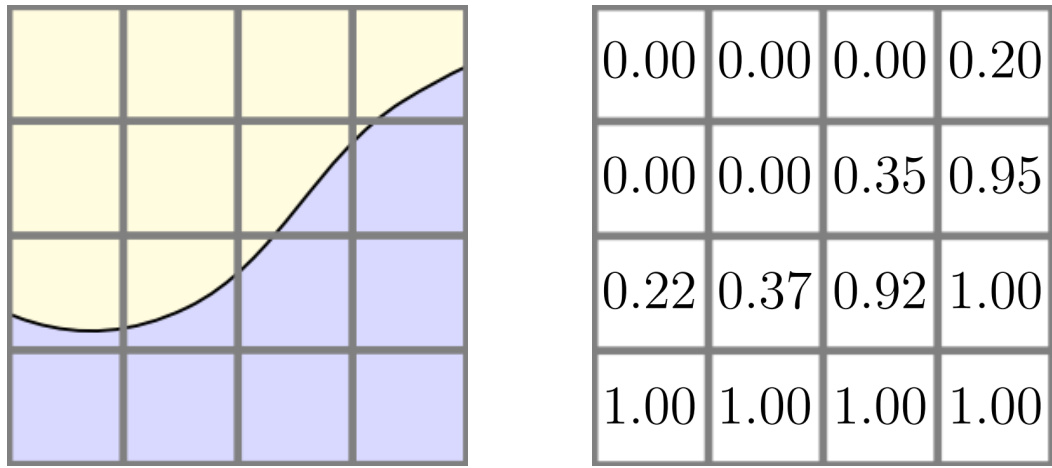


Figure 5.3: Two dimensional example of grid cells containing segments of the fluid-fluid boundary with (left) the fluid-fluid interface, and (right) the corresponding values of the volume fraction (5.2.1) within each cell.

Given that during the course of a VoF simulation, the fluid interface is only identified by finding cells with $0 < C_{ij} < 1$, techniques are implemented to *reconstruct* the fluid interface to obtain the orientation of the unit normal within each cell and the value of the interfacial curvature. The unit normal is fundamental for advecting the volume fraction (and so the fluid interface) in time, while the interfacial curvature is required to calculate the surface tension force at the fluid interface. Reconstruction of fluid interfaces is one of the primary difficulties of implementing a VoF method, and multiple schemes have been developed to achieve this [179]. This contrasts with BEMs where the computational mesh (typically nodes with interpolating splines) *define* the location and shape of the interface and this leads to VoF implementations producing less accurate approximations of interfacial properties such as the surface area [179]. Ultimately, the level of accuracy will turn out to be sufficient for our pur-

poses, especially considering the benefits a VoF implementation provides in allowing drop impacts with multiple topological changes to be simulated.

Once the interface has been reconstructed, the volume fraction C_{ij} and other flow variables are advected across the computational domain; this is the other primary difficulty of VoF implementations and will not be discussed here as it is outside the scope of this thesis. Suffice it to say that the discrete solution of the governing equation (5.1.12), solved in conjunction with applied boundary conditions, is combined with the reconstructed surface unit normal and interfacial curvature to evolve the system to a future time, where the process begins anew by reconstructing the evolved interface. We will now move on to describe how this VoF method is implemented in Basilisk, and the setup for our simulations.

5.2.2 Basilisk Implementation

The techniques used in Basilisk to reconstruct and advect fluid interfaces are given in [177], with descriptions of the schemes these techniques were built upon (in Gerris) found in [182–184]. To solve the discrete version of the global Navier-Stokes equations (5.1.12) and advect the flow in time, Basilisk uses the Bell-Colella-Glaz advection scheme [185] coupled with an implicit viscosity solver, and a CFL-limited time advancement scheme.

The size of the fluid domain in Basilisk is set prior to simulation and cannot be expanded while the simulation is running. For this reason, the domain is chosen to be *much* larger in our simulations than the region in which interesting activity occurs. Fortunately, Basilisk allows for adaptive mesh refinement so particular regions of the domain are resolved using a large number of small cells, and less interesting regions are resolved with a small number of large cells. For our purposes, we use small cells to resolve regions where there are large gradients in both the flow velocity, and in the characteristic function χ (that is, at the location of the fluid interface), with large cells used far from the fluid-fluid interface, or where the aforementioned gradients are small. This allows simulations to be run efficiently as the majority of the fluid domain is devoid of activity.

Simulating Drop Impact

When simulating drop impact (see Chapter 6), we use a domain size of 24×24 (and two dimensional area of $24^2 = 576$), which is *much* larger than the two dimensional area covered by the spherical drop prior to impact (which has radius 1 and so a two dimensional area of $\pi/2$, recalling that our model is axisymmetric so a sphere is represented by half a circle). In addition to the adaptive mesh refinement described above, we also utilise (at every time step) an in-built function in Basilisk called “remove_droplets()” to remove small air bubbles that can form in drop impact simulations either due to small-scale spurious interfacial phenomena, or between the drop and substrate as the two come into contact; a well known phenomenon [186] which has little influence on the subsequent drop’s dynamics. Given their limited influence, removing these bubbles allows our simulations to run more efficiently because otherwise, the adaptive mesh refinement scheme would trigger upon the appearance of interfacial cells *inside* the drop, *increasing* the number of computations due to an over-refined mesh. This function works by identifying *distinct* regions of a specified fluid domain, and ‘flipping’ the value of the volume fraction in some of these regions to match the *other* fluid, and by doing so eliminating any local gradients in the fluid properties. For drop impacts, we remove any region of the gas subdomain that spans an area of less than 16 of the smallest grid cells we utilise, so a (dimensionless) area of size $16 \times 0.00586^2 \approx 0.0005$ (or dimensionally as 50nm^2).

Simulating Surface Viscosity for Liquid Marble Formation

When simulating liquid marble formation, as described in Chapters 6-7, we extract the state of a *clean* drop impact simulation at a specified point in time and use this as the initial condition for the simulation. We therefore use the same size domain as drop impact simulations. Our simulations for liquid marble formation involve surface viscous effects that are incorporated using an effective surface tension, which has a *unique* evaluation at each distinct fluid-fluid interface. As is discussed in detail in §5.3, we are able to alter the surface tension in Basilisk simulations, but this is more easily done *globally*, with a single effective surface tension affecting every fluid-fluid interface. For this reason, and that the shapes of powder coated satellite drops are uninteresting (with no clear opportunity to become liquid marbles themselves), we again use the in-built function “remove_droplets()”, this time to remove *all* drops

other than the primary drop in surface viscous simulations found in Chapter 7. This means we only consider the encapsulated primary drop at the start of the surface viscous liquid marble simulations, and remove any subsequent satellites (if formed). Given that the satellite drops are not expected to interact significantly with the primary drop once ejected, their removal greatly increases computational efficiency without any identified adverse effects.

Boundary Conditions

Boundary conditions applied on the fluid domain (at the axis of symmetry, the solid substrate, and ‘at infinity’) are implemented by assigning values to appropriate variables in the ghost cells that are *inside* the computational domain but *outside* the fluid domain (as in Figure 5.2). Although we have specified boundary conditions ‘at infinity’ (5.1.10), we find that applying the default (in Basilisk) symmetry boundary conditions are adequate. The computational domain is necessarily *finite* and so we identify the ‘at infinity’ boundary by two boundaries: one defined by the vertical line at $r = r_{max}$, and the other by the horizontal line at $z = z_{max}$. For the boundary defined by $r = r_{max}$, the same symmetry conditions are applied as at the axis of symmetry (5.1.18). The boundary defined by $z = z_{max}$ is *perpendicular* to the axis of symmetry, so the imposed symmetry conditions are rotated by 90° , giving

$$\tilde{\mathbf{u}} \cdot \mathbf{e}_z = 0, \quad \frac{\partial}{\partial z} (\tilde{\mathbf{u}} \cdot \mathbf{e}_r) = 0, \quad \frac{\partial \chi}{\partial z} = 0. \quad (5.2.2)$$

These boundaries are far from where the drop dynamics occur and we find that the use of these particular boundary conditions does not adversely affect fluid flow.

For the most part, applying boundary conditions is done using in-built functions within Basilisk. These functions, when given values to assign *at* a boundary, look at the appropriate variable as evaluated in the adjacent *non-ghost* cell and assign whatever value necessary to the adjacent *ghost* cell so that linearly-interpolating between the two satisfies the condition *at* the boundary. There are in-built functions in Basilisk called “dirichlet()” and “neumann()” with which we can impose Dirichlet and Neumann boundary conditions at a fluid domain boundary, assigning a chosen value to the designated variable (or its derivative for the Neumann condition) at that boundary. We use these to apply the impermeability condition (3.2.11) at the solid substrate, and the symmetry conditions, (5.1.18) and (5.2.2), at the other boundaries.

The function “contact_angle()” is used to assign the desired contact angle at the contact line.

For the Navier-slip boundary condition (3.2.10), the implementation requires a bit of work because the value being assigned at the interface is *not* constant. We will now describe how this condition is applied at the solid substrate.

Recalling the derivation of this condition in §3.2.2, we can equivalently characterise it in terms of a slip length \bar{d}_p , that is, the linearly-extrapolated distance through the substrate corresponding to zero radial flow velocity. Consider a non-ghost cell adjacent to the solid substrate (at $z = 0$), and let Δ denote its width (recall that all cells are square), so the centre of this cell is located at $z = \Delta/2$. Let $\tilde{u}_r^{(1)}$ denote the radial velocity at the cell centre. Having a slip length of \bar{d}_p means that the radial velocity vanishes at $z = -\bar{d}_p$, so by linearly interpolating between the two, we obtain the equation

$$\tilde{u}_r(z) = \tilde{u}_r^{(1)} \frac{\bar{d}_p + z}{\bar{d}_p + \Delta/2}. \quad (5.2.3)$$

So in particular we have that at $z = 0$,

$$\tilde{u}_r(0) = \tilde{u}_r^{(1)} \frac{\bar{d}_p}{\bar{d}_p + \Delta/2}, \quad (5.2.4)$$

where we clearly see that (5.2.4) is equivalent to the Navier-slip condition (3.2.10) using the approximation (5.2.3). So this condition is implemented in Basilisk by calling the “dirichlet()” function with the right hand side of (5.2.4) as the argument.

Calculation of the Unit Normal and Interfacial Curvature in Basilisk

We note that Basilisk provides in-built functionality to approximate both the unit normal $\underline{\mathbf{n}}$ and curvature $\nabla_s \cdot \underline{\mathbf{n}}$; what follows is a brief description of how this is achieved. For any cell, the ‘height function’ h provides, in each coordinate direction, the distance from the cell centre to the nearest fluid-fluid interface. For each cell *containing* the fluid-fluid interface (that is, those in which $0 < C_j < 1$), a finite-difference *like* approximation is conducted, in each coordinate direction, on the value of the h at the centre of the identified interfacial cell as well as its immediate neighbours (that is, the surrounding 8 cells in an axisymmetric setting). Approximations of the first-order derivatives of h are used to calculate the orientation of the unit normal n in each interfacial cell, and by also approximating the second-order derivatives of h in each coordinate direction, the curvature $\nabla_s \cdot \underline{\mathbf{n}}$ is obtained. An interested reader is

directed to [177] for further details regarding the calculation of h , $\underline{\mathbf{n}}$, and $\nabla_s \cdot \underline{\mathbf{n}}$ in Basilisk.

5.3 Added Functionality: Implicit Scheme to Solve for the Effective Surface Tension

Basilisk is fully capable of simulating viscous multi-phase flow including interactions with the boundary of the fluid domain, in particular, we are able to simulate liquid drop impacts onto a rigid substrate with subsequent rebound dynamics immersed in a passive gas phase using in-built functionality. Additionally, the value of surface tension is alterable in Basilisk, so the implementation of our effective surface tension at first appears trivial. However, simply using the value of the effective surface tension as calculated using variables from the *current* time (that is, with an explicit scheme) leads to numerically unstable simulations. This therefore led to the construction of an *implicit* scheme to calculate the effective surface tension so that simulations remain stable.

We start with a description of how this new functionality (developed for this body of research) is implemented, followed with a validation by comparing to results using our BEM for drop oscillations (from Chapter 4). Also discussed is a limitation on interfacial curvature that was enforced when simulating liquid marble formation for a certain set of parameters; these parameters were ultimately *not* used when gathering results for Chapter 7, but the description of its implementation and justification are given here for completeness.

5.3.1 Finding an Implicit Solution Iteratively

According to our model (see §3.2.4), dilatational surface viscosity is incorporated into the flow dynamics via an effective surface tension that requires solving surface integrals taken along the liquid-gas interface between the drop and surrounding gas. In VoF methods, as mentioned in §5.2.1, interfacial quantities are in general *not* as well-approximated as in numerical implementations that track the interface directly (for example, BEMs). We find that, particularly for large drop deformations, calculating the effective surface tension explicitly (in time) in Basilisk leads to simulations

quickly becoming unstable, and that reducing the time step alone is insufficient in alleviating the instability. To rectify this, a scheme was devised to find an implicit solution (in time) for the effective surface tension through an iterative process, which is described here.

Numerical Procedure

We search for an implicit value of the effective surface tension iteratively by repeatedly reverting the VoF simulation to a stored state at some given time step, and then evolving the simulation forward to the next time step with an altered value of σ_{eff} . We continue doing so until a certain criterion, described below, is satisfied. By doing so, we obtain a suitable implicit approximation for σ_{eff} , with which we make one final reversion to the stored state and evolve ahead with this approximation, thus beginning the process anew by storing the state of the simulation at the evolved time step. We now describe this process in detail below.

Suppose that we have stored the state of the simulation at the $(j - 1)$ -th time step t_{j-1} , for integer j . We wish to evolve the flow forward to the j -th time step, $t_j = t_{j-1} + \tau$ for $\tau > 0$ say, such that the simulation remains stable. We do this by finding the number Λ_{j-1} such that evolving forward the simulation from time step t_{j-1} to t_j with $\sigma_{\text{eff}} = \Lambda_{j-1}$ results in the explicitly calculated value of σ_{eff} (using equation 3.2.38, repeated here for convenience):

$$\sigma_{\text{eff}} = 1 + W = 1 + \lambda^s \left(\frac{\int_{S_{LG}} (\nabla_s \cdot \underline{\mathbf{n}})(\underline{\mathbf{u}} \cdot \underline{\mathbf{n}}) \, dS}{\int_{S_{LG}} 1 \, dS} \right),$$

evaluated at the time step t_j , being equal to Λ_{j-1} . If we consider the function

$$F(\Lambda_{j-1}) = \Lambda_{j-1} - (1 + W_j(\Lambda_{j-1})), \quad (5.3.1)$$

where $(1 + W_j(\Lambda_{j-1}))$ denotes the evaluation of the aforementioned equation for σ_{eff} at time step t_j , with the velocities and geometry of the system having evolved from t_{j-1} with $\sigma_{\text{eff}} = \Lambda_{j-1}$, then we seek to solve

$$F(\Lambda_{j-1}) = 0. \quad (5.3.2)$$

We will denote the solution to (5.3.2) by $\Lambda_{j-1} = \sigma_{\text{eff}}^*$. We note here that the difference between the time steps, $\tau = t_j - t_{j-1}$ depends on the value of $t_{j-1} - t_{j-2}$ and is limited by a CFL-condition, which is based on the arrangement of the computational mesh

and the magnitude of flow velocities at the *current* time, and *not* on the value of the surface tension. Changing the value of σ_{eff} during repeated reversions importantly does *not* alter the CFL-limit, so we can ensure that τ remains fixed during this procedure so that we are always evolving forward to the *same* t_j .

Our initial guess for Λ_{j-1} is the previous approximate solution of (5.3.2) that allowed us to evolve from time step t_{j-2} to t_{j-1} . If this is the first time evolution of the surface viscous regime, the initial guess is $\Lambda_{j-1} = 1$. In either case, the initial guess is denoted by $\sigma_{\text{eff}}^{(0)}$. If at any point in this iterative process, evolving ahead to t_j provides us with *exactly* $F = 0$, then the system at t_j is stored and instantly becomes the new time step from which we evolve the system, and the value of Λ_{j-1} that led to this (which is precisely σ_{eff}^*) becomes the new $\sigma_{\text{eff}}^{(0)}$.

If $F(\sigma_{\text{eff}}^{(0)}) \neq 0$, then we return to the stored state at t_{j-1} and evolve instead with $\Lambda_{j-1} = \sigma_{\text{eff}}^{(0)} + \eta$, with $\eta > 0$. If we see that $F(\sigma_{\text{eff}}^{(0)})$ and $F(\sigma_{\text{eff}}^{(0)} + \eta)$ have opposing signs, then (assuming monotonicity of F) a solution of (5.3.2) *must* lie in the interval $(\sigma_{\text{eff}}^{(0)}, \sigma_{\text{eff}}^{(0)} + \eta)$. Using linear interpolation, we approximate the solution as

$$\sigma_{\text{eff}}^* \approx \sigma_{\text{eff}}^{(0)} - \eta \frac{F(\sigma_{\text{eff}}^{(0)})}{F(\sigma_{\text{eff}}^{(0)} + \eta) - F(\sigma_{\text{eff}}^{(0)})}, \quad (5.3.3)$$

which we use to evolve to t_j , which then becomes the new set time step from which we evolve the system. If at any point in this entire procedure, a sign change is detected in F when comparing consecutive guesses for Λ_{j-1} (that is, between guesses with a difference of η) then linear interpolation as in (5.3.3) is how the solution of $F = 0$ is approximated.

Now consider $F(\sigma_{\text{eff}}^{(0)})$ and $F(\sigma_{\text{eff}}^{(0)} + \eta)$ to have the *same* sign. Note that we *could* decide, because of the assumed monotonicity of F , that just by looking at the sizes of $F(\sigma_{\text{eff}}^{(0)})$ and $F(\sigma_{\text{eff}}^{(0)} + \eta)$, whether continuing to *increase* the size of our guesses will lead us to the solution, or whether we should be heading in the other direction (that is, by looking below $\sigma_{\text{eff}}^{(0)}$). However, we are wary of small numerical errors that may erroneously send us down the wrong path (which is more likely if there are only two data points), so out of an abundance of caution we continue to make guesses around $\sigma_{\text{eff}}^{(0)}$ until we gather more data points, or find a solution.

We return now to the system at t_{j-1} , and try evolving the system again with $\Lambda_{j-1} = \sigma_{\text{eff}}^{(0)} - \eta$. As stated earlier, if $F(\sigma_{\text{eff}}^{(0)} - \eta) = 0$, or there is a change of sign between $F(\sigma_{\text{eff}}^{(0)} - \eta)$ and $F(\sigma_{\text{eff}}^{(0)})$, then we either have an exact solution, or can find an

approximate solution with (5.3.3), and move on to time step t_j and seek to evolve to t_{j+1} . If neither is true, we revert to t_{j-1} and evolve forward with $\Lambda_{j-1} = \sigma_{\text{eff}}^{(0)} + 2\eta$. At this point, assuming none of the conditions for finding a solution previously mentioned are satisfied, we have enough data points to determine the direction in which we can find the solution. If we have

$$\left|F(\sigma_{\text{eff}}^{(0)} - \eta)\right| > \left|F(\sigma_{\text{eff}}^{(0)})\right| > \left|F(\sigma_{\text{eff}}^{(0)} + \eta)\right| > \left|F(\sigma_{\text{eff}}^{(0)} + 2\eta)\right|, \quad (5.3.4)$$

then we know that *increasing* our guesses for the effective surface tension is leading us closer to a solution for $F = 0$. In this case we will *only* consider positive increments for future guesses until we observe a sign change in F . If instead we have

$$\left|F(\sigma_{\text{eff}}^{(0)} - \eta)\right| < \left|F(\sigma_{\text{eff}}^{(0)})\right| < \left|F(\sigma_{\text{eff}}^{(0)} + \eta)\right| < \left|F(\sigma_{\text{eff}}^{(0)} + 2\eta)\right|, \quad (5.3.5)$$

then we only consider *negative* increments (decreasing from $\Lambda_{j-1} = \sigma_{\text{eff}}^{(0)} - \eta$). If neither (5.3.4) nor (5.3.5) holds, then we continue the procedure by alternating future guesses between negative (positive) increments of the lowest (highest) existing guess and switch to a single direction if a chain of four guesses satisfies either (5.3.4) or (5.3.5).

For the sake of efficiency, we allow the increment to increase dynamically if we see that the solution to (5.3.2) is being approached *slowly*. If one of the sequential conditions (5.3.4)-(5.3.5) is satisfied *and* the difference in F for two sequential guesses is less than $1/5$ times the absolute value of F for the latest guess, then the size of the increment η is doubled for future guesses. If a sign change is eventually found with an enlarged η , the increment is reduced to its initial value and further guesses are made in appropriate directions until a sign change is found with a gap of η between the guesses. Linear interpolation as in (5.3.3) is then used to find the approximate solution. If after 30 guesses have been made, a solution is *not* found, then we keep the effective surface tension at the same value (so evolve from t_{j-1} to t_j with $\Lambda_{j-1} = \sigma_{\text{eff}}^{(0)}$), and hope to find a solution of $F(\Lambda_j) = 0$ in order to evolve from t_j to t_{j+1} .

In most cases, there are no occurrences of the function F *not* being monotonic, nor a solution not being found within the allotted 30 guesses, and so much of the above does not make a difference. However in some rare cases, probably due to some unfavourable free surface shapes within the grid cells (related to a poor reconstruction of the fluid interface in Basilisk), non-monotonicity in F can be observed, and solutions are sometimes not found. In these scenarios, the processes described above

allow us to move through these tricky periods, which end up being very brief and can crash the respective simulations if left unchecked. A more efficient algorithm taking into account these edge cases can be constructed, but considering the rarity of these problems and the success of our algorithm, we feel no need to do so.

Figure 5.4 shows a diagram illustrating a simple example of this iterative process; beginning with the initial guess $\sigma_{\text{eff}}^{(0)}$ and incrementing until the solution σ_{eff}^* to (5.3.2) is found. For our simulations, we use an initial increment of $\eta = 0.05$, and set a maximum value of $\eta = 1$ (which can only be reached through doubling of η as described above).

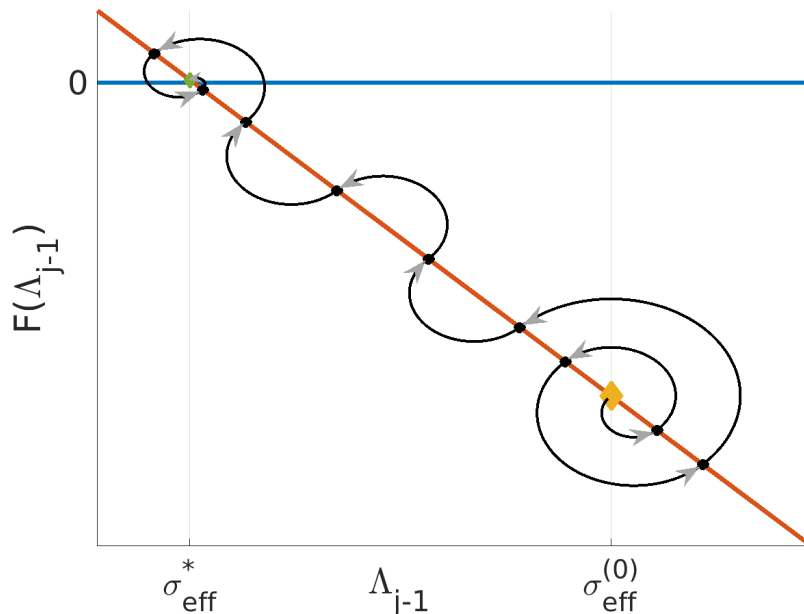


Figure 5.4: Diagram illustrating the search for the implicit value of the effective surface tension, beginning with an initial guess $\sigma_{\text{eff}}^{(0)}$ and ending with σ_{eff}^* .

5.3.2 Validation of Dilatational Surface Viscosity Implementation

We validate the implementation of dilatational surface viscosity in Basilisk as described in §5.3.1 by comparing drop oscillations affected by dilatational surface viscosity to those shown for our high-accuracy BEM in §4.6.1. These comparisons are made for a high deformation (nonlinear) case where bulk inertia is dominant, and with values of the dilatational surface viscous coefficient λ^s varying across multiple orders of magnitude. We will see that not only are fine details reproduced in the

Basilisk implementation with respect to oscillation amplitude, but that this is the case even though the VoF simulations obtain relatively poor approximations for the total energy.

Matching our BEM simulations (which assume inviscid bulk flows in the liquid and gas), we set $\tilde{\mu} = 0$ in (5.1.12) and consider the motion of a suspended drop (that is, without the effects of gravity) initially at rest with the shape given by (4.6.6) with $\epsilon = 0.5$, repeated here for convenience:

$$(R(\psi), Z(\psi)) = [1 + \epsilon P_2(\cos \psi)] (\sin \psi, \cos \psi),$$

where (R, Z) denote the radial and axial coordinates of the axisymmetric drop boundary, with polar angle $\psi \in [0, \pi]$, and second-order Legendre polynomial P_2 . The details for the numerical simulations in our BEM are found in §4.8. The VoF simulations are run in a fluid domain of size 6×6 with an adaptive mesh and a minimum (square) cell width of $6/2^9 \approx 0.0117$. Adaptive mesh refinement is implemented using the in-built function “`adapt_wavelet()`”, which tells the simulation to have greater resolution in regions with large gradients of its given arguments; which in our case is the flow velocity and volume fraction.

As shown in Figure 5.5, the VoF simulations in Basilisk show very good agreement with their BEM counterparts for the height of the drop apex (with respect to the centre of mass of the drop); reproducing many of the intricate peaks and troughs over the course of the simulations. Likewise, Figure 5.6 portrays very good agreement between the two implementations with respect to the effective surface tension, which is especially impressive given that the effective surface tension depends on the position of the interface that (as previously mentioned) VoF methods struggle to reconstruct accurately (compared to BEMs). The difference between the methods in their ability to reconstruct the interface is highlighted in Figure 5.7 for the total drop energy, whereby the VoF simulations experience large fluctuations, which is due entirely to a poor calculation of the surface energy (which is equivalent to the surface area of the drop). Even though quantitatively the approximation for the energy is poor, there is good qualitative agreement with the BEM simulations; increasing λ^s within this range leads to a faster decay in energy.

Similarly for larger λ^s , Figure 5.8 shows good agreement between the numerical methods for the height of the drop apex, showing additional examples of the Basilisk implementation reproducing fine details in drop oscillations. Figure 5.9 shows that

the Basilisk implementation is still able to provide good agreement with the BEM regarding the effective surface tension even with large λ^s where the simulations experience long periods of overdamping (where σ_{eff} is near zero). Finally, we see in Figure 5.10 that the Basilisk simulations continue to agree *qualitatively* with the BEM simulations for total energy; an increase in λ^s in general now *slows* the energy decay.

What these figures collectively highlight is that complicated (dilatational) surface viscous effects can be incorporated into simulations of high-deformation drop oscillations using a VoF method (in Basilisk), and that such simulations can yield accurate drop shapes. Importantly, this occurs while the surface energy (equivalent to the surface area) is relatively poorly approximated. We move now to a discussion on numerical considerations associated with persistent high-curvature regions of the drop interface for a specific class of simulations.

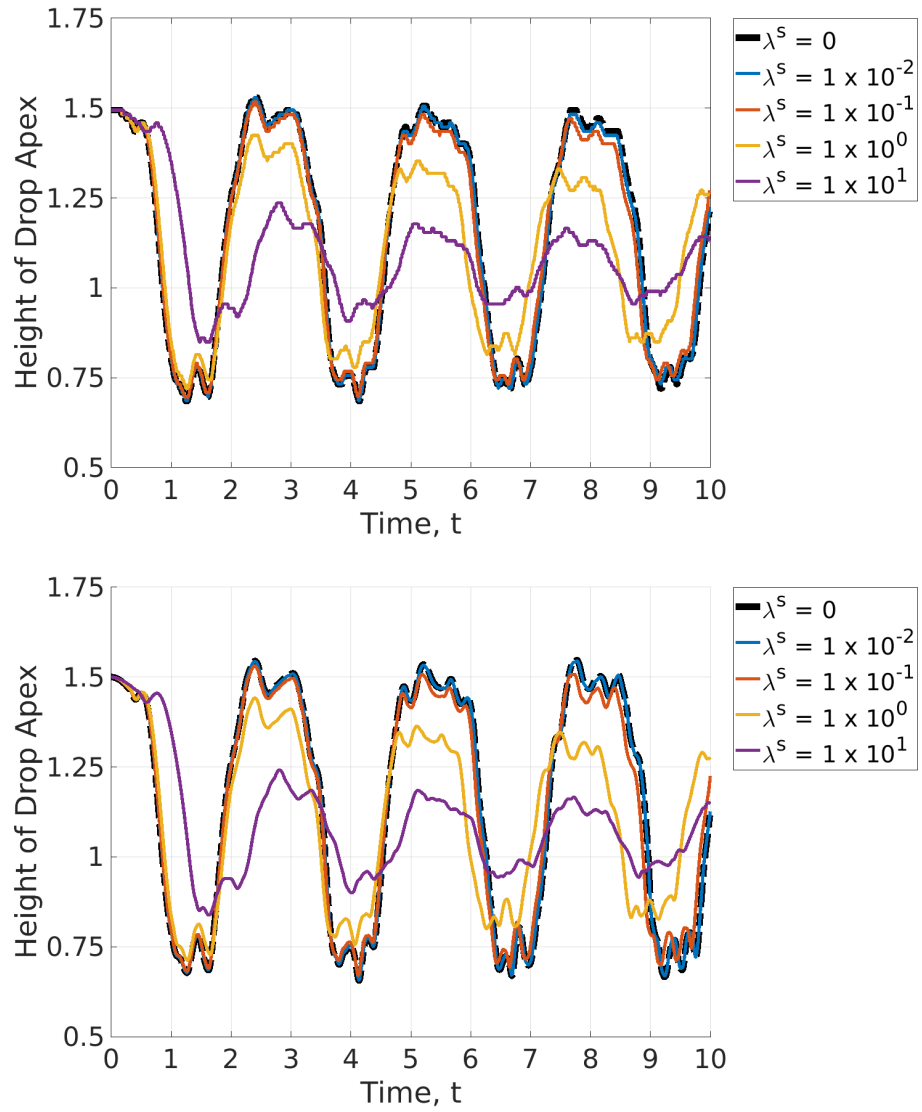


Figure 5.5: Comparison for the height of the drop apex (from the centre of mass of the drop) for suspended drops released from rest with initial shape (4.6.6) with $\epsilon = 0.5$, and small λ^s , from simulations using (top) a VoF implementation using Basilisk, and (bottom) a BEM implementation using purpose-built code described in §4.5. The details of the BEM simulations can be found in the caption of Figure 4.32. The VoF simulations are run in a 6×6 domain with adaptive mesh refinement and a smallest grid cell diameter of $6/2^9 \approx 0.01$.

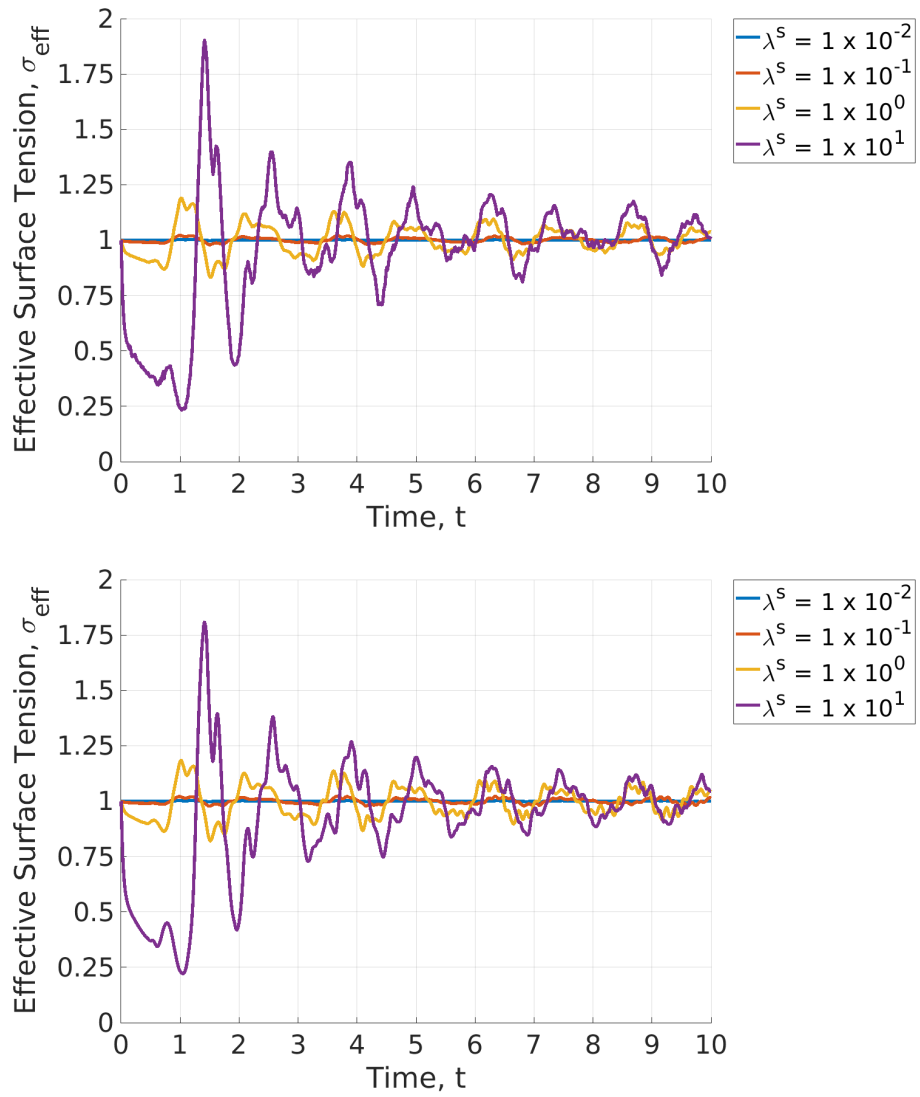


Figure 5.6: Comparison for the effective surface tension for suspended drops released from rest with initial shape (4.6.6) with $\epsilon = 0.5$, and small λ^s , from simulations using (top) a VoF implementation using Basilisk, and (bottom) a BEM implementation using purpose-built code described in §4.5. The details of the BEM simulations can be found in the caption of Figure 4.32, and for the VoF simulations in the caption of Figure 5.5.

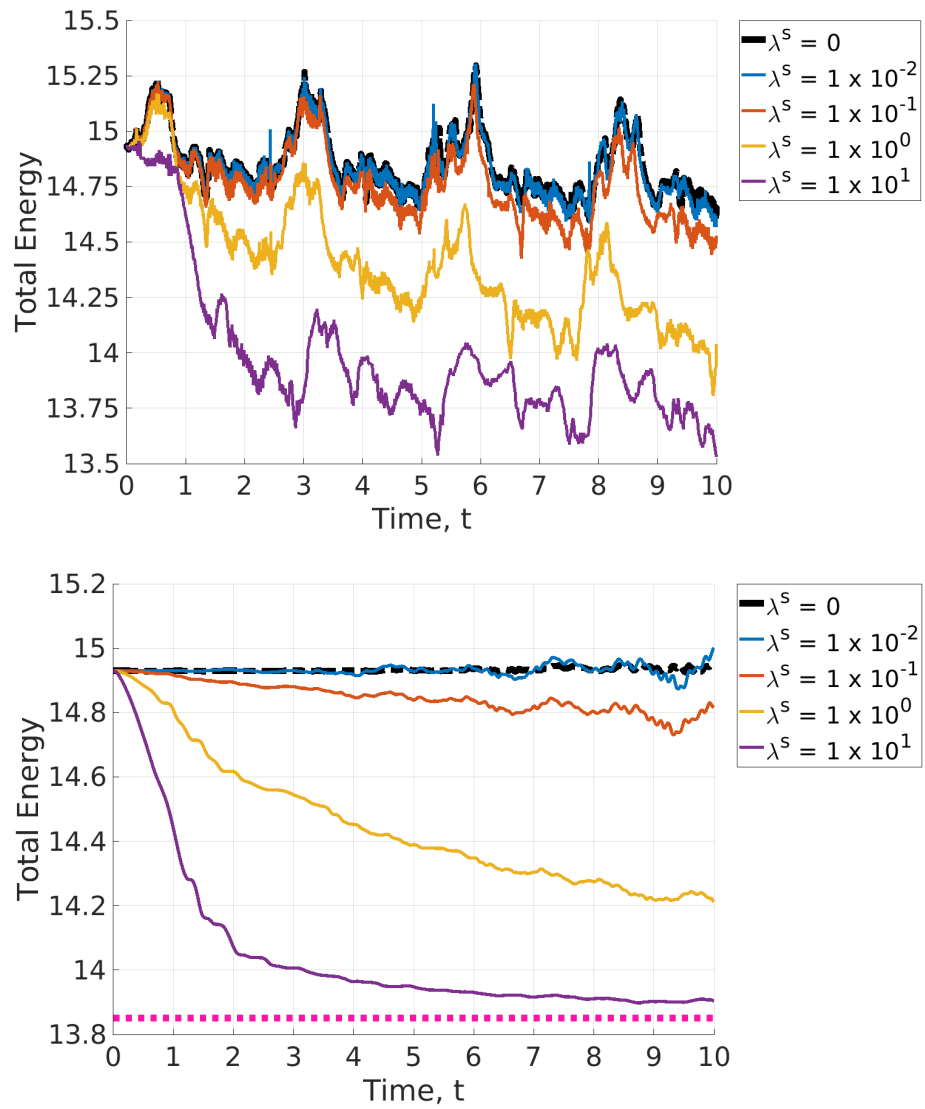


Figure 5.7: Comparison for the total energy for suspended drops released from rest with initial shape (4.6.6) with $\epsilon = 0.5$, and small λ^s , from simulations using (top) a VoF implementation using Basilisk, and (bottom) a BEM implementation using purpose-built code described in §4.5. The details of the BEM simulations can be found in the caption of Figure 4.32, and for the VoF simulations in the caption of Figure 5.5.

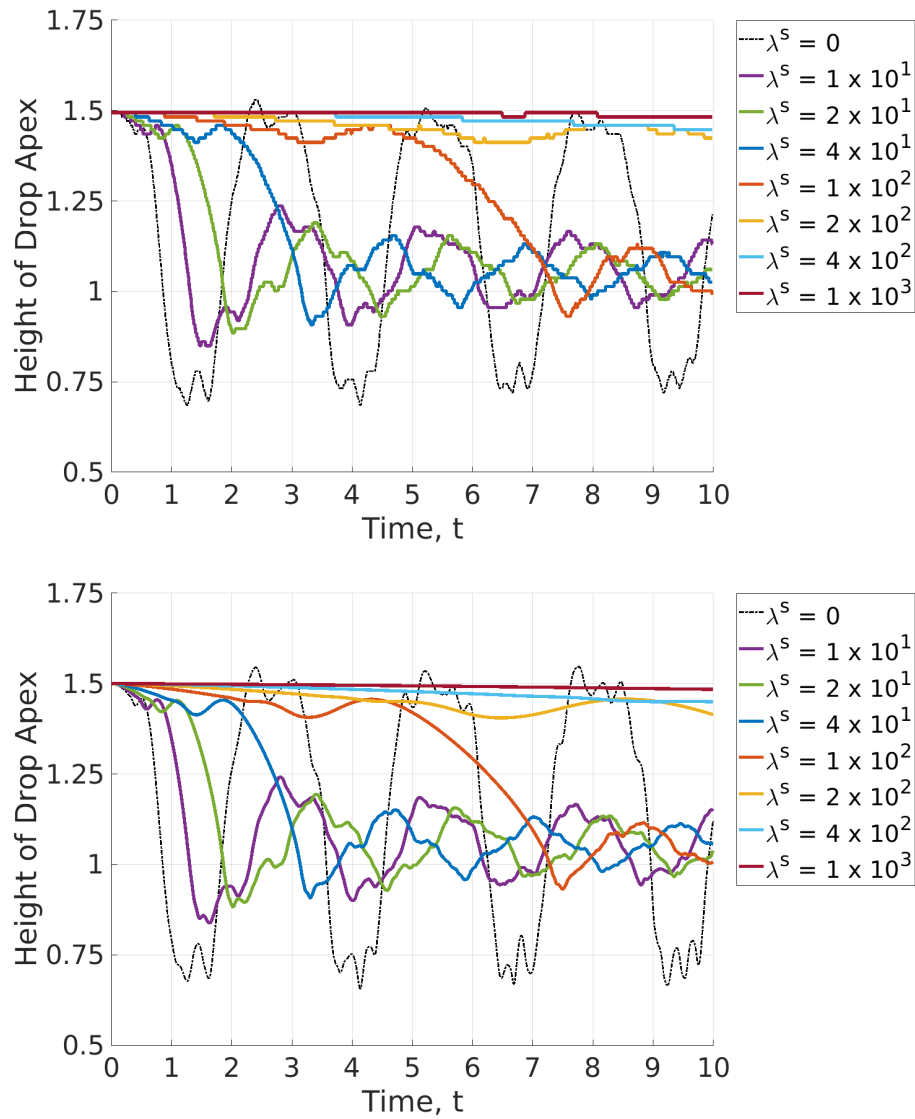


Figure 5.8: Comparison for the height of the drop apex (from the centre of mass of the drop) for suspended drops released from rest with initial shape (4.6.6) with $\epsilon = 0.5$, and large λ^s , from simulations using (top) a VoF implementation using Basilisk, and (bottom) a BEM implementation using purpose-built code described in §4.5. The details of the BEM simulations can be found in the caption of Figure 4.32, and for the VoF simulations in the caption of Figure 5.5.

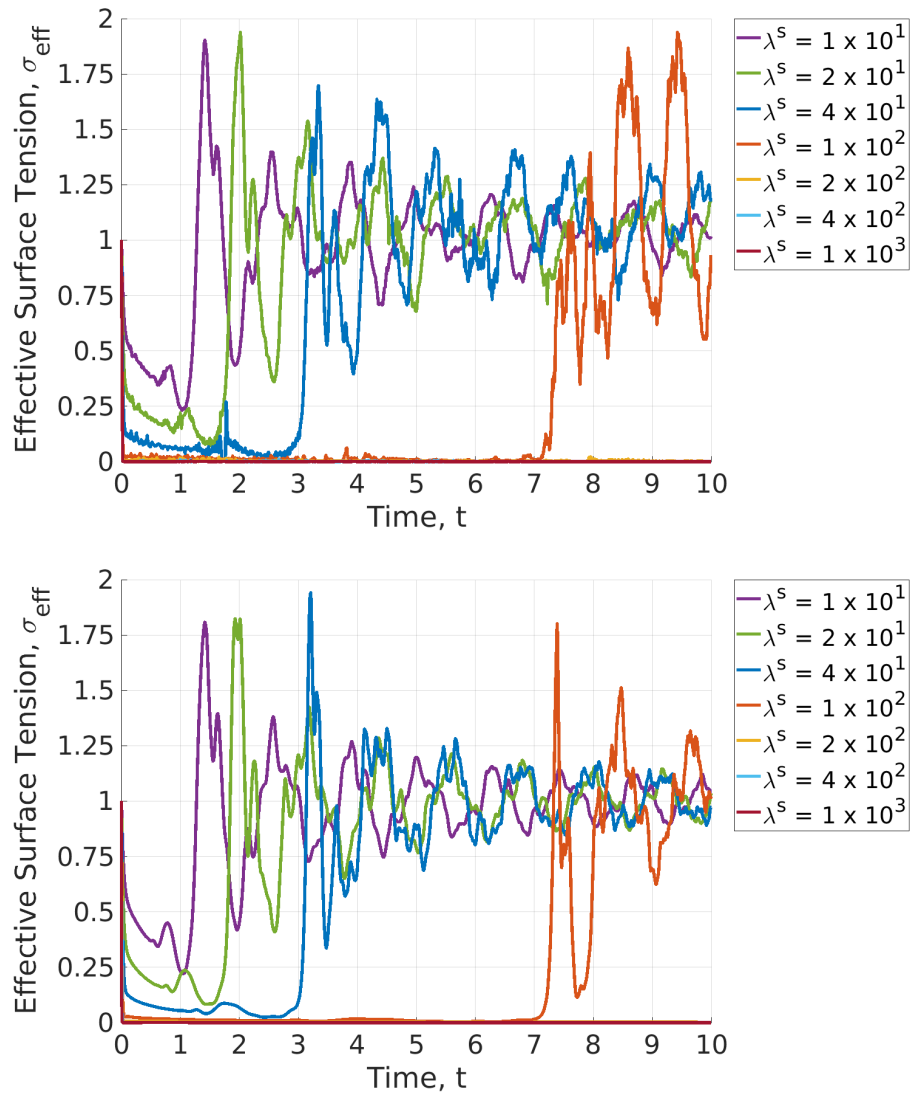


Figure 5.9: Comparison for the effective surface tension for suspended drops released from rest with initial shape (4.6.6) with $\epsilon = 0.5$, and large λ^s , from simulations using (top) a VoF implementation using Basilisk, and (bottom) a BEM implementation using purpose-built code described in §4.5. The details of the BEM simulations can be found in the caption of Figure 4.32, and for the VoF simulations in the caption of Figure 5.5.

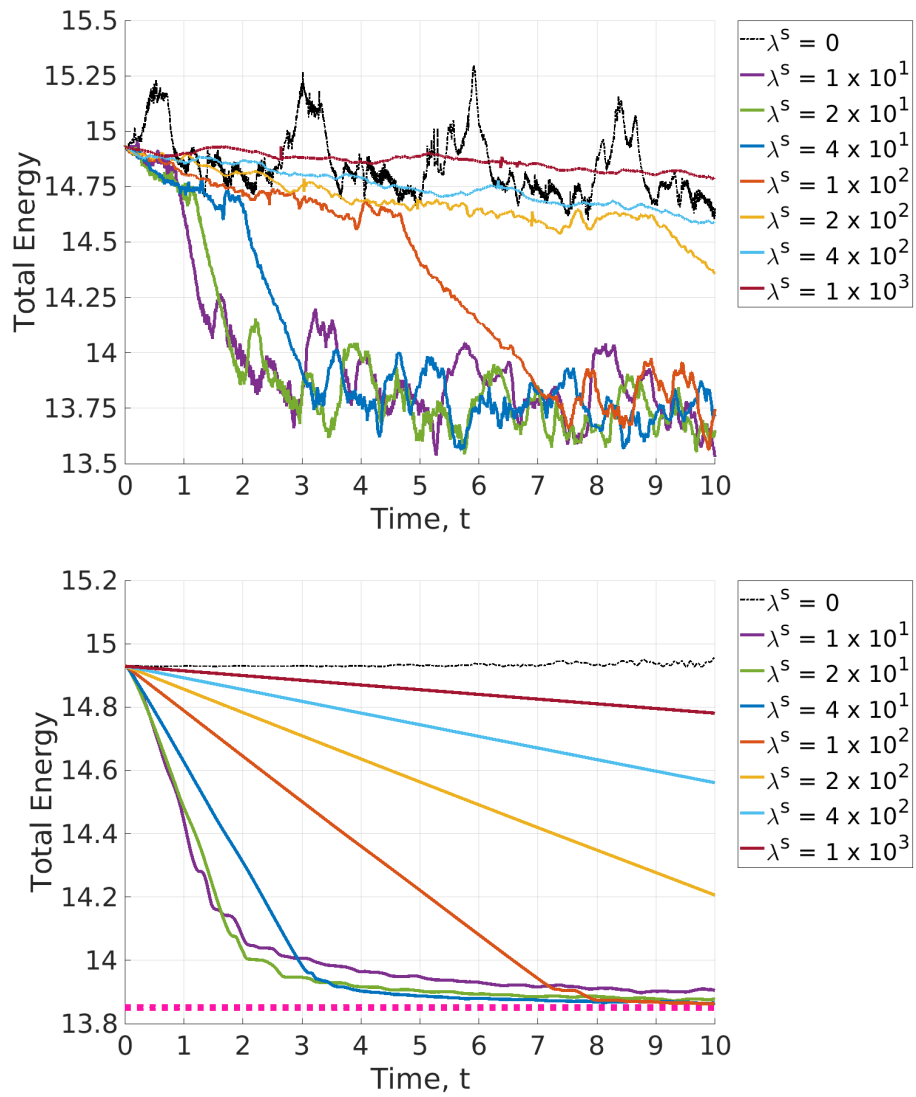


Figure 5.10: Comparison for the total energy for suspended drops released from rest with initial shape (4.6.6) with $\epsilon = 0.5$, and large λ^s , from simulations using (top) a VoF implementation using Basilisk, and (bottom) a BEM implementation using purpose-built code described in §4.5. The details of the BEM simulations can be found in the caption of Figure 4.32, and for the VoF simulations in the caption of Figure 5.5.

5.3.3 Curvature Limitation

In §7.2, we discuss how we choose the parameter β in the constitutive equation for the dilatational surface viscous coefficient λ^s (3.2.37) to best match our simulations to experiments. We find for comparatively large values of β that numerical problems arise relating to regions experiencing high curvature readings (in absolute terms) for long period of time, and so we impose a condition to ‘limit the curvature’. Ultimately, it is only simulations using values of β orders of magnitude higher than the eventual chosen value where this condition is needed and is applied frequently enough to affect the results significantly, but we include a discussion here for completeness.

VoF methods have difficulty dealing numerically with regions of high curvature, particularly when the absolute value of the curvature approaches the reciprocal of the smallest cell diameter resolving the interface [182]. Note that we cannot increase resolution indefinitely as we are limited in the computing power we have available as a resource for this body of research. For a simulation where the surface tension is unity (its value for a clean interface, in dimensionless terms), these regions are smoothed quickly enough so that numerical issues associated with high curvatures are limited in their effects. However, an effective surface tension close to zero allows high-curvature regions to persist in time and can become even ‘sharper’ depending on the behaviour of bulk flow within the drop (contributions from the gas flow are likely small). Left unchecked, these regions can cause spurious dynamics whereby, for example, the interfacial curvature continues to increase and bends the interface significantly over the length of a handful of grid cells and causes increases in the local surface area and allows small interior bubbles to form. As previously mentioned, Basilisk (and VoF methods in general) has difficulty accurately approximating interfacial quantities, and so further complications involving spurious small-scale dynamics only makes these approximations worse.

To avoid these issues, we impose a simple curvature-limiting condition, motivated by the fact that a true powder coated drop interface is likely to have a natural limit on its curvature relating to the size of the powder particles adsorbed onto the drop interface. Reasonably, the (absolute) curvature of a region of the drop interface should *not* exceed the curvature on the surface of the typical powder particle located on that particular region. The powder particles used in our experiments are spherical, and the mean particle diameter is found to be $\bar{d}_p = 23.72\mu\text{m}$ (see §2.1), so following this

reasoning, the curvature of the drop interface should be limited by C/\bar{d}_p , for some constant C .

For our model, we impose this condition by replacing the effective surface tension term $\sigma_{\text{eff}}(t)$ in the global momentum equation (5.1.12) with the following spatially dependent function,

$$\Sigma(\underline{\mathbf{x}}, t) = \begin{cases} \sigma_{\text{eff}}(t), & |\nabla_s \cdot \underline{\mathbf{n}}|(\underline{\mathbf{x}}) < C/\bar{d}_p \\ 1, & |\nabla_s \cdot \underline{\mathbf{n}}|(\underline{\mathbf{x}}) \geq C/\bar{d}_p. \end{cases} \quad (5.3.6)$$

So whenever the local curvature on the drop interface exceeds the preset limit, the surface tension is locally set to unity, and so this region is smoothed until the curvature falls below the limit. Our global conservation of momentum equation then ends up as

$$\tilde{\rho} \left[\frac{\partial \tilde{\underline{\mathbf{u}}}}{\partial t} + (\tilde{\underline{\mathbf{u}}} \cdot \nabla) \tilde{\underline{\mathbf{u}}} \right] = -\nabla \tilde{p} + \tilde{\rho} \underline{\mathbf{g}} + \nabla \cdot (2\tilde{\mu} \text{Oh} \underline{\underline{\mathbf{D}}}) - \delta(n) \Sigma(\underline{\mathbf{x}}, t) (\nabla_s \cdot \underline{\mathbf{n}}) \underline{\mathbf{n}}. \quad (5.3.7)$$

For the simulations of liquid marble generation where this is triggered, (for $\beta \geq 10$), we use $C = 1$. We find that this condition alleviates the problems faced by the simulations that use it, but as noted earlier, the value of β chosen for our simulations to best match experiments is much lower than for those cases where this condition is triggered.

Chapter 6

Drop Impact

In this chapter, we discuss the results of *clean* (that is, with $\lambda^s \equiv 0$) drop impact simulations in Basilisk, using the VoF method introduced in Chapter 5; which is a numerical implementation of the viscous model developed in §3.2.5. We simulate drop impacts onto a rigid substrate with multiple impact Weber numbers, from which we then extract the drop shapes and velocity profiles at the moment of encapsulation (which, recall, occurs post-rebound in our model following experimental observations). This extracted data then provides initial conditions for surface viscous simulations (that is, where $\lambda^s \neq 0$) of liquid marble formation (presented in Chapter 7). The impact Weber numbers in simulations are (approximately) the same as those for the drop impact experiments in Chapter 2.

We will show that our drop impact simulations exhibit good agreement with our powder bed experiments in terms of the spreading factor γ (recall this is the ratio of the maximum spreading diameter over the initial drop diameter), for the *spreading time* (the time from moment of contact with the substrate to when maximum spread is reached) and the *contact time* (the time from the moment of contact to the moment the drop rebounds from the substrate). Reproducing the spreading factor is particularly important as it determines the values of the drop surface area corresponding to drop encapsulation, and liquid marble formation (discussed initially in §2.3.4). We will also see that by introducing a ‘pinning radius’, justified by referencing rigid substrate impact experiments in §2.3.1, we can make our simulations better match drop impact experiments onto a rigid superhydrophobic substrate in terms of the contact time.

This chapter concludes with a presentation of extracted drop profiles from our

simulations overlaid onto our experiments of drop impacts onto both types of substrate. This will then lead into Chapter 7 which uses the results described in this chapter as a basis for simulations of liquid marble formation.

6.1 Spread Dynamics and Timescales for Interaction with the Substrate

We will show that the spreading factors from the drop impact simulations agree with the spreading factors observed in our experiments, and others from the literature. We will also show the agreement in the spreading times and contact times between our simulations and powder bed experiments, and that by introducing a pinning radius (motivated experimentally) we can increase the contact times to match those of the rigid superhydrophobic substrate experiments. We will start with a discussion on the validity of the chosen slip lengths between the drop and solid substrate.

6.1.1 Slip Length: Numerical Justification

In our discussion of the viscous model (see §3.2.5), we justify the inclusion of a boundary condition at the liquid-solid interface (between the drop and the rigid impermeable superhydrophobic substrate) in terms of a slip length. In that section, we reason that the slip length in the case of drop impacts onto powder beds is likely to be on the order of the mean powder particle diameter, $\bar{d}_p = 23.72\mu\text{m}$. In simulations, the limitation on the smallest computational cell size is determined by the computing power we have available as a resource; in our case, with a square domain of length 24mm, we can routinely simulate drop impacts with cell sizes no smaller than $24\text{mm}/2^{12} \approx 5.86\mu\text{m}$ (mesh refinement involves routinely splitting ‘parent’ cells into 4 constituent ‘child’ cells with *half* the length of the parent). Given that the slip length is multiple times *larger* than the smallest cell size, we are confident that its effects are resolved relatively accurately in our simulations.

In Figure 6.1 we see the spreading factor as calculated for multiple simulations with different impact Weber numbers and for different imposed slip lengths. For imposed slip lengths *larger* than the minimum computational cell size, there is clear variation in the spreading factor, in particular we see that the spreading factor is an

increasing function of the slip length, which seems intuitive. When the imposed slip length is *smaller* than the minimum cell size, we see *little* variation in the spreading factor; indicating that the simulations are instead being governed by an effective ‘numerical’ slip length on the scale of the minimum cell size itself. Taking the imposed slip length to zero is equivalent to approaching a no-slip condition (whereby the tangential velocity at the interface is zero), so if we were capable of refining the mesh indefinitely (with the minimum cell size tending to zero), we would expect to see the calculated spreading factor tending to unity as the imposed slip length tends to zero. This spreading factor data for minimum cell sizes *smaller* than our own would then form a monotonic curve when combined with the current data for slip lengths *larger* than $5.86\mu\text{m}$ (our current minimum cell size).

The ‘true’ slip length of the *clean* rigid superhydrophobic substrates used in our experiments (see §2.3.1) is likely to be on the order of $1\mu\text{m}$ (approximate size of the surface asperities), which is *smaller* than our minimum cell size of $5.86\mu\text{m}$, meaning we are therefore unable to accurately resolve at the appropriate scale when simulating impacts of this nature. However, in Figure 6.1 we see that the spreading factor is relatively insensitive to a change in slip length (for slip lengths larger than the minimum cell size); with a maximum increase of approximately 10% (seen in the $We = 66$ case) for a two order of magnitude increase in the slip length (from 10^{-2}mm to 10^0mm). This insensitivity is also observed in Figure 6.3, where the spreading factors from drop impact experiments onto surfaces exhibiting the Leidenfrost effects (represented by filled markers) are *not much* larger than those from impacts onto micro-textured superhydrophobic surfaces (represented by un-filled markers), even though the slip length for the former case is likely *much larger* than the latter due to the impacting drop skating along a thin vapour film above the solid surface rather than spreading along, and interacting with, the solid surface itself. Therefore, although we cannot reach the desired resolution to match the approximate slip length of the rigid superhydrophobic substrates from our experiments, we are satisfied in our ability to obtain meaningful results for simulations of impacts onto such surfaces by imposing an artificially *larger* slip length that *is* resolvable in our simulations. For simplicity, we choose the same slip length as in simulations of powder bed impacts; the mean powder particle diameter, $\bar{d}_p = 23.72\mu\text{m}$.

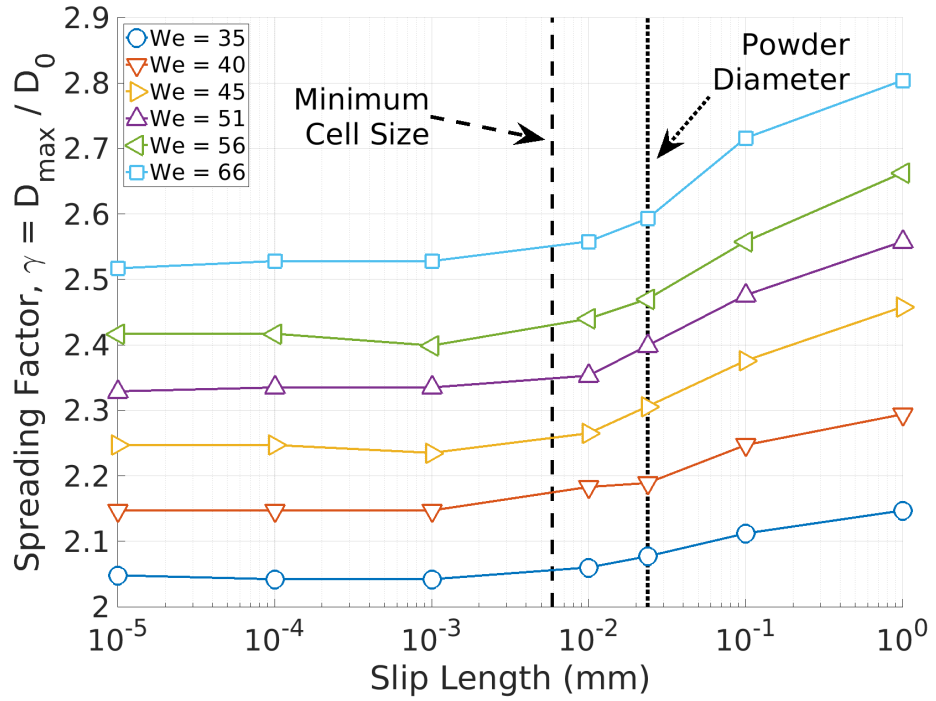


Figure 6.1: Spreading factor as a function of imposed slip length for multiple impact Weber number drop impact simulations. The minimum cell size in all simulations is approximately $5.86\mu\text{m}$. For reference, note that the mean powder particle diameter is $23.72\mu\text{m}$, and the initial drop diameter is 2mm . Data points on the *left* of the minimum cell size correspond to a ‘numerical’ slip length on the order of the minimum cell size, and simulations for the data points on the *right* are assumed to be well-resolved at their imposed slip lengths.

6.1.2 Pinning Radius

As described in §2.3.1, for drop impact experiments onto rigid impermeable superhydrophobic substrates, we often see that once the contact line has receded sufficiently from its position at maximum spread, there is a significant reduction in the dynamic contact angle. In experiments, we observe that this reduction in contact angle occurs when the (dimensionless) contact line radius lies somewhere between $r_{CL} = 0.25$ and $r_{CL} = 0.50$ (recall the initial drop radius is unity), and that the contact angle decreases from approximately 160° to 120° . For our simulations of rigid substrate drop impacts, we impose this reduction of the dynamic contact angle between the drop and substrate at $r_{CL} = 0.50$. Importantly, this phenomenon is *not* observed in our drop impact experiments onto powder beds and so this is not included in simulations of that situation.

Alternative models have been developed for modelling drop interactions with solid substrates, including more complicated dynamic contact angle models [187, 188], but the experimentally-guided simple approach taken here provides an adequate approximation of the drop dynamics considering the scope of this body of research.

6.1.3 Validation against Experiments

We now validate our drop impact simulations against experiments by comparing the observed spreading factors, spreading times, and contact times. In Figure 6.2 we see for $35 \leq We \leq 89$ (the interval of impact Weber numbers that exhibit interesting behaviour in powder bed experiments), the spreading times and contact times for our drop impact experiments onto rigid impermeable superhydrophobic substrates, and onto superhydrophobic powder beds. This figure also includes data from simulations with and without an imposed pinning radius, noting that the spreading time is the same in both cases because the pinning radius only affects drop *retraction*. We see that the spreading times in our simulations agree with both types of experiments, and that *without* a pinning radius, the contact time (spreading time plus retraction time) for simulations agrees with those observed in the powder bed experiments, and by *including* the pinning radius, the contact time is extended and agrees with the rigid impermeable superhydrophobic substrate experiments.

Of note in Figure 6.2 is that the spreading time and contact time (with and without a pinning radius) observed in our experiments and simulations, are each *independent* of the impact Weber number. Prior research found that the contact time for drop impacts onto rigid superhydrophobic substrates was independent of the *impact speed* [189], which is consistent with our finding because the liquid in our experiments is always the same (de-ionised water, see §2.1), and its material properties are used in *all* our simulations, so the variation in the impact Weber number is *entirely* due to change in impact speed. Further research confirmed this observation, additionally finding that the *spreading time* of a drop on a superhydrophobic substrate is *also* independent of the impact speed [190, 191], consistent with our results.

In Figure 6.3, we see very good agreement between our simulations and our experiments in terms of the spreading factor across a wide range of impact Weber numbers. The data points in the second plot (initially collated in [126]) are also from

drop impact experiments onto superhydrophobic substrates, and show exceptional agreement with our own results. In this plot we see data from impacts onto rigid micro-textured superhydrophobic surfaces [125, 126, 190, 192] (given by the un-filled markers), and from impacts onto surfaces exhibiting the Leidenfrost effect [193, 194] (given by the filled markers), where superhydrophobicity is a consequence of the substrate being at a very high temperature, which causes the impacting drops to spread along a thin vapour film above the substrate.

Finally, in Figures 6.4-6.5 we see, for 10 distinct impact Weber numbers, outlines of the drop during the spreading stage of our drop impact simulations overlaid onto images from our rigid substrate and powder bed experiments, respectively, at those same (or similar) impact Weber numbers. The experiments shown for each impact Weber number are representative of the other experiments at those We . Further, the simulations and experiments are aligned in time, so that the (dimensionless) time of $t = 0.00$ is the moment of contact between the drop and substrate for both situations. The images show the drops moments after contact with the rigid substrate or powder bed, then part way through the spreading regime, and when the drops are at their maximum spread. The overlaid simulations show exceptional agreement with both rigid substrate impact experiments and powder bed impact experiments, even when the powder bed experiments exhibit glimpses of axisymmetry breaking waves on the drop surface at high impact Weber numbers.

Now that we have confirmed the agreement between our simulations and experiments with regards to the spreading factor, spreading time and contact time, we move on to a comparison of the retraction, and rebound dynamics.

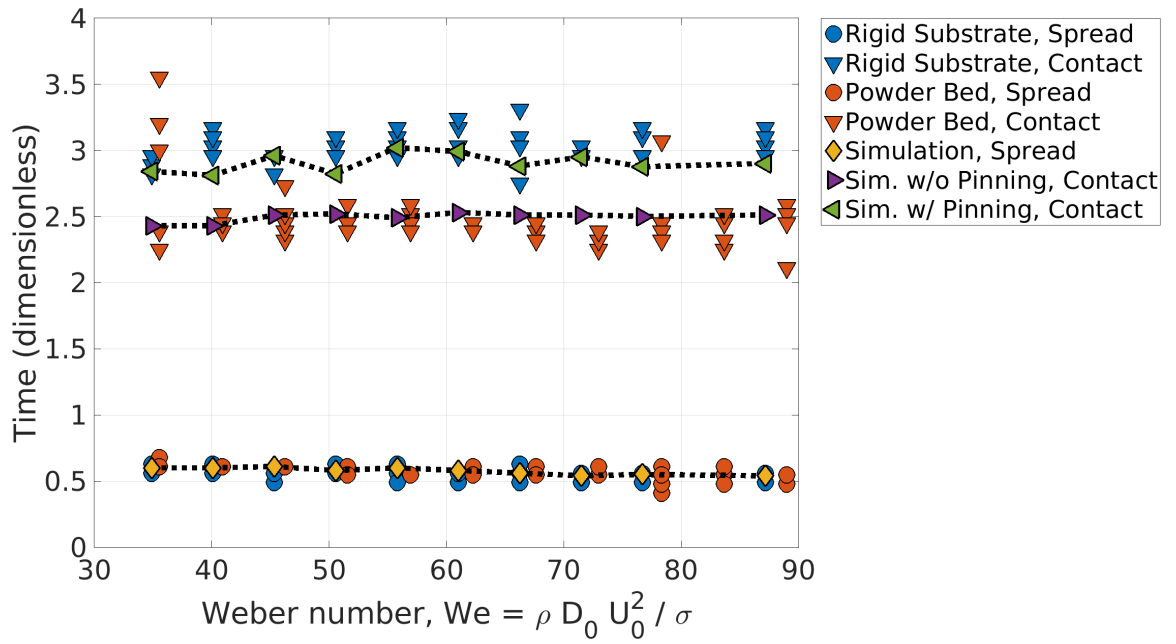


Figure 6.2: Spreading time (from the moment of contact with the substrate to the moment maximum spread is reached) and contact time (total time on the substrate, so spreading time plus retraction time) for drop impact experiments and simulations. Experimental data is gathered from rigid impermeable superhydrophobic substrate experiments and superhydrophobic powder bed experiments discussed in Chapter 2. The simulations are run in Basilisk using our VoF implementation, with contact times given with and without the inclusion of a pinning radius (see §6.1.2), and with the spreading time shared by both types of simulation.

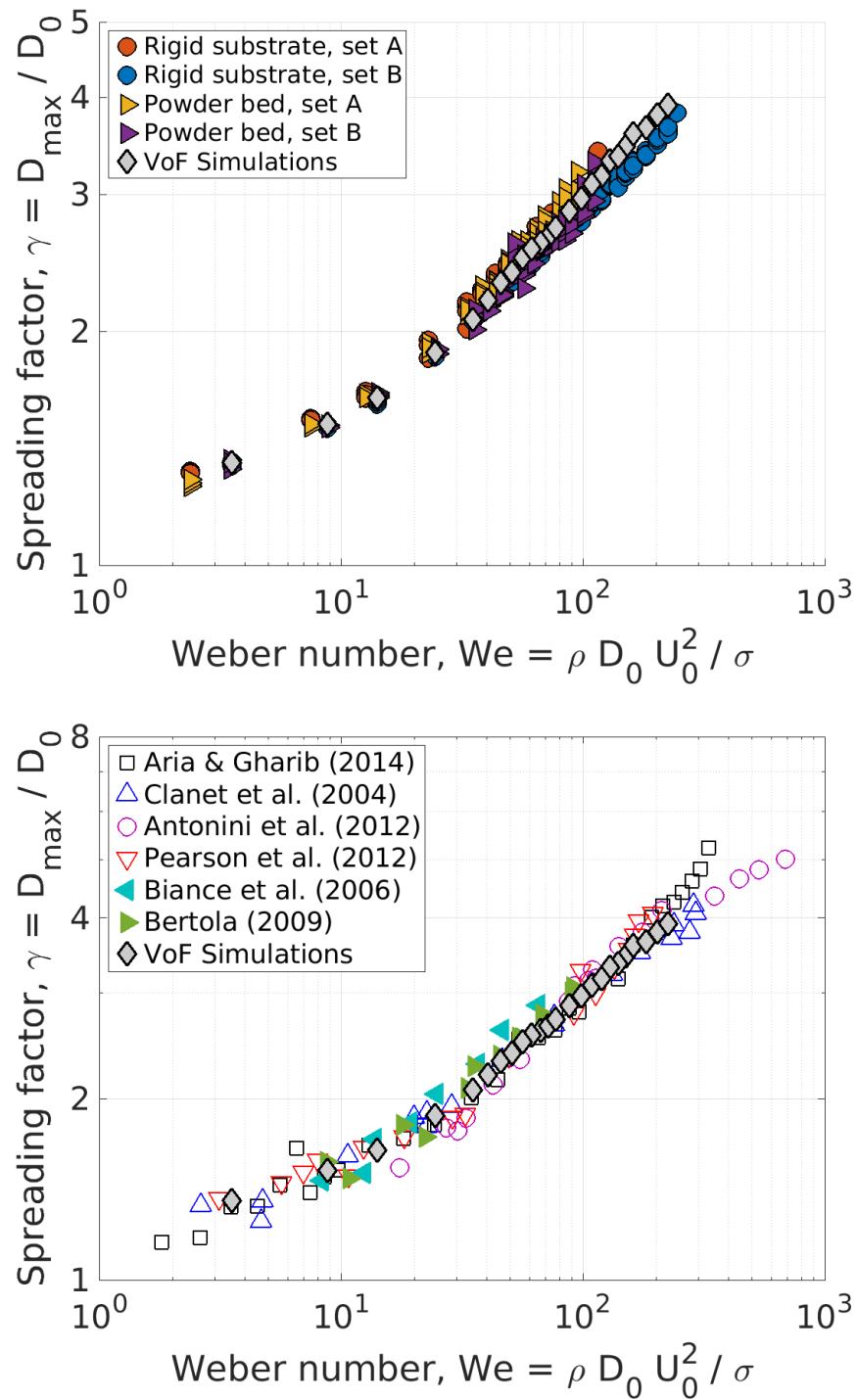


Figure 6.3: Spreading factor plotted against the impact Weber number for our VoF drop impact simulations using Basilisk, along with data from (top) our drop impact experiments on rigid impermeable superhydrophobic substrates and superhydrophobic powder beds, and from (bottom) drop impact experiments on micro-textured rigid superhydrophobic substrates (un-filled markers) [125, 126, 190, 192], and surfaces exhibiting the Leidenfrost effect (filled markers) [193, 194].

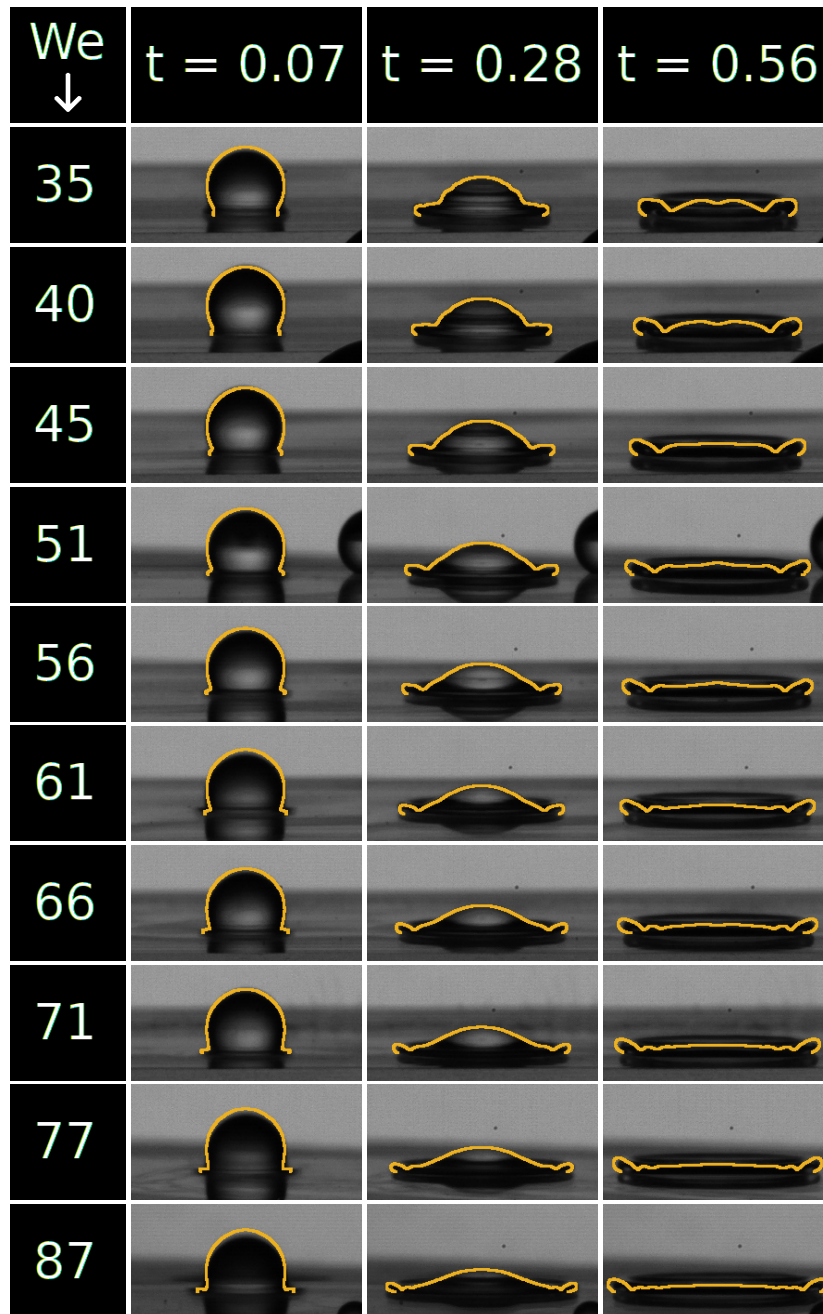


Figure 6.4: Outlines of drops from drop impact simulations with VoF using Basilisk, overlaid onto drop impact experiments on rigid impermeable superhydrophobic substrates (as shown in Chapter 2). The dimensionless time of $t = 0.00$ indicates the moment of contact between the drop and substrate in both the simulations and experiments. The images on the right with $t = 0.56$ are at the approximate time when the drops reach their maximum spread (recall that this is We -independent). The experiments shown are representative of other experiments with their impact Weber numbers.

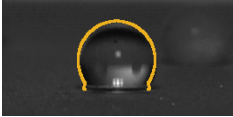
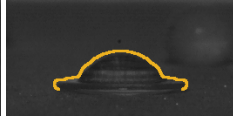
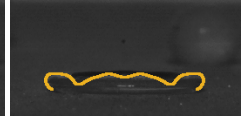
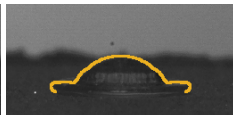
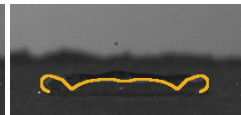
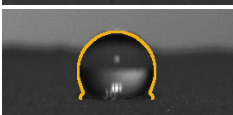
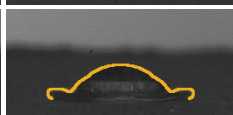
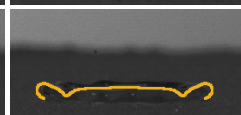
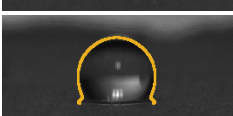
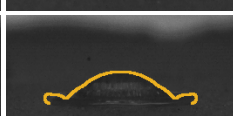
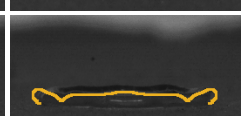
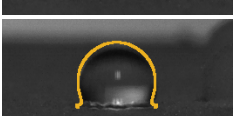
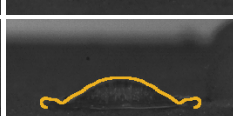
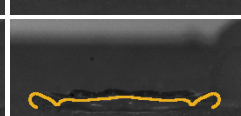
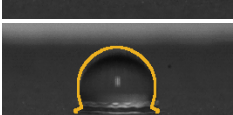
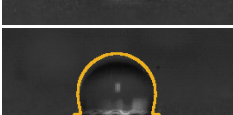
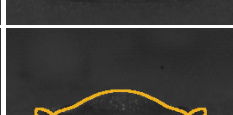
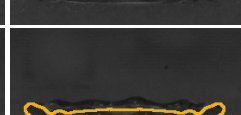
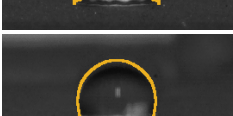
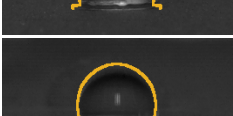
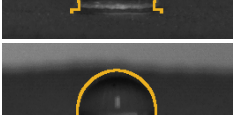
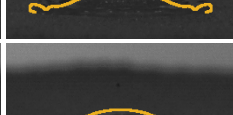
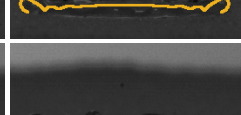
We Sim. ↓ Exp.	$t = 0.07$	$t = 0.28$	$t = 0.56$
35 36			
40 41			
45 46			
51 52			
56 57			
61 62			
66 68			
71 73			
77 78			
87 89			

Figure 6.5: Outlines of drops from drop impact simulations with VoF using Basilisk, overlaid onto drop impact experiments on superhydrophobic powder beds (as shown in Chapter 2). The dimensionless time of $t = 0.00$ indicates the moment of contact between the drop and substrate in both the simulations and experiments. The images on the right with $t = 0.56$ are at the approximate time when the drops reach their maximum spread (recall that this is We -independent). The experiments shown are representative of other experiments with their impact Weber number.

6.2 Retraction and Rebound Dynamics

We now compare the retraction and rebound dynamics of our drop impact simulations against our experiments. We begin with a demonstration of how the inclusion of the pinning radius (which was motivated by experiments in §2.3.1) leads to better agreement between our simulations and experiments of drop impacts onto rigid superhydrophobic substrates. We follow this with a comparison between our simulations and experiments of drop impacts onto powder beds up to the point of encapsulation in our simulations (as determined by the spreading factor, see Chapter 7) in which, we recall, no pinning radius is required.

6.2.1 Rigid Substrate Impacts

In Figures 6.6-6.8 we see examples of our drop impact simulations overlaid onto drop impact experiments on rigid impermeable superhydrophobic substrates, with the dimensionless time $t = 0.00$ corresponding to the moment of contact with the substrate for the simulation and experiment. Provided in each figure are the simulations at that particular impact Weber number *with* and *without* the pinning radius as described in §6.1.2.

As shown in Figure 6.2, the inclusion of the pinning radius means the contact time of the drop on the substrate *increases* and better matches that of the rigid substrate experiments. This is confirmed visually from the drop shapes also, with the overlays of simulations on experiments at times $t = 2.94$ in Figure 6.6, $t = 2.73$ in Figure 6.7, and $t = 2.87$ in Figure 6.8 showing that the simulations *without* a pinning radius have already rebounded from the substrate, while the simulations *with* a pinning radius remain in contact with the substrate, like the drops in the experiments. In Figure 6.6, we note that the simulation *with* the pinning radius shows exceptional agreement with respect to the shape of the primary drop during post-rebound oscillations, doing significantly better than the simulation *without* the pinning radius. In Figures 6.7-6.8, including the pinning radius does not produce as exceptional agreement between simulations and experiments, but the resemblance is improved, noting in particular that the simulations with the pinning radius better trace the height and shape of the bottom of the primary drop in experiments for some time after rebound. We do however note the inclusion of the pinning radius does not

provide significant improvement in recreating the shape and breakup dynamics of the jet formed prior to rebound, which contributes greatly to post rebound dynamics (particularly for higher We), and appears to be the primary cause in the discrepancy in drops shapes between our simulations and the experiments.

Including a pinning radius has enabled us to slightly improve agreement between our simulations and experiments for impacts onto rigid substrates, but we will see in §6.2.2 that it has had no benefit for improving agreement with experiments for impacts onto powder beds. As the latter type of impact is our focus, we henceforth do *not* include a pinning radius for contact with the substrate when simulating liquid marble formation in Chapter 7.

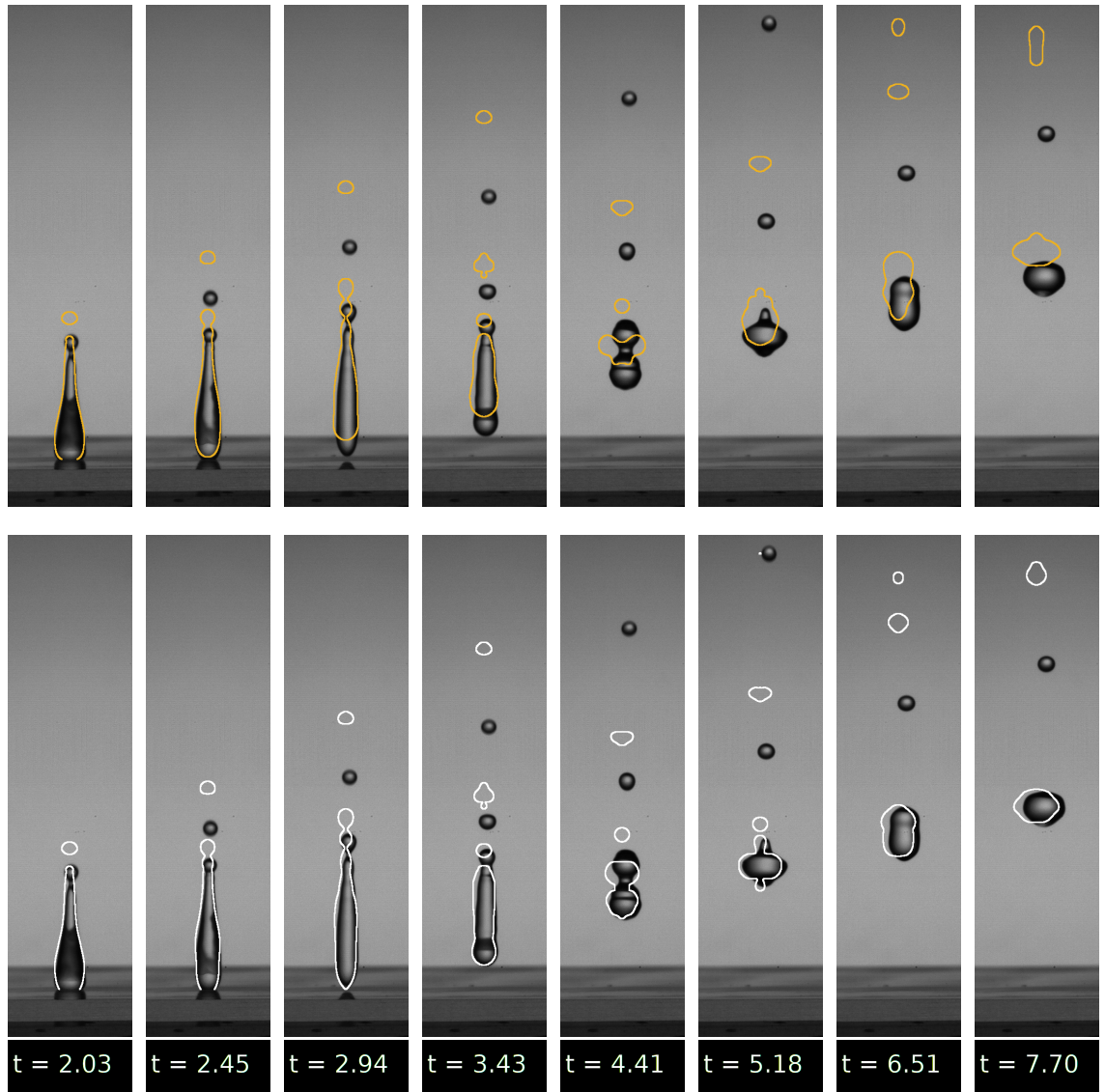


Figure 6.6: Drop shape from a $We = 45$ ($\gamma = 2.31$) simulation overlaid onto a $We = 45$ ($\gamma = 2.27$) rigid substrate experiment. The moment of contact (at dimensionless time $t = 0.00$) is synchronised between the simulation and experiment. The top row of images is overlaid with a simulation *without* a pinning radius. The bottom row of images is overlaid with a simulation *with* a pinning radius of $r_{pin} = 0.5$ reducing the dynamic contact angle from 160° to 120° when reached by the receding contact line.

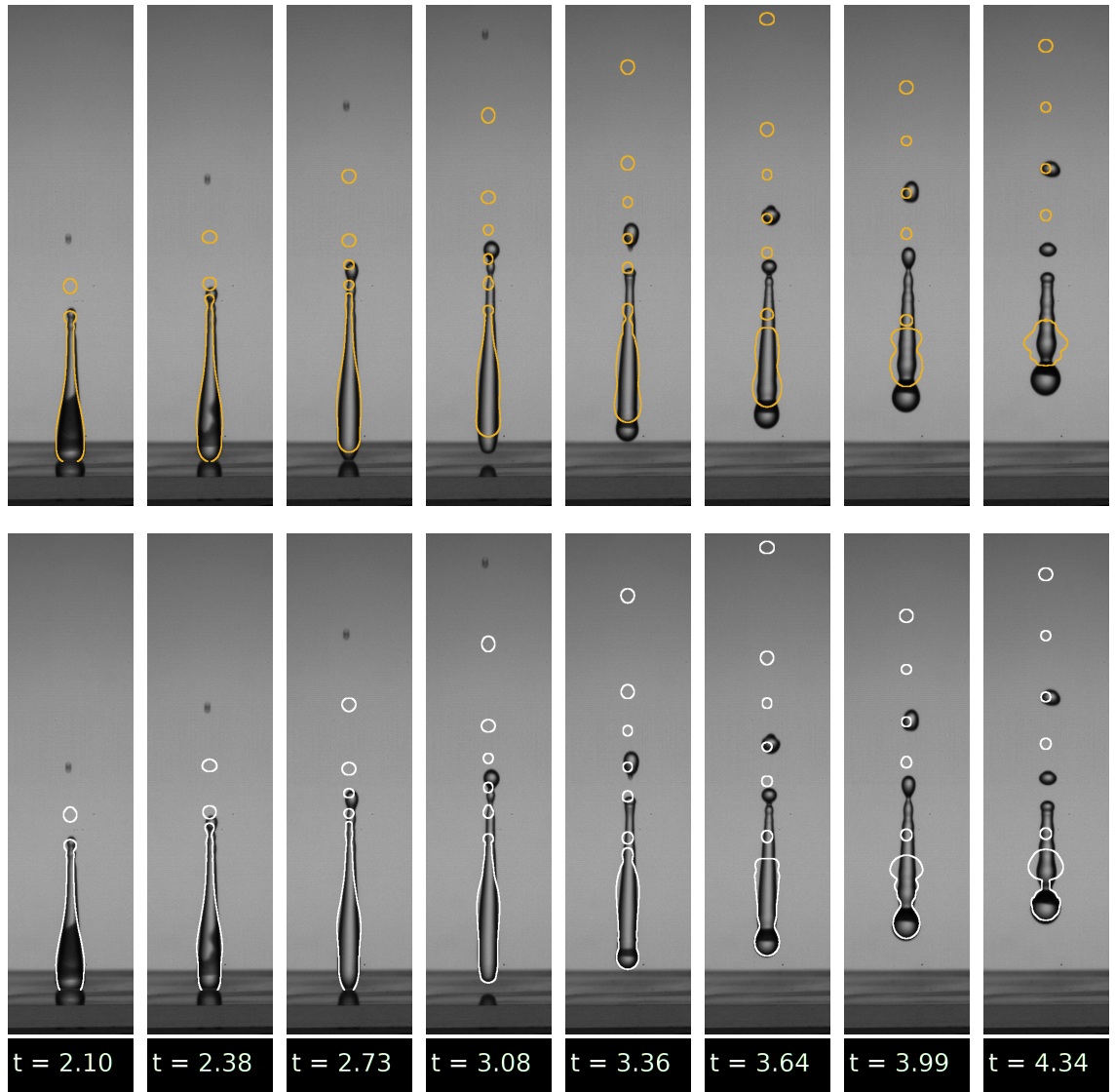


Figure 6.7: Drop shape from a $We = 61$ ($\gamma = 2.53$) simulation overlaid onto a $We = 61$ ($\gamma = 2.49$) rigid substrate experiment. The moment of contact (at dimensionless time $t = 0.00$) is synchronised between the simulation and experiment. The top row of images is overlaid with a simulation *without* a pinning radius. The bottom row of images is overlaid with a simulation *with* a pinning radius of $r_{pin} = 0.5$ reducing the dynamic contact angle from 160° to 120° when reached by the receding contact line.

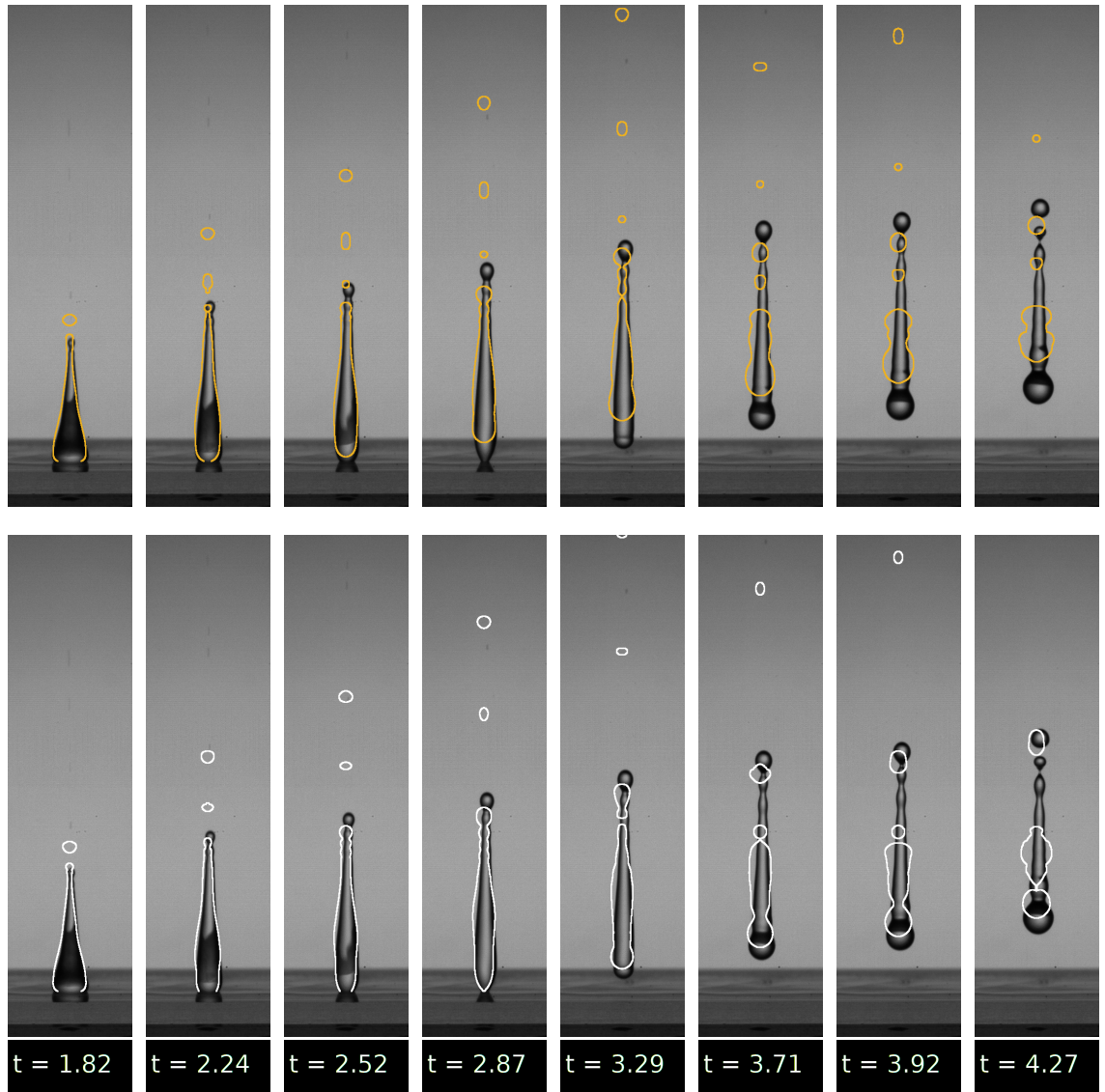


Figure 6.8: Drop shape from a $We = 66$ ($\gamma = 2.59$) simulation overlaid onto a $We = 68$ ($\gamma = 2.53$) rigid substrate experiment. The moment of contact (at dimensionless time $t = 0.00$) is synchronised between the simulation and experiment. The top row of images is overlaid with a simulation *without* a pinning radius. The bottom row of images is overlaid with a simulation *with* a pinning radius of $r_{pin} = 0.5$ reducing the dynamic contact angle from 160° to 120° when reached by the receding contact line.

6.2.2 Powder Bed Impacts

In Figures 6.9-6.11 we see examples of our drop impact simulations overlaid onto drop impact experiments on superhydrophobic powder beds, with the dimensionless time $t = 0.00$ corresponding to the moment of contact with the substrate for the simulation *and* experiment. We show the simulations that are eventually used in

Chapter 7 for liquid marble formation (with a constant contact angle), as well as the simulations with the pinning radius (as described in §6.1.2, with a reduction in the dynamic contact angle part way through retraction) that were implemented to better match rigid substrate impact experiments. The images begin with the drop during retraction, and end at the moment of encapsulation for the primary drop in the simulation *without* the pinning radius. Recall (see §2.3.4 and the discussion surrounding equation 3.2.32) that the moment of encapsulation is the first point in time, post-rebound, when the surface area of the drop falls below the ‘initial encapsulation area’ $A_{encap}^{(0)}$; itself defined as the maximum contact area between the drop and substrate, multiplied by a parameter, α_{encap} . The dependence of α_{encap} on the spreading factor, with which we obtain the values of α_{encap} to use in our drop impact simulations, is discussed in §7.1.

We see in these figures that our simulations are not in perfect agreement with the experiments of drop impacts onto powder beds; our simulations are much more prone to forming long thin jets prior to rebound, which is *not* something observed in these experiments. However, what we *actually* desire from these simulations are drop shapes at encapsulation that resemble those observed in powder bed experiments. These shapes (along with the velocity profile) then constitute the initial conditions for surface viscous simulations described in Chapter 7, which in turn produce liquid marbles. As previously mentioned, the moment of encapsulation is determined by the spreading factor; which we have already matched to our powder bed experiments (see §6.1). The intermediary period in our simulation between reaching maximum spread along the substrate, and encapsulation, is ultimately not very important; we see particularly in Figure 6.9 that although our simulations produce long vertical jets, once these have detached from the primary drop, the shape at encapsulation *is* reminiscent of the drop shape in the associated powder bed experiment. The same is also true for Figures 6.10-6.11, with further comparisons between drops at the moment of encapsulation in simulations and experiments shown and discussed in §7.3.1.

In Figures 6.9-6.11, the difference between the simulations with and without a pinning radius is subtle; their contact times are different and although, as shown in Figure 6.6-6.8 (note that these are the same simulations), significant differences in drop shapes emerge post-rebound, this is largely *after* encapsulation will have

occurred (for the simulation *without* the pinning radius). The simulations *with* the pinning radius form *longer* threads than the simulations *without* a pinning radius due to the extended contact time with the substrate, which are themselves longer than those seen in the powder bed experiments, but the difference between the two simulations for the shown stretches of time are not dramatic. Ultimately, we expect the two types of simulation to provide similar drop shapes at encapsulation, but given we do not observe any pinning of the contact line in our powder bed experiments, we use the simpler model (that utilises a constant contact angle) in our drop impact simulations, to then obtain initial conditions for our surface viscous liquid marble simulations (see Chapter 7).

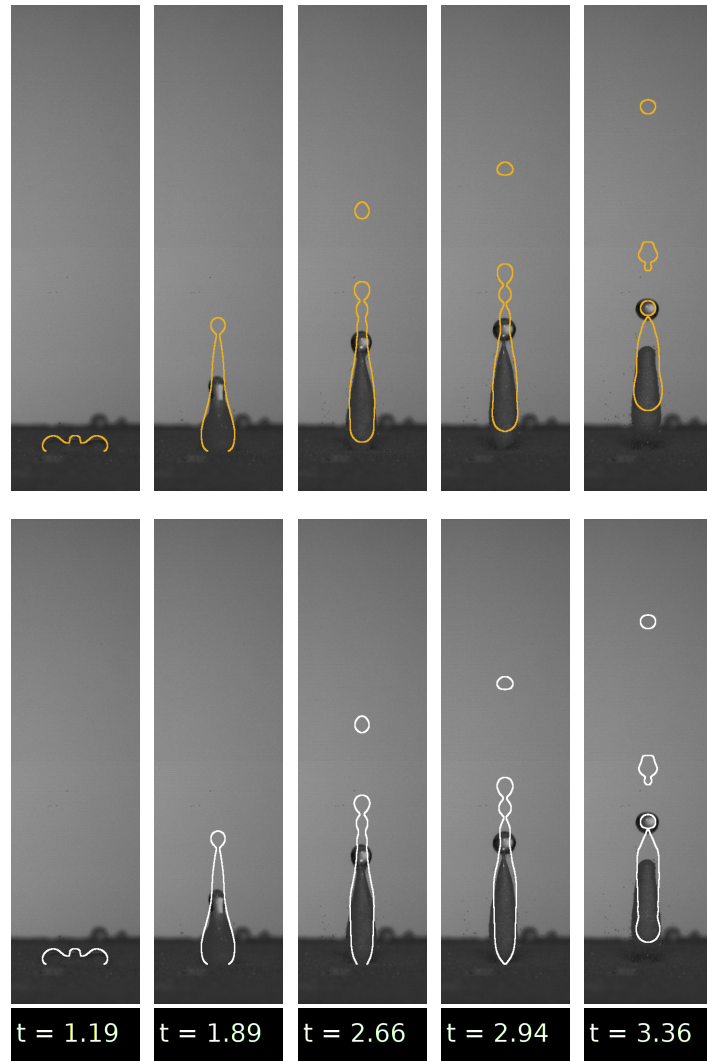


Figure 6.9: Drop shapes from $We = 45$ ($\gamma = 2.31$) simulations overlaid onto a $We = 46$ ($\gamma = 2.23$) powder bed experiment. The moment of contact (at dimensionless time $t = 0.00$) is synchronised between the simulation and experiment. The top (bottom) row is overlaid with a simulation *without* (*with*) a pinning radius of r_{pin} which reduces the otherwise constant contact angle when passed over by the receding contact line. Images span from part way through retraction along the powder bed to the moment of encapsulation for the primary drop in the non-pinning simulation.

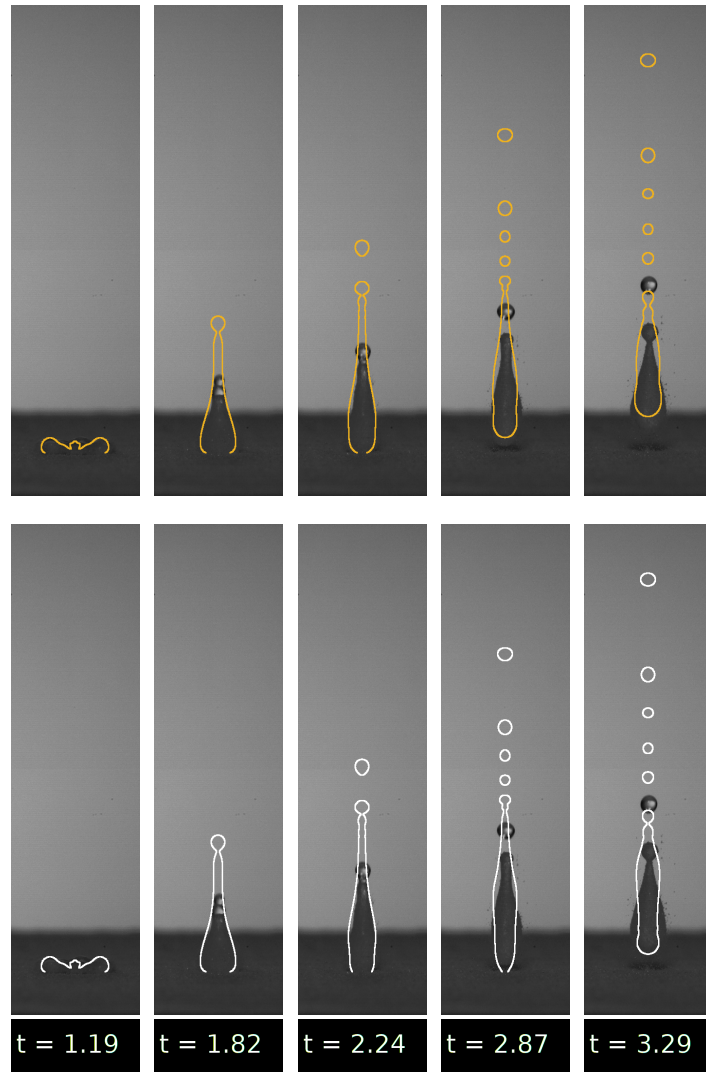


Figure 6.10: Drop shapes from $We = 61$ ($\gamma = 2.53$) simulations overlaid onto a $We = 62$ ($\gamma = 2.53$) powder bed experiment. The moment of contact (at dimensionless time $t = 0.00$) is synchronised between the simulation and experiment. The top (bottom) row is overlaid with a simulation *without* (*with*) a pinning radius of r_{pin} which reduces the otherwise constant contact angle when passed over by the receding contact line. Images span from part way through retraction along the powder bed to the moment of encapsulation for the primary drop in the non-pinning simulation.

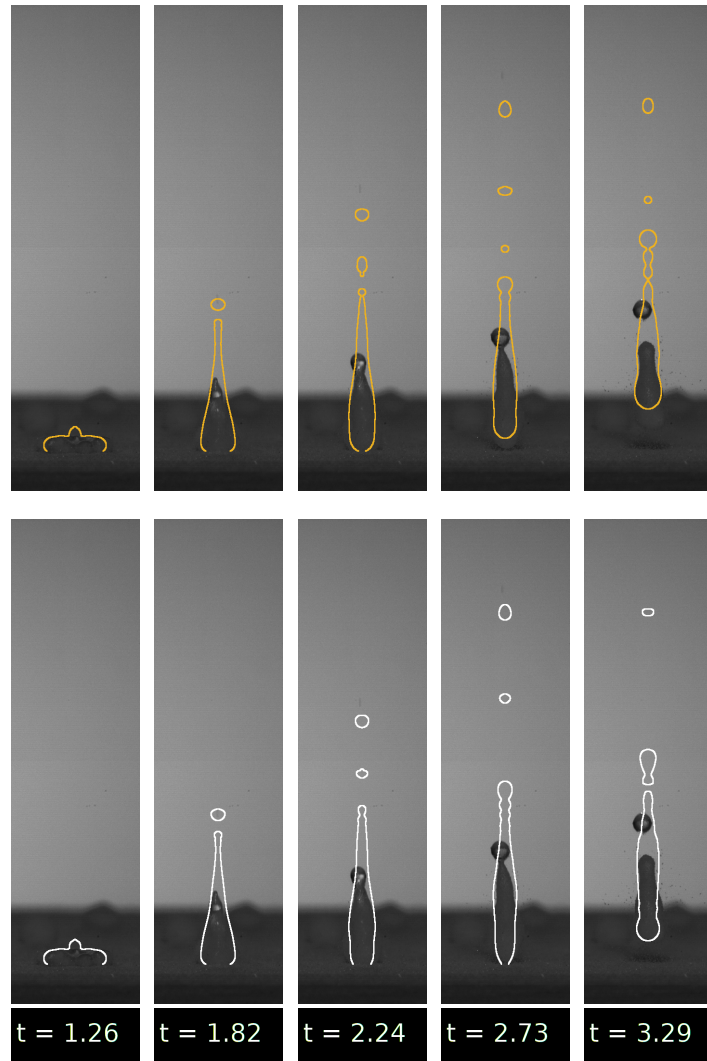


Figure 6.11: Drop shapes from $We = 66$ ($\gamma = 2.59$) simulations overlaid onto a $We = 68$ ($\gamma = 2.61$) powder bed experiment. The moment of contact (at dimensionless time $t = 0.00$) is synchronised between the simulation and experiment. The top (bottom) row is overlaid with a simulation *without* (*with*) a pinning radius of r_{pin} which reduces the otherwise constant contact angle when passed over by the receding contact line. Images span from part way through retraction along the powder bed to the moment of encapsulation for the primary drop in the non-pinning simulation.

Energy Loss in Powder Bed Experiments

Although our simulations exhibit good agreement with powder bed experiments with respect to the spreading factor, and the contact time with the substrate, the greatest rebound height of the drop in experiments is much *lower* than in our simulations. This indicates excess energy loss associated with interactions between the drop and powder bed that is *not* captured in our simulations, which will lower the rebound speed and affect rebound dynamics. We see evidence of excess energy loss in Figure 6.12 with the coefficient of restitution, ϵ , calculated for our experiments of drop impact onto rigid substrates and powder beds, and also for our simulations (*without* a pinning radius), across multiple impact Weber numbers. We define the coefficient of restitution as

$$\epsilon = \sqrt{\frac{h_R}{h_0}}, \quad (6.2.1)$$

where h_R is the greatest rebound height attained by the centre of mass for the primary drop, and h_0 is the height of the centre of mass of the drop that leads to the associated impact Weber number when the drop is released from rest. The coefficient of restitution, viewed as a measure of energy loss associated with the impact process, shows in Figure 6.12 that the impact experiments onto powder beds exhibit *greater* energy loss (that is, smaller ϵ) compared to impact experiments onto rigid substrates, and compared to our (non pinning radius) simulations, at similar impact Weber numbers.

Recall that our simulations have a drop impacting onto a rigid impermeable superhydrophobic substrate, with the effects of the powder incorporated into the viscous model (see §3.2.5) via a slip length at the substrate, and surface viscous effects on the drop surface post-encapsulation. Importantly, our simulations do *not* incorporate substrate deformation, which *does* occur in impact experiments onto powder beds, and may be the primary cause of the discrepancy in energy loss between the powder bed and rigid substrate experiments (and our simulations). Energy loss associated with liquid drop impact onto hydrophobic powder beds has also been reported in [16], in which an estimate for the energy loss is made due to viscous dissipation during *retraction* along the powder bed, however the model presented assumes that the final state of the drop is a spherical liquid marble, which is not the case we are interested in.

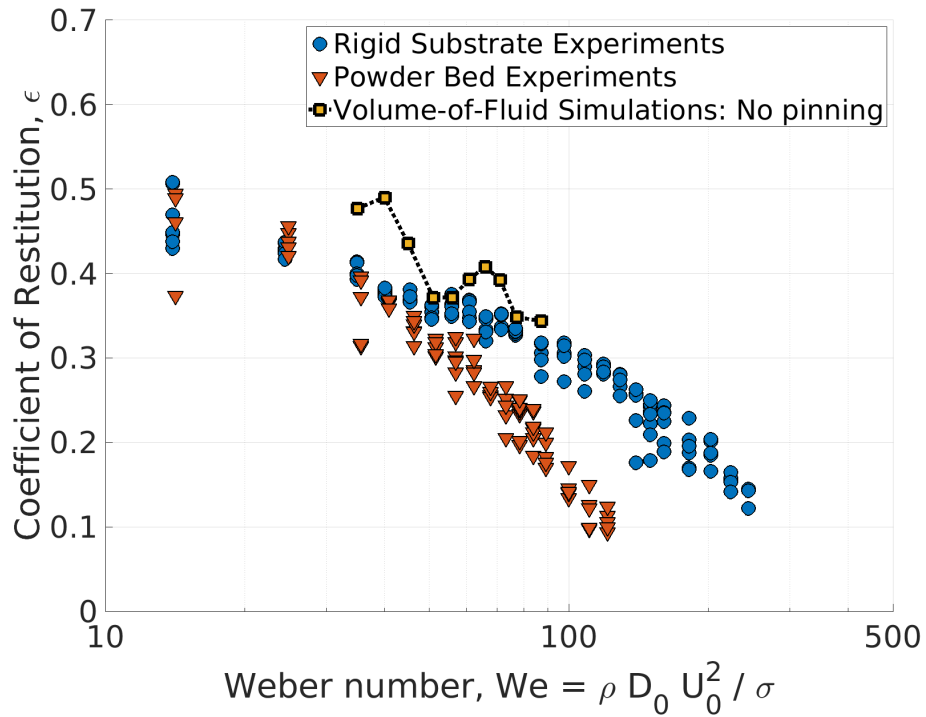


Figure 6.12: Coefficient of restitution as calculated for drop impact experiments onto rigid impermeable superhydrophobic substrates and superhydrophobic powder beds, for a wide range of impact Weber numbers. Also shown are data points from drop impact simulations *without* a pinning radius, for $35 \leq We \leq 87$. Coefficient of restitution is calculated as $\epsilon = \sqrt{h_R/h_0}$ for greatest rebound height, h_R , of the primary drop, and initial drop height h_0 (released from rest to obtain the associated impact Weber number).

Given that the excess energy loss affects rebound dynamics, we may be able to better ‘match’ our simulations and powder bed experiments by comparing simulations with a particular impact Weber number, to powder bed experiments with a somewhat larger impact Weber number, to accommodate the extra energy loss in the latter case. The idea then is that the total energy at rebound is approximately equal in the simulation and experiment, so then the rebound speed and subsequent rebound dynamics are more comparable. We see an example of such a comparison in Figure 6.13 where we see the retraction and rebound dynamics of a $We = 45$ simulation with a $We = 52$ powder bed experiment. We note that the two share a good agreement in rebound dynamics, especially highlighting the fact that both drops become encapsulated at the same time from initial contact with the substrate (the final frame), and with very similar shapes. The similarity in encapsulated shapes and

liquid marble shapes for simulations and experiments across different impact Weber numbers is discussed further in Chapter 7.

Finally, given the disparity in the coefficient of restitution (and thus the rebound velocity of the drop) between our powder bed experiments and simulations, comparisons between our simulations and experiments could instead be made for a similar spreading factor γ , instead of similar impact Weber numbers as is done in Chapter 7. However, we would expect similar conclusions to be made on the success of our computational model for liquid marble formation under such an analysis, as there is an observed monotonic increase in γ with We in experiments (on average) and in our simulations. Further, just as there are examples of good agreement between experiments and simulations for differing We , there are also examples of striking similarities for differing γ , with an example to be discussed in §7.3.3 (in particular, Figure 7.10) which differs in We and γ .

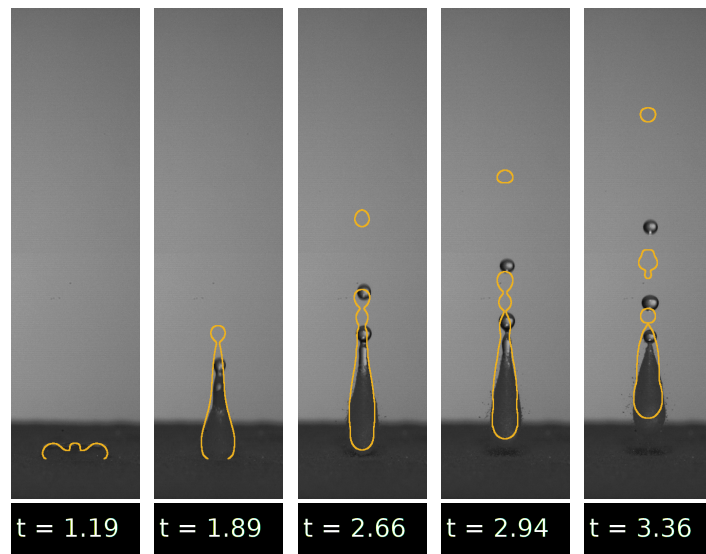


Figure 6.13: Drop shapes from $We = 45$ ($\gamma = 2.31$) simulations (without a pinning radius) overlaid onto a $We = 52$ ($\gamma = 2.35$) powder bed experiment. The moment of contact (at dimensionless time $t = 0.00$) is synchronised between the simulation and experiment. Images span from part way through retraction along the powder bed to the moment of encapsulation for the primary drop in the non-pinning simulation.

Chapter 7

Liquid Marble Formation

In this chapter, we describe modelling choices made for (novel) simulations of liquid marble formation, and present the results of these simulations with comparisons to experiments. These simulations use the viscous-bulk model for liquid marble formation described in Chapter 3 (specifically §3.2.5), which was motivated using observations made in drop impact experiments onto superhydrophobic powder beds (see Chapter 2) including similarities to rigid substrate impacts and effects that we argue may be described with surface viscosity. The simulations were solved numerically with a VoF method using the open-source software package Basilisk (see Chapter 5), with initial conditions extracted (at the moment of encapsulation) from drop impact simulations in Chapter 6.

We begin by reminding the reader of encapsulation and freezing areas for drop impacts onto powder beds, first introduced in Chapter 2 and incorporated into our model in Chapter 3, and how these are evaluated for our drop impact simulations, according to our experiments. We then discuss how an important parameter found within the constitutive equation for the dilatational surface viscous coefficient λ^s was chosen to best match our simulations of liquid marble formation to experiments. Finally, we show the results of our liquid marble simulations; discussing in detail how well the shapes formed at encapsulation, and the liquid marbles themselves (where formed) match those observed in our experiments.

7.1 Encapsulation of Simulated Drops

Prior to encapsulation of the drop interface in adsorbed powder, which is the moment that surface viscosity is ‘turned on’ in our model (see §3.2.4), the simulations presented in this chapter are the same as the drop impact simulations (*without* a pinning radius) presented in §6.2.2. Recall (see §2.3.4 and §3.2.4), the moment of encapsulation for each of these simulations is defined as the first time the surface area of the liquid-gas interface is the same as (or less than, due to a satellite drop ejection) the value of the initial encapsulation area $A_{encap}^{(0)}$; itself defined as the maximum contact area between the drop and the substrate multiplied by the parameter α_{encap} (3.2.32).

In §2.3.4, a relationship was found between the surface area of a drop at encapsulation and (deformed) liquid marble formation (assuming no loss of powder mass since reaching maximum spread), and the *spreading area* (2.3.2), which resulted in Figure 2.34 for the variables $\alpha_{encap}^{(spr)}$ and $\alpha_{freeze}^{(spr)}$. Also included were data points $\alpha_{final}^{(spr)}$ which are calculated for drops that attain spherical liquid marble status, using the same process as calculating $\alpha_{freeze}^{(spr)}$ for deformed liquid marbles. These data points act as an indicator of the minimum surface area attained as a proportion of the maximum spreading area, and are not part of the computational model. In Figure 7.1, we see all data points from the aforementioned graph *scaled* so that now they relate the surface area at encapsulation and (deformed) liquid marble formation, to the *maximum contact area*. Given these data points relate to the maximum contact area rather than the spreading area, they lose the superscript $^{(spr)}$ and match the variables introduced in §3.2.4, where they were motivated in terms of differing powder concentrations on the liquid-gas and liquid-solid interfaces of the drop. The scaling uses an observation made from the clean drop impact simulations conducted in Chapter 6; namely that the radius of the contact line, and the maximum *visible* drop radius, both at maximum spread, appear to differ (approximately) by a constant (see Figure 7.2). Let r_{max} and $r_{max}^{(CL)}$ denote the maximum *visible* radius and the maximum contact line radius of the drop, respectively, at maximum spread. Then, we scale the data points in Figure 2.34 to those in Figure 7.1 using the relation $r_{max}^{(CL)} \approx r_{max} - 0.16$.

The data points for α_{encap} in Figure 7.1, following scaling from values obtained directly from experiments, now exhibit a clear (on average) decreasing monotonic slope as the spreading factor γ is increased. We model the change in α_{encap} as γ is varied by imposing a linear fit to the scaled data, and given that the data for α_{freeze}

shows no clear monotonic trend, a horizontal line is drawn through their collective average value. We then evaluate, for simulations of drop impact for 10 distinct impact Weber numbers (conducted in Chapter 6), the value of α_{encap} according to the linear fit, using the value of the spreading factor γ calculated in each simulation (note that α_{freeze} is constant for all simulations). This determination of the parameters α_{encap} and α_{freeze} for each drop impact simulation then defines, when multiplied by the maximum contact area, the initial encapsulation area $A_{encap}^{(0)}$ and initial freezing area $A_{freeze}^{(0)}$ for each simulation, respectively. Note that the final simulation data point (for $We = 87$) lies on the horizontal line defining freezing instead of the linearly-decreasing line for encapsulation; if this point was not ‘lifted’, then the initial encapsulation area would be smaller than the initial freezing area, which is clearly impossible, so in this case, we instead say encapsulation and freezing occur simultaneously.

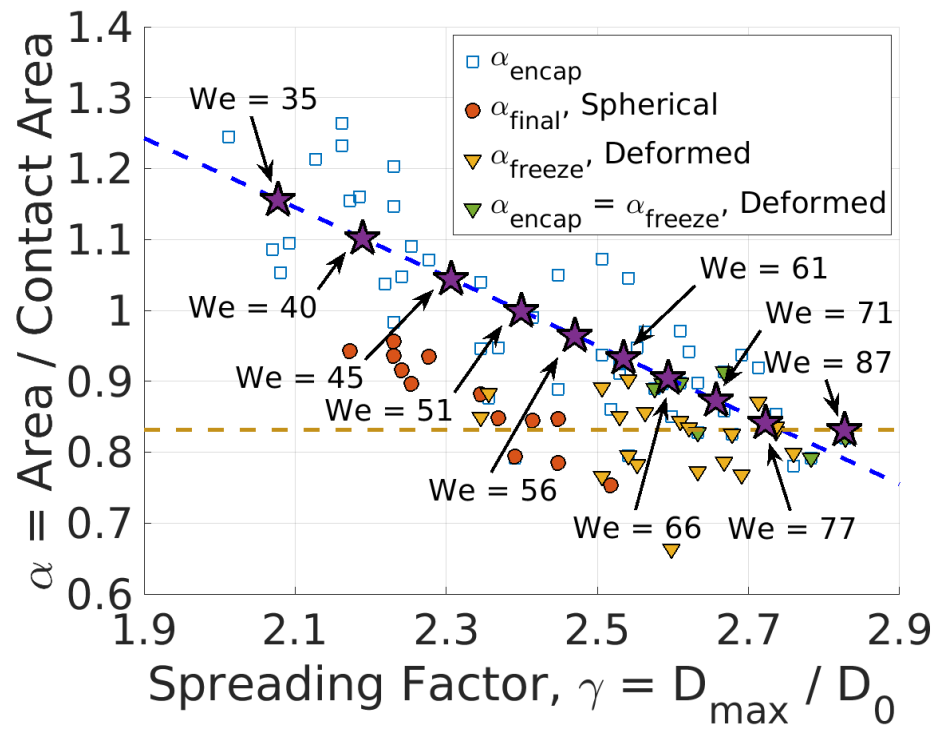


Figure 7.1: Amended plot from Figure 2.34, with the original data points $\alpha_{encap}^{(spr)}$, $\alpha_{freeze}^{(spr)}$, and $\alpha_{final}^{(spr)}$ scaled to relate to the maximum contact area with the substrate, rather than the spreading area. The scaled parameters α_{encap} , α_{freeze} , and α_{final} are shown as functions of the spreading factor γ , calculated for powder bed experiments from Chapter 2, supplemented with data points from drop impact simulations (purple stars) conducted in Chapter 6. These stars indicate the value of α_{encap} for each simulation according to the line-of-best-fit for the existing experimental data points. For the $We = 87$ data point, the corresponding value of α_{encap} sits on the horizontal α_{freeze} line, indicating simultaneous encapsulation and deformed liquid marble formation.

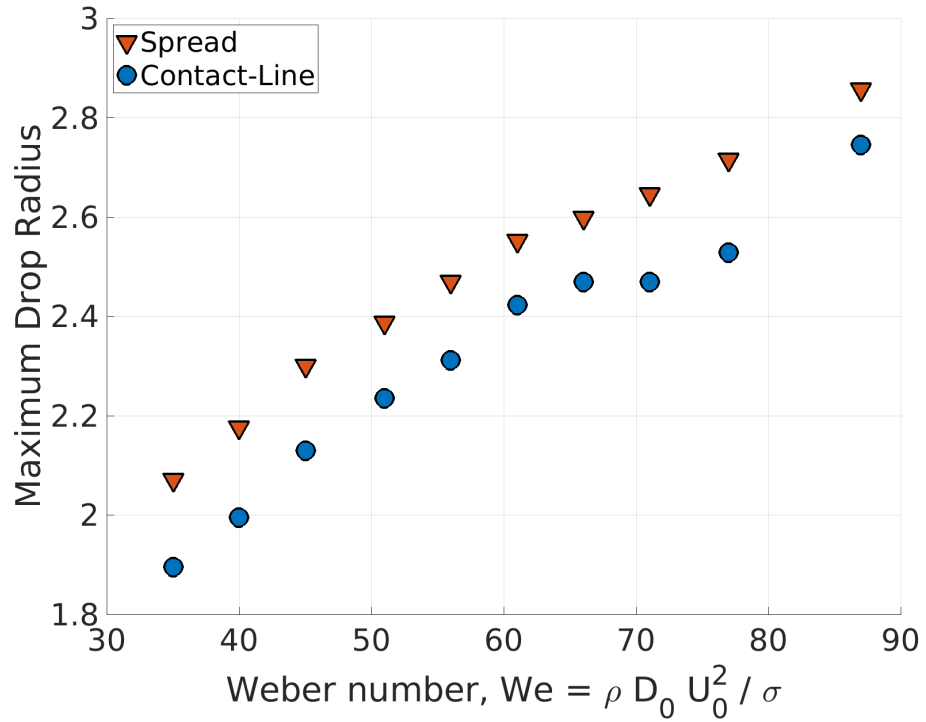


Figure 7.2: Maximum visible drop radius and maximum contact line radius, both taken at the moment of maximum spread for clean drop impact simulations as a function of the impact Weber number. See Figure 2.30 for a representation of the drop spread diameter compared to the contact line diameter.

7.2 Choice of β

The constitutive equation for the dilatational surface viscous coefficient λ^s (3.2.37), repeated here for convenience:

$$\lambda^s(A, t) = \beta \cdot \frac{(A_{encap}(t) - A)}{(A - A_{freeze}(t))},$$

contains a coefficient $\beta > 0$ that we choose to best match our simulations for liquid marble formation with experiments. This is done on at best a semi-quantitative basis as liquid marble formation by drop impact is a sensitive process and can exhibit large variability in shapes and drop behaviour, as will be shown here with the variety of drop shapes observed at the moment of encapsulation and for the liquid marbles themselves, so perfect agreement should not be expected.

For $We < 51$, the initial freezing areas for our simulations are *smaller* than the spherical surface areas for the primary drops, meaning deformed liquid marbles *cannot* be created, unless by some pinch-off event that manages to flip the ordering of

the (time dependent) freezing area and spherical surface area (which does not occur in our simulations for any tested β). Instead, these simulations exhibit a faster decay of drop oscillations as compared to their clean counterpart (where $\lambda^s = 0$). It is for these cases (specifically for $We = 40, 45$) where a value for β is chosen; according to Figure 7.1, the simulation with $We = 45$ has a spreading factor *larger* than many of our drop impact experiments that form spherical liquid marbles, whereas there is only a single example of a spherical marble forming with a spreading factor *less* than the $We = 40$ simulation. We therefore desire a value for β that will create a spherical liquid marble for $We = 45$ (that is, the drop forms and maintains a spherical shape before reaching the apex of rebound), but *not* for $We = 40$. Ultimately, a value of $\beta = 0.5$ was chosen to best suit this requirement, with the reasoning provided below.

7.2.1 Forming a Spherical Liquid Marble

To reiterate, we require a value of β such that the primary drop for the $We = 45$ simulation maintains a spherical shape before reaching the apex of its rebound from the substrate, while the $We = 40$ simulation continues to exhibit drop oscillations.

Recall from our nonlinear model for inviscid-bulk suspended drop oscillations with dominant dilatational surface viscosity effects (see §3.3), that for *every* positive value of λ^s , there exists a critical amplitude a_c such that oscillations are *underdamped* when the oscillation amplitude is *less* than a_c . For the simulations of post-rebound drop oscillations, it is clear that surface viscous effects dominate the bulk viscous effects. This is shown in the top plots of Figures 7.3-7.4, where we see that increasing β (and so implicitly increasing λ^s) causes a faster decay in drop oscillations than for the clean case (that is, with $\lambda^s = \beta = 0$), where only bulk viscosity acts. Once the amplitude of drop oscillations falls below the critical threshold, the subsequent oscillations are in the underdamped regime (importantly, with the decay rate due to dilatational surface viscosity going to zero as the oscillation amplitude goes to zero), and so we expect any future decay in oscillations to be approximately the same as it is in the clean case, which is entirely due to *bulk* viscosity. So even with a very large β (and so potentially large λ^s) where the drop surface area appears to stabilise at the spherical surface area, *small* drop oscillations will still persist. We have to therefore make the judgement call on how small drop oscillations are when deciding whether a spherical liquid marble is formed in simulations.

In Figure 7.3 we consider the effect of different values of β on the dynamics of a drop, post-encapsulation, for the $We = 40$ case. Both plots within this figure range from the time of encapsulation, to the time at which the apex of rebound is reached. We see that by increasing β , the surface area of the drop shows a faster decay in oscillations, with the drop tending towards a sphere and the $\beta = 5$ case reaching it and staying close long before the rebound apex is reached. Also shown in this figure is the ratio of drop length along its primary and secondary axes in the $\beta = 0.5$ simulation as compared to the same data taken from two drop impact experiments with $We = 41$. The experimental data also shows oscillations from the moment of encapsulation, with the time of encapsulation set to match the simulation. The experiments show the two extremes of decay in oscillations observed for $We = 41$; one (yellow line) showing the *only* example of spherical marble formation for this impact Weber number, and the other (red line) showing a much slower decay representative of the other experiments for this impact Weber number, the latter of which resembles the decay in our simulation.

A similar set of plots is shown in Figure 7.4 for simulations with $We = 45$. This time, $\beta = 0.5$ shows a decay to the spherical surface area, as desired. For the ratio of axes plot (showing drop oscillations) in this figure, we see the $\beta = 0.5$ simulation compared against two experiments with $We = 46$ representing the extremes of decay in drop oscillations (both of which form a spherical marble). The decay in oscillations for our simulation, keeping in mind the persistence of small amplitude oscillations as previously mentioned, appears to lie between these two extremes and so we are able to justifiably state that a spherical marble is ‘formed’ in our simulation and that it is consistent with experiments.

Therefore, in summary, the $\beta = 0.05$ simulations provided only negligible damping and resulted in the $We = 40$ and $We = 45$ cases both unable to form spherical marbles, and the $\beta = 5$ simulations made spherical marbles in both cases. The $\beta = 0.5$ simulations performed as required and *only* formed a spherical marble for $We = 45$. Furthermore, the damping rate for both cases (when using $\beta = 0.5$) lies within the extremes observed in experiments, confirming that this value of β is better than just an order-of-magnitude estimate. For this reason, $\beta = 0.5$ was chosen for all future liquid marble simulations.

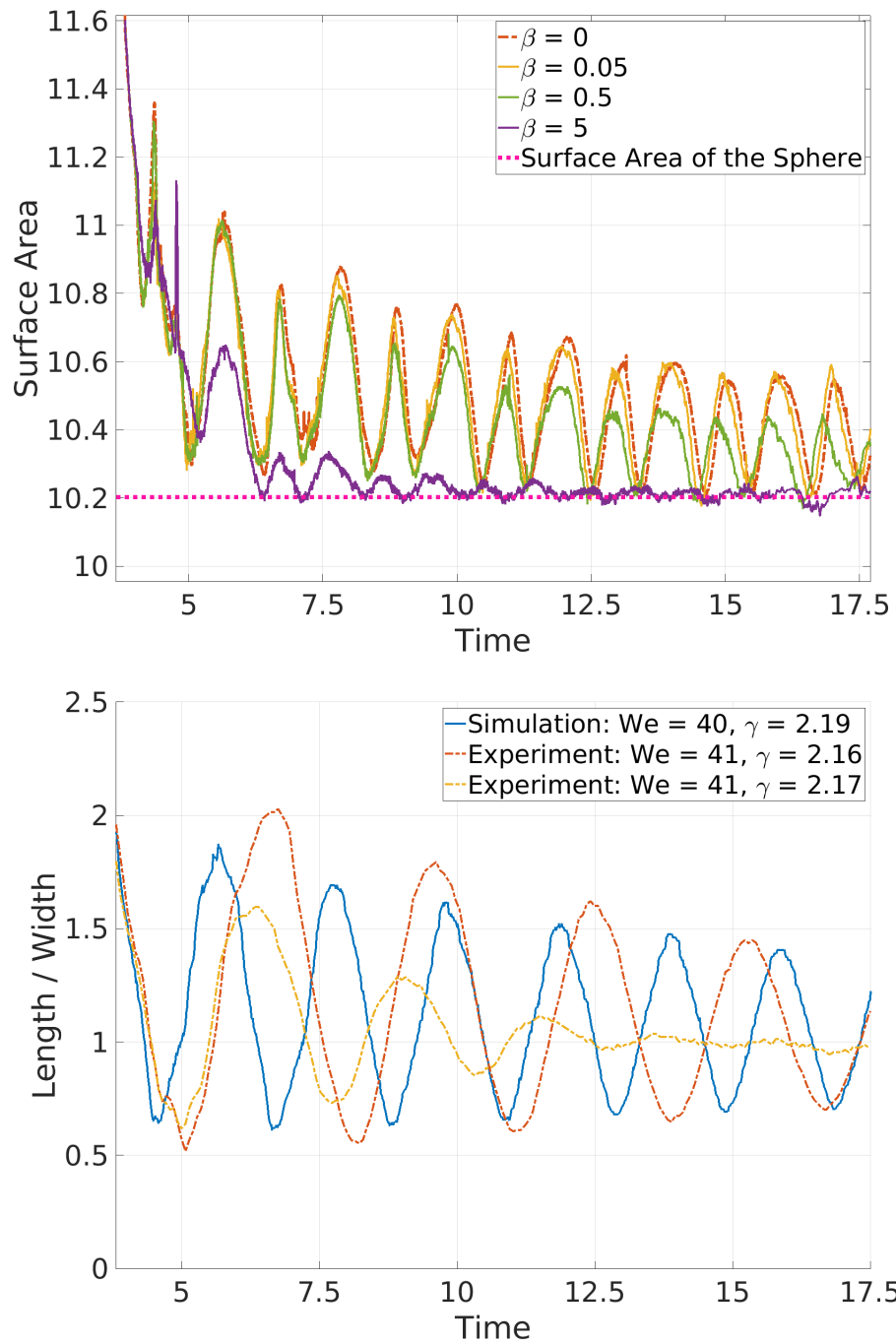


Figure 7.3: Plots from encapsulation to when the drop reaches the apex of its rebound from the substrate for simulations with $We = 40$ ($\gamma = 2.19$), with (top) a surface area plot showing the clean case, along with surface viscous simulations with $\beta = 0.05, 0.5, 5$, and also showing the spherical surface area. Also shown is (bottom) the ratio of the drop's primary and secondary axes for $\beta = 0.5$, overlaid with the same data taken from powder bed experiments with $We = 41$ ($\gamma = 2.16, 2.17$) representing the extreme cases for this We . Encapsulation in experiments is matched to occur at the start of the plot.

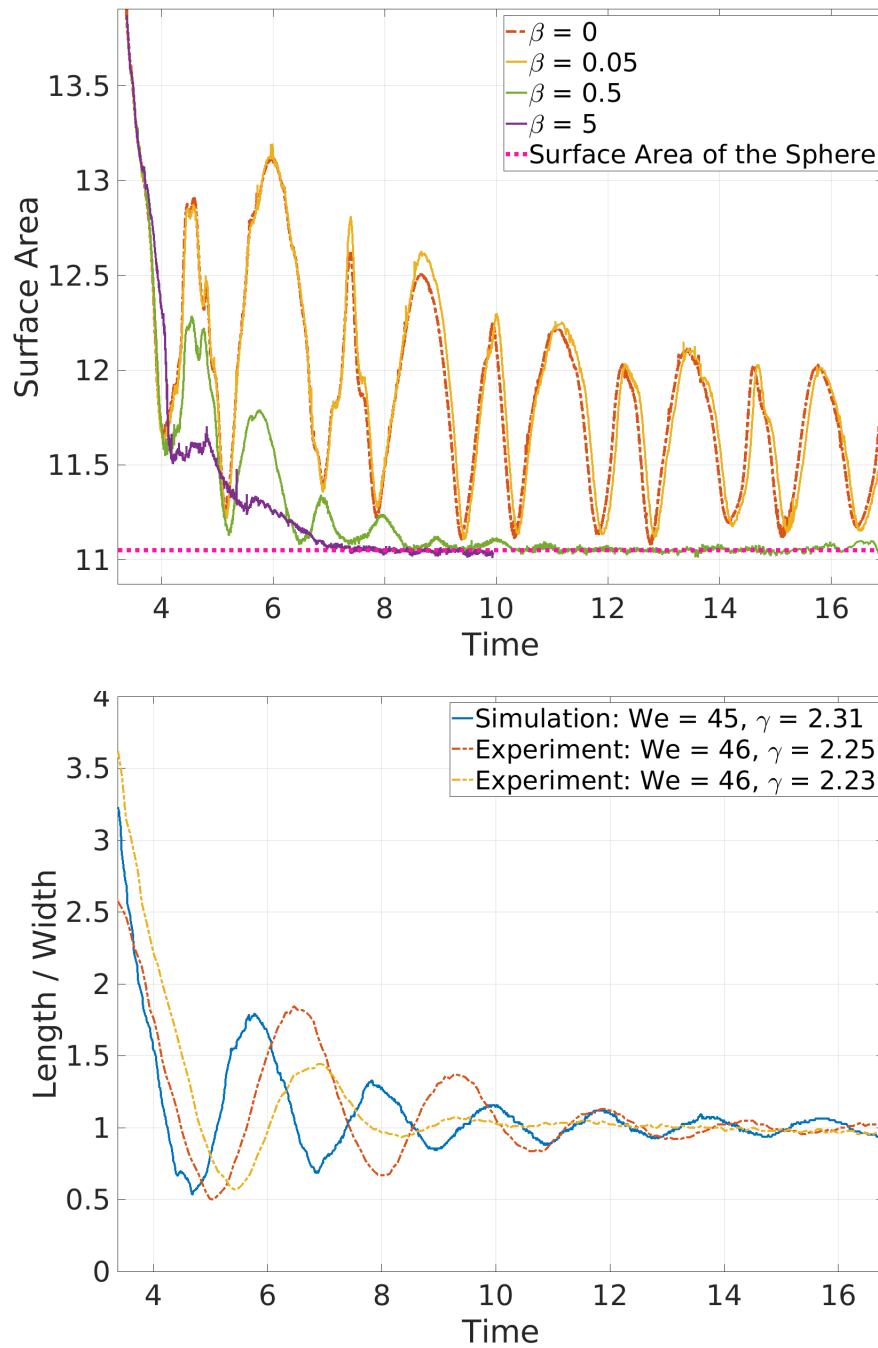


Figure 7.4: Plots from encapsulation to when the drop reaches the apex of its rebound from the substrate for simulations with $We = 45$ ($\gamma = 2.31$), with (top) a surface area plot showing the clean case, along with surface viscous simulations with $\beta = 0.05, 0.5, 5$, and also showing the spherical surface area. Also shown is (bottom) the ratio of the drop's primary and secondary axes for $\beta = 0.5$, overlaid with the same data taken from powder bed experiments with $We = 46$ ($\gamma = 2.23, 2.25$) representing the extreme cases for this We . Encapsulation in experiments is matched to occur at the start of the plot.

7.3 Simulation Results

In this section we will discuss the results from the liquid marble simulations; we will go through the different phenomena that can occur during the formation (or not) of liquid marbles from drop impacts onto superhydrophobic powder beds, and compare simulations to experiments. It is worth noting that there is large variability, in experiments, in drop shapes at encapsulation and for the liquid marbles themselves (where formed), so considering this and also that, as discussed in §6.2.2, the drop shapes do not perfectly match pre-encapsulation shapes from experiments, we should not expect perfect quantitative agreement between simulations and experiments.

7.3.1 Overview of Liquid Marble Formation

We begin by showing the drop shapes at encapsulation for our simulations at the 10 different impact Weber numbers that we consider, and provide images from experiments at the same moment for (almost) the same impact Weber number¹. These comparisons are provided in Figures 7.5-7.6. In these images, we see that in experiments with a given impact Weber, there is significant variation in drop shapes at the moment of encapsulation, so it is unsurprising that we do not see *perfect* agreement in our simulations, although as will be discussed, we consider the resemblance to be good overall. Interestingly (as mentioned in §6.2.2), we see in these images of encapsulated drops that a simulation for a particular impact Weber number can resemble experiments that have a somewhat *different* impact Weber number. A particular example of this is in Figure 7.5 where the drop shape at encapsulation in the simulation for $We = 45$ bears a good resemblance to the encapsulation in the experiment with $We = 52$ and $\gamma = 2.35$ (a comparison of pre-encapsulation dynamics is shown in Figure 6.13). Another example, shown later in §7.3.3 for the same simulation ($We = 45$) shows that in the initial stages following encapsulation, the dynamics of the drop matches well with an experiment with $We = 57$.

Another observation from Figures 7.5-7.6 is that there are examples of encapsulated drops in *experiments* looking similar to one another even though their impact Weber numbers are different. For example, in Figure 7.5 we observe the similarity

¹Simulations are run with a value of We from the rigid substrate experiments, which vary slightly from those of powder bed experiments due to minor differences in experimental setup.

between the ($We = 41, \gamma = 2.16$) and ($We = 52, \gamma = 2.52$) experiments, as well as the similarity between the ($We = 36, \gamma = 2.07$), ($We = 41, \gamma = 2.17$), and ($We = 46, \gamma = 2.23$) experiments.

So when we see seemingly greater resemblance between the drop shapes at encapsulation for our simulations at a given impact Weber number, to particular experiments at a somewhat *different* impact Weber number, we offer two possible rationalisations. The first possibility (first discussed in §6.2.2) is that the energy loss in experiments associated with the drop impacting onto a *deformable* powder bed is not captured in our simulations, and so the total energy of the drop at rebound *in experiments* at a particular impact Weber number is closer to the total energy of a drop from a lower impact Weber number *simulation*, rather a simulation with a *similar* impact Weber number. In this scenario, one imagines the similarity in total energy at rebound then leads to similar rebound dynamics and advection of the powder coating up to the point of encapsulation. At the same time, the fact that these simulations resemble experiments with different impact Weber numbers does not rule out the possibility that similar shapes at the same Weber number are also possible, but have not yet been observed. We have already noted that experiments with the same impact Weber number can produce a variety of drop shapes and that some of these match other impact Weber number experiments, so perhaps with more experiments we will uncover more examples of this.

Returning to Figures 7.5-7.6 and looking more generally, we observe a trend in simulations and experiments whereby the drop shape at encapsulation becomes elongated for higher We , owing to the fact that more powder has been adsorbed from the substrate and manages to spread along the liquid-gas interface sufficiently to trigger earlier encapsulation. For the final set of images in Figure 7.6, the simulation and experiments experience simultaneous encapsulation and freezing, and the experimental images for this case were taken from a later time (the shapes are maintained due to freezing) where their shapes have better visibility.

In Figure 7.7, we see all deformed liquid marbles formed in simulations and experiments from the drops shown encapsulated in Figures 7.5-7.6. The low impact Weber number simulations are absent from this figure as they either do *not* form liquid marbles ($We = 35, 40$) or only form spherical marbles ($We = 45$), which is visually uninteresting. Also not included is the $We = 87$ case, as the liquid marble is formed

at encapsulation and is shown in Figure 7.6. We see in simulations and experiments that the increase in impact Weber number (and in general the spreading factor) moves us from obtaining pseudo-spherical liquid marbles to (sometimes intricate, see for example the experimental shape for $We = 78$ and $\gamma = 2.63$) elongated liquid marbles. Again we highlight that the shapes of the liquid marbles in experiments can vary considerably even when the impact Weber numbers and spreading factors are similar, so given this, the resemblance of our simulations to the shapes seen in experiments is good.

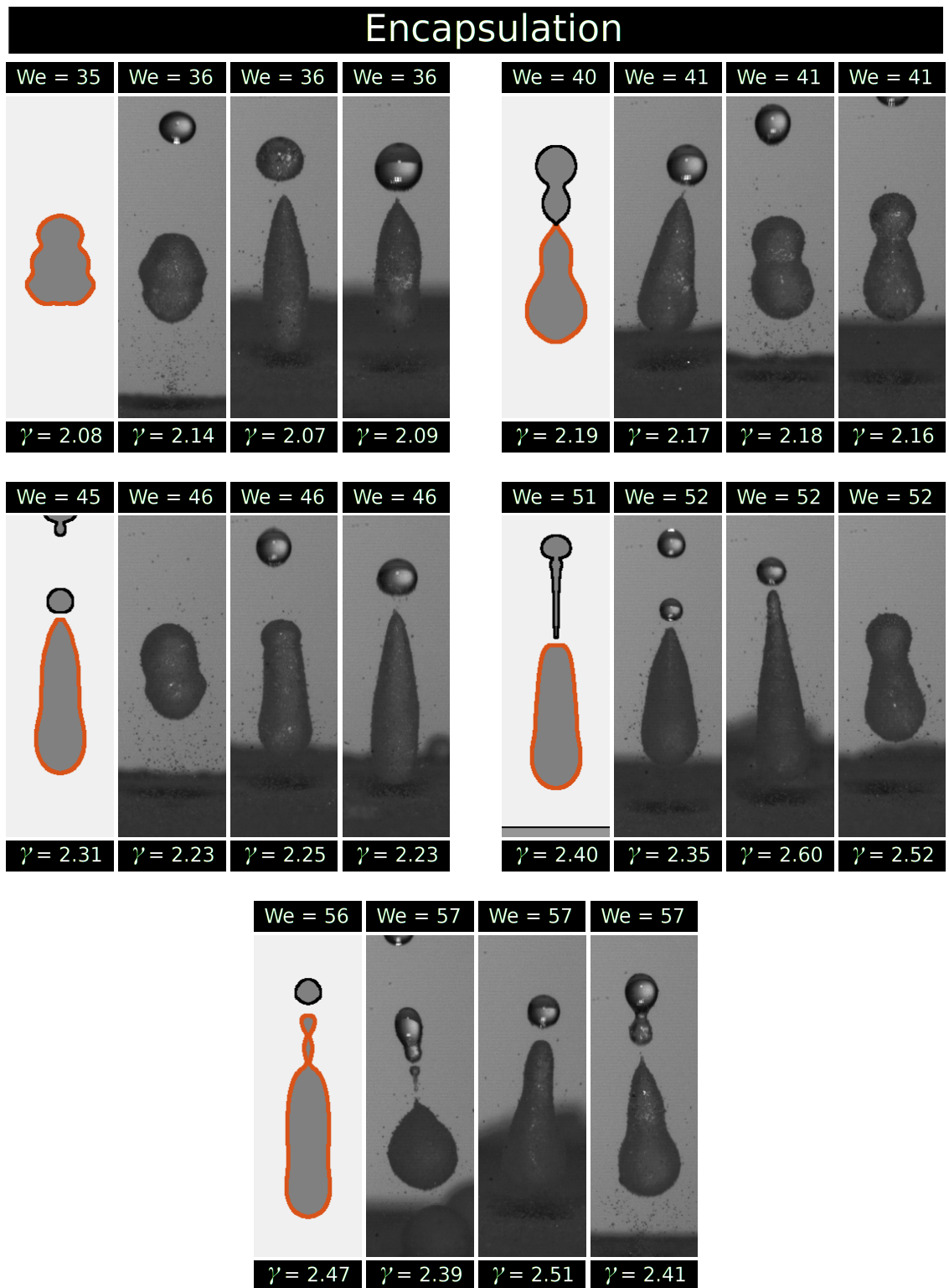


Figure 7.5: Drop profiles at encapsulation for $35 \leq We \leq 57$. The red outlines indicate the primary drop at the moment of encapsulation - any other drops in the simulation are ignored in the subsequent dynamics. The impact Weber number for each simulation or experiment is provided above each drop profile, with the spreading factor provided below.

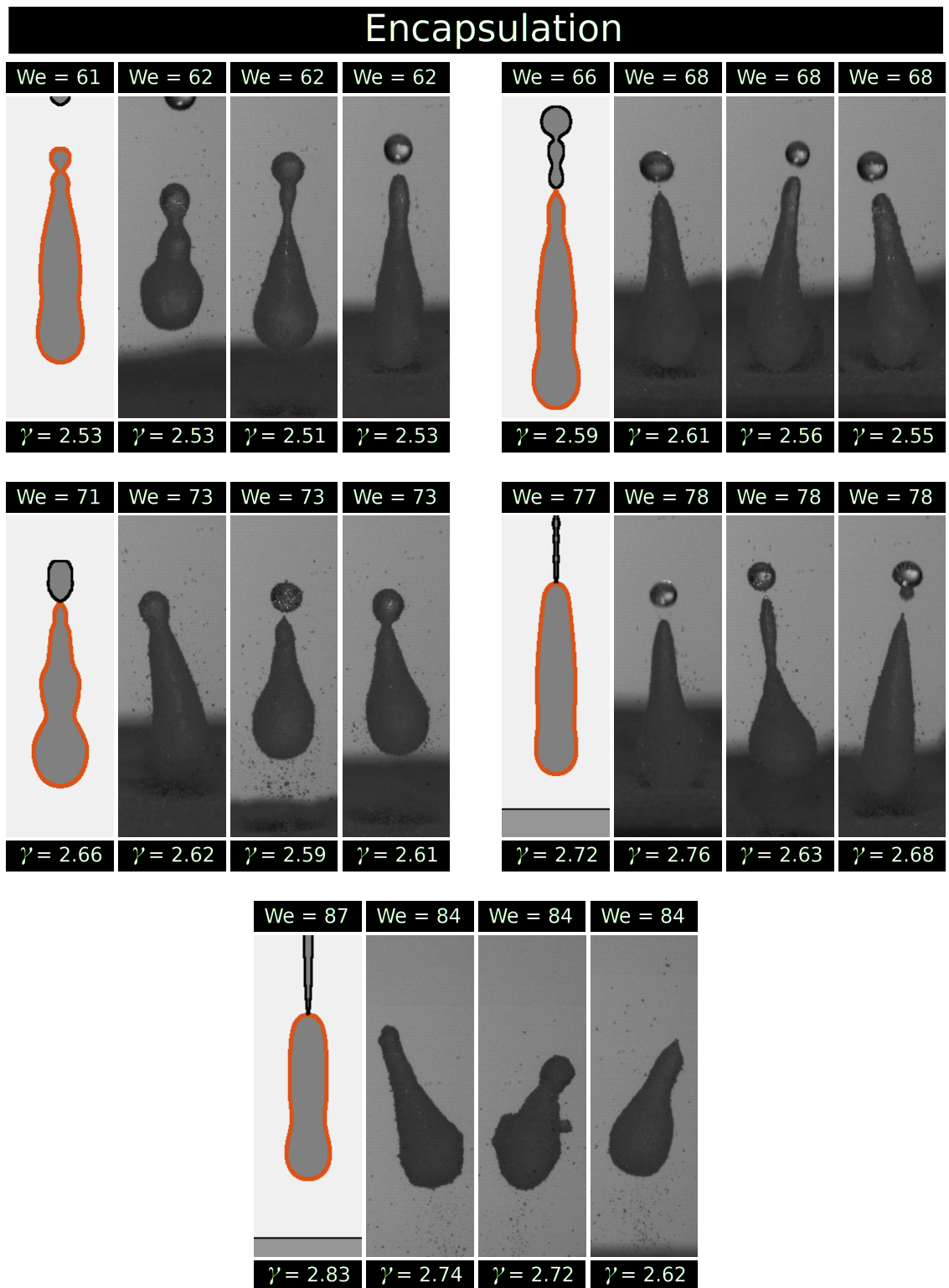


Figure 7.6: Drop profiles at encapsulation for $61 \leq We \leq 87$. The red outlines indicate the primary drop at the moment of encapsulation - any other drops in the simulation are ignored in the subsequent dynamics. The impact Weber number for each simulation or experiment is provided above each drop profile, with the spreading factor provided below.

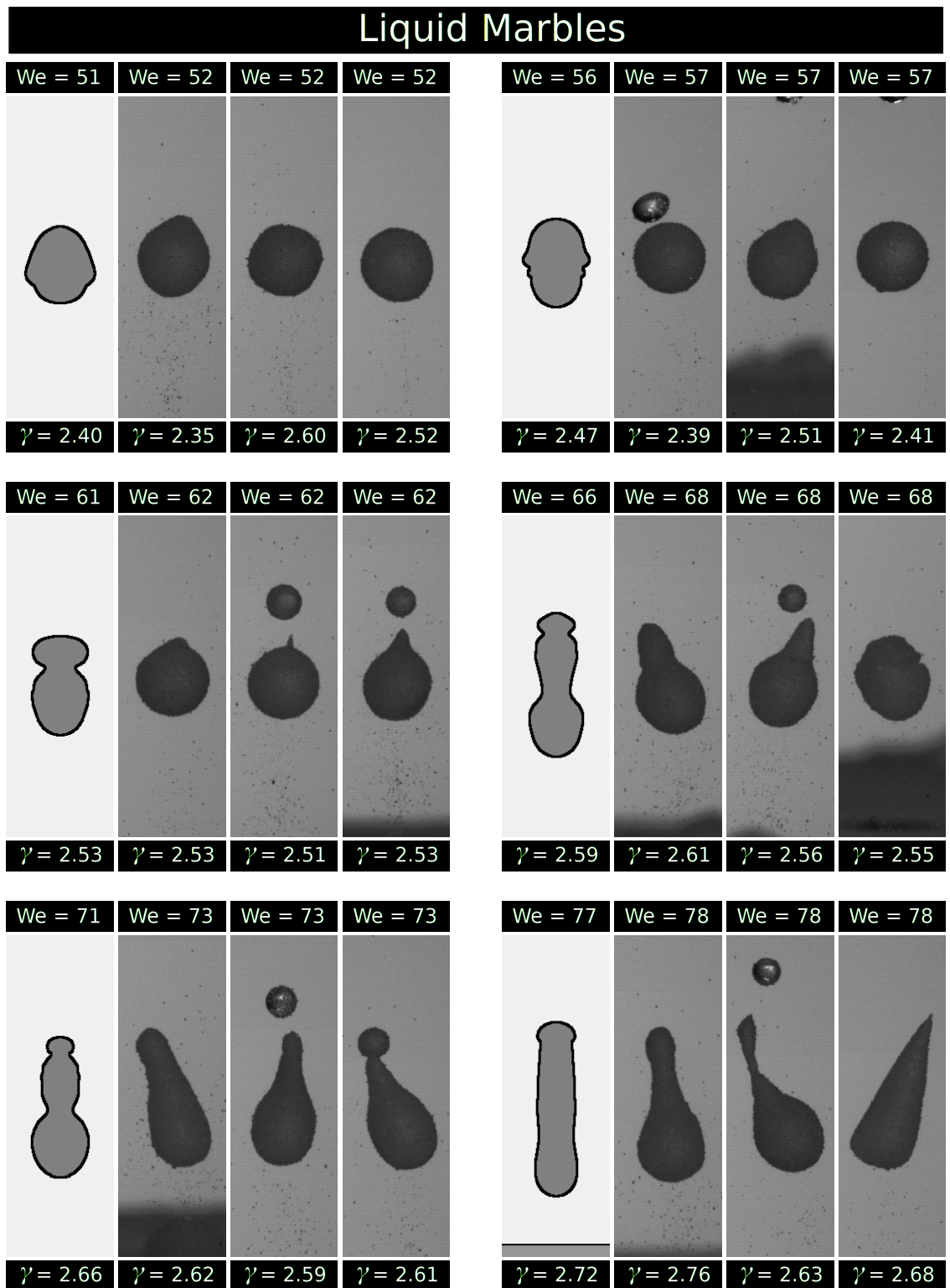


Figure 7.7: Drop profiles for deformed liquid marbles obtained for $51 \leq We \leq 78$. The impact Weber number for each simulation or experiment is provided above each drop profile, with the spreading factor provided below.

We will now discuss the different outcomes that emerge from these simulations; no liquid marble formation, spherical liquid marble formation, and deformed liquid

marble formation. Each discussion will include data from experiments that exhibit this behaviour.

7.3.2 No Liquid Marble Formation

We have chosen the value of β in the constitutive equation for λ^s such that simulations with $We < 45$ do *not* form liquid marbles of any kind (see §7.2). As we should therefore expect, and as we see in Figure 7.8, the surface area of the drop for $We = 40$ does not differ greatly from the clean case, and the effective surface tension does not take values far from unity. Recall that as per our model, we only allow encapsulation (and therefore also interfacial freezing) to occur post-rebound, and so the encapsulation and freezing thresholds $A_{encap}(t)$ and $A_{freeze}(t)$, respectively, are only plotted in the following figure (and others in this chapter) post-rebound. A point of interest in this case is one that occurs in almost all other simulations; encapsulation is caused by a satellite drop ejection, indicated by the sudden drop in liquid-gas surface area. This also causes a fall in the encapsulation and freezing areas, which have reduced from their initial values to account for the mass of powder permanently removed from the primary drop. This method of encapsulation (by satellite ejection) is common among our simulations and is also seen to occur in experiments, but there are exceptions in our simulations that will be highlighted.

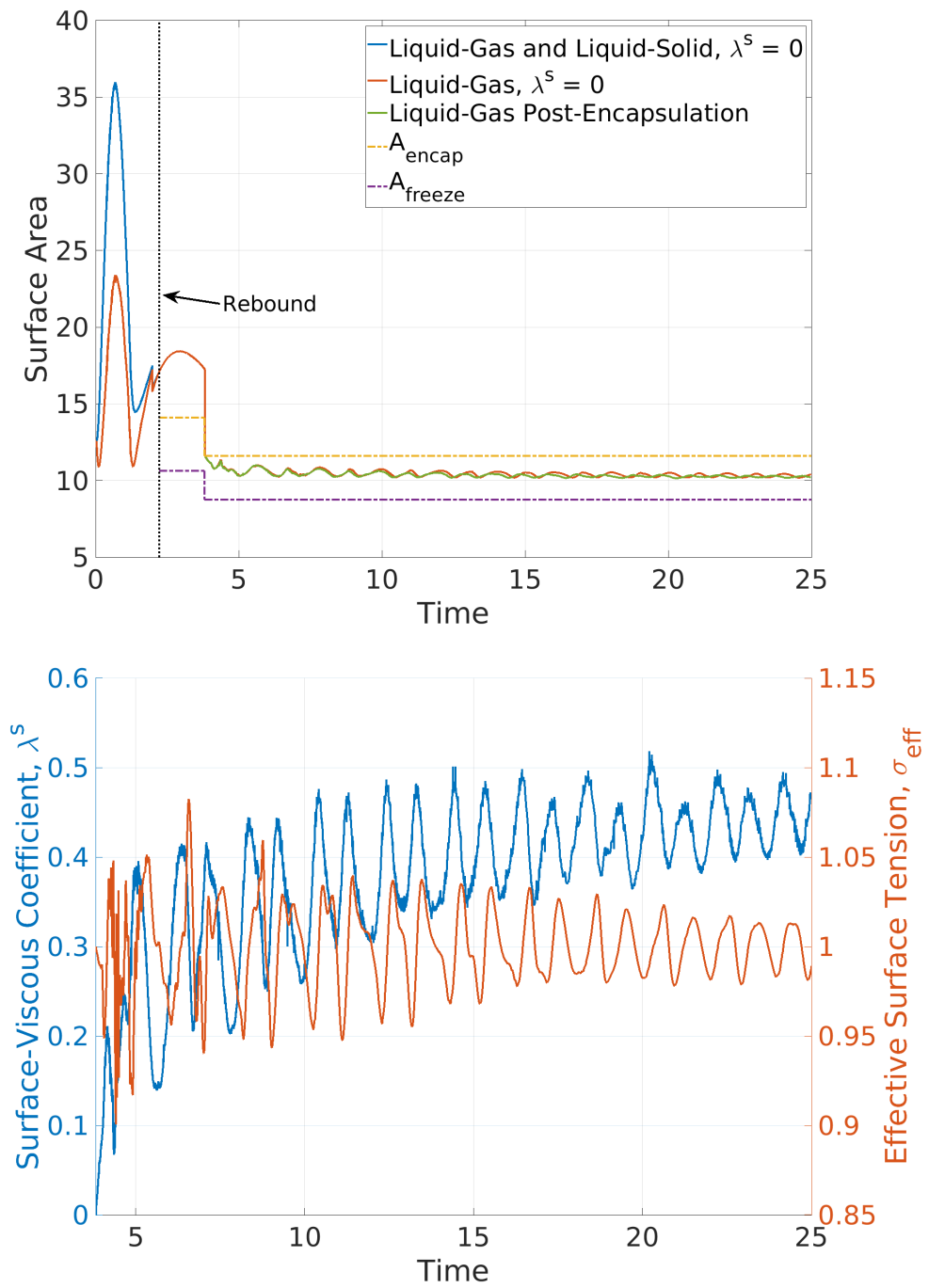


Figure 7.8: Plots for the liquid marble simulation arising from a $We = 40$ impact. (Top) The surface areas of both liquid-solid and liquid-gas interfaces, along with the encapsulation and freezing areas up to the point of encapsulation. Once encapsulated, the liquid-gas surface area for the surface viscous simulation is overlaid, and the (time dependent) encapsulation and freezing areas are continued accordingly. (Bottom) The dilatational surface viscous coefficient λ^s and effective surface tension σ_{eff} over the course of the simulation.

7.3.3 Spherical Liquid Marble Formation

Similar to the previous subsection whereby there was *no* liquid marble formation, this case, where a spherical liquid marble *is* formed, is guaranteed by our choice of β . Provided in Figure 7.9 is the surface area plot for the full liquid marble simulation for $We = 45$; a similar plot is shown in §7.2 but it excluded the pre-encapsulation dynamics. Also shown in Figure 7.9 is the value of λ^s (in log-scale) and the effective surface tension σ_{eff} over the course of the simulation. We note that as expected (because the surface area approaches the sphere which is *very* close to the freezing area), λ^s takes a much larger value than seen when no liquid marble was formed. The effective surface tension *does* experience large changes as it nears zero and briefly exceeds $\sigma_{\text{eff}} = 2$ in the initial stages of the post-encapsulation dynamics, but as λ^s becomes larger, σ_{eff} moves to oscillate around unity, owing to the greatly reduced drop velocities due to the surface viscous damping effects. We see a brief spike in both the surface viscous coefficient λ^s and therefore also in the effective surface tension σ_{eff} prior to $t = 14$; this is due to the surface area of the drop being very close to the freezing area by this point in the simulation and so slight variations in the surface area approximation are magnified in the calculation of λ^s .

As we have seen in Figure 7.4, the decay rate of oscillations in the $We = 45$ simulation sits between the extremes observed in experiments at $We = 46$. However, it is not a $We = 46$ experiment with which this simulation bears the greatest resemblance; as alluded to earlier, there are examples of simulations and experiments showing good agreement (at least for a short time) even though they have different impact Weber numbers (and spreading factors). An example of this is shown here in Figure 7.10 comparing drop profiles from the moment of encapsulation to the formation of a spherical marble, between the simulation with $We = 45$ and $\gamma = 2.31$ and an experiment with $We = 57$ and $\gamma = 2.45$. The first six pairs of images from this figure highlight the initial window of time in which the two show very good agreement, and the final two pairs taken much later, after the simulation and experiment have drifted out of phase with one another. There are other examples of lower impact Weber number simulations resembling higher impact Weber number experiments, but this is the clearest example where two disparate cases (in terms of parameters) come together for a brief period of time post-rebound.

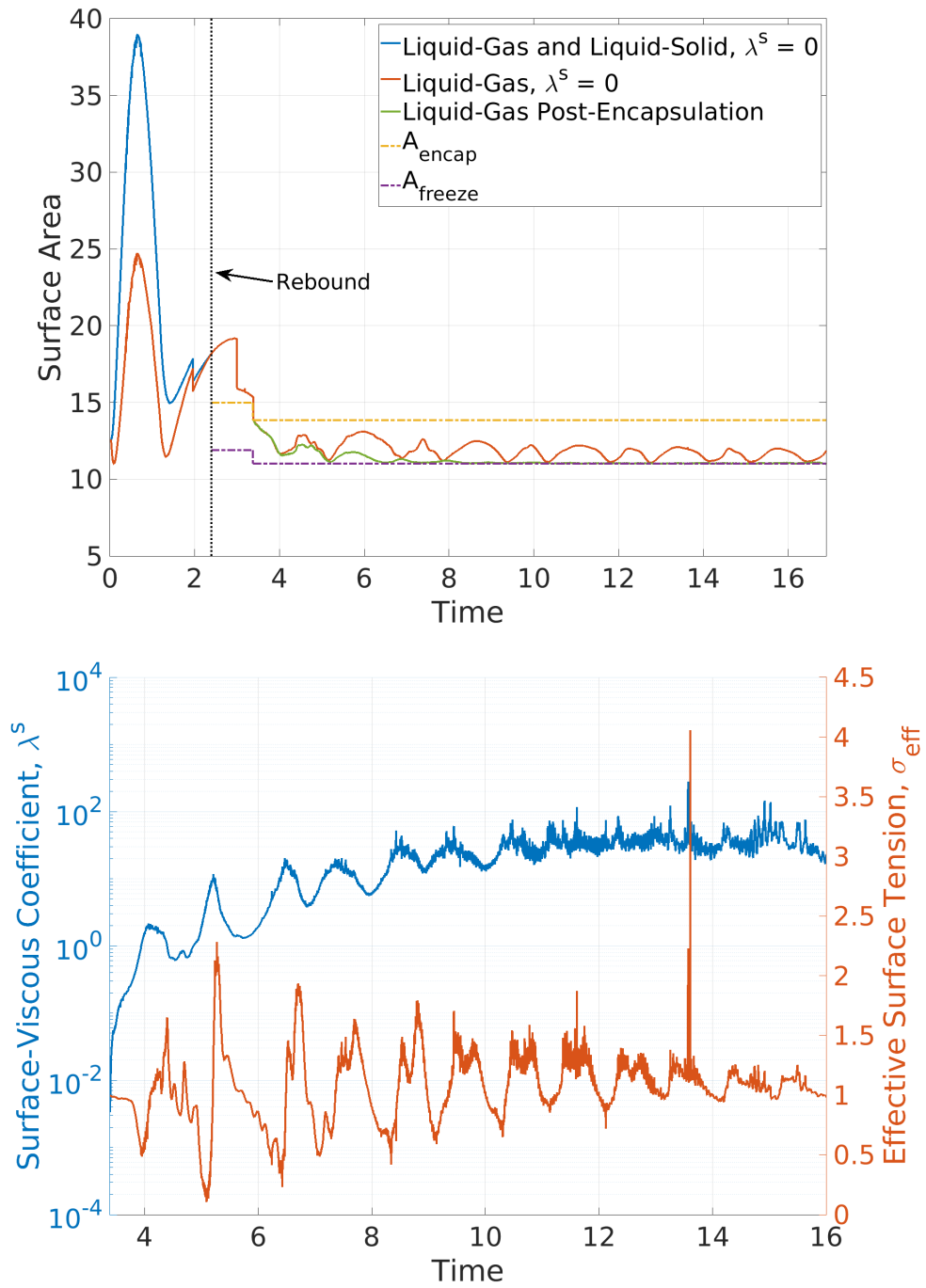


Figure 7.9: Plots for the liquid marble simulation arising from a $We = 45$ impact. (Top) The surface areas of both liquid-solid and liquid-gas interfaces, along with the encapsulation and freezing areas up to the point of encapsulation. Once encapsulated, the liquid-gas surface area for the surface viscous simulation is overlaid, and the (time dependent) encapsulation and freezing areas are continued accordingly. (Bottom) The dilatational surface viscous coefficient λ^s (log-scale) and effective surface tension σ_{eff} over the course of the simulation.

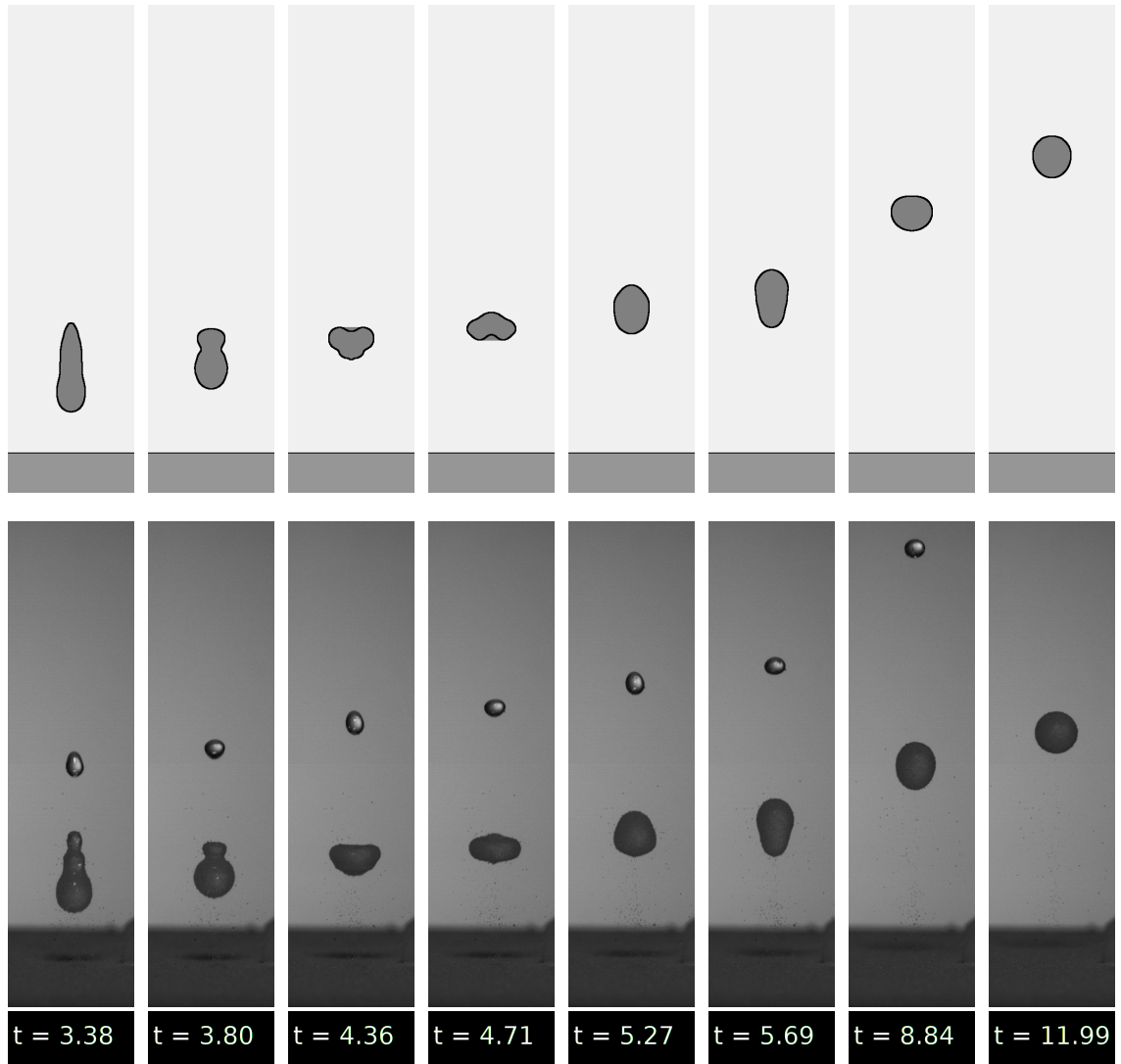


Figure 7.10: Drop profile comparisons from the moment of encapsulation between the simulation with $We = 45$ and $\gamma = 2.31$, and a powder bed experiment with $We = 57$ and $\gamma = 2.45$. The dimensionless time taken between images in the experiment is the same as that in the simulation, and $t = 3.38$ is the time of encapsulation for the primary drop in the simulation. The first six pairs of images show where the simulation and experiment match best (just post-encapsulation), and end with images showing that they eventually move out of phase with one another.

7.3.4 Deformed Liquid Marble Formation

In this subsection we combine results from simulations for different impact Weber numbers, all of which exhibit non-spherical liquid marble formation. We will begin with deformed liquid marbles that are ‘pseudo-spherical’, that is, with the freezing area close to (but larger than) the spherical surface area. We then discuss liquid marbles that are more elongated, and how the increase in impact Weber number (and so the spreading factor) leads to liquid marbles forming closer to the time of encapsulation, until reaching We large enough that encapsulation and freezing occur simultaneously. Included in this are descriptions and images of interesting phenomena observed in simulations, with examples of the same (or similar) phenomena occurring in experiments.

Pseudo-Spherical Marbles

We look now at the $We = 51$ simulation; the first example of a deformed liquid marble forming in our simulations. In Figure 7.11 we see the surface area plot for this simulation, alongside the clean case where $\lambda^s = 0$ during the encapsulated drop regime. From the moment of encapsulation until $t = 3.5$, the liquid-gas surface area for the surface viscous simulation is almost indistinguishable from the clean case; we can see in Figure 7.12 that this corresponds to the period where $\lambda^s < 1$ and the effective surface tension shows little change from unity. As the liquid-gas surface area moves closer to the freezing area, we start to see the surface viscous effects, with λ^s (now consistently taking a value greater than unity) driving more noticeable variations in σ_{eff} . At approximately $t = 5$ we see the simulation passes closely by the freezing area but has not reached it (just yet), which causes a spike in λ^s to above 100 and drives the effective surface tension to briefly reach greater than 4 times its base value. The surface area increases for a short time after this pass-by, but eventually finds itself reaching the freezing area just prior to $t = 6$, with λ^s diverging and σ_{eff} seeming to oscillate around a value close to zero. Recall (see §3.2.4) that we impose a minimum non-negative value on σ_{eff} for stability purposes, but it appears that allowing the effective surface tension to become negative in this case would likely yield the same results as the negative values would only be imposed briefly as σ_{eff} oscillates above and below zero. The time spent in the surface viscous regime is relatively long (longer than the contact time with the substrate), giving

the drop plenty of time to reform back into a pseudo-spherical shape, rather than an elongated shape that we see with higher We .

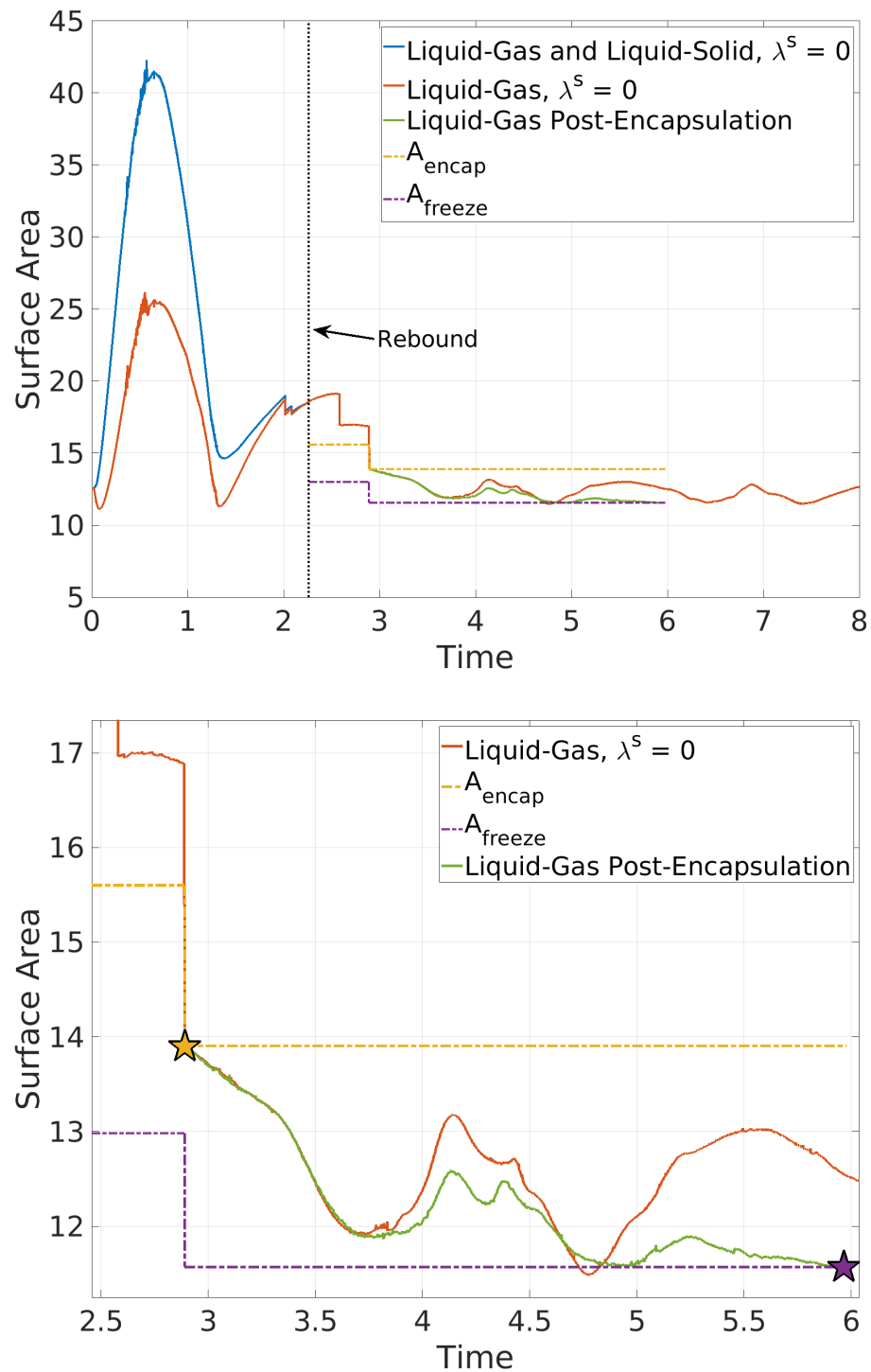


Figure 7.11: Surface area plot for the clean $We = 51$ simulation and overlaid surface viscous simulation post-encapsulation. (Top) Includes pre-encapsulation behaviour. (Bottom) Focus on the surface viscous case from encapsulation to liquid marble formation (both marked with stars). The lines for the liquid-gas surface area, encapsulation area and freezing area terminate at freezing; where the simulation ends.

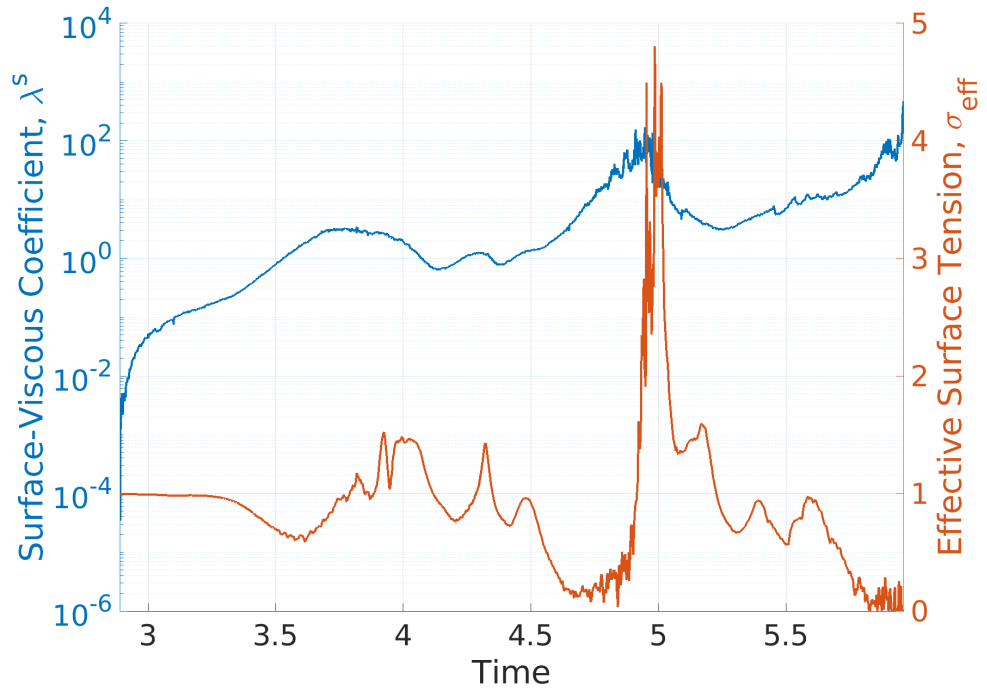


Figure 7.12: Post-encapsulation plot of the dilatational surface viscous coefficient λ^s (log-scale) and effective surface tension σ_{eff} over the course of the $We = 51$ liquid marble simulation.

In Figure 7.13 we see the drop shape evolution from the moment of encapsulation to the moment of pseudo-spherical deformed liquid marble formation for the $We = 51$ ($\gamma = 2.40$) simulation and a powder bed experiment with $We = 52$ ($\gamma = 2.60$). There are similarities between these results; liquid marble formation occurs approximately 3 units of (dimensionless) time after encapsulation in both cases, and the encapsulated shape is much more elongated than the eventual marble. Further, the encapsulated drop is able to substantially change its shape (becoming short and wide in the fourth panel of both cases), and the vertical distance travelled is very similar. Collectively, we take this as evidence of good qualitative agreement between the simulation and experimental data.

A point of difference between the simulation and experiment in Figure 7.13 is that the bottom of the drop in the experiment appears more rigid and unable to deform as easily as the simulation. This is likely due to powder being more tightly packed on the bottom of the drop, which in turn is related to it being the last region to leave the substrate; our model by contrast assumes a spatially constant powder concentration on the liquid-gas interface and so neglects any such effect.

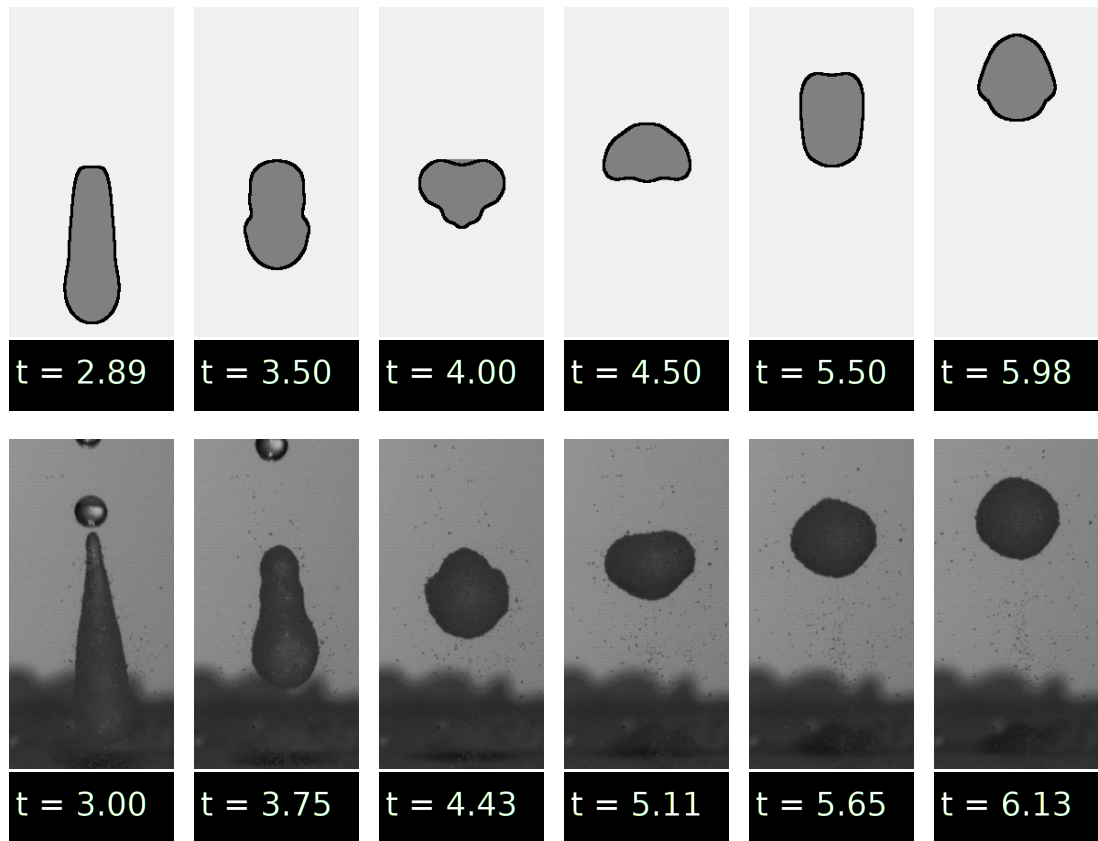


Figure 7.13: Drop profile comparison from the moment of encapsulation to the moment of deformed liquid marble formation between the simulation with $We = 51$ and $\gamma = 2.40$, and a powder bed experiment with $We = 52$ and $\gamma = 2.60$. The dimensionless time $t = 0.00$ corresponds to the moment the drop first comes into contact with the substrate.

Elongated Marbles

We now focus on higher impact Weber number cases, where as per our linear fit (see Figure 7.1), α_{encap} is moving closer to α_{freeze} (so $A_{encap}^{(0)}$ is moving closer to $A_{freeze}^{(0)}$), leaving only a small window of time between encapsulation and freezing, and so causing the deformed liquid marbles to be less spherical and more elongated (as their corresponding shapes at encapsulation are) when they form. We will discuss three distinct simulations that fall into this category; one that exhibits numerous interesting phenomena, a higher We case one where only a slight reduction in surface area separates encapsulation and freezing, and the highest We that we consider, where encapsulation and freezing occur simultaneously.

We first consider the liquid marble simulation with $We = 61$. Looking at the surface area plots in Figure 7.14, where we note that this is the first liquid marble simulation shown where encapsulation does *not* occur as the direct consequence of a satellite drop ejection. There are many examples in the experiments where, like this simulation, encapsulation is due to a continuous reduction in surface area, as the drop attempts to minimise its surface energy. In Figure 7.16(a) we see a very similar encapsulation scenario occurring in a $We = 62$ ($\gamma = 2.53$) experiment as in the $We = 61$ ($\gamma = 2.53$) simulation, whereby a *clean* satellite drop is ejected; a short period of time passes in which the drop retracts in on itself, and *then* encapsulation occurs.

Also looking at Figure 7.15, we see from the moment of encapsulation until $t = 3.6$, a gradual decrease in the effective surface tension from unity to approximately 0.8 as λ^s monotonically increases to approximately unity from zero, all the while showing little variation in surface area from the clean case (where $\lambda^s = 0$). As in the clean case, the now-encapsulated drop experiences a satellite drop ejection (slightly earlier in fact) and unlike the satellites in previous simulations, this satellite is *fully*-coated and leaves the primary drop with a concentration of powder *greater* than at encapsulation (due to the powder coated surface area shrinking post-encapsulation). Shown in Figure 7.16(b) is a similar post-encapsulation satellite drop ejection occurring in an experiment with $We = 62$ and $\gamma = 2.53$ (recall that satellite drops are removed from the computational domain in liquid marble simulations).

Following this satellite drop ejection (so for $t > 3.6$), the surface area of the (primary) drop continues to reduce and move closer to the (now-reduced) freezing area, with λ^s continuing to increase. This then causes rapid variations in the effec-

tive surface tension as the relatively poor approximations of interfacial quantities in Basilisk are magnified. Soon after $t = 4$, λ^s diverges towards infinity and the effective surface tension reaches the lowest value permitted (set at $\sigma_{\text{eff}} = 10^{-5}$) as the drop surface area reaches the freezing area.

With dilatational surface viscosity in effect, encapsulation delayed the surface area of the drop reaching the freezing area when compared to the clean case (where approaching the freezing area has no effect on dynamics). We can see how this happened in Figure 7.16(c); with a small value of the effective surface tension, a region of relatively high (negative) curvature was allowed to persist, which kept the surface area above the freezing area until the bottom of the drop (still moving upwards after rebound) managed to compress the shape, squashing this negative curvature region until the freezing area was reached. This ‘squashing’ of the drop shape is not observed in the clean simulation nor in our drop impact experiments onto a rigid superhydrophobic substrate, because the surface tension of water is sufficiently strong to smooth these regions before this can occur. There is an example of this occurring in a powder bed experiment and is shown alongside the simulation in Figure 7.16(c) with $We = 68$ and $\gamma = 2.56$; we see that the physical presence of powder particles prevents the re-connection of the fluid interface with itself, with a crevice forming in the experimental liquid marble similar to what is shown in our simulation.

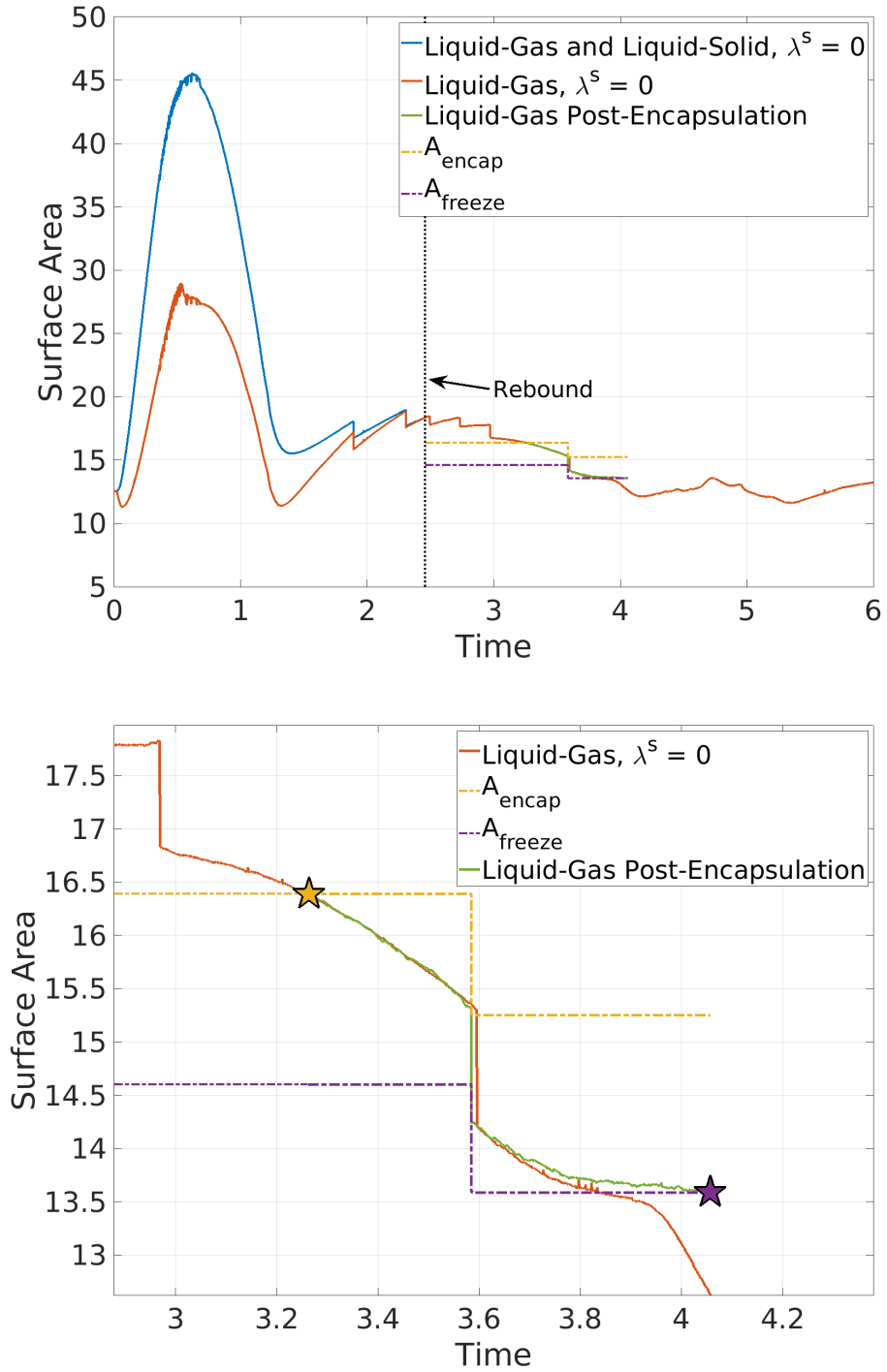


Figure 7.14: Surface area plot for the clean $We = 61$ simulation and overlaid surface viscous simulation post-encapsulation. The encapsulation and freezing areas change according to the surface viscous simulation. (Top) Includes pre-encapsulation behaviour. (Bottom) Focus on the surface viscous case from encapsulation to liquid marble formation.

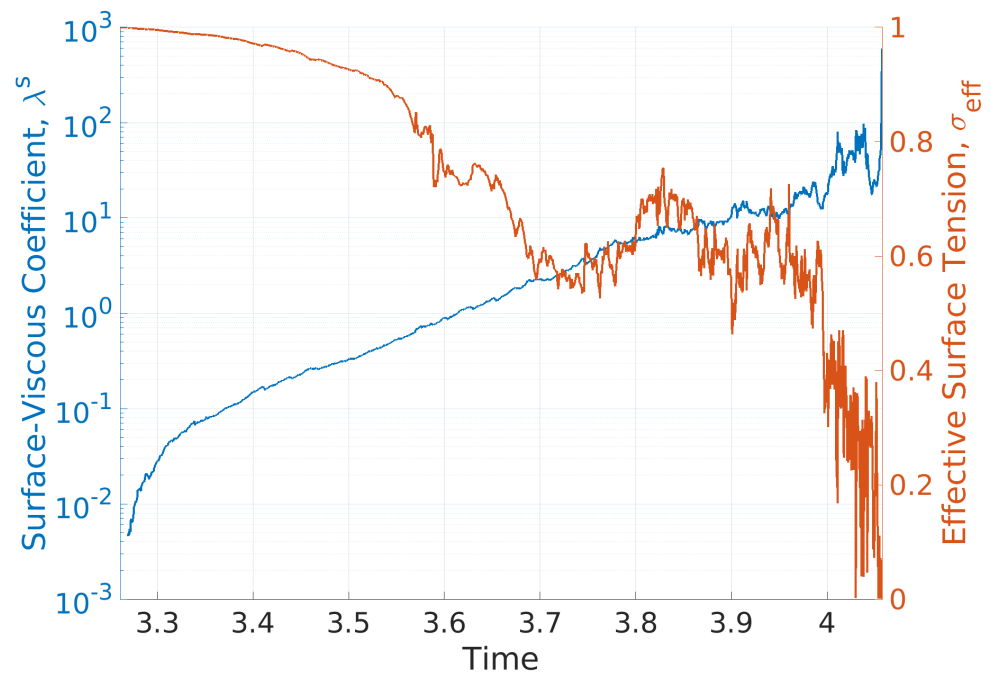


Figure 7.15: Post-encapsulation plot of the dilatational surface viscous coefficient λ^s (log-scale) and effective surface tension σ_{eff} over the course of the $We = 61$ liquid marble simulation.

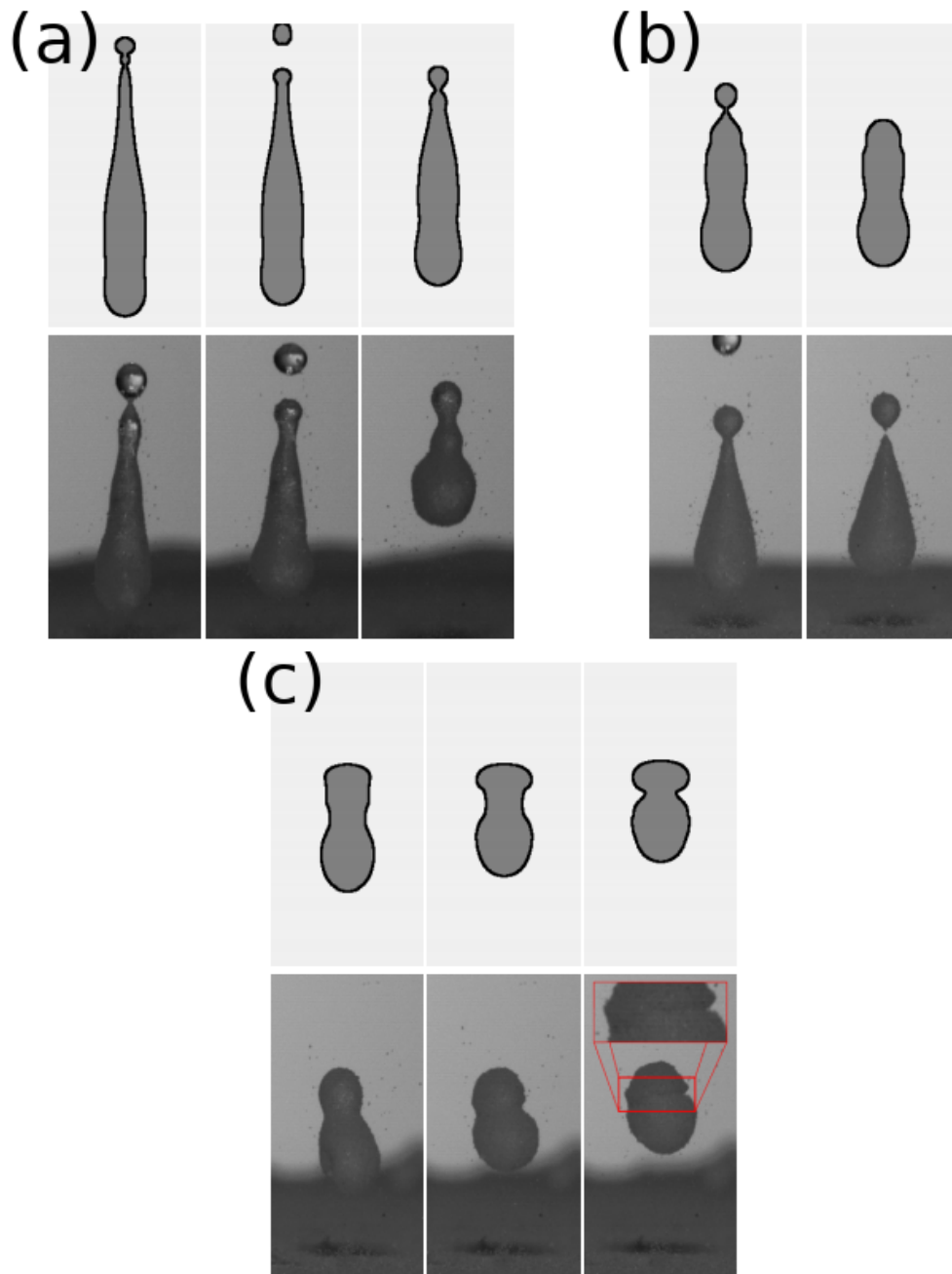


Figure 7.16: Comparisons of interesting observed phenomena in the $We = 61$ ($\gamma = 2.53$) simulation, with examples of the same phenomena occurring in our drop impact experiments: (a) $We = 62$ ($\gamma = 2.53$) experiment showing ejection of a clean satellite followed by a continuous reduction in surface area to encapsulation in the right-most image. (b) $We = 62$ ($\gamma = 2.53$) experiment showing ejection of a satellite post-encapsulation. (c) $We = 68$ ($\gamma = 2.56$) experiment showing the ‘squashing’ of the drop surface leading to deformed liquid marble formation in the right-most image.

We now consider the liquid marble simulation with $We = 71$. As shown in Figure 7.17, the difference in initial encapsulation and initial freezing areas has become very small, and for the short time between encapsulation and liquid marble formation, the difference in surface area between the clean and surface viscous case is *not* significant. In Figure 7.18 a steady increase in λ^s is matched by a steady *decrease* in the effective surface tension towards zero, reaching it shortly before λ^s diverges and the freezing area is reached. If we look at the drop shapes for this simulation in Figure 7.19, we see little change between the drop at encapsulation and liquid marble formation; the retraction of the drop apex into the rest of the drop is sufficient to close the gap between the encapsulation and freezing areas. Also shown in this figure is an example from a $We = 78$ ($\gamma = 2.69$) experiment similarly showing that the short retraction of the drop apex into the remainder of the drop is sufficient to freeze an encapsulated drop.

When the encapsulation and freezing areas are as close as in this case (and beyond), the surface viscous model becomes less important in the formation of deformed liquid marbles; what matters here is the threshold we have developed in terms of the parameters α_{encap} and α_{freeze} constructed following observations of experiments (see Figure 7.1). There is simply not enough time for surface viscosity to have a significant effect on drop dynamics, barring a poor choice for β (see §7.3.5), for the shape of the liquid marble to be drastically altered.

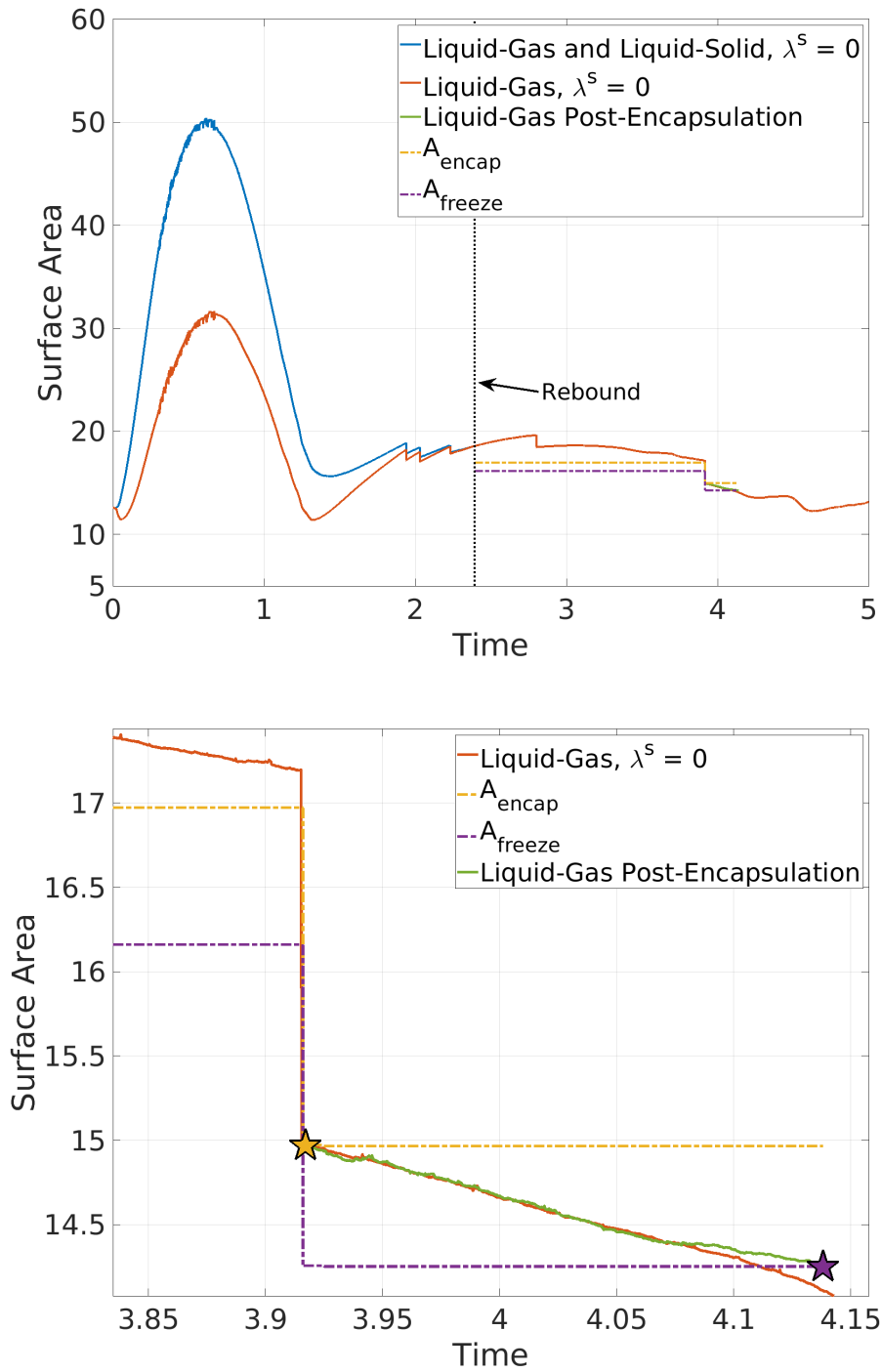


Figure 7.17: Surface area plot for the clean $We = 71$ simulation and overlaid surface viscous simulation post-encapsulation. The encapsulation and freezing areas change according to the surface viscous simulation. (Top) Includes pre-encapsulation behaviour. (Bottom) Focus on the surface viscous case from encapsulation to liquid marble formation.

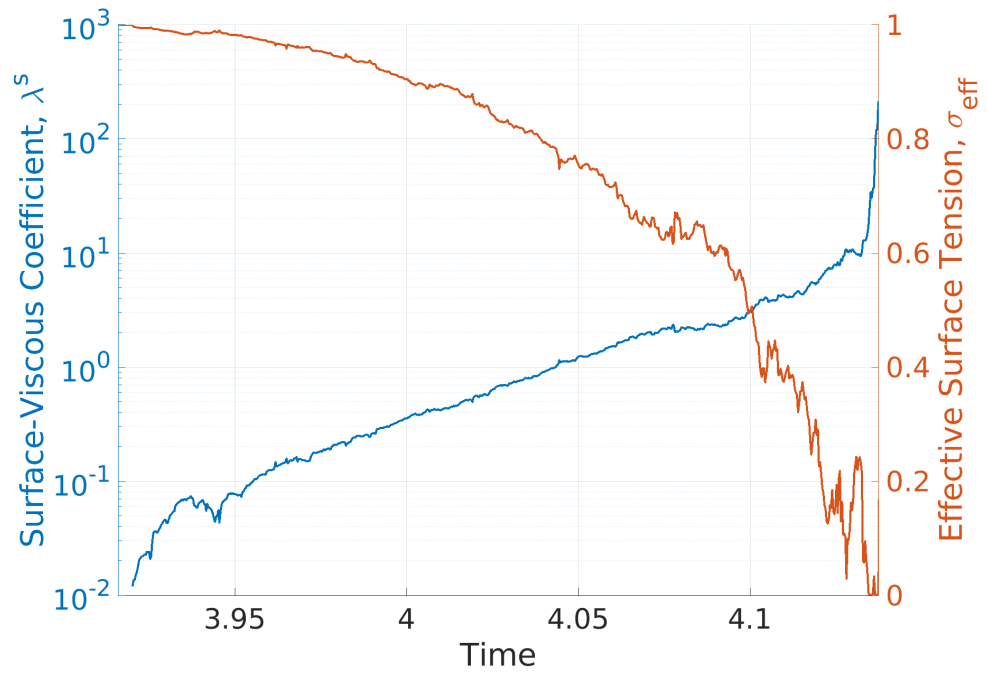


Figure 7.18: Plot of the dilatational surface viscous coefficient λ^s (log-scale) and effective surface tension σ_{eff} over the course of the $We = 71$ liquid marble simulation.

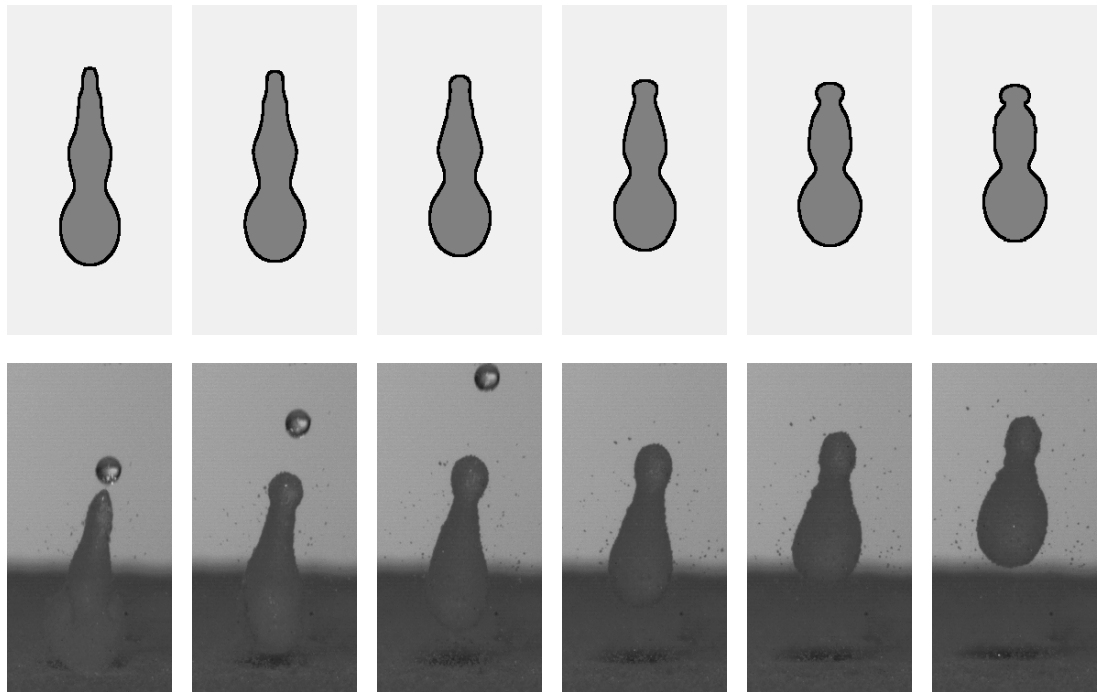


Figure 7.19: Drop profile comparison from the moment of encapsulation to the moment of deformed liquid marble formation between the simulation with $We = 71$ and $\gamma = 2.66$, and a powder bed experiment with $We = 78$ and $\gamma = 2.69$. Encapsulation is on the far left, with the deformed liquid marble on the far right, and intermediary images between them. In both cases there is little variation between the shape at encapsulation and of the deformed liquid marble; a slight retraction of the drop neck into the bulk of the drop is sufficient to cause interfacial freezing.

Finally, we consider the $We = 87$ ($\gamma = 2.83$) simulation, in which encapsulation and freezing occur simultaneously, meaning there are *no* surface viscous dynamics, and the shape of the liquid marble is determined entirely by the preceding clean drop impact simulation (from Chapter 6). In terms of our model, this occurs because the concentration of the adsorbed powder on the drop interface is already at the critical freezing threshold when encapsulation occurs.

In Figure 7.20 we see our instantaneously-formed liquid marble compared to other such liquid marbles observed in our experiments. There is reasonable agreement between our simulation and these experiments, but there are signs that we are close to the limits of the validity of our model for liquid marble formation, which are discussed here.

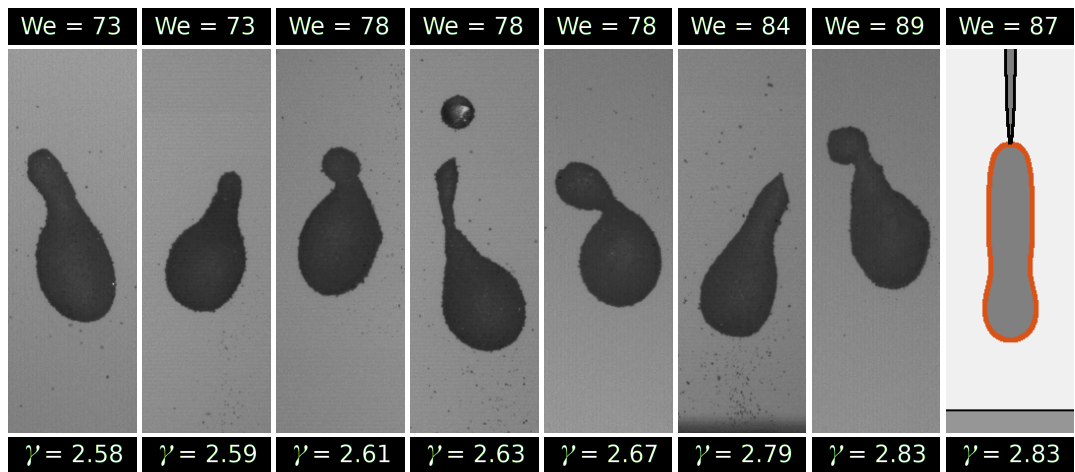


Figure 7.20: Examples of deformed liquid marbles created at the moment of encapsulation in powder bed impact experiments, and the $We = 87$ ($\gamma = 2.83$) simulation. The deformed liquid marble in the simulation (outlined in red) forms as an immediate result of a satellite drop ejection.

For all of the experiments shown in Figure 7.20, we see that the liquid marbles are ‘bottom heavy’, with apparent *local jamming* of the interface prior to encapsulation (before the drop apex has been coated in powder), with the motion of the bottom of the drops being similar to that of a rigid body translation. This property of the surface dynamics at high We is *not* present in our simulations. Recall that our model for liquid marble formation states that powder-related effects (a nonzero surface viscous contribution to the effective surface tension, and potential freezing of the interface) are not triggered until after encapsulation has occurred. Therefore, a

partially-coated drop in our simulations is dynamically equivalent to a clean drop, which will *not* have parts resembling rigid bodies when in a non-equilibrium shape. Further, our model assumes that the powder concentration within a powder coated region is spatially independent, so that, after encapsulation, there can be only *global*-jamming (with the entire drop forming a liquid marble) as the powder concentration reaches the critical freezing threshold *everywhere* simultaneously, rather than distinct regions freezing at different times.

However, recall (see Figure 7.1) that the extrapolated value of α_{encap} for this particular simulation ($We = 87$, $\gamma = 2.83$), predicted using our simple experimentally-motivated model for α_{encap} and α_{freeze} , is *lower* than the value of α_{freeze} used in our simulations. In terms of the model we have constructed for liquid marble formation, this would indicate that freezing of the drop interface (and so formation of a liquid marble) would *precede* encapsulation, which is impossible, so we ‘lifted’ α_{encap} and set it equal to α_{freeze} so that both occur simultaneously. At the same time, our result $\alpha_{encap} < \alpha_{freeze}$ may be interpreted as a scenario where the powder coated region of the drop interface reaches the critical freezing threshold for powder concentration prior to encapsulation. This could then correspond to the local-jamming effect as observed in the experiments within those regions coated in powder. In summary, although our current model for liquid marble formation is insufficient in capturing these dynamics related to apparent local-jamming, we can hypothesise from our experimentally-motivated model in Figure 7.1 that by removing some of our simplifying assumptions, we may be able to capture these local-jamming dynamics observed at higher We .

Another point of discrepancy, as discussed in §6.2.2, is our inability to perfectly recreate the pre-encapsulation rebound dynamics for drops impacting onto super-hydrophobic powder beds, partly due to our inability to capture the energy loss associated with the interactions between the drop and powder while on the substrate. While our simulations for lower We (and lower spreading factors) have not perfectly recreated pre-encapsulation dynamics, they have reached qualitatively similar shapes at encapsulation and liquid marble formation to those in experiments due to satellite drop ejections and breakup of the jet formed prior to rebound (see Figures 7.5-7.7). For the $We = 87$ ($\gamma = 2.83$) simulation, although the shape at encapsulation/freezing does resemble the drops from experiments in Figure 7.20, it does so due

to the fortunate ejection of a particularly long satellite droplet, and forms a more cylindrical shape than any of the experiments. Furthermore, our drop impact model is axisymmetric, and for higher impact Weber numbers, drops exhibit minor breaks in this symmetry which can affect retraction and rebound dynamics, and cannot be captured with our current model.

In summary, the substrate deformation and local jamming of the drop interface limits our model’s capability to describe liquid marble formation, and no comparisons for higher We are made.

7.3.5 Effect of large β

As an extra assurance that our choice of $\beta = 0.5$ in §7.2 is reasonable, we see in Figure 7.21 the drop at encapsulation compared to a set of liquid marbles formed with $\beta = 0.5, 5, 10$ for $We = 71$ ($\gamma = 2.66$). As discussed in the previous section and shown in Figure 7.7, the liquid marble formed with $\beta = 0.5$ is similar to those observed in experiments for similar impact Weber numbers and spreading factors. However, for the $\beta = 5$ and $\beta = 10$ cases, the liquid marbles are far removed from those seen in experiments for this impact Weber number (and those similar to it), where the formed liquid marbles typically differ *little* from the shapes at encapsulation.

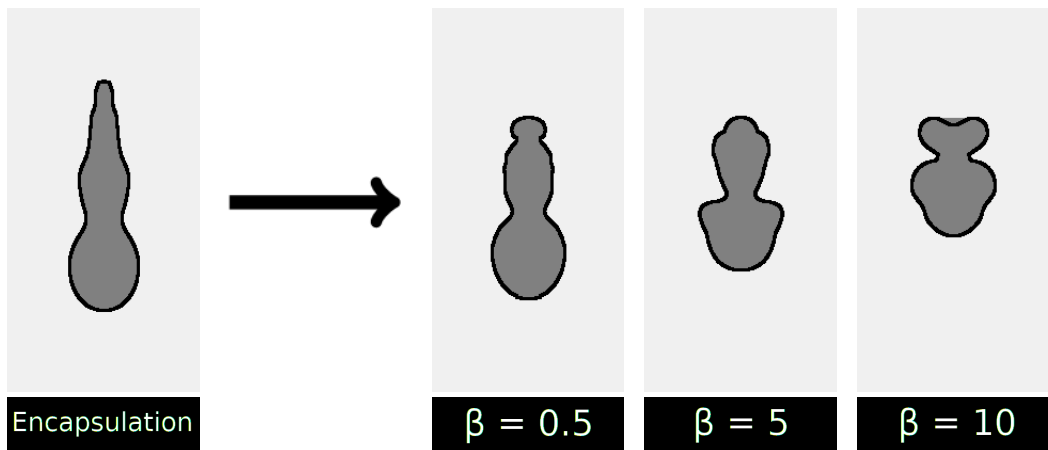


Figure 7.21: Drop profiles showing (left) the drop at encapsulation for $We = 71$ ($\gamma = 2.66$) and the remaining images show the liquid marble created using $\beta = 0.5$, $\beta = 5$, and $\beta = 10$.

Chapter 8

Summary and Future Work

For the research in this thesis, experimental and computational modelling investigations were conducted into the processes governing the formation of liquid marbles via drop impact onto a superhydrophobic powder bed. In summary, this thesis presents:

- *Experiments of water drop impacts onto rigid impermeable superhydrophobic substrates and superhydrophobic powder beds* (see Chapter 2) - A novel relationship was presented between the maximum spreading diameter of the drop on the powder bed, and the surface area of the rebounded drop at the moment of encapsulation and spherical/deformed liquid marble formation. The experiments presented in this chapter were used to motivate (Chapter 3) and validate (Chapters 6-7) our model for liquid marble formation.
- *A formulation of (two) mathematical models describing the formation of liquid marbles via drop impact onto a superhydrophobic powder bed* (see Chapter 3) - The powder bed was treated as a rigid impermeable superhydrophobic substrate, and the adhered particle coating as a continuum which provided (dilatational) surface viscous properties to the drop interface. The surface viscous effects manifested themselves in a spatially independent effective surface tension, which deviated from the surface tension of a bare drop only after encapsulation. The expression for the effective surface tension arose from assuming inviscid bulk flows in the liquid and gas phases, along with negligible particle inertia, and negligible surface shear viscosity. This expression was then imposed on a model with viscous bulk flows (viscosity being a necessary factor to accurately simulate the impact itself). Some assumptions made in our model

were motivated by observations from our experiments, whereas others were made for modelling/numerical simplicity. Ultimately, the model was validated empirically following comparisons between our numerical simulations and experiments. Relaxing underlying assumptions to better match experiments can be the focus of future work (discussed further below).

- *A detailed formulation of a BIM and corresponding computational BEM for the inviscid model (from Chapter 3) for liquid marble formation via drop impact, developed for this body of research (see Chapter 4) - While novel techniques were devised to model the spreading of the drop on the substrate, that were validated empirically for low We impacts, simulations of the impact phase for values of We required for liquid marble formation were unable to be conducted using the methods described in this chapter, which necessitated VoF simulations. BEM simulations (using the implementation described in this chapter) of suspended inviscid drops undergoing large (nonlinear) oscillations while experiencing (dilatational) surface viscous effects were used to validate the implementation of surface viscosity in subsequent VoF simulations.*
- *The first report of numerical simulations conducted for the formation of liquid marbles via drop impact onto a superhydrophobic powder bed (see Chapters 5-7) - A VoF method (see Chapter 5) was applied to the viscous model from Chapter 3 and simulations were conducted using a well-established piece of software (Basilisk), with results presented for a range of impact Weber numbers, $35 \leq We \leq 87$. Novel functionality was added to Basilisk to incorporate our time dependent effective surface tension. The novel relationship for the maximum spreading diameter and drop surface area (derived in Chapter 2) was used to determine the surface area at which encapsulation and interfacial freezing (jamming) occur. A parameter describing the ‘strength’ of (dilatational) surface viscous effects, which govern energy dissipation due to the adhered particles, was calibrated to match data from our experiments. In general terms, the events transpiring in simulations were of drop encapsulation followed by either: (i) a *slow* decay of drop oscillations, (ii) a *rapid* decay of drop oscillations with a spherical liquid marble formed prior to the drop reaching the apex of rebound, or (iii) the freezing of the drop interface in which a deformed liquid marble is created. The drop shapes at encapsulation and liquid marble formation in*

simulations, as well as post-encapsulation dynamics, were found to match well qualitatively and semi-quantitatively with experiments. The impact phases of these simulations (in which there were no surface viscous effects) were presented in Chapter 6, with liquid marble formation and the preceding surface viscosity effects presented in Chapter 7.

- *A novel third-order model for the oscillations of a suspended inviscid drop in the presence of a nonzero dilatational component of surface viscosity, and zero shear component* (see Chapter 3) - A novel damped nonlinear oscillator was developed, which predicted that for any value of λ^s , sufficiently large amplitude oscillations will transition from overdamped to underdamped motion when the oscillation amplitude crosses below a critical threshold. This critical amplitude threshold was derived, as was an analytic solution for the drop amplitude in the overdamped limit. The transition between regimes was subsequently validated in numerical simulations (using the BIM/BEM from Chapter 4) and is not predicted with existing (linear) models. A numerical investigation was then conducted for *large* (nonlinear) drop deformations by comparing BEM simulations and a ‘toy’ nonlinear oscillator model based upon our own third-order model, with qualitative similarities shown between the simulations and the ‘toy’ oscillator even though the latter is suited for small amplitude oscillations.

Future work that builds upon the results presented in this thesis will likely focus on relaxing some of the simplifying assumptions of our model and simulating more complex/realistic models. Avenues for future research therefore include:

- *Formulating the effects of dilatational surface viscosity alongside an assumption of viscous bulk flows* - Dilatational surface viscosity is incorporated into the viscous model (see §3.2.5), and hence within our simulations for liquid marble formation, by using the spatially independent effective surface tension obtained from the inviscid model (see §3.2.4). The effective surface tension appears (partly) as a result of there being no contributions from the (inviscid) bulk flows either side of the interface in the tangential stress balance equation (3.2.20). Under a viscous assumption, there would be contributions from both bulk flows in the form of quantities related to their bulk rate-of-strain tensors (3.2.42)-(3.2.43), which would (importantly) be spatially dependent. As

a result, encapsulation would no longer be required for (dilatational) surface viscous effects to be felt along the drop interface, and so the complexity of the model would increase, in part because surface viscous effects could no longer be neglected when the drop is on the substrate. This is done so in our model because we adopt the observation that encapsulation always occurs in our experiments post-rebound. An advection equation for the surface concentration is then necessary to track the extent of powder coverage, as the conservation of powder coated surface area that holds in our model is also partly the result of the inviscid bulk assumption. Using such a model, we could investigate our claim in Chapter 3 that because the drops experience large deformations post-rebound, the Reynolds number is likely still high, and so post-rebound surface viscous effects from the inviscid model would well approximate surface viscous effects from a fully formulated model built upon a bulk viscous assumption. This fully-viscous model would also allow predictions for liquid marble formation via drop impact to be made for liquids with larger viscosities than water.

- *Considering a nonzero surface shear viscosity coefficient, μ^s , in the Boussinesq-Scriven constitutive law (1.3.1)* - Considering $\mu^s > 0$ would likewise cause additional terms to appear in the normal and tangential stress balance equations (3.2.19)-(3.2.20) at the liquid-gas interface that would make surface viscous effects spatially dependent, with similar expected implications on model complexity as with the previous bullet point. Incorporating the shear component of surface viscosity may provide a plethora of additional effects that we do not currently observe in our model, nor appear when considering a fully (bulk) viscous formulation (as just described), because both cases only consider the degenerate case of $\mu^s = 0$. For this reason, a parameter study to determine the range of possible effects in the liquid marble formation process by varying λ^s and μ^s deserves attention.
- *Incorporating deformation of the substrate* - Including substrate deformation in our model would likely be achievable within the continuum description of the powder particles, and would involve the development of a solid mechanics or viscoelastic model for the substrate. Given there would be additional energy dissipation associated with the impact, we expect that the rebound speed

for drops would decrease compared to our simulations, so that the coefficient of restitution calculated in simulations would likely better match powder bed experiments than with the current model (see Figure 6.12). An important consequence may be that via this additional loss of energy, the drop profiles in simulations may better match those in powder bed experiments, particularly for high We impacts where the difference between our simulations and experiments is most apparent.

- *Comparing our model to drop impact experiments using different powders* - The ‘strength’ of surface viscous effects in our model could be calibrated, as was done in §7.2 for our own experiments, to another set of drop impact experiments (onto superhydrophobic powder beds) that exhibit liquid marbles, but with different particle characteristics. Choosing an appropriate value of β , by determining when spherical liquid marbles start to form in the new set of experiments, would test the predictive power of our model by comparing the liquid marbles obtained in these new simulations to the new experiments for various values of We . This could also provide additional revelations that are not apparent in our case because we only consider a single combination of liquid drop and solid particles.
- *Using particle-based approaches to validate modelling assumptions* - While particle-based simulations are computationally expensive to run, they could be utilised to investigate the validity of some of our simplifying assumptions on smaller computational domains. For example, by modelling the receding motion of a drop rim over a subset of powder particles, we could determine whether a transition of (approximately constant) powder concentrations *does* occur (over a small finite time) as the contact line recedes and particles move to the liquid-gas interface. Additionally, a dependence of λ^s on the adhered particle concentration could be derived empirically (instead of assumed) from particle-based simulations, where the computational domain is of small patches of particle coated liquid-gas interface with varying curvatures. Finally, when particle jamming occurs in our model, the entire drop interface is frozen at once, when in fact we appear to observe local jamming for high impact Weber number experiments (as discussed in Chapter 7). A particle-based simulation on locally jammed regions of a liquid-interface, alongside non-jammed regions, could provide insight

into how we should treat this phenomenon in our model, and whether using the Boussinesq-Scriven constitutive law is appropriate when part of the interface is immobilised.

Bibliography

- [1] P. Aussillous and D. Quéré. Liquid marbles. *Nature*, 411:924–927, 2001.
- [2] L. Mahadevan. Non-stick water. *Nature*, 411(6840):895–896, 2001.
- [3] G. McHale and M. I. Newton. Liquid marbles: principles and applications. *Soft Matter*, 7(12):5473–5481, 2011.
- [4] N. Eshtiaghi and K. P. Hapgood. A quantitative framework for the formation of liquid marbles and hollow granules from hydrophobic powders. *Powder technology*, 223:65–76, 2012.
- [5] E. Bormashenko. New insights into liquid marbles. *Soft Matter*, 8(43):11018–11021, 2012.
- [6] G. McHale and M. I. Newton. Liquid marbles: topical context within soft matter and recent progress. *Soft Matter*, 11:2530–2546, 2015.
- [7] C. Ooi and N. Nguyen. Manipulation of liquid marbles. *Microfluidics and Nanofluidics*, 19(3):483–495, 2015.
- [8] E. Bormashenko. Liquid marbles, elastic nonstick droplets: From minireactors to self-propulsion. *Langmuir*, 33(3):663–669, 2017.
- [9] N. M. Oliveira, R. L. Reis, and J. F. Mano. The potential of liquid marbles for biomedical applications: a critical review. *Advanced healthcare materials*, 6(19):1700192, 2017.
- [10] P. Singha, C. Ooi, N. Nguyen, K. Sreejith, J. Jin, and N. Nguyen. Capillarity: revisiting the fundamentals of liquid marbles. *Microfluidics and Nanofluidics*, 24(10):1–15, 2020.

- [11] P. Aussillous and D. Quéré. Properties of liquid marbles. *Proceedings of the Royal Society A: Mathematical, Physical and Engineering Sciences*, 462(2067):973–999, 2006.
- [12] N. Eshtiaghi, J. S. Liu, W. Shen, and K. P. Hapgood. Liquid marble formation: Spreading coefficients or kinetic energy? *Powder Technology*, 196(2):126 – 132, 2009.
- [13] J. O. Marston, Y. Zhu, I. U. Vakarelski, and S. T. Thoroddsen. Deformed liquid marbles: Freezing drop oscillations with powders. *Powder Technology*, 228:424 – 428, 2012.
- [14] J. O. Marston, Y. Zhu, I. U. Vakarelski, and S. T. Thoroddsen. Freezing drops with powders. *Physics of fluids*, 25(9):091107, 2013.
- [15] T. Supakar, M. Moradiafrapoli, G. F. Christopher, and J. O. Marston. Spreading, encapsulation and transition to arrested shapes during drop impact onto hydrophobic powders. *Journal of colloid and interface science*, 468:10–20, 2016.
- [16] A. Mozhi Devan Padmanathan, A. Sneha Ravi, H. Choudhary, S. Varanakkottu, and S. V. Dalvi. Predictive framework for the spreading of liquid drops and the formation of liquid marbles on hydrophobic particle bed. *Langmuir*, 35(20):6657–6668, 2019.
- [17] X. Li, H. Shi, Y. Wang, H. Wang, J. Huang, and M. Duan. Liquid marbles from soot films. *Soft Matter*, 16(18):4512–4519, 2020.
- [18] L. Forny, I. Pezron, K. Saleh, P. Guigon, and L. Komunjer. Storing water in powder form by self-assembling hydrophobic silica nanoparticles. *Powder technology*, 171(1):15–24, 2007.
- [19] Y. Zhao, J. Fang, H. Wang, X. Wang, and T. Lin. Magnetic liquid marbles: manipulation of liquid droplets using highly hydrophobic fe₃o₄ nanoparticles. *Advanced materials*, 22(6):707–710, 2010.
- [20] K. Rykaczewski, J. Chinn, M. L. Walker, J. H. J. Scott, A. Chinn, and W. Jones. Dynamics of nanoparticle self-assembly into superhydrophobic liquid marbles during water condensation. *Acs Nano*, 5(12):9746–9754, 2011.

- [21] M. Abkarian, S. Protière, J. M. Aristoff, and H. A. Stone. Gravity-induced encapsulation of liquids by destabilization of granular rafts. *Nature communications*, 4(1):1–8, 2013.
- [22] N. Pike, D. Richard, W. Foster, and L. Mahadevan. How aphids lose their marbles. *Proceedings of the Royal Society of London. Series B: Biological Sciences*, 269(1497):1211–1215, 2002.
- [23] M. Kasahara, S. Akimoto, T. Hariyama, Y. Takaku, S. Yusa, S. Okada, K. Nakajima, T. Hirai, H. Mayama, S. Okada, et al. Liquid marbles in nature: Craft of aphids for survival. *Langmuir*, 35(18):6169–6178, 2019.
- [24] E. Bormashenko, Y. Bormashenko, A. Musin, and Z. Barkay. On the mechanism of floating and sliding of liquid marbles. *ChemPhysChem*, 10(4):654–656, 2009.
- [25] Z. Liu, Y. Zhang, C. Chen, T. Yang, J. Wang, L. Guo, P. Liu, and T. Kong. Larger stabilizing particles make stronger liquid marble. *Small*, 15(3):1804549, 2019.
- [26] D. Quéré. Wetting and roughness. *Annual Review of Materials Research*, 38(1):71–99, 2008.
- [27] E. Bormashenko and A. Musin. Revealing of water surface pollution with liquid marbles. *Applied Surface Science*, 255(12):6429–6431, 2009.
- [28] H. Y. Erbil. Evaporation of pure liquid sessile and spherical suspended drops: A review. *Advances in colloid and interface science*, 170(1-2):67–86, 2012.
- [29] U. Cengiz and H. Y. Erbil. The lifetime of floating liquid marbles: the influence of particle size and effective surface tension. *Soft Matter*, 9(37):8980–8991, 2013.
- [30] A. Tosun and H. Y. Erbil. Evaporation rate of ptfе liquid marbles. *Applied surface science*, 256(5):1278–1283, 2009.
- [31] M. Dandan and H. Y. Erbil. Evaporation rate of graphite liquid marbles: comparison with water droplets. *Langmuir*, 25(14):8362–8367, 2009.
- [32] P. S. Bhosale, M. V. Panchagnula, and H. A. Stretz. Mechanically robust nanoparticle stabilized transparent liquid marbles. *Applied Physics Letters*, 93(3):034109, 2008.

- [33] H. Polwaththe-Gallage, C. Ooi, J. Jin, E. Sauret, N. Nguyen, Z. Li, and Y. Gu. The stress-strain relationship of liquid marbles under compression. *Applied Physics Letters*, 114(4):043701, 2019.
- [34] D. Zang, Z. Chen, Y. Zhang, K. Lin, X. Geng, and B. P. Binks. Effect of particle hydrophobicity on the properties of liquid water marbles. *Soft Matter*, 9(20):5067–5073, 2013.
- [35] S. Asare-Asher, J. N. Connor, and R. Sedev. Elasticity of liquid marbles. *Journal of Colloid and Interface Science*, 449:341 – 346, 2015.
- [36] E. Bormashenko, R. Pogreb, R. Balter, H. Aharoni, Y. Bormashenko, R. Grynyov, L. Mashkevych, D. Aurbach, and O. Gendelman. Elastic properties of liquid marbles. *Colloid and Polymer Science*, 293(8):2157–2164, 2015.
- [37] A. Rendos, N. Alsharif, B. L. Kim, and K. A. Brown. Elasticity and failure of liquid marbles: influence of particle coating and marble volume. *Soft Matter*, 13(47):8903–8909, 2017.
- [38] S. Azizian, S. Fujii, M. Kasahara, H. Butt, and M. Kappl. Effect of particle morphology on mechanical properties of liquid marbles. *Advanced Powder Technology*, 30(2):330–335, 2019.
- [39] M. I. Newton, D. L. Herbertson, S. J. Elliott, N. J. Shirtcliffe, and G. McHale. Electrowetting of liquid marbles. *Journal of physics D: Applied physics*, 40(1):20, 2006.
- [40] K. P. Hapgood and B. Khanmohammadi. Granulation of hydrophobic powders. *Powder Technology*, 189(2):253–262, 2009.
- [41] Y. Xue, H. Wang, Y. Zhao, L. Dai, L. Feng, X. Wang, and T. Lin. Magnetic liquid marbles: a “precise” miniature reactor. *Advanced materials*, 22(43):4814–4818, 2010.
- [42] T. Arbatan and W. Shen. Measurement of the surface tension of liquid marbles. *Langmuir*, 27(21):12923–12929, 2011.
- [43] Y. Zhao, Z. Xu, M. Parhizkar, J. Fang, X. Wang, and T. Lin. Magnetic liquid marbles, their manipulation and application in optical probing. *Microfluidics and nanofluidics*, 13(4):555–564, 2012.

- [44] C. P. Whitby, X. Bian, and R. Sedev. Spontaneous liquid marble formation on packed porous beds. *Soft Matter*, 8(44):11336–11342, 2012.
- [45] V. Sivan, S. Tang, A. P. O’Mullane, P. Petersen, N. Eshtiaghi, K. Kalantarzadeh, and A. Mitchell. Liquid metal marbles. *Advanced Functional Materials*, 23(2):144–152, 2013.
- [46] E. Bormashenko, Y. Bormashenko, R. Grynyov, H. Aharoni, G. Whyman, and B. P. Binks. Self-propulsion of liquid marbles: Leidenfrost-like levitation driven by marangoni flow. *The Journal of Physical Chemistry C*, 119(18):9910–9915, 2015.
- [47] Z. Liu, X. Fu, B. P. Binks, and H. Shum. Mechanical compression to characterize the robustness of liquid marbles. *Langmuir*, 31(41):11236–11242, 2015.
- [48] J. R. Dorvee, A. M. Derfus, S. N. Bhatia, and M. J. Sailor. Manipulation of liquid droplets using amphiphilic, magnetic one-dimensional photonic crystal chaperones. *Nature materials*, 3(12):896–899, 2004.
- [49] B. Wang, Y. Liu, Y. Zhang, Z. Guo, H. Zhang, J. H. Xin, and L. Zhang. Bioinspired superhydrophobic Fe_3O_4 @ polydopamine@ Ag hybrid nanoparticles for liquid marble and oil spill. *Advanced Materials Interfaces*, 2(13):1500234, 2015.
- [50] M. Khaw, C. Ooi, F. Mohd-Yasin, R. Vadivelu, J. St John, and N. Nguyen. Digital microfluidics with a magnetically actuated floating liquid marble. *Lab on a Chip*, 16(12):2211–2218, 2016.
- [51] T. C. Draper, C. Fullarton, N. Phillips, B. P. J. de Lacy Costello, and A. Adamatzky. Liquid marble interaction gate for collision-based computing. *Materials Today*, 20(10):561–568, 2017.
- [52] E. Bormashenko, R. Pogreb, Y. Bormashenko, A. Musin, and T. Stein. New investigations on ferrofluidics: ferrofluidic marbles and magnetic-field-driven drops on superhydrophobic surfaces. *Langmuir*, 24(21):12119–12122, 2008.
- [53] J. Jeon, J. Lee, S. Chung, and D. Kim. Magnetic liquid metal marble: characterization of lyophobicity and magnetic manipulation for switching applications. *Journal of Microelectromechanical Systems*, 25(6):1050–1057, 2016.

- [54] C. Ooi, J. Jin, A. V. Nguyen, G. M. Evans, and N. Nguyen. Picking up and placing a liquid marble using dielectrophoresis. *Microfluidics and Nanofluidics*, 22(12):142, 2018.
- [55] J. Jin, C. Ooi, K. Sreejith, J. Zhang, A. V. Nguyen, G. M. Evans, D. Dao, and N. Nguyen. Accurate dielectrophoretic positioning of a floating liquid marble with a two-electrode configuration. *Microfluidics and Nanofluidics*, 23(7):85, 2019.
- [56] D. Zang, J. Li, Z. Chen, Z. Zhai, X. Geng, and B. P. Binks. Switchable opening and closing of a liquid marble via ultrasonic levitation. *Langmuir*, 31(42):11502–11507, 2015.
- [57] E. Bormashenko, Y. Bormashenko, and A. Musin. Water rolling and floating upon water: marbles supported by a water/marble interface. *Journal of colloid and interface science*, 333(1):419–421, 2009.
- [58] E. Bormashenko. Liquid marbles: properties and applications. *Current Opinion in Colloid & Interface Science*, 16(4):266–271, 2011.
- [59] N. Nguyen, C. Ooi, P. Singha, J. Jin, K. Sreejith, H. Phan, and N. Nguyen. Liquid marbles as miniature reactors for chemical and biological applications. *Processes*, 8(7):793, 2020.
- [60] B. O. Carter, D. J. Adams, and A. I. Cooper. Pausing a stir: heterogeneous catalysis in “dry water”. *Green Chemistry*, 12(5):783–785, 2010.
- [61] Y. Miao, H. Lee, W. Chew, I. Phang, T. Liu, and X. Ling. Catalytic liquid marbles: Ag nanowire-based miniature reactors for highly efficient degradation of methylene blue. *Chemical Communications*, 50(44):5923–5926, 2014.
- [62] W. Wei, R. Lu, W. Ye, J. Sun, Y. Zhu, J. Luo, and X. Liu. Liquid marbles stabilized by fluorine-bearing cyclomatrix polyphosphazene particles and their application as high-efficiency miniature reactors. *Langmuir*, 32(7):1707–1715, 2016.
- [63] Z. Rozynek, K. Khobaib, and A. Mikkelsen. Opening and closing of particle shells on droplets via electric fields and its applications. *ACS applied materials & interfaces*, 11(25):22840–22850, 2019.

- [64] X. Han, H. Lee, Y. Lee, and X. Ling. Dynamic rotating liquid marble for directional and enhanced mass transportation in three-dimensional microliter droplets. *The Journal of Physical Chemistry Letters*, 8(1):243–249, 2017.
- [65] T. Arbatan, L. Li, J. Tian, and W. Shen. Liquid marbles as micro-bioreactors for rapid blood typing. *Advanced healthcare materials*, 1(1):80–83, 2012.
- [66] H. Li, P. Liu, G. Kaur, X. Yao, and M. Yang. Transparent and gas-permeable liquid marbles for culturing and drug sensitivity test of tumor spheroids. *Advanced healthcare materials*, 6(13):1700185, 2017.
- [67] R. K. Vadivelu, H. Kamble, A. Munaz, and N. Nguyen. Liquid marble as bioreactor for engineering three-dimensional toroid tissues. *Scientific reports*, 7(1):1–14, 2017.
- [68] J. Tian, N. Fu, X. Chen, and W. Shen. Respirable liquid marble for the cultivation of microorganisms. *Colloids and Surfaces B: Biointerfaces*, 106:187–190, 2013.
- [69] Y. Chu, Z. Wang, and Q. Pan. Constructing robust liquid marbles for miniaturized synthesis of graphene/ag nanocomposite. *ACS applied materials & interfaces*, 6(11):8378–8386, 2014.
- [70] Y. Sheng, G. Sun, J. Wu, G. Ma, and T. Ngai. Silica-based liquid marbles as microreactors for the silver mirror reaction. *Angewandte Chemie*, 127(24):7118–7123, 2015.
- [71] Y. Sheng, G. Sun, and T. Ngai. Dopamine polymerization in liquid marbles: A general route to janus particle synthesis. *Langmuir*, 32(13):3122–3129, 2016.
- [72] H. Gu, B. Ye, H. Ding, C. Liu, Y. Zhao, and Z. Gu. Non-iridescent structural color pigments from liquid marbles. *Journal of Materials Chemistry C*, 3(26):6607–6612, 2015.
- [73] J. Tian, T. Arbatan, X. Li, and W. Shen. Liquid marble for gas sensing. *Chemical Communications*, 46(26):4734–4736, 2010.
- [74] S. Fujii, M. Suzaki, S. P. Armes, D. Dupin, S. Hamasaki, K. Aono, and Y. Nakamura. Liquid marbles prepared from ph-responsive sterically stabilized latex particles. *Langmuir*, 27(13):8067–8074, 2011.

- [75] D. Shin, T. Huang, D. Neibloom, M. A. Bevan, and J. Frechette. Multifunctional liquid marble compound lenses. *ACS applied materials & interfaces*, 11(37):34478–34486, 2019.
- [76] B. P. Binks and R. Murakami. Phase inversion of particle-stabilized materials from foams to dry water. *Nature materials*, 5(11):865–869, 2006.
- [77] K. Sreejith, L. Gorgannezhad, J. Jin, C. Ooi, T. Takei, G. Hayase, H. Stratton, K. Lamb, M. Shiddiky, D. Dao, et al. Core-shell beads made by composite liquid marble technology as a versatile microreactor for polymerase chain reaction. *Micromachines*, 11(3):242, 2020.
- [78] A. Frohn and N. Roth. *Dynamics of droplets*. Springer Science & Business Media, 2000.
- [79] T. Supakar, A. Kumar, and J. O. Marston. Impact dynamics of particle-coated droplets. *Physical Review E*, 95(1):013106, 2017.
- [80] D. E. Tambe and M. M. Sharma. The effect of colloidal particles on fluid-fluid interfacial properties and emulsion stability. *Advances in colloid and interface science*, 52:1–63, 1994.
- [81] S. Reynaert, P. Moldenaers, and J. Vermant. Interfacial rheology of stable and weakly aggregated two-dimensional suspensions. *Physical Chemistry Chemical Physics*, 9(48):6463–6475, 2007.
- [82] A. Stocco, W. Drenckhan, E. Rio, D. Langevin, and B. P. Binks. Particle-stabilised foams: an interfacial study. *Soft Matter*, 5(11):2215–2222, 2009.
- [83] D. Y. Zang, E. Rio, D. Langevin, B. Wei, and B. P. Binks. Viscoelastic properties of silica nanoparticle monolayers at the air-water interface. *The European Physical Journal E*, 31(2):125–134, 2010.
- [84] A. P. Kotula and S. L. Anna. Probing timescales for colloidal particle adsorption using slug bubbles in rectangular microchannels. *Soft Matter*, 8(41):10759–10772, 2012.
- [85] A. G. Bykov, B. A. Noskov, G. Loglio, V. V. Lyadinskaya, and R. Miller. Dilational surface elasticity of spread monolayers of polystyrene microparticles. *Soft Matter*, 10(34):6499–6505, 2014.

- [86] S. Barman and G. F. Christopher. Simultaneous interfacial rheology and microstructure measurement of densely aggregated particle laden interfaces using a modified double wall ring interfacial rheometer. *Langmuir*, 30(32):9752–9760, 2014.
- [87] A. J. Mendoza, E. Guzmán, F. Martínez-Pedrero, H. Ritacco, R. G. Rubio, F. Ortega, V. M. Starov, and R. Miller. Particle laden fluid interfaces: dynamics and interfacial rheology. *Advances in colloid and interface science*, 206:303–319, 2014.
- [88] B. A. Noskov, P. A. Yazhgur, L. Liggieri, S. Lin, G. Loglio, R. Miller, and F. Ravera. Dilational rheology of spread and adsorbed layers of silica nanoparticles at the liquid-gas interface. *Colloid Journal*, 76(2):127–138, 2014.
- [89] A. Maestro, E. Santini, D. Zabiegaj, S. Llamas, F. Ravera, L. Liggieri, F. Ortega, R. G. Rubio, and E. Guzman. Particle and particle-surfactant mixtures at fluid interfaces: assembly, morphology, and rheological description. *Advances in Condensed Matter Physics*, 2015, 2015.
- [90] S. Barman and G. F. Christopher. Role of capillarity and microstructure on interfacial viscoelasticity of particle laden interfaces. *Journal of Rheology*, 60(1):35–45, 2016.
- [91] H. Katepalli, V. T. John, A. Tripathi, and A. Bose. Microstructure and rheology of particle stabilized emulsions: Effects of particle shape and inter-particle interactions. *Journal of colloid and interface science*, 485:11–17, 2017.
- [92] S. Mahmoudi Salehabad, S. Azizian, and S. Fujii. Shape-designable liquid marbles stabilized by gel layer. *Langmuir*, 35(27):8950–8960, 2019.
- [93] T. Krüger, S. Frijters, F. Günther, B. Kaoui, and J. Harting. Numerical simulations of complex fluid-fluid interface dynamics. *The European Physical Journal Special Topics*, 222(1):177–198, 2013.
- [94] J. Harting. Lattice-boltzmann simulations of colloidal particles at fluid interfaces. In *Computational Trends in Solvation and Transport in Liquids*, pages 511–531. Forschungszentrum Jülich, 2015.

- [95] K. Stratford, R. Adhikari, I. Pagonabarraga, J. Desplat, and M. E. Cates. Colloidal jamming at interfaces: A route to fluid-bicontinuous gels. *Science*, 309(5744):2198–2201, 2005.
- [96] E. Kim, K. Stratford, and M. E. Cates. Bijels containing magnetic particles: A simulation study. *Langmuir*, 26(11):7928–7936, 2010.
- [97] F. Jansen and J. Harting. From bijels to pickering emulsions: A lattice boltzmann study. *Physical Review E*, 83(4):046707, 2011.
- [98] F. Günther, F. Janoschek, S. Frijters, and J. Harting. Lattice boltzmann simulations of anisotropic particles at liquid interfaces. *Computers & Fluids*, 80:184–189, 2013.
- [99] Q. Xie, G. B. Davies, F. Günther, and J. Harting. Tunable dipolar capillary deformations for magnetic janus particles at fluid–fluid interfaces. *Soft Matter*, 11(18):3581–3588, 2015.
- [100] Q. Xie, G. B. Davies, and J. Harting. Controlled capillary assembly of magnetic janus particles at fluid–fluid interfaces. *Soft Matter*, 12(31):6566–6574, 2016.
- [101] Q. Xie, G. B. Davies, and J. Harting. Direct assembly of magnetic janus particles at a droplet interface. *ACS nano*, 11(11):11232–11239, 2017.
- [102] S. Aland, J. Lowengrub, and A. Voigt. A continuum model of colloid-stabilized interfaces. *Physics of Fluids*, 23(6):062103, 2011.
- [103] P. C. Millett and Y. U. Wang. Diffuse-interface field approach to modeling arbitrarily-shaped particles at fluid–fluid interfaces. *Journal of colloid and interface science*, 353(1):46–51, 2011.
- [104] C. Gu and L. Botto. Buckling vs. particle desorption in a particle-covered drop subject to compressive surface stresses: a simulation study. *Soft matter*, 14(5):711–724, 2018.
- [105] S. Frijters, F. Günther, and J. Harting. Deformation of fluid droplets stabilized by colloids or surfactant. *arXiv preprint arXiv:1201.6562*, 2012.
- [106] C. Gu and L. Botto. Direct calculation of anisotropic surface stresses during deformation of a particle-covered drop. *The Royal Society of Chemistry*, pages 705–716, 2016.

- [107] W. Xiong, P. Cheng, X. Quan, and W. Yao. Droplet impact on a layer of solid particles placed above a substrate: A 3d lattice boltzmann study. *Computers & Fluids*, 188:18–30, 2019.
- [108] J. T. Petkov, K. D. Danov, N. D. Denkov, R. Aust, and F. Durst. Precise method for measuring the shear surface viscosity of surfactant monolayers. *Langmuir*, 12(11):2650–2653, 1996.
- [109] L. E. Scriven. Dynamics of a fluid interface equation of motion for newtonian surface fluids. *Chemical Engineering Science*, 12(2):98 – 108, 1960.
- [110] R. W. Flumerfelt. Effects of dynamic interfacial properties on drop deformation and orientation in shear and extensional flow fields. *Journal of colloid and interface science*, 76(2):330–349, 1980.
- [111] C. Pozrikidis. Effects of surface viscosity on the finite deformation of a liquid drop and the rheology of dilute emulsions in simple shearing flow. *Journal of non-newtonian fluid mechanics*, 51(2):161–178, 1994.
- [112] J T. Schwalbe, F. R. Phelan, Jr., P. M. Vlahovska, and S. D. Hudson. Interfacial effects on droplet dynamics in poiseuille flow. *Soft Matter*, 7:7797–7804, 2011.
- [113] J. Gounley, G. Boedec, M. Jaeger, and M. Leonetti. Influence of surface viscosity on droplets in shear flow. *Journal of Fluid Mechanics*, 791:464–494, 2016.
- [114] S. Mandal and S. Chakraborty. Influence of interfacial viscosity on the dielectrophoresis of drops. *Physics of Fluids*, 29(5):052002, 2017.
- [115] V. Narsimhan. Shape and rheology of droplets with viscous surface moduli. *Journal of Fluid Mechanics*, 862:385–420, 2019.
- [116] A. Nadim and B. M. Rush. Determination of interfacial rheological properties through microgravity oscillations of bubbles and drops. 2000.
- [117] B. M. Rush and A. Nadim. Shape oscillations in droplets strongly influenced by surfactants. 2006.
- [118] B. M. Rush and A. Nadim. Damping of drop oscillations by surfactants and surface viscosity. 1999.

- [119] L. Shen, F. Denner, N. Morgan, B. van Wachem, and D. Dini. Capillary waves with surface viscosity. *Journal of Fluid Mechanics*, 847:644–663, 2018.
- [120] D. Khojasteh, M. Kazerooni, S. Salarian, and R. Kamali. Droplet impact on superhydrophobic surfaces: A review of recent developments. *Journal of industrial and engineering chemistry*, 42:1–14, 2016.
- [121] C. Josserand and S. T. Thoroddsen. Drop impact on a solid surface. *Annual review of fluid mechanics*, 48:365–391, 2016.
- [122] J. H. Conway and N. J. Sloane. Sphere packings, lattices and groups, 1993. *Épringer-Verlag, New York*, 1993.
- [123] F. A. Dullien. *Porous media: fluid transport and pore structure*. Academic press, 2012.
- [124] W. H. Press and S. A. Teukolsky. Savitzky-golay smoothing filters. *Computers in Physics*, 4(6):669–672, 1990.
- [125] J. T. Pearson, D. Maynes, and B. W. Webb. Droplet impact dynamics for two liquids impinging on anisotropic superhydrophobic surfaces. *Experiments in Fluids*, 53:603–618, 2012.
- [126] A. I. Aria and M. Gharib. Physicochemical characteristics and droplet impact dynamics of superhydrophobic carbon nanotube arrays. *Langmuir*, 30(23):6780–6790, 2014.
- [127] Y. Renardy, S. Popinet, L. Duchemin, M. Renardy, S. Zaleski, C. Josserand, M. A. Drumright-Clarke, D. Richard, C. Clanet, D. Quéré, and et al. Pyramidal and toroidal water drops after impact on a solid surface. *Journal of Fluid Mechanics*, 484:69–83, 2003.
- [128] M. C. T. Wilson, J. L. Summers, Y. D. Shikhmurzaev, A. Clarke, and T. D. Blake. Nonlocal hydrodynamic influence on the dynamic contact angle: Slip models versus experiment. *Phys. Rev. E*, 73:041606, Apr 2006.
- [129] G. McHale, N. J. Shirtcliffe, and M. I. Newton. Contact-angle hysteresis on super-hydrophobic surfaces. *Langmuir*, 20(23):10146–10149, 2004.

- [130] R. Aris. *Vectors, tensors and the basic equations of fluid mechanics*. Courier Corporation, 2012.
- [131] J. Padrino Inciarte. Topics in viscous potential flow of two-phase systems. 2010.
- [132] J. P. Rothstein. Slip on superhydrophobic surfaces. *Annual Review of Fluid Mechanics*, 42:89–109, 2010.
- [133] G. K. Batchelor. *An Introduction to Fluid Dynamics*. Cambridge University Press, 1967.
- [134] Y. D. Shikhmurzaev. *Capillary flows with forming interfaces*. Chapman & Hall/CRC, 2008.
- [135] D. A. Edwards, H. Brenner, and D. T. Wasan. *Interfacial Transport Processes and Rheology*. Butterworth-Heinemann, 1991.
- [136] L. Botto et al. Stretching of a capillary bridge featuring a particle-laden interface: particle sedimentation in the interface. 2014.
- [137] C. Gu and L. Botto. Fipi: A fast numerical method for the simulation of particle-laden fluid interfaces. *Computer Physics Communications*, 256:107447, 2020.
- [138] G. S. Beavers and D. D. Joseph. Boundary conditions at a naturally permeable wall. *Journal of Fluid Mechanics*, 30(1):197–207, 1967.
- [139] Lord Rayleigh. On the Stability, or Instability, of certain Fluid Motions. *Proceedings of the London Mathematical Society*, s1-11(1):57–72, 11 1879.
- [140] H. Lamb. *Hydrodynamics*. Dover Books on Physics. Dover publications, 1945.
- [141] H. Weber and G. B. Arfken. *Mathematical methods for physicists*. Elsevier Academic, 2005.
- [142] G. R. Fowles, G. L. Cassiday, et al. *Analytical mechanics*. Belmont, CA: Thomson Brooks/Cole,, 2005.
- [143] A. H. Nayfeh, D. T. Mook, and P. Holmes. *Nonlinear oscillations*. 1980.

- [144] R. Natarajan and R. A. Brown. Quadratic resonance in the three-dimensional oscillations of inviscid drops with surface tension. *The Physics of fluids*, 29(9):2788–2797, 1986.
- [145] R. Natarajan and R. A. Brown. Third-order resonance effects and the nonlinear stability of drop oscillations. *Journal of Fluid Mechanics*, 183:95–121, 1987.
- [146] C. Pozrikidis. *A Practical Guide to Boundary Element Methods with the Software Library BEMLIB*. Chapman & Hall/CRC, 2002.
- [147] J. Rodríguez-Rodríguez, J. M. Gordillo, and C. Martínez-Bazán. Breakup time and morphology of drops and bubbles in a high-reynolds-number flow. *Journal of Fluid Mechanics*, 548:69–86, 2006.
- [148] M. R. Davidson. Boundary integral prediction of the spreading of an inviscid drop impacting on a solid surface. *Chemical Engineering Science*, 55(6):1159 – 1170, 2000.
- [149] M. R. Davidson. Spreading of an inviscid drop impacting on a liquid film. *Chemical Engineering Science*, 57(17):3639 – 3647, 2002.
- [150] W. A. Strauss. *Partial differential equations*. John Wiley & Sons New York, NY, USA, 1992.
- [151] H. L. Lebesgue. *Measure and the Integral*. Holden-Day, 1966.
- [152] S. Georgescu, J. Achard, and É Canot. Jet drops ejection in bursting gas bubble processes. *European Journal of Mechanics - B/Fluids*, 21(2):265 – 280, 2002.
- [153] E. Canot, L. Davoust, M. El Hammoumi, and D. Lachkar. Numerical simulation of the buoyancy-driven bouncing of a 2-d bubble at a horizontal wall. *Theoretical and computational fluid dynamics*, 17(1):51–72, 2003.
- [154] B. H. Bang, S. S. Yoon, H. Kim, S. D. Heister, H. Park, and S. C. James. Assessment of gas and liquid velocities induced by an impacting liquid drop. *International journal of multiphase flow*, 37(1):55–66, 2011.
- [155] A. Dadvand, B. Khoo, M. T. Shervani-Tabar, and S. Khalilpourazary. Boundary element analysis of the droplet dynamics induced by spark-generated bubble. *Engineering analysis with boundary elements*, 36(11):1595–1603, 2012.

- [156] M. Abramowitz and I. A. Stegun. *Handbook of Mathematical Functions with Functions, Graphs, and Mathematical Tables*. Dover Publications, Incorporated, 1974.
- [157] Q. Sun, E. Klaseboer, B. Khoo, and D. Y. C. Chan. Boundary regularized integral equation formulation of the helmholtz equation in acoustics. *Royal Society open science*, 2(1):140520, 2015.
- [158] A. Quarteroni, R. Sacco, and F. Saleri. *Numerical Mathematics*. Springer-Verlag Berlin Heidelberg, 2007.
- [159] D. Leppinen and J. R. Lister. Capillary pinch-off in inviscid fluids. *Physics of Fluids*, 15(2):568–578, 2003.
- [160] C. A. Spangler, J. H. Hilbing, and S. D. Heister. Nonlinear modeling of jet atomization in the wind-induced regime. *Physics of Fluids*, 7(5):964–971, 1995.
- [161] B. M. Rush and A. Nadim. The shape oscillations of a two-dimensional drop including viscous effects. pages 43–51, 2000.
- [162] T. S. Lundgren and N. N. Mansour. Oscillations of drops in zero gravity with weak viscous effects. *Journal of Fluid Mechanics*, 194:479–510, 1988.
- [163] R. Courant, K. Friedrichs, and H. Lewy. On the partial difference equations of mathematical physics. *Mathematische Annalen*, 100, 1928.
- [164] E. R. Setiawan and S. D. Heister. Nonlinear modeling of an infinite electrified jet. *Journal of Electrostatics*, 42(3):243 – 257, 1997.
- [165] H. N. Oğuz and A. Prosperetti. Bubble entrainment by the impact of drops on liquid surfaces. *Journal of Fluid Mechanics*, 219:143–179, 1990.
- [166] W. L. Wendland. *Boundary Element Methods and Their Asymptotic Convergence*. In: *Theoretical Acoustics and Numerical Techniques*, volume 277. Springer, Vienna, 1983.
- [167] A. W. Knapp. *Basic real analysis*. Springer Science & Business Media, 2005.
- [168] D. C. Vadillo, A. Soucemarianadin, C. Delattre, and D. C. D. Roux. Dynamic contact angle effects onto the maximum drop impact spreading on solid surfaces. *Physics of Fluids*, 21(12):122002, 2009.

- [169] J. H. Hilbing and S. D. Heister. Droplet size control in liquid jet breakup. *Physics of Fluids*, 8(6):1574–1581, 1996.
- [170] N. N. Mansour and T. S. Lundgren. Satellite formation in capillary jet breakup. *Physics of Fluids A: Fluid Dynamics*, 2(7):1141–1144, 1990.
- [171] R. M. S. M. Schulkes. The evolution and bifurcation of a pendant drop. *Journal of Fluid Mechanics*, 278:83–100, 1994.
- [172] Maria Garzon, Leonard J Gray, and James A Sethian. Numerical simulation of non-viscous liquid pinch-off using a coupled level set-boundary integral method. *Journal of Computational Physics*, 228(17):6079–6106, 2009.
- [173] L. Chen, L. Li, Z. Li, and K. Zhang. Submillimeter-sized bubble entrapment and a high-speed jet emission during droplet impact on solid surfaces. *Langmuir*, 33(29):7225–7230, 2017.
- [174] E. S. Quintero, G. Riboux, and J. M. Gordillo. Splashing of droplets impacting superhydrophobic substrates. *Journal of Fluid Mechanics*, 870:175–188, 2019.
- [175] P. Tsai, S. Pacheco, C. Pirat, L. Lefferts, and D. Lohse. Drop impact upon micro-and nanostructured superhydrophobic surfaces. *Langmuir*, 25(20):12293–12298, 2009.
- [176] M. Reyssat, A. Pépin, F. Marty, Y. Chen, and D. Quéré. Bouncing transitions on microtextured materials. *EPL (Europhysics Letters)*, 74(2):306, 2006.
- [177] S. Popinet. Basilisk flow solver and software library. <http://basilisk.fr/>.
- [178] G. Tryggvason, R. Scardovelli, and S. Zaleski. *Direct Numerical Simulations of Gas-Liquid Multiphase Flows*. Cambridge University Press, 2011.
- [179] R. Scardovelli and S. Zaleski. Direct numerical simulation of free-surface and interfacial flow. *Annual review of fluid mechanics*, 31(1):567–603, 1999.
- [180] A. Prosperetti and G. Tryggvason. *Computational methods for multiphase flow*. Cambridge university press, 2009.
- [181] S. Popinet. Gerris flow solver and software library. <http://gfs.sourceforge.net/>.

- [182] S. Popinet. An accurate adaptive solver for surface-tension-driven interfacial flows. *Journal of Computational Physics*, 228(16):5838–5866, 2009.
- [183] S. Popinet. Gerris: a tree-based adaptive solver for the incompressible euler equations in complex geometries. *Journal of Computational Physics*, 190(2):572–600, 2003.
- [184] P. Lagrée, L. Staron, and S. Popinet. The granular column collapse as a continuum: validity of a two-dimensional navier-stokes model with a $\mu(i)$ -rheology. *Journal of Fluid Mechanics*, 686:378, 2011.
- [185] J. B. Bell, P. Colella, and H. M. Glaz. A second-order projection method for the incompressible navier-stokes equations. *Journal of Computational Physics*, 85(2):257 – 283, 1989.
- [186] D. B. van Dam and C. Le Clerc. Experimental study of the impact of an ink-jet printed droplet on a solid substrate. *Physics of Fluids*, 16(9):3403–3414, 2004.
- [187] Y. Yao, C. Li, H. Zhang, and R. Yang. Modelling the impact, spreading and freezing of a water droplet on horizontal and inclined superhydrophobic cooled surfaces. *Applied Surface Science*, 419:52 – 62, 2017.
- [188] J. Qu, Y. Yang, S. Yang, D. Hu, and H. Qiu. Droplet impingement on nano-textured superhydrophobic surface: Experimental and numerical study. *Applied Surface Science*, 491:160 – 170, 2019.
- [189] D. Richard, C. Clanet, and D. Quéré. Contact time of a bouncing drop. *Nature*, 417:811, 2002.
- [190] C. Antonini, A. Amirfazli, and M. Marengo. Drop impact and wettability: From hydrophilic to superhydrophobic surfaces. *Physics of fluids*, 24(10):102–104, 2012.
- [191] C. Lv, P. Hao, X. Zhang, and F. He. Drop impact upon superhydrophobic surfaces with regular and hierarchical roughness. *Applied Physics Letters*, 108(14):141602, 2016.
- [192] C. Clanet, C. Béguin, D. Richard, and D. Quéré. Maximal deformation of an impacting drop. *Journal of Fluid Mechanics*, 517:199, 2004.

- [193] A. Biance, F. Chevy, C. Clanet, G. Lagubeau, and D. Quéré. On the elasticity of an inertial liquid shock. *Journal of Fluid Mechanics*, 554:47, 2006.
- [194] V. Bertola. An experimental study of bouncing leidenfrost drops: comparison between newtonian and viscoelastic liquids. *International journal of heat and mass transfer*, 52(7-8):1786–1793, 2009.
- [195] C. Morel. On the surface equations in two-phase flows and reacting single-phase flows. *International Journal of Multiphase Flow*, 33(10):1045–1073, 2007.
- [196] J. T. Katsikadelis. *The boundary element method for engineers and scientists: theory and applications*. Academic Press, 2016.
- [197] R. A. Białeccki, M. Merkel, H. Mews, and G. Kuhn. In-and out-of-core bem equation solver with parallel and non-linear options. *International journal for numerical methods in engineering*, 39(24):4215–4242, 1996.

Appendix A

Derivation of the Surface Divergence Operator in Axisymmetric Coordinates

Consider a three dimensional space and let (r, θ, z) denote cylindrical coordinates centred on an origin \mathcal{O} within the space. Consider an axisymmetric surface \mathcal{S} embedded in this space that can be decomposed via two orthogonal curvilinear coordinates $\underline{\mathbf{t}}$ and $\underline{\theta}$, where $\underline{\theta}$ is the azimuthal angle from the cylindrical coordinate system described above and $\underline{\mathbf{t}}$ is the tangent vector to the surface orthogonal to the $\underline{\theta}$ -axis and is parametrised by the arclength s across the surface for constant θ . The full divergence operator is given by

$$\nabla \equiv \underline{\mathbf{e}}_r \frac{\partial}{\partial r} + \frac{\underline{\mathbf{e}}_\theta}{r} \frac{\partial}{\partial \theta} + \underline{\mathbf{e}}_z \frac{\partial}{\partial z}. \quad (\text{A.0.1})$$

The surface divergence operator is given by

$$\nabla_s \equiv (\underline{\mathbf{I}} - \underline{\mathbf{nn}}) \cdot \nabla = (\underline{\mathbf{tt}} + \underline{\mathbf{e}}_\theta \underline{\mathbf{e}}_\theta) \cdot \nabla, \quad (\text{A.0.2})$$

and hence

$$\begin{aligned} \nabla_s &= \underline{\mathbf{tt}} \cdot \underline{\mathbf{e}}_r \frac{\partial}{\partial r} + \frac{\underline{\mathbf{tt}} \cdot \underline{\mathbf{e}}_\theta}{r} \frac{\partial}{\partial \theta} + \underline{\mathbf{tt}} \cdot \underline{\mathbf{e}}_z \frac{\partial}{\partial z} + \underline{\mathbf{e}}_\theta \underline{\mathbf{e}}_\theta \cdot \underline{\mathbf{e}}_r \frac{\partial}{\partial r} + \frac{\underline{\mathbf{e}}_\theta \underline{\mathbf{e}}_\theta \cdot \underline{\mathbf{e}}_\theta}{r} \frac{\partial}{\partial \theta} + \underline{\mathbf{e}}_\theta \underline{\mathbf{e}}_\theta \cdot \underline{\mathbf{e}}_z \frac{\partial}{\partial z} \\ &= \underline{\mathbf{tt}} \cdot \underline{\mathbf{e}}_r \frac{\partial}{\partial r} + \underline{\mathbf{tt}} \cdot \underline{\mathbf{e}}_z \frac{\partial}{\partial z} + \frac{\underline{\mathbf{e}}_\theta \underline{\mathbf{e}}_\theta \cdot \underline{\mathbf{e}}_\theta}{r} \frac{\partial}{\partial \theta} \\ &= \underline{\mathbf{t}} \frac{\partial}{\partial s} + \underline{\mathbf{e}}_\theta \frac{1}{r} \frac{\partial}{\partial \theta}, \end{aligned} \quad (\text{A.0.3})$$

where $\underline{\mathbf{e}}_r, \underline{\mathbf{e}}_\theta, \underline{\mathbf{e}}_z$ are mutually orthogonal and $\partial/\partial s \equiv \underline{\mathbf{t}} \cdot \underline{\mathbf{e}}_r \partial/\partial r + \underline{\mathbf{t}} \cdot \underline{\mathbf{e}}_z \partial/\partial z$. Consider an axisymmetric vector field $\underline{\mathbf{a}} \equiv a_t \underline{\mathbf{t}} + a_n \underline{\mathbf{n}}$ and note that $\underline{\mathbf{t}} \cdot \partial \underline{\mathbf{t}} / \partial s = 0$, $\partial \underline{\mathbf{e}}_r / \partial \theta = \underline{\mathbf{e}}_\theta$

and $\underline{\mathbf{n}} \cdot \nabla_s b = 0$ for any b . The surface divergence of this field is

$$\begin{aligned}
\nabla_s \cdot \underline{\mathbf{a}} &= \nabla_s \cdot (a_t \underline{\mathbf{t}} + a_n \underline{\mathbf{n}}) \\
&= a_t \nabla_s \cdot \underline{\mathbf{t}} + \underline{\mathbf{t}} \cdot \nabla_s a_t + a_n \nabla_s \cdot \underline{\mathbf{n}} + \underline{\mathbf{n}} \cdot \nabla_s a_n \\
&= a_t \left[\underline{\mathbf{t}} \cdot \frac{\partial \underline{\mathbf{t}}}{\partial s} + \frac{\underline{\mathbf{e}}_\theta}{r} \cdot \frac{\partial \underline{\mathbf{t}}}{\partial \theta} \right] + \underline{\mathbf{t}} \cdot \left[\underline{\mathbf{t}} \frac{\partial a_t}{\partial s} + \frac{\underline{\mathbf{e}}_\theta}{r} \frac{\partial a_t}{\partial \theta} \right] + a_n \nabla_s \cdot \underline{\mathbf{n}} \\
&= a_t \left[\frac{\underline{\mathbf{e}}_\theta}{r} \cdot \left(t_r \frac{\partial \underline{\mathbf{e}}_r}{\partial \theta} + t_z \frac{\partial \underline{\mathbf{e}}_z}{\partial \theta} \right) \right] + \frac{\partial a_t}{\partial s} + a_n \nabla_s \cdot \underline{\mathbf{n}} \\
&= a_t \left[\frac{t_r}{r} \underline{\mathbf{e}}_\theta \cdot \underline{\mathbf{e}}_\theta \right] + \frac{\partial a_t}{\partial s} + a_n \nabla_s \cdot \underline{\mathbf{n}} \\
&= \frac{\partial a_t}{\partial s} + \frac{a_t t_r}{r} + a_n \nabla_s \cdot \underline{\mathbf{n}}.
\end{aligned} \tag{A.0.4}$$

Appendix B

Proof of Surface Area

Conservation from Zero Surface

Divergence of Surface Velocity

Consider a surface \mathcal{S} with outward-pointing unit normal $\underline{\mathbf{n}}$, with a closed boundary curve \mathcal{C} with its own outward-pointing unit normal ν . Let $\underline{\mathbf{v}}^s$ denote the velocity of the surface \mathcal{S} , which we can express as

$$\underline{\mathbf{v}}^s = \underline{\mathbf{v}}_{\parallel}^s + (\underline{\mathbf{v}}^s \cdot \underline{\mathbf{n}}) \underline{\mathbf{n}}, \quad (\text{B.0.1})$$

so that its components are separated into those tangential to and normal to the surface \mathcal{S} , respectively, where $\underline{\mathbf{v}}_{\parallel}^s = \underline{\mathbf{v}}^s - (\underline{\mathbf{v}}^s \cdot \underline{\mathbf{n}}) \underline{\mathbf{n}}$. Taking the surface divergence of $\underline{\mathbf{v}}^s$, particularly of the representation in (B.0.1), we obtain

$$\begin{aligned} \nabla_s \cdot \underline{\mathbf{v}}^s &= \nabla_s \cdot \underline{\mathbf{v}}_{\parallel}^s + \underline{\mathbf{n}} \cdot \nabla_s (\underline{\mathbf{v}}^s \cdot \underline{\mathbf{n}}) + (\underline{\mathbf{v}}^s \cdot \underline{\mathbf{n}}) (\nabla_s \cdot \underline{\mathbf{n}}), \\ &= \nabla_s \cdot \underline{\mathbf{v}}_{\parallel}^s + (\underline{\mathbf{v}}^s \cdot \underline{\mathbf{n}}) (\nabla_s \cdot \underline{\mathbf{n}}), \end{aligned} \quad (\text{B.0.2})$$

where $\underline{\mathbf{n}} \cdot \nabla_s = \underline{\mathbf{n}} \cdot (\underline{\mathbf{I}} - \underline{\mathbf{nn}}) \cdot \nabla = n_i (\delta_{ij} - n_i n_j) \partial_j = n_i \partial_i - n_j \partial_j = \underline{\mathbf{n}} \cdot \nabla - \underline{\mathbf{n}} \cdot \nabla = 0$.

For a function f defined at the surface \mathcal{S} , the Reynolds transport theorem applied to \mathcal{S} states that [195]:

$$\frac{d}{dt} \int_{\mathcal{S}} f \, dA = \int_{\mathcal{S}} \left(\frac{\partial}{\partial t} f + f (\underline{\mathbf{v}}^s \cdot \underline{\mathbf{n}}) (\nabla \cdot \underline{\mathbf{n}}) \right) dA + \int_{\mathcal{C}} f \underline{\mathbf{v}}_{\parallel}^s \cdot \nu \, dC, \quad (\text{B.0.3})$$

where dA is an area element on \mathcal{S} , and dC is a line element on \mathcal{C} . Setting $f = 1$, we then obtain

$$\frac{d}{dt} \int_{\mathcal{S}} 1 \, dA = \int_{\mathcal{S}} (\underline{\mathbf{v}}^s \cdot \underline{\mathbf{n}}) (\nabla \cdot \underline{\mathbf{n}}) \, dA + \int_{\mathcal{C}} \underline{\mathbf{v}}_{\parallel}^s \cdot \nu \, dC. \quad (\text{B.0.4})$$

By the divergence theorem, the line integral on the right hand side of (B.0.4) can be expressed as an area integral over \mathcal{S} , namely:

$$\int_{\mathcal{S}} \nabla \cdot \underline{\mathbf{v}}_{\parallel}^s \, dA = \int_{\mathcal{C}} \underline{\mathbf{v}}_{\parallel}^s \cdot \nu \, dC, \quad (\text{B.0.5})$$

hence (B.0.4) can be rewritten as

$$\frac{d}{dt} \int_{\mathcal{S}} 1 \, dA = \int_{\mathcal{S}} [\nabla \cdot \underline{\mathbf{v}}_{\parallel}^s + (\underline{\mathbf{v}}^s \cdot \underline{\mathbf{n}}) (\nabla \cdot \underline{\mathbf{n}})] \, dA. \quad (\text{B.0.6})$$

For quantities defined only on the surface \mathcal{S} (such as $\underline{\mathbf{v}}^s$ and $\underline{\mathbf{n}}$), note that the divergence operator ∇ and surface divergence operator ∇_s are equivalent, so (B.0.6) can be rewritten as

$$\frac{d}{dt} \int_{\mathcal{S}} 1 \, dA = \int_{\mathcal{S}} [\nabla_s \cdot \underline{\mathbf{v}}_{\parallel}^s + (\underline{\mathbf{v}}^s \cdot \underline{\mathbf{n}}) (\nabla_s \cdot \underline{\mathbf{n}})] \, dA. \quad (\text{B.0.7})$$

Finally, we combine (B.0.2) with (B.0.7) to see that

$$\frac{d}{dt} \int_{\mathcal{S}} 1 \, dA = \int_{\mathcal{S}} \nabla_s \cdot \underline{\mathbf{v}}^s \, dA, \quad (\text{B.0.8})$$

and so $\nabla_s \cdot \underline{\mathbf{v}}^s = 0$ in \mathcal{S} means that the surface area of \mathcal{S} is constant in time.

Appendix C

Axisymmetric Kernels for the Boundary Integral Equation

Consider the following solution of Laplace's equation in three-dimensions:

$$G(\underline{\mathbf{x}}, \underline{\mathbf{x}}_0) = \frac{1}{4\pi|\underline{\mathbf{x}} - \underline{\mathbf{x}}_0|} \quad \text{for } \underline{\mathbf{x}} \in \Omega - \{\underline{\mathbf{x}}_0\} \quad (\text{C.0.1})$$

where $\underline{\mathbf{x}} = x\underline{\mathbf{e}}_x + y\underline{\mathbf{e}}_y + z\underline{\mathbf{e}}_z$ and $\underline{\mathbf{x}}_0 = x_0\underline{\mathbf{e}}_x + y_0\underline{\mathbf{e}}_y + z_0\underline{\mathbf{e}}_z$. For convenience, define

$$\begin{aligned} D &= |\underline{\mathbf{x}} - \underline{\mathbf{x}}_0|^2 \\ &= (x - x_0)^2 + (y - y_0)^2 + (z - z_0)^2 \end{aligned} \quad (\text{C.0.2})$$

Moving to cylindrical coordinates (r, θ, z) , we have $x = r \cos \theta$, $x_0 = r_0 \cos \theta_0$, $y = r \sin \theta$, $y_0 = r_0 \sin \theta_0$ and without loss of generality we take $\theta_0 = 0$ due to assumed axisymmetry of the domain. So,

$$\begin{aligned} D &= (r \cos \theta - r_0)^2 + r^2 \sin^2 \theta + (z - z_0)^2 \\ &= r^2 + r_0^2 + (z - z_0)^2 - 2rr_0 \cos \theta \\ &= (r + r_0)^2 + (z - z_0)^2 - 2rr_0 (1 + \cos \theta) \\ &= (r + r_0)^2 + (z - z_0)^2 - 4rr_0 \cos^2 u, \end{aligned} \quad (\text{C.0.3})$$

with $u = \theta/2$. Taking the partial derivative of (C.0.1) with respect to some variable, a say, gives

$$\frac{\partial G}{\partial a} = \frac{1}{4\pi} \cdot \frac{-1}{2} \cdot D^{-3/2} \cdot \frac{\partial D}{\partial a} = -\frac{1}{8\pi D^{3/2}} \frac{\partial D}{\partial a}. \quad (\text{C.0.4})$$

The requisite derivatives for the gradient are therefore

$$\frac{\partial G}{\partial r} = -\frac{1}{8\pi D^{3/2}} [2(r + r_0) - 4r_0 \cos^2 u] = -\frac{1}{4\pi D^{3/2}} [r + r_0 - 2r_0 \cos^2 u], \quad (\text{C.0.5})$$

and

$$\frac{\partial G}{\partial \theta} = \frac{1}{2} \frac{\partial G}{\partial u} = -\frac{1}{16\pi D^{3/2}} [4rr_0 \sin(2u)] = -\frac{1}{4\pi D^{3/2}} [rr_0 \sin(2u)], \quad (\text{C.0.6})$$

and

$$\frac{\partial G}{\partial z} = -\frac{1}{8\pi D^{3/2}} [2(z - z_0)] = -\frac{1}{4\pi D^{3/2}} [z - z_0], \quad (\text{C.0.7})$$

which provide the gradient

$$\nabla G = \frac{\partial G}{\partial r} \mathbf{e}_r + \frac{1}{r} \frac{\partial G}{\partial \theta} \mathbf{e}_\theta + \frac{\partial G}{\partial z} \mathbf{e}_z. \quad (\text{C.0.8})$$

The normal derivative of G is therefore given by

$$\frac{\partial G}{\partial n} = -\frac{1}{4\pi D^{3/2}} [n_r (r + r_0) + n_z (z - z_0) - 2n_r r_0 \cos^2 u + n_\theta r_0 \sin(2u)]. \quad (\text{C.0.9})$$

The following three terms are defined for convenience,

$$A = (r + r_0)^2 + (z - z_0)^2, \quad (\text{C.0.10})$$

$$B = (r - r_0)^2 + (z - z_0)^2, \quad (\text{C.0.11})$$

$$m = \frac{4rr_0}{A}, \quad (\text{C.0.12})$$

noting that $D = A[1 - m \cos^2 u]$ and $B/A = 1 - m$. Further, note that A , B , and m are independent of θ . To obtain the axisymmetric integration kernels, we integrate the normal derivative of G through θ . We do this here:

$$\begin{aligned} \int_0^{2\pi} \frac{\partial G}{\partial n} d\theta &= 2 \int_0^\pi \frac{\partial G}{\partial n} du \\ &= \frac{-1}{2\pi A^{3/2}} \left\{ [n_r (r + r_0) + n_z (z - z_0)] \int_0^\pi \frac{1}{(\sqrt{1 - m \cos^2 u})^3} du \right\} \\ &\quad + \frac{-1}{2\pi A^{3/2}} \left\{ -2n_r r_0 \int_0^\pi \frac{\cos^2 u}{(\sqrt{1 - m \cos^2 u})^3} du \right\} \\ &\quad + \frac{-1}{2\pi A^{3/2}} \left\{ r_0 \int_0^\pi \frac{n_\theta \sin(2u)}{(\sqrt{1 - m \cos^2 u})^3} du \right\}. \end{aligned} \quad (\text{C.0.13})$$

The third integral in the above equation is zero due to the periodicity of the sin function over the range of integration. For the first two integrals, we introduce the definitions of complete elliptic integrals of the first, second, and third kinds respectively:

$$K(m) = \frac{1}{2} \int_0^\pi \frac{1}{\sqrt{1 - m \cos^2 t}} dt, \quad (\text{C.0.14})$$

$$E(m) = \frac{1}{2} \int_0^\pi \sqrt{1 - m \cos^2 t} dt, \quad (\text{C.0.15})$$

and

$$\Pi(m, m) = \frac{1}{2} \int_0^\pi \frac{1}{(\sqrt{1 - m \cos^2 t})^3} dt, \quad (\text{C.0.16})$$

for $m \in (0, 1)$. Two useful identities are

$$\Pi(m, m) = \frac{E(m)}{1 - m}, \quad (\text{C.0.17})$$

and

$$\frac{1}{2} \int_0^\pi \frac{\cos^2 t}{(\sqrt{1 - m \cos^2 t})^3} dt = \frac{\Pi(m, m) - K(m)}{m}. \quad (\text{C.0.18})$$

The complete elliptic integrals $K(m)$ and $E(m)$ can be well approximated using polynomials so writing the integration kernels in terms of these allows for good numerical approximation. We therefore have

$$\begin{aligned} \int_0^{2\pi} \frac{\partial G}{\partial n} d\theta &= -\frac{n_r(r + r_0) + n_z(z - z_0)}{\pi A^{3/2}(1 - m)} E(m) + \frac{2n_r r_0}{\pi A^{3/2}} \frac{\Pi(m, m) - K(m)}{m} \\ &= -\frac{n_r(r + r_0) + n_z(z - z_0)}{\pi A^{1/2} B} E(m) + \frac{n_r}{2\pi r A^{1/2}} \left[\frac{E(m)}{1 - m} - K(m) \right] \\ &= \frac{1}{\pi A^{1/2}} E(m) \left[\frac{n_r}{2r} \cdot \frac{1}{1 - m} - \frac{n_r(r + r_0) + n_z(z - z_0)}{B} \right] - \frac{n_r}{2\pi r A^{1/2}} K(m). \end{aligned} \quad (\text{C.0.19})$$

For aesthetics, we seek b such that

$$\frac{n_r}{2r} \cdot \frac{1}{1 - m} = \frac{n_r}{2r} + b, \quad (\text{C.0.20})$$

which gives

$$\begin{aligned} b &= \frac{n_r}{2r} \cdot \left(\frac{1}{1 - m} - 1 \right) \\ &= \frac{n_r}{2r} \cdot \frac{m}{1 - m} = \frac{n_r}{2r} \cdot \frac{4rr_0}{B} = \frac{2n_r r_0}{B}. \end{aligned} \quad (\text{C.0.21})$$

Hence,

$$\int_0^{2\pi} \frac{\partial G}{\partial n} d\theta = \frac{1}{\pi A^{1/2}} E(m) \left[\frac{n_r}{2r} - \frac{n_r(r - r_0) + n_z(z - z_0)}{B} \right] - \frac{n_r}{2\pi r A^{1/2}} K(m). \quad (\text{C.0.22})$$

The other integration kernel is given by

$$\int_0^{2\pi} G d\theta = 2 \int_0^\pi G du = \frac{1}{2\pi A^{1/2}} \left\{ \int_0^\pi \frac{1}{\sqrt{1 - m \cos^2 u}} du \right\} = \frac{1}{\pi A^{1/2}} K(m). \quad (\text{C.0.23})$$

Appendix D

Computation of Spline Coefficients

Consider the interval $l_1 \leq l \leq l_{N+1}$ and let

$$l_1 < l_2 < \cdots < l_N < l_{N+1} \quad (\text{D.0.1})$$

be a partition of the original interval into N distinct subintervals. For each l_j , prescribe a coordinate $y_j \in \mathbb{R}$, where $j = 1, \dots, N+1$. We wish to interpolate the function y in the interval $l_1 \leq l \leq l_{N+1}$, where y_j are the function values at the subinterval endpoints l_j . Define

$$h_j := l_{j+1} - l_j, \quad (\text{D.0.2})$$

for $j = 1, \dots, N$ and

$$\lambda_k := \frac{h_{k+1}}{h_k}, \quad (\text{D.0.3})$$

for $k = 1, \dots, N-1$. We seek a collection of piecewise polynomials of degree $M \in \{3, 5\}$

$$S^{(j)}(l) := y_j + \sum_{m=1}^M a_m^{(j)}(l - l_j)^m, \quad (\text{D.0.4})$$

such that $S^{(j)}(l)$ interpolates y in the subinterval $l_j \leq l \leq l_{j+1}$, for $j = 1, \dots, N$. Trivially, each of these interpolating functions, or ‘splines’, takes the value of the function y when evaluated at the endpoints of the partition subintervals, that is,

$$S^{(j)}(l_j) = y_j, \quad (\text{D.0.5})$$

for $j = 1, \dots, N$. The splines are continuous across the interior subinterval endpoints,

$$S^{(j-1)}(l_j) = S^{(j)}(l_j) \quad (\text{D.0.6})$$

for $j = 2, \dots, N$, and the final spline evaluated at the endpoint of the original interval returns the final function value, that is,

$$S^{(N)}(l_{N+1}) = y_{N+1}. \quad (\text{D.0.7})$$

Moreover, the splines have continuous derivatives up to order $M-1$ across the interior points,

$$\frac{d^p S^{(j-1)}}{dl^p}(l_j) = \frac{d^p S^{(j)}}{dl^p}(l_j), \quad (\text{D.0.8})$$

for $j = 2, \dots, N$ and $p = 1, \dots, M-1$. The polynomial coefficients $a_m^{(j)}$ are determined uniquely by solving the continuity equations (D.0.6), (D.0.7), and (D.0.8), along with end conditions imposed at interval endpoints l_1 and l_{N+1} . When $M = 3$, the system of interpolating splines are referred to as ‘cubic splines’, and for $M = 5$, they are ‘quintic splines’. The remainder of this appendix details the calculations of these polynomial coefficients for cubic and quintic splines, with so-called ‘clamped-end’ conditions, which are those that specify the values for the derivatives of the splines at the original interval endpoints and are commonly used in axisymmetric BEMs [146].

D.1 Cubic Splines

For convenience, change the notation for the polynomial coefficients from $\{a_3^{(j)}, a_2^{(j)}, a_1^{(j)}\}$ to $\{a_j, b_j, c_j\}$. Cubic splines are then given by

$$S^{(j-1)}(l) = y_{j-1} + c_{j-1}(l - l_{j-1}) + b_{j-1}(l - l_{j-1})^2 + a_{j-1}(l - l_{j-1})^3, \quad (\text{D.1.1})$$

for $j = 2, \dots, N$.

D.1.1 Continuity at Interior Nodes

We rewrite the spline continuity equations (D.0.6), (D.0.7), and (D.0.8) in the form of (D.1.1). As such, we have the equations

$$y_{j-1} + c_{j-1}h_{j-1} + b_{j-1}h_{j-1}^2 + a_{j-1}h_{j-1}^3 = y_j, \quad (\text{D.1.2})$$

for continuity of position with $j = 2, \dots, N+1$,

$$c_{j-1} + 2b_{j-1}h_{j-1} + 3a_{j-1}h_{j-1}^2 = c_j, \quad (\text{D.1.3})$$

for continuity of the first derivative with $j = 2, \dots, N$, and

$$2b_{j-1} + 6a_{j-1}h_{j-1} = 2b_j, \quad (\text{D.1.4})$$

for continuity of the second derivative with $j = 2, \dots, N$.

D.1.2 Generating the Matrix Equation

Solving the system of equations (D.1.2) and (D.1.3) for a_{j-1} and b_{j-1} gives

$$a_{j-1}h_{j-1}^3 = -2(y_j - y_{j-1}) + c_j h_{j-1} + c_{j-1} h_{j-1}, \quad (\text{D.1.5})$$

and

$$b_{j-1}h_{j-1}^2 = 3(y_j - y_{j-1}) - c_j h_{j-1} - 2c_{j-1} h_{j-1}, \quad (\text{D.1.6})$$

for $j = 2, \dots, N$. Substitution (D.1.5) and (D.1.6) into (D.1.4) yields

$$\begin{aligned} c_{j-1} [\lambda_{j-1}^2 h_{j-1}] + c_j [2\lambda_{j-1}^2 h_{j-1} + 2h_j] + c_{j+1} [h_j] \\ = y_{j-1} [-3\lambda_{j-1}^2] + y_j [3\lambda_{j-1}^2 - 3] + y_{j+1} [3], \end{aligned} \quad (\text{D.1.7})$$

for $j = 2, \dots, N - 1$. We suppose the existence of a ‘ghost’ interval $l_{N+1} \leq l \leq l_{N+2}$ so that the continuity equations (D.1.3) and (D.1.4) hold for $j = 2, \dots, N + 1$. This means that equation (D.1.7) will now hold for $j = 2, \dots, N$, which enables it to be rewritten into the following matrix form

$$\underline{\underline{\mathbf{A}}} \cdot \underline{\mathbf{c}} = \underline{\mathbf{p}} + \underline{\hat{\mathbf{c}}}, \quad (\text{D.1.8})$$

where

$$\underline{\underline{\mathbf{A}}}_{i,j} = \begin{cases} \lambda_{j-1}^2 h_{j-1} & , j = i - 1 \text{ and } j \neq 2 \\ 2\lambda_{j-1}^2 h_{j-1} + 2h_j & , j = i \\ h_j & , j = i + 1 \text{ and } j \neq N \\ 0 & , \text{ otherwise,} \end{cases} \quad (\text{D.1.9})$$

for $i = 2, \dots, N$,

$$\underline{\mathbf{p}}_j = \{-3y_{j-1}\lambda_{j-1}^2 + y_j(3\lambda_{j-1}^2 - 3) + 3y_{j+1}, j = 2, \dots, N, \quad (\text{D.1.10})$$

and $\underline{\mathbf{c}} = (c_2, c_3, \dots, c_{N-1}, c_N)$, $\underline{\hat{\mathbf{c}}} = (-\lambda_1^2 h_1 c_1, 0, \dots, 0, -h_N c_{N+1})$.

We want to solve this system for the vector of unknowns, $\underline{\mathbf{c}}$. The matrix $\underline{\underline{\mathbf{A}}}$ is dependent only on the values of l_j , $j = 1, \dots, N + 1$, so is known. The vector $\underline{\mathbf{p}}$ depends on l_j and y_j , $j = 1, \dots, N + 1$, so is also known. The values for c_1 and c_{N+1} are imposed by the choice of end conditions for this system of splines.

D.1.3 End Conditions

Consider the end conditions

$$\frac{dS^{(1)}}{dl}(l_1) = 0, \quad \frac{dS^{(N)}}{dl}(l_{N+1}) = 0, \quad (\text{D.1.11})$$

and

$$\frac{d^2 S^{(1)}}{dl^2}(l_1) = 0, \quad \frac{d^2 S^{(N)}}{dl^2}(l_{N+1}) = 0, \quad (\text{D.1.12})$$

The clamped-end conditions (D.1.11) and (D.1.12) exist for the axial coordinate z and radial coordinate r when a two dimensional surface embedded in three-dimensions is axisymmetric. The endpoints l_1 and l_{N+1} refer to the points of contact with the axis of symmetry with the curve parametrising the surface.

Three dimensional axisymmetric z -conditions

The first condition in (D.1.11) applied to equation (D.1.3) gives

$$c_1 = 0, \quad (\text{D.1.13})$$

while the second condition yields

$$c_{N+1} = 0. \quad (\text{D.1.14})$$

Three dimensional axisymmetric r -conditions

For the conditions in (D.1.12), the first, applied to equation (D.1.4) gives

$$0 = 2b_1 = b_1 h_1^2 = 3(y_2 - y_1) - c_2 h_1 - 2c_1 h_1,$$

where we have used the equation (D.1.6). This means that

$$c_1 = \frac{1}{2h_1} [3(y_2 - y_1) - c_2 h_1]. \quad (\text{D.1.15})$$

The second condition gives

$$\begin{aligned} 0 &= 2b_N + 6a_N h_N = b_N h_N^2 + 3a_N h_N^3 \\ &= -12(y_{N+1} - y_N) + 6c_{N+1} h_N + 6c_N h_N + 6(y_{N+1} - y_N) - 2c_{N+1} h_N - 4c_N h_N, \end{aligned}$$

where we have used (D.1.5) and (D.1.6). So we have

$$c_{N+1} = \frac{1}{2h_N} [3(y_{N+1} - y_N) - c_N h_N]. \quad (\text{D.1.16})$$

D.2 Quintic Splines

For convenience, change the notation for the polynomial coefficients from

$\{a_5^{(j)}, a_4^{(j)}, a_3^{(j)}, a_2^{(j)}, a_1^{(j)}\}$ to $\{a_j, b_j, c_j, d_j, e_j\}$. Quintic splines are then given by

$$\begin{aligned} S^{(j-1)}(l) &= y_{j-1} + e_{j-1}(l - l_{j-1}) + d_{j-1}(l - l_{j-1})^2 + c_{j-1}(l - l_{j-1})^3 \\ &\quad + b_{j-1}(l - l_{j-1})^4 + a_{j-1}(l - l_{j-1})^5, \end{aligned} \quad (\text{D.2.1})$$

for $j = 2, \dots, N$.

D.2.1 Continuity at Interior Nodes

We rewrite the spline continuity equations (D.0.6), (D.0.7), and (D.0.8) in the form of (D.2.1). As such, we have the equations

$$y_{j-1} + e_{j-1}h_{j-1} + d_{j-1}h_{j-1}^2 + c_{j-1}h_{j-1}^3 + b_{j-1}h_{j-1}^4 + a_{j-1}h_{j-1}^5 = y_j, \quad (\text{D.2.2})$$

for continuity of position with $j = 2, \dots, N + 1$,

$$e_{j-1} + 2d_{j-1}h_{j-1} + 3c_{j-1}h_{j-1}^2 + 4b_{j-1}h_{j-1}^3 + 5a_{j-1}h_{j-1}^4 = e_j, \quad (\text{D.2.3})$$

for continuity of the first derivative with $j = 2, \dots, N$,

$$2d_{j-1} + 6c_{j-1}h_{j-1} + 12b_{j-1}h_{j-1}^2 + 20a_{j-1}h_{j-1}^3 = 2d_j, \quad (\text{D.2.4})$$

for continuity of the second derivative with $j = 2, \dots, N$,

$$6c_{j-1} + 24b_{j-1}h_{j-1} + 60a_{j-1}h_{j-1}^2 = 6c_j, \quad (\text{D.2.5})$$

for continuity of the third derivative with $j = 2, \dots, N$, and

$$24b_{j-1} + 120a_{j-1}h_{j-1} = 24b_j, \quad (\text{D.2.6})$$

for continuity of the fourth derivative with $j = 2, \dots, N$.

D.2.2 Generating the Matrix Equations

Introduce a ‘ghost’ interval $l_{N+1} \leq l \leq l_{N+2}$ so that the continuity equations (D.2.3 - D.2.6) holds for $j = 2, \dots, N + 1$. Solving the system of equations (D.2.2 - D.2.4) for a_{j-1} , b_{j-1} and c_{j-1} gives

$$a_{j-1}h_{j-1}^5 = 6(y_j - y_{j-1}) - 3e_jh_{j-1} - 3e_{j-1}h_{j-1} + d_jh_{j-1}^2 - d_{j-1}h_{j-1}^2, \quad (\text{D.2.7})$$

and

$$b_{j-1}h_{j-1}^4 = -15(y_j - y_{j-1}) + 7e_jh_{j-1} + 8e_{j-1}h_{j-1} - 2d_jh_{j-1}^2 + 3d_{j-1}h_{j-1}^2, \quad (\text{D.2.8})$$

and

$$c_{j-1}h_{j-1}^3 = 10(y_j - y_{j-1}) - 4e_jh_{j-1} - 6e_{j-1}h_{j-1} + d_jh_{j-1}^2 - 3d_{j-1}h_{j-1}^2, \quad (\text{D.2.9})$$

for $j = 2, \dots, N + 1$. These equations will be substituted into the equations for continuity of the third and fourth derivatives, respectively (D.2.5) and (D.2.6), to

generate two simultaneous matrix equations which, together with end conditions, can be solved for e_j and d_j , $j = 2, \dots, N$.

Substituting (D.2.7 - D.2.9) into the equation of continuity for the third derivative (D.2.5) yields

$$\begin{aligned} e_{j-1}[-4h_{j-1}\lambda_{j-1}^3] + e_j[-6h_{j-1}\lambda_{j-1}^3 + 6h_j] + e_{j+1}[4h_j] \\ + d_{j-1}[-h_{j-1}^2\lambda_{j-1}^3] + d_j[3h_{j-1}^2\lambda_{j-1}^3 + 3h_j^2] + d_{j+1}[-h_j^2] \\ = y_{j-1}[10\lambda_{j-1}^3] + y_j[-10\lambda_{j-1}^3 - 10] + y_{j+1}[10], \end{aligned} \quad (\text{D.2.10})$$

for $j = 2, \dots, N + 1$. In matrix form this is

$$\underline{\underline{\mathbf{D}}}^{(1)} \cdot \underline{\mathbf{d}} + \underline{\underline{\mathbf{e}}}^{(1)} \cdot \underline{\mathbf{e}} = \underline{\mathbf{p}}^{(1)} + \underline{\hat{\mathbf{d}}}^{(1)} + \underline{\hat{\mathbf{e}}}^{(1)}, \quad (\text{D.2.11})$$

where the matrices are

$$\underline{\underline{\mathbf{D}}}^{(1)}_{i,j} = \begin{cases} -\lambda_{j-1}^3 h_{j-1}^2 & , j = i - 1 \text{ and } j \neq 2 \\ 3\lambda_{j-1}^3 h_{j-1}^2 + 3h_j^2 & , j = i \\ -h_j^2 & , j = i + 1 \text{ and } j \neq N \\ 0 & , \text{ otherwise,} \end{cases} \quad (\text{D.2.12})$$

and

$$\underline{\underline{\mathbf{e}}}^{(1)}_{i,j} = \begin{cases} -4\lambda_{j-1}^3 h_{j-1} & , j = i - 1 \text{ and } j \neq 2 \\ -6\lambda_{j-1}^3 h_{j-1} + 6h_j & , j = i \\ 4h_j & , j = i + 1 \text{ and } j \neq N \\ 0 & , \text{ otherwise,} \end{cases} \quad (\text{D.2.13})$$

for $i = 2, \dots, N$,

$$\underline{\mathbf{p}}_j^{(1)} = \{10\lambda_{j-1}^3 y_{j-1} - 10(\lambda_{j-1}^3 + 1)y_j + 10y_{j+1}, \quad j = 2, \dots, N. \quad (\text{D.2.14})$$

and $\underline{\mathbf{d}} = (d_2, d_3, \dots, d_{N-1}, d_N)$, $\underline{\mathbf{e}} = (e_2, e_3, \dots, e_{N-1}, e_N)$,

$\underline{\hat{\mathbf{d}}}^{(1)} = (\lambda_1^3 h_1^2 d_1, 0, \dots, 0, h_N^2 d_{N+1})$, $\underline{\hat{\mathbf{e}}}^{(1)} = (4\lambda_1^3 h_1 e_1, 0, \dots, 0, -h_N e_{N+1})$.

Turning to the second matrix equation, substituting (D.2.7 - D.2.9) into the equation of continuity for the fourth derivative (D.2.6) yields

$$\begin{aligned} e_{j-1}[-7\lambda_{j-1}^4 h_{j-1}] + e_j[-8\lambda_{j-1}^4 h_{j-1} - 8h_j] + e_{j+1}[-7h_j] \\ + d_{j-1}[-2\lambda_{j-1}^4 h_{j-1}^2] + d_j[3\lambda_{j-1}^4 h_{j-1}^2 - 3h_j^2] + d_{j+1}[2h_j^2] \\ = y_{j-1}[15\lambda_{j-1}^4] + y_j[-15\lambda_{j-1}^4 + 15] + y_{j+1}[-15], \end{aligned} \quad (\text{D.2.15})$$

for $j = 2, \dots, N + 1$. In matrix form this is

$$\underline{\underline{\mathbf{D}}}^{(2)} \cdot \underline{\mathbf{d}} + \underline{\underline{\mathbf{e}}}^{(2)} \cdot \underline{\mathbf{e}} = \underline{\mathbf{p}}^{(2)} + \hat{\underline{\mathbf{d}}}^{(2)} + \hat{\underline{\mathbf{e}}}^{(2)}, \quad (\text{D.2.16})$$

where the matrices are

$$\underline{\underline{\mathbf{D}}}_{i,j}^{(2)} = \begin{cases} -2\lambda_{j-1}^4 h_{j-1}^2 & , j = i - 1 \text{ and } j \neq 2 \\ 3\lambda_{j-1}^4 h_{j-1}^2 - 3h_j^2 & , j = i \\ 2h_j^2 & , j = i + 1 \text{ and } j \neq N \\ 0 & , \text{ otherwise,} \end{cases} \quad (\text{D.2.17})$$

and

$$\underline{\underline{\mathbf{e}}}_{i,j}^{(2)} = \begin{cases} -7\lambda_{j-1}^4 h_{j-1} & , j = i - 1 \text{ and } j \neq 2 \\ -8\lambda_{j-1}^4 h_{j-1} - 8h_j + 6h_j & , j = i \\ -7h_j & , j = i + 1 \text{ and } j \neq N \\ 0 & , \text{ otherwise,} \end{cases} \quad (\text{D.2.18})$$

for $i = 2, \dots, N$,

$$\underline{\mathbf{p}}_j^{(1)} = \{15\lambda_{j-1}^4 y_{j-1} - 15(\lambda_{j-1}^3 - 1)y_j - 15y_{j+1}, \quad j = 2, \dots, N, \quad (\text{D.2.19})$$

and $\hat{\underline{\mathbf{d}}}^{(1)} = (2\lambda_1^4 h_1^2 d_1, 0, \dots, 0, -2h_N^2 d_{N+1})$, $\hat{\underline{\mathbf{e}}}^{(1)} = (7\lambda_1^4 h_1 e_1, 0, \dots, 0, 7h_N e_{N+1})$. The matrix system (D.2.11, D.2.16) can be solved for e_j, d_j for $j = 2, \dots, N$ after the imposition of end conditions that uniquely determine the values of $d_1, d_{N+1}, e_1, e_{N+1}$. Then equations (D.2.7 - D.2.9) can be used to solve for the remaining spline coefficients.

D.2.3 End Conditions

Consider the end conditions

$$\frac{dS^{(1)}}{dl}(l_1) = 0, \quad \frac{d^3 S^{(1)}}{dl^3}(l_1) = 0, \quad \frac{dS^{(N)}}{dl}(l_{N+1}) = 0, \quad \frac{d^3 S^{(N)}}{dl^3}(l_{N+1}) = 0, \quad (\text{D.2.20})$$

and

$$\frac{d^2 S^{(1)}}{dl^2}(l_1) = 0, \quad \frac{d^4 S^{(1)}}{dl^4}(l_1) = 0, \quad \frac{d^2 S^{(N)}}{dl^2}(l_{N+1}) = 0, \quad \frac{d^4 S^{(N)}}{dl^4}(l_{N+1}) = 0, \quad (\text{D.2.21})$$

and

$$\frac{dS^{(1)}}{dl}(l_1) = 0, \quad \frac{d^3 S^{(1)}}{dl^3}(l_1) = 0, \quad \frac{dS^{(N)}}{dl}(l_{N+1}) = 0, \quad \frac{d^2 S^{(N)}}{dl^2}(l_{N+1}) = 0, \quad (\text{D.2.22})$$

and

$$\frac{d^2 S^{(1)}}{dl^2}(l_1) = 0, \quad \frac{d^4 S^{(1)}}{dl^4}(l_1) = 0, \quad \frac{dS^{(N)}}{dl}(l_{N+1}) = -1, \quad \frac{d^2 S^{(N)}}{dl^2}(l_{N+1}) = 0. \quad (\text{D.2.23})$$

Conditions (D.2.20) and (D.2.21) exist for the axial coordinate z and radial coordinate r respectively, when a two dimensional surface embedded in three-dimensions is axisymmetric and intersects the axis of symmetry. The endpoints l_1 and l_{N+1} refer to the points of contact of the axis of symmetry with the curve parametrising the surface. Conditions (D.2.22) and (D.2.23) exist for the axial and radial coordinates z and r , respectively, for the case when the endpoint l_1 is in contact with the axis of symmetry, but the endpoint l_{N+1} is where the fluid boundary begins to be described by linear elements.

Three dimensional axisymmetric z -conditions

Consider the conditions in (D.2.20). The first condition when applied to equation (D.2.3) gives

$$e_1 = 0, \quad (\text{D.2.24})$$

while second condition yields

$$d_1 = \frac{1}{3h_1^2} [10(y_2 - y_1) - 4e_2 h_1 + d_2 h_1^2]. \quad (\text{D.2.25})$$

The third condition applied to equation (D.2.5) gives

$$e_{N+1} = 0, \quad (\text{D.2.26})$$

and the fourth condition gives

$$d_{N+1} = \frac{1}{3h_N^2} [-10(y_{N+1} - y_N) + 4e_N h_N + d_N h_N^2]. \quad (\text{D.2.27})$$

Three dimensional axisymmetric r -conditions

Consider the conditions in (D.2.21). The first condition when applied to equation (D.2.4) gives

$$d_1 = 0, \quad (\text{D.2.28})$$

while the second condition yields

$$e_1 = \frac{1}{8h_1} [15(y_2 - y_1) - 7e_2 h_1 + 2d_2 h_1^2]. \quad (\text{D.2.29})$$

The third condition applied to equation (D.2.6) gives

$$d_{N+1} = 0, \quad (\text{D.2.30})$$

and the fourth condition gives

$$e_{N+1} = \frac{1}{8h_N} [15(y_{N+1} - y_N) - 7e_N h_N - 2d_N h_N^2]. \quad (\text{D.2.31})$$

Three dimensional axisymmetric z -conditions with linear boundary

Consider the conditions in (D.2.22). The first two conditions are the same as in (D.2.20), so the same coefficient values hold, that is, (D.2.24) and (D.2.25),

$$e_1 = 0 \quad \text{and} \quad d_1 = \frac{1}{3h_1^2} [10(y_2 - y_1) - 4e_2 h_1 + d_2 h_1^2].$$

The third condition yields

$$e_{N+1} = -1, \quad (\text{D.2.32})$$

while the fourth condition gives

$$d_{N+1} = 0. \quad (\text{D.2.33})$$

Three dimensional axisymmetric r -conditions with linear boundary

Consider the conditions in (D.2.23). The first two conditions are the same as in (D.2.21), so the same coefficient values hold, that is, (D.2.29) and (D.2.28),

$$e_1 = \frac{1}{8h_1} [15(y_2 - y_1) - 7e_2 h_1 + 2d_2 h_1^2] \quad \text{and} \quad d_1 = 0.$$

The third condition yields

$$e_{N+1} = 0, \quad (\text{D.2.34})$$

while the fourth condition gives

$$d_{N+1} = 0. \quad (\text{D.2.35})$$

Appendix E

Populating the Matrices for the Discretised Boundary Integral Equation

This appendix focuses on populating the matrices $\underline{\underline{\mathbf{H}}}$ and $\underline{\underline{\mathbf{K}}}$ from the discrete boundary integral equation (4.5.20), and is the same process outlined in [131], provided here for the convenience of the reader. Every element of these matrices contains two surface integrals (except the first and last columns that contain just one).

When the singularity point is *not* adjacent to the elements being integrated over, standard Gauss-Legendre quadrature is used to approximate the integrals as they are non-singular. When the singularity point lies at a node adjacent to an element that is being integrated over, the complete elliptic integral $K(m)$ (approximated in equation 4.5.17) exhibits a logarithmic singularity as the integration variable approaches the singularity point. As $K(m)$ is a term in both axisymmetric integration kernels h and k (see equations 4.3.4)-(4.3.5), this singularity affects both matrices $\underline{\underline{\mathbf{H}}}$ and $\underline{\underline{\mathbf{K}}}$ and must be treated with care. Fortunately, this singularity still allows integration of these functions over boundary elements through the use of a specialist logarithmic Gauss-Legendre quadrature [196].

Consider the p -th element (bounded between nodes p and $p + 1$) for $p = 1, \dots, N$, we will now discuss how the surface integrals over this element are approximated when the singularity point $\underline{\mathbf{x}}_i$ is positioned at a node *away* from this element (that is, $i \notin \{p, p + 1\}$), and when it lies on a node at either end of the element (that is,

$i \in \{p, p + 1\}$). Before continuing, let f (known as the ‘shape function’) be given by

$$f(l) = \frac{s(l) - s_p}{s_{p+1} - s_p} \quad \text{or} \quad f(l) = \frac{s_{p+1} - s(l)}{s_{p+1} - s_p}, \quad (\text{E.0.1})$$

where the particular choice of f depends on which integral within a matrix element is being computed (see (4.5.24)-(4.5.25) and notice both forms of f).

Non-Singular Integrals, $i \notin \{p, p + 1\}$

When the singularity point $\underline{\mathbf{x}}_i$ is *not* located at either endpoint of the element, the integrands in (4.5.24) and (4.5.25) are non-singular and standard Gauss-Legendre quadrature can be used to approximate the surface integrals. To this end, introduce the local intrinsic coordinate $-1 \leq \eta \leq 1$ such that $\eta = -1$ for $l = l_p$, and $\eta = 1$ for $l = l_{p+1}$. Suppose that the spline parameter l depends monotonically on this coordinate, that is,

$$l(\eta) = l_p \left(\frac{1 - \eta}{2} \right) + l_{p+1} \left(\frac{1 + \eta}{2} \right). \quad (\text{E.0.2})$$

Integrals over the spline parameter l can then be changed to integrals over the intrinsic coordinate η , with

$$\int_{l_p}^{l_{p+1}} f(l) h(\underline{\mathbf{x}}_i, l) J(l) dl = \left(\frac{l_{p+1} - l_p}{2} \right) \int_{-1}^1 f(\eta) h(\underline{\mathbf{x}}_i, \eta) J(\eta) d\eta, \quad (\text{E.0.3})$$

and

$$\int_{l_p}^{l_{p+1}} f(l) k(\underline{\mathbf{x}}_i, l) J(l) dl = \left(\frac{l_{p+1} - l_p}{2} \right) \int_{-1}^1 f(\eta) k(\underline{\mathbf{x}}_i, \eta) J(\eta) d\eta. \quad (\text{E.0.4})$$

Then, standard Gauss-Legendre quadrature gives the approximation

$$\int_{l_p}^{l_{p+1}} f(l) h(\underline{\mathbf{x}}_i, l) J(l) dl \approx \sum_{\chi=1}^{M+1} w_\chi f(\eta_\chi) h(\underline{\mathbf{x}}_i, \eta_\chi) J(\eta_\chi), \quad (\text{E.0.5})$$

and

$$\int_{l_p}^{l_{p+1}} f(l) k(\underline{\mathbf{x}}_i, l) J(l) dl \approx \sum_{\chi=1}^{M+1} w_\chi f(\eta_\chi) k(\underline{\mathbf{x}}_i, \eta_\chi) J(\eta_\chi), \quad (\text{E.0.6})$$

for standard Gaussian weights w_χ and abscissae η_χ .

Singular Integrals, $i \in \{p, p + 1\}$

When the singularity point $\underline{\mathbf{x}}_i$ lies at either endpoint of the element, the integrand of a surface integral over that element exhibits a logarithmic singularity due to the presence of $K(m)$ that occurs as the integration point approaches $\underline{\mathbf{x}}_i$. To compute the

value of such an integral and avoid the (weak) singularity, notice that the complete elliptic integral $K(m)$ can be decomposed into

$$\begin{aligned} K(m) &\approx A_c(1-m) + B_c(1-m)\ln(1-m) \\ &= [A_c(1-m) + B_c(1-m)\ln(A)] - B_c(1-m)\ln(B). \end{aligned} \quad (\text{E.0.7})$$

Recall the definitions of A and B from (4.3.6). For field variable $\underline{\xi} = (R, Z) \in \bar{\Gamma}_p$, we have that as $\underline{\xi} \rightarrow \underline{x}_i$,

$$\begin{aligned} A &= (r_i + R)^2 + (z_i - Z)^2 \rightarrow 4r_i^2, \quad \text{and} \\ B &= (r_i - R)^2 + (z_i - Z)^2 \rightarrow 0, \end{aligned} \quad (\text{E.0.8})$$

and so $\ln(A)$ converges to a finite value, while $\ln(B)$ diverges. Looking back at (E.0.7), we have therefore segmented the singular component of $K(m)$ (the term containing $\ln(1-m)$) and we now have non-singular (the term within the square brackets), and singular parts (the remaining term). If $r_i = 0$, then $A = B$ and no decomposition as in (E.0.7) is necessary as $\ln(1-m) \equiv \ln(A/B) \equiv \ln(1) = 0$ and so there is no singularity, and in fact such an integral can be approximated as if $i \notin \{p, p+1\}$. What follows is the treatment of the singularity (for $r_i \neq 0$), with highlighted differences depending on whether the singularity point lies at l_p or l_{p+1} .

Singular Integrals, $i = p$

When $i = p$, the singular logarithm in the decomposition in (E.0.7) can be further decomposed as [197]

$$\ln(B) = 2 \ln \left[B^{1/2} \left(\frac{l_{p+1} - l_p}{l - l_p} \right) \right] + 2 \ln \left[\frac{l - l_p}{l_{p+1} - l_p} \right], \quad (\text{E.0.9})$$

where the first term on the right hand side is non-singular and the final term *is* singular (as $l \rightarrow l_p$).

For surface integrals containing the kernel k , the integrals themselves may now be decomposed into non-singular ('regular') and singular parts, denoted \mathcal{K}_{reg} and \mathcal{K}_{sng} respectively, so that

$$\int_{l_p}^{l_{p+1}} f k J \, dl = \mathcal{K}_{\text{reg}} + \mathcal{K}_{\text{sng}}. \quad (\text{E.0.10})$$

Using the full decomposition of $K(m)$ (see equations E.0.7 and E.0.9) with the expression of k in terms of $K(m)$ (see equation 4.3.4), the non-singular component of

(E.0.10) is given by

$$\begin{aligned} \mathcal{K}_{\text{reg}} = & \frac{(l_{p+1} - l_p)}{2\pi} \int_{-1}^1 f \frac{r_i}{A^{1/2}} [A_c(1 - m) \\ & + B_c(1 - m) \left\{ \ln(A) - 2 \ln \left(\frac{2B^{1/2}}{1 + \eta} \right) \right\}] J d\eta, \end{aligned} \quad (\text{E.0.11})$$

with intrinsic coordinate $-1 \leq \eta \leq 1$ such that

$$l(\eta) = l_p \left(\frac{1 - \eta}{2} \right) + l_{p+1} \left(\frac{1 + \eta}{2} \right).$$

Given \mathcal{K}_{reg} is non-singular, it can be numerically approximated using standard Gauss-Legendre quadrature as described earlier for $i \notin \{p, p + 1\}$. For the singular component, we again use the full decomposition of $K(m)$, this time to obtain

$$\mathcal{K}_{\text{sng}} = \frac{2(l_{p+1} - l_p)}{\pi} \int_0^1 f \frac{r_i}{A^{1/2}} B_c(1 - m) J \ln \left(\frac{1}{\hat{\eta}} \right) d\hat{\eta}, \quad (\text{E.0.12})$$

with intrinsic coordinate $0 \leq \hat{\eta} \leq 1$ such that

$$l(\hat{\eta}) = l_p(1 - \hat{\eta}) + l_{p+1}\hat{\eta}. \quad (\text{E.0.13})$$

The particular form of the singularity within the integrand of (E.0.12) is integrable, and we use a specialised Gaussian quadrature to approximate it. This approximation states that,

$$\int_0^1 f \frac{r_i}{A^{1/2}} B_c(1 - m) J \ln \left(\frac{1}{\hat{\eta}} \right) d\hat{\eta} \approx \sum_{\chi=1}^{M+1} \hat{w}_\chi f(\hat{\eta}_\chi) \frac{r_i}{A^{1/2}(\hat{\eta}_\chi)} B_c(1 - m(\hat{\eta}_\chi)) J(\hat{\eta}_\chi), \quad (\text{E.0.14})$$

where \hat{w}_χ and $\hat{\eta}_\chi$ represent the logarithmic-Gauss-Legendre weights and abscissae respectively as given in [196].

For surface integrals containing the kernel h , we similarly decompose these into nonsingular and singular parts (as was done in equation E.0.10). In this case,

$$\int_{l_p}^{l_{p+1}} f h J dl = \mathcal{H}_{\text{reg}} + \mathcal{H}_{\text{sng}}, \quad (\text{E.0.15})$$

for non-singular component \mathcal{H}_{reg} and singular component \mathcal{H}_{sng} . For convenience, rewrite the kernel h (recall its form in equation 4.3.5) as

$$h = \bar{h} - \frac{n_r}{2\pi A^{1/2}} K(m), \quad (\text{E.0.16})$$

where \bar{h} represents the terms *not* multiplied by $K(m)$. The term \bar{h} is therefore non-singular whereas the final term *is* singular. The process of using the full decomposition of $K(m)$ and introducing intrinsic coordinates to find the integral expressions

of \mathcal{H}_{reg} and \mathcal{H}_{sng} is almost identical to finding \mathcal{K}_{reg} and \mathcal{K}_{sng} ; because the form of the kernel h in (E.0.16) is almost identical (in terms of experiencing a singularity) as k (see equation 4.3.4). We therefore forego presenting this process and show the formulated integrals as

$$\begin{aligned} \mathcal{H}_{\text{reg}} = \frac{(l_{p+1} - l_p)}{4} \int_{-1}^1 f \left\{ \bar{h} - \frac{n_r}{\pi A^{1/2}} [A_c(1 - m) \right. \\ \left. + B_c(1 - m) \left\{ \ln(A) - 2 \ln \left(\frac{2B^{1/2}}{1 + \eta} \right) \right\} \right\} J d\eta, \end{aligned} \quad (\text{E.0.17})$$

and

$$\mathcal{H}_{\text{sng}} = -\frac{(l_{j+1} - l_j)}{\pi} \int_0^1 f \frac{n_r}{A^{1/2}} B_c(1 - m) J \ln \left(\frac{1}{\hat{\eta}} \right) d\hat{\eta}. \quad (\text{E.0.18})$$

The quadrature used to approximate of \mathcal{H}_{reg} and \mathcal{H}_{sng} is the same as is used for \mathcal{K}_{reg} and \mathcal{K}_{sng} , respectively.

Singular Integrals, $i = p + 1$

For $i = p + 1$, we decompose the final term in (E.0.7) with

$$\ln(B) = 2 \ln \left[B^{1/2} \left(\frac{l_{p+1} - l_p}{l_{p+1} - l} \right) \right] + 2 \ln \left[\frac{l_{p+1} - l}{l_{p+1} - l_p} \right], \quad (\text{E.0.19})$$

where the first term on the right hand side is non-singular and the final *is* singular (as $l \rightarrow l_{p+1}$). Once again, we decompose our integrals into \mathcal{K}_{reg} , \mathcal{K}_{sng} , \mathcal{H}_{reg} , and \mathcal{H}_{sng} .

For the non-singular components, we use the following variable transformation:

$$l(\eta) = l_p \left(\frac{1 - \eta}{2} \right) + l_{p+1} \left(\frac{1 + \eta}{2} \right),$$

with $-1 \leq \eta \leq 1$, and using the same techniques as outline for $i = p$, we obtain

$$\begin{aligned} \mathcal{K}_{\text{reg}} = \frac{(l_{p+1} - l_p)}{2\pi} \int_{-1}^1 f \frac{r_i}{A^{1/2}} [A_c(1 - m) \\ + B_c(1 - m) \left\{ \ln(A) - 2 \ln \left(\frac{2B^{1/2}}{1 - \eta} \right) \right\}] J d\eta, \end{aligned} \quad (\text{E.0.20})$$

and

$$\begin{aligned} \mathcal{H}_{\text{reg}} = \frac{(l_{p+1} - l_p)}{4} \int_{-1}^1 f \left\{ \bar{h} - \frac{n_r}{\pi A^{1/2}} [A_c(1 - m) \right. \\ \left. + B_c(1 - m) \left\{ \ln(A) - 2 \ln \left(\frac{2B^{1/2}}{1 - \eta} \right) \right\} \right\} J d\eta. \end{aligned} \quad (\text{E.0.21})$$

For the singular components, we use the following alternative variable transformation:

$$l(\hat{\eta}) = l_p \hat{\eta} + l_{p+1}(1 - \hat{\eta}), \quad (\text{E.0.22})$$

with $0 \leq \hat{\eta} \leq 1$, and again using techniques from the case of $i = p$, we obtain

$$\mathcal{K}_{\text{sng}} = -\frac{2(l_{p+1} - l_p)}{\pi} \int_0^1 f \frac{r_i}{A^{1/2}} B_c(1 - m) J \ln \left(\frac{1}{\hat{\eta}} \right) d\hat{\eta}, \quad (\text{E.0.23})$$

and

$$\mathcal{H}_{\text{sng}} = \frac{(l_{p+1} - l_p)}{\pi} \int_0^1 f \frac{n_r}{A^{1/2}} B_c(1 - m) J \ln \left(\frac{1}{\hat{\eta}} \right) d\hat{\eta}. \quad (\text{E.0.24})$$

We are now able to fully populate the matrices $\underline{\mathbf{H}}$ and $\underline{\mathbf{K}}$, and are therefore able to solve the discretised boundary integral equation (4.5.20) for all missing values of ϕ_j and $(\partial\phi/\partial n)_j$, for $j = 1, \dots, N + 1$.